ARO 35913.1-PH-CF

TECHNICAL DIGEST
1996

DIFFRACTIVE OPTICS AND MICRO-OPTICS

APRIL 29–MAY 2, 1996
BOSTON, MASSACHUSETTS

1996 TECHNICAL DIGEST SERIES
VOLUME 5

19961025 042



SPONSORED AND MANAGED BY
OPTICAL SOCIETY OF AMERICA

DISTRIBUTION STATEMENT A
Approved for public release;
Distribution Unlimited

REPORT DOCUMENTATION PAGE

Form Approved
OMB NO. 0704-0188

Public reporting burden for this collection of information is estimated to average 1 hour per response, including the time for reviewing instructions, searching existing data sources, gathering and maintaining the data needed, and completing and reviewing the collection of information. Send comment regarding this burden estimates or any other aspect of this collection of information, including suggestions for reducing this burden, to Washington Headquarters Services, Directorate for information Operations and Reports, 1215 Jefferson Davis Highway, Suite 1204, Arlington, VA 22202-4302, and to the Office of Management and Budget, Paperwork Reduction Project (0704-0188), Washington, DC 20503.

1. AGENCY USE ONLY *(Leave blank)*	2. REPORT DATE	3. REPORT TYPE AND DATES COVERED
	Septemher 13, 1996	Final August 19, 1996 - Feb. 18, 1997

4. TITLE AND SUBTITLE
Organization of the 1996 Diffractive Optics and Micro Optics Topical Meeting

5. FUNDING NUMBERS
DAAH04-96-1-0435

6. AUTHOR(S)
David W. Hennage

7. PERFORMING ORGANIZATION NAMES(S) AND ADDRESS(ES)
Optical Society of America
2010 Massachusetts Ave. NW
Washington, DC 20036

8. PERFORMING ORGANIZATION REPORT NUMBER

9. SPONSORING / MONITORING AGENCY NAME(S) AND ADDRESS(ES)
U.S. Army Research Office
P.O. Box 12211
Research Triangle Park, NC 27709-2211

10. SPONSORING / MONITORING AGENCY REPORT NUMBER
ARO 35913.1-PH-CF

11. SUPPLEMENTARY NOTES
The views, opinions and/or findings contained in this report are those of the author(s) and should not be construed as an official Department of the Army position, policy or decision, unless so designated by other documentation.

12a. DISTRIBUTION / AVAILABILITY STATEMENT
Approved for public release; distribution unlimited.

12 b. DISTRIBUTION CODE

13. ABSTRACT *(Maximum 200 words)*

The Diffractive Optics and Micro Optics Topical Meeting brought together scientists and engineeres of various backgrounds to discuss new developments in the various aspects of diffractive and refractive micro-optics. These included modeling and deisgn, fabrication and replication technology, and applications and products.

14. SUBJECT TERMS	15. NUMBER IF PAGES
	16. PRICE CODE

17. SECURITY CLASSIFICATION OR REPORT	18. SECURITY CLASSIFICATION OF THIS PAGE	19. SECURITY CLASSIFICATION OF ABSTRACT	20. LIMITATION OF ABSTRACT
UNCLASSIFIED	UNCLASSIFIED	UNCLASSIFIED	UL

CONFERENCE EDITION

Summaries of the papers

presented at the topical meeting

DIFFRACTIVE OPTICS AND MICRO-OPTICS

APRIL 29–MAY 2, 1996
BOSTON, MASSACHUSETTS

1996 TECHNICAL DIGEST SERIES
VOLUME 5



SPONSORED AND MANAGED BY
OPTICAL SOCIETY OF AMERICA

Optical Society of America
2010 Massachusetts Avenue NWS
Washington DC 20011-1023

DTIC QUALITY INSPECTED 3

Articles in this publication may be cited in other publications. To facilitate access to the original publication source, the following form for the citation is suggested:

Name of Author(s), "Title of Paper," in *Diffractive Optics and Micro-Optics*, Vol. 5, 1996 OSA Technical Digest Series (Optical Society of America, Washington DC, 1996), pp. xx-xx.

Optical Society of America

ISBN

Conference Edition	1-55752-432-7
Postconference Edition	1-55752-433-5
(Note: Postconference Edition includes postdeadline papers.)	
1996 Technical Digest Series	1-55752-417-3

Library of Congress Catalog Card Number

Conference Edition	95-72752
Postconference Edition	95-72753

Copyright © 1996, Optical Society of America

Individual readers of this digest and libraries acting for them are permitted to make fair use of the material in it, such as to copy an article for use in teaching or research, without payment of fee, provided that such copies are not sold. Copying for sale is subject to payment of copying fees. The code 1-55752-417-3/96/$6.00 gives the per-article copying fee for each copy of the article made beyond the free copying permitted under Sections 107 and 108 of the U.S. Copyright Law. The fee should be paid through the Copyright Clearance Center, Inc., 21 Congress Street, Salem, MA 01970.

Permission is granted to quote excerpts from articles in this digest in scientific works with the customary acknowledgment of the source, including the author's name and the name of the digest, page, year, and name of the Society. Reproduction of figures and tables is likewise permitted in other articles and books provided that the same information is printed with them and notification is given to the Optical Society of America. In addition, the Optical Society may require that permission also be obtained from one of the authors. Address inquiries and notices to Director of Publications, Optical Society of America, 2010 Massachusetts Avenue, NW, Washington, DC 20036-1023. In the case of articles whose authors are employees of the United States Government or its contractors or grantees, the Optical Society of America recognizes the right of the United States Government to retain a nonexclusive, royalty free license to use the author's copyrighted article for United States Government purposes.

Printed in the U.S.A.

Contents

Agenda of Sessions v
DMA Electromagnetic Theory 1
DMB Micro-Optics Fabrication 23
JMC Joint Session on Diffractive and Micro-Optics and Holography I 43
DMD Optical Interconnects 63
DTuA Applications I 83
JTuB Poster Previews 103
JTuC Joint Session on Diffractive and Micro-Optics and Holography II 207
DTuD Scalar Design 227
DWA Subwavelength Structures 245
DWB Micro-Optics Applications 265
DWC Testing and Evaluation 287
DWD Fabrication 309
DThA Replication Techniques 333
DThB Applications II 351
Key to Authors and Presiders 373

DIFFRACTIVE OPTICS AND MICRO-OPTICS TECHNICAL PROGRAM COMMITTEE

M.G. Moharam, *University of Minnesota, General Chair*

Jurgen Jahns, *University of Hagen, Germany, Program Chair*

J. Allen Cox, *Honeywell Technology Center, Program Chair*

Bernard V. Braunecker, *Leica AG, Switzerland*

Dale Buralli, *Sinclair Optics*

Thomas K. Gaylord, *Georgia Institute of Technology*

Michael J. Hayford, *Optical Research Associates*

H. Peter Herzig, *University of Neuchatel, Switzerland*

Michael Hutely, *National Physics Laboratory, UK*

Raymond K. Kostuk, *University of Arizona*

James Leger, *University of Minnesota*

Joseph Mait, *Army Research Laboratories*

Keith O. Mersereau, *AT&T Bell Laboratories*

G. Michael Morris, *University of Rochester*

M. Oikawa, *Nippon Sheet Glass, Japan*

SUNDAY
APRIL 28, 1996

3rd FLOOR REGISTRATION AREA
6:30pm-8:30pm
Registration

MONDAY
APRIL 29, 1996

3rd FLOOR REGISTRATION AREA
7:00am-5:30pm
Registration

GARDNER A&B

8:30–10:00am
DMA • Electromagnetic Theory
M. G. Moharam, *University of Central Florida, Presider*

8:30am (Invited)
DMA1 • Electromagnetic theory of X-ray gratings, M. Neviere, *U.R.A. CNRS, France.* The electromagnetic theory of bare metallic gratings, multilayer coated gratings, and Bragg-Fresnel gratings for soft x-ray is presented, as well as its extension to nonperiodic focusing elements like Bragg Fresnel zone plates. **(p. 2)**

9:00am
DMA2 • Optimal design of low-order diffractive structures, David C. Dobson, *Texas A&M Univ.*; J. Allen Cox, *Honeywell Technology Center.* Two new approaches to optimal design of low-order diffractive structures based on the Helmholtz equation are presented. One using a solid foundation for effective medium theory introduces completely new structures; the other admits more practical discrete structures. **(p. 5)**

9:15am
DMA3 • Boundary element method for analysis and design of one-dimensional diffractive optical elements, Dennis W. Prather, Joseph N. Mait, *U.S.Army Research Laboratory*; Mark S. Mirotznik, *Catholic Univ. America.* We present results on the application of the boundary element method to analyze the vector diffraction from finite, a periodic diffractive elements. We validate our implementation for both dielectrics and perfect conductors comparison with analytic techniques. **(p. 9)**

9:30am
DMA4 • Highly improved convergence of the coupled-wave method for TM polarization and conical mountings, Philippe Lalanne, *CNRS, France*; G. Michael Morris, *Univ. Rochester.* By reformulating the eigen-problem of the coupled-wave method for TM polarization and conical mounts, we demonstrate highly improved convergence rates for metallic and dielectric gratings. **(p. 15)**

9:45am
DMA5 • Mathematical justification for the recent improvement of the modal method by Fourier expansion, Lifeng Li, *Univ. Arizona.* Recently the convergence of the modal method by Fourier expansion for metallic gratings in TM polarization was dramatically improved. This empirically discovered result is given a rigorous mathematical justification. **(p. 19)**

INDEPENDENCE BALLROOM
10:00–10:30am
Coffee Break

GARDNER A&B

10:30am–12:00m
DMB • Micro-Optics Fabrication
Jurgen Jahns, *University of Hagen, Germany, Presider*

10:30am (Invited)
DMB1 • Aberration corrected etched microlens arrays, Keith Mersereau, Casimir R. Nijander, Wesley P. Townsend, Avi Y. Feldblum, *AT&T Bell Laboratories.* Refractive microlens arrays are made in fused silica through reactive ion etching. Aberration is reduced by controlling the relative etch rates of silica and photoresist. **(p. 24)**

11:00am
DMB2 • Microlens arrays formed by crossed thin-film deposition of cylindrical microlenses, R. Grunwald, R. Ehlert, S. Woggon, H.-J. Patzold, H.-H. Witzmann, *GOS, Germany.* Microlens arrays with high fill factors for laser beam shaping and image processing are produced by crossed thin-film deposition through silt mask arrays. **(p. 27)**

11:15am
DMB3 • Single step fabrication of glass microlenses for array and diode laser applications, Neil Fromer, Nabil M. Lawandy, *Brown Univ.* By use of a laser-driven thermal process in semiconductor-doped glasses, single microlenses of various shapes and sizes, as well as arrays, can be generated. **(p. 31)**

11:30am
DMB4 • Compact micro optical diode laser assembly using mass transported large-numerical aperture refractive microlenses, D.Z. Tsang, Z. L. Liau, J. N. Walpole, *MIT Lincoln Laboratory.* A mass-transported gallium phosphide microlens array has been directly attached to a laser/heatsink to form a compact assembly with a nearly diffraction-limited collimated output. **(p. 35)**

11:45am
DMB5 • Ion exchange in glass for the fabrication of continuous phase diffractive optical elements, Risto-Pekka Salmio, Jyrki Saarinen, Henri Saarikoski, *Helsinki Univ. Technology, Finland;*

Jari Turunen, *Univ. Joensuu, Finland*; Ari Tervonen, *Optonex Ltd., Finland.* High-efficiency diffractive elements produced by thermal ion exchange in glass and designed by fast numerical simulation of the ion exchange process are presented. **(p. 39)**

12:00m–1:30pm
Lunch on Own

GARDNER A&B

1:30pm-3:00pm
JMC • Joint Session on Diffractive and Micro-Optics and Holography I
Raymond Kostuk, *University of Arizona, Presider*

1:30pm (Invited)
JMC1 • Fabrication of micro-optics and diffractive lenses using analogue methods, M. C. Hutley, *National Physical Laboratory, UK.* We review mechanical and optical techniques for generating blazed diffracting components and consider how the lessons learned may be applied to current technological developments. **(p. 44)**

2:00pm
JMC2 • Laser-written diffraction gratings in quantum dot and island metal films, Yu. Kaganovskii, M. Rosenbluh, *Bar-Ilan Univ., Israel.* Pulsed laser interference diffraction gratings are written in thin films composed of quantum dots in glass and in thin metal island films. **(p. 48)**

2:15pm
JMC3 • High-efficiency transmission gratings fabricated in bulk fused silica, H. T. Nguyen, B. W. Shore, J. A. Britten, S. J. Bryan, S. Falabella, R. D. Boyd, M.D. Perry, *Lawrence Livermore National Laboratory.* We present the design and performance of high-efficiency transmission gratings fabricated in bulk fused silica for use in ultraviolet high-power laser systems. **(p. 52)**

2:30pm
JMC4 • Ultrahigh spatial-frequency, high-contrast periodic structures produced by interference lithography, H. T. Nguyen, J. A. Britten, R. D. Boyd, B. W. Shore, M. D. Perry, Lawrence Livermore National Laboratory. We develop a process to produce high-aspect ratio, high frequency periodic profiles recorded in a photoresist layer by interference lithography. **(p. 55)**

2:45pm
JMC5 • Diffractive diffusers at the fabrication limit, Hans Peter Herzig, Wolfgang Singer, *Institute of Microtechnology, Switzerland*; Eckhard Piper, Johannes Wangler, *Carl Zeiss, Germany.* The design and fabrication of diffractive elements, generating flattop intensity distributions for partial coherent lasers at short wavelengths, is presented. **(p. 59)**

INDEPENDENCE BALLROOM

3:00–3:30pm
Coffee Break

GARDNER A&B

3:30–5:00pm
DMD • Optical Interconnects
Keith Mersereau, *AT&T Bell Laboratories, Presider*

3:30pm (Invited)
DMD1 • Diffractive optics in free-space optoelectronic computing systems, Philippe J. Marchand, Frederick B. McCormick, Sadik C. Esener, *University of California, San Diego.* We discuss the design, optimization, and fabrication of the diffractive elements used in a particular free-space optical interconnection scheme: the Optical Transpose Interconnection System (OTIS). **(p. 64)**

4:00pm
DMD2 • Integration of diffractive optical elements with vertical-cavity surface-emitting lasers, M. E. Warren, T. C. Du, J.R. Wendt, G. A. Vawter, K. L. Lear, S. P. Kilcoyne, R. F. Carson, P. K. Seigal, M. Hagerott Crawford, H. Hou, R. P. Schneider, *Sandia National Laboratories.* Diffractive optics are integrated into the surfaces of vertical-cavity surface emitting arrays and on surfaces flipchip bonded to the arrays for various applications. **(p. 67)**

4:15pm
DMD3 • Diffractive spot-array generation using multimode surface emitting lasers and light emitting diodes, John S. Hoch, Joseph M. Kahn, *Univ. California-Berkeley*; Annette Grot, *Hewlett Packard Laboratories.* We discuss beam shaping of multimode surface-emitting lasers and light emitting diodes using diffractive spot-array generation. **(p. 71)**

4:30pm
DMD4 • 3 x 3 optoelectronic cross-bar switch using vertical-cavity surface- emitting laser arrays, N.Rajkumar, J. N. McMullin, B. P. Keyworth, R.I. MacDonald, *Telecommunication Research Labs, Canada.* The fabrication of a 3 x 3 optoelectronic switch that uses vertical cavity surface-emitting laser arrays is described. Optical signals, distributed by a dispensed polymer microlens and grating assembly, are detected and summed electrically by a 3 x 3 metal semiconductor-metal photodetector array to complete the cross-bar switch. **(p. 75)**

4:45pm
DMD5 • An extensible, diffractive optic system for interconnecting optoelectronic device arrays, Rick L. Morrison, *AT&T Bell Laboratories.* An extensible diffractive optical framework is proposed that combines dense spatial channel packing and long Gaussian relay lengths while achieving a reduced chromatic sensitivity. **(p. 79)**

INDEPENDENCE BALLROOM/BOYLSTON PARK CAFE

6:00–7:30pm
Conference Reception

3rd FLOOR REGISTRATION AREA

7:30am-5:30pm
Registration

GARDNER A&B

8:30–10:00am
DTuA • Applications I
Donald Sweeney, *Lawrence Livermore National Laboratory, Presider*

8:30am (Invited)
DTuA1 • The way of diffractive optics into the laser resonator, Heiko Schwarzer, Frank Wyrowski, *BIFO, Germany*. The effect of microstructured profiles on electromagnetic waves is the basic issue of diffractive optics. These profiles represent a significant extension of the possibilities to realize optical functions. Laser optics is of special importance for diffractive optics. In this paper examples of the use of diffractive elements outside and inside the laser resonator are given. Theoretical and experimental results are presented. **(p. 84)**

9:00am
DTuA2 • Diffractive optical element for chromatic confocal imaging, Sarah L. Dobson, Pang chen Sun, Yeshayahu Fainman, *Univ. California-San Diego*. A confocal microscope that uses a diffractive zone plate for wavelength-depth encoding and non-mechanical depth scanning is characterized and used for surface profile measurements. **(p. 86)**

9:15am
DTuA3 • Tunable diffractive optical filter for imaging applications, J. Allen Cox, Bernard S. Fritz, *Honeywell Technology Center*. We describe a new approach for a tunable, multi-spectral filter that uses diffractive elements suitable for high quality, wide FOV imaging, and out-of band rejection. The method admits both bandpass and notch rejection forms. **(p. 90)**

9:30am
DTuA4 • Diffractive optics technology for F-Theta scan lenses, Kevin J. McIntyre, G. Michael Morris, *Univ. Rochester*. Use of diffractive optics in F-Theta scan lens design allows for substantial improvements in system performance and size. **(p. 94)**

9:45am
DTuA5 • Optical design comparison of 60dg eyepieces, Wayne Knapp, Brian Volk, *Precision Optics Corp.*; Berge Tatian, *optical design specialist*; Gary Blough, Robert Michaels, *Rochester Photonics Corp.* A comparison of eyepieces, one with plastic aspherics and one with a diffractive optic, shows the improved chromatic aberration and MTF of the diffractive approach. **(p. 98)**

INDEPENDENCE BALLROOM

10:00am-10:30am
Coffee Break/Exhibits

COMMONWEALTH ROOM

10:30am–12:00m
JTuB • Poster Previews
G. Michael Morris, *University of Rochester and Rochester Photonics Corp., Presider*

10:30am
JTuB1a • Fabrication and experiment of a diffractive phase element that implements wavelength demultiplexing and focusing, Bizhen Dong, Guoqing Zhang, Guozhen Yang, Benyuan Gu, Shihai Zheng, Dehua Li, Yansong Chen, *Academia Sinica, China*. The design and fabrication of diffractive phase elements for wavelength demultiplexing and focusing are presented. Experimental results are in good coincidence with numerical simulations. **(p. 104)**

10:30am
JTuB1b • A new kind of diffractive phase element applied to wavelength demultiplexing and annular focusing, Benyuan Gu, Guoqing Zhang, Bizhen Dong, Guozhen Yang, *Academia Sinica, China*. A design of diffractive phase elements first applied to wavelength demultiplexing and annular focusing is presented. Numerical simulations are in good agreement with the desired performances. **(p. 108)**

10:32am
JTuB2 • Off-axis Talbot effect and array generation in planar optics, Markus Testorf, Jurgen Jahns, *Fern Univ. Hagen, Germany*; Nikolay A. Khilo, Andrey M. Goncharenko, *Belarussian Academy of Sciences*. The Talbot effect for oblique angles of light propagation is investigated. Experimental verifications and considerations on a planar integration of Talbot array illuminators are included. **(p. 112)**

10:34am
JTuB3 • Diffractive elements developed for uniform illumination in inertial confinement fusion, Qiu Yue, Fan Dianyuan, Deng Ximing, Chinese Academy of Sciences; Deng Xuegong, Li Yongpin, *China Univ. Science and Technology*. A type of diffractive element is designed and fabricated for uniform illumination in inertial confinement fusion. Experiment results are given. **(p. 116)**

10:36am
JTuB4 • Achromatization for multiple narrowband sources using hybrid multi-order diffractive lenses, Kevin J. McIntyre, G. Michael Morris, *Univ. Rochester*. Multiple refractive and diffractive lenses can be combined to form hybrid lenses suitable for systems with multiple narrowband sources. **(p. 119)**

10:38am
JTuB5 • Array generator design for an optical analog-to-digital converter, Joseph N. Mait, *U.S. Army Research Laboratory*; Barry L. Shoop, *U.S. Military Academy*. We present the design of an eight-level phase-only diffractive element that generates a 7 x 7 nonuniform array of spots. The array generator is used to implement error diffusion within an optical analog-to-digital converter. **(p. 123)**

10:40am
JTuB6 • Electric fields and Poynting vectors in dielectric gratings, Bruce W. Shore, Michael D. Feit, *Lawrence Livermore National Laboratory*; Lifeng Li, *Univ. Arizona*. We discuss and illustrate the use of electric field magnitudes, energy density, and Poynting vectors as tools for understanding phenomena associated with dielectric gratings. **(p. 126)**

10:42am
JTuB7 • Diffractive-refractive achromatic optical processor for white-light spatial filtering, P. Andres, *Univ. Valencia, Spain*; E. Tajahuerce, J. Lancis, V. Climent, M. Fernandez-Alonso, *Univ. Jaume I, Spain*. We present a novel diffractive-refractive achromatic optical processor, with very low residual chromatic aberrations, to perform white-light spatial-frequency filtering of color inputs. **(p. 128)**

10:44am
JTuB8 • Diffractive optical elements for tracking and receiving in optical space communication systems, P. Blattner, H. P. Herzig, K. J. Weible, *Univ. Neuchatel, Switzerland*. Different designs of a diffractive optical element used for tracking and receiving in laser communication terminal are presented. Elements based on these designs are realized and compared. **(p. 132)**

10:46am
JTuB9 • Scalar design of diffractive elements using direct and indirect optimization, Joseph N. Mait, *U.S. Army Research Laboratory*. We present a general procedure for the design of diffractive optical elements and use scalar diffraction theory to apply it to the design of three common diffractive elements. The procedure reveals that most common design techniques can be classified as either direct or indirect optimizations. **(p. 136)**

10:48am
JTuB10 • High efficiency dielectric reflection gratings, B. W. Shore, M. D. Perry, J. A. Britten, R. D. Boyd, M. D. Feit, H. Nguyen, R. Chow, G. Loomis, *Lawrence Livermore National Laboratory*; Lifeng Li, *Univ. Arizona*. We discuss the design and fabrication of all-dielectric reflection gratings that place theoretically 99% of the incident light into a single diffraction order. **(p. 140)**

10:50am
JTuB11 • Design of phase-shifting masks for enhanced-resolution optical lithography, Guo-Zhen Yang, Zhi-Yuan Li, Bi-Zhen Dong, Ben-Yuan Gu, Guo-Qing Zhang, *Academia Sinica, China*. An approach based on the general theory of amplitude-phase retrieval in optics is presented for the design of phase-shifting masks for enhanced-resolution optical lithography. **(p. 144)**

10:52am
JTuB12 • Flat-top beam generation using an iteratively designed binary phase grating, Jun Amako, Tomio Sonehara, *Seiko Epson Corp., Japan*. The grating phase, optimized by the simulated-annealing algorithm, produces in-phase diffracted waves that interfere constructively to form a uniform amplitude and phase profile in a Fourier domain. **(p. 148)**

10:54am
JTuB13 Surface-relief gratings with sharp edges: Improvement of the convergence of the coordinate transformation method, Lifeng Li, *Univ. Arizona*. The convergence of the coordinate transformation method of Chandezon et al. for surface-relief gratings with sharp edges is improved substantially with use of the correct Fourier factorization procedure. **(p. 151)**

10:56am
JTuB14 Liquid crystal phase modulation technique to reduce the spatial frequency of interferometric fringes, P. Douglas Knight Jr., *Univ. North Carolina-Charlotte*. A technique to reduce the spatial frequency of interferometric fringes is proposed with use of a spatial light modulator to perform phase modulation. **(p. 155)**

10:58am
JTuB15 Synthesis of fully continuous phase screens for tailoring the focal plane irradiance profiles, Sham Dixit, Mike Feit, *Lawrence Livermore National Laboratory*. We present an iterative procedure for constructing fully continuous phase screens for tailoring the focal plane intensity distributions. **(p. 159)**

11:00am
JTuB16 Fabrication of large aperture kinoform phase plates in fused silica for smoothing focal plane intensity profiles, Mike Rushford, Sham Dixit, Ian Thomas, Mike Perry, *Lawrence Livermore National Laboratory*. We have fabricated large aperture (40-cm) kinoform phase plates for producing super-Gaussian focal plane intensity profiles. **(p. 163)**

11:02am
JTuB17 Speckle-free phase Fresnel holograms and beam-shaping elements, Luiz Goncalves Neto, Yunlong Sheng, *Univ. Laval, Canada*. We describe optical speckle-free phase Fresnel holograms. We choose the constant initial phase for iterations, which can avoid the speckles caused by isolated point zeros in the reconstruction plane. **(p. 166)**

11:04am
JTuB18 High-efficiency fast diffractive lens for beam coupling, Yunlong Sheng, Dazeng Feng, *Univ. Laval, Canada*. Iterative simulated annealing is implemented in the design of a high-efficiency fast lens for focusing and shaping elliptical beams. The aberrations introduced in the design are evaluated. **(p. 170)**

11:06am
JTuB19 Effective medium theory of symmetric two-dimensional subwavelength periodic structures, Philippe Lalanne, *France*. We present the effective medium theory of two-dimensional symmetric periodic structures. Predictions are verified with rigorous computation. **(p. 174)**

11:08am
JTuB20 • Z-scan measurement in amorphous As2S3 thin film, Yeung Joon Sohn, Chong Hoon Kwak, Ok Shik Choe, *Yeungnam Univ., Korea*. The complex nonlinear refractive index is measured and analyzed in an amorphous As2S3 thin film by adaptation of the sensitive cw z-scan technique. **(p. 178)**

11:10am
JTuB21 • Simplified processing method of dichromated gelatin derived from Agfa 8E75HD plates, Yong Seok Im, Young Lak Lee, Chong Hoon Kwak, Ok Shik Choe, *Yeungnam Univ., Korea*; Sang Cheol Kim, *Samsung Aerospace Industries Ltd, Korea*. A simplified method to make dichromated gelatin hologram is presented. If one starts with Agfa 8E75HD plates, the complete processing time is just two hours and high diffraction efficiency of 81.5% is obtained. **(p. 182)**

11:12am
JTuB22 • Analysis of focal tolerance and fine pattern resolutions formed by phase conjugation in dichromated gelatin hologram, Yong Seok Im, Young Lak Lee, Chong Hoon Kwak, Ok Shik Choe, *Yeungnam Univ., Korea*. An image of 1 um line width formed by holographic phase conjugation is measured clearly within the focal tolerance of about 40 um and is analyzed theoretically.
(p. 186)

11:14am
JTuB23 • Wavelength-agile fluorescence microscopy filter using photorefractive barium titanate, Robert Kersten, Salvador Fernandez, Ciencia Inc.; George Fischer, Robert Boyd, *Univ. Rochester*. Holograms in photorefractive materials are used as passive wavelength-agile notch filters in fluorescence spectroscopy applications, thus filtering out coherent light while transmitting incoherent light. **(p. 190)**

11:16am
JTuB24 • Holographic interferometry methods for conducting stress analysis on quartz crystal components, Jill A. Brosig, *Motorola*. Holographic interferometry is used to study mechanical loading on quartz blanks resulting from mount structure. After identifying the magnitude and location of real-time-induced stresses, the design is optimized by change of such parameters as geometry and materials. **(p. 193)**

11:18am
JTuB25 • A computational model for holographic sensing, Ben Bakker, Val Bykovski, *Univ. Massachusetts-Lowell*. A novel analytical concept based on holographic recognition of light patterns from a sample is proposed and demonstrated computationally. **(p. 196)**

11:20am
JTuB26 • Computer-generated hologram for reconstruction of unusual mode image, Gao Wenqi, Tan Suqing, Zhou Jin, *Nanjing Univ., China*. Three kinds of computer-generated holograms of unusual reconstruction mode are reported. Theoretic analysis and corresponding experimental results are given. **(p. 199)**

11:22am
JTuB27 • Measurement and analysis of compound amplitude and phase holographic gratings, Y. J. Wang, M. A. Fiddy, Y. Y. Teng, D. A. Pommet, L. Malley, *Univ. Massachusetts-Lowell*. We describe the effect on the reconstruction of a bleached hologram of the inevitable presence of a residual amplitude hologram that is usually neglected. The modeling of this offers insights into its possible exploitation for some applications. **(p. 203)**

INDEPENDENCE BALLROOM

11:30am–1:30pm
Poster Session

12:00m-1:30pm
Lunch on Own

GARDNER A&B

1:30–3:00pm
JTuC • Joint Session on Diffractive and Micro-Optics and Holography II
Michael Gale, *Paul Scherrer Institute, Presider*

1:30pm (Invited)
JTuC1 • Diffraction optics—a century from basic studies to mass production, Erwin G. Loewen, *Spectronic Instruments, Inc.* It has taken 100 years to combine basic concepts for diffraction optics with a series of enabling technologies to arrive at commercially useful products. **(p. 208)**

2:00pm
JTuC2 • Liquid crystal grating based on modulation of circularly polarized light, Jay E. Stockley, Kristina M. Johnson, *Univ. Colorado-Boulder*; Gary D. Sharp, Steven A. Serati, Ping Wang, *Boulder Nonlinear Systems Inc.* We present theoretical and experimental results for analog phase modulators and gratings using chiral smectic liquid crystals as rotative wave plates acting on circular polarization. **(p. 211)**

2:15pm
JTuC3 • Diffractive optical elements for three-dimensional displays based on the partial pixel 3-D display architecture, G. P. Nordin, M. W. Jones, R. G. Lindquist, J. H. Kulick, S. T. Kowel, *Univ. Alabama-Huntsville*. We examine the use of diffractive optical elements to realize three-dimensional, holographic-like displays based on the partial pixel 3-D display architecture, and we describe our current implementations of real-time displays. **(p. 215)**

2:30pm
JTuC4 • Beam-pointing stabilization and increased ladar heterodyne mixing efficiency using a liquid crystal phased array device, Mark J. Missey, *Vincent Dominic, Univ.*; Edward A. Watson, *Wright Laboratory*. Active beam-pointing stabilization and increased coherent laser radar mixing efficiency applications for an addressable liquid crystal phased array are investigated. **(p. 219)**

2:45pm
JTuC5 • Programmable wave-front generation with two binary phase spatial light modulators, Guoguang Yang, Seth Broomfield, *Univ. Oxford, UK*. A programmable wave-front generation system that uses two binary phase SLMs is a space-variant system with high diffraction efficiency. It is implemented experimentally with two ferroelectric liquid crystal SLMs. **(p. 223)**

INDEPENDENCE BALLROOM

3:00–3:30pm
Coffee Break/Exhibits

GARDNER A&B

3:30–5:00pm
DTuD • Scalar Design
Joseph N. Mait, *U.S. Army Research Laboratory, Presider*

3:30pm (Invited)
DTuD1 • A rogues' gallery of CGH null tests, Steven Arnold, *Diffraction International Ltd.* CGH null testing of aspheric optics was first demonstrated by MacGovern and Wyant in 1971 but has only recently become available as a commercial product. This talk describes a variety of CGH null test configurations using both commercial and customized interferometers. Several of the aspheres and their associated CGH nulls will be shown to exhibit various pathological traits. **(p. 228)**

4:00pm
DTuD2 • Rigorous design of flat-top generators, Markku Kuittinen, Jari Turunen, Pasi Vahimaa, *Univ. Joensuu, Finland.* We present a novel rigorous method to solve diffraction problems of refractive-index-modulated apertures in a conducting screen and apply it to beam shaping. **(p. 229)**

4:15pm
DTuD3 • Diffraction efficiency of high-NA continuous-relief diffractive lenses, M. Rossi, C. G. Blough, D. H. Raguin, *Rochester Photonics Corp.*; E. K. Popov, D. Maystre, *Laboratoire d'Optique Electromagnetique, France.* A high efficiency F/2 diamond-turned diffractive lens is used as a fiber coupler. The diffraction efficiency is modeled with use of rigorous theory and a fast ray tracing algorithm. **(p. 233)**

4:30pm
DTuD4 • Pseudorandom encoding of fully complex modulation to biamplitude phase modulators, Robert W. Cohn, Wenyao Liu, Univ. Louisville. This algorithm maps analog amplitudes to unity or zero. Unity is randomly selected with a probability equal to the desired amplitude. This algorithm outperforms MEDOF. **(p. 237)**

4:45pm
DTuD5 • Analysis and synthesis of a two-dimensional diffractive lens using the local linear grating model and the coupled-wave theory, Yunlong Sheng, Simon Larochelle, Dazeng Feng, Univ. Laval, Canada. A simple local linear grating model and the coupled-wave theory are used for estimating and optimizing diffraction efficiency of large numerial aperture two-dimensional radially symmetrical lenses. **(p. 241)**

WEDNESDAY
MAY 1, 1996

3rd FLOOR REGISTRATION AREA
7:30am-5:30pm
Registration

GARDNER A&B

8:30–10:00am
DWA • Subwavelength Structures
Yeshayahu Fainman, *University of California ,San Diego, Presider*

8:30am (Invited)
DWA1 • Thin-film filters with diffractive and waveguiding layers, R. Magnusson, S. Tibuleac, Z. Liu, D. Shin, P. P. Young, *Univ. Texas at Arlington*; S.S. Wang, *Motorola Inc.* Guided-mode resonance effects in diffractive thin-film structures are applied to realize both reflection and transmission bandpass filters. **(p. 246)**

9:00am
DWA2 • Design of resonant grating filters, Scott M. Norton, G. Michael Morris, Turan Erdogan, Univ. Rochester. Resonant grating filters offer high-contrast, narrowband performance. We demonstrate approximate methods to obtain resonant width in resonant grating filters as well as the advantages of each method. **(p. 249)**

9:15am
DWA3 • Zeroth-order complex-amplitude modulation by lamellar surface profiles, Ville Kettunen, Pasi Vahimaa, Jari Turunen, Marko Honkanen, Olli Salminen, *Univ. Joensuu, Finland*; Eero Noponen, *Helsinki Univ. Technology, Finland.* The encoding of the signal wave amplitude and phase into variations of the efficiency and phase of the zeroth carrier-grating diffraction order is considered. **(p. 253)**

9:30am
DWA4 • Subnanometer linewidth resonant grating filters, Song Peng, G. Michael Morris, *Univ. Rochester.* Resonant grating structures can be designed to achieve narrower linewidth and higher peak efficiency than conventional interference filters. Issues related to device fabrication are addressed. **(p. 257)**

9:45am
DWA5 • Optimization of guided-mode resonance and Bragg gratings designed using rigorous diffraction theory, Ben Layet, Malcolm T. M. Lightbody, Mohammad R. Taghizadeh, *Heriot-Watt Univ., UK.* We use rigorous diffraction theory to design gratings acting as polarizers, beamsplitters, deflectors, or wavelength filters. The grating components potentially provide high performance and robustness. **(p. 261)**

INDEPENDENCE BALLROOM
10:00am-10:30am
Coffee Break/Exhibits

GARDNER A&B

10:30am–12:00m
DWB • Micro-Optics Applications
Ravindra A. Athale, *George Mason University, Presider*

10:30am (Invited)
DWB1 • Giant micro-optics: wide applications in LCD systems, Shigeru Aoyama, Tsuyoshi Kurahashi, Daidou Uchida, Masayuki Shinohara, Tsukasa Yamashita, *Omron Corp., Japan.* In recent years, giant microoptic devices based on microlens arrays, micro prism arrays and holograms have been developed for LCD systems. The attractive applications are reviewed. **(p. 266)**

11:00am
DWB2 • Color separation echelon gratings, Margaret B. Stern, Gary J. Swanson, *MIT Lincoln Laboratory.* Echelon-like grating structures are designed to separate the visible spectrum according to diffraction order rather than by dispersion within one diffraction order. The performance and fabrication of prototype gratings are described. **(p. 270)**

11:15am
DWB3 • A multiview fast optical tomography system using microlens arrays, K. P. Bishop, R. E. Pierson, E. Y. Chen, *Applied Technology Associates*; L. McMackin, *U.S. Air Force Phillips Laboratory.* The implementation of a fast optical tomography system with use of a microlens-based Hartmann wavefront sensor is described for use in interrogating a heated jet flow. **(p. 274)**

11:30am
DWB4 • Microlens lithography, R. Volkel, H. P. Herzig, Ph. Nussbaum, W. Singer, R. Dandliker, *Institute of Microtechnology, Switzerland.* Microlens lithography is a new lithographic method that uses microlens arrays. It provides a resolution of 2-5 um for an almost unlimited print area. **(p. 278)**

11:45am
DWB5 • Laser beam relaying with a phase-conjugate diffractive optical element, Siamak Makki, James Leger, *Univ. Minnesota.* A diffractive optical element is used to image a flat top laser beam by phase conjugation. It has the advantage over conventional afocal systems of avoiding concentration of light at the intermediate focal point. **(p. 282)**

12:00m-1:30pm
Lunch on Own

GARDNER A&B

1:30–3:00pm
DWC • Testing & Evaluation
Hans Peter Herzig, *University of Neuchatel, Switzerland, Presider*

1:30pm (Invited)
DWC1 • Interferometric tests for microoptics, J. Schwider, N. Lindlein, *Univ. Erlangen, Germany.* This paper considers mainly

the testing of refractive microlenses. The measurement of paraxial parameters, surface quality, and wave aberrations with the help of interferometers in reflected and transmitted light as well as the advantages and problems of these interferometers, are discussed. **(p. 288)**

2:00pm
DWC2 • Evaluation of wavefront sensors based on etched microlenses, R. E. Pierson, K. P. Bishop, E. Y. Chen, Applied Technology Associates; D. R. Neal, *Sandia National Laboratories*; L. McMackin, *U.S. Air Force Phillips Laboratory*. Binary etched microlenses enable fabrication of Shack-Hartmann wavefront sensors optimized for a particular application. We present a modeling and test approach to microlens optimization. **(p. 292)**

2:15pm
DWC3 • Realization of multilayer diffractive components experimental methods of characterization, H. Giovannini, H. Akhouayri, C. Amra, *CNRS, France*. Techniques of deposition already used in the field of thin films can be used to realize multilayer diffractive components. Methods of characterization based on ellipsometry, two-beam interferometry and photothermal deflection give the optical properties of coated gratings. These methods, together with a numerical simulation can help the design of diffractive components. All these techniques can be used to realize bi-dimensional gratings. **(p. 296)**

2:30pm
DWC4 • Experimental studies of Talbot array illuminators, Thomas J. Suleski, Donald C. O'Shea, *Georgia Institute of Technology*. Experimental studies of binary phase Talbot array illuminators are presented. Useful new results include stronger light concentration and spatial frequency doubling of Talbot intensity patterns. **(p. 300)**

2:45pm
DWC5 • Submicron gratings with dielectric overcoat: performance and stability, C. Heine, R. H. Morf, M. T. Gale, *Paul Scherrer Institute, Switzerland*. Measurements on broadband anti-reflection structures show that the combination of dielectric overcoating with grating microstructure leads to improved stability. Various types of designs are presented. **(p. 304)**

INDEPENDENCE BALLROOM

3:00pm-3:30pm
Coffee Break/Exhibits

GARDNER A&B

3:30–5:00pm
DWD • Fabrication
Michael Feldman, *Digital Optics Corporation, Presider*

3:30pm
DWD1 • Rapid fabrication of diffractive microlenses using excimer laser ablation, Xiaomei Wang, Robert H. Rediker, *Cynosure Inc.*; James R. Leger, *Univ. Minnesota*. We fabricate eight-level diffractive microlenses using excimer laser ablation through an imaging objective. These lenses exhibit diffraction-limited focusing and near theoretical diffraction efficiency (92%). **(p. 310)**

3:45pm
DWD2 • Excimer laser micromachining for rapid fabrication of binary and blazed diffractive optical elements, Michael T. Duignan, Gregory P. Behrmann, *Potomac Photonics Inc.* We demonstrate fabrication of two-level and ramped diffractive structures by a fast and flexible direct-write process using an excimer laser-based tabletop micromachining work station with an integrated optical surface profiler. **(p. 314)**

4:00pm
DWD3 • Fabrication of submicron feature diffractive elements using near-field direct-write ultraviolet lithography, Igor I. Smolyaninov, David L. Mazzoni, Christopher C. Davis, *Univ. Maryland*; Joseph N. Mait, *U.S. Army Research Laboratory*. We present the results of direct-write lithography implemented using the near-field optical interaction between an uncoated tapered fiber tip and a layer of photoresist. The nearfield arrangement allows for both lithography and shear force microscopic examination of the surface. **(p. 318)**

4:15pm
DWD4 • One-step lithography for mass production of multilevel diffractive optical elements using high energy beam sensitive gray-level mask, Walter Daschner, Robert Stein, Pin Long, Sing H. Lee, *Univ. California-San Diego*; Chuck Wu, *Canyon Materials Inc.* We present fabrication of multilevel DOEs using a HEBS-glass gray-level mask. Ebeam direct write of the mask avoids alignment errors and a transfer step generates monolithic DOEs. **(p. 322)**

4:30pm
DWD5 • Subwavelength diffractive elements fabricated in semiconductors for 975 nm, R. W. Smith, M. E. Warren, J. R. Wendt, G. A. Vawter, *Sandia National Laboratories*. The performance of high efficiency subwavelength anti-reflection structures and blazed gratings fabricated into semiconductor surfaces for 975 nm light are discussed. **(p. 325)**

4:45pm
DWD6 • Fabrication of zone plates for x-ray microscopy: diffractive optics for soft x-rays, S. J. Spector, C. J. Jacobsen, *SUNY Stony Brook*; D. M. Tennant, *AT&T Bell Laboratories*. We fabricate Fresnel zone plates and test them as the imaging optic in a soft xray microscope to resolve features approximately 30 nm in size. **(p. 328)**

Monday, April 29, 1996

Electromagnetic Theory

DMA 8:30 am-10:00 am
Gardner A&B

M.G. Moharam, *Presider*
University of Central Florida

Electromagnetic theory of X-ray gratings.

M. NEVIERE,
Laboratoire d'Optique Electromagnétique, U.R.A. CNRS n° 843
Faculté des Sciences de St-Jérôme, Case 262, 13397 Marseille Cédex 13, France

Diffracting and focusing elements become more and more popular in soft and hard X-ray spectral domain in view of achieving studies of spectroscopy, luminescence, photoemission, microscopy, etc ... Concerning diffraction elements, i.e. gratings, two main types have to be distinguished. The first type consists of bare metallic gratings, usually gold or platinum coated, which cover a wide range of wavelength, from 6 A° to 1000 A°, and are classical gratings used under grazing incidence. As "classical gratings" with finite conductivity, their theory was already published [1, 2] at the beginning of the 1970's. However, due to the high number of propagating orders resulting from wavelength-to-groove-spacing ratio (λ/d) less than 1/100 or even 1/1000, the use of the Integral Theory was precluded in this spectral domain, at least with the computers available at that time. It is only in 1979 that we recognized [3] that due to the specificities of X-ray gratings, namely low groove-depth-to-groove spacing ratios (h/d) plus refractive indices close to unity, the coupling between the eigenmodes or diffracted orders was weak enough so that it was possible to get accurate results with the Differential Theory by truncating the Fourier series of the field to an order much less than the number of propagating orders. This discovery opened the X-ray domain to the use of electromagnetic theory of gratings, and since that time, the Differential Theory was used to study and optimize many X-ray gratings for Synchrotron Radiation Instrumentation and important space missions [4-5]. A computer software was recently developed in order to determine a given number of grating parameters (e.g. groove depth, incidence, groove spacing ...) in order to optimize a desired efficiency in TE, TM polarization or natural light for a specified used. Spectacular agreement was found between theoretical predictions and measurements so that the diffraction of X-rays by a metallic grating can be considered as a well resolved problem. The modal method [6] developed in the mean time and used by several authors led to identical results with comparable computation time.

Such bare metallic gratings, however, have the inconvenience to give high efficiencies at grazing incidence only ; since nowadays, gratings are not only asked to diffract light, but also to focus it, the result is increased aberrations. Thus an alternative solution has been proposed, which leads to high efficiencies under near normal incidence. It consists of the second type of gratings, called multidielectric gratings. Here too, there are two ways of producing multidielectric gratings. The first way consists of evaporating a stack of pairs of dielectric layers, with alternatively high and low refractive index, leading to what will be

called a multilayer coated grating. The second way starts from plane multidielectric stack, in which a grating is carved via ion-etching technique. We then get what is called a Bragg-Fresnel multilayer grating.

Since both types of multidielectric gratings involve a high number of modulated interfaces, for a long time they appeared to be a challenge to grating theoreticians. The first type (i.e. multilayer coated gratings) was first adressed in 1991 [7] and the Differential Theory of gratings was extended to deal with such a multiprofile grating whose interfaces are not separable, i.e. they cannot be studied separately, and liked to each other through Rayleigh expansions. The method turned out to be successful to study gratings coated with several tens or a few hundred of dielectric layers, provided the groove depth is small enough, which is always almost the case in X-ray domain. The second type, i.e. Bragg-Fresnel multilayer gratings, was recently resolved [8] for any groove shape by computing the product of the transmission matrices of the elementary gratings carved in each dielectric layer. Such a method again, turned out to be efficient in X-ray domain with a few hundred of dielectric layers.

For both multidielectric gratings however, when the groove depth increases, contamination linked with growing exponential functions in the numerical integration process limits the validity of the method. This difficulty has been resolved recently by several authors [9] who proposed a scheme called R (and S)-matrix propagation algorithm and variants [10]. The use of such algorithms has enabled the Differential Theory to deal with high blaze angle (e.g. 10°) gratings coated with several tens of dielectic layers and used in an order as high as 60. Such an X-ray echelle turns out to be of special interest for achieving ultra-high resolution ($\approx 10^5$) in X-ray fluorescence experiment. The study of an echelle working at extremely low λ/d ratio requires being able to integrate 150x150 or 200x200 equation sets without numerical instability. It has been resolved in [11] and numerical results for X-ray echelles will be published in [12].

As a consequence of the new possibilities in grating computation, unperiodic focusing devices such as Bragg-Fresnel linear zone plates can be studied via the electromagnetic theory. It suffices to consider the limited zone plate as a bump of a lamellar Bragg-Fresnel grating (with a groove period high enough to avoid coupling between adjacent bumps) and to resolve the grating problem.The influence of parameters which are out of the scope of the physical optics theory (e.g. the groove depth) on the focusing potentialities can then be analyzed [13].

Spectacular comparisons between theorerically predicted grating efficiencies and measurements in soft and hard X-rays will be presented at the conference.

REFERENCES

[1] D. Maystre, "Sur la diffraction d'une onde plane par un réseau métallique de conductivité finie", Opt. Commun., 6, pp. 50-54, 1972.

[2] M. Nevière, P. Vincent, R. Petit, "Sur la théorie du réseau conducteur et ses applications à l'optique", Nouv. Rev. Optique 74, pp. 65-77, 1974.

[3] M. Nevière, one communication at the "Synchrotron Radiation Instrumentation Symposium", N.B.S., Gaithersburg, Maryland, USA, 4-6 June 1979 ; three communications at the "VI International Conference on Vacuum Ultraviolet Radiation Physics", University of Virginia, Charlottesville, Virginia, USA, 2-6 June 1980.

[4] M. Nevière, J. Flamand, "Electromagnetic theory as it applies to X-ray and XUV gratings", Nucl. Instr. Meth., 172, pp. 273-279, 1980.

[5] M. Nevière, J. Flamand, J.M. Lerner, "Optimization of gratings for soft X-ray monochromators", Nucl. Instr. Meth., 195, pp. 183-189, 1982.

[6] L.C. Botten, M.S. Craig, R.C. Mc Phedran, J.L. Adams, and J.R. Andrewartha, "The finitely conducting lamellar diffraction grating", Opt. Acta 28, pp. 1087-1102, 1981.

[7] M. Nevière, "Multilayer coated gratings for X-ray diffraction : differential theory", J. Opt. Soc. Am. A 8, pp. 1468-1473, 1991.

[8] M. Nevière, "Bragg-Fresnel multilayer gratings : electromagnetic theory", J. Opt. Soc. Am. A 11, pp. 1835-1845, 1994.

[9] Lifeng Li, "Multilayer modal method for diffraction gratings of arbitrary profile, depth and permitivity", J. Opt. Soc. Am. A 10, pp. 2581-2591, 1993.

[10] M.G. Moharan, D.A. Pommet, E.B. Grann and T.K. Gaylord, "Stable implementation of the rigorous coupled-wave analysis for surface relief gratings : enhanced transmission matrix approach", J. Opt. Soc. Am. A 12, pp. 1077-1086, 1995.

[11] F. Montiel, M. Nevière, "Differential theory of gratings : extension to deep gratings of arbitrary profile and permittivity via the R-matrix propagation algorithm", J. Opt. Soc. Am. A 11, pp. 3241-3250, 1994.

[12] M. Nevière, F. Montiel, "Soft X-ray multilayer coated echelle gratings : electromagnetic and phenomenological study", J. Opt. Soc. Am. A, to be published.

[13] F. Montiel, M. Nevière, "Electromagnetic theory of Bragg-Fresnel linear zone plates", J. Opt. Soc. Am. A, to be published.

Optimal Design of Low Order Diffractive Structures

David C. Dobson
Dept. of Mathematics
Texas A&M University
College Station, TX 77843-3368
409-845-3261
Fax: 409-862-4190

J. Allen Cox
Honeywell Technology Center
3660 Technology Drive
Minneapolis, MN 55418
612-956-4769
Fax: 612-956-4517

1. Introduction. A low order diffractive structure has a period Λ of the same magnitude as the incident wavelength (λ), $\Lambda \approx \mathcal{O}(\lambda)$, and thus admits only a few ($\mathcal{O}(1)$) propagating orders. An important subclass is defined by $\Lambda < \lambda$, for which only zero order propagates, and includes antireflective ("moth-eye") structures, form birefringent phase plates, wire grid polarizers, and resonant guided wave filters. An example lying in the broader class is represented by the outer zones of a fast ($\tilde{f}/1$) Fresnel phase lens, where $\Lambda \approx 2\lambda$.

An important problem for this class of diffractive structures is the design of the detailed structure in the unit cell of the periodic array to achieve optimal performance in some sense. Usually, this means finding a surface profile which maximizes diffraction efficiency within a prescribed tolerance in either a specified order or a set of orders. In the case of moth-eye gratings, previous efforts in this direction have been constrained by ansatzes of the profile shape, e.g., either polynomial form [1] or other analytical forms [2]. The difficulty of the problem for the broader class of structures has been pointed out recently [3]. Because $\Lambda \approx \lambda$, it is well known that phase reconstruction methods based on the Fourier approximation are inadequate and that a more rigorous approach is needed.

Here we present two methods for optimal design of low order diffractive structures based on the Helmholtz equation developed by one of authors (DCD) and reported in the mathematics literature [4, 5] and only briefly in the optics literature [7]. The first method, relaxed optimization, typically yields structures in the unit cell which either are continuous in the refractive index or are multiply-connected regions in discrete indices. Because of their "relaxed" form, such structures provide exceptional performance, giving, for example, very low reflectivity moth-eye gratings with extremely low aspect aspect ratio. Theoretically, the relaxed method also forms the basis for theorems placing effective medium theory [8] of zero-order gratings on a sound mathematical foundation. The second method, shape optimization, yields a more practical simply-connected profile as the interface between two regions of constant index. This method can provide, for example, relatively high efficiency in staircase profiles having only three or four steps.

We start with a concise statement of the mathematical problem and proceed to illustrate the two optimization approaches with examples in subsequent sections. Only brief a summary of each approach is presented here. Mathematical details can be found in the references [4, 5, 7]. A more detailed paper will appear in the optics literature.

2. Statement of the Problem. The starting point for our approach is rigorous grating theory. We consider a periodic structure defined by some surface profile S which separates two homogeneous materials. In principle this surface can be nonsmooth, and it does not have to be the graph of a function of one variable. In the case of E-parallel polarization on a linear grating, Maxwell's equations reduce to the scalar Helmholtz equation

$$(\triangle + a_S)u = 0$$

where $\triangle = \frac{\partial^2}{\partial x^2} + \frac{\partial^2}{\partial y^2}$, and the function a_S is defined by

$$a_S(x,y) = \begin{cases} k_1^2 & \text{if } (x,y) \text{ is above } S, \\ k_2^2 & \text{if } (x,y) \text{ is below } S, \end{cases}$$

where k_1, k_2 are the (complex, in general) refractive indices of the two materials. Our general approach is applicable to other polarization cases including the full vector Maxwell equations, although the details are more difficult. Our analysis and numerical methods are based on a variational formulation of the problem. Analysis including existence and uniqueness results, as well as the convergence of numerical finite element methods for the problem has appeared in the applied mathematics literature [6].

The general form of the design problem we consider is: determine a profile S which generates a specified "output" for a given incident beam, or range of incident beams. The "output" consists of the intensity (or phase and intensity) of the outward propagating reflected and transmitted orders. One way to turn this into a mathematically viable problem is to state it as a minimization:

$$\min_S J(S) = \|F(S) - g\|_2^2, \tag{1}$$

where $F(S)$ is the vector containing the reflected and transmitted orders diffracted from the surface profile S, and g is the desired "output" of the grating. Note that calculating $F(S)$ requires solving the Helmholtz equation.

The problem, as stated, is "ill-posed". In this case the meaning of ill-posedness is that sequences of admissible design profiles S_n exist which minimize $J(S)$ but do not converge to an admissible design. There are basically two remedies. First is to "relax" the problem by enlarging the class of admissible designs to include "mixtures" of the two materials. This approach is mathematically sound and is closely related to ideas in effective media theory. One practical consequence of the associated analysis is that *structures with graded refractive indices $k(x,y)$ with $k_1 \le k(x,y) \le k_2$ can always be realized as a limit of (possibly highly oscillatory) surface profiles separating two homogeneous materials.*

The second remedy to ill-posedness to to constrain the class of admissible designs to eliminate the nonconvergent sequences. Typical approaches used in inverse problems involve smoothness constraints. Such constraints are not appropriate for gratings, since mask-etch type fabrication processes often yield profiles with edges. Our approach is a "total variation" constraint which allows nonsmooth profiles, but limits the total amount of oscillation in the profile. More precisely, if S is given by the graph of a function $s(x)$, we insist that

$$TV(s) = \int |s'(x)|\, dx \le C,$$

where C is a bound on the allowed oscillation. One potential disadvantage of this approach is that choosing C too small may produce sub-optimal designs. However we have found that generally C can be adjusted to give a satisfactory tradeoff between optimality and complexity of the structure. This approach is also mathematically sound [5].

For both approaches (relaxed design and shape design), we employ large-scale numerical optimization algorithms to solve the discretized minimization problem (1). These algorithms take advantage of the underlying structure of the problem for improved efficiency, and use "adjoint-state" techniques from optimal control theory to calculate derivative information from the partial differential equations.

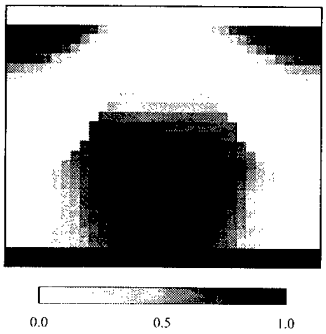


FIG. 1. *Optimized moth-eye profile. Plot shows the volume fraction of substrate in each cell (black is substrate, white is air).*

3. Design Examples.

3.1 Relaxed Optimization. Our first example illustrates the relaxed design approach. In this problem, we optimize a dielectric grating structure in such a way that the total reflected energy is minimized over a given range of incidence angles.

The parameters for this example are: $k_1 = 1$, $k_2 = 1.6$, $\lambda = 1$, $\Lambda = 0.5$. The range of incidence angles is chosen to be ± 1.2 radians (about ± 69 degrees). An initial triangular-shaped profile had low reflectivity near normal incidence, but as expected showed much increased reflectivity at sharper angles. The profile shown in Figure 1 was obtained using our method and exhibits reflectivity below 0.2% over ± 1.1 radians. The highest reflectivities still occur at the sharpest angles, but are reduced by orders of magnitude over the triangular profile.

As noted earlier, the analysis leading to the relaxed design approach shows that graded index structures of the type illustrated in Figure 1 can be realized as a limit of sharp interfaces between two materials. In [4] we calculated the reflectivity of such a structure and found that the performance was not greatly degraded.

3.2 Shape Optimization. Consider the problem of maximizing the energy in the +1 transmitted order, given a normally incident plane wave on a grating which supports nine transmitted orders. The material parameters are $k_1 = 1$, $k_2 = 1.5$. Figure 2 shows a design for such a structure obtained by optimization under the Fourier approximation. This design is very intuitive. It directs 70% of the incident energy into the +1 transmitted order. However, the figure clearly shows the disturbances in the diffracted field which result in wasted energy.

Using the profile in Figure 2 as an initial guess, we applied our minimization algorithm with the total variation constraint to obtain a 95% efficient profile S. The profile was judged to exhibit a satisfactory tradeoff between shape complexity and efficiency. To obtain a "manufacturable" profile, we then approximated S by the 4-level structure shown in Figure 3. The efficiency decreased from 95% to 87%, but this still represents a gain of 17% efficiency over the ramp profile of Figure 2. We should note that by loosening the total variation constraint on the profile, designs with up to 99.9% efficiency were achieved. However they were too oscillatory to be of practical use.

We have applied this method with success to many other design problems. For some classes of problems, the method yields relatively simple profiles with efficiency close to 100%.

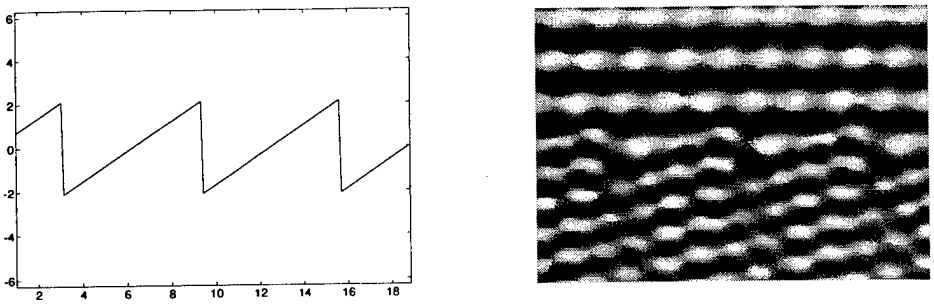


FIG. 2. *Optimal ramp profile. Gray-scale plot shows the real part of the diffracted field. The structure directs 70% of the incoming energy into the +1 transmitted order.*

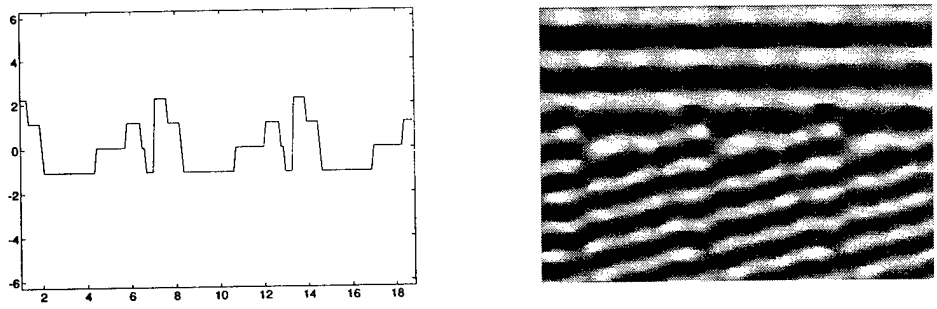


FIG. 3. *An 87.0% efficient 4-level approximation to an optimal profile, and the real part of the diffracted field.*

4. Summary. We have presented a brief overview of two optimal design methods for low order diffractive structures. Both methods are based directly on rigorous grating theory, utilize the full partial differential equation model, and are mathematically sound. These methods have been implemented numerically and have been used to generate high efficiency structures. The first method is closely related to effective medium theory and generates "relaxed" designs. The second method finds an optimal interface between two homogeneous materials and can be used to generate highly efficient continuous profiles, as well as practical stairstep profiles by approximation.

REFERENCES

[1] W.H. Southwell, *Pyramid-array surface-relief structures producing antireflection index matching on optical surfaces*, J. Opt.S oc. Am. A, Vol. 8, 549-53 (1991).

[2] E.B. Grann, M.G. Moharam, D.A. Pommet, *Optimal design for antireflective tapered two-dimensional subwavelength grating structures*, J. Opt. Soc. Am. A, Vol. 12, 333-9 (1995).

[3] J. Turunen, E. Noponen, and F. Wyrowski, *Diffractive optics beyond the paraxial domain*, in Diffractive Optics Vol. 11, 1994 OSA Technical Digest Series (OSA, Washington, DC 1994) pp. 186-9.

[4] D.C. Dobson, *Optimal design of periodic antireflective structures for the Helmholtz equation*, Euro. Jnl of Applied Math. vol. 4, pp. 321-40 (1993).

[5] D.C. Dobson, *Controlled scattering of light waves: optimal design of diffractive optics*, in "Control Problems in Industry", I. Lasiecka and B. Morton, eds., Birhäuser, Boston (1995), pp. 97-118.

[6] G. Bao, *Finite elements approximation of time harmonic waves in periodic structures*, SIAM J. on Numerical Analysis, to appear.

[7] G. Bao, D.C. Dobson, J.A. Cox, *Mathematical studies in rigorous grating theory*, J. Opt. Soc. Am. A, Vol. 12, 1029-42 (1995).

[8] S.M. Rytov, *Electromagnetic properties of a finely stratified medium*, Soviet Physics JETP, vol. 2, pp. 466-74 (1976).

Boundary Element Method for Analysis and Design of One-Dimensional Diffractive Optical Elements

Dennis W. Prather, Mark S. Mirotznik,† and Joseph N. Mait

U.S. Army Research Laboratory

AMSRL-SE-EO

2800 Powder Mill Road

Adelphi, Maryland 20783

phone: (301) 394-2520, fax: (301) 394-4214, e-mail: prather@arl.mil

†The Catholic University of America

Department of Electrical Engineering

Washington, D.C. 20064

The boundary element method (BEM) is a numerical technique to solve the boundary integral equations for the vector analysis of diffraction.[1,2] Boundary integral methods model the interaction between an incident field and a diffractive optical element (DOE) using distributions induced on the surface of the DOE by the incident field. For a conductor the surface distribution is a current and, for a dielectric, it is a polarization field. Re-radiation from the surface distribution, in turn, generates a diffracted field. The objective of the BEM is the determination of the surface distribution given the incident field and DOE.

Alternative approaches to the solution of vector-based diffraction include differential methods,[3,4] volume integral methods,[1,5,6] and variational techniques.[7,8] However, the advantages of the BEM over these other methods are that it is applicable to finite aperiodic, as well as infinitely periodic, DOEs, only the surface of the DOE needs to be sampled, and once the surface distribution is known for a given incident field, it can be used to determine the complex vector field amplitudes anywhere in space or over independent regions of space. However, the BEM requires a Green's function, which limits its application to homogeneous, or discretely inhomogeneous, media. In this paper we present our work on the analysis of finite extent, aperiodic, homogeneous conducting and dielectric DOEs using the BEM.

We assume that the incident field is a uniform TE-polarized plane wave, in which case only the transverse component of the electric field needs to be considered. As shown in Fig. 1 the solution space is divided into two homogeneous regions: region I, which contains the DOE, and region O, which is free space. The boundary integral equations that describe the coupling between the fields on the surface of the DOE and those in free space are[1,2]

$$\begin{aligned} 0 &= \mathbf{E}^{sc}(\mathbf{r}_s)\left(1-\frac{\theta}{2\pi}\right)+\oint_C\left[\mathbf{E}^{sc}(\mathbf{r}')\frac{\partial G_I(\mathbf{r}_s,\mathbf{r}')}{\partial\hat{n}}-G_I(\mathbf{r}_s,\mathbf{r}')\frac{\partial\mathbf{E}^{sc}(\mathbf{r}')}{\partial\hat{n}}\right]dl' \\ &+ \mathbf{E}^{inc}(\mathbf{r}_s)\left(1-\frac{\theta}{2\pi}\right)+\oint_C\left[\mathbf{E}^{inc}(\mathbf{r}')\frac{\partial G_I(\mathbf{r}_s,\mathbf{r}')}{\partial\hat{n}}-G_I(\mathbf{r}_s,\mathbf{r}']\frac{\partial\mathbf{E}^{inc}(\mathbf{r}')}{\partial\hat{n}}\right]dl' \end{aligned} \tag{1a}$$

$$0=\mathbf{E}^{sc}(\mathbf{r}_s)\left(\frac{\theta}{2\pi}\right)+\oint_C\left[G_O(\mathbf{r}_s,\mathbf{r}')\frac{\partial\mathbf{E}^{sc}(\mathbf{r}')}{\partial\hat{n}}-\mathbf{E}^{sc}(\mathbf{r}')\frac{\partial G_O(\mathbf{r}_s,\mathbf{r}')}{\partial\hat{n}}\right]dl' \tag{1b}$$

where where $\oint$ is Cauchy's principal value of integration, $\mathbf{E}^{inc}(\mathbf{r})$ and $\mathbf{E}^{sc}(\mathbf{r})$ are the incident and scattered fields, respectively, $\mathbf{r}_s$ is a point on the DOE surface C, and $G_O(\mathbf{r}_s,\mathbf{r}')$ and $G_I(\mathbf{r}_s,\mathbf{r}')$ are the Green's functions for the regions O and I. The phase θ is the angle subtended by the boundary at the point $\mathbf{r}_s=\mathbf{r}'$, which is a point in the contour integral at which a singularity occurs.[1] The total field $\mathbf{E}^{tot}(\mathbf{r})$ is the sum of $\mathbf{E}^{inc}(\mathbf{r})$ and $\mathbf{E}^{sc}(\mathbf{r})$.

To determine the total electric field using the BEM one samples the contour C, which reduces Eqs. (1a) and (1b) to a single matrix equation in terms of the incident field values at the sample points

E_n^{inc} and $Q_n^{inc} = \partial E_n^{inc}/\partial \hat{n}$ and the unknown scattered field values E_n^{sc} and $Q_n^{sc} = \partial E_n^{sc}/\partial \hat{n}$. Solution of the matrix equation yields the scattered field values only at the sampled nodes; the field values elsewhere are determined via interpolation:

$$\mathbf{E}^{sc}(\mathbf{r}'(\xi)) = \sum_{n=1}^{N} \hat{E}_n^{sc}(\xi) = \sum_{n=1}^{N} E_n^{sc}\phi_1(\xi) + E_{n+1}^{sc}\phi_2(\xi) \tag{2a}$$

$$\mathbf{Q}^{sc}(\mathbf{r}'(\xi)) = \sum_{n=1}^{N} \hat{Q}_n^{sc}(\xi) = \sum_{n=1}^{N} Q_n^{sc}\phi_1(\xi) + Q_{n+1}^{sc}\phi_2(\xi). \tag{2b}$$

In our analysis we used linear interpolation,

$$\phi_1(\xi) = (1-\xi)/2, \tag{3a}$$

$$\phi_2(\xi) = (1+\xi)/2, \tag{3b}$$

where $\xi = [-1, 1]$. The interpolated field values are used to determine the scattered field everywhere,

$$\mathbf{E}^{sc}(\mathbf{r}) = \int_C \left[\mathbf{Q}^{sc}(\mathbf{r}')\, G_O(\mathbf{r},\mathbf{r}') - \mathbf{E}^{sc}(\mathbf{r}')\, \frac{\partial G_O(\mathbf{r},\mathbf{r}')}{\partial \hat{n}}\right] dl',\ \mathbf{r} \in O, \tag{4}$$

and the total field is obtained by summing the scattered field with the incident field.

To validate our implementation of the BEM, we used it to analyze the diffraction of a 1.0-μm wavelength TE-polarized plane wave, i.e., electric field perpendicular to the plane of incidence, by an infinitely long, 0.5-μm radius dielectric cylinder that has a relative permiability of 2.25. In Fig. 2 we compare the electric field magnitude determined by BEM to that of the analytic solution.[9] Agreement between the two is apparent. The boundary of the cylinder was sampled at $\lambda/47$.

The analysis presented above is applicable to both dielectrics and imperfect conductors. For perfect conductors, the coupled integral equations are reduced to a single equation because the total electric field both inside a perfect conductor and on its boundary is zero. Thus, Eq. (1a) degenerates to zero and Eq. (1b) reduces to

$$\mathbf{E}^{sc}(\mathbf{r}_s) = -\int_C \mathbf{Q}^{sc}(\mathbf{r}')\, G_O(\mathbf{r}_s,\mathbf{r}')\, dl'. \tag{5}$$

For convenience, the unit normal is now pointing into region O. If we restrict ourselves to one-dimensional elements, we can simplify Eq. (5) further to

$$\mathbf{E}^{inc}(x_s,y_s) = \frac{\omega\mu}{4}\int_C \mathbf{J}(x',y')\,H_0^{(2)}\left(\beta_O\sqrt{(x_s-x')^2+(y_s-y')^2}\right)dl', \tag{6}$$

where we have used the relationships $\mathbf{E}^{inc}(\mathbf{r}_s) = -\mathbf{E}^{sc}(\mathbf{r}_s)$, $\mathbf{J}(\mathbf{r}') = (1/j\omega\mu)[\partial\mathbf{E}^{tot}(\mathbf{r}')/\partial\hat{n}]$, and, for diffraction in two dimensions, $G_O(\mathbf{r},\mathbf{r}') = (1/4j)H_0^{(2)}\left(\beta_O\sqrt{(x-x')^2+(y-y')^2}\right)$. The function $H_0^{(2)}(\cdot)$ is the zeroth order Hankel function of the second kind.

As before, to determine the total electric field in O, one first samples the contour C and solves for the current values at the sample points. In terms of the surface current values at the sample points, the total electric field is

$$\begin{aligned}\mathbf{E}^{tot}(x,y) &= \mathbf{E}^{inc}(x,y) - \frac{\omega\mu}{8}\sum_{n=1}^{N}\Delta\ell_n \\ &\times \int_{-1}^{1}\left[J_n\phi_1(\xi)+J_{n+1}\phi_2(\xi)\right]\,H_0^{(2)}\left(\beta_O\sqrt{\left[x-\hat{x}_n(\xi)\right]^2+\left[y-\hat{y}_n(\xi)\right]^2}\right)\,d\xi,\end{aligned} \tag{7}$$

where $\phi_1(\xi)$ and $\phi_2(\xi)$ are the same linear interpolation functions used above, $\Delta\ell_n$ is the length of the nth segment, and

$$\begin{aligned}\hat{x}_n(\xi) &= x_n\phi_1(\xi)+x_{n+1}\phi_2(\xi), \\ \hat{y}_n(\xi) &= y_n\phi_1(\xi)+y_{n+1}\phi_2(\xi).\end{aligned}$$

Our implementation of the BEM for conductors was validated by comparing the far-field magnitude of the diffracted field from a perfectly conducting plate as determined by BEM to that predicted by scalar theory. The plate dimensions were 20.0 μm $\times$ 1.0 μm and its surface was sampled at $\lambda/23.7$. The comparison presented in Fig. 3 indicates agreement between the two theories at a distance of 100λ behind the plate.

1 REFERENCES

[1] S. Kagami and I. Fukai, IEEE Trans. Ant. and Prop. **AP-32** (1984), 455–461.

[2] K. Yashiro and S. Ohkawa, IEEE Trans. Ant. and Prop. **AP-33** (1985), 383–389.

[3] T. K. Gaylord and M. G. Moharam, Proc. IEEE **73** (1985), 894–937.

[4] K. S. Kunz and R. J. Luebbers, *The Finite Difference Time Domain Method for Electromagnetics* (CRC Press, Boca Raton FL, 1993).

[5] C. A. Brebbia, *The Boundary Element Method for Engineers* (Wiley, New York, 1978).

[6] J. J. Wang, *Generalized Moment Methods in Electromagnetics* (John Wiley, New York, 1991).

[7] B. Lichtenberg and N. C. Gallagher, Opt. Eng. **33** (1994), 3518–3526.

[8] D. C. Dobson and J. A. Cox, in *International Conference on the Application and Theory of Periodic Structures*, J. M. Lerner and W. R. McKinney, eds., Proc. SPIE **1545** (1991), 106–113.

[9] C. A. Balanis, *Advanced Engineering Electromagnetics* (John Wiley, New York, 1989).

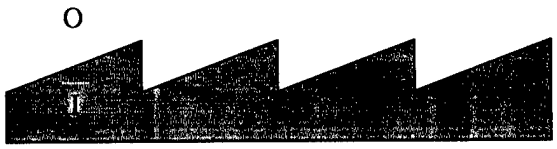


Figure 1. Representation of diffractive element for analysis using the boundary element method.

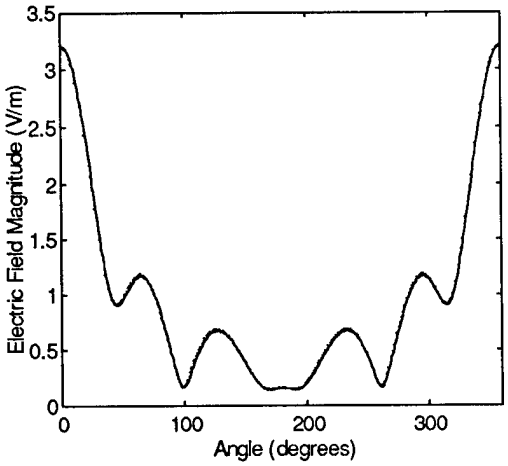


Figure 2. Comparison of diffracted electric field magnitude from a dielectric cylinder calculated using BEM (dotted line) to magnitude determined analytically (solid line).

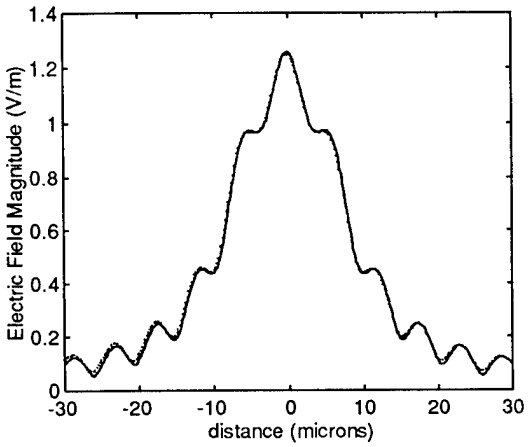


Figure 3. Comparison of diffracted electric field magnitude from a conducting plate into the far-field calculated using BEM (dotted line) to magnitude predicted by scalar theory (solid line).

Highly improved convergence of the coupled-wave method for TM polarization and conical mountings

Philippe Lalanne and G. Michael Morris*
Institut d'Optique Théorique et Appliquée, CNRS, BP 147, 91403 Orsay Cedex, France
tel: 33-1-69-41-68-46 fax: 33-1-69-41-31-92 e-mail: philippe.lalanne@iota.u-psud.fr
*The Institute of Optics, University of Rochester, Rochester, NY 14627
tel: (716)-275-5140 fax: (716)-271-1027 e-mail: morris@joker.optics.edu

1. Introduction

Several methods exists to analyze grating diffraction problems by solving rigorously Maxwell's equations. In some circumstances, all these methods suffer from some numerical instabilities and difficulties. We focus on a method originally derived from the integral method, namely the coupled-wave method (RCWA) formulated by Moharam and Gaylord[1]. This method is known to be slowly converging especially for TM polarization of metallic lamellar gratings. The slow convergence-rate has been analyzed in detail by Li and Haggans[2]. In this paper, we provide numerical evidence that the coupled-wave method is slowly converging for conical mounts of one-dimensional metallic grating. By reformulating the eigenproblem of the coupled-wave method, we provide numerical evidence that highly improved convergence-rates similar to the TE polarization case can be obtained for conical mounts. Of course, this result can be applied to the case of TM polarization for non-conical mounting, which is a particular case of the general conical mounting diffraction problem. We reveal that the origin of the slow convergence in the original RCWA method is not due to the use of Fourier expansions (as was argued by Li and Haggans), but to an inadequate formulation of the eigenproblem.

2. Reformulation of the eigenproblem

The RCWA computation is twofold. The Fourier expansion of the field inside the grating provides a system of differential equations. Once the eigenvalues and eigenvectors of this system are found, the boundary conditions at the grating interfaces are matched in order to compute the diffraction efficiencies. In the following, we focus on the eigenproblem of one-dimensional gratings.

Notations
The notation used in this paper are strictly those of Ref. 3. Let us consider a one-dimensional periodic structure along the x axis with an arbitrary permittivity profile $\varepsilon(x)$, see Fig. 1. The z axis is perpendicular to the grating boundaries. The grating is invariant in the y direction. Magnetic effects are not considered. ε_0 is the permittivity of the vacuum. The period of the structure is denoted by Λ and the grating vector K is equal to $2\pi/\Lambda$. An incident plane-wave makes an angle α with the z direction in a conical mounting ($\delta \neq 0$). ψ is the angle between the polarization vector and the plane of incidence. k_0 and k_1 represents the incident plane-wave vector in a vacuum and in the incident medium, respectively. A temporal dependence in $e^{j\omega t}$ of the wave is assumed ($j^2=-1$). ε_m will denote the mth Fourier coefficient of $\varepsilon(x)/\varepsilon_0$ and a_m will be used to denote the mth Fourier coefficients of $\varepsilon_0/\varepsilon(x)$.

new formulation
The new eigenproblem formulation linking the normalized vector amplitudes of the ith space-harmonic fields inside the grating region, $\mathbf{S}_i$ and $\mathbf{U}_i$, to their first derivative, is

$$k_0^{-1}\begin{bmatrix} S_y' \\ S_x' \\ U_y' \\ U_x' \end{bmatrix} = \begin{bmatrix} 0 & 0 & K_y E^{-1} K_x & I - K_y E^{-1} K_y \\ 0 & 0 & K_x E^{-1} K_x - I & -K_x E^{-1} K_y \\ K_x K_y & A^{-1} - K_y^2 & 0 & 0 \\ K_x^2 - E & -K_x K_y & 0 & 0 \end{bmatrix} \begin{bmatrix} S_y \\ S_x \\ U_y \\ U_x \end{bmatrix}. \quad (1)$$

* **I** is the identity matrix,
* **E** is the matrix formed by the permittivity harmonic coefficients,
* **A** is the matrix formed by the inverse-permittivity harmonic coefficients,
* $\mathbf{K}_x$ is a diagonal matrix with the i,i element being $((k_1 \sin\alpha \cos\delta - iK))/k_0$,
* $\mathbf{K}_y$ is a diagonal matrix equal to $\mathbf{I} \cdot (k_1 \sin\alpha \sin\delta)/k_0$,

The only difference between the conventional formulation (see Eq. (57) of Ref. 3) and the new formulation of Eq. (1) is in the third row of the second column, where matrix $\mathbf{E} - \mathbf{K}_y^2$ has been replaced by $\mathbf{A}^{-1} - \mathbf{K}_y^2$. Since $\mathbf{A}^{-1}$ is identical to **E** when an infinite number of orders are retained, Eqs. (1) and (57) in Ref. 3 are fully equivalent. As will be shown with numerical examples in the next Section, this equivalence is only true when an infinite number of orders is retained. When truncating the matrices for simulation purposes, we will see that the two eigenproblem formulations provide highly different convergence-rates.

Using the second derivative of the field vector, the eigenproblem of Eq. (1) reduces to

$$k_0^{-2}[U_x''] = [K_y^2 + K_x^2 - E][U_x], \text{ and}$$
$$k_0^{-2}[S_x''] = [K_x E^{-1} K_x A^{-1} + K_y^2 - A^{-1}][S_x]. \quad (2)$$

Equations (2) are new formulations of Eq. (60) in Ref. 3, and can be used to save computational time.

3. Numerical example

The grating problem analyzed here is shown in Fig. 1. The incident medium is air and the substrate is a highly absorbent metal, with a optical index 0.22+j6.71. The incident wavelength, grating depth and period are equal to 1 μm. The fill factor is 0.5. The diffraction geometry correspond a 30° angle of incidence, a 30° azimuthal angle, and a 45° angle between the electric-field vector and the plane of incidence (α = 30°, δ = 30°, and ψ = 45°). In Fig. 2 the diffraction efficiencies of the negative first- and zeroth-order are shown as a function of the number of retained orders. The solid lines are obtained with the conventional formulation of Eq. (57) in Ref. 3, and the dotted lines are obtained with the new eigenvalue formulation. We first note that the conventional formulation provides slow (oscillating) convergence-rates. We also note that the new formulation provides faster and smoother convergence-rates. For example, for the zeroth-order diffracted plane wave, the numerical values of the diffraction efficiencies are 10.58%, 10.11%, 10.08% and 10.07% when 25, 51, 75, and 125 orders are retained with the new formulation. With the conventional formulation, the corresponding diffraction efficiencies are 1.38%, 7.70%, 8.99%, and 9.42%.

We conclude that the new formulation with 25 retained orders provides more accurate results than the conventional formulation with 125 retained orders. The improved convergence rates illustrated in Fig. 2 is not an isolated case. All our simulation results show an improvement even for dielectric and non-lamellar gratings, and for small or large period-to-wavelength ratios. Two other cases are reported in Ref. 4. Also in Ref. 4, an interpretation of the convergence-rate improvement is provided by considering the eigenvalue problem in the quasi-static limit, where the grating period is very small compared to the wavelength.

For a given reasonable accuracy, the new eigenproblem formulation saves considerable time and computer memory since fewer orders have to be retained. This is especially true when arbitrary profile-surfaces are approximated by a stack of lamellar gratings, or when several grating depths are studied for a given diffraction problem. We hope that this new formulation will be helpful when analyzing grating diffraction problems with RCWA.

This work was supported by the Direction Générale de l'Armement for financial support under contract DRET-DGA # 94-1123 and by the U.S. Army Research Office.

References

[1] M.G. Moharam and T.K. Gaylord, "Rigorous coupled-wave analysis of grating diffraction - E-mode polarization and losses", J. Opt. Soc. Am. **73**, 451-455 (1983).

[2] L. Li and C.W. Haggans, "Convergence of the coupled-wave method for metallic lamellar diffraction gratings", J. Opt. Soc. Am. A **10**, 1184-1189 (1993).

[3] M.G. Moharam, E.B. Grann and D.A. Pommet, T.K. Gaylord, "Formulation for stable and efficient implementation of the rigourous coupled-wave analysis of binary gratings", J. Opt. Soc. Am. A **12**, 1068-1086 (1995).

[4] Ph. Lalanne and G.M. Morris, "Highly improved convergence of the coupled-wave method for TM polarization", accepted for publication in JOSA A.

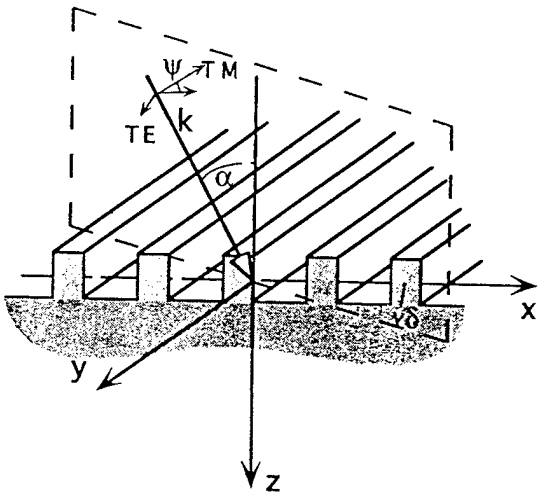


Fig. 1 Geometry for the conical grating diffraction problem analysed in this paper ($\alpha = 30°$, $\delta = 30°$ and $\psi = 45°$). The grating parameters are given in Section 3.

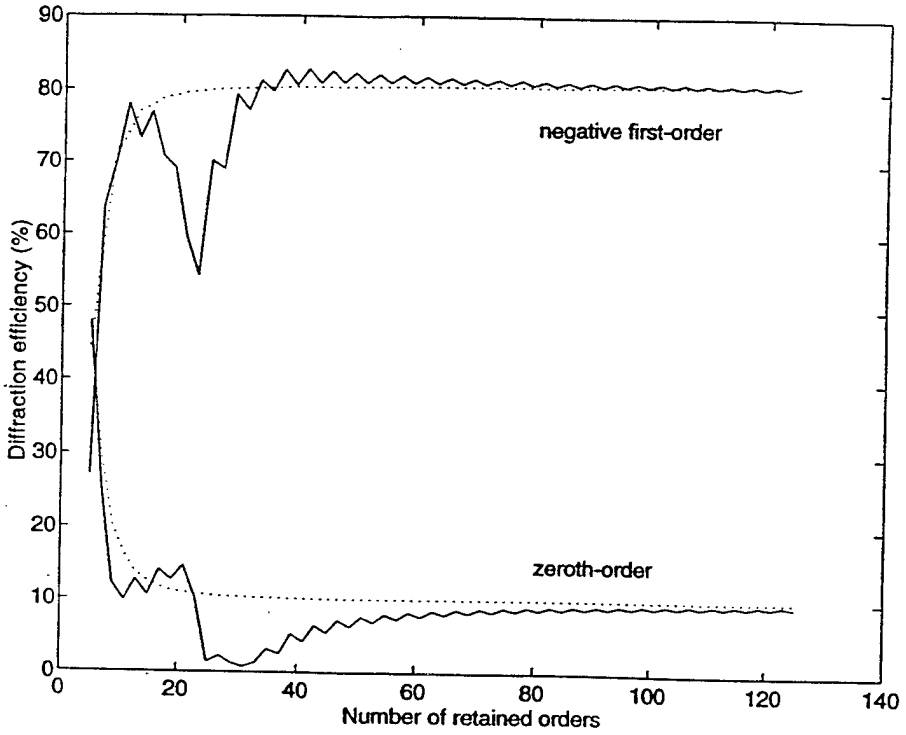


Fig. 2 Diffraction efficiencies of the reflected negative first- and zeroth-orders of the metallic grating of Fig. 1. The solid lines are obtained with the conventional eigenproblem formulation of Ref. 3. The dotted lines are obtained with the new formulations of Eqs. (1) or (2).

Mathematical Justification for the Recent Improvement of the Modal Method by Fourier Expansion

Lifeng Li
Optical Sciences Center, University of Arizona, Tucson, Arizona 85721
Tel: (520) 621-1789, Fax: (520) 621-4358

1. Introduction

Recently, Lalanne and Morris[1], and Granet and Guizal[2] numerically achieved dramatic improvement in the convergence rate of the modal method by Fourier expansion (MMFE, also called the coupled-wave method) for metallic gratings in TM polarization by reformulating the algebraic eigenvalue problem. Figure 1 shows a numerical comparison between the old and new formulations for a case studied in Ref. 3. Their work convincingly proved that the cause of the slow convergence of the MMFE is not the use of the Fourier series but the way in which the Fourier series of the permittivity and reciprocal permittivity functions are used.

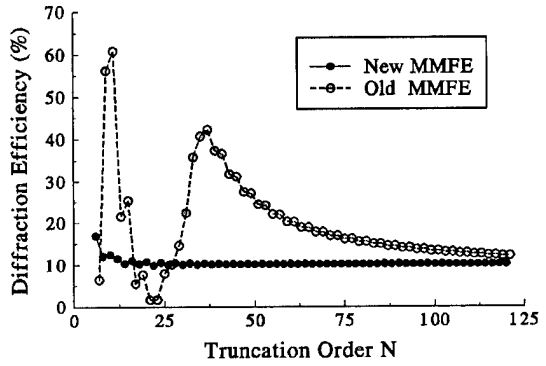


Fig. 1 Comparison between the new and old formulations of the MMFE.

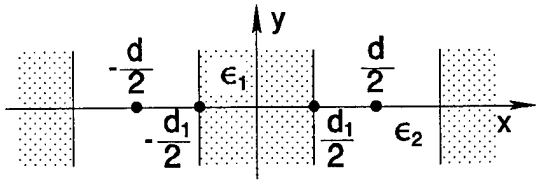


Fig. 2 A periodic, piecewise-constant medium.

In the old formulation, one solves the second order differential system[4] [the Gaussian system of units, the coordinate system of Fig. 2, and the time dependence $\exp(-i\omega t)$ are used in this paper]

$$\frac{d^2 H_{zn}}{dy^2} = \sum_m \epsilon_{n-m} \sum_p \left(\alpha_m \left[\frac{1}{\epsilon} \right]_{m-p} \alpha_p - \mu_0 k_0^2 \delta_{mp} \right) H_{zp}. \tag{1}$$

Here, k_0 is the vacuum wavenumber, $\mu_0 = 1$, δ_{mp} is the Kronecker symbol, ϵ_n and $[1/\epsilon]_n$ are the Fourier coefficients of the permittivity and reciprocal permittivity functions, H_{zn} is the y dependent Fourier coefficient of the magnetic field, and $\alpha_n = \alpha_0 + n K$, with $K = 2\pi/d$ and α_0 being the Floquet exponent. In the new formulation, one solves[1,2]

$$\frac{d^2 H_{zn}}{dy^2} = \sum_m \left[\left[\frac{1}{\epsilon} \right] \right]^{-1}_{nm} \sum_p \left(\alpha_m [\![\epsilon]\!]^{-1}_{mp} \alpha_p - \mu_0 k_0^2 \delta_{mp} \right) H_{zp}, \tag{2}$$

where $[\![f]\!]$ denotes a matrix generated by the Fourier coefficients of f such that its (n,m) entry is f_{n-m}, and -1 denotes matrix inverse. Thus, the only difference between the new and old formulations is the manner in which the permittivity function appears in the equations: the new formulation uses $[\![1/\epsilon]\!]^{-1}$ and $[\![\epsilon]\!]^{-1}$ instead of $[\![\epsilon]\!]$ and $[\![1/\epsilon]\!]$, respectively. It should be mentioned

that there is another version of the old formulation, recently presented by Moharam *et al.*[5], in which the matrix $[\![1/\epsilon]\!]$ in Eq. (1) is replaced by $[\![\epsilon]\!]^{-1}$:

$$\frac{d^2 H_{zn}}{dy^2} = \sum_m \epsilon_{n-m} \sum_p \left(\alpha_m [\![\epsilon]\!]^{-1}_{mp} \alpha_p - \mu_0 k_0^2 \delta_{mp} \right) H_{zp} . \tag{3}$$

The authors of Refs. 1 and 2 did not provide any answer to the question: what is the fundamental difference between the two formulations? They also did not say how they discovered the new equation. Indeed, their discovery appears all too accidental or empirical.

In this paper, I prove that the reason for the success of the new formulation is that it uniformly preserves the continuity of the appropriate field components across the discontinuities of the permittivity function; by inference, the old formulations do so only nonuniformly. I will provide the mathematical basis for the new formulation. Furthermore, I will describe the correct procedures for Fourier-analyzing the electromagnetic field components in Maxwell's equations such that the required field continuity is preserved across the discontinuities of the permittivity function.

2. Mathematical Theorems

All functions in this section are assumed to be periodic in x with periodicity d. For convenience I assume that all piecewise continuous functions have only one jump in $[0,d)$. The generalization of the results given below to functions having a finite number of jumps is straightforward. Two piecewise continuous functions, $f(x)$ and $g(x)$, are said to have a pair of concurrent jumps at x_0 if

$$\begin{aligned} f(x_0 + 0) - f(x_0 - 0) &\neq 0, \\ g(x_0 + 0) - g(x_0 - 0) &\neq 0. \end{aligned} \tag{4}$$

The jumps are said to be complementary if

$$f(x_0 - 0)\, g(x_0 - 0) = f(x_0 + 0)\, g(x_0 + 0) . \tag{5}$$

As in Section 1, a function name with an integer subscript is used to denote a Fourier coefficient of that function. The Fourier series of the function $f(x)$ is denoted by $S(f,x)$, which is not necessarily equal to f. The partial sum of the first N terms (from $-N$ to N) of $S(f,x)$ is denoted by $S_N(f,x)$. Fourier factorization means the expression of the Fourier coefficient of a product in terms of the Fourier coefficients of its factors. The following results are stated without proof (please see Ref. 6 for the proofs).

Theorem 1 (Fourier factorization of a product of a continuous function and a piecewise continuous function) *If both $f(x)$ and $g(x)$ are piecewise smooth and at least one of them, say $g(x)$, is continuous everywhere, then the Fourier coefficient of $h(x) = f(x)\, g(x)$ is given by the Cauchy product of $\{f_n\}$ and $\{g_n\}$:*

(*Rule* 1)
$$h_n = \sum_m f_{n-m} g_m . \tag{6}$$

Theorem 2 *If functions f and g are piecewise smooth with a pair of concurrent jumps at x_0, and the trigonometric series generated by the formal multiplication of $S(f,x)$ and $S(g,x)$ converges, then the convergence of the resultant series is nonuniform in the neighborhood of x_0, and*

$$h_n \neq \sum_m f_{n-m} g_m , \tag{7}$$

where h_n is the Fourier coefficient of $h(x)$ that is defined by

$$h(x) = \begin{cases} f(x)\,g(x), & x \neq x_0; \\ \frac{1}{2}[f(x_0+0)\,g(x_0+0) + f(x_0-0)\,g(x_0-0)], & x = x_0. \end{cases} \tag{8}$$

Theorem 3 (Fourier factorization of a product of two functions with complementary jumps) *If functions f and g satisfy the conditions of Theorem 2 and their jumps at x_0 are complementary, then the conclusions of Theorem 2 hold. Furthermore, if $f(x) \neq 0$ for $x \in [0,d)$, then*

(*Rule* 2)
$$h_n = \sum_m \left[\!\left[\frac{1}{f} \right]\!\right]^{-1}_{nm} g_m . \tag{9}$$

Corollary *If $f(x)$ is a piecewise smooth function having a finite number of jumps in $[0,d)$, then*

$$[\![f]\!]^{-1} \neq \left[\!\left[\frac{1}{f} \right]\!\right]. \tag{10}$$

To demonstrate the practical significance of the abstract mathematical results, I provide the following example. Let

$$f(x) = \begin{cases} A \\ \\ B \end{cases}, \qquad g(x) = \begin{cases} \frac{2C}{d_1}\,|x|, & |x| < d_1/2, \\ D\,\frac{d - 2|x|}{d - d_1}, & d_1/2 < |x| \leq d/2. \end{cases} \tag{11}$$

Furthermore, let us assume that $A \neq B$, $AC = BD \neq 0$; therefore, f and g have complementary jumps at $x = \pm d_1/2$, and $h(x)$ as defined by Eq. (8) is continuous. Figure 3 shows the three functions in three different line thicknesses. Figure. 4 contains two close-up plots of $S_N(h,x)$ in the neighborhood of $x = d_1/2$. The oscillatory curve is obtained using h_n given by Eq. (6). The nonuniform, slow convergence and the deviation from $h(x)$ at $x = d_1/2$ is quite prominent. In contrast, the non-oscillatory line is computed using h_n given by Eq. (9). The convergence is fast and uniform, and continuity of $h(x)$ at $x = d_1/2$ is perfectly preserved.

If the three types of products $f(x)\,g(x)$ with which Theorems 1, 3, and 2 are concerned are referred to as products of type 1, 2, and 3, respectively, then the mathematical results of this section can be summarized as follows:

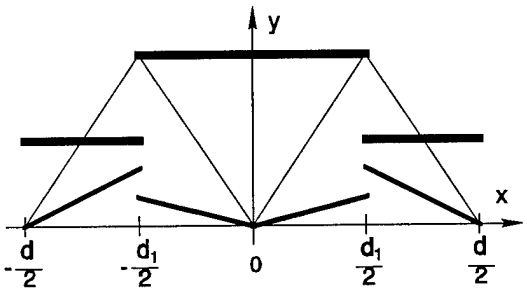


Fig. 3 Schematic representations of functions $f(x)$ and $g(x)$ in Eq. (11) and their product $h(x)$, in order of decreasing line thickness.

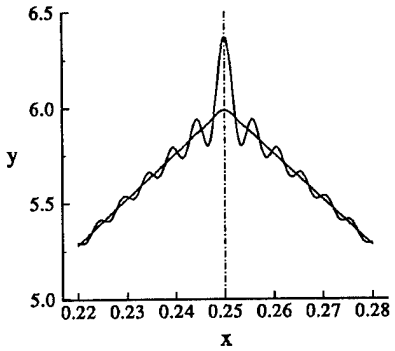


Fig. 4 Plots of $S_N(h,x)$ in the neighborhood of the discontinuity at $x = d_1/2$. Here, $N = 200, d = 1$, $d_1 = 0.5, A = 6, B = 3, C = 1$, and $D = 2$.

(1) A product of type 1 (two piecewise smooth functions, of which at least one is continuous) can be Fourier factorized by Rule 1 (the Cauchy rule).
(2) A product of type 2 (two piecewise smooth functions with a pair of complementary jumps) can be Fourier factorized by Rule 2, but not by Rule 1.
(3) A product of type 3 (two piecewise smooth functions with a pair of concurrent but non-complementary jumps) cannot be Fourier factorized.

3. Application to the Grating Problem

The x-dependent equation corresponding to Eqs. (1) through (3) is

$$-\frac{\partial^2 H_z}{\partial y^2} = \epsilon\left[\frac{\partial}{\partial x}\left(\frac{1}{\epsilon}\frac{\partial H_z}{\partial x}\right) + \mu_0 k_0^2 H_z\right]. \tag{12}$$

Now, a reader, well-equipped with the mathematical theory of Section 2, can immediately see why Eqs. (1) and (3) are incorrect and why Eqs. (2) is correct. Based on the physics, we know that $(1/\epsilon)(\partial H_z/\partial x)$ and the entire right hand side of Eq. (12) are continuous. Since ϵ is discontinuous at $x = \pm d_1/2$, the two products must both be of type 2. Equations (1) and (3) are incorrect because they derive from the application of the factorization Rule 1 to at least one of the type 2 products. In contrast, Eq. (2) is correct because it derives from the application of the factorization Rule 2 to both of the type 2 products. Note that there is no ambiguity in the way that Eq. (12) can be Fourier analyzed. For example, suppose that the right hand side of Eq. (12) is multiplied out to yield two or more terms, then there will be terms that are products of type 3, which cannot be Fourier factorized.

Based on the above and many other examples, the procedure for Fourier analyzing Maxwell's equations that contain a discontinuous permittivity function can be summarized as follows:

(1) From the basic Maxwell's equations, derive the coupled first order equations or the second order equation in terms of the vector field component(s) of interest.
(2) Arrange the resulting equation(s) in such a way that the combinations of the permittivity function and the field components form products of type 1 and type 2 only; avoid type 3 products.
(3) Substitute the Fourier coefficients for the field components that are not multiplied or divided by the permittivity function, and apply the factorization rules 1 and 2 to the products of type 1 and 2, respectively.

4. Conclusion

The significance of this paper is by no means limited to the MMFE. In a broad sense, any numerical work that requires the Fourier analysis of a product of two periodic functions with complementary jumps could benefit. In particular, this research may have an important implication to the classical differential method for gratings. The lesson learned from this research is that, in converting Maxwell's equations in spatial variables to equations in the discrete Fourier space, one cannot blindly substitute the Fourier series of every term and every factor into the spatial equations; appropriate factorization rules must be applied when discontinuities are present in the factors of the products.

References

1. P. Lalanne and G. M. Morris, J. Opt. Soc. Am. A (to be published).
2. G. Granet and B. Guizal, J. Opt. Soc. Am. A (to be published).
3. L. Li and C. W. Haggans, J. Opt. Soc. Am. A **10**, 1184 (1993).
4. K. Knop, J. Opt. Soc. Am. **68**, 1206 (1978).
5. M. G. Moharam *et al.* J. Opt. Soc. Am. A **12**, 1068 (1995).
6. L. Li, "Use of Fourier series in the analysis of discontinuous periodic structures," J. Opt. Soc. Am. A (to be published).

Monday, April 29, 1996

Micro-Optics Fabrication

DMB 10:30 am-12:00 m
Gardner A&B

Jurgen Jahns, *Presider*
Fern University of Hagen, Germany

Aberration-corrected etched microlens arrays

Keith Mersereau, Casimir R. Nijander, Wesley P. Townsend, Avi Y. Feldblum
AT&T Bell Laboratories Engineering Research Center
P. O. Box 900
Princeton, NJ 08542-0900

ABSTRACT

Refractive microlens arrays can be made through reactive ion etching of melted photoresist microlenses. We report fabrication of fused silica microlens arrays with reduced aberration by controlling the relative etch rates of silica and photoresist. An example is presented and implications are discussed.

1. Etched Microlens Arrays

Fabrication of photoresist microlenses and microlens arrays has been known for several years.[1,2,3,4,5,6] Researchers have also reported reactive ion etching or ion milling of these into substrates such as fused silica and silicon.[7,8,9,10,11,12]

Since 1989, AT&T has been making refractive microlens arrays at the Bell Laboratories Engineering Research Center. Most of these arrays are made of fused silica. Lenses made range in size from 10 to 400 microns diameter with F-numbers from about F/1.5 to F/6.

The general process for making these microlens arrays is illustrated in Figure 1. Positive photoresist is patterned in the desired array pattern, resulting in an array of photoresist "pill boxes." The wafer is then heated until the resist melts, forming a nearly spherical shape. These photoresist microlenses can be themselves used as lenses, but if a more rugged material is desired, the pattern can be transferred into fused silica (or another material) using reactive ion etching (RIE).

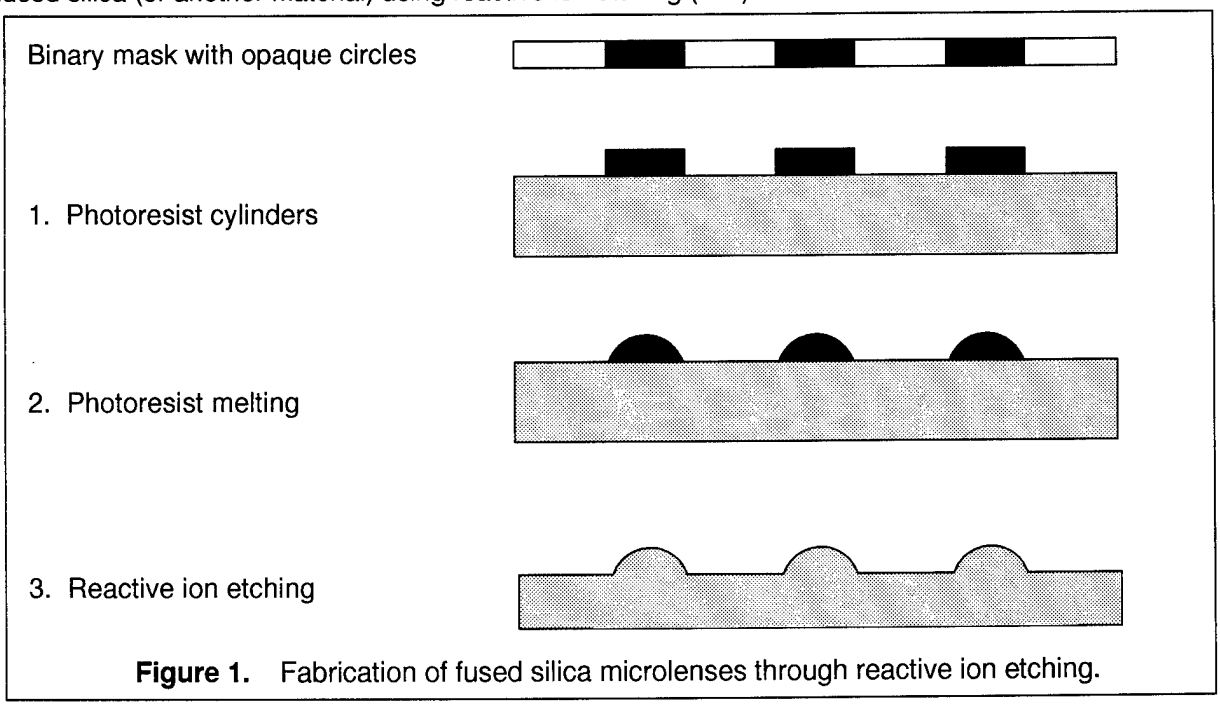


Figure 1. Fabrication of fused silica microlenses through reactive ion etching.

We have found that the process of reactive ion etching introduces aberration into microlenses. For some applications, such as free-space optical interconnect, the level of this aberration (often greater than 1 wave OPD at 633 nm) is unacceptable. Therefore we report a method for correcting this aberration by controlling the reactive ion etching process.

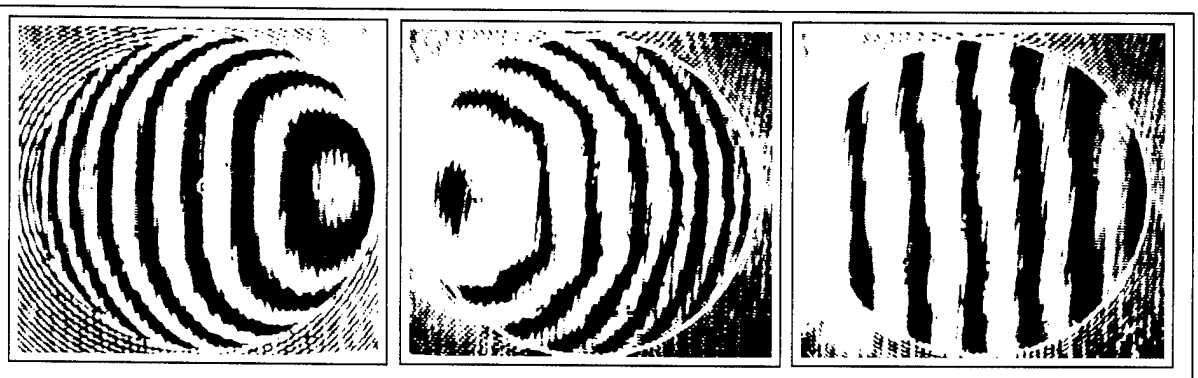
2. Aberration Correction

Our method of aberration reduction is to adjust the etch rates of photoresist and silica during the etching process. By etching the resist faster than the SiO_2, one obtains a "flatter" (and therefore slower) lens. By etching the resist more slowly, we get a "taller" (and faster) lens. We can use these two effects to shape our microlenses by, for example, etching the resist faster than the SiO2 at the beginning of the etch to "slow down" the lens edge and etching the resist more slowly toward the end of the etch to "speed up" the center of the lens.

An example is shown in Figure 2. Figure 2 (a) shows the Mach-Zehnder interferogram[13,14,15] from a 230 μm diameter microlens etched into fused silica with a nominal 1:1 etch ratio, meaning that the lens height after etching is nearly the same as the lens height in photoresist (before etching). This is accomplished by etching for 740 minutes with 3.6% oxygen and 96.4% CHF_3 based on volume. The interferometer fringe pattern indicates that this microlens has about one and one-half waves of optical path difference (OPD) wavefront aberration, peak-to-valley. The fringe shape is characteristic of spherical aberration.

For demanding applications such as free-space optical interconnect, this degree of aberration is unacceptable. To reduce the aberration, we need to etch the photoresist more quickly at the beginning of the etch than at the end. We elected to etch in three steps, starting with high oxygen and ending with lower oxygen. In Figure 2 (b), we show the result of etching 5.3% oxygen for 280 minutes, 4.4% for 320 minutes, and 3.6% for 400 minutes. The lens is almost as badly aberrated as in the previous case, but in the opposite direction. This is akin to overcorrected spherical aberration compared to undercorrected (in the Fig. 2a case). However, the aberration looks less like pure spherical aberration because there are sharp discontinuities in the fringe pattern. These are present because of the sudden changes in etching gas composition.

Figure 2 (c) shows the interferogram resulting from a microlens etched at 4.7% oxygen for 280 minutes, 4.1% for 320 minutes, and 3.6% for 400 minutes. This lens appears to have less than one-quarter wave of aberration. The radius of curvature for this lens is about 250 μm, for a focal length of 547 μm (F/2.4) at a wavelength of 633 nm.



(a) (b) (c)

Figure 2. Mach-Zehnder interferograms from (a) uncorrected, (b) overcorrected, and (c) well-corrected RIE-etched microlenses.

3. Conclusions

The example above illustrates the way we have made aberration-corrected microlens arrays. Microlenses made in this way will be aspheric; thus one can etch the lens shape to suit the application requirements. As the example shows, using only 3 different gas ratios we can achieve quarter-wave OPD results. In practice, one would make a better lens by making continuous RIE gas composition changes. One can also alter etch rates to achieve effects other than aberration correction, such as to adjust the focal length of the resulting microlenses.

The advantage of this method is its great flexibility in creating the desired microlens shape.

4. References

1. O. Wada, "Ion Beam Etching of InP and Its Application to the Fabrication of High Radiance InGaAsP/InP Light Emitting Diodes," *J. Electrochem. Soc.* **131**(10), 2373-2380 (1984).

2. Z. D. Popovic, R. A. Sprague, and G. A. N. Connell, "Technique for the Monolithic Fabrication of Microlens Arrays," *Applied Optics* **27**(7), 1281-1284 (1984).

3. M. C. Hutley, "The Manufacture and Testing of Microlens Arrays," *Optics in Complex Systems*, F. Lanzl, H.-J. Preuss, G. Weigelt, Eds., *Proc. SPIE* **1319**, 492-493 (1990).

4. T. R. Jay, M. B. Stern, and R. E. Knowlden, "Effect of Refractive Microlens Array Fabrication Parameters on Optical Quality," *Proc. SPIE* **1751**, 236-245(1992).

5. T. R. Jay and M. B. Stern, "Preshaping Photoresist for Refractive Microlens Fabrication," *Proc. SPIE* **1992**, 275-282 (1993).

6. D. R. Purdy, "Fabrication of Complex Micro-Optic Components Using Halftone Transmission Masks to Photosculpt Positive Resist," *Microlens Arrays*, M. C. Hutley, Ed., *European Optical Society Topical Meetings Digest Series* **2**, 20-25 (1993).

7. K. Mersereau, C. Nijander, A. Feldblum, and W. Townsend, "Fabrication and Measurement of Fused Silica Microlens Arrays," *Proc. SPIE* **1751**, 229-233 (1992).

8. J. Schwider, et al., "Production and Control of Refractive and Diffractive Microlenses," *Proc. SPIE* **1992**, 102-113 (1993).

9. M. B. Stern and T. R. Jay, "Dry Etching -- Path to Coherent Refractive Microlens Arrays," *Proc. SPIE* **1992**, 283-292 (1993).

10. E. J. Gratrix, "Evolution of a Microlens Surface Under Etching Conditions," *Proc. SPIE* **1992**, 266-274 (1993).

11. H. Sankur, E. Motamedi, R. Hall, W. J. Gunning, and M. Khoshnevisan, "Fabrication of Refractive Microlens Arrays," *Proc. SPIE* **2383**, 179-183 (1995).

12. P. Savander, "Microlens Arrays Etched into Glass and Silicon," *Optics and Lasers in Engineering* **20**, 97-107 (1994).

13. M. C. Hutley, D. Daly, and R. F. Stevens, "The Testing of Microlens Arrays," *Microlens Arrays*, M. C. Hutley, Ed., *Institute of Physics Short Meetings Series* **30**, 67-81 (1991).

14. D. Daly and M. C. Hutley, "Microlens Measurement at NPL," *Microlens Arrays*, M. C. Hutley, Ed., *European Optical Society Topical Meetings Digest Series* **2**, 50-54 (1993).

15. K. Mersereau, R. J. Crisci, C. R. Nijander, and W. P. Townsend, "Testing and Measurement of Microlenses," *Proc. SPIE* **1992**, 210-215 (1993).

Microlens arrays formed by crossed thin-film deposition of cylindrical microlenses

R. Grunwald, R. Ehlert, S. Woggon, H.-J. Pätzold, H.-H. Witzmann

Gesellschaft zur Förderung angewandter Optik, Optoelektronik, Quantenelektronik und Spektroskopie e.V. (GOS), Labor für Mikrooptik und Laserstrahlformung
Rudower Chaussee 5 (im IGZ), 12489 Berlin, Federal Republic of Germany
phone / fax: (030) 6392 1453, email: grunwald@mbi.fta-berlin.de

1. INTRODUCTION

Crossed 1D patterning allows to generate regular 2D optical microstructures like refractive microlens arrays with high fill factors which are of interest for photonics and laser applications (image sensing / processing, coupling, beam shaping, mode selection **[1]**). In general, a surface can be treated sequentially or simultaneously by *(a)* subtractive, *(b)* additive or *(c)* modifying processes thus forming a deepened or elevated relief or a periodically changed refractive index. *Type (a)* has been published for excimer laser ablation by means of crossed linear scans with laser spots or contour masks **[2]** and by direct writing laser lithography with two subsequent (crossed) exposures by linear intensity arrays followed by a tranfer into the substrate by ion etching **[3]**. Problems emerge from the unwanted deposition of debris, nonlinearities and the necessary control of the laser beam quality during a sufficiently long time. A well-known approach is the holographic method of *Cowan* **[4,5]** with three beam interference in a recording photoresist medium. By this method, high-definition, replicable hexagonal hole arrays with extremely small element diameters have been found. On the other hand, the set-up is not flexible enough for a fast change of the geometry and requires a proper adjustment, a homogeneous beam and the knowledge of the nonlinearities. Direct changes of the refractive index (e.g. in photorefractive media) can be used for a process of *type (b)*. We report on an alternative, relatively simple technology of *type (c)* for the fabrication of close-packed arrays (orthogonal, hexagonal) based on the crossed vapour deposition which is preferentially suitable for moderate microlens parameters (pitches, focal lengths).

2. FABRICATION METHOD

Thin-film components of periodically modulated phase and/or reflectance profiles (microlens/ micro-mirror arrays) can be produced by 3D or multiple mask shading in a vacuum deposition apparatus with electron beam vaporizer (schematically in **fig.1**) **[1,6]**. A computer code has been developed to simulate the geometrical conditions which are defined by the substrate position on a rotating substrate mount, the distance between the plane of substrate movement and source, the angular characteristics of the vaporizer, mask distance, shape and profile of the mask. In the simplest case, slit masks with parallel, perpendicular walls have been used. By exploiting the additional degree of freedom of the depth of the mask, the thickness profile can be optimized to fit a parabolic function, as we could show theoretically and experimentally. By shading with properly formed slit masks, linear arrays of cylindrical (nearly parabolic) microlenses can be deposited. A sequential, crossed deposition of 2 or 3 linear arrays delivers (analogous to the *type-a-* and *type-b*-technologies) orthogonal or hexagonal 2D arrays by a simple way. A scheme of the system geometry for crossed deposition is shown in **fig.2**. Contour plots of the expected thickness distributions for a 3- and 2-step deposition with optimized masks are drawn in **fig.3** and **fig.4**. In the experiments, monolithic and compound laser drilled masks with conical or stairway profiles have been rotated in angular steps of 60°

or 90°. A substrate holder with a stepwise rotatable mask has been constructed for this purpose. The overgrowths of the masks should determine the lower limit for the slit width. For sufficiently thin layers (thickness << mask dimensions), however, this effect is negligible. Limitations by the mechanical properties of the layers arise from the (by a factor 2 or 3) higher maximum thicknesses, compared with a 1-step un-crossed deposition through hole masks.

3. RESULTS

First experiments to produce periodical (orthogonal and hexagonal, refractive and/or reflective) SiO_2 and/or HfO_2 structures of high fill factors by crossed deposition have been realized successfully. A micrograph of a part of a linear array with 50 x 50 cylindrical microlenses (HfO_2 layer on BK7 substrate, 500 μm pitch, f = 11 mm) measured with an UBM laser diode profilometer is shown in **fig.5**. The result of a 2-step crossed deposition (0°+90°, SiO_2 on quartz) is demonstrated in **fig.6** and the intensity pattern of a laser beam in the focal plane of a lenslet array with a very long focal length and a small numerical aperture (f = 80 mm, NA = $5*10^{-3}$) in **fig.7**. The minimum generated pitch (element diameter) was about 100 μm. Despite of the high geometrical fill factor (nearly 100 %), we found that an effective fill factor has to be defined by the optical properties. A further enhancement of the array quality by improved masks is under investigation. UV-laser resistant arrays and the deposition of thin-film microoptics on polymer substrates have been tested **[7]**.

4. CONCLUSIONS

Crossed deposition of linear thin-film arrays in a rotating vacuum deposition system with shading slit mask arrays has been shown to be a relatively simple method to manufacture 2D microoptical arrays (microlenses, micromirrors) of different structure with high fill factors. Limitations are given by the accuracy of mask geometry and positioning, mask overgrowth and maximum layer thickness. The thickness profile functions of the lenslets can be controlled by using multiple or extended (3D) masks. A computer simulation of the vapour deposition geometry allows to optimize the mask parameters. The method of crossed deposition works in the diameter range 100...500 μm for slits with a length-to-width ratio of 50:1.

5. REFERENCES

[1] R. Grunwald, U. Griebner, R. Ehlert, S. Woggon: Micro-optical array components for novel-type lasers and artificial compound eyes. - National Workshop on Microlens Arrays, National Physical Laboratory, Teddington, May 11-12, A4, pp. 85-88 (1995).

[2] K. Zimmer, F. Bigl: 3D-Strukturierung von Polymeren durch Excimerlaserablation. - 11. International Symposium "Quality and Information Management", Mittweida, Hochschule für Technik und Wirtschaft Mittweida, November 24-26, 1994.

[3] G. Przyrembel: Continous-relief microoptical elements fabricated by laser beam writing. - Micro System Technologies '94, Berlin, October 19-21, 1994, pp. 219-228.

[4] J. J. Cowan: The holographic honeycomb microlens. - Proc. SPIE Vol. **523**, pp. 251-259 (1985).

[5] N. J. Phillips, Ch. A. Barnett: Micro-optic studies using photopolymers. - Proc. SPIE Vol. **1544**, pp. 10-21 (1991).

[6] R. Grunwald, U. Griebner, D. Schäfer: Graded reflectivity micro-mirror arrays. - Proc. SPIE Vol. **1983**, pp. 49-50 (1993).

[7] R. Grunwald, R. Ehlert, S. Woggon, H.-H. Witzmann: Thin-film microlens arrays on flexible polymer substrates. - submitted to Micro System Technologies 1996.

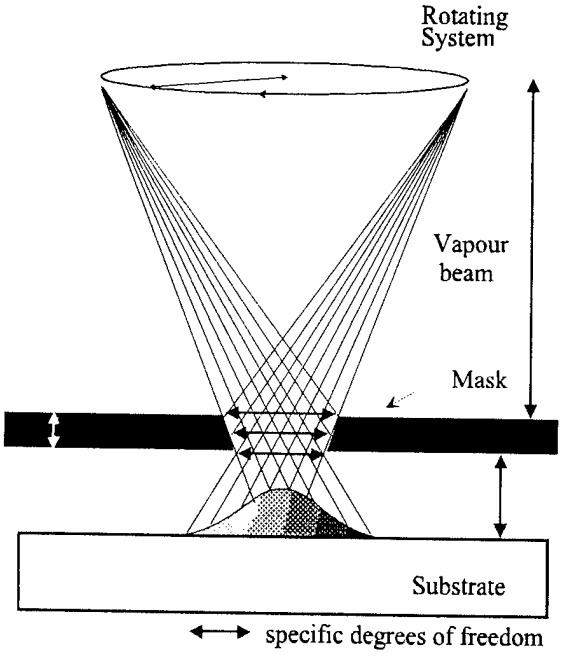


Fig. 1: Deposition of thickness modulated layers through thick shading masks (schematically)

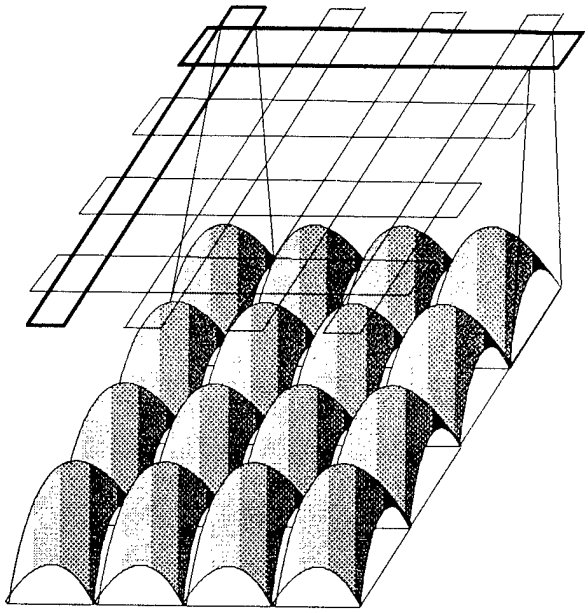


Fig. 2: Crossed deposition of linear arrays of cylindrical microlenses (schematically)

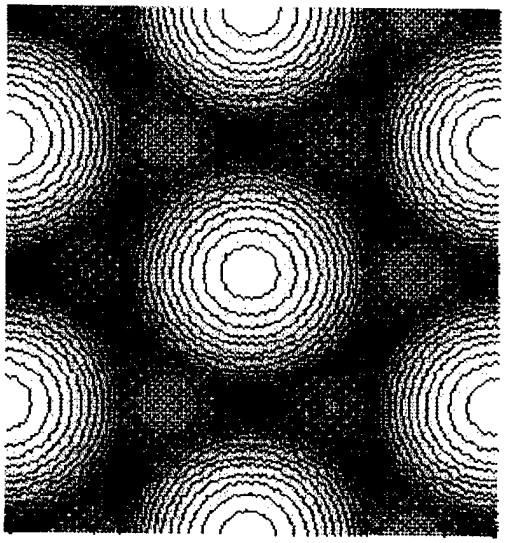


Fig. 3: Calculated thickness distribution for a hexagonal array structure generated by a 3-step deposition with optimized slit masks (0°+60°+120°)

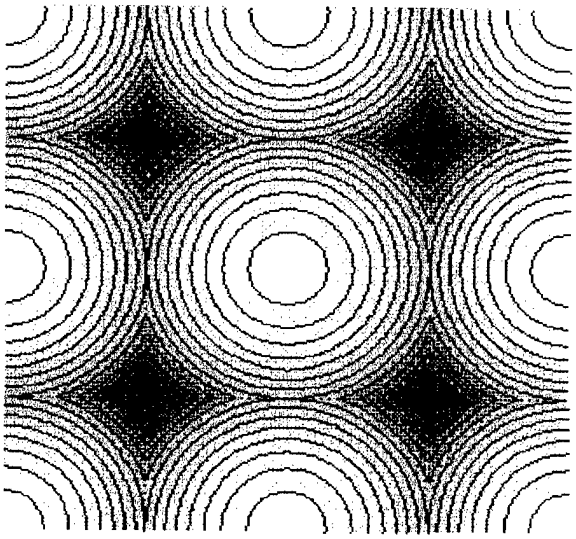


Fig. 4: Calculated thickness distribution for a orthogonal array structure generated by a 2-step deposition with optimized slit masks (0°+90°)

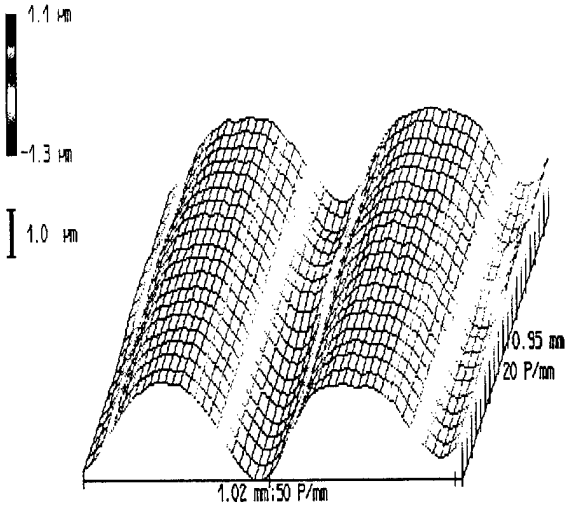


Fig. 5: Thickness profile of a part of a 1D thin-film array of cylindrical microlenses (measured with UBM laser diode profilometer)

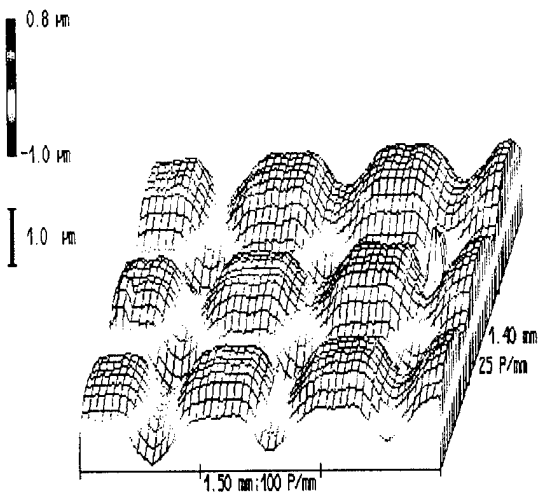


Fig. 6: Thickness profile of a part of a 2D thin-film microlens array fabricated by crossed deposition (measured with UBM laser diode profilometer)

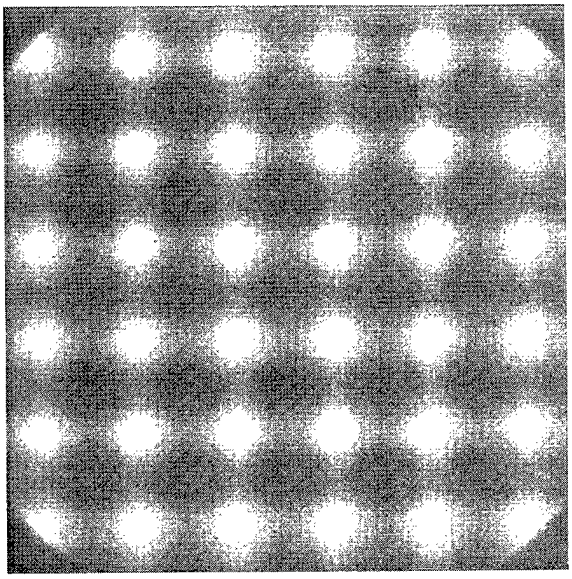


Fig. 7: Intensity distribution in the focal plane of a microlens array (crossed cylindrical microlenses, 50 x 50 elements, 500 mm pitch, SiO_2 on quartz substrate) monitored by a CCD camera

Single Step Fabrication of Glass Microlenses for Array and Diode Laser Applications

Neil Fromer and N. M. Lawandy
Department of Physics and Division of Engineering, Box D
Brown University, Providence RI, 02912
Tel: (401) 863-3961 Fax:(401) 863-1157 email: neil_fromer@brown.edu

Recently, a single step technique for the fabrication of microlenses was reported, in which a laser induced thermal runaway process caused a local melting transition near the surface of a semiconductor doped glass. [1] These microlenses were produced on time scales of a fraction of a second and in a single step, a dramatic improvement over conventional fabrication techniques, where multiple processing steps and long processing times are required. Using this method, we have produced micro -elliptical lenses and demonstrated their capability to correct the output of a diode laser. In addition, microlens arrays have been produced using diffractive spot generators to irradiate the glass. Because of heat transfer effects, this approach had to be modified to produced equivalent microlenses throughout the array. The appropriate spot grating phase mask design to generate uniform arrays has been addressed and is also discussed in the work that follows.

Elliptical Microlens Formation

The experimental setup used to fabricate the lenses is shown in figure 1. The material used was Schott RG 610 filter glass, a borosilicate glass doped with CdS_xSe_{1-x} nanocrystals, used as long pass wavelength filters with a cutoff at 610 nm. The laser used in the experiments was an Ar^{++} ion laser operating in single line mode at 514.5 nm. By focusing the argon ion laser beam with a cylindrical lens, an elliptical spot is formed on the glass. When the laser intensity is sufficiently high, absorption of the light causes a melting transition and welling up of glass in an elliptical region, creating the desired lens shape. By modifying such parameters as laser power and beam waist size a large range of different focal lengths and lens sizes can be achieved, as shown in figure 2. The elliptical lens is crudely characterized by two focal lengths; the shorter one we label $f_\perp$ and the longer one $f_{||}$. These focal lengths were readily calculated by assuming

the lens cross section along the major and minor axes to be spherical. and found to agree with the measured values to within 3%.

Diode lasers are small, inexpensive sources of laser emission. However, the output beam is elliptical, astigmatic, and rapidly diverging. Standard methods for correcting the beam involve as many as eight separate optical elements.[2] However, when one is interested in a simply producing a round beam, the fabrication method described can be used to create an elliptical microlens directly on the laser diode package, by replacing the standard output window with a semiconductor doped glass.

Using the beam divergence angles and diode chip dimensions, we calculated the position and focal lengths required to create a collimated circular output beam, using a single elliptical microlens:

$$f_{\perp} = L = \frac{d}{2\left(\tan(\theta_{\perp}) - \tan(\theta_{\parallel})\right)} \quad (1)$$

$$f_{\parallel} = L + \frac{d}{2\tan(\theta_{\parallel})} \quad (2)$$

where $f_{\perp}$ and $f_{||}$ are the half width half maximum divergence angles in the two directions, d is the width of the active (light-emitting) layer, and L is the distance between the diode and the elliptical lens required to produce a circular output beam. Once the focal lengths have been determined, the lens can be made through correct choices of power and beam size.

We are currently in the process of having several laser diodes packaged with RG 610 glass as the output window. This will allow us to manufacture a lens directly onto the diode package, correcting the beam without the need for external optics. As a feasibility study, we modeled the larger (perpendicular) divergence of the diode using single slit diffraction of a HeNe laser beam. We chose a slit width to give the same far field divergence as the diode laser, and then used the elliptical microlens to collimate the beam. The result was an almost circular output beam as seen in figure 3. The power throughput of this lens was measured to be 70%. A large amount of the power lost was due to the discrepancy between the diffracted beam's parallel divergence and $f_{||}$.

Microlens Arrays

The fabrication technique described provides an extremely rapid and low cost method for fabricating single lenses. Through the use of a binary phase mask, one can turn a single laser beam into an array of equal intensity spots, which can be focused onto the glass sample to form a microlens array.

We were able to create lens arrays ranging from an array size of 3x3 to 8x8; however, with disparate lens sizes radially distributed with the central ones being the largest. Figure 4 shows a 4x4 array of lenses produced using this technique. This simple radial pattern implies a temperature gradient created by the array of heat sources, causing the center of the array to accumulate more heat than at the sides. This effectively lowers the threshold intensity, leading to larger lenses. Using the temperature distribution function for a point source on a surface, we showed that this temperature gradient was predicted by the diffusion equation.[3]

Our models indicate that by adjusting the relative intensities and/or the spot sizes, we can correct this effect and form an array of equal sized lenses. This may be done by attenuating the power of certain spots before focusing onto the glass, using SLM technology, or by having a specially designed phase mask to give us the proper intensity distribution.

References:

[1] G. Beadie and N. M. Lawandy, Opt. Lett. **20** (21) , 2153 (1995)
[2] P L Fuhr, Appl. Optics **24**, 2820 (1985)
[3] Ready, John F., Effects of High-Power Laser Radiation, Academic Press, NY, 1971

Figures

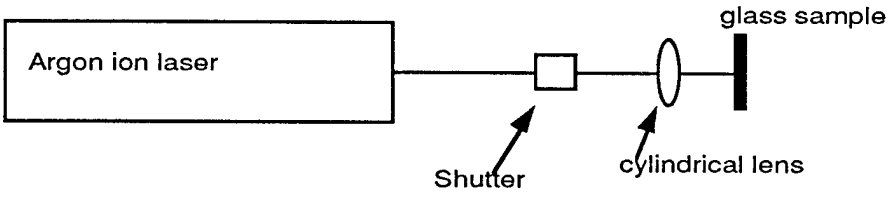
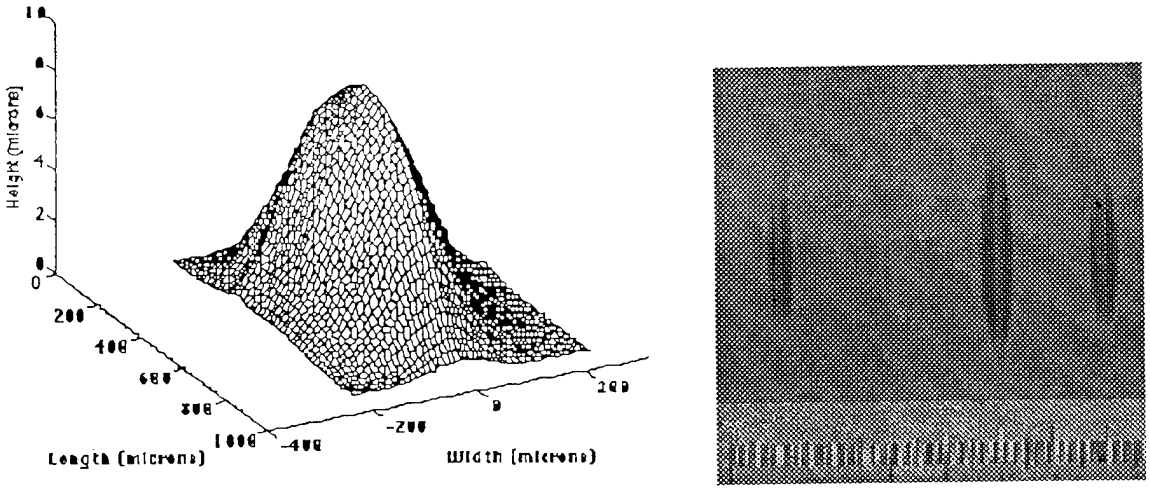
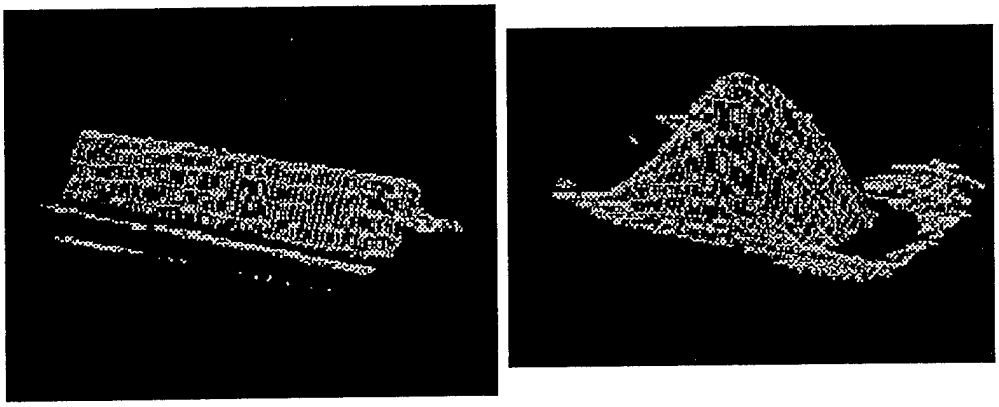


Figure 1: Experimental Setup. Additional lenses were to focus the beam through the shutter and re-collimate at a different size for some lens sizes.



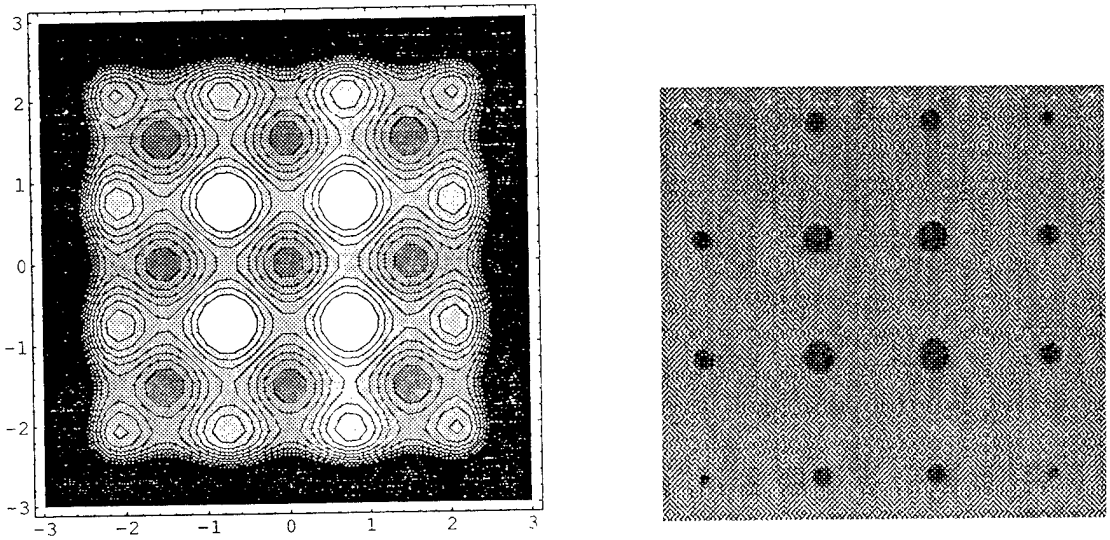
(2a) (2b)

Figure 2 Elliptical microlenses. (a) three dimensional profile of a single lens; (b): several lenses of different sizes.



(3a) (3b)

Figure 3: HeNe lsaer beam intensity profile. (3a) is the diffracted beam, and (3b) shows the same beam focused through an elliptical lens.



(4a) (4b)

Figure 4: Theoretical prediction of the heat transfer problem in microlens arrays (4a) is seen to correlate match experimental lens sizes (4b).

COMPACT MICRO-OPTICAL DIODE LASER ASSEMBLY USING MASS-TRANSPORTED LARGE-NUMERICAL-APERTURE REFRACTIVE MICROLENSES

D. Z. Tsang, Z. L. Liau, and J. N. Walpole

Lincoln Laboratory, Massachusetts Institute of Technology
Lexington, MA 02173-9108
(617) 981-4427
FAX: (617) 981-5793

The advancement of semiconductor laser materials growth and device fabrication technology has brought the cost of the laser chip well below the cost of the associated optics, precision alignment, and packaging required to effectively utilize the device in systems applications.[1] We report here a novel compact packaging approach that utilizes unique microlenses for simplified lens support and alignment. In this scheme, a microlens fabricated on a planar substrate is directly attached to the laser/heatsink to form a precision optical assembly providing a collimated (or focused) output beam. The approach is applicable to either single lasers or laser arrays.

To collimate or focus the output of semiconductor diode lasers, the microlens must be precisely aligned with regard to *xyz* translation and to tip and tilt angle. In our approach, shown in Fig. 1, a mass-transport lenslet fabricated on a planar substrate is mounted on the device to automatically reduce the number of alignment operations. For a collimated laser output, the lenslet is designed to have a focal length f equal to the substrate thickness. The lens is placed in direct contact with the laser chip and its heatsink, thereby eliminating the need for a separate lens mounting fixture. The laser can be mounted either flush with the edge or allowed to extend several micrometers beyond the heatsink, as shown.

Mass-transported GaP microlenses[2-6] are very attractive for this application because they can be made with high numerical aperture (NA) for good light-collection efficiency and because the high refractive index of GaP allows much looser tolerances for errors in the microlens fabrication or in the optical alignment. The microlens fabrication technique is illustrated in Fig. 2. A multiple-mesa preform is first etched in a GaP substrate by using precision photolithography followed by ion-beam-assisted Cl_2 etching. The lens profile is accurately encoded in the mesa-width variations in the preform [see Fig. 2(a)]. The wafer is then heat-treated at 1100°C for 20 h in a protective environment, during which vapor transport occurs for the minimization of the surface energy, and the preform smooths to become the desired microlens [see Fig. 2(b)]. One main advantage of this technique is its capability for accurate formation of almost any desired lens profile. This is best illustrated in our recent work of anamorphic microlenses[3,5] which feature two distinct curvatures for the astigmatic output of high-power lasers with a laterally tapered gain region.[7-10] With one single anamorphic microlens, the taper-laser's astigmatic output was corrected, made nearly round, and efficiently coupled into a single-mode fiber.[3,5] This is much simpler and more compact compared to the cumbersome bulk lens system. In the present work, however, more basic spherical microlenses were used for the initial demonstration of the packaging technology.

The present spherical microlenses were fabricated in two-dimensional arrays with a nominal diameter of 140 μm on a pitch of 300 μm. The lens wafer was carefully polished to a thickness of 423 μm, because these 0.46-NA lenses have a depth of focus of approximately $\pm$ 4 μm in GaP. The lens array chip was 2 mm long in the vertical direction to minimize tilt misalignment. The lenses were coated for low reflection with a quarter-wavelength thickness of SiO_2.

For this initial demonstration we used an edge-emitting 980-nm ridge-waveguide laser array with a pitch of 150 μm. The array was soldered to a heatsink using conventional die attachment techniques with attention to ensure that the solder did not flow beyond the laser output facet and interfere with subsequent lens attachment. In this case, each edge of the laser array protruded 10 mm above the heatsink and the 68-μm-thick laser chip was mounted stripe up. The lens array was actively aligned to the laser array with micropositioners. The lateral and transverse positions and the rotation of the lens array were adjusted such that each lens was centered on a laser emitter. No adjustment of the lens position along the z-axis in the direction of laser emission or of the tip and tilt angle of the lens was necessary because those are set by

the fabrication of the lens and the mounting arrangement. The lens was then attached directly to the laser heatsink with ultraviolet-curable adhesive. The heatsink is Au-coated silicon with a lapped and polished flat edge used for the lens attachment surface. The tilt of the lens relative to the heatsink can be estimated from the laser protrusion and the length of the lens array chip to be about 0.3°. In the composite infrared and visible photograph of the assembly in Fig. 3, two of the lasers are covered by a lens and are collimated, while the other two are not aligned to a lens. Far-field scans taken in the directions parallel and perpendicular to the laser junction have a full width at half-maximum of about 0.8° and 0.6° (see Fig. 4), respectively, much narrower than the far-field pattern of the laser without the lens. The far-field pattern is narrower perpendicular to the junction because the lens is more completely filled by the wider divergence of the laser in that direction.

Estimates of the effects of misalignment based on optical path length differences for this approach are encouraging. Lens aberrations and misalignments can produce optical path length differences that result in phase front distortions that are large enough to reduce coupling efficiencies to single-mode fiber. While biconvex lenses can be corrected for spherical aberration with the lens centered on the laser, significant phase front distortions can still result if the lens is laterally misaligned even slightly, e.g., 1 μm off axis. By using this approach with planoconvex lenses, the high refractive index of the GaP allows light rays to remain paraxial even at large numerical apertures, and the phase front distortion can remain small. For the lens used in this experiment, the maximum distortion in the outer regions of the lens is estimated to be no more than $\lambda/10$ over lateral misalignments of $\pm$ 10 μm. Negligible phase front distortions are important for applications such as efficient coupling to single-mode fiber.

This microlens packaging approach, which is very compact and does not require rigid external lens mounts, can reduce the number of independent axes required to align laser arrays and lens arrays in future free-space and fiber-coupled optical systems. The scheme is particularly attractive when large wafers of precise lenses can be manufactured at low cost. Applications include optical interconnects, optical computing, and lens-coupled fiber-optical systems. Work is currently under way to use the approach to align anamorphic lenses to tapered lasers[7-10] to show the feasibility of a compact optical assembly with high coupling efficiency to single-mode fiber.

This work was sponsored by the Department of the Air Force.

REFERENCES

1. See, for example, *Micro-Optics/Micromechanics and Laser Scanning and Shaping*, M.E. Motamedi and L. Beiser, eds., Proc. SPIE 2383 (1995).
2. Z. L. Liau, D. E. Mull, C. L. Dennis, R. C. Williamson, and R. G. Waarts, *Appl. Phys. Lett.* **64**, 1484 (1994).
3. Z. L. Liau, J. N. Walpole, D. E. Mull, C. L. Dennis, and L. J. Missaggia, *Appl. Phys. Lett.* **64**, 3368 (1994).
4. J. S. Swenson, Jr., R. A. Fields, and M. H. Abraham, *Appl. Phys. Lett.* **66**, 1304 (1995).
5. Z. L. Liau, J. N. Walpole, J. C. Livas, E. S. Kintzer, D. E. Mull, L. J. Missaggia, and W. F. DiNatale, *IEEE Photon. Technol. Lett.* **7**, 1315 (1995).
6. *Solid State Research Report, Lincoln Laboratory, MIT* 1994: 4, p. 1.
7. J. N. Walpole, E. S. Kintzer, S. R. Chinn, C. A. Wang, and L. J. Missaggia, *Appl. Phys. Lett.* **61**, 740 (1992).
8. D. Mehuys, D. F. Welch, and L. Goldberg, *Electron. Lett.* **28**, 1944 (1992).
9. S. H. Groves, J. P. Donnelly, J. N. Walpole, J. D. Woodhouse, L. J. Missaggia, R. J. Bailey, and A. Napoleone, *IEEE Photon. Technol. Lett.* **6**, 1286 (1994).
10. *Solid State Research Report, Lincoln Laboratory, MIT*, 1994:2, p. 8.

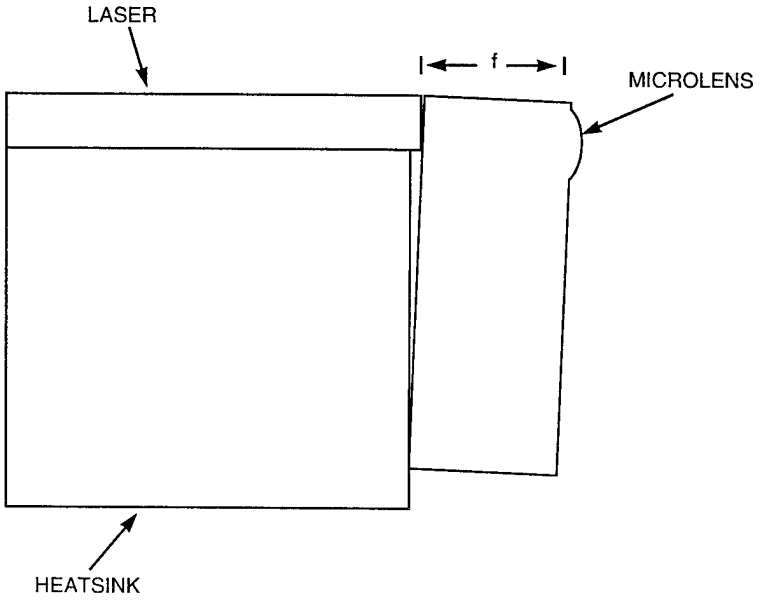


Figure 1. Diagram showing a side view of diode laser and lens assembly with direct contact between laser and lens. In this approach a microlens fabricated on a planar substrate is attached to the laser heatsink.

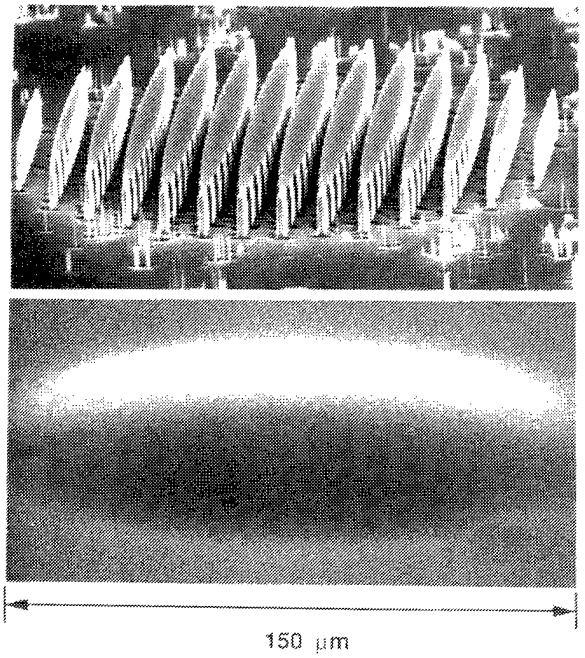


Figure 2. Fabrication of large-numerical-aperture spherical microlens in GaP substrate by mass transport. These SEM perspective views show the multiple-mesa preform (upper) defined by precision photolithography and ion-beam-assisted Cl_2 etching, and the lens formed (lower) after heat treatment at 1100°C for 20 h in a protective environment.

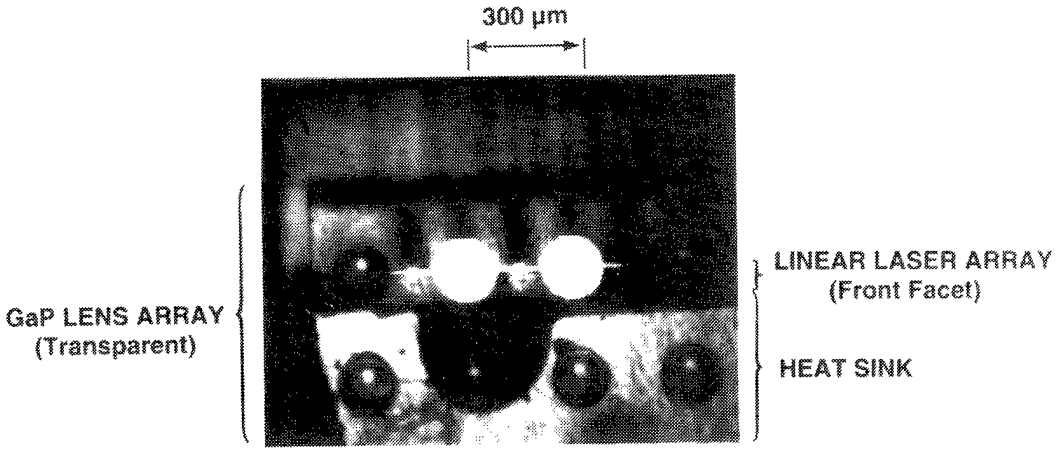


Figure 3. Photographs of head-on view of assembly in which the GaP lens array contacts the laser array. Although covered by the lens, the laser array is visible because the GaP is transparent. The lasers have twice the pitch of the lenses so that only two of the four lasers that are turned on are collimated by the lenslets.

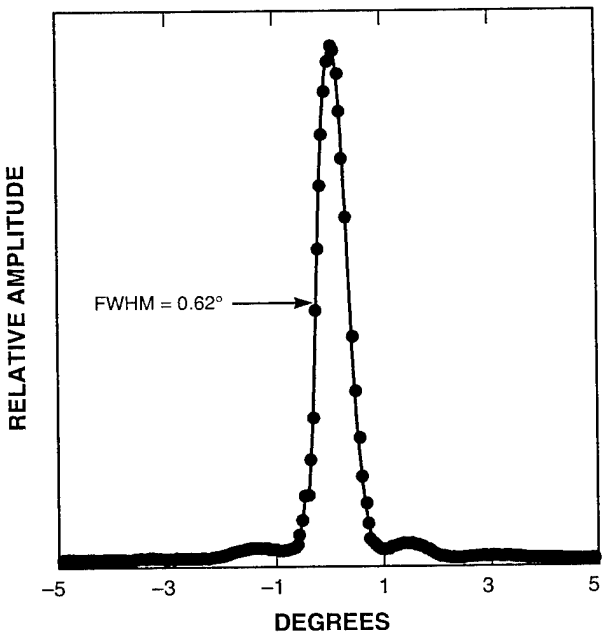


Figure 4. Far-field measurement of optical assembly perpendicular to the laser junction.

ION EXCHANGE IN GLASS FOR THE FABRICATION OF CONTINUOUS-PHASE DIFFRACTIVE OPTICAL ELEMENTS

Risto-Pekka Salmio, Jyrki Saarinen, and Henri Saarikoski
Department of Technical Physics, Helsinki University of Technology, FIN-02150 Espoo, Finland, Tel./Fax: +358 0 451 3156/3164, e-mail risto.salmio@hut.fi

Jari Turunen
Department of Physics, University of Joensuu, P.O.Box 111, FIN-80101 Joensuu, Finland

Ari Tervonen
Optonex Ltd., P.O.Box 128, FIN-02101 Espoo, Finland

Diffractive phase elements, which only modulate the phase of an incident wavefront, provide high diffraction efficiencies. Such elements can be fabricated in the form of surface-relief profiles by a variety of methods including selective etching or material deposition, and diamond turning. Binary surface-relief elements have diffraction efficiencies of the order of 30–75% depending on the symmetries of the signal, while efficiencies even in excess of 90% are only possible if one employs continuous surface profiles fabricated, e.g., by direct-write laser beam or electron-beam lithography. Then, however, accurate exposure control is needed. Continuous surface profiles can be approximated by multilevel profiles, which may be fabricated by successive lithography steps, where careful mask alignment is then required.

Gradient-index profiles are used extensively in diffractive optics. For example, all volume holograms are of this type. On the other hand, ion exchange in glass is widely applied method for the fabrication of graded-index refractive lenses and waveguide components. The benefit of gradient-index structures is a flat surface, which allows easy anti-reflection coating, cleaning, and the stacking of several elements together.

Recently we have proposed and demonstrated the fabrication of continuous-phase diffractive free-space elements by thermal ion exchange in glass [1]. This is achieved by patterning a binary metallic mask on top of a glass substrate, which is then immersed into a molten salt bath to achieve an exchange of ions between the glass substrate and an external salt source through mask apertures. In contrast to aiming at binary phase modulation [2 – 5], which would reflect the mask pattern, we deliberately employ the inevitable side diffusion to obtain a smoothly varying continuous phase profile. This ensures a high diffraction efficiency with only one mask/ion-exchange step.

The optimal mask pattern and ion-exchange time are found using optimization algorithms aiming to maximize diffraction efficiency η and to minimize array uniformity error ΔR. The efficiency η is the ratio of power diffracted into the signal to the total transmitted power. The signal can be a continuous one or a discrete spot array formed by a grating. The uniformity error ΔR is defined as the maximum deviation of a signal beam from the average. Every time the aperture configuration is changed, the ion exchange process, i.e., the change of ion concentrations in the substrate, must be numerically simulated. Refractive index change Δn is assumed to be linearly dependent on C, which is the relative concentration of the incoming ions normalized to the interval $[0, 1]$. With this formalism $C = 1$ corresponds to the situation in which all exchangeable ions in glass have been replaced by the incoming ions.

The theory of the ion-exchange process is well established for the fabrication of waveguide components [6]. Perhaps the most fundamental difference in the design of ion-exchanged free-space elements in comparison to typical waveguide structures is that in the former deep ion exchanged structures are required. Thus, for the simulation of the ion-exchange process, the errors introduced by assuming the basic diffusion equation

$$\frac{\partial C}{\partial t} = D\nabla^2 C \tag{1}$$

are likely to become significant, and a more accurate model is needed, which takes into account the different self-diffusion coefficients and electrical equilibrium of the two ions taking part in the process: incoming ions A and outgoing ions B. So, we use the nonlinear ion-exchange model

$$\frac{\partial C}{\partial t} = \nabla \cdot \frac{D\nabla C}{(M-1)C+1}. \tag{2}$$

The ratio M of the self-diffusion coefficients of the incoming and outgoing ions is $M = D_A/D_B$, which is assumed to be an invariant constant. The boundary conditions are $C = 1$ at the surface under the mask apertures and $\partial C/\partial y = 0$ under the mask, where y is the direction perpendicular to the glass surface. Furthermore, periodic boundary conditions must be applied for the gratings. In all our experiments, we have used Corning 0211 glass and Ag^+-Na^+ -exchange with $M = 0.7$ and Δn=0.049.

To solve Eq. (2) by finite difference algorithms, we divide the cross-section of a glass substrate within one grating period in a rectangular grid and the ion-exchange time in discrete time steps. In the work of Ref. 1, we exploited explicit Dufort-Frankel finite difference schemes. For the simulation of relatively long ion exchange processes (on the order of 20 h), we have implemented an implicit Crank-Nicholson algorithm. This algorithm is unconditionally stable allowing the use of long time steps. A decrease in computation time of two orders of magnitude compared with the explicit method has been achieved using both adaptive grid spacing and adaptive time step.

The optical response of the ion-exchanged element is determined by a thin-element approximation, which is valid if the grating period is much larger than the wavelength of light, grating thickness h is on the order of a few wavelengths, and/or the refractive index modulation is small ($\Delta n < 0.1$). These conditions are valid for all structures that we have fabricated by thermal ion exchange. The transmitted field is then related to the incoming field through the complex-amplitude transmission function

$$t(x, y) = A(x, y) \exp[i\phi(x, y)], \tag{3}$$

where $A(x, y)$ is an amplitude modulation and $\phi(x, y)$ is a phase modulation. For a lossless material $A(x, y) = 1$, refractive index n is real, and the phase function is given by the optical path through the element

$$\phi(x, y) = \int_0^h kn(x, y, z)\mathrm{d}z. \tag{4}$$

Here $k = 2\pi/\lambda$ and λ is the wavelength of light in vacuum. The far-field diffraction pattern is readily obtained by Fourier-transforming $\exp[i\phi(x, y)]$. The validity of the thin-element approximation has been checked using beam-propagation methods, which are valid for thick elements [7].

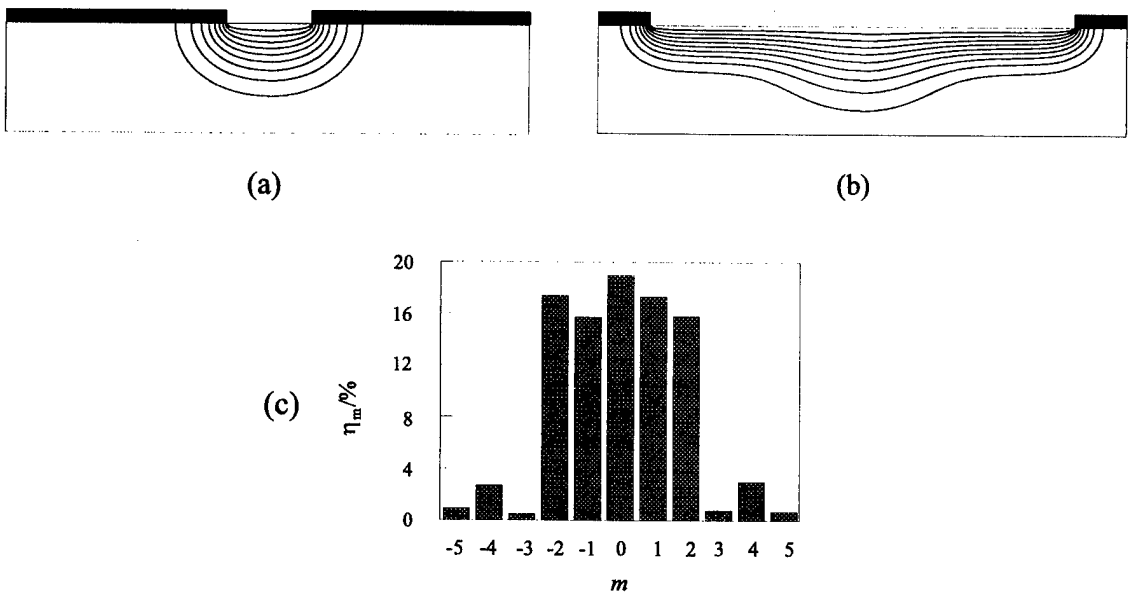


Fig. 1: Fabrication of a one-to-five beam splitter by two mask/ion-exchange steps in glass. Concentration curves of one grating period after (a) the first and (b) the second mask/ion-exchange step are plotted from 0.1 to 0.9 times the maximum concentration with spacings of 0.1. (c) Far-field efficiencies η_m of the diffraction orders m of the component.

Small mask apertures result in sharp spatial variations in the phase function, which cause diffraction into high spectral orders and consequently reduce η. Allowing two or more consecutive ion-exchange steps with different masks, one can produce far smoother phase profiles. A one-to-five beam splitter fabricated by two-step mask/ion-exchange process has been demonstrated (Fig. 1.). The grating period is 123 μm, the process times are 455 min and 154 min, and the widths of the mask apertures are 19.7 μm and 98.4 μm in the first and in the second step, respectively. The measured diffraction efficiency is $\eta = 85.2\%$ and the array uniformity error is $\Delta R = 12\%$. The differences with the theoretical values, $\eta = 91.1\%$ and $\Delta R = 0.3\%$, are expected to be primarily due to mask alignment errors and the variation of temperature of the furnace used in these experiments. According to our numerical analysis, however, mask alignment in the multistep ion-exchange process is not as critical as in the fabrication of discrete multilevel surface profiles. We also point out that the diffraction efficiency is significantly higher than that in the case of four-level surface-relief element (η =78.1%) obtained by two photolithography steps.

In addition to the multiple-step process, post baking of the ion-exchanged element in a furnace without an ion source provides a smoothly varying phase function by additional diffusion of ions. Theoretical results for a one-to-nine beam splitter fabricated by a single ion-exchange step followed by post baking are presented in Fig. 2, where the phase functions resulting from 1027 min ion exchange and 233 min post baking are shown. The element is a symmetric grating with a period of 256 μm. There are eight apertures in the mask: the largest aperture with a width of 38 μm is surrounded by small apertures with widths of 2.75 μm, 1 μm, 1 μm, and 1 μm at distances 31.9 μm, 40.8 μm, 67.8 μm, and 128 μm from the center of the largest aperture, respectively. The theoretical diffraction efficiency is $\eta = 98.3\%$ and the array uniformity error is $\Delta R = 0.9\%$.

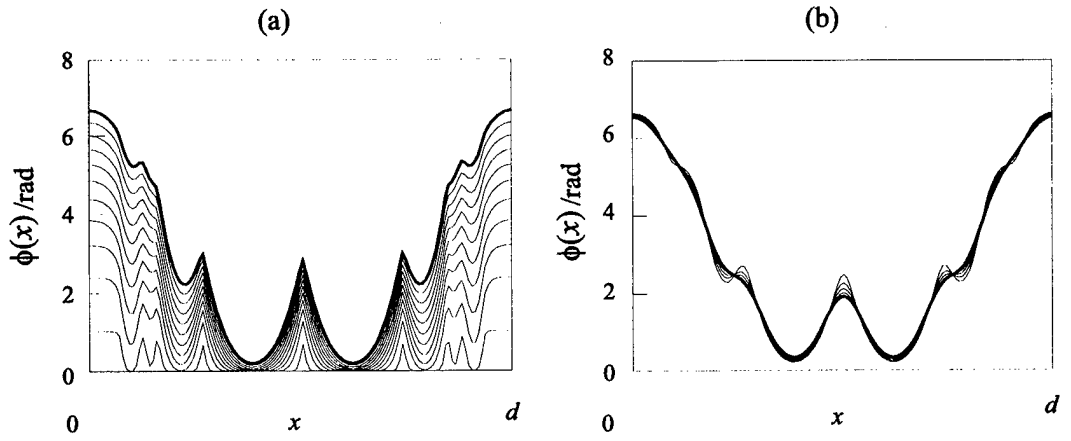


Fig. 2: (a) Development of phase function within one grating period d during ion-exchange for a one-to-nine beam splitter. (b) Phase function in post bake following (a). The final result in both steps is shown with a bold line. The curves have been plotted with a 6000 s time interval in (a) and 3000 s interval in (b).

Equation (2) seems to be accurate for processes up to several hours. However, deviations from the theory have been noticed in long ion exchanges more than 6 hours. One source of the inaccuracies is that the glass surface swells. We have observed this both by a profilometer scan and a liquid-gate test. Another source is the retardation of the diffusion as a result of an electrochemical potential over the apertures in a metallic mask [8]. By following the procedure in Ref. 8 to anodize aluminum masks, we have confirmed significant differences in the optical functions of gratings fabricated using metallic and oxidized masks.

As a conclusion, in this paper we have further developed the method of designing and fabricating high-efficiency diffractive elements by ion exchange in glass. The method gives higher diffraction efficiencies than those obtainable by an equal number of material removal or deposition steps. The numerical simulation of the process has been sped up by an implicit finite difference method allowing the use of sophisticated optimization algorithms. The use of nonmetallic mask material has been applied in the case of long processes to avoid the saturation of the diffusion.

[1] R.-P. Salmio, J. Saarinen, J. Turunen, and A. Tervonen, *Appl. Phys. Lett* **66**, 917 (1995).
[2] T. Yatagai, R. Sugawara, H. Hashizume, and M. Seki, *Opt. Lett.* **13**, 952 (1988).
[3] E. J. Patej and B. Oroń, *Proc. SPIE* **1085,** 436 (1989).
[4] H. C. Bolstad, T. Yatagai, and M. Seki, *Opt. Eng.* **31,** 1259 (1992).
[5] J. Saarinen, A. Tervonen, J. Turunen, and S. Honkanen, in *Meeting Digest – Frontiers in Information Optics*, Topical Meeting of ICO, Kyoto, Japan, 1994, p. 76.
[6] A. Tervonen, in *Introduction to glass integrated optics*, S. I. Najafi, ed., (Artech House, Boston, 1992), pp. 73–105.
[7] J. Saarinen, J. Turunen, and J. Huttunen, *Appl. Opt.* **33**, 1035 (1994).
[8] R. G. Walker, C. D. W. Wilkinson, and J. A. H. Wilkinson, *Appl. Opt.* **22**, 1923 (1983).

Monday, April 29, 1996

Joint Session on Diffractive and Micro-Optics and Holography I

JMC 1:30 pm-3:00 pm
Gardner A&B

Raymond Kostuk, *Presider*
University of Arizona

Fabrication of micro-optics and diffractive lenses using analogue methods

M C Hutley
National Physical Laboratory
Teddington
TW11 0LW, UK
Tel (44) 181 943 6122 Fax (44)181 943 2945

Introduction

The most important aspect of producing a diffracting optical component that will compare well with its refracting or reflecting counterpart is to achieve an adequate level of diffraction efficiency. Binary diffracting structures in amplitude and phase forms have been available for about a century but since their efficiency is limited to 10% and 40% respectively they have not found significant application. In order to achieve high efficiency it is necessary to exercise some control over the form of the grooves and for most practical cases it is necessary to generate a saw-tooth "blazed" profile. A blazed profile is one in which the individual facets behave, to a first approximation, like tiny prisms which send the light by reflection or refraction in the same direction that the spacing of the grooves sends it by diffraction.

Much of the current development in diffracting optics is based on producing a digitised approximation to the ideal profile by the superposition of a series of binary steps using the technology of photolithography. The purpose of the present paper is to review other attempts to achieve diffracting components with the ideal groove profile, to summarise the lessons that have been learned from this experience, and to consider the extent to which they are appropriate to the new generation of technology.

2. Mechanical methods.

Until recently the only diffracting component that had any widespread application was the diffraction grating. The production of gratings was the supreme challenge to mechanical and machine control engineering. It is interesting to note that the justification for the effort of making a grating was that the chromatic dispersion was far greater than that of a prism. In many modern applications for diffracting optics, dispersion is a disadvantage. It is also interesting to note that the much of the machine control technology developed for ruling engines has been carried over to photomask writers on which the current diffracting optics boom is based.

The production of blazed plane gratings was first achieved by Strong in 1935 (1). For a plane grating of constant pitch the appropriate facet angle may be achieved by the correct orientation of the diamond ruling tool. This no longer holds for a concave grating and severely limits the numerical aperture over which a concave grating will work. This led to the development of "multi-partite" gratings in which different sections were ruled at different angles (2) or to complex toolholders in which the diamond rotated as ruling progressed.

More complex structures such as Fresnel-zone plates can be generated mechanically by single point diamond turning.(3) In this case the facet angle and the width of the groove both vary across the aperture so a far higher degree of control is required. The current best quality machines are capable of producing good quality diffracting components, particularly if they are to be used in the infrared where mechanical tolerances are comparatively relaxed. The only question that arises is "why bother?". If one has the capability to produce a surface that will control the optical phase

across the aperture, why introduce a phase step of π every time one crosses the Fresnel zone boundary ? The sharp edges of the groove are likely to produce scattering and one needs a sharper tool than is required to turn a lens. The savings in weight and material are negligible, even for germanium. Why not simply make an aspheric lens ? In most practical cases the answer lies in hybrid designs in which aberrations (particularly chromatic) of the diffracting component are balanced against those of refracting components. As stand-alone devices they have little to offer optically, but the thinner structure may be easier to replicate or may absorb less energy.

3. Interference techniques

Standing waves

The recording of interference fringes to produce diffracting structures has been used for over a century. In 1875 Cornu photographed Newton's rings to generate a zone plate and in 1901 Cotton (4) recorded standing waves and proposed the holographic reconstruction of arbitrary wavefronts. Sheridan in 1968 recorded standing waves in photoresist to generate blazed holograms and Hutley refined the technique for the production of spectroscopic quality gratings (5). During exposure the photoresist is aligned obliquely to the fringe pattern so there are within the bulk of the resist, layers which are alternately soluble and insoluble. After development the shape of the profile is determined by the shape of the oblique insoluble layers near the surface.

The shortcoming of this approach is that the separation of the standing waves is equal to half the wavelength of light in the photoresist. This defines the separations of the planes of the facets of the grooves (which in turn is half the Littrow blaze wavelength). In theory the blaze wavelength should be equal to the recording wavelength divided by the refractive index of the resist. In practice it less than that so that with an argon laser at 458 nm the blaze wavelength is about 220 nm. This is ideal for ultraviolet and visible spectroscopy but is too shallow by a factor of about ten for transmission diffracting optics.

The technique can readily be applied to zone plates by placing a point source at the centre of curvature of a concave mirror. A longer blaze wavelength is achieved if light is incident through the substrate and it can be increased still further by selective reactive ion etching of the structure into the substrate so that it is possible to achieve high efficiency in transmission.

The great advantage of this approach is that it is possible to produce in a few minutes, components which combine large area (>100 mm), high numerical aperture and spectroscopic quality.

Fourier Synthesis

The fringes in a two beam interferometer possess a sinusoidal variation of intensity. It is possible to build up any desired intensity profile by superimposing a Fourier series of sinusoidal patterns of appropriate amplitude and phase. This approach has been adopted (6,7) for plane gratings and good results obtained for two Fourier components. However, the best results were obtained for gratings in which a single sinusoid would have been quite efficient and the technological difficulties were significant. It is difficult to see how the technique could practically be applied to any component other than plane gratings. The author has attempted to obtain the second Fourier component by frequency doubling the output of an argon laser but with limited success.

Multiple beam interferometry

With multiple beam interferometers it is possible to obtain an intensity profile that is other than sinusoidal. For example, by carefully selecting the reflectance and phase change on reflection of the mirrors in a Fabry Perot interferometer it is possible to produce asymmetric fringes which are a good approximation to a saw-tooth.(8) These may then be recorded directly in photoresist or photographic plates which are bleached and swollen to yield blazed zone plates.(9)

An alternative approach is to use the symmetrical transmission fringes of a Fabry-Perot interferometer of high finesse. The fringes can be considered as delta functions and have approximately the same spatial distribution as the Fresnel zone boundaries. If the fringes are recorded in photoresist and the plates are scanned in such a way that the fringes expand by one period, it is possible to control the exposure so as to build up a saw-tooth profile (10,11). By this means good saw tooth profiles and efficiencies of the order of 80% were obtained for transmission zone plates in the visible.

General Photosculpture Techniques

The term "photosculpture" applies when the shape of a photosensitive surface is determined by the intensity distribution to which it is exposed. The simplest manifestation of this is to scan the area with a focussed laser beam and vary the intensity to achieve the correct exposure. This can be achieved either on an optical lathe (12) or on a rectangular raster (13). Both are capable of producing items with both rectangular and circular symmetry. This approach gives a far greater flexibility of design than is available from interferometry, but the price that one pays is that it is slow and therefore requires extreme mechanical stability. In some cases the writing time is so great that the latent image recorded at the beginning of the process begins to fade before it can be developed. A very detailed knowledge of the properties of the resist is therefore required in order to compensate for this.

For items which have circular symmetry a simpler system may be used in which blazed circular grooves are generated by rotating the photosensitive material under an image of a triangular light source (14, 15). After exposing one groove, the projection system is translated radially, the width of the image is adjusted and the next zone is exposed. This has the advantage that the optical projection system is working on axis with a relatively small field but has the disadvantage that as the zones become narrower, the energy from the source is reduced and exposure times become longer. The production of items of large aperture and high numerical aperture is therefore difficult.

Finally, it is possible to generate a desired exposure pattern by producing a variable density mask.(12,16,17) Strictly this is not an "analogue" technique because the variable density is usually produced as a half-tone dot pattern. However, if this is then reduced photographically the detail of the dots is lost.

General Summary of Results

All of the techniques described above have been able to produce blazed diffracting structures with reasonable efficiencies . For very coarse structures the efficiency can be very high (90% or so) but for the finer structures needed for high numerical apertures the efficiency is lower. The reason is that the efficiency depends upon the spatial resolution of the recording system. In order to

achieve 90% of the maximum theoretical efficiency it is necessary that the steep facet of the saw-tooth should occupy no more than 5% of the width of the groove. The finest groove width **d** for which one might expect 90% efficiency is twenty times the spatial resolution δ. For an optical recording system $\delta = 1.22\,\lambda_0 / NA_{(system)}$ If **d** is the width of the outermost zone on a zone plate, we have from the grating equation that $\mathbf{d} = m\lambda / NA_{(zone\ plate)}$. If $\mathbf{d} = 20\delta$ we may now write:

$$NA_{(zone\ plate)} = m\lambda \frac{NA_{(system)}}{\lambda_0 25}$$

This means that **whatever** optical system is used to generate a diffracting structure the maximum numerical aperture (for 90% of theoretical efficiency, used at the same wavelength in first order) is one twenty fifth of the numerical aperture of the system used to record the structure. Thus, if the recording system has f/1 optics, the best that can be achieved is f/25. Given that $NA_{(system)}$ is limited, the only possibilities to improve on the factor of 25 are:

Increase **m** and work at higher orders of diffraction. This approach has been adopted by Gale and colleagues (13). The consequences are that the modulation depth is greater. The chromatic behaviour is changed in that the free spectral range is reduced and the efficiency performance is that of an echelle. In the limit, when the order number is equal to the Fresnel number, one has re-invented the lens!

Increase λ. This is not usually an option but it does mean that one can use visible light to generate devices for use in the infrared at around 10 μm (18)

Decrease λ_0. One can gain some improvement (perhaps a factor of 4) by using UV to record optics for use in the visible, but if one really needs to combine high efficiency in first order with high numerical aperture one is forced to use higher resolution lithography such as e-beam. If one also requires a large physical aperture, this is likely to be very expensive.

Happily, there are applications for components of low NA and for those with small apertures. So diffracting optics does have a rôle but there remain some severe technological challenges.

References

1. Strong J (1935) Phys Rev **48**,480
2. Hutley M C (1982)" Diffraction Gratings" Academic Press. London (and references therein)
3. Goto K, Mori K, Hatakoshi G,Takahashi S. (1987) Jpn Jnl App Phys. **26** supp 26-4. 135-140
4. Cotton A. (1901) Seances Soc Français Phys 70-73
5. Hutley M C (1975) Opica Acta **22**,1-13
6. Schmahl G (1974) Proc 4th Int Conf Vac UV Radiation Phys. Hamburg.
7. Breidne M, Johansson S, Nilson L-E and Åhlen H. Optica Acta **26.** 1427-1441
8. Aebischer N. Nouv Rev d'Opt App (1971)**2**,351-366
9. Ferrière R, Andres P, Illueca C. (1984) J Opt(Paris) **15**,213-218
10. Claire J J, Françon M and Laude J-P. (1970) C R Acad Sc Paris **270,**1600-1603.
11. Hutley M C, Stevens R F, Wilson S J. (1988) J Mod Opt**2**,265-280.
12. Koronkovich V P et al. (1984) Optik **67** ,257-266
13. Gale M T, Rossi M, Schütz (1994) Proc SPIE **2045**
14. Schwider J, Grzanna J, Spolaczyk R and Burov R, (1980) Optica Acta **27**,683-698
15.Emerton N, Smith R W,and Cañas R G. (1987) IERE **76** 99-103 (Holographic systems components and applications. Cambridge.)
16.Moreno V,Hutley M C, Tyrer J R. (1989)IEE**311,**76-79(Holographic systems components and applications, Bath)
17. Purdy D.(1994) Pure Appl Opt.**3**,167-175.
18. Hutley M C, Stevens R F, Wilson S J. (1991) Opt Engg **30** 1005-1010

LASER WRITTEN DIFFRACTION GRATINGS IN QUANTUM DOT AND ISLAND METAL FILMS

Yu. Kaganovskii and M. Rosenbluh
Department of Physics, Bar-Ilan University, Ramat-Gan 52900, Israel
Phone: 972-3-531-8296; fax: 972-3-535-3298

We demonstrate a new direct method of recording of interference patterns which are stable under high light intensities. The patterns are written on thin glass films containing quantum dots or on metal island films by the interference of two pulsed laser beams. A pulsed dye laser at 584 nm, with a 7 nsec pulse, and pulse intensities of 2-5 MW/cm^2 produced gratings with a period l depending on the angle, α, between the two beams according to $l = \lambda/2\sin(\alpha/2)$.

The quantum dot films were obtained by the simultaneous vacuum condensation, onto a glass substrate, of SiO and Cu from two separate sources. The Cu concentration was varied from 1 to 10 at%, and the overall film thickness varied from 20 to 300 nm (the thinnest films were prepared for TEM examination of the Cu distribution). The average size of the Cu particles in the films, after condensation, was about 10 nm.

Electron microscope micrographs reveal that the gratings form as a result of two processes: SEM shows a local buildup of the film on the substrate along lines of high light intensity (Fig. 1). A similar but random buildup, seen as separate round hillocks, is also observed after heat treatment of the films at ~500°C temperature.

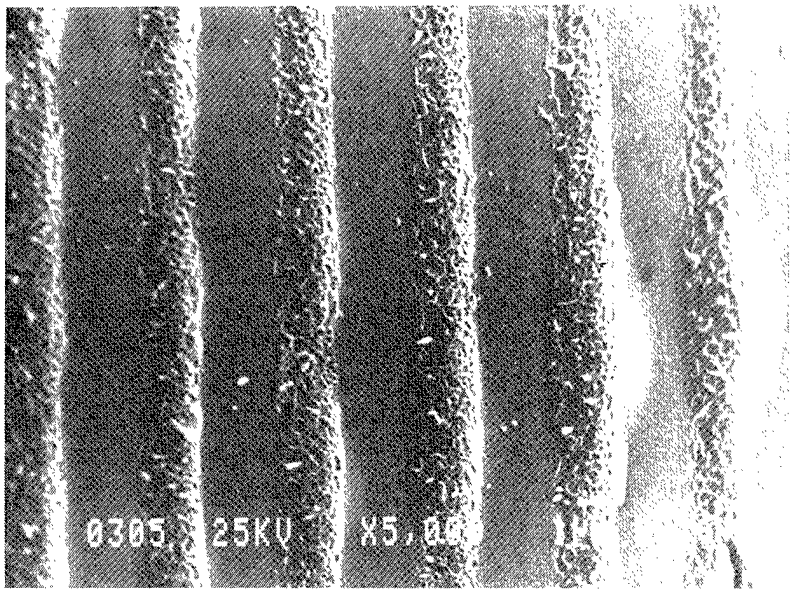


Figure 1. SEM micrograph of 6.2 μm grating in a SiO glass film containing quantum dots of Cu.

The second mechanism responsible for the grating formation is revealed in a TEM micrograph, (Fig. 2), which shows an increase of Cu particle size in the high light intensity regions. The average growth rate of the Cu particle radius is very high, about 10^{-9} cm per laser pulse, so that the average radius grows by a factor of 2 after 10^3 pulses. In regions with low light intensity the Cu particles do not change their size and the film remains stable.

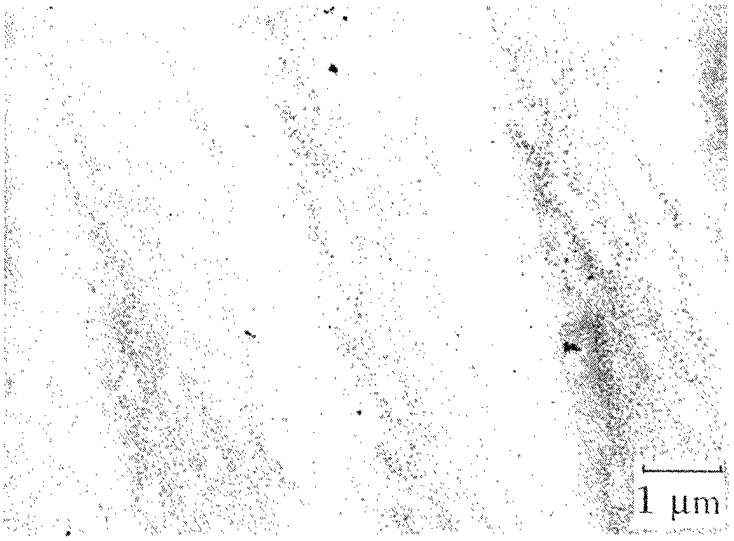


Figure 2. TEM picture of 3 μm grating written in a SiO glass film containing quantum dots of Cu.

In separate experiments island films of Cu, Au and In with a thickness of 10-20 nm, were vacuum condensed on a heated glass or NaCl substrate. TEM studies, (Fig. 3), of the island film morphology after laser irradiation show gratings which are made up of lines containing metal

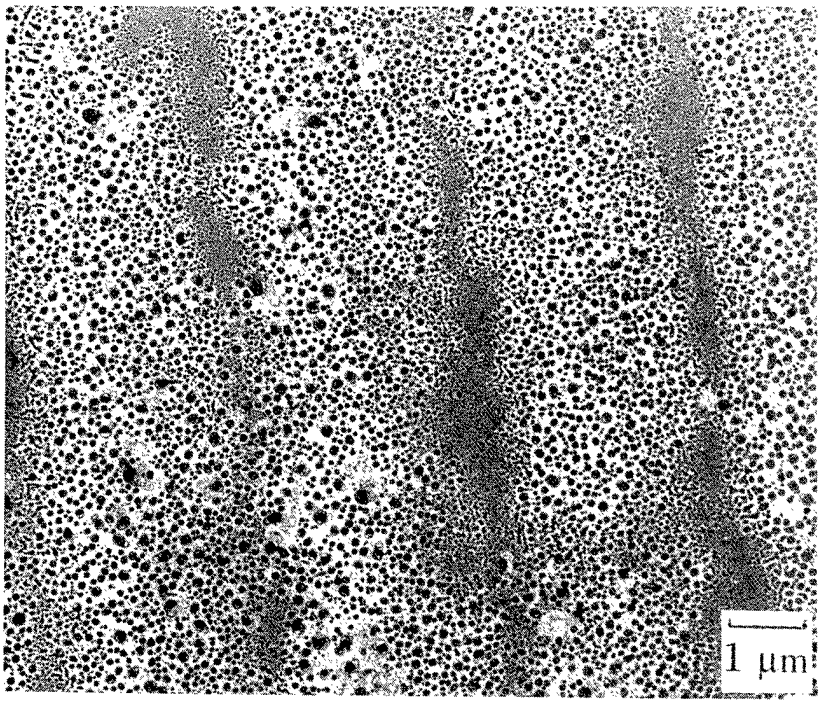


Figure 3. 3 μm period grating written in a Cu island film of 20 nm thickness.

islands of an average size which are bigger than islands in surrounding areas. The average island size in regions of high intensity illumination as well as the width of the line, grows with exposure time, indicating a very fast surface coalescence of the islands, while the island size in the low intensity regions (interference minima) does not change with time.

To determine the mechanism of grating formation for both types of sample we consider the heat distribution near the absorbing particle, of radius R, in a transparent matrix during the laser pulse with duration τ. The particle's temperature changes as a result of a balance between the absorbed energy and the conductive heat loss to the glass matrix. The time dependent particle temperature, $T_1(t)$, is determined by the equation:

$$\frac{dT_1}{dt} = \frac{\Delta q}{\tau c_1 v} + 4\pi R^2 \kappa c_2 \left.\frac{\partial T_2}{\partial r}\right|_{r=R}, \qquad (1)$$

where $\Delta q/\tau = \alpha I v$ is the energy absorbed by particle per unit time; α is the absorption index, κ is the heat conductivity of the glass, I is the pulse intensity, $v = 4\pi R^3/3$ is the volume of the particle, c_1 and c_2 are the heat capacities per unit volume of the particle and glass matrix, and $T_2(r,t)$ is the temperature distribution near the particle. Considering the problem for a 7 nanosecond pulse, we may suppose $\partial T_2/\partial t \approx 0$ and look for a steady state solution, because the characteristic time, $t_{ch} \approx l^2/6\kappa$, for heat spreading over the average distance l between particles, is much less than τ. Thus, with $l \approx 5\text{x}10^{-6}$ cm and $\kappa \approx 10^{-2}$ cm^2/s we obtain $t_{ch} \approx 5\text{x}10^{-10}$s, which is at least an order of magnitude less than τ. Thus except for a short time of order t_{ch} at the start and end of the pulse we may consider the particle's temperature as a constant.

In this case the temperature distribution around the particle is determined by the expression

$$T_2(r) = T_m + \frac{(T_R - T_m)R}{r} \qquad (2)$$

where T_m is the temperature of the matrix and T_R is the temperature of a particle with the radius R. It follows from (2), that $(\partial T_2/\partial r)_{r=R} = -(T_R - T_m)/R$. Substituting this into (1) with $\partial T_1/\partial t = 0$, we obtain

$$T_R = T_m + \frac{\alpha I}{3c_1\kappa} R^2, \qquad (3)$$

i.e. the temperature of a particle is proportional to the square of its radius. With $\alpha = 10^7$ cm^{-1}, $c_1 \approx 4\text{x}10^6$ J/Km^3, $\kappa \approx 10^{-2}$ cm^2/s, $I \approx 6\text{x}10^6$ W/cm^2, $R \approx 10$ nm, we obtain $T_R - T_m \approx 500$ K, and for a particle with $R \approx 20$ nm the difference is $T_R - T_m \approx 2500$ K.

The atom flux directed towards the Cu particle from the glass matrix, is $J = -D(dC/dr)_{r=R} \approx D\Delta C/R$, where D is the Cu atomic diffusion coefficient in glass around the particle, C is the Cu concentration in SiO glass and ΔC is the difference between concentration of Cu in the glass matrix the equilibrium concentration at the particle temperature. This flux leads to a growth of the Cu particles with a rate

$$dR/dt = J\,\Omega = D\Omega\Delta C/R, \qquad (4)$$

where Ω is the atom volume. With $D=10^{-6}$ cm^2/s (the glass surrounding the Cu particle becomes liquid during the laser pulse); $\Omega\Delta C = 10^{-1}$; $R= 10^{-6}$ cm we obtain $dR/dt= 10^{-1}$ cm/s, which is in a good agreement with the experimental value.

The theoretical analysis of the heat distribution on the glass surface surrounding a metal island is similar to what was presented above for the metal particle inside the transparent matrix. This indicates that the island temperature during the 7 nanosecond laser pulse can be as high as 2500°C (for an $R \approx 20$ nm island size) and increases with size proportional to R^2. Thus two-dimensional diffusional coalescence[1] cannot explain the observed results. We propose a new mechanism for the coalescence of the metal particles which is connected with the overall random surface motion of liquid islands in a local temperature gradient, and collisions during this motion. The temperature distribution around each metal particle on the substrate is described by an expression similar to Eq. 2. Small random drifts of a liquid drop in a temperature gradient must lead to an overall directed average motion to colder regions. During this motion, the biggest (and therefore hottest) liquid drops coalesce with the smaller solid particles. In the Figure 3 the tracks of such motion and coalescence can be discerned as areas besides the larger coalesced particles that were left empty of metal particles.

1. I. M. Lifshits and V. V. Slyozov, J. Phys. Chem. Solids, **19**, 35 (1961).

High-Efficiency Transmission Gratings Fabricated in Bulk Fused Silica

H.T. Nguyen, B.W. Shore, J.A. Britten, R.D. Boyd, S.J. Bryan, S. Falabella, and M. D. Perry
Lawrence Livermore National Laboratory, P.O. Box 808, L-443, Livermore, CA 94550
Tel. (510) 423-2111, FAX (510) 422-9294

I. Introduction

High power ultraviolet lasers are now widely used in the semiconductor industry and inertial confinement fusion research, and are finding increased application in medical therapy. Whether based on excimers or frequency converted solid-state, high power ultraviolet lasers continue to be plagued by issues of optical damage and a limited choice of optical components for beam manipulation. In particular, system performance is often limited by the damage threshold of cavity and transport mirrors. Beam transport and steering based on refractive optics are limited not by surface damage as is the case with reflective systems but instead by bulk damage induced by two photon absorption, color center formation and self-focusing. These limitations can, in principle, be overcome in many applications by the use of transmission gratings fabricated in high damage threshold, transparent materials.

We present the design and performance of high-efficiency transmission gratings fabricated in bulk fused silica for use in ultraviolet high-power laser systems. By controlling the shape, depth, and duty cycle of the grooves we have achieved a diffraction efficiency exceeding 95% in the $m = -1$ order. By directly etching the grating profile in bulk fused silica we have achieved damage threshold greater than 13 J/cm^2 for 1 nsec pulses at 351 nm.

II. Theory

The efficiency of a grating depends, for given wavelength λ, polarization and angle of incidence α, on groove period d, groove depth h, and the shape of the grating profile. For suitable choice of these parameters the transmission efficiency can approach 100%. The most efficient gratings are obtained when only two orders can propagate, namely the zero order (specular reflection) and the -1 order, and when the incident radiation impinges

close to the Littrow angle, arcsin($\lambda/2d$) (autocollimation). By suitably choosing the groove spacing d for given wavelength λ we can exclude all other orders. This possibility follows from the basic grating equation relating angle of incidence α to angle of diffraction β_m for order m,

$$\sin \beta_m = \sin \alpha + (m\lambda / d). \qquad (1)$$

Our goal for permitting only two orders can be assured by fixing the grating period to be smaller than the wavelength. For light of wavelength 351 nm this implies a groove period of 351 nm or less.

The geometry of diffraction is entirely set by the grating equation, and is independent of groove depth or profile. With period = 350 nm the Littrow angle, at which reflective diffraction into order -1 coincides with incident radiation, is 30°. With this incident angle the transmitted light into order -1 emerges into air at an angle of 30°. Thus there will be a 60° angle between the two transmitted orders as they emerge into air.

Taking the groove spacing to be 350 nm, we found that there was a range of parameters at which the efficiency was 97% or better. Our target design is for a period of 350 nm, a depth of around 600 nm, and with duty cycle of 0.5 (i.e. the grooves have width 175 nm) to be used with TE polarized light. Figure 1 illustrates the profile and efficiency for this design. This design has a theoretical efficiency of 98% into m = -1 order.

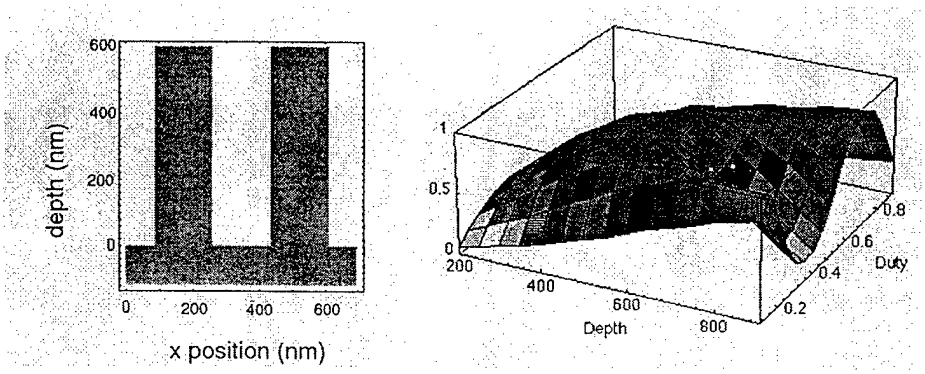


Figure 1. Right: Theoretical transmission efficiency, λ = 351 nm, order -1 and TE polarization, as a function of groove depth (nm) and duty cycle for a rectangular-profile grating etched into silica (left frame). Incident angle is Littrow angle, groove spacing is d = 350 nm. The peak efficiency (97.6%) occurs for depth of 600 nm and duty cycle 0.5.

III. GRATING FABRICATION

Our fabrication of gratings proceeds through several steps. We first prepare, on suitably flat and polished substrates, carefully controlled thickness of photoresist. We next use laser interference lithography to pattern the photoresist with the desired profiles. We develop the resultant latent image to form a corrugated photoresist grating, which we transfer etch into the substrate. A typical photoresist grating and a grating etched into bulk fused silica is shown in Figure 2.

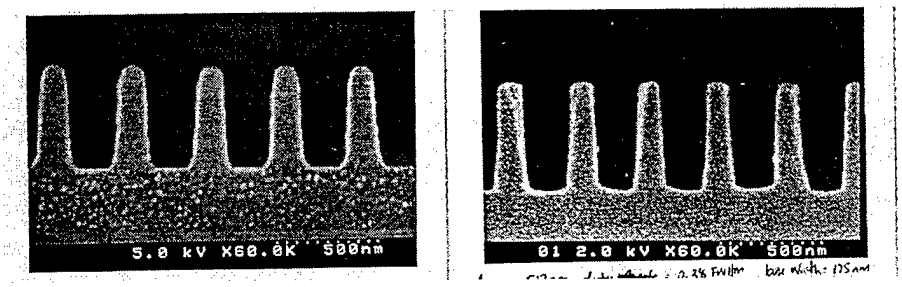


Figure 2A. Grating profile patterned in photoresist, 2B) Grating profile etched into bulk fused silica.

IV. EXPERIMENTAL RESULTS

We have fabricated a grating that exhibits a diffraction efficiency in excess of 95% in the $m = -1$ order and 2% in the transmitted 0 order at the Littrow angle of the grating. The light that is not present in these two orders appears to be diffusely scattered. This can be seen from the hazy appearance of the sample. We attribute this to the defects in the bulk fused silica substrate that was used. This can be corrected by using super polished fused silica substrates (fused silica substrates that have been etched/polished to minimize substrate polishing damage). It is expected that with these substrates a diffraction efficiency of greater than 97% can be obtained. Experimental results are in good agreement with our theoretical computations.

In addition, we have conducted damage test of these transmission grating using a 3 ns pulse from a frequency-tripled Q-switched Nd:YAG laser. The grating was situated to the TE-polarized laser beam at the use angle of 30°. Both front and back surfaces had a damage threshold of 13.2 J/cm^2. These values are typical for standard bulk fused silica.

Ultrahigh Spatial-Frequency, High-Contrast Periodic Structures Produced by Interference Lithography

H.T. Nguyen, J.A. Britten, R.D. Boyd, B.W. Shore, and M. D. Perry
Lawrence Livermore National Laboratory, P.O. Box 808, L-443, Livermore, CA 94550
Tel. (510) 423-2111, FAX (510) 422-9294

I. Introduction

During efforts to produce multilayer high efficiency dielectric reflection gratings in oxides, 351nm high efficiency transmission gratings, and other development work, we required very high-contrast grating profiles in photoresist. High-contrast profiles are profiles with very steep sidewalls, greater than 80 degrees. It is quite difficult to achieve high-contrast profiles using interference lithography. The electric field distribution is sinusoidal. Therefore, one would conclude that the profile would resemble a sinusoid, as shown in Figure 1a. Early work with interference lithography produced grating profiles similar to the ones shown in Figure 1a.[1-3] We have learned that if great care is taken in the processing steps, very different profiles can be achieved. Figure 1b shows a very high-contrast, high-aspect ratio grating profile in photoresist. The difference between Figure 1a and Figure 1b is that 1) the photoresist profile in Figure 1b has completely developed through to the substrate, and 2) the contrast characteristics of the photoresist used in Figure 1b are superior over the photoresist used in Figure 1a.

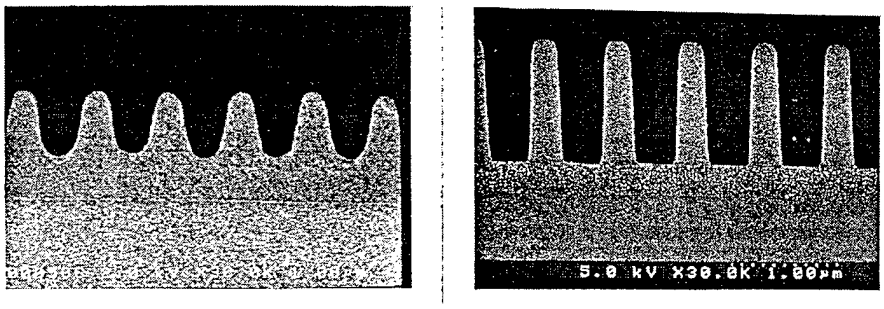


Figure 1a) Scanning electron micrograph of sinusoidal profile in photoresist, 1b) Scanning electron micrograph of high-contrast profile photoresist.

In addition to high-contrast photoresist and the complete dissolution of the grating troughs to the substrate, the exposure laser must operate single-frequency. This is essential for the production of high-aspect ratio, high-contrast grating profiles since the contrast of the exposure laser is transferred to the photoresist during exposure.

Etched structures such as grating profiles etched into a SiO_2 layer atop a multilayer dielectric stack, and a ultraviolet transmission grating etched into bulk fused silica, require high-contrast for high-efficiency. These are more easily made with a high-contrast mask.

It is also important to mention that a high-contrast profile is not always desired or needed for all applications. In fact, a distorted sinusoidal profile is used for all of our metallic overcoated gratings.[4] Additionally, we have developed a process to control the duty cycle, the full-width-at-half-maximum of the structure divided by its period, of the structures from 0.6 to 0.17.

II. Vertical Sidewalls

The use of different types of photoresist has become very important to our processing technique. We have discovered that each of the different photoresists used have individual advantages and disadvantages. By choosing a particular photoresist we can now control the photoresist profiles, from a distorted sinusoid to a rectangular profile, from a duty cycle of greater than 0.6 to less than 0.17. For instance, Photoresist A used to produce very steep side walls has excellent contrast characteristics but low sensitivity, requiring exposure fluence >120mJ/cm^2. On the other hand, Photoresist B has very high sensitivity, requiring an exposure fluence of about 20mJ/cm^2, but its contrast characteristics are lower. Figures 2a and 2b show grating profiles of these photoresist exposed under similar conditions.

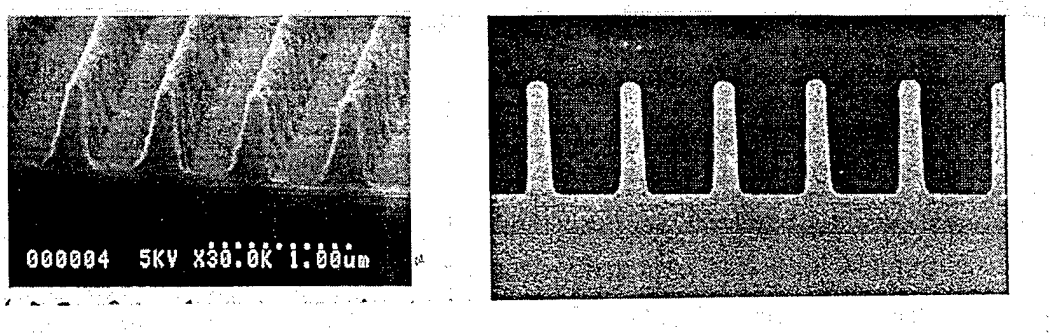


Figure 2a) Typical profiles produced with Photoresist A, 2b) Typical high-contrast profile produced with Photoresist B

The difference in the grating profiles shown is a function of the photoresist used. Even though all of the resist are diazonapthoquinone-based (DNQ), they exhibit different contrast characteristics. The basic differences between these resist are the transparency of the resin, synthesizer, and concentration of the photoactive compound. Photoresist B uses a more transparent resin which results in less UV light being absorbed, and lateral scattering yielding steeper side walls.

Diffractive diffusers at the fabrication limit

Hans Peter Herzig, Wolfgang Singer

Institute of Microtechnology, Rue A.-L. Breguet 2, CH-2000 Neuchâtel, Switzerland
Phone +41 38 234 251, Fax +41 38 254 276

Eckhard Piper, Johannes Wangler

Carl Zeiss, Postfach 1369/1380, D-73446 Oberkochen, Germany
Phone +49 7364 20 3823, Fax +49 7364 20 4509

1 Introduction

Diffractive micro-optical elements gained increasing interest for beam-shaping, e.g., the laser treatment of materials,[1] and for illumination systems. The fabrication technologies for diffractive micro-optical elements bring in advance high accuracy and reproducibility, especially of the periodicity of the elements. In monochromatic applications, diffractive micro-optical elements are only restricted by the limits of the fabrication technology.

In this paper we discuss the design and fabrication of optical diffusers for deep UV lithography. The diffusers generate a flat-top intensity distribution,[2] for a partially coherent excimer-laser at 248nm. We investigated far-field distributions with a uniform intensity over a rectangular shape. High efficiency and a space-invariant response of the diffractive elements are required. In detail, the diffusers have to be almost independent of the size, the shape, and the homogeneity of the illumination.

The fabrication limits due to the restricted resolution of the fabrication technology are a severe restriction for the design of diffractive elements for short wavelengths applications. Therefore, a conventional design was preferred to the IFTA-algorithm.[3] In this case, the utilization of arrays of binary micro Fresnel lenses[4] with adapted geometry is straight forward. The lenses generate the desired angular spectrum, while the array property warrants the space invariance of the element. However, binary Fresnel lenses suffer usually from binarization noise and a large zeroth diffraction order, which violates the homogeneity condition of flat-top distributions. The small oscillations in the far-field due to the binarization noise can be smoothed out with partially coherent or, in the limit, incoherent illumination. Furthermore, we show that the zeroth order is reduced by the addition of a constant phase offset to the transmission phase function of the lens array.

Binary diffractive elements with two phase levels usually have low diffraction efficiency (40.5 %).[5] For the generation of symmetrical intensity distributions, however, both the plus and the minus first diffraction order contribute to the desired intensity distribution, increasing the diffraction efficiency (~ 80 %). In order to improve the efficiency, multi-level elements have to be employed. We investigated also elements with varying numbers of phase levels, where the number of levels is chosen according to the resolution limit of the fabrication technology. As will be shown, these elements have a locally varying diffraction efficiency.

2 Design considerations

The basic set-up is shown in Fig. 1. A diffractive element is illuminated by a multi-mode excimer-laser with given beam divergence in x- and y-direction at a wavelength of 248nm. The required intensity distribution is then obtained in the Fourier-plane of the second lens system.

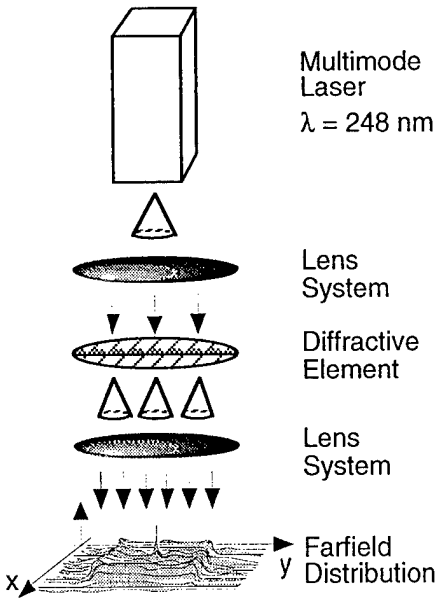


Fig. 1. Set-up for the generation of flat-top distributions (simplified).

The phase grating to generate the flat-top intensity distribution is designed as an array of micro-Fresnel lenses of rectangular shape. For a given focal length, the shape of a single diffractive lens defines the shape and the diameter of the far-field distribution. Due to the divergent illumination with a partially incoherent source, the far-field of the lenses is added incoherently and with small displacements. In the following, we assume that the source is ideally incoherent. The modal distribution of the laser is approximated roughly by a rect-function. The intensity distribution in the far-field is therefore given by a convolution of the square of the amplitudes with a rect-function. As will be shown in detail, the incoherent source has a smoothing effect to the fine oscillations of the coherent intensity distribution.

3 Calculation methods for the far-field distribution

Phase gratings or Fresnel zone lenses are conventionally fabricated as a binary or multilevel phase grating. In that case the direct computation of the far-field according to the Fresnel series by a sum of Bessel-functions can be applied.[6] For this reason, first the transition points tp_n of the m-level Fresnel lens with focal length f for the wavelength λ have to be calculated. The phase values φ_n of the transmission function are given by

$$\varphi_n = n\frac{2\pi}{m} = \frac{2\pi}{\lambda}\left(\sqrt{f^2 + tp_n^2} - f\right) + \varphi_{off}\,, \qquad (1)$$

where we have introduced a constant offset-phase φ_{off}. The offset-phase defines the interference between the first few contributions to the Fresnel series. The first and second contribution, e.g., can be adjusted that they are destructively interfering in the center of the far-field distribution. The influence of the offset-phase to the high-frequencies is negligible.

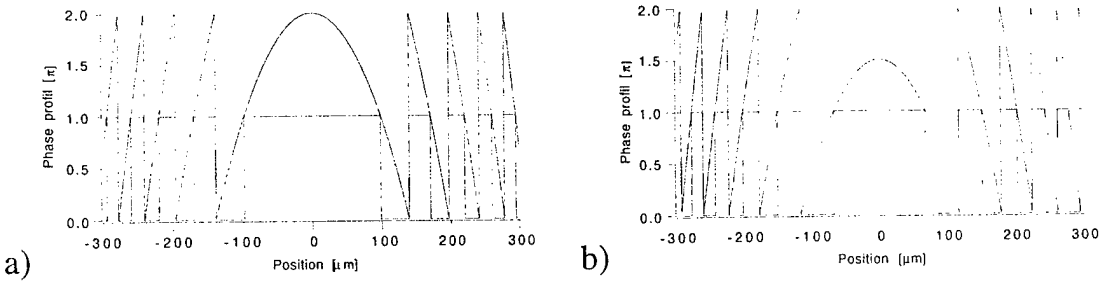


Fig. 2. Continuous phase function and binary approximation (a) without offset-phase, (b) with offset-phase of 0.45 π.

4 Effect of offset-phase and incoherent illumination

Due to the approximation of the continuous phase profile by a binary or staircase grating (Fig. 2), the far-field shows rapid oscillations or binarization noise (Fig. 3). This noise is smoothed out by the incoherent illumination (Fig. 4). In the center of the zone plate, the approximation of the phase function by a binary phase grating is poor (Fig. 2). With a constant offset-phase of 0.45 π, the large central part of the zone plate, which is not diffracting at all, is decreased (Fig. 2b). The large unmodulated region in the spectrum of a zone plate (Fig. 3a) without phase offset is modulated (Fig. 3b). After convolution of the power spectrum with the spectrum of the incoherent source, the large zero order vanishes almost completely (Fig. 4b) :

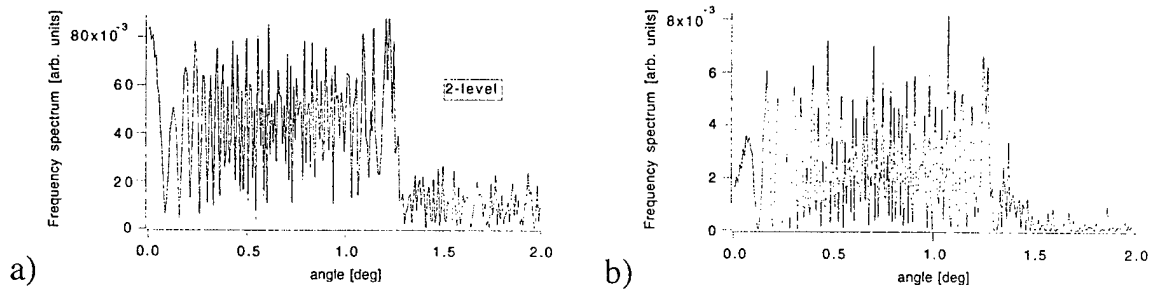


Fig. 3. Spectrum of the binary elements given in Fig. 3.

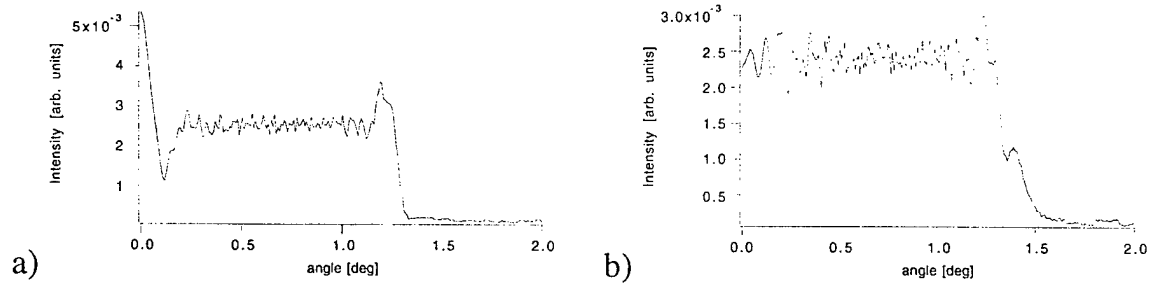


Fig. 4. Far-field distribution after incoherent illumination (divergence 1 mrad).

A further comparison is concerned with diffusers of different size, but constant numerical aperture. The number of Fresnel zones and thus the number of contributions to the Fresnel sum increases with the size of the Fresnel zone plate. The frequency spectra exhibit an increasing modulation with increasing element size. Therefore, the homogeneity of the intensity distribution after convolution improves reasonably with increasing element size. However, with increasing element size of the micro-Fresnel lenses the space invariance of the diffuser is reduced. The optimum is a trade-off between homogeneity of the intensity distribution and space-invariance of the element.

A first design of a rectangular far-field distribution was performed with an array of rectangular binary Fresnel lenses without offset-phase. The design angles were 4 and 5.5 degrees in x and y, respectively. Figure 5 shows the results for the x-direction. In a second design, a Fresnel zone plate was fabricated with a constant offset phase. The results for the simulation and for the measurement are compared in Figs. 5 and 6. Both measurements show a significant deviation from the simulation result in the zeroth order due to fabrication errors, while the design angles (4 degree and 5.5 degree) are obeyed. The elements were fabricated in quartz by RIE and they have a smallest feature size in the order of 1 µm.

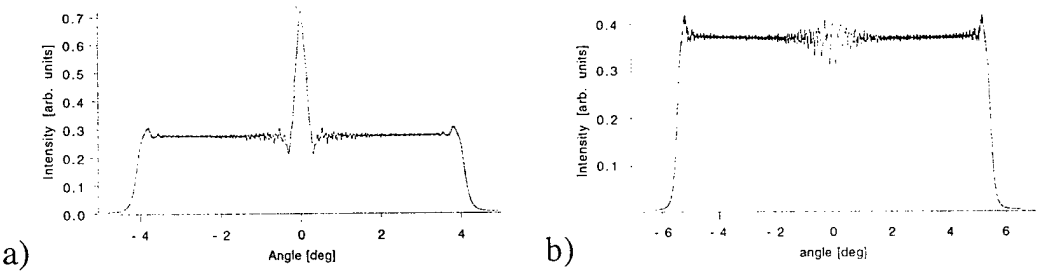


Fig. 5. Simulation result for a binary phase element (a) without offset-phase (design angle 4 degrees) and (b) with offset-phase (design angle 5.5 degrees).

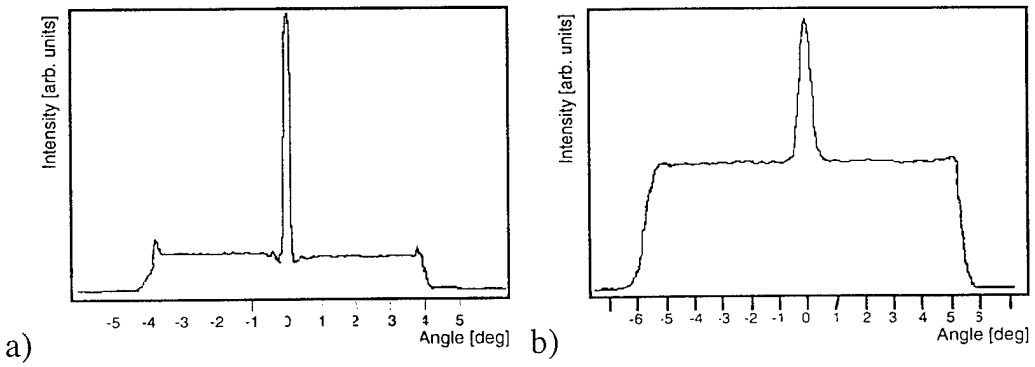


Fig. 6. Measurement result for the elements given in Fig. 5.

In summary, we have shown that by a simple addition of a constant offset-phase to the continuous phase profile, the spectrum of the binary or multilevel phase grating can be modified. The offset-phase design can especially be applied to improve the homogeneity of the far-field distribution.

However, etch depth errors induce an enlargement of the zeroth order. Therefore we found a large zeroth order from the measurements even for the optimized micro Fresnel lens. However, the total amount of energy in the central peak remains very small and it is therefore advantageous to defocus or to block the zeroth order.

References

1 Ch. Budzinski, H.J. Tiziani, "Radiation resistant diffractive optics generated by micro electroforming", Laser und Optoelektronik **27** (1), 54 - 61 (1995)

2 T.H. Bett, et al., "A binary phase zone plate array for laser beam spatial intensity distribution conversion", in *Holographic Systems, Components and Applications*, Conference Publication 379, Neuchâtel 1993, pp. 249 - 254 (1993)

3 Joseph N. Mait, "Understanding diffractive optic design in the scalar domain", J. Opt. Soc. Am. A **12**, pp. 2145 - 2158 (1995)

4 H. Nishihara and T. Suhara, "Micro Fresnel Lenses", in *Progress in Optics* Vol. **24**, Elsevier 1987, p. 4 (1987)

5 E. Hasman, N. Davidson and A.A. Friesem, "Efficient multilevel phase holograms for CO_2-Lasers", Optics Letters **16**, pp. 423 - 425 (1991)

6 I.N. Ross, D.A. Pepler, C.N. Danson, "Binary phase zone plate design using calculations of far-field distributions", Opt. Commun. **116**, 55 - 61, (1995)

Monday, April 29, 1996

Optical Interconnects

DMD 3:30 pm-5:00 pm
Gardner A&B

Keith Mersereau, *Presider*
AT&T Bell Laboratories

Diffractive Optics in Free-Space OptoElectronic Computing Systems

Philippe J. Marchand, Frederick B. McCormick, and Sadik C. Esener

University of California, San Diego
Department of Electrical and Computer Engineering
9500 Gilman Drive
La Jolla, CA 92093-0407
http://soliton.ucsd.edu

Optical interconnections have been shown to have advantages over electrical interconnections in terms of speed, energy, and density for global links[1]. In addition, the flexibility of optical interconnections permits efficient electronic layouts that can improve the performance of electrical connections in an opto-electronic computing system. Optical interconnections systems are currently a very active area of research[2,3,4,5]. These systems typically combine electronic circuits, opto-electronic transmitters and receivers, and optical elements. Electronic circuits are usually designed, optimized, and fabricated using standard VLSI technology. Many technologies are available for opto-electronic transmitters and receivers; in our case, we will use either Si/PLZT[6,7] or Si/MQW[8] technologies. Similarly, there is a wide choice of technologies available for the optical elements in the system. In this paper we first present some results on diffractive elements for Free-Space Interconnection systems fabricated using e-beam direct write technology. Then we discuss the design and optimization of the diffractive elements used in a particular free-space optical interconnection scheme: the optical transpose interconnection system (OTIS); where we have used CodeV®[9] optical system design software package to design and optimize several different systems based on both refractive and diffractive micro-optic technologies. In addition, we have explored the possibility of using a volume holographic element to replace the need for a polarizing beam splitter in the system.

E-Beam Direct Write Diffractive Element for OptoElectronic Computing Systems

We will present experimental results of analytic-type diffractive optical elements for Free Space Optical Interconnects systems. These elements were all designed using CodeV® and fabricated using e-beam direct write techniques. Arrays of lenslets were fabricated to provide a 64x64 shuffle-exchange and a 8x8 twin-butterfly interconnections.

Computer Simulation and Optimization of OTIS Optical Elements

We have modeled, using Code V® software, various 256 channel OTIS systems. First order geometrical approximations determine the initial design of each system given fixed parameters such as 500 μm source spacing, f/4 optics, and unit system magnification. The optimization goal is to maximize the amount of light captured by a small (typically 20μm x 20μm) aperture on the output plane, representing a detector element on an opto-electronic chip. The various models include systems consisting of refractive lenslets as well as spherical and aspheric diffractive lenslets. Lenslet array systems are defined as those in which all lenslets within an array are identical. The individual lenslet systems are more complex, having each lenslet independently optimized for the particular interconnect paths it is required to support. The four systems chosen for study represent a progression in increasing design complexity and fabrication cost as well as expected performance.

Design and Optimization Approach

Traditional optical system design software is not well suited to modeling a highly parallel 256 channel free-space optical interconnection system. The limits on the total number of field points (25) and the enormous computational task of optimizing large non-sequential surface (NSS) ranges, needed for defining the individually optimized lenslets, prohibit the implementation of a complete model of the system. To accurately model OTIS we take advantage of the large degree of symmetry inherent in the system in order to reduce the complexity to a manageable amount.

The sources, representing either optical modulator or vertical cavity surface emitting laser (VCSEL) arrays, are modeled as object field points. To increase efficiency and reduce cross-talk, the chief rays of each source is aimed at its respective interconnect lenslet using the CRA command. Modeling all of the interconnect paths is impossible

because of the limited number of field points allowed by the design software. A sub-set of interconnection paths must therefore be selected. For the 256 channel system, there are three unique lenslet functions on each lenslet plane. The paths are chosen such that each pairing of the lenslets functions between the two planes is represented; only unique paths are included. Each field point is weighted according to the total number of paths it represents.

The directed illumination of the modulators is formed by uniformly illuminating an array of off-axis lenslets having square apertures. As a result the modulated light will have a sinc^2 profile. We have approximated this as a Gaussian, as this type of apodization is much easier to implement in CodeV®. This approach is also valid if VCSELs are used rather than modulators. All systems have two glass plates included which represent the lenslet substrates. We have included 1.2mm thick low-expansion (LE) glass plates as this is the substrate used for the in-house fabrication of CGH's.

Each interconnect lenslet plane is defined as a non-sequential surface range. Our initial designs were accomplished by specifying a single element and using the ARR command to replicate it into an array. For the individual lenslet systems we needed to set up a plane of non-identical lenslets. To insure that all rays intersect the proper lenslet we had to use non-sequential surfaces (NSS). Both NSS ranges have zero thickness; they are located on the surface of the substrates. Within each range the x-y location (decentration) and size (clear aperture and edge location) of all the lenslets are defined.

As a result of such modeling, it is shown that aspheric individually optimized lenslets provide the best optical performance, although some limitations on uniformity and aberrations are still evident. The CodeV files are also used to generate the fabrication data for the lenslets.

Birefringent Computer Generated Holograms

In the case where the optical transmitters are modulators, we are studying different methods of illumination. In order to maximize light coupling into the OTIS interconnect optics, the modulators should be illuminated off normal. The most promising approach to achieve this uses an area-multiplexed off-axis diffractive lenslet array. Such a system provides the necessary directed illumination. For reflection-mode modulators the system must be 'folded' onto itself. In this case, both the illumination and interconnection optics can be combined into the same optical element using the technology of birefringent computer generated holography (BCGH)[10]. A BCGH is a computer generated hologram (CGH) with two different phase functions, one for each state of linear polarization. If multiple quantum well (MQW) electro-absorptive modulators are used, then a quarter-wave retardation plate is needed between the BCGH and the lenslet plane. No waveplate is needed if Lead Lanthanum Zirconate Titanate (PLZT) electro-optic modulators are used, as these provide the necessary polarization rotation. With such an illumination system the off-axis performance of the modulators may be an issue. MQW's have been shown to have a suitably wide (10°-15°) angular acceptance range[11]. We are presently evaluating the off-axis performance of PLZT modulators; preliminary results show acceptable performance ±15° from the normal.

The BCGH technology can be used to implement both the area-multiplexed illumination lenslets and the OTIS lenslets in a modulator based system and we are in the process of fabricating and testing in a system environment the first such array.

Photorefractive Beam Splitter

Interconnection systems with light modulators as transmitters require a beamsplitter or equivalent component. This element is necessary to direct illumination light to the modulators and provide low losses on the interconnect path. The traditional component used is a Polarizing Beam Splitter (PBS) in combination with a quarter-wave retardation plate; however PBS's have major drawbacks in OTIS. PBS's have a limited angular acceptance range, typically ±5°; exceeding this range results in polarization 'crosstalk' and lessened overall efficiency. Staying within this range leads to high f# optics, given by:

$$f_{\#} \geq \frac{1}{\sqrt{2}}\left(\frac{\sqrt{M}}{\sqrt{M}+1}+\frac{\sqrt{N}}{\sqrt{N}+1}\right)\bullet\frac{1}{\tan 5^{\circ}}$$

For example, a 256 channel system ($M = N = 16$) would be limited to f/12.9 or greater optics, and a 4096 channel system ($M = N = 64$) would be limited to f/14.1. Note that the total system length is proportional to the f# and low f# lenses, both refractive and diffractive, are available. Thus, a PBS unnecessarily increases the system length.

We replace the PBS with a volume hologram recorded in Iron doped Lithium Niobate (Fe:LiNbO3). Such an element utilizes the Bragg selectivity of a volume grating rather that the polarization selectivity of a PBS to distinguish between the illumination and interconnect paths. Incident plane wave illumination may be diffracted towards the modulators with good efficiency, since only one hologram is recorded; while the interconnection paths (composed of off-axis convergent and divergent beams not meeting the Bragg condition) suffer only minimal losses due to surface reflections and absorption.

Theoretical analysis is promising. Analysis based on coupled mode equations predicts peak efficiency (theoretically 100%, but practically we can expect ~60% for a single volume transmission grating in Fe:LiNbO3) achievable over a wide range of incident angles, given the proper exposure; and a Bragg selectivity (angular deviation away from Bragg condition at which the diffraction efficiency has fallen to $1/e^2$ of maximum) of better than 6 arc-minutes. Experiments to verify these performance predictions are in progress; results will be presented.

References

1. M. R. Feldman, S. C. Esener, C. C. Guest, and S. H. Lee, "Comparison between electrical and free-space optical interconnections based on power and speed considerations," *Applied Optics*, **27**, 1742-1751, 1988.
2. F. B. McCormick, A. L. Lentine, R. L. Morrison, J. M. Sasian, T. J. Cloonan, R. A. Novotny, M. G. Beckman, M. J. Wojcik, S. J. Hinterlong, and D. B. Buchholz, "155 Mb/s operation of a FET-SEED free-space switching network," *IEEE Photonics Technology Letters*, **6** (12), 1479-81, 1995.
3. D. A. Baillie, F. A. P. Tooley, S. M. Prince, N. L. Grant, J. A. B. Dines, M. P. Y. Desmulliez, and M. R. Taghizadeh, "Implementation of a 16-channel sorting module," *OSA Topical Meeting on Optical Computing*, 5-7, Salt Lake City, 1995.
4. S. Araki, M. Kajita, K. Kasahara, K. Kubota, K. Kurihara, I. Redmond, E. Schenfeld, and T. Suzaki, "Massive optical interconnections (MOI): interconnections for massively parallel processing systems," *OSA Topical Meeting on Optical Computing*, 263-265, Salt Lake City, 1995.
5. D. V. Plant, B. Robertson, H. S. Hinton, W. M. Robertson, G. C. Boisset, N. H. Kim, Y. S. Liu, M. R. Otazo, D. R. Rolston, and A. Z. Shang, "16 channel FET-SEED based optical backplane interconnection," *OSA Topical Meeting on Optical Computing*, 272-274, Salt Lake City, 1995.
6. B. Mansoorian, G. Marsden, V. Ozguz, C. Fan, and S. Esener, "Characterization of a free-space optoelectronic interconnect system based on a Si/PLZT smart pixel," *OSA Topical Meeting on Spatial Light Modulators and Applications*, 128-131, Palm Springs, 1993.
7. B. Mansoorian, V. Ozguz, C. Fan, and S. Esener, "Design and implementation of flip-chip bonded Si/PLZT smart pixels," *LEOS Summer Topical Meeting on Smart Pixels*, 128-131, Santa Barbara, 1993.
8. K. W. Goosen, A. L. Lentin, J. A. Walker, L. A. D'Asaro, S. P. Hui, B. Tseng, R. Leibenguth, D. Kossives, D. Dahringer, L. M. F. Chirovsky, and D. A. B. Miller, "Demonstration of a dense, high-speed optoelectronic technology integrated with silicon CMOS via flip-chip bonding and substrate removal," *OSA Topical Meeting on Optical Computing*, 142-144, Salt Lake City, 1995.
9. Code V® is a registered trademark of Optical Research Associates, Pasadena, CA
10. F. Xu, J. E. Ford, and Y. Fainman, "Polarization-selective computer-generated holograms: design fabrication, and applications," *Applied Optics*, **34**, 256-266, 1995.
11. F. B. McCormick, T. J. Cloonan, A. L. Lentine, J. M. Sasian, R. L. Morrison, M. G. Beckman, S. L. Walker, M. J. Wojcik, S. J. Hinterlong, R. J. Crisci, R. A. Novotny, and H. S. Hinton, "5-Stage free-space optical switching network with field effect transistor self-electro-optic-effect device smart-pixel arrays," *Applied Optics*, **33**, 1601-1618, 1994.

Integration of Diffractive Optical Elements with Vertical-Cavity Surface-Emitting Lasers

M.E. Warren, T.C. Du, J.R. Wendt, G.A. Vawter, K.L. Lear, S.P. Kilcoyne, R.F. Carson, P.K. Seigal, M. Hagerott Crawford, H. Hou and R.P. Schneider

Sandia National Laboratories, P.O. Box 5800 MS 0603
Albuquerque, NM 87185-0603, ph. (505) 844-7208; fax 844-8985

Vertical-cavity surface-emitting lasers (VCSELs) are very desirable sources for a variety of optical system applications. In particular, the inherent planarity of arrays of VCSELs makes them ideal for compact 3-dimensional optical interconnect systems[1]. Despite smaller beam divergence than edge emitting lasers, spreading of the beam emerging perpendicular to the surface of the VCSEL limits the range of free space transmission, reduces the device density in an array and can introduce cross-talk. Although an external optical system using a separate lens array is a possible solution, the idea may be impractical or expensive due to constraints such as space limitations or the additional need for an optomechanical system to position the lenses. An alternative approach is the integration of high efficiency diffractive optics and VCSELs on a single transparent substrate. Such a compact source is also very attractive for miniature optical instrumentation applications. Integrating diffractive optical elements with substrate-emitting VCSELs provides a method for manipulating the propagation properties of the exiting beams[2]. With diffractive structures, a broad range of optical elements can be easily designed and fabricated and high diffraction efficiencies can be achieved with current processing technologies.

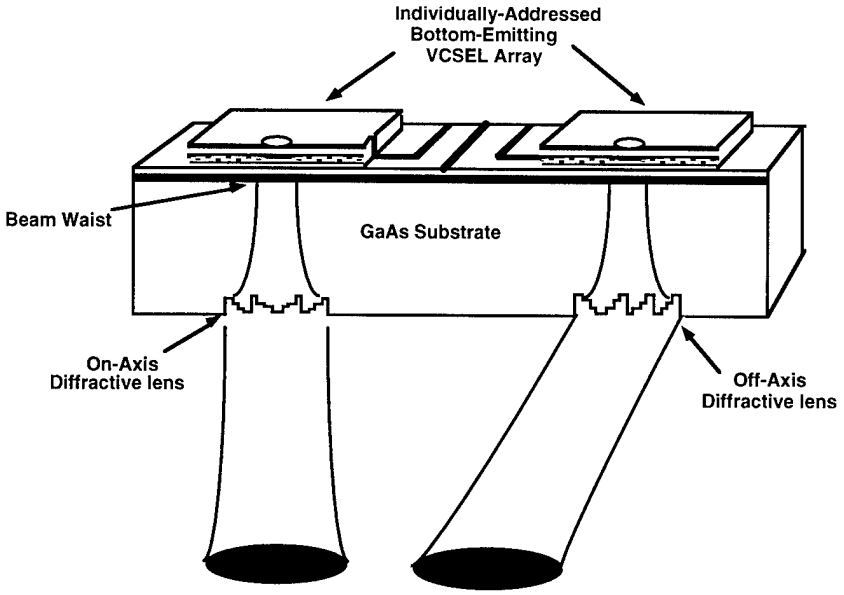


Figure 1. Drawing of VCSEL array with diffractive lenses etched into the transparent substrate.

The basic device concept is illustrated in Figure 1. The integrated device with on-axis lens is designed for use as a laser source with controlled beam properties for a prototype

vertical optical interconnect system for stacked multichip modules. For this interconnect system, the VCSELs transmit an optical signal to photoreceivers located 850 microns away, through 100-micron diameter vias in the silicon mounting module shown in Figure 2.

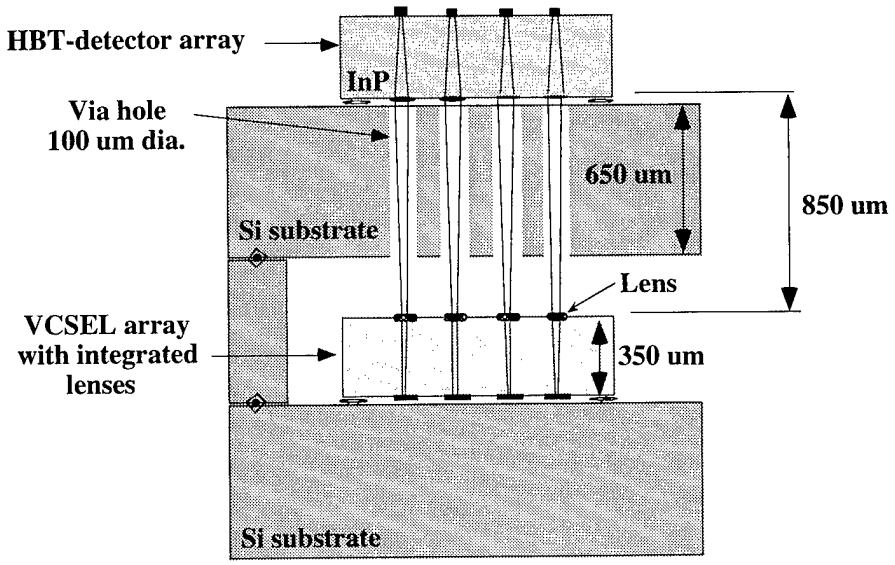


Figure 2. Drawing of one channel of prototype optical interconnect system for stacked multi-chip modules.

The monolithic integrated device is comprised of an independently addressable VCSEL array on top of a 350-micron thick GaAs substrate with an 8-phase level diffractive lens etched on the opposite surface. The VCSELs are fabricated as 4 x 4 arrays on a 500-micron pitch with top-side n and p contacts. The emitted light has a typical wavelength of 970 nm, which allows use of the transparent substrate as an optical medium. The VCSEL array is fabricated first on a substrate already thinned and polished to the desired thickness. The lenses are then fabricated by a sequence of direct-write e-beam lithography steps and reactive ion beam etching steps. Scanning electron micrographs of a finished lens are shown in Figure 3. The efficiency of power transmission through a 100 micron pinhole 850 microns from the lens was measured for devices with and without lenses. The efficiency of transmission through the pinhole increases from about 15% without a lens to over 80% with the lens.

Off-axis lenses have also been fabricated on VCSEL substrates by the same process. The off-axis lens shown in Figure 4 is similar in performance to the on-axis lens with a collimated beam tilted 20 degrees. The off-axis lens integrated into the VCSEL substrate is being developed for position sensing applications that require extremely compact geometries. The off-axis beam allows a simple design for reading of a reflective pattern on a moving surface. Integration of the off-axis lens demonstrates a capability to control the direction as well as the divergence of a VCSEL beam with integrated diffractive lenses.

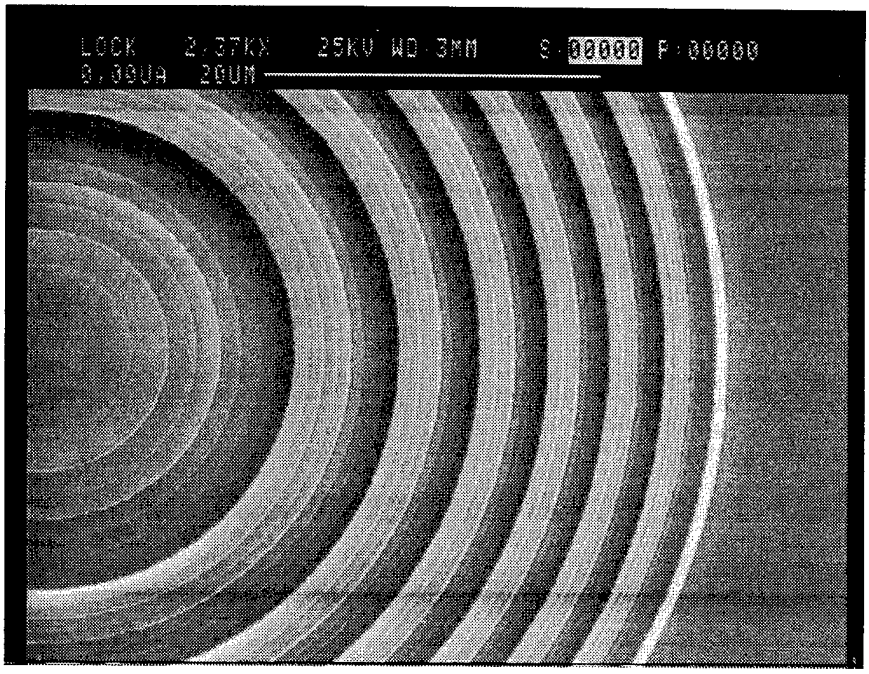


Figure 3. Scanning electron micrograph of diffractive lens fabricated on the GaAs substrate of a VCSEL array. The lens is 80 microns in diameter and has a 110 micron focal length. The smallest features are approximately 0.25 micron.

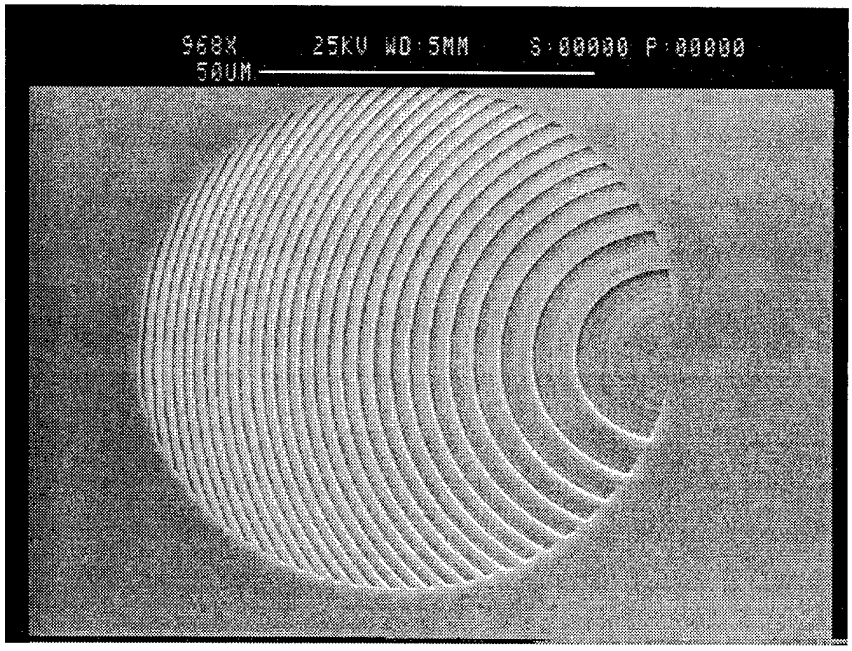


Figure 4. Scanning electron micrograph of an off-axis diffractive lens integrated into a VCSEL array substrate. The specifications are similar to the lens in Figure 3, except the lens is designed to direct the VCSEL beam 20 degrees off-normal.

A top-emitting device cannot use the substrate material as an optical medium as previously described. One approach to combining a top-emitting VCSEL array with diffractive optical elements in a compact package is to use flip-chip bonding of the

VCSELs to a transparent substrate on which the various optical elements can be fabricated[3]. This technique is especially applicable to visible-wavelength VCSEL structures for which the substrate is not transparent. In this case we have fabricated diffractive optical elements in fused silica substrates that the VCSEL arrays can be flip-chip bonded to. We are developing this approach for miniaturized instruments for applications that include displays, scanning and chemical sensing. Figure 5 is a photograph of a VCSEL array flip-chip bonded to a silica substrate, taken from the silica side.

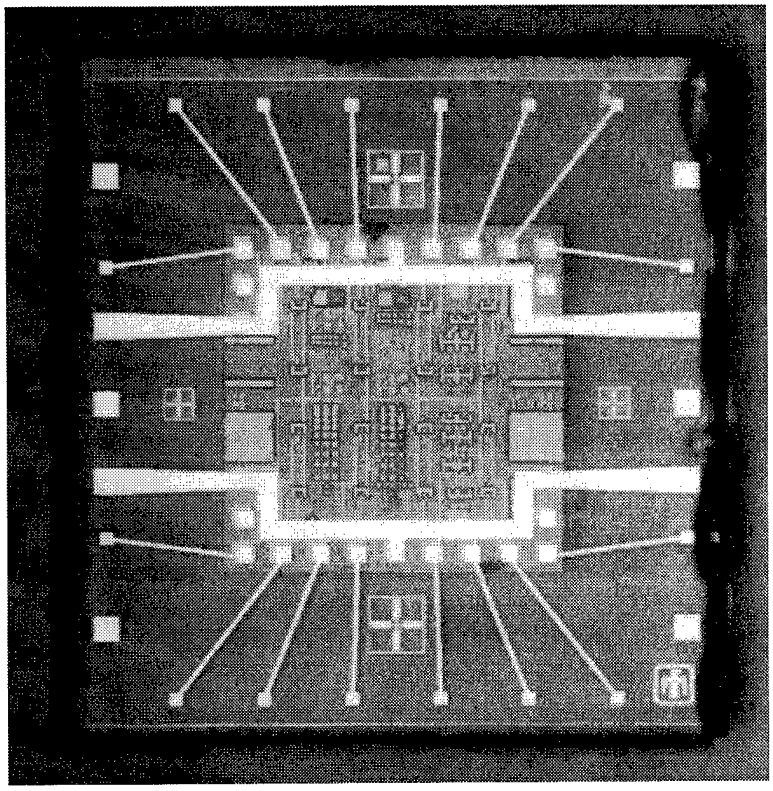


Figure 5. Photograph of a VCSEL array flip-chip bonded to a fused silica substrate, taken through the silica substrate showing the top of the array.

The authors would like to thank S. Samora and T.R. Carter for their expert technical support. T.C. Du is now with Intel Corp. and R.P. Schneider is now with Hewlett-Packard Corp. This work was supported by the Department of Energy under contract DE-AC04-94AL85000.

1. R.F. Carson, P.K. Seigal, D.C. Craft, M.L. Lovejoy, "Future Manufacturing Techniques for Stacked MCM Interconnections", Journal of Metals, **46**, pp. 51-55, 1994.

2. K. Rastani, M. Orenstein, E. Kapon, A.C. Von Lehmen, "Integration of planar Fresnel microlenses with Vertical-Cavity Surface-Emitting Laser arrays", Optics Letters, **16**, pp. 919-921, 1991.

3. J. Jahns, R.A. Morgan, H.N. Nguyen, J.A. Walker, S.J. Walker, and Y.M. Wong, "Hybrid Integration of Surface-Emitting Microlaser Chip and Planar Optics Substrate for Interconnect Applications", IEEE Phot. Techn. Lett., **4**, pp. 1369-1372, 1992.

Diffractive Spot-Array Generation Using Multimode Surface-Emitting Lasers and Light-Emitting Diodes

John S. Hoch, Annette Grot,* T. S. Tan* and Joseph M. Kahn

Department of Electrical Engineering and Computer Sciences
514 Cory Hall, University of California, Berkeley, CA 94720
Phone: (510) 643-8848, Facsimile: (510) 642-2739

* Hewlett Packard Laboratories
3500 Deer Creek Road, Palo Alto, CA 94304
Phone: (415) 857-6848, Facsimile: (415) 857-6241

1. Introduction

The ability to shape the diverging beam from a surface-emitting laser or a light-emitting diode is important for future micro-optic illumination systems. In this paper, we consider using two surface-relief diffractive optical elements (DOEs) to shape the output from a 980-nm multimode vertical-cavity surface-emitting laser (VCSEL) into a closely spaced rectangular spot array in the near field (approximately 10 mm from the laser). We also describe a similar system for illumination by an 850-nm resonant-cavity light-emitting diode (RCLED). With small intensity variation from spot to spot, the rectangular spot array is intended to approximate a profile that is completely uniform from point to point. This design strategy is particularly valuable with the VCSEL, as its complicated multimode emission profile makes it nearly impossible to guarantee absolute uniformity within the rectangle, but creating a rectangular array of light spots spaced very close together is still feasible.

The VCSEL emission profile is determined by the width of the active region and the bias current. The linewidth of our typical 980-nm VCSEL, with a 24-μm active width, increases with bias current and varies from 0.3 nm to 0.7 nm. The far-field divergence angle (FWHM) varies from 3 to 10 degrees, again increasing with bias current. The linewidth of our typical 850-nm RCLED is much broader and equals about 13 nm. The RCLED also emits a nearly Lambertian profile with a far-field divergence angle (FWHM) of approximately 100 degrees. In terms of modeling, the narrow emission spectrum of the VCSEL allows it to be considered as perfectly coherent, whereas the RCLED is modeled more accurately as narrowband and spatially incoherent.

2. The Cascaded Approach

The cascaded-DOE approach that we investigated uses a phase Fresnel zone plate (FZP) and an array generator to produce a rectangular spot array with small intensity variation (see Fig. 1). The rectangular spot array is meant to be observed in the image plane of the phase FZP. This technique of using two DOEs instead of one is advantageous in that the focusing function of the total optical system can be assigned to the phase FZP. This allows the array generator and the phase FZP to be designed independently. Furthermore, this cascaded approach works well with either VCSEL or RCLED illumination.

The first element in our cascaded approach, the phase FZP, determines the size of an individual spot in the image plane. A phase FZP is merely a staircase approximation to a phase Fresnel lens, and it has increasing efficiency for an increasing number of phase levels. For example, a two-phase FZP can be shown to have a maximum diffraction efficiency of 40.5%, and a four-phase FZP to have an upper limit of 81%. The second element in our cascaded approach, the array generator, determines the overall shape and spacing of the closely spaced spots in the image plane. In this paper, we are interested in rectangular spot arrays, but the array generator is capable of creating arbitrary shapes.

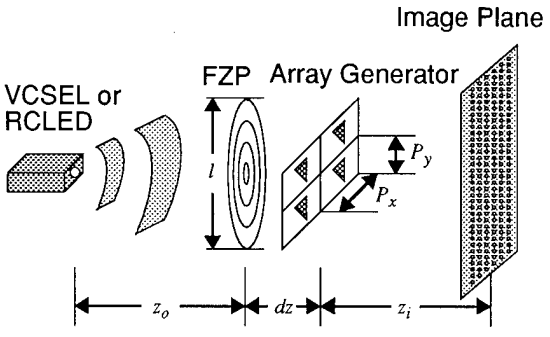


Fig. 1 Cascaded-DOE approach to achieving a rectangular spot array.

3. Theory of Spot-Array Generation with Multimode VCSELs

The total optical system is nearly invariant to the complicated multimode profile of the VCSEL. This can be seen by computing the field that results in an arbitrary observation plane. Modeling the VCSEL field as monochromatic and using the Fresnel approximation [1], the complex electric-field amplitude in a plane a distance z behind the array generator is given by

$$\mathbf{U}_1(x_1, y_1) = \left(\frac{\pi l^2}{4\lambda^2 z^2}\right)\mathbf{U}_{V1}(x_1, y_1) * \sum_{m,n=-\infty}^{\infty} \alpha_{mn} \frac{2J_1\left(\frac{\pi l}{\lambda z}\sqrt{\left(x_1 - \frac{m\lambda z}{P_x}\right)^2 + \left(y_1 - \frac{n\lambda z}{P_y}\right)^2}\right)}{\frac{\pi l}{\lambda z}\sqrt{\left(x_1 - \frac{m\lambda z}{P_x}\right)^2 + \left(y_1 - \frac{n\lambda z}{P_y}\right)^2}}, \quad (1)$$

where * represents convolution, $J_1(x_1, y_1)$ is the Bessel function of the first kind of order one, λ is the wavelength, l is the diameter of the phase FZP, and α_{mn} are the Fourier series coefficients of the array generator, which has periods P_x and P_y along x and y, respectively. $\mathbf{U}_{V1}(x_1, y_1)$ is the complex electric-field amplitude in the observation plane due to the phase FZP acting alone on the VCSEL field. If the observation plane is restricted to the image plane of the phase FZP, $\mathbf{U}_{V1}(x_1, y_1)$ is the VCSEL image. Equation (1) indicates that $\mathbf{U}_{V1}(x_1, y_1)$ is widened in the observation plane, and that multiple replicas of this field occur periodically. Thus, regardless of the VCSEL profile, a rectangular spot array can be produced in the image plane, as the array generator can be designed to selectively create VCSEL images.

4. Coherent Impulse Response of Optical System

The coherent impulse response of the total optical system can be used to determine the field in any observation plane given an arbitrary field in the exit aperture of the VCSEL. More importantly, it can also be used in the analysis of the two-element system with RCLED illumination. Using Fresnel diffraction theory, the impulse response can be derived exactly and then used to arrive at the same expression as in (1). However, this particular impulse response is not a simple expression, which complicates the analysis of the optical system with RCLED illumination. The impulse response is considerably simplified if the observation plane is restricted to the image plane, and the lens law is assumed to hold. The lens law is given by $1/z_i + 1/z_o = 1/f$, where z_o is the object distance, z_i is the image distance, and f is the focal length of the phase FZP. With this assumption, the impulse response is given by

$$h(x_i, y_i; x_o, y_o) = \left(\frac{\pi l^2}{4\lambda^2 z_i z_o}\right)\exp\left[\frac{j\pi}{\lambda}\left(\frac{x_i^2 + y_i^2}{z_i} + \frac{x_o^2 + y_o^2}{z_o}\right)\right] \sum_{m,n=-\infty}^{\infty} \alpha_{mn} \frac{2J_1\left(\frac{\pi l}{\lambda z_i}\sqrt{\left(x_i + Mx_o - \frac{m\lambda z_i}{P_x}\right)^2 + \left(y_i + My_o - \frac{n\lambda z_i}{P_y}\right)^2}\right)}{\frac{\pi l}{\lambda z_i}\sqrt{\left(x_i + Mx_o - \frac{m\lambda z_i}{P_x}\right)^2 + \left(y_i + My_o - \frac{n\lambda z_i}{P_y}\right)^2}}. \quad (2)$$

As an example, using (2) allows the amplitude in the image plane, $\mathbf{U}_i(x_i, y_i)$, to be expressed as

$$\mathbf{U}_i(x_i, y_i) = \left(\frac{\pi l^2}{4\lambda^2 z_i^2}\right)\exp\left[j\frac{\pi}{\lambda z_i}\left(x_i^2 + y_i^2\right)\right] \int\int_{-\infty}^{\infty} \frac{1}{M}\mathbf{U}_{Vo}\left(\frac{x_i - \tilde{x}_o}{-M}, \frac{y_i - \tilde{y}_o}{-M}\right)\exp\left(j\frac{\pi}{\lambda z_o}\left[\left(\frac{x_i - \tilde{x}_o}{M}\right)^2 + \left(\frac{y_i - \tilde{y}_o}{M}\right)^2\right]\right) \sum_{m,n=-\infty}^{\infty} \alpha_{mn} \frac{2J_1\left(\frac{\pi l}{\lambda z_i}\sqrt{\left(\tilde{x}_o - \frac{m\lambda z_i}{P_x}\right)^2 + \left(\tilde{y}_o - \frac{n\lambda z_i}{P_y}\right)^2}\right)}{\frac{\pi l}{\lambda z_i}\sqrt{\left(\tilde{x}_o - \frac{m\lambda z_i}{P_x}\right)^2 + \left(\tilde{y}_o - \frac{n\lambda z_i}{P_y}\right)^2}} d\tilde{x}_o d\tilde{y}_o, \quad (3)$$

where $\mathbf{U}_{Vo}(x_o, y_o)$ is the complex amplitude in the exit aperture of the VCSEL (the object), and M is defined as z_i/z_o. Equation (3) can be interpreted as a convolution between the VCSEL image according to geometric optics and the same function as in (1). Thus, Eq. (3) is an approximation to Eq. (1), if (1) is restricted to the image plane. Equation (3) can be directly compared to the result derived for the RCLED.

5. Theory of Spot-Array Generation with RCLEDs

Unlike the VCSEL, which can be modeled as a monochromatic source whose near-field characteristics can be described with Fresnel diffraction, the RCLED must be treated in a different manner. Specifically, it can be considered as an extended collection of independent radiators, and consequently, it can be modeled as a narrowband and spatially incoherent field. Within the theory of partial coherence [2], the spatial and temporal-coherence properties of a general electric field can be described with a mutual-coherence function, which is defined as

$$\Gamma_{12}(\tau) = \langle \boldsymbol{u}(P_1, t+\tau)\, \boldsymbol{u}^*(P_2, t)\rangle, \quad (4)$$

where the angle brackets refer to a time average. The function $\boldsymbol{u}(P_1, t)$ is called the analytic signal evaluated

at point P_1 and time t, and it is not the same as the complex electric-field amplitude considered previously in the monochromatic case. The analytic signal can be defined for a monochromatic field and a nonmonochromatic field. The intensity at point P_1 is related to the mutual-coherence function by

$$I_1(P_1) = \Gamma_{11}(0) . \tag{5}$$

For propagation, it is often easier to use the Fourier transform of the mutual-coherence function, known as the cross-spectral density. Using this approach, and after some manipulation, the intensity in the image plane of the phase FZP can be expressed as

$$I_i(x_i, y_i) = \int_0^{\infty} \int_{-\infty}^{\infty} \int I_{RCo}(x_o, y_o, \lambda) \left| h(x_i, y_i ; x_o, y_o) \right|^2 dx_o dy_o d\lambda , \tag{6}$$

where $I_{RCo}(x_o, y_o, \lambda)$ is the intensity spectrum of the RCLED. Substituting (2) into (6) yields

$$I_i(x_i, y_i) = \left(\frac{\pi l^2}{4\lambda^2 z_i z_o} \right)^2 \int_0^{\infty} \int_{-\infty}^{\infty} \int \frac{1}{M^2} I_{RCo}\left(\frac{x_i - \tilde{x}_o}{-M}, \frac{y_i - \tilde{y}_o}{-M}, \lambda \right)$$

$$\left| \sum_{m,n=-\infty}^{\infty} \alpha_{mn} \frac{2J_1\left(\frac{\pi l}{\lambda z_i} \sqrt{\left(\tilde{x}_o - \frac{m\lambda z_i}{P_x} \right)^2 + \left(\tilde{y}_o - \frac{n\lambda z_i}{P_y} \right)^2} \right)}{\frac{\pi l}{\lambda z_i} \sqrt{\left(\tilde{x}_o - \frac{m\lambda z_i}{P_x} \right)^2 + \left(\tilde{y}_o - \frac{n\lambda z_i}{P_y} \right)^2}} \right|^2 d\tilde{x}_o d\tilde{y}_o d\lambda . \tag{7}$$

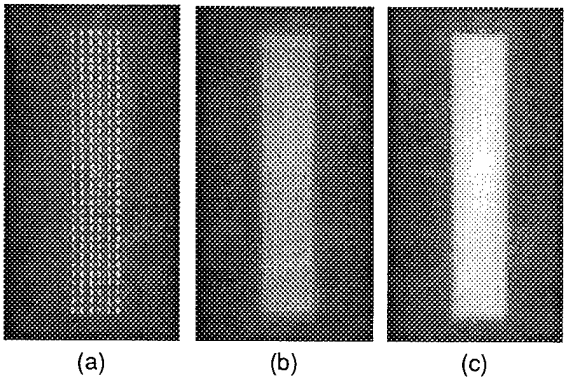
For a fixed wavelength λ, (7) is a convolution between the geometric image of the RCLED and a function that has multiple peaks. This means that the RCLED image is widened and replicated in the image plane of the phase FZP, just like for the VCSEL (cf. Eq. (3)). On the other hand, unlike (3), Eq. (7) is a convolution between two real and non-negative functions, instead of two complex functions. This means that if the peaks of the squared impulse response in (7) are spaced close enough together, the rectangular region will tend to be uniform everywhere, even between the spots. When the two functions are complex, as in (3), coherent interference will lead to a lack of uniformity. Thus, the lack of spatial coherence in the RCLED will serve to smooth the image.

For other wavelengths, the widened images are shifted, where the maximum shift for an RCLED of bandwidth $\Delta\lambda$ equals $m\Delta\lambda z_i / P_x$ along x_i and $n\Delta\lambda z_i / P_y$ along y_i. The shift is larger for images that are farther from the axis, which correspond to larger values of m and n. Thus, the lack of temporal coherence in the RCLED also plays a significant role in smoothing the image.

6. Experimental Results with VCSEL Illumination

We have fabricated the two elements necessary to shape the multimode profile from a 980-nm VCSEL with a 24-μm active-region diameter to a rectangular spot array approximately 200 μm × 1240 μm. The total path length from the VCSEL to the image plane is about 10 mm, making it a very compact system. The phase FZP and the array generator were fabricated on the front and back side of a quartz wafer of thickness 500 μm. The focal length of the phase FZP is 2405 μm. Using Gaussian beam theory as an approximation, the spot diameter in the image plane equals 18 μm for a 14-μm emission diameter. The zone plate was fabricated with four levels and an $f/\#$ of about unity (diameter = 2500 μm), leading to a minimum zone width of approximately 0.5 μm for the outer zone. The array generator, designed with the "even-orders-missing" (EOM) technique [3], is a two-phase element with a minimum feature size of 0.5 μm. The fundamental cell has a period of 245 μm in each direction, which determines the 40-μm spot separation in the image plane. The array generator produces a 6 × 32 spot array to form the desired rectangle. Theoretically, it has a diffraction efficiency of 75% and a uniformity deviation of 0.3% (the uniformity deviation is defined as $(\eta_{max} - \eta_{min}) / (\eta_{max} + \eta_{min})$, where η_{max} and η_{min} are the maximum and minimum diffraction efficiencies to individual spots). In the fabricated array generator, the fundamental cell was stepped 41 times in each direction, making it about 1 cm on a side.

Figure 2a shows an image captured by a lensless CCD camera (Electrophysics 1370) that was produced by the two-element system. The VCSEL was biased below threshold to prevent complete camera saturation. The uniformity deviation was measured to be 8.8% by using the captured image and assigning the value of η to



(a) (b) (c)

Fig. 2 Images produced with (a) VCSEL illumination (bias = 2 mA), (b) RCLED illumination (bias = 1 mA) and (c) RCLED illumination (bias = 1.5 mA).

each spot according to the largest intensity value within the spot. Upon close examination of this image, it is evident that the intensity of the zero-order beam was less than any of the spots in the desired array, which is consistent with the EOM design technique that theoretically eliminates this order. The zero-order beam is very sensitive to etch-depth errors in particular. The overall efficiency of the total optical system, for a VCSEL biased above threshold, was measured to be 52% by using an aperture to block light outside the desired rectangle. The theoretical maximum overall efficiency of this system is 61%, which is the product of the array-generator theoretical diffraction efficiency (75%) and the phase-FZP theoretical diffraction efficiency (81%).

7. Experimental Results with RCLED Illumination

Similar to the VCSEL case, the two elements necessary to image the profile from an RCLED have been fabricated on the front and back side of a quartz wafer. The four-phase FZP is very similar to its VCSEL counterpart, as is the two-phase array generator, only here the phase FZP has a focal length of 2480 μm and the array generator has a period of 212 μm. The period of the array generator was altered to maintain the 40-μm spacing between the spots for the 850-nm source. The theoretical diffraction efficiency and uniformity deviation of the array generator are 74% and 0.6%, respectively. Using geometric optics, the spot diameter in the image plane is 37 μm for an RCLED with a 30-μm emitting aperture.

Figures 2b and 2c show two images captured by the lensless CCD camera for two different RCLED bias conditions. The captured images appear significantly different than those produced with VCSEL illumination. In particular, the replicated RCLED images are not distinguishable, and the rectangular region appears very uniform throughout due to the size of the magnified spot and also due to temporal and spatial-coherence effects. In fact, for this case it is necessary to compute a point-to-point uniformity deviation instead of a spot-to-spot uniformity deviation, as was done for the VCSEL. For Fig. 2b, where the camera did not saturate, and ignoring edge regions, the uniformity deviation was 9.3%. The overall efficiency was measured to be 3.4%, which is low due the small fraction of the incident light captured by the phase FZP. Assuming a Lambertian source, the maximum overall efficiency is given by the squared numerical aperture of the phase FZP (7.2%) multiplied by the maximum diffraction efficiency of the cascaded DOEs (60%), which equals 4.3%. It is evident from Fig. 2 that very little of the zero-order beam was present in the image, as desired. Fig. 3 shows part of a magnified image produced by the two-element system in which the individual spots were partially resolvable. The image was magnified by increasing the ratio of z_i to z_o, while still maintaining focus according to the lens law. Close examination of this image indicates that regions of very low intensity were not present between the spots, which agrees with our analysis of this partially coherent imaging system.

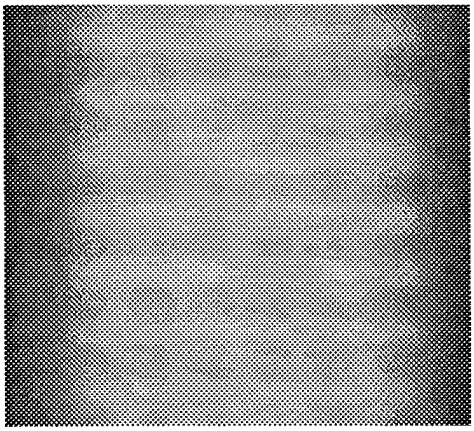


Fig. 3 Part of magnified image from two-element system with RCLED illumination.

References

[1] J. W. Goodman, *Introduction to Fourier Optics* (McGraw-Hill, New York, 1968).

[2] M. J. Beran and G. B. Parrent, Jr., *Theory of Partial Coherence* (Prentice-Hall, Englewood Cliffs, NJ, 1964).

[3] A. Vasara, M. R. Taghizadeh, J. Tarunen, J. Westerholm, E. Noponen, H. Ichikawa, J. M. Miller, T. Jaakkola, and S. Kuisma, "Binary surface-relief gratings for array illumination in digital optics," *Appl. Opt.* **31**, 3320-3336 (1992).

3 X 3 Optoelectronic Cross-Bar Switch Using Vertical Cavity Surface Emitting Laser Arrays

N. Rajkumar, J. N. McMullin, B. P. Keyworth, R. I. MacDonald
Telecommunication Research Labs
800 Park Plaza
10611 - 98 Ave., Edmonton
Canada, T5K 2P7
Phone: (403)4413800, Fax: (403)4413600
e-mail: rnagaraj@edm.trlabs.ca

Introduction: In an electronic space division switch matrix, the system performance at high frequencies is subject to degradation because of crosstalk due to electromagnetic coupling in adjacent signal paths. A substantial improvement in performance can be obtained if the incoming signals were optical and the outgoing electrical with optical detectors acting as the cross points[1,2]. As the incoming paths are optical, a great degree of immunity to crosstalk can be gained, and the crosstalk that may arise in the outgoing electrical lines could be reduced by proper shielding as the adjacent conductor lines are no longer electrically connected. Such switching matrices may also be applied in high speed analog and digital signal processing applications [3,4]. The signal distribution in optoelectronic switches has been done in the past using 1:N multimode fibre splitters and butt-coupling the fibres to the MSM detectors by prealigning the fibres in etched silicon V-groove arrays. Two drawbacks of the fibre distribution method are that it is very fragile and handling large number of fibres is difficult and time-consuming. Alternative approaches are the use of integrated waveguide devices for power division or free space interconnect. A 3X3 free space switch prototype using three discrete lasers has been previously reported [5]. In this paper a modified version using vertical cavity surface emitting lasers (VCSEL's) driven by electrical inputs is described.

Design and fabrication: The basic design of the optoelectronic switch is shown in Fig. 1. The switch has three input electrical lines (1,2,3) which can be switched to any of the three output electrical lines (A,B,C). The incoming signals excite a VCSEL array which generates three light beams at 850 nm. The light is collimated and split three ways by a lens-grating arrangement [5]. In order to split the light three ways we have fabricated 1:3 Damman binary gratings [6] on a quartz substrate. The grating period is 20 μm and the etch depth is 0.924 μm giving a 1:3 equal

intensity split with 67% efficiency at 850 nm. On the backside of the quartz substrate we have dispensed polymer microlenses at 250 μm centres using a patented technique [7].

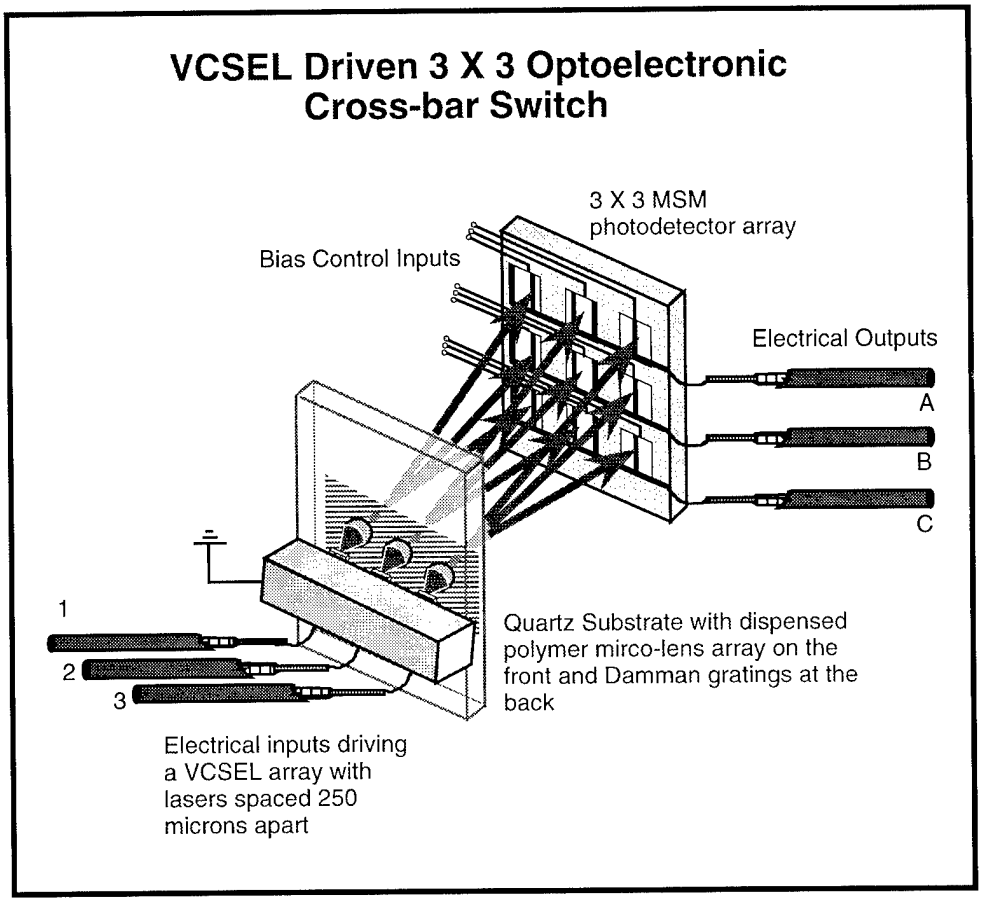


Fig. 1

The three collimated beams are split in the vertical direction by the Damman grating and at a distance of 6 mm from the grating the separation between the 0 and ± 1 diffraction orders reaches 250 μm. Thus there are nine spots of equal intensity in a 3X3 matrix separated by 250 μm in each direction. A camera image of the optical distribution at the detector plane is shown in Fig. 2. A 3X3 metal-semiconductor-metal (MSM) array with detectors at the same spacing is placed at this plane and the detected signals are summed horizontally to complete the optoelectronic switch.

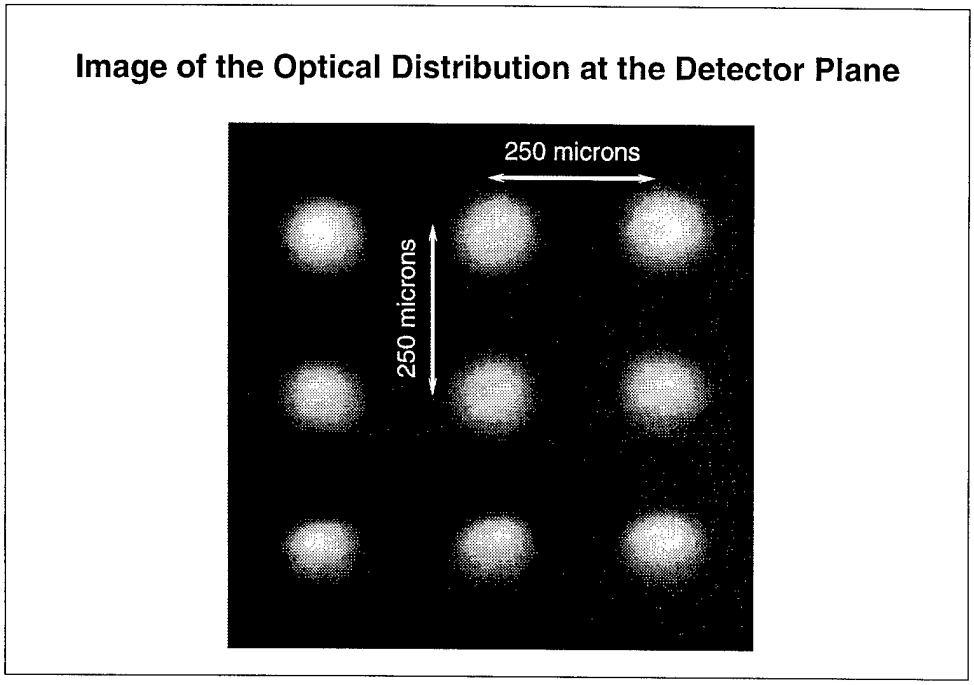


Fig. 2

Experimental Measurements and Discussion: DC cross talk measurements on the detectors were done by illuminating one column of the detectors and measuring the detected current in the detectors of the neighbouring columns. This procedure was repeated for each of the columns, and the average crosstalk was found to be -38.1dB. A crosstalk of -38.1 dB indicates that the switch is well-suited for digital switching applications. The on-off contrast measurements was also done on the detectors by switching the MSM detectors ON and noting the current and then repeating the same by grounding both ends of the detector. The ON-OFF contrast was found to be -37.7 dB. A better contrast is easily achieved by precision biasing the off-state so that the current goes to zero. This has been experimentally verified by biasing one of the detectors to 17.6 mV. The contrast then obtained was -69.5 dB.

Conclusion: A VCSEL driven 3X3 optoelectronic switch with electrical input/output has been designed and fabricated using free space optical distribution. The crosstalk is around -38.1 dB and the ON-OFF contrast around -69.5 dB. The diffraction grating dispensed micro-lens assembly is a highly compact device and could easily be mass produced. The main critical issue to be dealt here

is the proper alignment of the various components. This could be achieved with a suitable precision housing which could also be mass produced.

References

1. R. I MacDonald, E. H. Hara, "Optoelectronic broadband switching array", Electron. Lett., vol. 16, pp. 502-503, 1978.

2. M. Veilleux, R. I. MacDonald, "An optoelectronic switching Matrix with high isolation", JLT, vol. 10, pp. 988-991, 1992.

3. B. E. Swekla, R. I. MacDonald, "Optoelectronic transversal filter", Electron. Lett., 27, pp.1769-1770, 1991.

4. R. I MacDonald, S.S. Lee, "Photodetector sensitivity control for weight setting in optoelectronic neural networks:, Appl. Opt., vol. 30, pp.176-178, 1991.

5. R. Nagarajan, J. N. McMullin, B. P. Keyworth, R. I. MacDonald, "3X3 optoelectronic switch using diffractive optics", MJJ5, OSA Annual Meeting, Portland, Oregon, September, 1995.

6. H. Dammann, E.Koltz, "Coherent-optical generation and inspection of two-dimensional periodic structures", Opt. Acta, Vol. 24, pp.505-515, 1977

7. B. P. Keyworth, J. N. McMullin, D. Corazza, L. Mabbott, T. Neufeld, T. Rosadiuk, "Dispensed polymer microlenses", WVV52, OSA Annual Meeting, Portland, Oregon, September, 1995.

An extensible, diffractive optic system for interconnecting opto-electronic device arrays

Rick L. Morrison
AT&T Bell Laboratories
Naperville, IL 60566

Introduction

The melding of silicon electronic processing circuits with GaAs quantum well optical modulators and receivers provides the opportunity to significantly increase system communication throughput by virtue of integrated high-speed, free-space, optical channels as demonstrated in a recent experiment[1]. A second accomplishment of this experiment, the mounting of the optical platform in an electronics cabinet, illustrates the progress toward adapting the optical infrastructure to more traditional packaging schemes. The challenge of blending opto-electronic techniques into contemporary electronic architectures lies in further reducing the opto-mechanical system volume and cost.

Although several system demonstrators have employed standard refractive lenses (figure 1a), these optics typically have a physical size that is much greater than the opto-electronic chip, while the longitudinal dimension of the system expands as the imaged area is increased. The demanding requirements on spot quality, low field distortion and precision alignment discourage significant cost reductions except through possible large manufacturing volumes.

One alternative optical architecture is based on defining individual optical microchannels[2] between each transmitter and receiver (figure 1b). Typically, each channel utilizes a microlens to collimate and relay a gaussian beam to a secondary microlens that would refocus the beam. Such a space-variant configuration allows great flexibility in creating general interconnections. The primary consideration in this scheme is the density of optical channels that limit the size of the microlenses and thus the maximum range that the beam can be relayed. Unfortunately, a packing density of several tens of channels per square millimeter would nominally limit the interconnection range to a few millimeters.

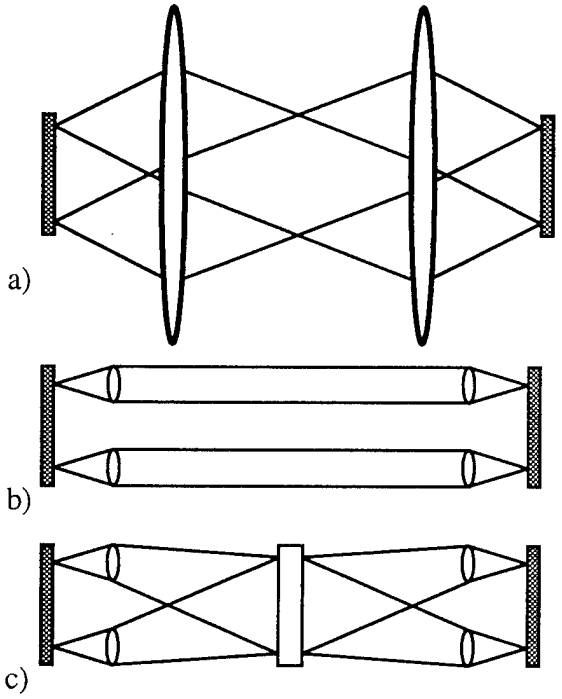


Figure 1. Optical frameworks: a) refractive system, b) microchannel system, c) proposed diffractive system.

The approach presented here (figure 1c), grounded in the microchannel architecture, provides extended interconnection ranges and partitions the optical framework in a manner that allows expansion to very large opto-electronic chips. In addition, domains of low chromatic sensitivity provide operation over a remarkably large wavelength range.

New Optical Framework

The proposed optical structure is a three lens gaussian beam relay constructed explicitly of diffractive lenses as illustrated in figure 2. The slow relay lens is shared by a 2-dimensional group of faster microlenses that generate collimated gaussian beams. Each microlens is designed to create a geometric focus at the center of the relay lens thereby reducing the speed of the relay lens and also enclosing the lateral extent of the system within the bounds of the emitting/receiving area. The purpose of the relay lens is to form a 2f-2f relay system that images the apertures of one microlens array to a secondary set.

The primary advantages of this diffractive optical relay framework are:

- the effective range of the channel is extended several fold over that of the simple microchannel system,
- larger opto-electronic chips can be laterally partitioned into many groups of relays thus leading to great extensibility, and,
- by using diffractive elements, the lenses can be microlithographically defined resulting in precision alignment and uniformly well determined focal lengths.

There are two issues that should be examined whenever diffractive components predominate in a system. First is the subject of the highly chromatic nature of diffractive elements and how this influences operation[3]. The second is the question of diffraction efficiency.

The chromatic properties of the system can be examined by noticing that a ray emitted at the source will have a calculated lateral offset at the image plane equal to,

$$y = \frac{8f \cdot u_0}{(2x-1)^2} \cdot \left(\frac{\delta\lambda}{\lambda} x^2 - 2\left(\frac{\delta\lambda}{\lambda}\right)^3 x^3 \right)$$

where f is the focal length of the microlens, x is the ratio of the focal lengths of the relay lens to the microlens, u_0 is the initial ray slope, and λ is the operating wavelength. By using a small beams (i.e. $f*u_0$ small), the chromatic sensitivity is minimized. Also, the appearance of $\lambda/\delta\lambda$ as a third order dependence indicates that conditions exist where three wavelengths will be properly focused and thus the potential for a flat spectral response region. These predictions have been verified in a more rigorous gaussian beam simulation.

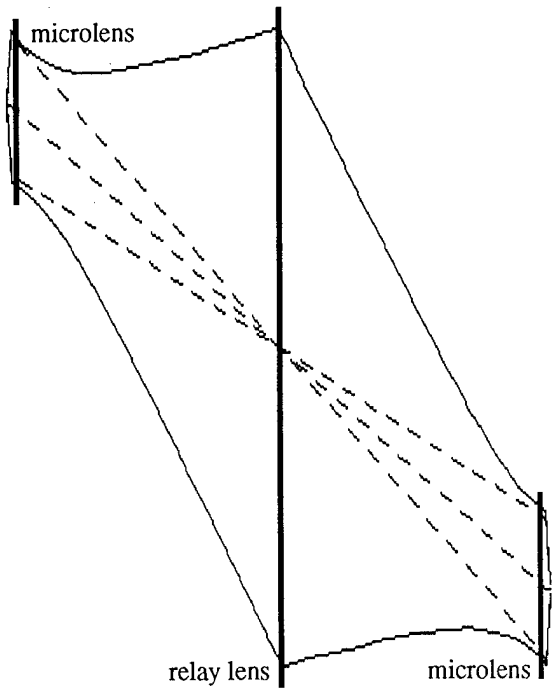


Figure 2. Raytrace of proposed optical framework. An array of diffractive microlenses directs collimated gaussian beams to a slower relay lens that images the waists onto a second microlenses array. Geometric traces are shown as dashed lines.

The reduced chromatic sensitivity for this framework is achieved for relatively short focal length microlenses. This is illustrated by the beam size plots in figure 3 where the system was simulated with gaussian optics in Mathematica™ and verified using CodeV™. The simulated results assume two 340 μm focal length microlens arrays and a 11,000 μm focal length relay lens operating at 850nm. A 5μm gaussian waist diameter is used as the source. The solid curve shows that the final spot size never grows larger than twice its optimal size (5μm diameter) over a 200nm wavelength range. The dashed curve shows the

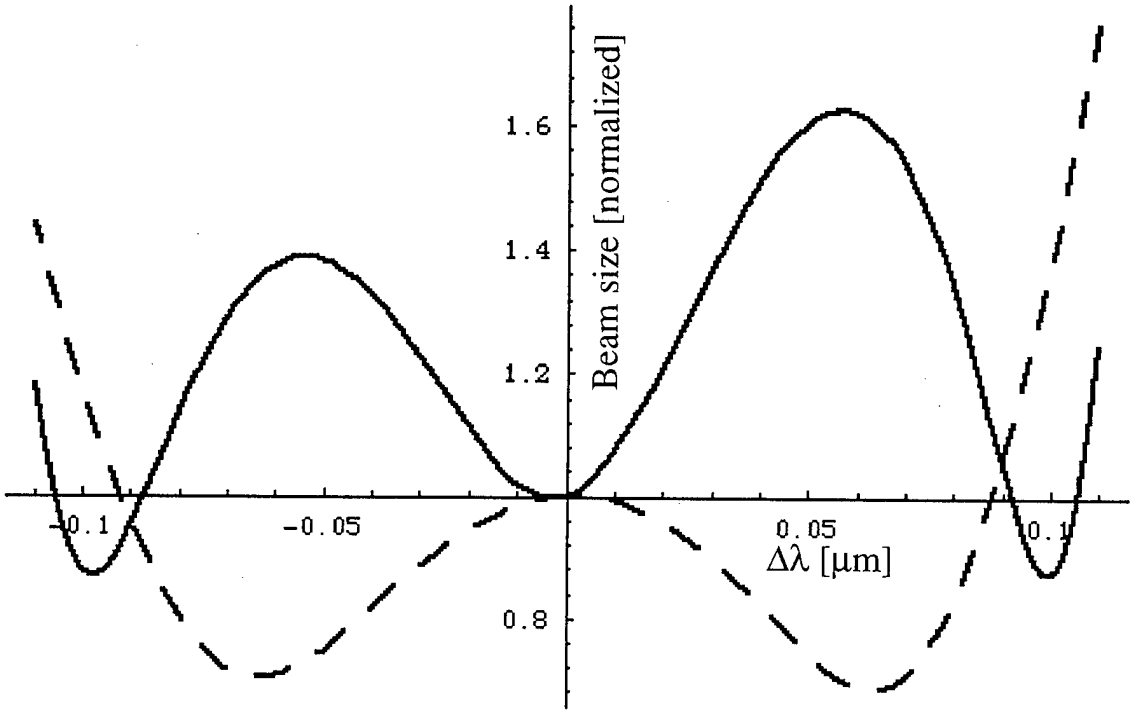


Figure 3. Beam size at entrance to second microlens (dashed) and final image size (solid) normalized to design wavelength operation. Normalizations are 75 and 5 μm diameters respectively at 850nm.

normalized beam size at the entrance to the final microlens. Whenever the beam is smaller than this aperture, there is less concern of coupling light into neighboring channels.

It should be noted that the spot size at the image plane is not the only chromatic effect. For example, wavelengths shifts lead to beam expansion at the relay lens and small to moderate beam steering for sources that are offset from the relay lens optical axis. Therefore initial designs should provide suitably larger apertures than are required at the optimal wavelength. Fortunately, almost all moderate size wavelength shifts result in a smaller beam size at the receiver microlens.

The light coupled between transmitter and receiver will be reduced by the product of diffraction efficiencies of the lenses. Clearly the fast microlenses will account for the most serious power loss. Assuming efficiencies as low as 75% of for each microlens and 90% for the relay lens still provides 50% coupling for a single pass. It is therefore advantageous to consider vertical cavity surface emitting lasers (VCSELs) rather than modulators which would require a double pass through the optics. A further consideration is how the uncoupled light might lead to cross talk between optical channels. This last issue will be examined more rigorously in a future experiment that incorporates this optical framework.

As configured, the system is able to perform operations equivalent to a typical singlet lens system, such as magnification. Thus modules can be constructed to create perfect shuffle interconnections and space-invariant interconnections.

Demonstration

An experiment was assembled from available diffractive optic elements to demonstrate the imaging and chromatic properties of the proposed optical system. The collimating microlenses were part of two 8-level linear microlens arrays etched into fused silica having a focal lengths of 1051μm at an operating

wavelength of 850 nm. These lenses have a circular aperture of 250 μm with centers separated by 250 μm. The first microlens was used to collimate the beam emitted from a single mode fiber. The relay lens was a 5mm circular aperture multilevel diffractive element having a 35mm focal length at an operating wavelength of 850nm also etched into fused silica. A Ti:Sapphire laser coupled into the optical fiber served as the tunable optical source. The tuning range was limited to wavelengths from 790-880 nm.

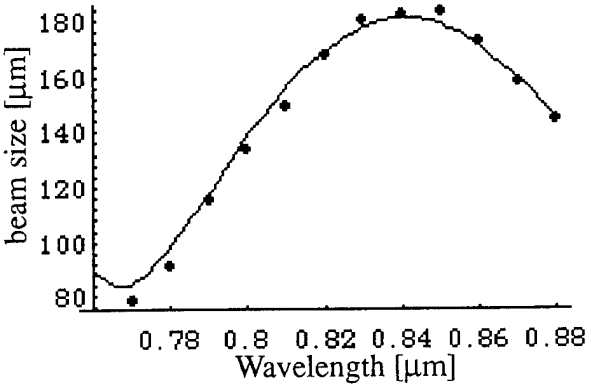


Figure 4. Measured and simulated beam size vs. wavelength at entrance to final microlens.

In this experiment, the optical axes of all lenses were aligned with each other so that the beam was centered with each lens. Lenses were positioned for operation at 850nm. Due to the limited distance between the surface of the final microlens and the image point, and the recessed sensing region in the slit based beam profiler, it was necessary to reimage and magnify the final image spot. This was accomplished using a large field of view 15.6mm focal length lens and a 50mm achromatic lens. The image measurements have been scaled to remove the magnification.

Chromatic effects influencing the beam size at the entrance to the 2nd microlens are illustrated in figure 4. A curve predicted by the simulation traces the measured beam size.

The beam size at the final image as measured and predicted by simulation are shown in figure 5. From the measurement, it can be seen that the image size changes by less than a factor of 3 over a range of about 100nm.

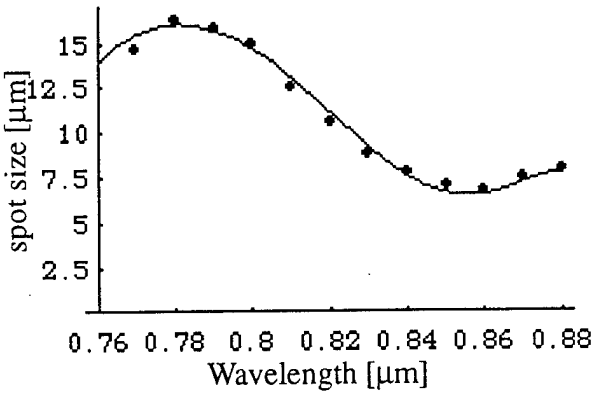


Figure 5. Measured and simulated spot size vs. wavelength at image plane of last microlens.

Summary

The extensibility of this diffractive optical architecture is well suited for both chip-to-chip and backplane optical interconnections. Additionally, the low chromatic sensitivity achieved suggest that either reduced wavelength tolerances or multiwavelength channels can be supported.

The author wishes to thank D.B.Buchholz, J. Jahns, C. Nijander, A. Feldblum, and W. Townsend for suppling the diffractive lenses used in the experiment. This work was partially sponsored by ARPA under Air Force Rome Laboratories contract number F 30602-93-C-0166.

References

1. A.L. Lentine, et.al., "Demonstration of an experimental single chip optoelectronic switching system", post-deadline paper PD2.5, LEOS '95.
2. F.B. McCormick, et. al., "Optical interconnections using microlens arrays," Opt. and Quan. Elect. **24**, S465-477 (1992).
3. For example, R. Kostuk, J. Yeh, M. Fink, "Distributed optical data bus for board-level interconnects", Appl. Opt. **32**, 5010-5021 (1993).

Tuesday, April 30, 1996

Applications I

DTuA 8:30 am-10:00 am
Gardner A&B

Donald Sweeney, *Presider*
Lawrence Livermore National Laboratory

The way of diffractive optics into the laser resonator

Heiko Schwarzer and Frank Wyrowski

Berliner Institut für Optik, Rudower Chaussee 5, D-12484 Berlin, Germany

Abstract

The effect of microstructured profiles on electromagnetic waves is the basic issue of diffractive optics. These profiles represent a significant extension of the possibilities to realize optical functions. Laser optics is of special importance for diffractive optics. In this paper examples of the use of diffractive elements outside and inside the laser resonator are given. Theoretical and experimental results are presented.

Introduction

Diffractive elements (DE) allow the manipulation of the complex amplitude and the polarization of an electromagnetic wave. Moreover, the dispersion caused by diffraction may be used. In the paraxial domain of diffractive optics, the optical effects of a DE always include dispersion. In the non-paraxial domain, also the polarization is typically influenced. Depending on the optical function, scalar or/and rigorous electromagnetic diffraction theory have to be used. In a few situations, even geometrical optics is sufficient to caculate the structure of a DE.

Applications outside the laser resonator

Beam splitting is of interest, not only in optical computing, but also in materials processing. One example is the interconnection between high power Nd:YAG-Laser and a fiber bundle [1]. The optical function is to split the laser beam into 2-9 individual beams. The constraints are: (1) a uniformity error not larger than about $\pm 5\%$, (2) a diffraction efficiency higher than 80 % with as few quantization levels as possible, (3) a given minimum diffraction angle between orders, and (4) a splitting ratio which is independent of polarization. Constraints (1) and (2) can be satisfied by design theory and suitable grating design methods known in the paraxial domain of diffractive optics [2]. Due to constraint (3), the limits of the validity of scalar diffraction theory are reached for higher splitting ratios and not only the uniformity error may become too large but also (4) may be violated. Therefore, a rigorous diffraction analysis has to be performed. The actual results will be presented.

Besides diffraction gratings also non-periodic DEs are of concern in laser optics. Paraxial beam shaping elements are of special interest. Iterative Fourier transform algorithms (IFTA) may be used to design very general beam shaping DEs [3]. Here the initial phase is crucial. Various versions with different features may be chosen. For the special class of beam shaping elements transforming a super-Gaussian beam (separable or circular symmetric function in two dimensions) into another super-Gaussian beam a stationary phase approach is appropriate to design a beam shaping element with continuous profile. In this case the IFTA may be applied to quantize the profile without causing significant errors. Examples will illustrate the beam shaping techniques.

Applications inside of the laser resonator

Leger et al. have introduced the use of diffractive resonator mirros for beam shaping inside the resonator [4]. This step may be understood as a generalization of resonator design which offers fascinating new features. On the basis of this work the use of the IFTA to improve the mode shaping quality has been considered. Several DEs have been designed for various modes.

The mode shaping within the resonator is done by diffractive phase elements, that is the mirros work in the paraxial domain and only the phase of the incident light wave is affected. Also non-paraxial diffractive mirrors are of interest in resonator design [5]. The use of a diffraction grating working in autocollimation (zeroth order is coupled out) has been used to realize a 1.444 μm-Nd:YAG laser with a stable resonator. To this end, a copper grating has been fabricated by optical recording and Cu-galvanic after optimizing the height-to-period ratio by an electromagnetic diffraction method (integral method with parametrization of grating profile [6]). The dispersion of the grating has been used to suppress the strong 1.06 μm-line of the Nd:YAG-slab. Moreover, a similar grating has been introduced to realize an unstable resonator for 1.06 μm-Nd:YAG-laser. To this end, the height of the grating has been modulated by a Gaussian to realize an apodization. The diffraction losses are very small in both situations because only two diffraction orders appear, whereby the zeroth order is used as the outgoing laser light.

Acknowledgement

The authors like to thank Harald Aagedal, Georg Bostanjoglo, Janett Guhr, Bernd Kleemann, Andreas Mitreiter, Hans-Jürgen Rostalski, and Stephan Teiwes for their contributions to the mentioned applications of diffractive optics in laser technology.

References

[1] F. Wyrowski and R. Zuidema, "Diffractive interconnection between high power Nd:YAG-laser and fibre bundle", *Appl. Opt.* **33**, 6732–6740 (1994).

[2] F. Wyrowski and O. Bryngdahl, "Digital holography as part of diffractive optics", *Rep. Prog. in Physics* **54**, 1481–1571 (1991).

[3] H. Aagedal, M. Schmid, T. Beth, S. Teiwes, and F. Wyrowski, "Theory of speckles in diffractive optics and its application in general beam shaping", *J. Mod. Opt.* **43** (1996), in press.

[4] J. R. Leger, D. Chen, and Z. Wang, "Diffractive optical element for mode shaping of a nd:yag laser", *Opt. Lett.* **19**, 108–110 (1994).

[5] A. Mitreiter, J. Guhr, H.-J. Rostalski, and G. Bostanjoglo, "Apodized diffraction grating as outcoupling element for a 1.06 μm nd:yag-laser", in *Diffractive Optics*, 1994 OSA Technical Digest Series **11**, 282–285 (1994).

[6] B.H. Kleemann, A. Mitreiter, and F. Wyrowski, "Integral equation method with parametrization of grating profile: theory and experiments", *J. Mod. Opt.* **43** (1996), in press.

Diffractive Optical Element for Chromatic Confocal Imaging

Sarah L. Dobson, Pang-chen Sun, and Yeshayahu Fainman

University of California at San Diego
Department of Electrical and Computer Engineering
La Jolla, CA 92093-0407

Confocal scanning imaging technique is attractive for various microscopic imaging applications due to its superior resolution, rejection of scattered light, and depth discrimination [1-3]. This method attracted special interest in such applications as imaging biological and semiconductor materials, where high definition in both the transverse and longitudinal dimensions is required. The unique property of the depth discrimination enables the confocal microscope to measure the depth image of a 3-D object by moving different parts of the object transversally and longitudinally into the focal region. The precision of the depth measurement depends on the depth Point-Spread-Function (PSF) of the confocal imaging system as well as the depth resolution of the depth scanning device. To achieve high depth resolution, most of the existing confocal imaging systems use a high precision and very stable mechanical scanning methods. In contrast, chromatic confocal microscope alleviates the requirement of the mechanical depth scanning by employing a broadband light source (e.g., white light source) and a dispersive objective lens for wavelength-depth coding [2-4]. With this method different spectral components of the source are focused onto different depth planes of the object, and the measured output power spectrum is directly translated into the depth information of the object. Furthermore, the chromatic confocal microscope can perform parallel depth measurements when the output power spectrum components are detected and analyzed in parallel.

The existing chromatic confocal microscopes suffer from technological limitations that need to be resolved. For example, commercially available microscope objectives are designed to compensate for chromatic dispersion, thereby limiting the chromatic microscope scanning range. In addition, the dispersive properties of microscope objectives depend on the specific design and lens material characteristics, thus requiring individual calibration. Finally, the dispersion curve of the objective is usually nonlinear resulting in wavelength-dependent sensitivity. In this manuscript, we resolve these technological limitations by using a diffractive optical zone plate for wavelength-depth coding [5]. In contrast to the previous designs that use refractive lenses, the diffractive element provides important features uniquely suitable for this application: (i) the dispersion resulting from diffraction phenomena is, in general, stronger than that from refraction providing a more sensitive wavelength-depth coding; (ii) the dispersion from the diffractive element can be characterized analytically allowing for derived calibration curves. The focal length corresponding to the first diffraction order of a zone plate is given by

$$f(\lambda) = f(\lambda_c)\frac{\lambda_c}{\lambda}, \qquad (1)$$

where λ_c is the center wavelength for the zone plate design, $f(\lambda_c)$ is the focal length of the first diffractive order of the zone plate for the center wavelength, and λ is the operating wavelength. Notice that the focal length vs. wavelength described by Eq. 1 depends only on the design focal length for the center wavelength, and it is not affected by the material properties and type of the zone plate (i.e., amplitude or phase). Due to strong diffractive dispersion effects, a diffractive optical element can provide a desired depth scanning range for a narrower spectral bandwidth of the source. Furthermore, the focal length vs. wavelength relation can be approximated by a linear curve for a relatively narrow wavelength scanning range. The diffraction efficiency of the element is determined by the number of phase quantization levels for the center wavelength and gradually deteriorates when the operating wavelength is changed.

The diffractive optical element used in our experiments was a binary phase zone plate designed for a focal length of 250 mm at a center wavelength of 800 nm. A quartz wafer was first patterned using E-beam lithography, and subsequently, chemically etched in a Hydrofluoric (HF) acid bath. The measured diffraction efficiency of the first diffraction order was about 40%. From Eq. 1, the focal length for the first diffraction order of the zone plate is given by

$$f(\lambda)_{(mm)} = \frac{2\times 10^5}{\lambda_{(nm)}} \approx 470.59 - 0.277\lambda_{(nm)}, \qquad (2)$$

where a Taylor expansion is used to obtain the approximate result with the last term corresponding to the linear approximation for a narrow spectral bandwidth of our laser source at 850 nm. We experimentally measured the focal length of the zone plate over a total spectral range of 150 nm. The measured focal length dependence on the wavelength exactly followed Eq. 2, and the total focal length change covered a range of about 42 mm. The total focal length change corresponds to about 16.8% of the designed focal length. Such a large scanning range in depth has not be achieved using refractive elements.

The experimental setup depicted in Fig. 1 is a confocal microscope system combined with a diffractive optical zone plate to introduce chromatic dispersion. A light beam from a tunable Ti:sapphire laser source (λ=775 to 925 nm) is spatially filtered, expanded, and collimated. The collimation of the beam alleviates the requirement of using an identical optical setup for illumination and detection. After passing through the beam splitter, the light beam was focused by the diffractive optical zone plate. The depth position of this focal point is determined by the operating wavelength. For a tuning range of 150 nm, the focal length of the zone plate varies by 42 mm. The wave transmitted through the diffractive element is introduced into a telecentric imaging system composed of a lens with a focal length of 100 mm and a 40X microscope objective with a focal length of 4.5 mm. The telecentric setup is used to demagnify and image the focal point of the zone plate into the focal plane of the microscope objective. Again, the position of the focal plane is determined by the wavelength of the source. The demagnification process combined with wavelength tuning enables a fine change of the focal plane in depth, which can be characterized by the definition of the wavelength-to-position mapping. A sample introduced in the focal plane of the objective lens will reflect the optical wave back through the telecentric imaging system. After passing through the diffractive zone plate, the resultant collimated diffracted beam is redirected by the beam splitter and focused onto the pinhole-detector assembly of the confocal microscope. The higher order diffraction beams are focused onto different planes in the longitudinal direction and are significantly attenuated by the pinhole. To compare our system to the conventional confocal microscope, we performed mechanical depth scanning by employing a piezoelectric micropositioner assembly (PI Physik Instrumente, PZ54 E-180) used for mounting the microscope objective. The micropositioner is capable of a 100 μm expansion for mechanical depth scanning with 0.01 μm resolution.

For system characterization, we experimentally measured the wavelength-to-depth mapping and the depth PSF. The measurement result (see Fig. 2a) of wavelength-to-position mapping shows, as predicted, a highly linear relation, with a constant sensitivity over a broad wavelength range. A linear curve fit of the experimental data gives the wavelength-to-position mapping,

$$d(\lambda)_{(\mu m)} = (-0.568)\lambda_{(nm)} + 476.79, \qquad (3)$$

where d is the deviation of the focal point, at wavelength λ, from the focal length obtained at the center wavelength of 850 nm. A wavelength tuning of 100 nm is used to achieve an axial position change of 58 μm. The deviation from the linear fit is ±0.15 μm corresponding to 0.5% of the entire depth position range, which is better than that obtained from measurement of the diffractive zone plate alone. This may occur due to the chromatic dispersion compensation between the diffractive element and the refractive microscope objective. We used the

magnification of the telecentric imaging system to verify the result above. The magnification of a telecentric imaging system is equal to the ratio of the focal lengths of the lenses employed. Alternatively, the longitudinal magnification is a square of the transverse magnification. Therefore, the transverse magnification M of the telecentric imaging system can be calculated from our experimental results by taking the square root of the ratio between the linear coefficients in equations (2) and (3)

$$M = \sqrt{\frac{0.277 \times 10^3}{0.568}} = 22.1 = \frac{F}{f_{MO}}, \qquad (4)$$

where F and f_{MO} are the focal lengths of the lens and the microscope objective, respectively. This result is consistent with the data provided by the manufacturer (Oriel Corporation, 40X microscope objective f= 4.5 mm and the second lens F=100 mm, resulting M=22.2). Figure 2b shows the measurement result of the longitudinal point spread function from the chromatic confocal system. We estimated a Full Width Half Maximum (FWHM) of $\Delta\lambda$=4.49 nm that corresponds to Δd=2.55 μm in depth. This value is approximately equal to the measured FWHM value of point spread function (Δd=2.56 μm) using the piezoelectric micropositioner assembly in a conventional confocal system arrangement. Figure 3 depicts the measured profile of an experimental sample using both the chromatic (see Fig. 3b) and the conventional (see Fig. 3a) confocal microscope. The sample is a binary grating coated with a 20 nm thin film of gold to provide higher reflectivity. From the measured data, we estimate that the chromatic confocal method provides a grating depth of 8.47 μm, while the conventional method provides a grating depth of 8.44 μm. The two resultant profiles are found to be in good agreement.

In conclusion, we demonstrate a chromatic confocal microscope that uses a diffractive zone plate for wavelength-depth encoding and non-mechanical depth scanning. Our method provides such advantages as nonmechanical depth scanning, high linearity, and high sensitivity in wavelength-to-depth mapping. The chromatic confocal microscope was characterized in terms of the measured depth PSF and the wavelength-to-depth mapping curves. Finally, a sample profile was measured experimentally and the results were found in good agreement with these obtained with conventional confocal microscope. In the future we intend to use multi-phase level diffractive element for better efficiency, incorporate an eletro-optic wavelength scanner for high speed depth scanning, and use broadband source and multiple detectors for parallel measurements.

Authors thank Fang Xu and Rob Stein for preparing the diffractive optical element and providing the measurement sample. The research is funded by the National Science Foundation.

References

1. T. Wilson and C. Colin, *Theory and Practice of Scanning Optical Microscopy,* Academic Press, London (1984).
2. M.A. Browne, O. Akinyemi, and A. Boyde, "Confocal Surface Profiling Utilizing Chromatic Aberration," Scanning, **14**:145 (1992).
3. O. Akinyemi, A. Boyde, M.A. Browne, M. Hadravsky, and M. Petran, "Chromatism and Confocality in Confocal Microscopes," Scanning, **14**:136 (1992).
4. M. Maly and A. Boyde, "Real-Time Stereoscopic Confocal Reflection Microscopy Using Objective Lenses with Linear Longitudinal Chromatic Dispersion," Scanning **16**:187, (1994).
5. M.C. Hutley and R.F. Stevens, "The Use of a Zone-Plate Monochrometer as a Displacement Transducer," J. Phys. E **21**:1037 (1988).

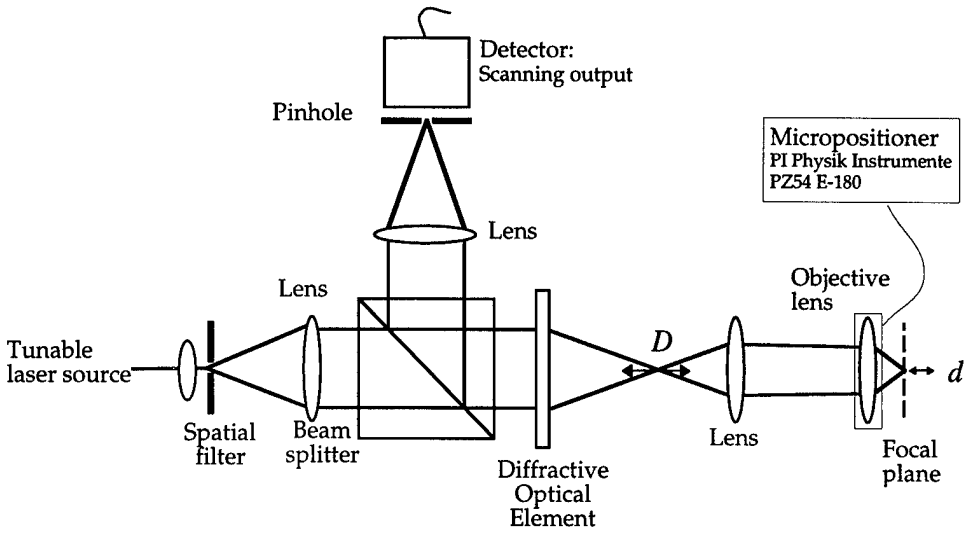


Fig. 1 Schematic diagram of a chromatic confocal microscope with a diffractive optical element

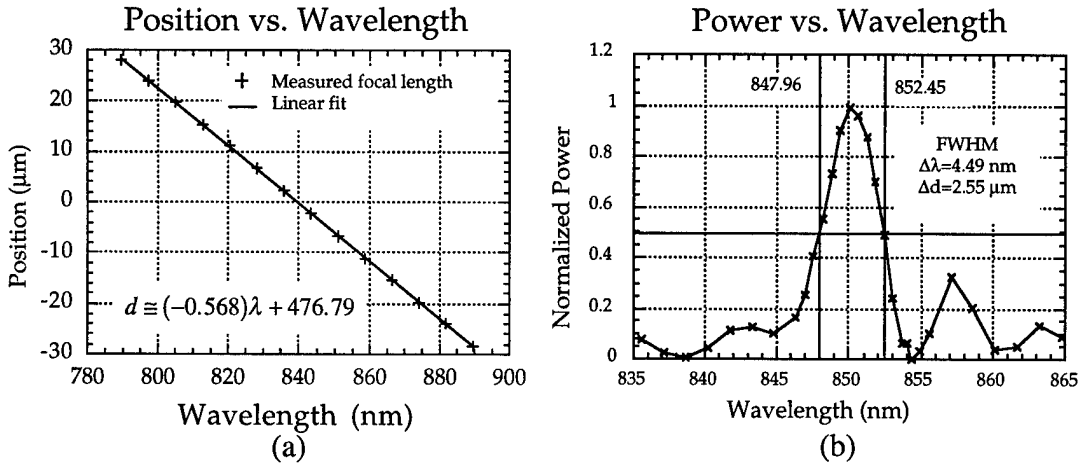


Fig. 2 Experimental results of system characterization: (a) wavelength-to-depth mapping (b) longitudinal point spread function

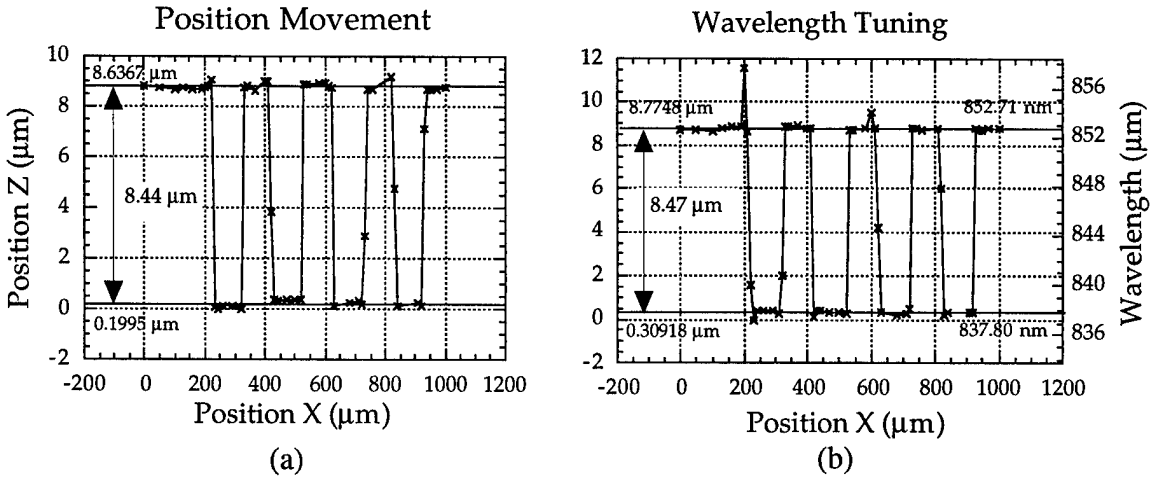


Fig. 3 Experimental result of measuring a binary grating profile: (a) conventional confocal microscope and (b) chromatic confocal microscope.

Tunable Diffractive Optical Filter for Imaging Applications

J. Allen Cox and Bernard S. Fritz
Honeywell Technology Center MN65-2500
3660 Technology Drive
Minneapolis, MN 55418

1. Introduction

Remote detection and monitoring of scenes, objects, and materials in selective spectral bands is an increasingly important field with many applications. A variety of optical filtering concepts have been suggested for the sensors used for this purpose, ranging from fixed dielectric filters and rotating filter wheels to more advanced techniques based on acousto-optical gratings and interferometric devices (Fabry-Perot and Michelson). These latter methods (acousto-optic and interferometric) have been demonstrated(1,2) and have shown the value provided by tunability and spectral agility in the optical filter. More recently, methods based on diffractive optics have been proposed for tunable spectral filtering. Specifically, the large degree of longitudinal dispersion in a diffractive element has been exploited both by Hinnrichs and Morris(3) and by the authors(4).

Hinnrichs and Morris use a single diffractive Fresnel phase lens to disperse the image of a scene along the longitudinal axis and sample it with a two-dimensional detector array. By changing the separation between the lens and the detector array, one can select the wavelength, or narrow band of wavelengths, which is in sharp focus, and thus obtain a tunable spectral sensor. At a given separation, all out-of-band wavelengths are defocused and detected as a essentially structureless background. Signal processing techniques, such as frame differencing, can be used to remove the background and provide a two-dimensional map of the scene in the selected narrow waveband. Because focal length varies with wavelength in this method, it is clear that magnification of the scene also varies and must be compensated in the signal processing. Further, since only a single diffractive element is used, field-of-view is limited by off-axis aberrations (coma and astigmatism). Intuitively, one expects this method to work well for detecting point objects and edges in relatively uncluttered backgrounds but that it's performance would be limited in forming high quality spectral images of extended cluttered scenes and objects subtending wide angles.

Here, we describe an alternative method for a spectrally agile filter based on diffractive optics which provides high quality spectral imagery directly and which performs well in highly cluttered scenes. There are two complementary forms of the approach: one provides conventional spectral bandpass filtering in the sense described above, while the other provides notch rejection filtering and is useful in rejecting specific wavelengths from the image, produced, for example, by laser jamming. We describe the concept in both forms in the next section and give an example in Section 3.

2. Description of Concept

Our concept makes use of hybrid optics consisting of highly dispersive diffractive elements and conventional elements (refractive lenses and reflective mirrors). In conventional broadband imaging applications diffractive optical elements with significant amounts of optical power are generally used in pairs due to their highly dispersive nature, with the second one used to compensate for the chromatic aberration of the first. We have generalized this idea to implement our approach.

Figure 1 illustrates the concept's three major components for a single axial field point. A foreoptics module that includes a diffractive element is used to form an intermediate image of the scene that is spread longitudinally in wavelength along the optical axis. A relay optical module, which also includes a diffractive element, recombines the longitudinally spread images and reimages them achromatically onto a detector array. The third component

consists of an aperture array placed in the intermediate image region of the optical train where the scene has been dispersed longitudinally, and by translating it to the appropriate position, one can select a given waveband from the scene to be passed (Fig. 1A) to, or blocked from (Figure 1B), the detector array depending on the nature of the aperture array. Spectral filtering is thus achieved by using the aperture array as a spatial filter in the image plane of the fore-optics. Only one aperture in the array is shown in Fig. 1 for clarity. The relay optical module maps the aperture array one-to-one onto the elements of the detector array. By scanning the aperture array along the longitudinal axis, a tunable filter has been created. The length of the longitudinal scan is related to the filter's bandwidth as measured, for example, by the full-width-at-half-maximum. Although this concept is not a solid state device, it requires only a one-dimensional translation of a substrate containing the aperture array through a few millimeters to achieve good bandwidths over a wide spectral band and thus is capable of fast response time.

Best performance for the notch rejection form is obtained by actually using a third stage at the front of the system shown in Figure 1B. This stage consists of a chromatically well-corrected imaging optic with an array of pinhole aperture to sample the image. This sampled image is then passed to the system shown in Figure 1B, again with pinhole mapped to blocking aperture mapped to detector element. The use of this addition stage greatly reduces crosstalk and provides superior laser rejection.

Three basic optical properties must be fulfilled for the actual implementation of this concept:

1. Large longitudinal color at an intermediate image plane
2. Relatively constant Airy disc size with wavelength at this intermediate image plane
3. Telecentric objective, with no variation in magnification with color (zero lateral color) at the intermediate image plane

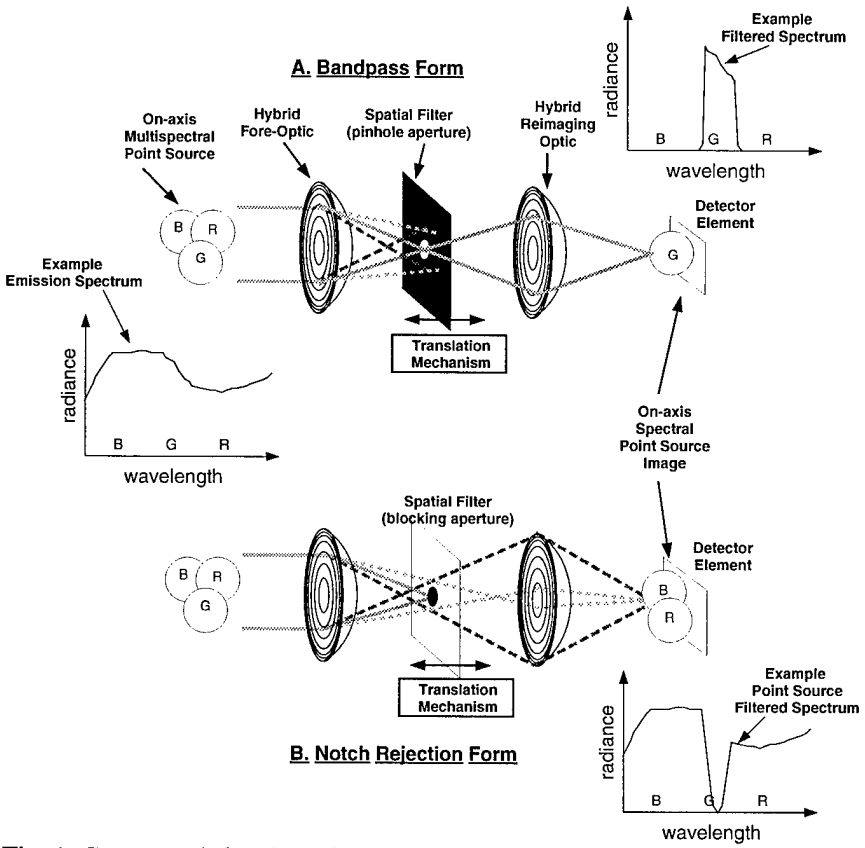


Fig. 1. Conceptual sketches of tunable diffractive optical filter in two forms.

By introducing a large amount of longitudinal color into a lens system, the image can be spread out longitudinally in wavelength along the optical axis. The zero lateral color condition in conjunction with the telecentric requirement in image space, means all images in the waveband are of identical magnification , or size, in spite of being displaced axially. If the spots (Airy disc) can be made independent of wavelength, one can use a two-dimensional spatial filter array with apertures related in size to the Airy disc to select a given waveband at this intermediate image plane. The longitudinal wavelength spread of a diffractive element is an order of magnitude greater than that of a refractive element, making the spatial filtering feasible. One also finds for a diffractive element used at infinite conjugates that the Airy disc size is independent of wavelength, unlike a refractive element in which it is a nonlinear function of wavelength.

By placing the diffractive element at the stop of a lens system and also making this the lens system's focal point (telecentric condition), we satisfy the requirements to achieve a tunable filter using a spatial filter. By being coincident with the stop, the diffractive element will introduce no lateral color. Figure 2 shows an off-axis field point for the foreoptics. Following the spatial filter with a set of relay optics that recombines the various wavebands and images them onto the focal plane array completes the system. The relay optics maps each clear aperture in the spatial filter array onto the active area of a corresponding detector. We can avoid the requirement of small distortion in the relay optic by pre-distorting the aperture distribution in the spatial filter, thus keeping the relay optics simple.

3. Example

We have done optical designs of this concept for wavebands in the visible, midwave IR, and longwave IR and for both bandpass and notch rejection forms. A design of a prototype bandpass system for use in the visible waveband is shown in Figure 3. This design is made up of spherical elements using standard optical glasses. The parameters for this design are listed in Table 1. We calculated the system's transmission function, and an example for the system tuned to 580 nm is shown in Figure 4. The out-of-band spectral transmittance, representing leakage, approaches the area fill factor of the transmitting aperture for wavelengths which are far out-of-band. The width of the spectral transmission function is related to the design's longitudinal waveband spread at the transmitting aperture array and the transmitting aperture fill factor. These parameters can be adjusted to give the desired ratio of out-of-band energy to inband energy at the image plane detector. As an example,the system gives a passband from 566 nm to 601 nm (see Fig. 4) over a total band from 486-656 nm. The ratio of inband to out-of-band energy is 5.40. The inband transmittance compared to the ideal rectangle function is 0.56. In practice, there is always some variation of blur diameter with wavelength in a hybrid system, leading to some variation in the filter's spectral bandpass characteristics with center wavelength as shown in Figure 5. There is sufficient freedom in the design parameters to account for this in most system requirements.

4. Summary

A multispectral imaging tunable filter concept making use of diffractive optics is presented as viable option to such applications as remote sensing. A simple spatial filtering technique is used which allows for fields of view of over 20 degrees, high system transmittance (50-90%), fast modulation capability (~ milliseconds), low power, and wavelength independence (using appropriate optical and detector materials).

5. References

1. Greg Vane, Editor, *Imaging Spectroscopy II*, Proceedings SPIE, Vol. 834 (1987).

2. Reinhart Beer, *Remote Sensing by Fourier Transform Spectrometry* (John Wiley, New York, 1992).

3. M. Hinnrichs and G.M. Morris, "Image multispectral sensing," International Patent Application WO 94/15184 (7 July 1994).

4. B.S. Fritz and J.A. Cox, "Tunable diffractive optical filter for multispectral imaging," in *Diffractive and Holographic Optics Technology II*, Ivan Cindrich, Sing H. Lee, Editors, Proc. SPIE **2404**, 194-200 (1995).

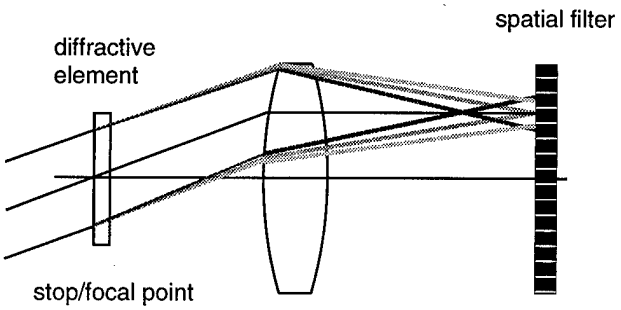


Fig. 2. Foreoptics for an off-axis point and telecentric condition.

Table 1

PROTOTYPE OPTICAL SYSTEM PARAMETERS	
FIELD OF VIEW	20 degs
WAVEBAND	656-486 nm
SCAN LENGTH	2.5 mm
ENTRANCE PUPIL DIAMETER	15 mm
IMAGE SPACE F/#	1.5
IMAGE SIZE	8 mm x 8mm
IMAGE PIXEL FILL FACTOR (area)	30%
IMAGE PIXELS	700 x 700
TRANSMITTING ARRAY SIZE	30 mm
TRANSMITTING APERTURE FILL FACTOR (area)	9%

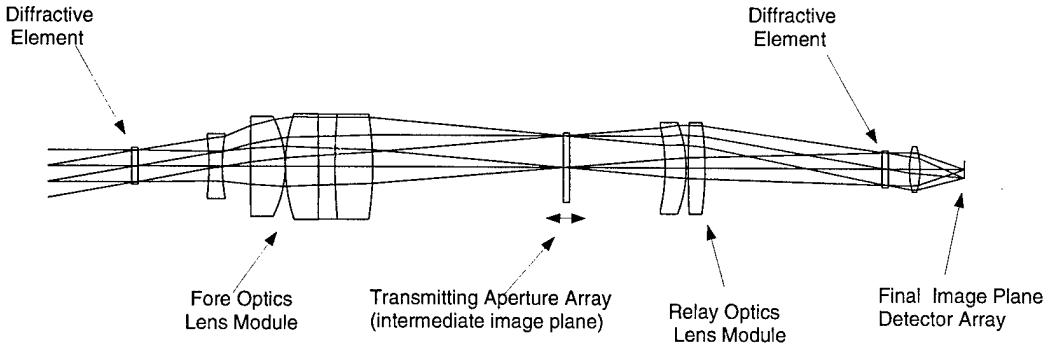


Fig. 3. Prototype optical system for visible waveband

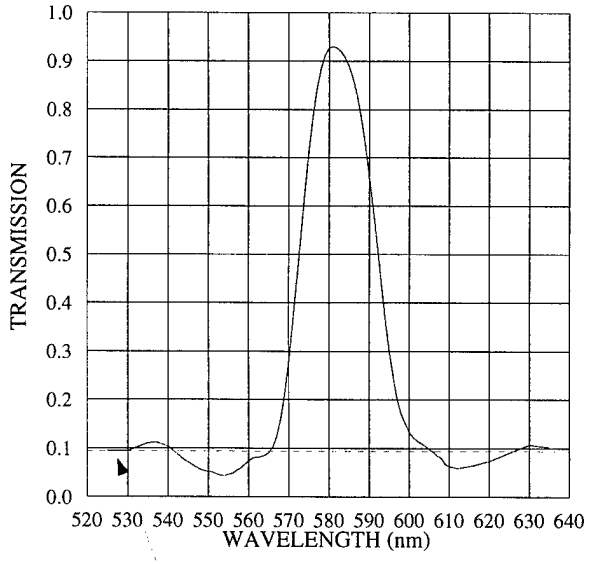


Fig. 4. Aperture array transmission function

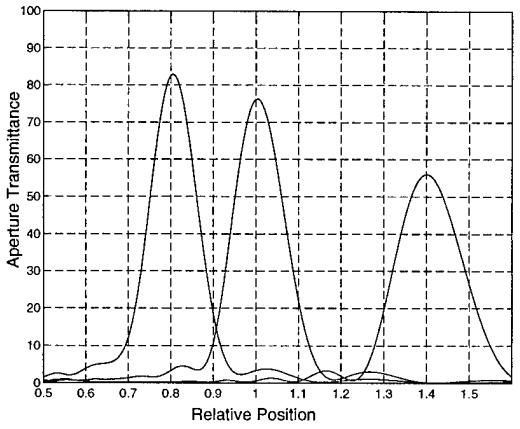


Fig. 5. Aperture array transmission versus center wavelength.

Diffractive Optics Technology for F-Θ Scan Lenses

Kevin J. McIntyre and G. Michael Morris, Institute of Optics, University of Rochester
Rochester, NY 14627, (716) 275-2322, (716) 271-1027 (FAX)

Introduction

A variety of optical systems utilize F-θ lenses to focus a scanned laser beam to a small spot. Typical applications include laser printing and laser machining. Since scan lenses usually operate at discrete laser wavelengths, diffractive optical components can be incorporated into these designs without the efficiency losses normally associated with broadband applications. This paper will examine the use of diffractive optical elements in F-θ scan lens design. A discussion of some basic design principles is provided. This is followed by a comparison between a refractive system and a hybrid system which illustrates how diffractive optics can significantly enhance the performance of F-θ scan lenses.

F- Θ Lens Design

F-θ lenses are distinguished from many other types of lenses in that they possess negative distortion to make the image height directly proportional to the field angle. This allows for a linear mapping between the image height and the angle of a scanning element, which typically consists of a rotating or oscillating mirror element. F-θ lenses also feature an external aperture stop. The resulting asymmetric forms make it difficult to correct transverse chromatic aberration and coma but aid in producing the required distortion. Transverse color correction is critical if the design must accommodate the spectral variability exhibited by semiconductor lasers. An appropriate design bandwidth, which accounts for temperature related fluctuations as well as manufacturing variability, is 20 nm. Correction of coma becomes a greater issue as the speed of the scan lens increases.

The use of diffractive optics in F-θ scan lens design has been previously reported. Ono and Nishida[1] discussed the use of a holographically recorded F-θ lens formed from the interference pattern of two spherical waves. This type of design lacks the flexibility of a generalized polynomial phase structure which is now available in the form of a surface relief diffractive element. Burrali and Morris[2] reported use of these elements as they proposed a system consisting of a single diffractive element. Their design is free of 3rd order coma, astigmatism, and Petzval curvature, but its large track length reduces its practicality. These all-diffractive systems suffer from large amounts of chromatic aberration if the operating wavelength deviates even slightly from the design wavelength. This makes their utility with diode laser sources troublesome since the lasers would have to be screened for their nominal wavelength as well as temperature controlled during operation. Stephenson[3] published an article which discusses some of the advantages of incorporating diffractive optics into various scanning systems. He notes a 30% increase in resolution obtained for a graphics arts scanner when diffractive optics are included in the design.

Refractive versus Hybrid Designs

The example used in the following comparison is a laser writing system designed to operate at a wavelength of 780 nm. The total scan length is chosen to be 220 mm, which allows for coverage of a standard 8.5" x 11" piece of paper. Assuming a scan range of +/- 30 degrees, the focal length is set equal to 210 mm. Both the refractive and the hybrid systems contain two elements which provide enough degrees of freedom to obtain an optical resolution of at least 300 dpi. Systems which utilize polygonal scanners usually incorporate anomorphic optical components to accommodate mirror wobble[4], but for simplicity this issue is not addressed in this example.

The refractive system shown in figure 1(a), consists of a negative-positive lens combination. The design, which utilizes a high index (n_d = 1.785) flint glass for both lens elements, provides diffraction limited performance (quarter-wave criterion) at f/35. The basic form is similar to other two element designs[5,6,7] in that the first element is a negative meniscus lens, and the second element is a positive, nearly plano-convex lens. Across a 20 nm bandwidth this lens exhibits an unacceptable amount of transverse chromatic aberration as the maximum spot shift is approximately equal to the spot size. This effect can be reduced by nearly 50% if a lower dispersion crown glass is used. However, the lower refractive index nearly doubles the wavefront error. A third lens element is required to provide acceptable chromatic performance while maintaining control of the monochromatic aberrations.

The hybrid system shown in figure 1(b), also consists of a negative-positive lens combination with a positive power diffractive surface on first surface of the second element. Both of the lens elements are comprised of the same high index flint glass used in the refractive lens, which allows for diffraction limited performance at f/22. The diffractive surface provides for color correction over a 20 nm bandwidth, as well as higher order aspheric correction, and comprises approximately 10 % of the total power of the second element. The minimum diffractive zone spacing, which occurs at the edge of the lens, is equal to 12 waves. This can be readily increased by manufacturing the surface as a MOD[8,9] lens structure in which the phase steps are equal to $m2\pi$, where m is an integer greater than unity.

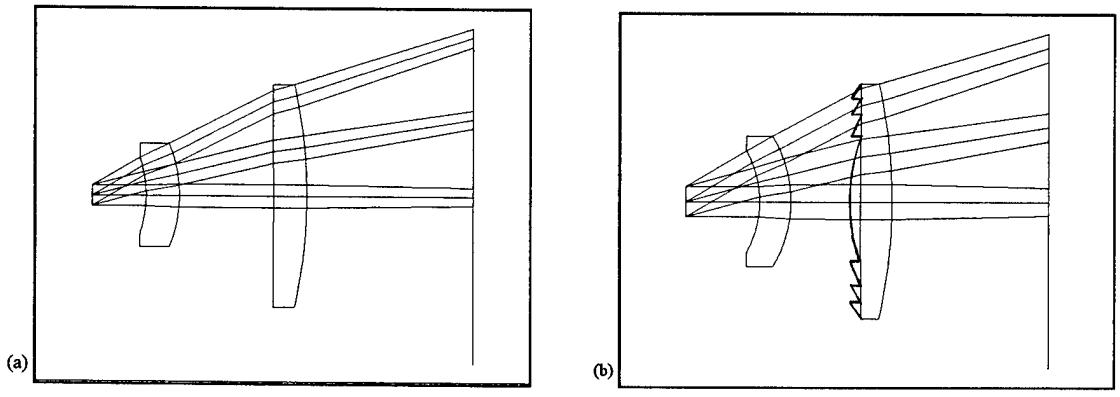


Figure 1. Two element fθ scan lenses: focal length = 210 mm, scan angle = +/- 30 degrees. (a) refractive design operating at F/35. (b) hybrid design operating at F/22. First surface of second refractive element is a diffractive surface.

Transverse ray aberration plots for both lenses are shown below in Figs. 4 and 5. All of the axes are drawn to the same scale resulting in a reduced plot width for the refractive lens due to the larger f-number. The plots for the refractive lens reveal that the design is limited by coma, and a 20 nm bandwidth cannot be accommodated. The plots for the hybrid lens reveal that reasonable color correction is achieved, and spherical aberration is the primary remaining aberration. Note that distortion does not show up in these ray fans since the transverse errors are relative to the real (not paraxial) chief ray.

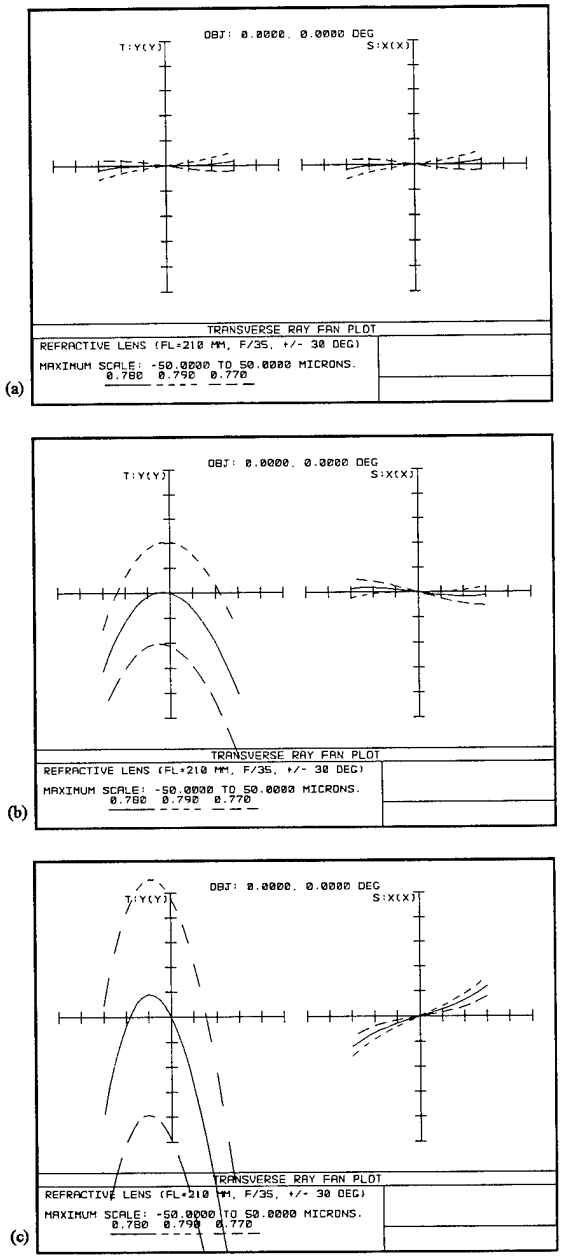


Figure 4. Ray fan plots for the refractive design. a, b, c correspond to the center, mid and full fields, respectively. Horizontal scale is the same as for the hybrid lens which leads to reduced plot width due to the larger f#.

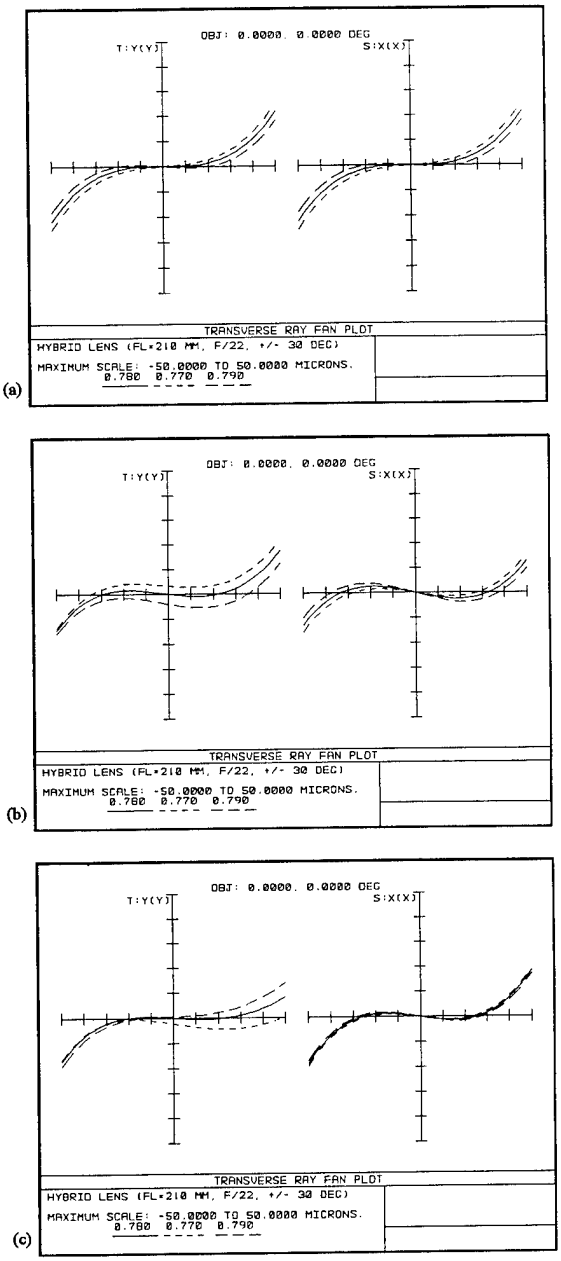


Figure 5. Ray fan plots for the hybrid design. a, b, c correspond to the center, mid, and full fields, respectively.

The scan linearity is often expressed as a percent error. This quantity, referred to as the F-θ characteristic, is defined as [y(θ)-Fθ]/[Fθ] x 100%, where y(θ) is the real chief ray image height. Figure 6 shows that both systems exhibit nearly identical behavior since they were constrained in the same manner during the optimization process.

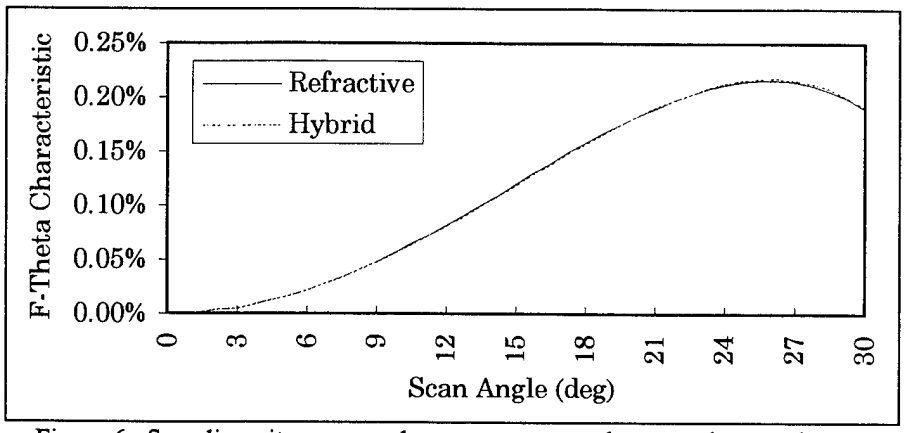


Figure 6. Scan linearity expressed as a percent error between the actual image height and the target image height.

Summary

The comparison between the refractive and the hybrid lenses illustrates the substantial improvements that can be obtained if diffractive optical surfaces are incorporated into the design of F-θ scan lenses. Adding a single diffractive surface can drastically increase the speed of the system allowing for, in this example, a spot size reduction of nearly 40%. An equivalent refractive design would require at least one more element, thereby adding to the weight and size of the final system. Since achromatization with diffractive optics does not require the use of different glass types, all of the elements can be designed with a single high index material, which further aids in the correction of monochromatic aberrations. Of course, many scanning systems require the use of anomorphic wobble-correction optics that typically utilize at least one toric surface. It may be possible, however, to eliminate the need for such a costly surface by incorporating diffractive optics technology into the design of these systems as well.

References

[1] N. Nishida and Y. Ono, "Holographic Zones Plates for fθ and Collimating Lenses", Appl. Opt. **25** 794-797 (1986)
[2] D. Burrali and G.M. Morris, "Design of Diffractive Singlets for Monochromatic Imaging", Appl. Opt. **30** 2151-2158 (1991)
[3] D. Stephenson, "Diffractive Optical Elements Simplify Scanning Systems", Laser Focus World, 75-80, (June 1995)
[4] G. Marshall, (editor), Optical Scanning, Marcel Dekker, Chpt. 2, (1991)
[5] K. Takanashi and N. Sakuma, U.S. Patent #4,707,085, (Nov 17, 1987)
[6] N. Sakuma, U.S. Patent #4,770,517, (Sep 13, 1988)
[7] A. Ohta, U.S. Patent #4,789,230, (Dec 17, 1987)
[8] D. W. Sweeney and G. Sommargren, "Single Element Achromatic Diffractive Lens", in Diffractive Optics, Vol. 11 of 1994 OSA Technical Digest Series (Optical Society of America, Washington, D.C., 1994), pp. 26-29
[9] G. M. Morris and D. Faklis, "Achromatic and Apochromatic Diffractive Singlets", in Diffractive Optics, Vol. 11 of 1994 OSA Technical Digest Series (Optical Society of America, Washington, D.C., 1994), pp. 53-56

OPTICAL DESIGN COMPARISON OF 60° EYEPIECES ONE WITH ASPHERICS and ONE WITH A DIFFRACTIVE SURFACE FINAL RESULTS

Authors:

Wayne Knapp
Precision Optics Corporation
22 East Broadway
Gardner, MA 01440
Tel: 508-630-1800
Fax: 508-630-1487

Brian Volk
Precision Optics Corp.
22 East Broadway
Gardner, MA 01440
Tel: 508-630-1800
Fax: 508-630-1487

Berge Tatian
Optical Design Specialist
204 North Street
Stoneham, MA 02180
Tel: 508-438-9281

Gary Blough
Rochester Photonics Corporation
330 Clay Road
Rochester, NY 14623
Tel: 716-272-3010
Fax: 716-272-9374

Robert Michaels
Rochester Photonics Corporation
330 Clay Road
Rochester, NY 14623
Tel: 716-272-3010
Fax: 716-272-9374

Eyepiece optical designs were developed for a wide angle eyepiece with a large exit pupil and eye relief. In addition to the design criteria listed below in Table 1, one design was of a conventional configuration (aspherics and plastics permitted) and the other design was to include a diffractive optic.

Table 1
Design Criteria

Parameter	Development Criteria
Field of View	60°
Format Covered	25mm
Focal Length	24mm
Distortion	-10%
Glass Length	<41mm
Glass Diameter	<46mm
Glass Weight	<120gm
Focus Range	± 2 Diopter
Field Curvature	± .25 Diopter
Astigmatism	< .5mm Diopter
Exit Pupil (All Field Angles)	≥ 12mm Diameter
Normal Eye Relief	≥ 20mm
Spectral Band	540.0nm - 558.0nm
Transmission	80%
MTF 5mm Centered and Decentered Pupil's Located within 5mm of Optical Axis	Various Criteria to 56 lp/mm

This paper presents the optical design results via a sample design of each type without regard to cost or potential performance limits of the fabricated optics. Although each design represents an optimized state relative to the design criteria, as is the case in optical design, there is always potential for further improvement.

The eyepieces are part of a 1X power image intensifier system with matched -10% objective and eyepiece distortions. The eye is to view a flat surface image intensifier tube phosphor output with a 25mm diameter. The most significant drivers of the design included the 60° field of view, eye relief/pupil size, flat object, field/astigmatism requirements, glass weight, and diameters. These parameters, in combination, severely constrained the design solution space. Additionally, the 56 lp/mm MTF requirement at four field locations with seven pupil positions each provided for lengthy performance analysis during design iterations. As an example of the constraint problem, consider the 46mm glass diameter limit. At a 30° semi angle, 20mm eye relief, and 6mm semi pupil, the upper rim ray would require a 35.1mm aperture at the element closest to the eye. Any convex curvature exacerbates this problem, and a 1mm edge allowance quickly places one at the 46mm limit.

The diameter limit stated above, the total length, and the need to refract the rays in a short space led to designs with high index glass materials for the positive elements. The resulting optical designs are shown in Figure 1a (conventional configuration) and Figure 1b (diffractive optic configuration).

Figure 1a - Conventional (with Aspheres)

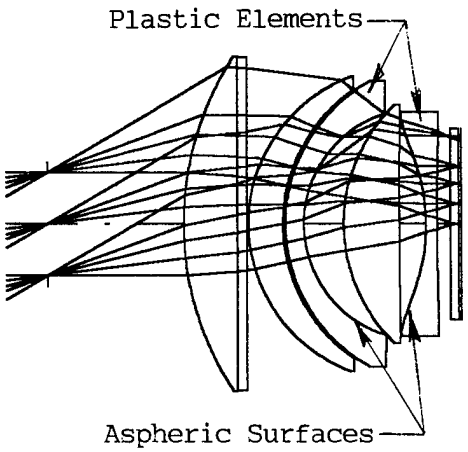
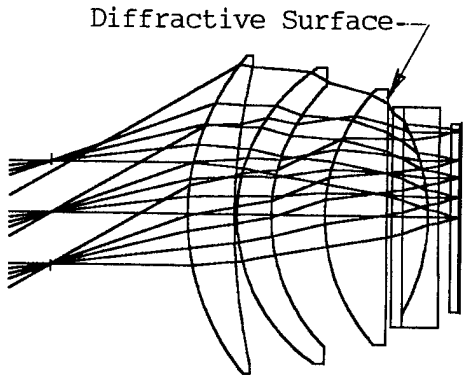


Figure 1b - Diffractive



The optical components just met the 120gm weight constraint, with the two plastic elements in the conventional design offsetting its one extra element. The reduced curvature of the lens closest to the eye in the conventional design permitted less vignetting of the upper marginal ray and still meet the 46mm aperture constraint. The meniscus elements of the conventional design are more curved than those of the diffractive design. Both designs exhibit some fairly acute angles of incidence, particularly in the near 30° semi-field region.

Transverse aberration curves for each design are presented in Figures 2a and 2b. Spherical aberration over the 15mm pupil represented in these plots is similar for both lenses as are field curvature and maximum astigmatism. The most obvious benefit of the diffractive design is the reduction in lateral color, which results in improved off-axis MTF performance. Field and distortion curves are presented, Figures 3a and 3b.

Modulation Transfer Function data for each design was obtained over the field of view and various pupil positions. The data matrix contained 192 points, and a sample output is shown for the conventional eyepiece out to 20° semi-field, Table 2. The data presents the radial and tangential modulation (0-100), and the focal position for the matrix of pupil positions indicated. The average change from the specification was used as a single merit value for the design; this number appears in the lower left of the data. Centered pupil focus data is used to determine MTF based field curve and astigmatism values.

Figure 2a - Conventional (with Aspheres)

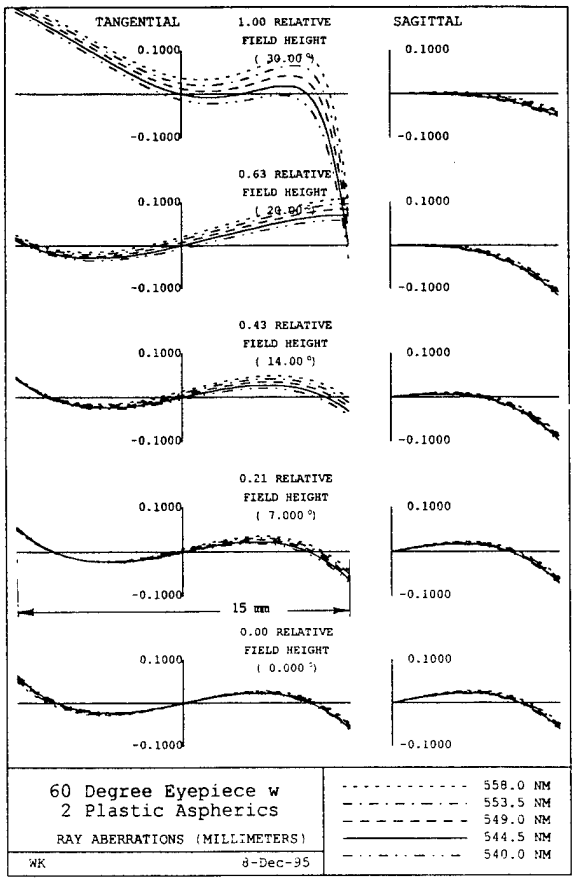


Figure 2b - Diffractive

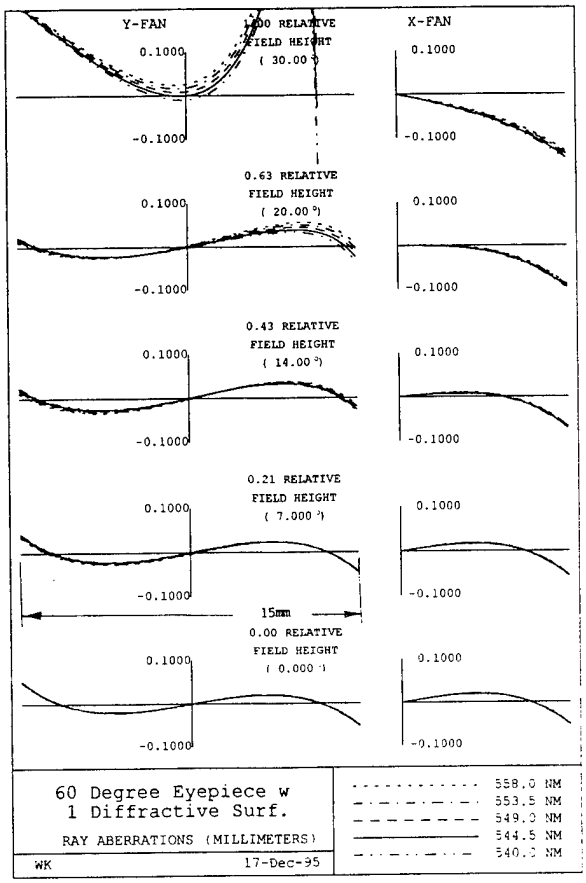


Figure 3a - Conventional (with Aspheres)

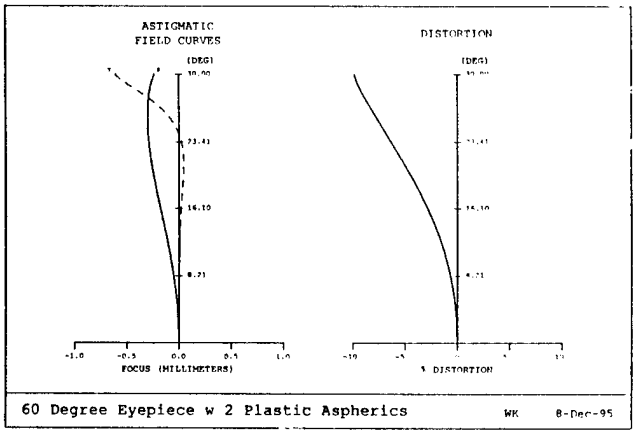


Figure 3b - Diffractive

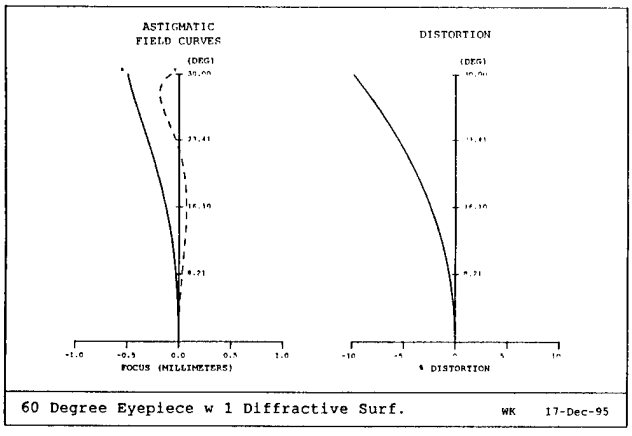


Table 3 presents a summary of the field curves, astigmatism, and average MTF residual over specification to a 30° semi-field. The diffractive eyepiece design has a better average MTF due to its reduced chromatic aberration. MTF derived field curves and astigmatism are also less for the diffractive eyepiece design.

The conclusion is drawn that the diffractive element has yielded a better optical design from a chromatic, field curves, and MTF standpoint. Previous work has also shown that diffractive elements can be effectively used to decrease the number of optical components required to obtain suitable performance in the design of eyepiece systems.[1,2] It is hoped that this optical design trade indicates the differences between these two approaches and can be used as a guide to future design efforts.

Table 2 - Sample MTF Data

Eyepiece MTF Data

	Radial					Tangential				
Pupil Location	**14.0**	**28.0**	**42.0**	**56.0**	**Δ Focus mm**	**14.0**	**28.0**	**42.0**	**56.0**	**Δ Focus mm**
Centered Pupil On Axis	95	88	82	76	0.000	95	88	82	76	0.000
+2mm Vertical On Axis	93	82	71	61	-0.110	94	87	80	72	-0.055
+5mm Vertical On Axis	65	46	36	26	0.440	89	72	54	38	-0.220
Centered Pupil 14D Field	95	89	83	76	-0.180	92	79	66	54	-0.020
+2mm Vertical 14D Field	93	82	71	61	-0.260	91	76	61	47	-0.020
+5mm Vertical 14D Field	59	43	33	27	-0.500	87	65	45	30	-0.180
+2mm Horizontal 14D Field	94	87	80	73	-0.180	91	77	63	50	-0.100
-2mm Horizontal 14D Field	94	88	81	74	-0.180	89	70	52	37	-0.100
+5mm Horizontal 14D Field	91	76	60	46	-0.340	83	56	38	29	-0.420
-5mm Horizontal 14D Field	91	75	59	45	-0.340	76	43	25	15	-0.420
Centered Pupil 20D Field	94	86	77	69	-0.225	89	70	54	40	0.025
+2mm Vertical 20D Field	93	83	72	62	-0.260	88	68	50	35	0.025
+5mm Vertical 20D Field	70	47	38	29	-0.500	85	60	39	24	-0.100
+2mm Horizontal 20D Field	92	79	65	50	-0.180	88	69	51	37	-0.100
-2mm Horizontal 20D Field	93	84	74	65	-0.180	86	64	46	34	0.025
+5mm Horizontal 20D Field	90	73	56	41	-0.340	83	56	35	25	-0.350
-5mm Horizontal 20D Field	94	85	76	67	-0.340	78	48	28	25	-0.100

+10.4441

Table 3- Performance Summary

	Eyepiece Configuration	
Parameter	**Conventional**	**Diffractive**
Average MTF to 30°	9.4 Over Spec	13.4 Over Spec
Field Curvature @ 0°	0 Diopter	0 Diopter
Field Curvature @ 14°	-.17 Diopter	0 Diopter
Field Curvature @ 20	-.17 Diopter	-.08 Diopter
Field Curvature @ 30	-.73 Diopter	-.58 Diopter
Astigmatism @ 0°	0 Diopter	0 Diopter
Astigmatism @ 14°	.27 Diopter	.30 Diopter
Astigmatism @ 20°	.42 Diopter	.45 Diopter
Astigmatism @ 30°	.63 Diopter	.45 Diopter

The authors and their corporate affiliations acknowledge the support of ITT Night Vision and the Army's Night Vision and Electronic Sensors Directorate. These designs were developed under the Army's Night Vision and Electronic Sensors Directorate "Advanced Image Intensification - Advanced Technology Demonstration" or "AI^2 - ATD".

[1]M.D.Missig and G.M.Morris, "Diffractive optics applied to eyepiece design," Appl. Opt. 34,2452 (1995)
[2]C.G.Blough, M.J.Hoppe, D.R.Hand, and W.G.Peck, "Achromatic eyepieces using acrylic diffractive lenses", SPIE 2600, (1995)

Poster Previews

JTuB 10:30 am-12:00 m
Commonwealth Room

G. Michael Morris, *Presider*
University of Rochester and Rochester Photonics Corp.

Fabrication and Experiment of Diffractive Phase Element That Implements Wavelength Demultiplexing and Focusing

Bizhen Dong, Guoqing Zhang, Guozhen Yang, Benyuan Gu,
Shihai Zheng, Dehua Li, and Yansong Chen
Institute of Physics, Academia Sinica, P. O. Box 603
Beijing 100080, China
Phone: +86-10-2559131 ext. 229 Fax: +86-10-2562605

I. Introduction

Recently, the diffractive optics has extensively attracted interest of researchers because diffractive optical elements(DOE's) can incorporate several optical functions in a single optical element.[1–4] This is important in a number of areas such as integrated optics, optical computing, optical sensors, and so on. For example, one can design diffractive optical elements to perform wavelength multiplexing/demultiplexing, and focusing. Various designs and fabrication schemes for DOE's that modulate only the phase of an incident lightwave have been proposed. In this paper we present the design and fabrication of diffractive phase element (DPE) that incorporates simultaneous wavelength demultiplexing and focusing in the optical system illuminated by a light beam with three wavelength components. Optical lithography and reactive-ion etching are used to fabricate the surface-relief structure with 8 levels. Experiments demonstrate the feasibility of three wavelength demultiplexing and focusing simultaneouslly.

II. Design and Numerical Simulation

The sketch of a typical optical system considered here is illustrated in Fig. 1. This optical system is assumed to be illuminated by a uniform beam of incident light with mutually incoherent components with different wavelength. P_1 and P_2 represent the input and output plane, respectively. A wave function at wavelength λ_α on the input planes is denoted by $U_{1\alpha}$; the corresponding wave function on the output plane is denoted by $U_{2\alpha}$. The wave functions are generally complex. For brevity of notation we consider a one-dimensional case in our design and experiment. The output wave function $U_{2\alpha}$ is linked to the input wave function $U_{1\alpha}$ at wavelength λ_α by a linear transform function $G(X_2, X_1, \lambda_\alpha)$ of the form[5]

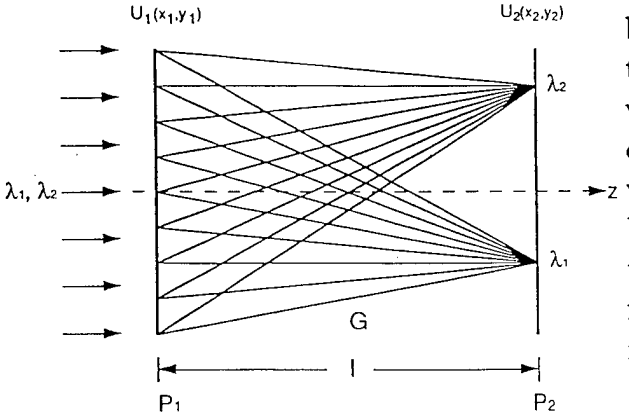


Fig. 1 : Schematic diagram of a diffractive optical system.

$$U_2(X_2, \lambda_\alpha) = \int G(X_2, X_1, \lambda_\alpha) U_1(X_1, \lambda_\alpha) dX_1. \quad (1)$$

Equation (1) can be recast in a compact form

$$U_2(X_2, \lambda_\alpha) = \hat{G}(\lambda_\alpha) U_1(X_1, \lambda_\alpha), \quad (2)$$

where $\hat{G}$ represents an integral operator. In the general case or nonparaxial case, $\hat{G}$ may be nonunitary, i. e., $\hat{G}^+\hat{G} = \hat{A} \neq \hat{I}$, where the superscript + stands for Hermitian conjugation

operation; $\hat{I}$ is an identity transform; and $\hat{A}$ is an Hermitian operator. In numerical simulations, the every continuous functions is approximately sampled in a discrete way and represented by its values at a set of sampling points (or pixels). Assume that the total numbers of the sampling points are N_1 on the input plane and $N_2 = N_{2s} \times N_\lambda$ on the output plane, where N_{2s} is the number of spatial sampling points on the output plane and N_λ is the number of different wavelengths. Thus, we have

$$U_{1n}(\lambda_\alpha) = \rho_{1n\alpha} \exp(i2\pi h_{1n}/\lambda_\alpha), \tag{3a}$$

$$U_{2m\alpha} = \rho_{2m\alpha} \exp(i\phi_{2m\alpha}), \tag{3b}$$

$$U_{2m\alpha} = \sum_{l=1}^{N_1} G_{mn}(\lambda\alpha) U_{1n\alpha},$$

$$n = 1, 2, 3, ..., N_1, \quad m = 1, 2, 3, ..., N_{2s}, \quad \alpha = 1, 2, 3, ..., N_\lambda. \tag{4}$$

The design problem of the DPE can be put into the framework of phase retrieval: If the linear transform kernel $\hat{G}$ and the amplitude information of $U_{1\alpha}$ and $U_{2\alpha}$ are known, how can the profile of the surface-relief kinoform be determined so that Eq. (2) is satisfied to a high accuracy ?

To describe the closedness of the calculated wavefront $\hat{G}U_1$ to the desired wavefront U_2, we introduce a distance measure D in an L_2 norm[5] as

$$D^2 = \sum_\alpha \| U_{2\alpha} - \hat{G}(\lambda_\alpha) U_{1\alpha} \|^2 \tag{5}$$

The design problem of the DPE's may be formulated as the search for the minimum of D^2 with respect to function arguments h_1 and $\phi_{2\gamma}$. Through evaluating the functional variations, we can derive a set of equations for determining h_1 and $\phi_{2\gamma}$.

$$\exp(i2\pi h_{1k}/\lambda_0) = \frac{\tilde{Q}_k^*}{|\tilde{Q}_k|}$$

$$k = 1, 2, 3, ..., N_1, \tag{6a}$$

where

$$\lambda_0 = \frac{\lambda_{max} + \lambda_{min}}{2}$$

$$\tilde{Q}_k = \sum_\alpha \left[\sum_{j \neq k}^{I} \rho_{1j\alpha} \exp(-i2\pi h_{1j}/\lambda_\alpha) A_{jk}(\lambda_\alpha) - \sum_j \rho_{2j\alpha} \exp(-i\phi_{2j\alpha}) G_{jk}(\lambda_\alpha) \right]$$

$$\times (2\pi/\lambda_\alpha) \rho_{1k\alpha} \exp[i(2\pi h_{1k}/\lambda_0)(\lambda_0/\lambda_\alpha - 1)].$$

$$\exp(-i\phi_{2k\gamma}) = \frac{\sum_j G_{kj}(\lambda_\gamma) \rho_{1j\gamma} \exp(i2\pi h_{1j}/\lambda_\gamma)}{\left| \sum_j G_{kj}(\lambda_\gamma) \rho_{1j\gamma} \exp(i2\pi h_{1j}/\lambda_\gamma) \right|}$$

$$k = 1, 2, 3, ..., N_{2s}, \quad \gamma = 1, 2, 3, ..., N_\lambda. \tag{6b}$$

Generally speaking, no analytical solutions to Eqs.(6a) and (6b) may be expected, but they can be numerically solved by use of Yang-Gu iterative algorithm described in Refs.

[6-7] in detail. According to the general theory of optical wave propagation, this system shown in Fig. 1 performs the linear transform given by Eq.(1) with a transform kernel $G(x_2, x_1; l, \lambda_\alpha)$ at wavelength λ_α. In the paraxial approximation, G can be expressed as

$$G(x_2, x_1; l, \lambda_\alpha) = \left(\frac{1}{i\lambda_\alpha l}\right)^{1/2} \exp(i2\pi l/\lambda_\alpha) \exp[i\pi(x_2 - x_1)^2/\lambda_\alpha l]. \quad (7)$$

The relevant physical and structural parameter values were chosen as follows: The number of wavelengths of illumination light is $N_\lambda = 3$. The corresponding wavelengths are $\lambda_1 = 0.5145\mu m$, $\lambda_2 = 0.5900\mu m$, and $\lambda_3 = 0.6328\mu m$. The central wavelength is $\lambda_0 = 0.5(\lambda_1 + \lambda_3) = 0.57365\mu m$. The sizes of the apertures on the input and output planes are $x_{1max} = 7.66mm$ and $x_{2max} = 15.32mm$. The numbers of sampling points on the input and output planes are $N_1 = 256$ and $N_{2s} = 12$, respectively. A uniform intensity at all wavelengths on the input plane is assumed, i.e., $\rho_{1\alpha}$ is a constant. The intensity and positions of diffractive light focused in the focal plane, and focal distance can be arbitrary. In our design, the intensities of three wavelength demultiplexing are assumed identical, the consecutive positions of three wavelength foci are designed 0.128mm and 0.256mm, and the focal spacing between the input and output planes also is designed $l = 400mm$. Fig. 2 shows the designed quantized relief depth of 8-level DPE, and the numerical simulation of the intensity distribution generated by the DPE on the output plane is displayed in Fig. 3. From Fig. 3 it can be seen that a local maximum of intensity for each wavelength is demultiplexed and occurred at its predesignated position in the desired plane.

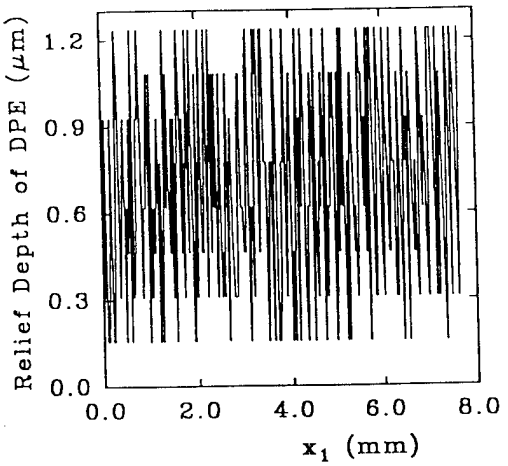


Fig. 2 : Profile of 8-level relief depth of the DPE.

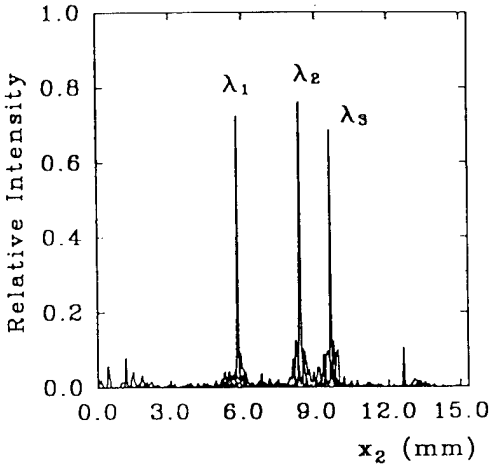


Fig. 3 : Numerical simulation of output pattern generated by the DPE.

III. Fabrication and Experimental Results

Optical lithography and reactive-ion etching are used in forming the surface-relief structure of the designed DPE. To fabricate the surface-relief structure with 8 levels, three lithographic masks shown in Fig. 4 were designed and used to fabricate the surface-relief structure in our experiment. The DPE was fabricated in fused silica(index refraction = 1.459). To demonstrate the validity of the numerical simulation, a optical system shown in Fig. 5 was chosen as the experimental setup. Identical intensities of three laser beams with

wavelength, $\lambda = 0.6328\mu m$ (He-Ne laser), $\lambda = 0.5145\mu m$ (Argon laser), and $\lambda = 0.5900\mu m$ (Dye laser), consist a coaxial collimated beam to illuminate the DPE.

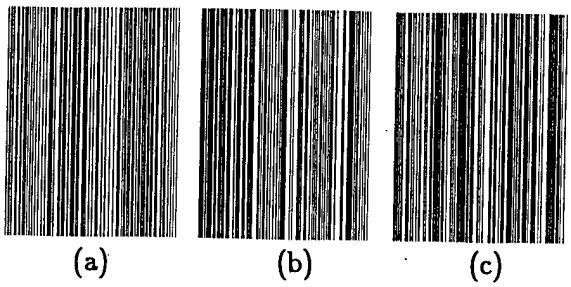


Fig. 4 : Lithographic masks for 8-level DPE, (a) mask1, (b) mask2 and (c) mask3.

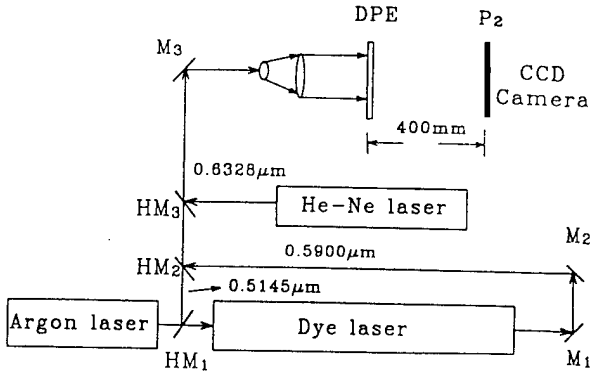


Fig. 5 : Experimental setup.

Figs. 6 depict the experimental output images recorded by the CCD camera and photo camera, respectively, at the focal plane for three wavelength demultiplexing and focusing from the DPE. It is clear that the experimental results shown in Fig. 6(a) are in good coincidence with the numerical simulation shown in Fig. 3.

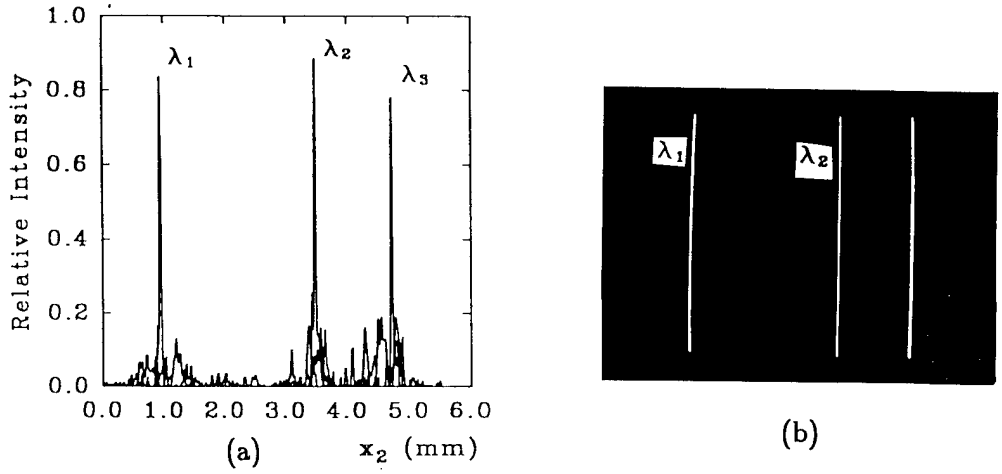


Fig. 6 : Experimental results for three wavelength demultiplexing and focusing: (a) Intensity distribution measured by CCD camera; (b) Photography.

References

[1] M. Kato and K. Sakuda, Appl. Opt. **30**, 630–635(1992).

[2] M. Bernhardt, F. Wyrowski, and O. Bryngdahl, Appl. Opt. **30**, 4629–4639(1991).

[3] Y. Ishii and T. Kubota, Appl. Opt. **32**, 4415–4422(1993).

[4] Y. Amitai, Opt. Commun. **98**, 24–28(1993).

[5] G. Z. Yang, B. Z. Dong, B. Y. Gu, J. Y. Zhuang, and O. K. Ersoy, Appl. Opt. **33**, 209–218(1994).

[6] B. Y. Gu, G. Z. Yang, B. Z. Dong, J. Y. Zhuang, and O. K. Ersoy, Appl. Opt. **34**, 2564–2570(1995).

[7] M. P. Chang, O. K. Ersoy, B. Dong, G. Yang, B. Gu, Appl. Opt. **34**, 3069–3076(1995).

A New Kind of Diffractive Phase Elements Applied to Wavelength Demultiplexing and Annular Focusing

Benyuan Gu, Guoqing Zhang, Bizhen Dong, Guozhen Yang
Institute of Physics, Academia Sinica, P. O. Box 603
Beijing 100080, P. R. China
Phone: +86-10-2559131 ext. 229 Fax: +86-10-2562605
e-mail: guby@aphy01.iphy.ac.cn

1. Introduction

In recent years much effort has been devoted to the designs of diffractive optical elements (DOE's) because of considerable progress in DOE microfabrication technology. In the previous papers various designs of DOE's have been presented, these elements produce focal annuli for monochromatic illuminating system[1], or implement wavelength demultiplexing and straight line or spot focusing.[2-5]

The goal of this article is to propose a design of a new kind of diffractive phase elements (DPE's), these DPE's are able to integrated above all functions, i.e. DPE's implement simultaneously wavelength demultiplexing and produce annuli with each wavelength focusing at desired focal plane.

2. Formulas Used for the Design of DPE's

A schematic representation of a typical optical system for design DPE's is shown in Fig. 1. The system is assumed to be illuminated by a beam of incident light consisting of mutually incoherent components with different wavelengths. P_1 and P_2 represent the input plane and output planes, respectively. A wave function at wavelength λ_α on the input plane P_1 is denoted by $U_{1\alpha}$; the corresponding wave function on the output plane P_2 is denoted by $U_{2\alpha}$. The wave functions are generally complex. In numerical simulations, the every continuous functions are sampled and represented by their values at a set of sampling points(or pixels). Consequently, at a given wavelength λ_α, the wave function on the input plane is

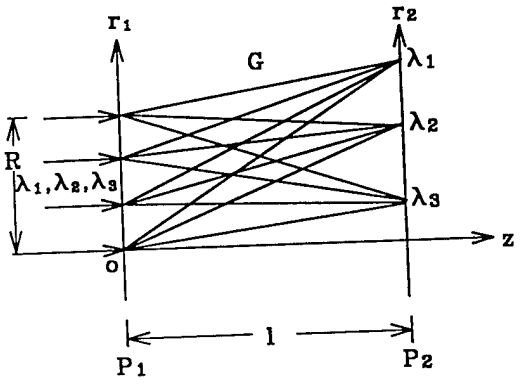


Fig. 1 : Configuration of a diffractive optical system.

$$U_{1n}(\lambda_\alpha) = \rho_{1n\alpha}\exp(i2\pi h_{1n}/\lambda_\alpha),$$
$$n = 1,2,3...N_1, \quad \alpha = 1,2,3...N_\lambda. \tag{1}$$

The corresponding wave function on the output plane is

$$U_{2m\alpha} = \rho_{2m\alpha}\exp(i\phi_{2m\alpha}), \quad m = 1,2,3..N_{2s}. \tag{2}$$

The coordinate system is such that the $z-$axis is along the optical axis of the system, the system considered here is rotationally symmetric, our description can be in terms of polar coordinates, radial coordinates on the input and output planes are described r_1 and r_2. The output wave function is linked to the input wave function at wavelength λ_α by a linear transform function $G(r_2, r_1, \lambda_\alpha)$ of the form

$$U_{2m\alpha} = \sum_{n=1}^{N_1} G_{mn}(\lambda_\alpha) U_{1n\alpha}. \tag{3}$$

The design problem for the DPE's can be generally addressed as follows : From known the transform kernel G and the amplitudes of $U_{1\alpha}$ and $U_{2\alpha}$ determinate the profile of the surface-relief kinoform, satisfying Eq. (3) to a high accuracy.

To describe the closeness of the calculated wavefront $\hat{G}U_1$ to the desired wavefront U_2, we introduce a distance measure D^2 in an L_2 norm[6],

$$D^2 = \sum_\alpha \| \left[U_{2\alpha} - \hat{G}(\lambda_\alpha) U_{1\alpha} \right] \|^2 . \tag{4}$$

By evaluating the functional variation of D^2 with respect to h_1 and $\phi_{2k\gamma}$, one obtain

$$\exp(i2\pi h_{1k}/\lambda_0) = \frac{\tilde{Q}_k^*}{|\tilde{Q}_k|}, \quad k = 1, 2, 3....N_1, \tag{5}$$

where λ_0 is the mean wavelength, and can be chosen as the center wavelength, given by $\lambda = (\lambda_{max} + \lambda_{min})/2$, λ_{max} and λ_{min} are maximum and minimum of wavelengths in polychromatic illumination. and

$$\tilde{Q}_k = \sum_\alpha \{ \sum_{j \neq k}{}' \rho_{1j\alpha} \exp(-i2\pi h_{1j}/\lambda_\alpha) A_{jk}(\lambda_\alpha)$$

$$- \sum_j \rho_{2j\alpha} \exp(-i\phi_{2j\alpha}) G_{jk}(\lambda_\alpha) \} (2\pi/\lambda_\alpha) \rho_{1k\alpha} \exp[i(2\pi h_{1k}/\lambda_0)(\lambda_0/\lambda_\alpha - 1)].$$

and

$$\exp(i\phi_{2k\gamma}) = \frac{\sum_j G_{kj}(\lambda_\gamma) \rho_{1j\gamma} \exp(i2\pi h_{1j}/\lambda_\gamma)}{|\sum_j G_{kj}(\lambda_\gamma) \rho_{1j\gamma} \exp(i2\pi h_{1j}/\lambda_\gamma)|},$$

$$k = 1, 2, 3....N_{2s}, \ \gamma = 1, 2, 3...N_\lambda. \tag{6}$$

Eqs. (5) and (6) can be numerically solved with use of the YG iterative algorithm described in Ref. 6.

3. Numerical Simulation Results for the Design of DPE's

In Fig. 1 the focal spacing between the input plane P_1 and the output plane P_2 is l, and the DPE is placed on the input plane. According to the general theory of optical wave propagation,[7] this system performs the linear transform given by Eq.(3) with a transform kernel at wavelength λ_α,

$$G(r_2, r_1; l, \lambda_\alpha) = \frac{2\pi}{i\lambda_\alpha l} \exp(i2\pi l/\lambda_\alpha) \exp[i\pi(r_2^2 + r_1^2)/\lambda_\alpha l] \times J_0(\frac{2\pi r_2 r_1}{\lambda_\alpha l}) r_1. \tag{7}$$

where J_0 is the zeroth–order Bessel function of the first kind.

We now present the results obtained in the design of DPE's which simultaneously perform wavelength demultiplexing and annular focusing of each wavelength. In our computations, the number of wavelengths of illumination light of the optical system, intensities and radii of diffractive annuli focused in the focal plane, and focal distance can be arbitrarily chosen. The relevant physical and structural parameter values chosen as follows: The sizes of the apertures on the input and output planes are $R_1 = 3.0mm$ and $R_2 = 9.0mm$. The numbers of sampling points on the input and output planes are $N_1 = 512$ and $N_{2s} = 32$, respectively. A uniform intensity at all wavelengths on the input plane is assumed, i.e., $\rho_{1\alpha}$ is a constant. In our design, the intensities of focusing annuli for wavelength demultiplexing are assumed identical, and the focal spacing between the input and output planes also is predesignated $l = 400mm$.

In the first two examples of design, the number of wavelengths of illumination light is chosen $N_\lambda = 2$. Figs.2 (a) and (b) show a depth distribution of the designed DPE and corresponding intensity of focusing annuli, respectively. In Fig. 2(b) two peaks of intensity with each wavelength ($\lambda = 0.6328\mu m$ and $0.5145\mu m$) occur at predesignated radii $r_2 = 5.28mm$ and $7.29mm$, respectively. It means that the designed DPE implements simultaneously two annuli with each wavelength separating and focusing at desired positions.

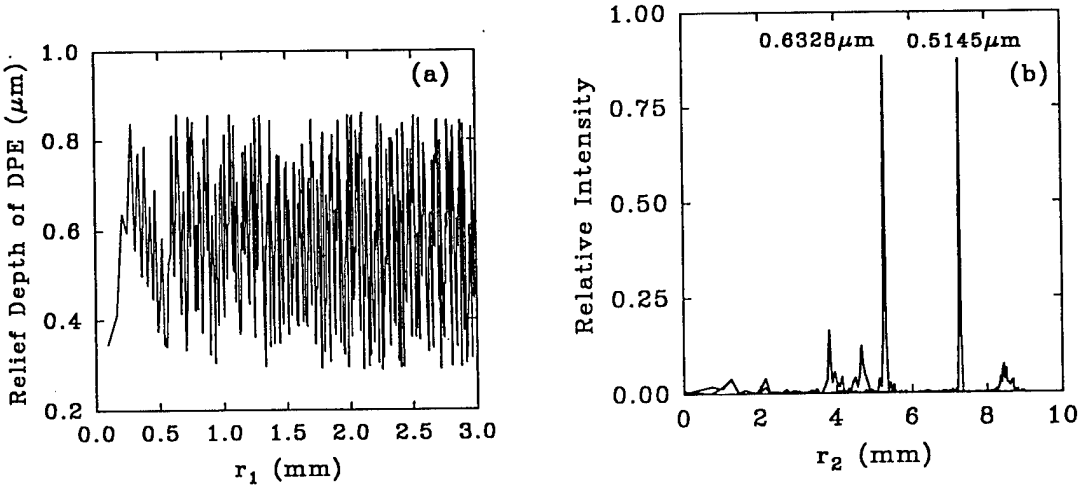


Fig. 2: (a) Profile of depth of the designed DPE, (b)Output pattern with two wavelengths demultilexing and annuli focusing generalized from the designed DPE shown in Fig.2 (a).

To verify further the validity of the design method, we now demonstrate more examples by changing the relevant parameter values. Fig. 3 also present successful result by using different wavelengths and radii from that in Fig. 2. Fig. 3 describes the corresponding output pattern of intensity, two annuli with each wavelength ($\lambda = 0.5145\mu m$ and $0.5900\mu m$) are divided and focusing at desired radii $r_2 = 3.56mm$ and $6.56mm$, respectively.

For second example, N_λ is taken 3, and radii of focal annuli are predesignated ar-

bitrarily. Fig. 4 present a satisfactory design again. Three peaks of intensity raise in the output pattern shown in Fig. 4, the peaks with each wavelength ($\lambda = 0.5900\mu m$, $0.6328\mu m$, and $0.5145\mu m$) still demultiplex, and focus at expected radii $r_2 = 1.59mm$, $3.89mm$, and $7.29mm$, respectively, in the focal plane.

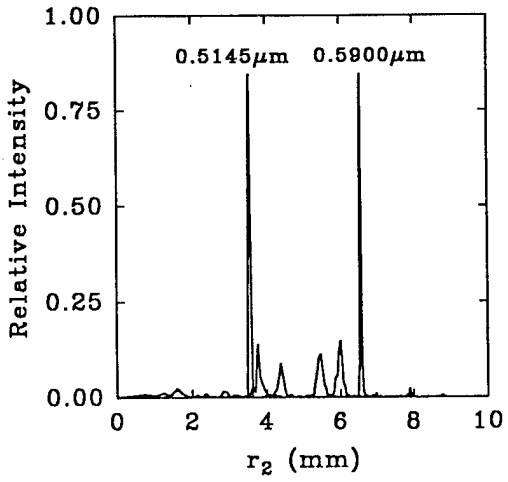


Fig. 3 : Output pattern with two wavelengths demultilexing and annuli focusing generated from the designed DPE.

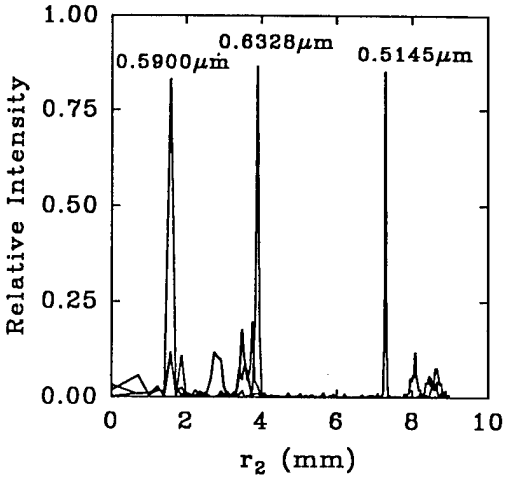


Fig. 3 : Output pattern with three wavelengths demultilexing and annuli focusing generated from the designed DPE.

4. Conclusions

The design of DPE's that simultaneously implement wavelength demultiplexing and annular focusing is present based on the theory of amplitude-phase retrieval and an iterative YG algorithm. The calculated results shows that the diffractive patterns obtained by the designed DPE's are in good agreement with the desired patterns. It may be expected that this design method will be useful and effective for the design of DPE's in micro-optical system.

References

1. G. Zhang, G. Yang, and B. Gu, Appl. Opt. **35**, 1995. in press.
2. M. Kato and K. Sakuda, Appl. Opt. **30**, 630-635 (1992).
3. Y. Amitai, Optics Communications **98**, 24-28 (1993).
4. B. Gu, G. Yang, B. Dong, M–P. Chang, and O. K. Ersoy, Appl. Opt. **34** , 2564-2570 (1995).
5. M–P. Chang, O. K. Ersoy, B. Dong, G. Yang, and B. Gu, Appl. Opt. **34** , 3069-3076 (1995).
6. G. Z. Yang, B. Z. Dong, B. Y. Gu, J. Y. Zhuang and O. K. Ersoy, Appl. Opt. **33**, 209–218 (1994).
7 J. W. Goodman, Introduction to Fourier Optics (McGraw-Hill, San Francisco, 1969).

Off-axis Talbot effect and array generation in planar optics

Markus Testorf, Jürgen Jahns
FernUniversität Hagen, LG ONT, Elberfelderstr. 95, 58084 Hagen, Germany,
fax.: +49-2331-332904, e-mail: markus.testorf@fernuni-hagen.de.

Nikolay A. Khilo, Andrey M. Goncharenko
Division for Optical Problems in Information Technology (DOPIT), Belarussian Academy of Sciences, P.O. B. 1, Minsk 220072, Republic of Belarus, fax: +375-172-324553
e-mail: dopit@bas.minsk.by

I. Introduction

Recently, planar optics was introduced as a concept for the micro integration of free space optics[1]. For the planar optics approach passive optical elements are arranged on the surface of a thick transparent substrate. The light signal travels within the substrate along a folded zig-zag path, reflected at the surfaces of the substrate. Since planar optics was first proposed, various applications were successfully demonstrated, like integrated split and shift modules[2] or integrated optical imaging systems[3].

Typically, the light signal reflects off the optical elements, positioned on the surfaces of the substrate under a certain angle with respect to the plane in which the elements are located. The oblique angle of light propagation has to be considered for the analysis of planar optics and related optical systems. In order to develope a foundation for the treatment of integrated planar optical systems incorporating self-imaging phenomena, we investigate the Talbot effect for oblique angles of light propagation.

II. Free space propagation and self-imaging

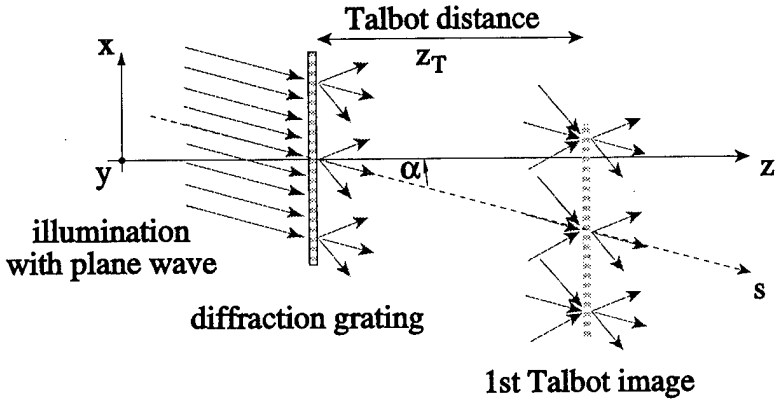


Fig. 1: Configuration for observing the off-axis Talbot effect

We consider the configuration shown in Fig. 1. A grating is illuminated by a tilted plane wave. The transmission function of the grating is assumed to be separable in x and y. The propagation direction s of the initial wave front and the grating axis z deviate by an angle α within the x-z plane.

As self-imaging is based on free space propagation of diffracted wave fields, we first calculate the transfer function $\tilde{h}(k_x,k_y,z)$ of free space starting from the solution of Helmholtz's equation in frequency space[4]. We assume small diffraction angles centered around the propagation direction $k_{x0}= (2\pi/\lambda)\cdot\sin(\alpha)$ of the incident wave. Substituting $k'_x = k_x - k_{x0}$ and disregarding constant factors we find

$$\tilde{h}(k'_x, k_y, z) = \exp\left[\underbrace{-i k'_x z \tan(\alpha)}_{\text{shift in space}} \underbrace{- \frac{i k'^2_x z}{2k\cos^3(\alpha)} - \frac{i k_y^2 z}{2k\cos(\alpha)}}_{\text{parabolic approximation}} \underbrace{- \frac{i k'^3_x z\sin(\alpha)}{2k^2\cos^5(\alpha)} - \frac{i k'_x k_y^2 z\sin(\alpha)}{k^2\cos^3(a)}}_{\text{aberrations}}\right] \quad (1)$$

with $k=2\pi/\lambda$. Eq. (1), can be split into three terms. The phase linear in k'_x corresponds to a lateral shift of the diffraction pattern in real space. The second part contains the parabolic approximation, including on-axis Fresnel diffraction ($\alpha=0$) as a special case. The last term describes aberrations which arise from the off-axis propagation of the light signal.

The effect of self-imaging can be explained within the parabolic approximation. From the parabolic term, in Eq. (1), we find different Talbot distances for x and y:

$$z_{T,x} = m_x \frac{2d_x^2}{\lambda}\cos^3(\alpha); \quad \text{and} \quad z_{T,y} = m_y \frac{2d_y^2}{\lambda}\cos(\alpha) \quad \text{with} \quad m_x, m_y = 1,2,3,..., \quad (2)$$

where indices x and y denote the lateral coordinates. For self-imaging of two dimensional gratings both conditions in Eq. (2) have to be fulfilled simultaneously.

III. Experimental verification

A) The Talbot distance

To verify Eq. (2) experimentally a one-dimensional amplitude Ronchi grating with a period $d=50\mu m$ was illuminated under different angles α by a collimated laser beam (He-Ne laser $\lambda=0.633mm$). The grating lines were oriented in y-direction. For angles $\alpha=5$, 10, 15 and 20 degrees we determined the Talbot distance. The results are summarized in Fig. 2 where the measurements are compared to the theoretical values. The deviations of the experimental

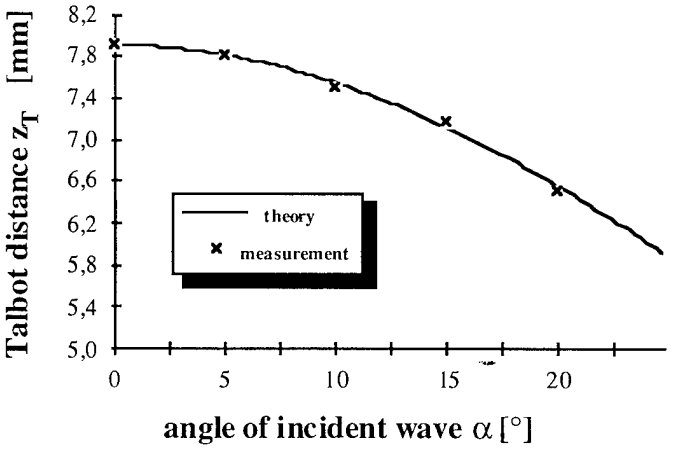


Fig. 2: Determination of the Talbot distance

and the theoretical results were found to be approximately 1%.

B) Aberrations

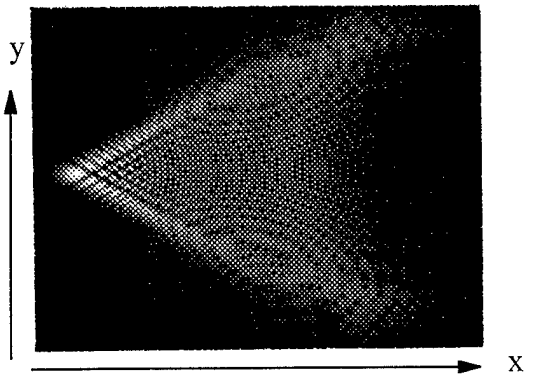


Fig. 3: Point-spread function of aberrations

To study the aberrations we numerically calculate the Fourier transformation of the last term in Eq. (1). The result, presented qualitatively in Fig. 3 as a gray scale picture, can be regarded as the point spread function for off-axis self-imaging. The ideal self-image has to be convoluted by a coma like amplitude distribution.

To compare the numerical calculations with experiments we use again a one-dimensional amplitude Ronchi grating with a period of 50μm. The grating consists of 200 lines which is sufficient to avoid edge effects at the center of the grating image. We determine the intensity distribution of the diffracted wave front of the grating at the first Talbot plane (Fig. 4a). The intensity line scan, Fig. 4a shows strongly modulated bright lines and a moderate contribution of background noise.

For comparison we computed the theoretical intensity distribution from Eq (1). The resulting intensity distribution, Fig. 4b, corresponds fairly good to the measurement, in Fig. 4a. Deviations are caused by intensity variations of the illuminating laser beam and alignment errors. During the experiment, we found that the shape of the fringes strongly depends on α and z.

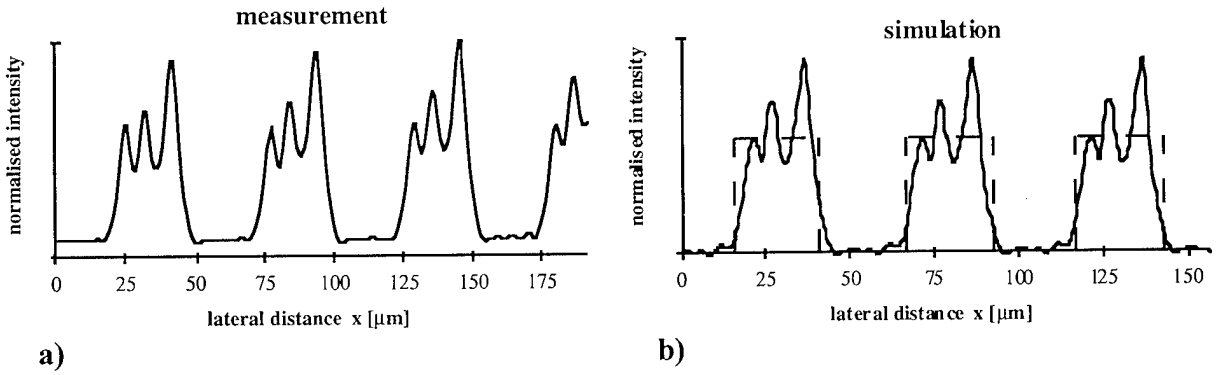


Fig. 4: Experiment and simulation of the intesity pattern in the first Talbot plane.

IV. Application to planar optics: spot array generation

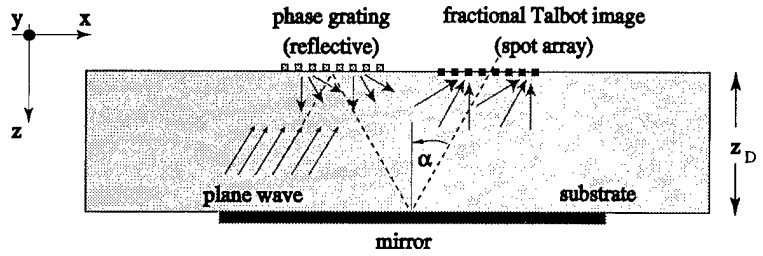


Fig. 5: Planar optical setup

One useful application for the off-axis Talbot effect is array illumination[5]. This can be efficiently performed by use of the fractional Talbot effect, where the diffraction grating is a phase only element and the bright spots appear in rational fractions of the Talbot distance[6]. A planar optical configuration is shown in Fig. 5.

For array illumination, the portion of light intensity diffracted to the desired output spots is important rather than the specific shape of the spots. Therefore, aberrations of the self-images are of less importance as long as only the line shape is influenced. From simulations we found that more than 95% of the light energy can be used in a planar optical setup. This portion, depending on α, is found to be a maximum for angles between $\alpha=20^{\circ}$ and $\alpha=30^{\circ}$.

V. Conclusion

In this paper we investigated the Talbot effect for oblique angles of light incidence. The Talbot distance depending on the illumination angles turns out to be different for both lateral coordinates. Aberrations arising from the off-axis configuration cause a significant modulation and distortion of the ideal self-images. For array generation by means of the fractional Talbot effect, however, these distortions are of less importance. Therefore, Talbot array illuminators are well applicable to planar optical integration.

References

1. J. Jahns and A. Huang, "Planar integration of free space optical components," Appl. Opt. **28**, 1602 (1989).
2. J. Jahns and B. A. Brumback, "Integrated-optical split and shift module based on planar optics," Opt. Comm. 79(5,6), 318 (1989).
3. J. Jahns and J. S. Walker, "Imaging with planar optical systems," Opt. Comm. **76**(5,6), 313 (1990).
4. J. Goodman, Introduction to Fourier optics, (McGraw Hill, New York 1968).
5. N. Streibl, "Beam shaping with optical array generators," J. Mod. Opt. **36**, 1559-1573 (1989).
6. J. R. Leger and G. J. Swanson,"Efficient aray illuminators using binary-optics phase plates at fractional Talbot planes," Opt. Lett. **15**, 288 (1990).

Diffractive Elements Developed for Uniform Illumination in Inertial Confinement Fusion

Qiu Yue Fan Dianyuan Deng Ximing
Shanghai Institute of Optics and Fine Mechanics, Chinese Academy of Sciences
P.O.Box 800-211, Shanghai 201800, P.R.China
Tel: 86-21-59534890 Ext.291, Fax: 86-21-59528812

Deng Xuegong Li Yongpin
Department of Physics, China University of Science and Technology
Hefei Anhui 230026, P.R.China

1. Introduction

In inertial confinement fusion(ICF) experimental researches, especially in direct drive ICF experimental researches, energy of the incident high power laser beam must be focused onto the target surface very uniformly. To achieve high illumination uniformity for target, several techniques have been developed, such as random phase plate (PR)[1], induced spatial incoherence (ISI)[2], smoothing by spectral dispersion (SSD)[3], lenslet array (LA)[4], etc.. Although these techniques have proven valuable in ICF applications, all of them have some limitations and can't meet all of the requirements of the applications.

Recently, we've been investigating the possibility of introducing the diffractive optical technology into our uniform illumination for ICF applications. Using a modified Gerchberg-Saxton algorithm, a kind of pure-phase elements (PPE)s are designed[5,6]. The results show it is a very promising method. Meanwhile, scientists in Lawrence Livermore National Laboratory developed a kind of kinoform phase plate for ICF uniform illumination[7,8]. In this paper, we will give out our fabricate and experiment results of PPE.

2. Design

We've developed a 2-D PPE design code according to a modified Gerchberg-Saxton algorithm[5,6], which enable us to design PPEs which can generate focal spots of arbitrary shapes and sizes with varied intensity profiles. During the design of the PPE, we

choose λ=0.6328μm., the size is 40mm × 40mm. The iteration is start up with a lens like initial phase profile. With a uniform plane incident beam, the focal spot intensity profile is chosen to be a super-Gaussian function:

$$U_t(x_t, y_t) = \exp\left(\left|\frac{x}{w_x}\right|^n + \left|\frac{y}{w_y}\right|^n\right) \tag{1}$$

with n=50 and w_x=w_y=500μm. Figure 1(a) shows the phase distribution of the PPE after 100 iterations, Figure 1(b) is the focal spot intensity distribution. As we expect, the focal spot is of very sharp edge and low sidelobes. Statistically, the intensity profile tends to have a flat-top envelope, but resembles a speckle pattern with very large intensity modulations. This may be caused by the limits of the algorithm, such as self-trapping phenomena, etc. It is a problem need to be solved. However, by using PPE array, the modulation nonuniformity can be statistically averaged out, furthermore, the intensity distribution on the target plane will not be sensitive to the near-field distribution of the incident laser beam[4]. The interference fringes can also be smoothed out with some existing techniques, such as SSD or partially coherent light, etc.. To make a PPE array is very difficult and very expensive, but it is the most effective method available up date.

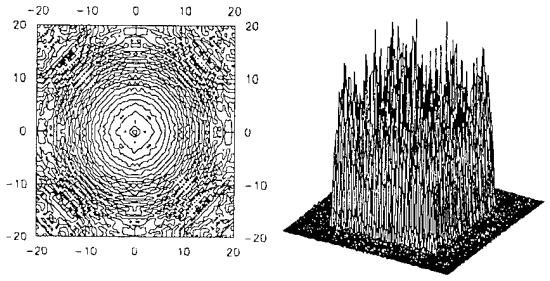


Figure 1. (a) The profile of the PPE obtained by the iterative algorithm (b) The intensity of the focal spot

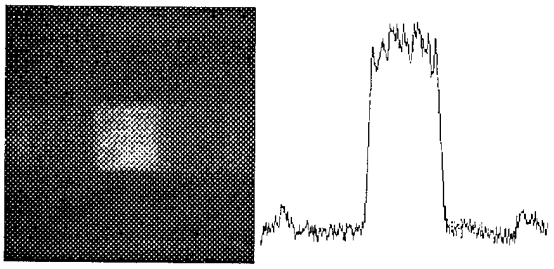


Figure 2. (a) The experimental focal spot pattern. (b) Horizontal line-scan through the profile.

3. Experiment

Using technology of ion etching, a 40mm × 40mm in square size, 16 levels PPE has been fabricated. We have tested the PPE's performance using a 2D-image measurement system. An expanded He-Ne laser beam incident to the PPE and focused by a main focusing lens with a focal length of 340mm. A 500 × 582 pixel, 1/3" CCD imager is fixed in the target position. Figure 2(a) is the focal spot intensity profile, and Figure 2(b) is the horizontal line-scans through the profile. As expected, the focal spot is a 500μm × 500μm in size with very sharp edges. The intensity distribution within the spot is very modulated. These properties are fit with the theoretical result in the previous section. However, the pattern is a little different from the theoretical result in detail because of the drawback during the PPE's fabrication and the near-field distortion of the incident beam. The size of

the PPE is a little larger than that is fit to the ion etching equipment, this reduces the accurate of the masks' alignment. The misalignment cause a additional grating structure with a period of about 200μm in horizontal and vertical direction on the PPE's surface phase relief pattern, especially in the horizontal direction, as shown in Figure 2. We believe that this drawback can be overcome by enhance the accurate of the masks' alignment during the PPE's fabrication. Another simple but effective technique to fabricate the PPE is under developing.

Reference

[1] Y.Kato & K.Mima, "Random Phase Shifting of Laser Beam for Absorption Profile Smoothing and Instability Suppression in Laser Produced Plasmas", *Appl.Phys.B:* , 29(3), 186, (1982)

[2] R.H.Lehmberg & S.P.Oenschain, "Use of Induced Spatial Incoherence for Uniform Illumination of Laser Fusion Targets", *Opt.Commun.*, 46(1), 27, (1983)

[3] S.Skupsky, R.W.Short, T.Kessler, et al, "Improved Laser-Beam Uniformity Using the Angular Dispersion of Frequency-Modulated Light", *J.Appl.Phys.*, 66(8), 3456, (1989)

[4] Ximing Deng, Xiangchun Liang, Zezun Chen, et al, "Uniform Illumination of large targets Using a Lens Array", *Appl. Opt.* , 25(3), 377, (1986)

[5] Qiu Yue, Wen Guojun, Fan Dianyuan, Dengximing, Li Yongping, Deng Xuegong, "Using Kinoform Phase Plates to Generate Uniform Focal Profiles", *International Atomic Energy Agency Technical Committee Meeting on Drives for Inertial Confinement Fusion, Paris, France*, Nov.1994.

[6] Deng Xuegong, Li Yongping, Qiu Yue, Fan Dianyuan, "Phase-Mixture Algorithm Applied to Design of Pure Phase Elements", *Chinese Journal of Lasers* B4(5), 447, (1995)

[7] J.K.Lawson, S.N.Dixit, D.Eimerl, et al, "Phase Screens for the Control of the Focal Irradiance of the Nova Laser", *Proc. SPIE*, 1870, 88, (1993)

[8] S.N.Dixit, J.K.Lawson, K.R.Manes, et al, "Kinoform Phase Plates for Focal Plane Irradiance Profile Control", *Opt.Lett.* 19(6), 417, (1994)

Achromatization for Multiple Narrowband Sources using Hybrid Multi-Order Diffractive Lenses

Kevin J. McIntyre and G. Michael Morris, Institute of Optics, University of Rochester
Rochester, NY 14627, (716) 275-2322, (716) 271-1027 (FAX)

Introduction

Surface relief diffractive lenses that utilize multiple diffracted orders were first introduced by Sweeney and Sommargren[1] and Morris and Faklis[2]. More comprehensive discussions of these lenses were later presented[3,4,5]. These multi-order diffractive (MOD) lenses were shown to have the same optical power at a discrete set of resonance wavelengths within a chosen spectral region. The physical difference between a standard diffractive lens and a MOD lens is that the OPD at the zone boundaries of a standard diffractive lens is equal to the design wavelength, whereas, for a MOD lens the OPD is equal to an integer (>1) multiple of the design wavelength. As a result, the diffraction efficiency for each order of a MOD lens has a reduced spectral bandwidth. This efficiency reduction indicates that MOD lenses may be best suited for optical systems which utilize discrete wavelength sources as opposed to broadband sources. This paper will investigate the use of MOD lenses in this class of systems by examining the combination of refractive and diffractive lens power to achieve proper achromatic control in a manner analogous to the standard hybrid lens approach. These hybrid lens combinations may be well suited for applications such as color laser printing and laser machining. Several first order design examples are provided including a two-color hybrid achromat with nearly 100% diffraction efficiency and a three-color hybrid apochromat made from a single material.

Background

The expression for the power of a MOD lens is given as $\Phi(\lambda) = m\lambda\phi_0/p\lambda_0$, where m is the diffracted order, λ is the wavelength, ϕ_0 is the design power, p is a physical design parameter (integer), and λ_0 is the design wavelength. At the resonance wavelengths given by, $\lambda_{res} = p\lambda_0/m$, the optical power of the lens is equal to ϕ_0. It is likely that the operating wavelengths of a given system will not be the same as the resonance wavelengths making it necessary to add refractive power to achromatize the lens. To make use of the unique spectral properties of MOD lenses and to ensure a minimum level of diffraction efficiency, the operating wavelengths should be nearly equal to the resonance wavelengths. In terms of diffraction efficiency, the ideal operating wavelengths are those for which the efficiency equals 100 %. These wavelengths can be determined through use of the expression for the mth order diffraction efficiency, $\eta_m = \mathrm{sinc}^2[\alpha(\lambda)p - m]$, where $\alpha(\lambda) = [\lambda_0(n(\lambda)-1)]/[\lambda\,(n(\lambda_0)-1)]$ is a wavelength detuning factor, and $n(\lambda)$ is the refractive index of the material. Since the effect of material dispersion is relatively small, the efficiency maxima occur near the resonance wavelengths.

Adding refractive power also results in a reduction in the rate of change of power as a function of wavelength. This dispersion reduction may be enough to accommodate the spectral fluctuations exhibited by diode lasers. The design bandwidth for such devices it typically 20 nm. For diode systems which are relatively fast, this dispersion may need to be constrained directly in the first-order design.

Theory

The concept of overlaying multiple diffractive lenses was recently introduced[1] for a broadband imaging application. In this case a standard diffractive lens was combined with a MOD lens to offset the effects of material dispersion. Generalizing this idea, the following expression is written for the power of N_{ref} thin refractive lenses and N_{diff} diffractive lenses in contact at an operating wavelength, λ_k,

$$\Phi(\lambda_k) = \sum_{i=1}^{N_{ref}} c_i (n_i(\lambda_k)-1) + \sum_{j=1}^{N_{diff}} A_j m_{jk} \lambda_k . \quad (1)$$

The curvature and refractive index of the ith refractive element are given by c_i and n_i, respectively. The factor, m_{jk}, represents the diffraction order of the jth diffractive element for the wavelength, λ_k, and A_j is a physical design parameter given by

$$A_j = \frac{\phi_j}{p_j (\lambda_{des})_j} . \quad (2)$$

In this expression p_j is an integer that specifies the integer number of waves of OPD at the edge of each diffractive zone, $(\lambda_{des})_j$ is the design wavelength of the jth diffractive lens, and ϕ_j is the power of the jth diffractive lens at the resonant wavelengths, $p(\lambda_{des})_j$ /m . The parameter, A_j, is analogous to the curvature c_i, since it describes the physical structure of a lens and remains unchanged as the operating wavelength, λ_k, is varied. A similar expression for the derivative of the lens power can be written as

$$\Phi'(\lambda_k) = \sum_{i=1}^{N_{ref}} c_i n_i'(\lambda_k) + \sum_{j=1}^{N_{diff}} A_j m_{jk} \quad (3)$$

where the prime symbol denotes the derivative with respect to wavelength. The resulting system of equations can be expressed as

$$\begin{bmatrix} n_1(\lambda_1)-1 & n_2(\lambda_1)-1 & \cdots & m_{11}\lambda_1 & m_{21}\lambda_1 & \cdots \\ n_1(\lambda_2)-1 & n_2(\lambda_2)-1 & \cdots & m_{12}\lambda_2 & m_{22}\lambda_2 & \cdots \\ \cdots & \cdots & \cdots & \cdots & \cdots & \cdots \\ n_1'(\lambda_1) & n_2'(\lambda_1) & \cdots & m_{11} & m_{21} & \cdots \\ n_1'(\lambda_2) & n_2'(\lambda_2) & \cdots & m_{12} & m_{22} & \cdots \\ \cdots & \cdots & \cdots & \cdots & \cdots & \cdots \end{bmatrix} \cdot \begin{bmatrix} c_1 \\ c_2 \\ \cdots \\ A_1 \\ A_2 \\ \cdots \end{bmatrix} = \begin{bmatrix} \Phi_{tot} \\ \Phi_{tot} \\ \cdots \\ 0 \\ 0 \\ \cdots \end{bmatrix} \quad (4)$$

where Φ_{tot} represents the target power at each of the operating wavelengths, and the value of the derivative of the power is arbitrarily set equal to zero. Each row corresponds to a specific operating wavelength and each column corresponds to a specific lens element. If the number of rows in the matrix equals the number of variables given in the column vector on the LHS, then at least one solution exists. This assumes that no two columns in the matrix are multiples of one another since they could be combined causing a reduction in the number of variables by one. This assumption implies a restriction on overlapping multiple diffractive lenses which can be expressed solely in terms of the diffraction orders as

$$\frac{m_{jk}}{m_{j'k}} = \text{constant}, \qquad \text{for all k in two columns } (j \neq j'). \quad (5)$$

If this condition is satisfied, the two diffractive lenses are not independent and therefore degenerate into one. This restriction prohibits designing a diffractive lens by simply multiplying the values for p and m of another diffractive lens by a fixed scale factor. Note that this degeneracy condition is analogous to defining two refractive lenses with the same material (i.e. refractive index). Examples of valid combinations of overlaid diffractive lenses include: 1) a diffractive lens which uses the same diffracted order for two or more operating wavelengths combined with another diffractive lens which utilizes at least two different orders for different operating wavelengths 2) a MOD lens, used in a system of three operating wavelengths, which uses three consecutive diffracted orders and a second MOD lens which utilizes orders such that there are an unequal number of orders between the operating wavelengths.

Design Examples

In all of the following examples, the glass is BK7 and the nominal focal length is 60 mm. The diffraction efficiency for multiple diffractive lenses is calculated as the product of the individual lens efficiencies at each wavelength.

Three-color hybrid apochromat

This lens is designed to have the same power at three different wavelengths and is formed with a single refractive lens and two overlaid diffractive lenses. A potential application for this lens type is a color laser writer which writes to a spectrally sensitive substrate such as photographic film. This type of application may require a relatively fast system making achromatic correction particularly important. The following operating wavelengths are assumed: $\lambda_1 = 670$ nm, $\lambda_2 = 750$ nm, $\lambda_3 = 880$ nm. The first diffractive lens is the conventional type ($p = 1$; $m = 1$) with a design wavelength given by $(\lambda_{des})_1 = \lambda_2 = 750$ nm. The second diffractive lens is a MOD lens with following design parameters, which are chosen to maximize the diffraction efficiency at each of the operating wavelengths: $p = 6$; $m = 6, 7, 8$; $(\lambda_{des})_2 = 880$ nm. The resonance wavelengths of the MOD lens are $\lambda_{res,8} = 660$ nm, $\lambda_{res,7} = 754$ nm, and $\lambda_{res,6} = 880$ nm. Using equation 4, one can solve for the refractive lens curvature, c, and the diffractive lens parameters, A_1 and A_2. The total power of the hybrid lens is distributed among the three lenses as: 101.63% : 2.69% : -4.32% (ref : standard diff : mod).

The chromatic behavior of this lens is illustrated in Fig. 1(a) which shows the focal length and the diffraction efficiency as functions of wavelength. The diffraction efficiencies at each of the operating wavelengths (shortest to longest) are equal to 94%, 98%, and 93%, respectively. The slopes of the focal length curves are roughly the same and given by 3.7μm/nm. A wavelength shift of 10 nm for one of the lasers results in a focus error of 0.037 mm. For an F/5 system, this is nearly equal to the depth of focus. In this case the laser spectral output would have to be better controlled. For slower systems, this focus error may be tolerable but it might be more appropriate to use a standard hybrid achromat designed to unite the focii for the wavelengths, λ_1 and λ_3.

Two-color hybrid achromat

This lens is designed to have the same power at two wavelengths and a value of zero for the derivative of the power at one of the wavelengths. It is formed with a single refractive lens and two overlaid diffractive lenses. Such chromatic properties may be appropriate for a high speed system which incorporates a diode alignment laser without any special controls over the emitted wavelength and a spectrally stable laser. A potential application is high resolution laser machining. The following wavelengths are assumed: $\lambda_1 = 500$ nm (primary beam), $\lambda_2 = 670$ nm (diode). The derivative of the power is set equal to zero at the diode wavelength. The first diffractive lens is the conventional type ($p = 1$; $m = 1$) with a design wavelength given by $(\lambda_{des})_1 = \lambda_1 = 500$ nm. The second diffractive lens is a MOD lens with the following design parameters: $p = 4$; $m = 3, 4$; $(\lambda_{des})_2 = \lambda_1 = 500$ nm. The resonance wavelengths of the MOD lens are $\lambda_{res,4} = 500$ nm and $\lambda_{res,3} = 667$ nm. The total power of the hybrid lens is distributed among the three lenses as: 97.69% : 0.92% : 1.39% (ref : standard diff : mod).

Fig. 1(b) shows the focal length and the diffraction efficiency as functions of wavelength. The diffraction efficiencies at each of the operating wavelengths, λ_1 and λ_2, are 100% and 79%, respectively. The reduced efficiency for λ_2 results from setting the design wavelength of the standard diffractive lens to be equal to λ_1.

Two-color hybrid achromat

This lens is similar to the previous two-color hybrid achromat but with no constraint on the derivative of the power and is formed with a single refractive lens and a single MOD lens. This lens type may be useful in a two laser application where the diffraction efficiencies must approach 100% at both of the operating wavelengths. The following relevant parameters are assumed: $\lambda_1 = 500$ nm, $\lambda_2 = 670$ nm ; $p = 3$; $m = 4, 3$; $(\lambda_{des})_1 = 665$ nm. The total power of the hybrid lens is distributed among the two lenses as: 25.77% : 74.23% (ref : mod).

Fig. 1(c) shows the focal length and the diffraction efficiency as functions of wavelength. The diffraction efficiencies at each of the operating wavelengths, λ_1 and λ_2, are 99.3% and 99.8 %, respectively. The relatively steep slope of the focal length curves, due to the strong diffractive component, dictates that the laser wavelengths should not deviate from their design values.

Summary

By combining multiple diffractive lenses with one or more refractive lenses, a variety of achromatic lens types can be designed. These lenses are particularly suited to laser applications which require achromatic behavior at a discrete set of operating wavelengths. These lens types offer the same advantages that conventional hybrid achromats provide including fewer lens materials (i.e. elements) and reduced surface curvatures. In fact, it is possible to design a three-color apochromat using a single lens material. The design of these lenses involves making judicious choices for the diffractive design wavelengths as well as the physical parameter, p, described earlier. For a system where the operating wavelengths are relatively close to one another, a conventional doublet design (either refractive or standard hybrid) may be the most appropriate choice, since the change in power over the small spectral band may be tolerable. However, for high speed systems in which chromatic aberration must be tightly controlled or systems in which the spectral separation is relatively large, these new hybrid lenses provide an alternative to existing achromatic design forms.

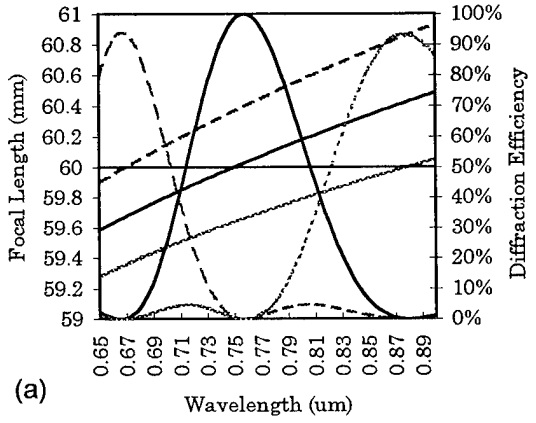


Figure 1. In the three graphs shown, the bell shaped curves correspond to the diffraction efficiencies, η_m, and the other curves correspond to the focal lengths. The same line type is used for the focal length and the diffraction efficiency for each diffracted order. (a) three-color apochromat - dashed, m=8; solid, m=7; dotted, m=6, (b) two-color achromat - dashed, m=4; solid, m=3, (c) two-color achromat - dashed, m=4; solid, m=3.

References

[1] D. W. Sweeney and G. Sommargren, "Single element achromatic diffractive lens", in Diffractive Optics, Vol. 11 of 1994 OSA Technical Digest Series (Optical Society of America, Washington, D.C., 1994), pp. 26-29

[2] G. M. Morris and D. Faklis, "Achromatic and apochromatic diffractive singlets", in Diffractive Optics, Vol. 11 of 1994 OSA Technical Digest Series (Optical Society of America, Washington, D.C., 1994), pp. 53-56

[3] D. Faklis and G. M. Morris, "Spectral properties of multiorder diffractive lenses", Appl. Opt. **34**, 2462-2468 (1995)

[4] D. W. Sweeney and G. Sommargren, "Harmonic diffractive lenses", Appl. Opt. **34**, 2469-2475 (1995)

[5] M. Rossi, R.E. Kunz, and H.P. Herzig, "Refractive and Diffractive Properties of Planar Micro-Optical Elements", Appl. Opt. **34**, 5996-6007 (1995)

Design Examples

In all of the following examples, the glass is BK7 and the nominal focal length is 60 mm. The diffraction efficiency for multiple diffractive lenses is calculated as the product of the individual lens efficiencies at each wavelength.

Three-color hybrid apochromat

This lens is designed to have the same power at three different wavelengths and is formed with a single refractive lens and two overlaid diffractive lenses. A potential application for this lens type is a color laser writer which writes to a spectrally sensitive substrate such as photographic film. This type of application may require a relatively fast system making achromatic correction particularly important. The following operating wavelengths are assumed: $\lambda_1 = 670$ nm, $\lambda_2 = 750$ nm, $\lambda_3 = 880$ nm. The first diffractive lens is the conventional type ($p = 1$; $m = 1$) with a design wavelength given by $(\lambda_{des})_1 = \lambda_2 = 750$ nm. The second diffractive lens is a MOD lens with following design parameters, which are chosen to maximize the diffraction efficiency at each of the operating wavelengths: $p = 6$; $m = 6, 7, 8$; $(\lambda_{des})_2 = 880$ nm. The resonance wavelengths of the MOD lens are $\lambda_{res,8} = 660$ nm, $\lambda_{res,7} = 754$ nm, and $\lambda_{res,6} = 880$ nm. Using equation 4, one can solve for the refractive lens curvature, c, and the diffractive lens parameters, A_1 and A_2. The total power of the hybrid lens is distributed among the three lenses as: 101.63% : 2.69% : -4.32% (ref : standard diff : mod).

The chromatic behavior of this lens is illustrated in Fig. 1(a) which shows the focal length and the diffraction efficiency as functions of wavelength. The diffraction efficiencies at each of the operating wavelengths (shortest to longest) are equal to 94%, 98%, and 93%, respectively. The slopes of the focal length curves are roughly the same and given by 3.7μm/nm. A wavelength shift of 10 nm for one of the lasers results in a focus error of 0.037 mm. For an F/5 system, this is nearly equal to the depth of focus. In this case the laser spectral output would have to be better controlled. For slower systems, this focus error may be tolerable but it might be more appropriate to use a standard hybrid achromat designed to unite the focii for the wavelengths, λ_1 and λ_3.

Two-color hybrid achromat

This lens is designed to have the same power at two wavelengths and a value of zero for the derivative of the power at one of the wavelengths. It is formed with a single refractive lens and two overlaid diffractive lenses. Such chromatic properties may be appropriate for a high speed system which incorporates a diode alignment laser without any special controls over the emitted wavelength and a spectrally stable laser. A potential application is high resolution laser machining. The following wavelengths are assumed: $\lambda_1 = 500$ nm (primary beam), $\lambda_2 = 670$ nm (diode). The derivative of the power is set equal to zero at the diode wavelength. The first diffractive lens is the conventional type ($p = 1$; $m = 1$) with a design wavelength given by $(\lambda_{des})_1 = \lambda_1 = 500$ nm. The second diffractive lens is a MOD lens with the following design parameters: $p = 4$; $m = 3, 4$; $(\lambda_{des})_2 = \lambda_1 = 500$ nm. The resonance wavelengths of the MOD lens are $\lambda_{res,4} = 500$ nm and $\lambda_{res,3} = 667$ nm. The total power of the hybrid lens is distributed among the three lenses as: 97.69% : 0.92% : 1.39% (ref : standard diff : mod).

Fig. 1(b) shows the focal length and the diffraction efficiency as functions of wavelength. The diffraction efficiencies at each of the operating wavelengths, λ_1 and λ_2, are 100% and 79%, respectively. The reduced efficiency for λ_2 results from setting the design wavelength of the standard diffractive lens to be equal to λ_1.

Two-color hybrid achromat

This lens is similar to the previous two-color hybrid achromat but with no constraint on the derivative of the power and is formed with a single refractive lens and a single MOD lens. This lens type may be useful in a two laser application where the diffraction efficiencies must approach 100% at both of the operating wavelengths. The following relevant parameters are assumed: $\lambda_1 = 500$ nm, $\lambda_2 = 670$ nm ; $p = 3$; $m = 4, 3$; $(\lambda_{des})_1 = 665$ nm. The total power of the hybrid lens is distributed among the two lenses as: 25.77% : 74.23% (ref : mod).

Fig. 1(c) shows the focal length and the diffraction efficiency as functions of wavelength. The diffraction efficiencies at each of the operating wavelengths, λ_1 and λ_2, are 99.3% and 99.8 %, respectively. The relatively steep slope of the focal length curves, due to the strong diffractive component, dictates that the laser wavelengths should not deviate from their design values.

Summary

By combining multiple diffractive lenses with one or more refractive lenses, a variety of achromatic lens types can be designed. These lenses are particularly suited to laser applications which require achromatic behavior at a discrete set of operating wavelengths. These lens types offer the same advantages that conventional hybrid achromats provide including fewer lens materials (i.e. elements) and reduced surface curvatures. In fact, it is possible to design a three-color apochromat using a single lens material. The design of these lenses involves making judicious choices for the diffractive design wavelengths as well as the physical parameter, p, described earlier. For a system where the operating wavelengths are relatively close to one another, a conventional doublet design (either refractive or standard hybrid) may be the most appropriate choice, since the change in power over the small spectral band may be tolerable. However, for high speed systems in which chromatic aberration must be tightly controlled or systems in which the spectral separation is relatively large, these new hybrid lenses provide an alternative to existing achromatic design forms.

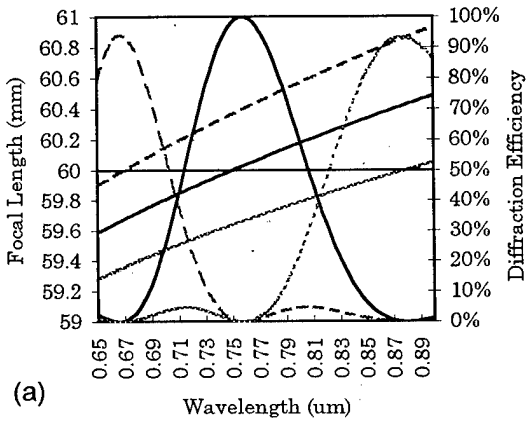


Figure 1. In the three graphs shown, the bell shaped curves correspond to the diffraction efficiencies, η_m, and the other curves correspond to the focal lengths. The same line type is used for the focal length and the diffraction efficiency for each diffracted order. (a) three-color apochromat - dashed, m=8; solid, m=7; dotted, m=6, (b) two-color achromat - dashed, m=4; solid, m=3, (c) two-color achromat - dashed, m=4; solid, m=3.

References

[1] D. W. Sweeney and G. Sommargren, "Single element achromatic diffractive lens", in Diffractive Optics, Vol. 11 of 1994 OSA Technical Digest Series (Optical Society of America, Washington, D.C., 1994), pp. 26-29

[2] G. M. Morris and D. Faklis, "Achromatic and apochromatic diffractive singlets", in Diffractive Optics, Vol. 11 of 1994 OSA Technical Digest Series (Optical Society of America, Washington, D.C., 1994), pp. 53-56

[3] D. Faklis and G. M. Morris, "Spectral properties of multiorder diffractive lenses", Appl. Opt. **34**, 2462-2468 (1995)

[4] D. W. Sweeney and G. Sommargren, "Harmonic diffractive lenses", Appl. Opt. **34**, 2469-2475 (1995)

[5] M. Rossi, R.E. Kunz, and H.P. Herzig, "Refractive and Diffractive Properties of Planar Micro-Optical Elements", Appl. Opt. **34**, 5996-6007 (1995)

Array Generator Design for an Optical Analog-to-Digital Converter

Joseph N. Mait
U.S. Army Research Laboratory
AMSRL-SE-EO
2800 Powder Mill Road
Adelphi, Maryland 20783
e-mail: mait@arl.mil

Barry L. Shoop
Photonics Research Center
Department of Electrical Engineering and Computer Science
United States Military Academy
West Point, New York 10996

Within the context of image processing, digital image halftoning is an important class of analog-to-digital (A/D) conversion. Halftoning can be thought of as an image compression technique whereby a continuous-tone, gray-scale image is printed or displayed using only binary-valued pixels. One method to achieve digital halftoning is error diffusion, wherein the error associated with a nonlinear quantization process is diffused within a local region. One of us (BLS) has developed a neural network architecture based on the mathematical foundation of the error diffusion algorithm that is called an error diffusion neural network [1]. The error diffusion neural network computes the halftoned image asymptotically faster than a conventional Hopfield-type neural network, provides full-rank connectivity across the entire image (other error diffusion techniques provide only local error diffusion), and, because of its parallel implementation, does not generate any artifacts commonly associated with sequential halftoning. Figure 1 is a representation of a smart-pixel-based architecture for an optical implementation of the error diffusion algorithm. The functionality required of the error diffusion neural network is implemented using gallium arsenide (GaAs) and aluminum gallium arsenide (AlGaAs) multiple quantum well modulators. The two-dimensional spatial distribution and intensity weighting required of the error diffusion filter is accomplished using a diffractive array generator. We report here on the design of the array generator.

The desired diffusion matrix is

0.0003	0.0019	0.0051	0.0068	0.0051	0.0019	0.0003
0.0019	0.0103	0.0248	0.0328	0.0248	0.0103	0.0019
0.0051	0.0248	0.0583	0.0766	0.0583	0.0248	0.0051
0.0068	0.0328	0.0766	0	0.0766	0.0328	0.0068
0.0051	0.0248	0.0583	0.0766	0.0583	0.0248	0.0051
0.0019	0.0103	0.0248	0.0328	0.0248	0.0103	0.0019
0.0003	0.0019	0.0051	0.0068	0.0051	0.0019	0.0003

These weights describe the intensity of the desired generated array. Because of the sensitivity of the human visual system to directional artifacts, circular symmetry of the frequency response is a key requirement in the design of this filter. If an eight-level phase-only array generator is assumed, the diffraction efficiency upper bound for this array is 91.15% [2]. We used the upper

bound solution as an initial input to the iterative Fourier transform algorithm [3] to design a 128 × 128 eight-level phase-only array generator. The phase function for a single period of the array generator is represented in Fig. 2. The calculated diffraction efficiency of the array generator is 91.97% and root-mean-square fluctuation in amplitude is only 0.0026.

The geometry of the opto-electronics is such that the horizontal spacing between quantum well modulators is twice that of the vertical. This is evident in Fig. 3, which is a representation of the mask set necessary to fabricate the array generator. The element has been submitted for fabrication to the diffractive optics foundry run sponsored by the ARPA CO-OP. The specifics of the design are indicated below.

Given
wavelength $\lambda = 850$ nm
focal length $f = 50$ mm
spot spacing $d_x \times d_y = 160\ \mu m \times 80\ \mu m$
DOE size $D_x \times D_y = 1\ cm \times 1\ cm$
minimum feature $\Delta_x \times \Delta_y = 2.1\ \mu m \times 4.2\ \mu m$

Calculated
grating period $W_x \times W_y = \lambda f/d_x \times \lambda f/d_y = 265.625\ \mu m \times 531.25\ \mu m$
number of replicas $M_x \times M_y = D_x/W_x \times D_y/W_y = 37.647 \times 18.824$
lattice size $L_x \times L_y = W_x/\Delta_x \times W_y/\Delta_y = 126.49 \times 126.49$

Designed
128×128 array generator replicated 37×18 times
grating period $(128 \cdot 2.1\ \mu m) \times (128 \cdot 4.2\ \mu m) = 268.8\ \mu m \times 537.6\ \mu m$
DOE size $(37 \cdot 268.8\ \mu m) \times (18 \cdot 537.6\ \mu m) = 9.9456\ mm \times 9.6768\ mm$
spot spacing $(850\ nm \cdot 50\ mm) \cdot (1/268.8\ \mu m \times 1/537.6\ \mu m) = 158.11\ \mu m \times 79.06\ \mu m$
spot size $\sim(850\ nm \cdot 50\ mm)/1\ cm = 4.25\ \mu m$

MAJ Shoop was supported by the Army Research Office and the Advanced Research Projects Agency.

1. B. L. Shoop, J. N. Mait, and E. K. Ressler, "Optical error diffusion for analog-to-digital conversion," submitted to the 1996 Army Science Conference.
2. F. Wyrowski, Opt. Lett. **16**, 1915-1917 (1991).
3. F. Wyrowski, J. Opt. Soc. Am. A **10**, 1553-1561 (1993).

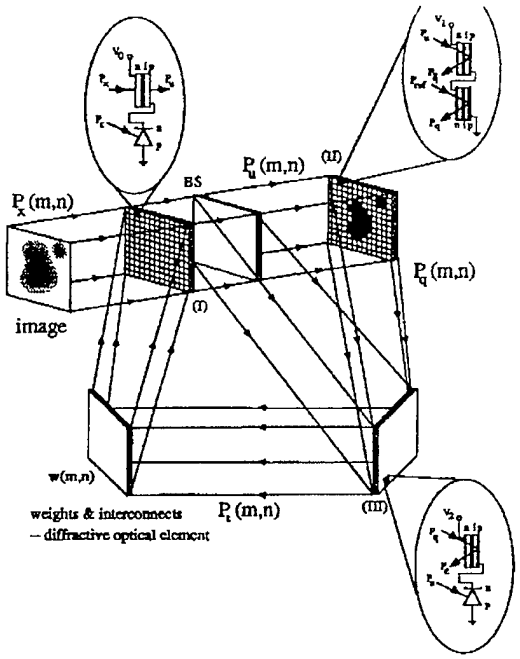


Figure 1. Architecture for optical implementation of error diffusion neural network.

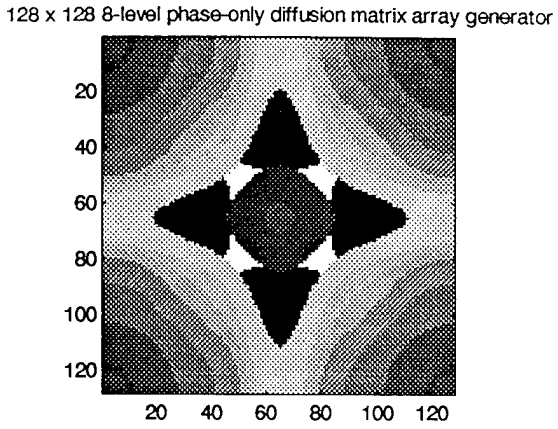


Figure 2. Representation of single period of phase for an eight-phase level diffusion matrix array generator.

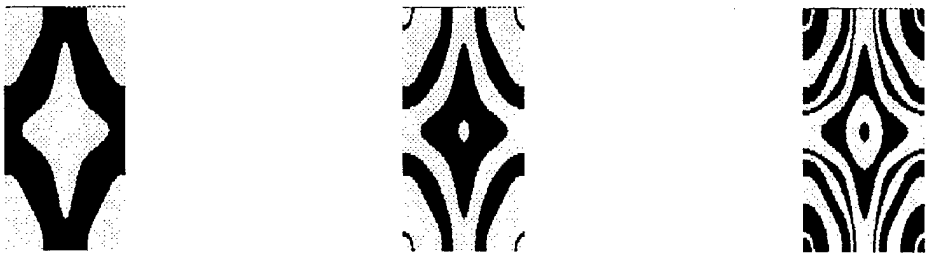


Figure 3. Representation of single period of mask set necessary to fabricate eight-phase level diffusion matrix array generator. Binary mask for (a) π-phase, (b) π/2-phase, and (c) π/4-phase etches.

Electric Fields and Poynting Vectors in Dielectric Gratings

Bruce W. Shore
Lawrence Livermore National Laboratory, Livermore CA 94550
phone (510) 455-0627 email shore2@LLNL.GOV
Lifeng Li
Optical Sciences Center, University of Arizona, Tucson AZ 85721
and Michael D. Feit
Lawrence Livermore National Laboratory, Livermore CA 94550

The electric field E is the most significant of the several fields of electromagnetic radiation, because it indicates regions of dielectric response. The nodes and antinodes of plane wave structure are clearly visible in plots of the E field, as are regions of localized enhancement near grating surfaces. It is in these enhanced field regions that one expects to find the strongest photoelectric response, or the first damage as the field is increased.

The electromagnetic energy density W , though uniform for simple standing wave patterns (above a mirror or high efficiency grating) reveals more structure around the grating interface than does the E field. It reveals mode structure and evanescent waves. However, patterns of nodes and antinodes in energy density do not become visible through photoelectric response, and regions of high energy density are not necessarily the regions in which damage occurs.

When there are no dissipative or absorptive sources and sinks of electromagnetic radiation, as is the case for an ideal dielectric material, then the Poynting vector **S** is a divergenceless field. It can have curls and saddle points as well as planes along which there is uniform flow. These structures do not correspond in an intuitively obvious way with the more important structure of nodes and peaks of the electric field, although the patterns of the two fields are closely tied.

When applied to resistive electromagnetic circuits, the Poynting vector describes Joule heating. The Poynting vector has been used to provide insight into the behavior of metallic gratings, whose surfaces are, like resistors, sinks for electromagnetic energy . In particular, Popov [1-3] has offered plots of the Poynting vector as a means of understanding how grating efficiency varies with groove depth, passing through regimes of high and low diffraction efficiency, interspersed with regimes of high and low specular reflection [3].

Such studies have had great value for the understanding of metal gratings. It is natural to hope that the Poynting vector will offer insight into the behavior of all-dielectric gratings.

Our studies, based on numerical solutions to the Maxwell equations using the multilayer modal method [4], have shown that although it is possible to associate changes of **S** with changes in grating construction, not all of these changes are evident in the far field. It is particularly noteworthy that small changes in groove shape of a dielectric grating may, without influencing the far field pattern (i.e. the grating efficiency) or the near E field cause

dramatic changes in the near-field Poynting vector: rows of curls may shift from above grating valleys to above grating peaks. Furthermore, the planes of steady flow of **S** may flow in either direction. Unlike the situation with absorbing material (metallic surfaces), the flow lines of **S** in a dielectric do not provide indication of Joule heating or other observable effects.

From examining the appearance of E, W and **S** in representative cases, we conclude that plots of **S** may not be as useful for dielectric gratings as they are for metallic structures. The energy density W is a much more intuitive field to examine than is **S**

This work was supported under the auspices of the U.S. Department of Energy at Lawrence Livermore National Laboratory under contract W-7405-Eng-48.

References

[1]. E. Popov, L. Tsonev and D. Maystre, "Gratings - general properties of the Littrow mounting and energy flow distribution" J. Mod. Opt. **37,** 367-377 (1990)

[2]. E. Popov, L. Tsonev and D. Maystre, "Losses of plasmon surface waves on metallic grating" J. Mod. Opt. **37,** 379-387 (1990)

[3]. E. Popov and L. Tsonev, "Total absorption of light by metallic gratings and energy flow distribution" Surface Science **230,** 290-294 (1990)

[4]. L. Li, "Multilayer modal method for diffraction gratings of arbitrary profile, depth, and permittivity" JOSA A **10,** 2581-91 (1993)

Diffractive-refractive achromatic optical processor for white-light spatial filtering

P. Andrés, E. Tajahuerce*, J. Lancis*, V. Climent*, and M. Fernández-Alonso*

Universidad de Valencia, Departamento de Optica, 46100 Burjassot, Spain.
**Universitat Jaume I, Departamento de Ciencias Experimentales, 12080 Castellón, Spain.*

1. INTRODUCTION

White-light Fourier processing techniques allow to improve the signal-to-noise ratio, to use non-laser sources, and, of course, to deal with color input signals. Nevertheless, conventional optical processing operations performed with broadband illumination are severally limited due to the wavelength dependence of the diffraction phenomenon. In this way, the Fraunhofer diffraction pattern of the input transparency is chromatic dispersed, both axial and laterally and, furthermore, the insertion of spatial filters at the frequency plane produces additional chromatic effects at the output plane.

Achromatic Fourier transformers are designed to partially compensate for the chromatic dispersion of the Fraunhofer diffraction pattern [1]. In this direction, two different optical architectures, constituted by a small number of diffractive lenses and achromatic objectives, providing the achromatic representation of the optical Fourier transform of any color input signal with low chromatic aberration under white-light point source illumination have been recently proposed [2,3]. The optical Fourier transform provided by the above optical setups is located, in a first-order approximation, in a single real plane and with the same magnification for all the wavelengths of the incident light. In a different context, it is also possible to design achromatic imaging systems using diffractive optical elements and conventional lenses [4,5].

Combining both achromatic Fourier transforming concepts and diffractive imaging methods, in this contribution we report a novel achromatic Fourier processor under white-light point source illumination. The first part of our optical proposal is an achromatic Fourier transformer that uses solely two on-axis blazed diffractive lenses. By adding only an achromatic objective and a third zone plate, the whole arrangement acts as an achromatic imaging configuration that, thus, images the input transparency into the output plane preserving the achromatic correction in the intermediate Fraunhofer plane. With a different approach, other achromatic Fourier processors have been previously reported [6-8]. However, they are constituted by a large number of optical components and/or the residual chromatic errors are very important. The formation of the final image can be understood in all the above cases as a double achromatic Fourier transforming process in cascade.

Our configuration provides an intermediate achromatic Fourier transform with low chromatic aberration and, neglecting the secondary chromatic aberration of the refractive objective, a final image with no chromatic error. This achromatic optical processor is well-adapted to extend the conventional monochromatic spatial filtering techniques to white-light with noteworthy results. Now, our optical processor can perform the same spatial filtering operation for all the spectral components of the broadband illumination simultaneously.

2. ACHROMATIC FOURIER TRANSFORMER

Let us consider an input transparency illuminated by a broadband spherical wavefront beam converging towards the point source S located at a normal distance z from the aperture. It is possible to recognize that a separated diffractive doublet, which consists of two on-axis zone plates ZP_1 and ZP_2 in such a way that ZP_2 is positioned at the source plane, is able to provide an achromatic representation of the Fourier transform of the input, as is depicted in Fig.1. If we denote Z_o and Z'_o as the focal length of ZP_1 and ZP_2, respectively, for the reference wave number σ_o, the achromatic condition leads to the constraint [3]

$$d^2 = -Z_o\, Z'_o \quad , \qquad (1)$$

where d is the separation between the two zone plates.

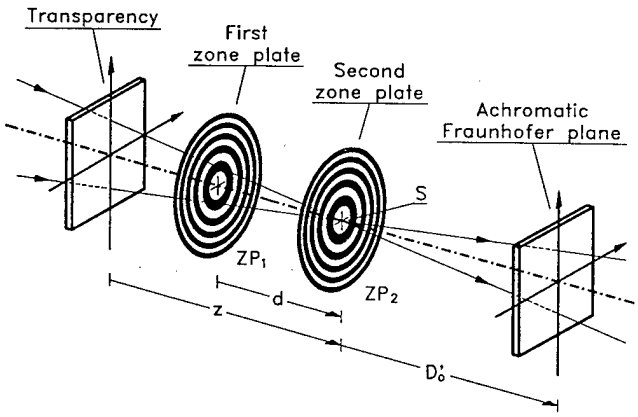


Figure 1.

In this way, the Fraunhofer diffraction pattern of the diffracting screen is obtained, in a first-order approximation, at a distance D'_o from ZP_2 such that

$$D'_o = \frac{-d^2}{d + 2\,Z_o} = \frac{\alpha}{\sqrt{\alpha} - 2}\, Z_o \quad , \qquad (2)$$

where the dimensionless parameter α is defined as $\alpha = -\,Z'_o / Z_o$. In order to manipulate the spectral content of the input object we must obtain a real achromatic Fraunhofer plane, i.e. $D'_o > 0$. This later fact implies that ZP_1 and ZP_2 should be a diverging and a converging zone plate, respectively, and α must satisfy the inequality $0 < \alpha < 4$.

Since we develop a first-order theory, the setup suffers from residual chromatic aberrations. For $\sigma_o = \sqrt{\sigma_1\, \sigma_2}$, being σ_1 and σ_2 the end wave numbers of the incoming radiation, it is possible to show that the greatest value of both the axial and the lateral geometrical chromatic error, CA_M, expressed as a percentage, is given by

$$CA_M = \frac{100}{1 + \beta\,(2 - \sqrt{\alpha})} \quad , \qquad (3)$$

where $\beta = \sqrt{\sigma_1\, \sigma_2}\,/(\sqrt{\sigma_1} - \sqrt{\sigma_2})^2$ takes into account the spectral bandwidth of the incident light. It is important to note that the achromatization of the Fourier transforming process in intensity remains unaltered by the position of the input along the optical axis of the system.

3. ACHROMATIC IMAGING SYSTEM

In order to design the achromatic Fourier processor we think about the whole optical setup as an achromatic imaging system whose first half performs an achromatic Fourier transformation of the input transparency. Following Morris' study [5], we consider an imaging system constituted by two on-axis zone plates, ZP_2 and ZP_3, with focal length Z'_o and Z''_o, respectively, for the design wave number σ_o, and an achromatic objective L, with focal distance f, located between the two, as is shown in Fig.2.

Let an input object O, illuminated by a polychromatic light beam, be located at a distance d of ZP_2. It is apparent that if we are able, in some way, to compensate the action of the two zone plates, the final image, O', supplied by the optical system will be simply given by the action of the refractive objective L. Thus, neglecting the secondary chromatic aberration of the achromatic lens, we will obtain a wavelength-independent image at the output plane. It is easy to recognize that this compensation can be accomplished if the next two conditions are satisfied. First, ZP_2 and ZP_3 are located at conjugate planes through the lens L. In mathematical terms, the distances l and l' (see Fig.2) must be related by

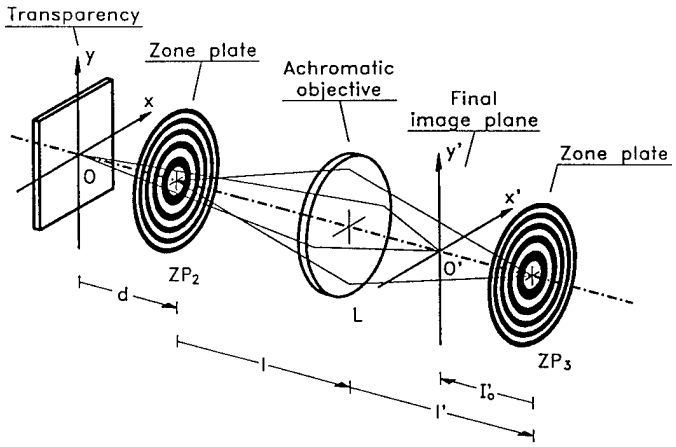


Figure 2.

$$l' = \frac{l\,f}{l-f} = -M\,l \quad , \tag{4}$$

where M is the lateral magnification between the conjugate planes. Second, in order that the image of ZP_2 through L has the same scale than ZP_3, i.e., the same focal distance (aside from a sign change), the focal lengths Z'_0 and Z''_0 must be linked by the relation

$$Z''_0 = -M^2\,Z'_0 \quad . \tag{5}$$

In this way, the image O' appears just at the conjugate plane of O through L. That is, at a distance I'_0 from ZP_3 such that

$$I'_0 = \frac{-f^2\,d}{(l-f)(l+d-f)} = -M\,M_0\,d \quad , \tag{6}$$

where M_0 is the lateral magnification between O and O' given by the objective. Although I'_0 is in principle negative, a real final image can be obtained by simply adding a second achromatic objective at the end of the setup.

4. ACHROMATIC PROCESSOR

The appropriate combination of the optical setups shown in Figs.1 and 2 provides an achromatic Fourier processor as we show next. The whole setup corresponding to our optical processor is shown in Fig.3. The first two zone plates, ZP_1 and ZP_2, perform the achromatic Fourier transformation of the input transparency. Our Fourier-transform configuration is constructed following the prescriptions of section 3. Thus, the achromatic condition is fixed by Eq.(1) and the achromatic Fraunhofer plane is located at a distance D'_0 from ZP_2 given by Eq.(2). The Fourier processor is then achieved by adding the achromatic objective L and the third zone plate ZP_3 in such a way that the position and the focal length of ZP_3 are determined by Eqs.(4) and (5), respectively. In this way, the three optical elements ZP_2, L, and ZP_3 act as an achromatic imaging system provided that the input transparency be located just against the first zone plate ZP_1. The final image plane is then located at a distance I'_0 from

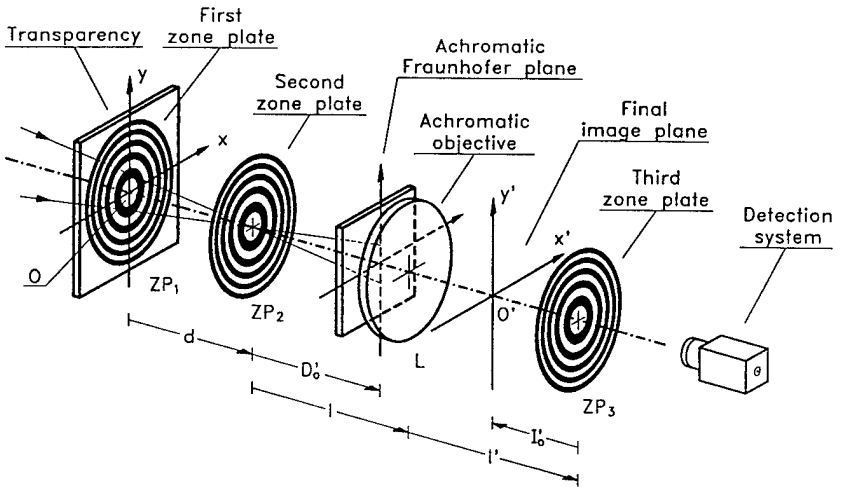


Figure 3.

ZP_3 given by Eq.(6). We can define the total length of our processor as the distance $e = d + l + l'$.

To optimize the optical system, the focal distances Z_0 and Z'_0 are selected in such a way that α has a small value. In this way, we obtain the Fourier transform of the input with low residual chromatic aberrations. To minimize the total length of the setup, it is convenient to choose l' such that $l' = l = 2f$, and thus $M = -1$. By inserting this result into Eq.(5), we derive that $Z''_0 = -Z'_0$. Finally, for inserting a spatial filter at the achromatic Fraunhofer plane of the setup the distance l must be grater than D'_0 and, thus, the focal length f must fulfill the inequality $f > D'_0/2$.

We will report some experimental verifications of the above procedure. In particular, the novel spatial filtering capabilities of our achromatic Fourier processor will be illustrated in a color multiple imaging experiment.

5. REFERENCES

1. G. M. Morris, "Diffraction theory for an achromatic Fourier transformer," Appl. Opt. **20**, 2017-2025 (1981).
2. P. Andrés, J. Lancis, and W. D. Furlan, "White-light Fourier transform with low chromatic aberration," Appl. Opt. **31**, 4682-4687 (1992).
3. J. Lancis, P. Andrés, W. D. Furlan, and A. Pons, "All-diffractive achromatic Fourier transform setup," Opt. Lett. **19**, 402-404 (1994).
4. S. J. Bennet, "Achromatic combinations of hologram optical elements," Appl. Opt. **15**, 542-545 (1976).
5. D. Faklis and G. M. Morris, "Broadband imaging with holographic lenses," Opt. Eng. **28**, 592-598 (1989).
6. R. H. Katyl, "Compensating optical systems. Part 3: Achromatic Fourier transformation," Appl. Opt. **11**, 1255-1260 (1972).
7. G. M. Morris and N. George, "Frequency-plane filtering with an achromatic optical transform," J. Opt. Soc. Am. **5**, 446-448 (1980).
8. S. Leon and E. N. Leith, "Optical processing and holography with polychromatic point source illumination," Appl. Opt. **24**, 3638-3642 (1985).

Diffractive Optical Elements for Tracking and Receiving in Optical Space Communication Systems

P. Blattner, H. P. Herzig, K. J. Weible
Institute of Microtechnology, University of Neuchâtel,
Rue A.- L. Breguet 2, 2000 Neuchâtel, Switzerland
Tel +41 38 234 494, Fax +41 38 254 276

1 Introduction

The design of first generation free space laser communication systems is based on laser diodes with output powers in the order of 100 mW [1]. The data rate transmission is in the order of 100 Mbit/s. This leads to terminals with large transmitter and receiver telescope diameters and, consequently, to high terminal mass and dimensions. The optical systems are usually designed with refractive lenses and reflective mirrors. Alternatives are planar diffractive optical elements (DOEs). By relying on diffraction and interference rather than on reflection and refraction, unique and novel properties can be realized. Almost any structure shape, including non-rotationally symmetric aspherics, can be manufactured, which provides all degrees of freedom for the design. Other interesting aspects of DOEs are their low weight, their strong dispersion, and the possibility to make segmented elements, large arrays of elements, beamsplitters, and polarizers. These properties are useful for many applications of DOEs in space, including: filters for image data processing [2], beam shaping [3, 4], and antireflection structures [5, 6]. Furthermore, the combination of refractive and diffractive surfaces (hybrid elements) offers new possibilities for optical design. The negative dispersion of DOEs can be used to compensate the chromatic aberrations of refractive lenses [7, 8]. Hybrid elements can also be used to compensate the temperature induced variations of their mounting system [9, 10]. Diffractive optical elements for space applications must comply with a number of requirements, including mechanical, thermal and optical stability [8]. Suitable techniques for realizing the microstructures in space qualified materials are based on a variety of high resolution lithographic and optical processes [11].

In this paper, we discuss the design and experimental realization of a ring pattern generator allowing tracking and data transmission within one optical element. This work has been done in the framework of an ESA project [12, 13].

2 Tracking/Receiver System

A schematic of a typical tracking/receiver system of the optical head of a laser communication system is shown Fig. 1. The tracking sensor consists of a 4-quadrant detector with a central hole which acts as a field stop for the subsequent receiver optics. The specific task of the diffractive optical element, situated at the entrance of the tracking/receiver system, consists of focusing the incoming beam into the central hole (receiver signal) while generating a ring intensity pattern in the tracking detector

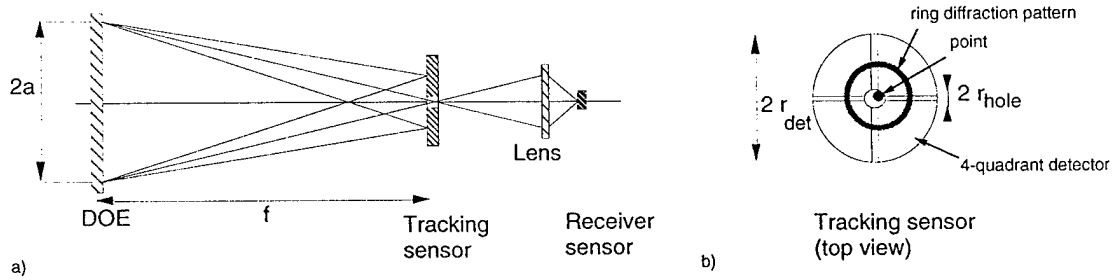


Figure 1: Principles of the tracking/receiving system. a) side view, b) top view. Changes of the relative positions of the sending and receiving communication terminals are directly translated into a shift of the ring intensity pattern on the tracking sensor, which can be measured by means of the 4-quadrant detector.

plane (tracking signal). Changes of the relative positions of the sending and receiving communication terminals are directly translated into a shift of the ring intensity pattern on the tracking sensor, which can be measured by means of the 4-quadrant detector.

Different design methods exist for the tracking/receiver DOE. The two specific tasks may be made by a segmented element. This means that the surface of the DOE is divided into two parts: A simple lens function in one part for the focusing point, and a radially shifted lens function in the other part for generation of the ring pattern (segmented aperture design). An alternative technique is to generate the ring pattern by the first diffraction order of a rotational blazed grating structure combined with a focusing function. The focal point in the center is then realized by the zero order of the grating structure. In this case, both functions are generated by the whole element, thus have the same aperture (common aperture design). The two design strategies are shown in Fig. 2 a) and b).

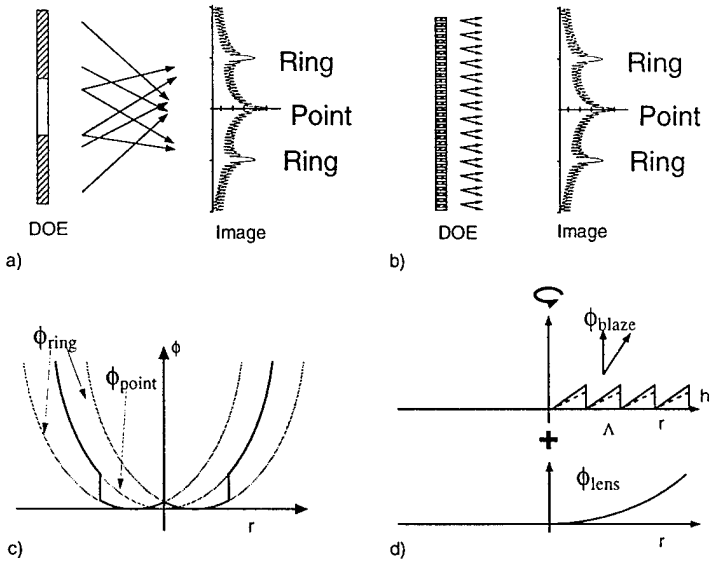


Figure 2: Two different design approaches for the tracking/receiver element. a) Segmented aperture design, b) common aperture design, c) the phase function of the segmented element, d) the phase function of the common aperture element.

DOEs are mainly described by their phase function. For the segmented aperture design each segment has its own phase function. In the case of the tracking/receiver DOE the phase function ϕ is then given by

$$y = \begin{cases} -\frac{k}{2f}r^2 & for \quad r_{seg} < r < a \\ -\frac{k}{2f}(r - r_{ring})^2 & for \quad 0 < r < r_{seg} \end{cases}, \tag{1}$$

where k is the wave vector, f the focal length of the tracking system, r_{ring} the radius of the ring intensity pattern on the 4-quadrant detector, $2a$ the diameter of the DOE, and r_{seg} the radius of separation of the two different segments. The function $\phi(r)$ is shown in Fig. 2 c). The advantage of this concept is that the ratio of the energy used for tracking (ring) and the energy used for the receiver (focal point) is directly given by the ratio of the surfaces of the two segments (i.e. $(r_{seg}/a)^2$). Furthermore, the two optical functions can be tested and characterized independently by covering one of the segments. However, a drawback of this concept might be that the system is not shift invariant, i.e. a change of the input intensity distribution directly affects the output functions. Also, the radius of the diffraction spot of the focus and the width of the ring are given by the aperture of the corresponding segments. This can lead to design problems. In particular, if much more energy has to be in the central point than in the ring, the surface of the segment used to generated the ring becomes small, thus, the width of the ring gets very large due to diffraction. On the other hand, if much more energy has to be in the ring than in the point, the point becomes very large. Depending on the design specifications the segmented approach may not be satisfying. The above mentioned problem can be avoided by the common aperture design.

The phase function of the common aperture design is composed of a lens function and a blazed grating structure defined over the entire aperture

$$\phi(r) = -\frac{k}{2f}r^2 + h \bmod(\frac{r}{\Lambda}, 1), \tag{2}$$

where Λ is the period of the grating structure, h is the phase depth of the grating structure and $mod(a, b)$ is the modulo function (also referred to the fractional part of the division a/b) . The phase function $\phi(r)$ is shown in Fig. 2 d). The grating period Λ determines the beam deflection of the first diffraction order, thus, the radius of the ring, while the phase depth of the grating structure h determines the energy distribution in the different diffraction orders. The diffraction efficiency of the first order of a blazed phase grating is given by

$$\eta_1 = \sin^2\left(\frac{h}{4}\right). \tag{3}$$

For a 2π-deep blazed structure only the first diffraction order has energy, therefore, only a ring structure without central peak is generated. If the phase depth differs from 2π, then the zero order will also get some energy, but also higher orders appear, i. e. rings of radius $2r_{ring}$, $3r_{ring}$, etc are created. However, these higher order rings don't affect the functionality of the tracking system. In this approach the diameter of the diffraction spot is given by the aperture of the whole DOE, and is therefore smaller than in the first approach.

Based on the design discussed above a set of visible light demonstrators (633 nm) for the ring/point-generation has been made, with a focal length of 400 mm and a diameter of the generated ring of 15 mm. The DOE were realized in fused silica. The resulting 8-phase level elements have smallest features in the order of 4 μm for the segemented design, respectively, 1 μm for the common aperture design.

Figure Fig. 3 a) shows the diffraction pattern of the common aperture design. Scans trough the focus in the image plan, together with the calculated function are presented in Fig. 3 b) and c) for the segmented aperture and the common aperture design, respectively. The measured intensity distribution shows excellent agreement with the expected theoretical data. The difference between theory and measurements can be explained by etch depth errors in the fabrication. Also it turned out that the common aperture element is more sensitive to etch depth errors than the segement element.

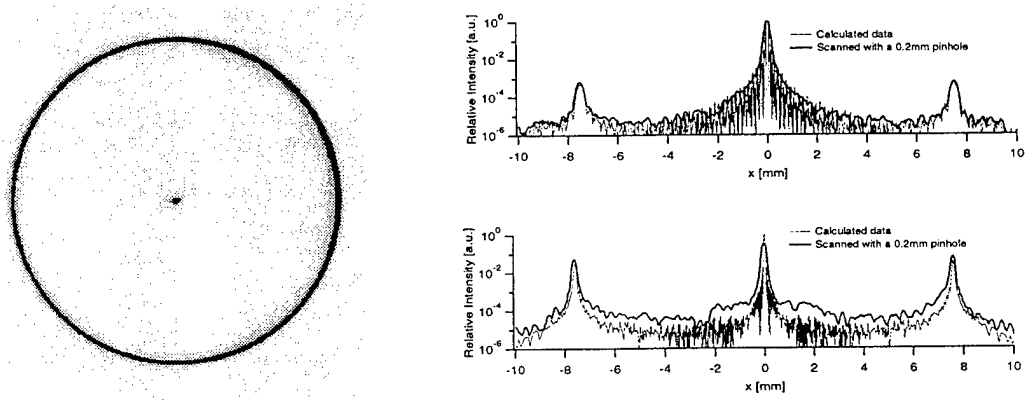


Figure 3: a) The diffraction pattern of the common aperture design. b) and c) Scans trough the focus in the image plan together with the calculated curve for the segment aperture, for the common aperture design, respectively.

3 Conclusions

On the example of the tracking/receiving element, it has been shown that diffractive optical elements may simplify optical systems, by including several functionalities in a single DOE. The task of this DOE is to generate a point/ring pattern. For this purpose two different design strategies have been investigated. One is based on a segmented aperture, the other on a common aperture approach. The realized elements showed a good agreement with the theory for both types of design. However, it

turned out that the segmented aperture based system may give some problems for specific point-ring energy ratios. The elements have satisfied the given severe specifications for space applications, which encourages to use DOEs in other systems.

References

[1] R. H. Czichy, M. Wittig, "Diffractive optics for advanced free space laser communication terminals," IEE Conference Publication No 379, Holographic Systems, Components and Applications, Neuchâtel, 1993, 255 - 259.

[2] F. Wyrowski, "Digital phase encoded inverse filters for optical pattern recognition", Appl. Opt. **30**, 4650-4657 (1991).

[3] M. T. Eisenmann, A. M. Tai, J. N. Cederquist. "Iterative design of a holographic beamformer," Appl. Opt. **28**, 2641-2650 (1989).

[4] P. Ehbets, H. P. Herzig, R. Dändliker, P. Regnault and I. Kjelberg, " Beam shaping of high power laser diode arrays by continous surface-relief elements," J. Mod. Opt. **40**, 637-645 (1993).

[5] Y. Ono, Y. Kimura, Y. Ohta, N. Nishida, "Antireflection effect in ultrahihg spatial-frequency holographic relief gratings," Appl. Opt. **26**, 1142-1146 (1987).

[6] D. Raguin and G. M. Morris, " Analysis of antireflection-structured surfaces with continous one-dimensional surface profiles," Appl. Opt. **32**, 2582-2598 (1993).

[7] T. Stones and N. George, "Hybrid diffractive-refractive lenses and achromats", App. Opt. **27**, 2960-2971 (1988).

[8] R. H. Czichy, "Hybrid optics for space applications," ESA Scientific/Technical Monographs SP-1158, ESA Publications Division, The Netherlands, 1993.

[9] G. P. Bohrmann and J. P. Bowen,"Influence of temperature on diffractive lens performance," Appl. Opt. **32**, 2483-2489 (1993).

[10] C. Londoño, et al., "Athermalization of a single-component lens with low diffractive optics", Appl. Opt. **32**, 2295-2302 (1972).

[11] H. P. Herzig, et al.,"Diffractive components: Computer generated elements," in Perspectives for Parallel Interconnects, Ph. Lalanne, P. Chavel, eds. (Springer, Berlin, 1993) 71-107.

[12] ESA project Co10566/93/NL/JV

[13] R. H. Czichy, "Miniaturised optical tracking sensor/receiver combination," ESA/PAT/274 (1992)

Scalar Design of Diffractive Elements using Direct and Indirect Optimization

Joseph N. Mait
U.S. Army Research Laboratory
AMSRL-SE-EO
2800 Powder Mill Road
Adelphi, Maryland 20783
e-mail: mait@arl.mil

1. Introduction

Although analysis of diffractive optical elements (DOEs) is critical to an understanding of the technology, equally important for their widespread application is an understanding of their design or, in counterpoint to analysis, their synthesis. The problem of design is essentially a casting of a designer's understanding of physics into an optimization problem: the DOE is to be determined so that it achieves some desired performance, preferably optimally, subject to the constraints of fabrication.

A large portion of the design literature consists of a discussion of algorithms. Unfortunately, this clouds a more fundamental distinction in synthesis, namely, whether the design is "direct" or "indirect." Direct designs are those that attempt to optimize directly the desired performance measure, subject to the constraints of fabrication. In contrast, indirect designs are those that first seek to determine a solution to the design problem unconstrained by fabrication and then impose the constraints of fabrication onto the unconstrained solution. To make this point clear, rather than concentrating on design for only a single application, the design of DOEs is considered for different applications, including focussing, array generation, and correlation. For each application the same methodic approach to design is followed: model the optical system, model the DOE fabrication, identify freedoms available for design, and define a performance measure. The problem is then solved in both a direct and an indirect manner. To insure that the discussion remains uncluttered, only design in the scalar domain is considered. However, the procedure is general enough that is easily applicable to the vector design of DOEs.

2. Design Procedure

The design of DOEs can be divided into three basic stages: understand the physics of the design problem (analysis); translate the physical understanding into mathematics and define an appropriate optimization problem (synthesis); and execute the design and fabricate the element (implementation). Each of these stages can be broken down further as indicated in the following.

Analysis: Understand the physics of image formation using the DOE.
Understand the fabrication of the DOE from data generated by computer.

These first two steps are perhaps obvious, but are critical to design. By *understand* we mean to imply the selection of a model. In this work, we consider only applications where scalar diffraction theory is valid. Simple integral transforms can then be used to model optical systems and the DOE is modelled as a thin phase transformation element. In selecting a fabrication model,

the designer must address how much detail to include. In our examples we model the DOE as a multilevel quantized phase element.

Synthesis: Define the design metric.
Define the optimization problem.

The essence of the synthesis step is to cast the design into an appropriate optimization problem. However, two basic approaches to optimization have emerged in the DOE literature: indirect and direct approaches. The distinction between the two is represented in Fig. 1. For both approaches, it is necessary to define a design metric based on those physical parameters that are used to characterize system performance. Whereas a direct approach to the design problem optimizes the design metric subject to the constraints of fabrication, in an indirect approach, the design metric is optimized without regard to these constraints. The solution to the unconstrained problem is then mapped onto the fabrication constraints using an alternative design metric.

The uni-directional and bi-directional methods refered to are based on the error-reduction and input-output algorithms defined by Fienup [1]. We prefer the nomenclature bidirectional and unidirectional to indicate the nature of data flow.

Implementation: Select a design algorithm and perform the optimization.
Fabricate the DOE from the computer-generated data.
Test the DOE.

The implementation steps are straight forward, but require many practical decisions to be made and, most importantly, considerable expenditure of resources. As indicated in Fig. 1, for direct approaches it is the primary design metric that is optimized. For indirect approaches, optimization of an alternate metric is necessary to solve the mapping problem, which is the imposition of fabrication constraints onto the unconstrained solution.

3. Diffractive Lens Design

The first design example is that of a diffractive lens. The function of the desired, but as yet unknown, DOE is to focus the energy from an incident plane wave to a point in space at a distance z_0 behind the lens. Under the assumptions of scalar diffraction theory the relationship between the input wavefield and the output wavefield is given by Fresnel diffraction [2]. For DOE fabrication, we assume a multiple-step etch procedure with binary masks, which achieves multilevel quantized phase. Further, we assume that the ability of the DOE to focus light is measured by its diffraction efficiency at the focal point.

The solution of the unconstrained problem is a quadratic phase function which maximizes the diffraction efficiency to unity. One can impose the constraints of fabrication by quantizing the unconstrained phase values to the constrained values. Table 1 summarizes the calculated diffraction efficiencies for a 100-μm diameter *f*/1 lens designed by quantization with a minimum feature size of 1.0 and 0.5 μm [3]. Direct solution of the lens design problem has been achieved with the rotationally symmetric iterative discrete on-axis (RSIDO) method [4,5]. The improvement in diffraction efficiency for lens designs generated by RSIDO is also presented in Table 1 [3].

4. Fourier Array Generator

We consider next DOEs that produce an array of point sources with illumination from a single point source. A coherent Fourier optical system is used to achieve this, thus a Fourier transform relationship exists between the diffractive element in the pupil plane and its response in the image plane. We assume again that the diffractive element is fabricated to have multilevel quantized phase. The performance of the diffractive array generator is measured by its ability to generate the desired spot array with high diffraction efficiency and minimum intensity error. To measure this we use the absolute distance measure between the generated intensity and the intensity that corresponds to the upper bound solution [6].

The upper bound solution is the solution to the unconstrained problem, but, unlike diffractive lens design, it does not have an analytic expression. However, upper bound arrays have been reported for a few one- and two-dimensional fan-outs [7,8]. As in Sec. 3, one can impose the constraints of fabrication via quantization. Table 2 summarizes the performance of 3 $\times$ 3 array generators designed by sampling and quantization. The results of the direct solution to the design problem using both the iterative Fourier transform algorithm and simulated annealing are also summarized in Table 2.

5. Correlation Filter

The details of the correlation design problem are presented in Ref. 9, however the results of both direct and indirect optimizations are presented in Table 3.

6. Conclusion

The examples and designs presented herein have been chosen for pedagogical reasons and are meant to be illustrative. That is, the intent of this work is not to make specific contributions to the design of diffractive lenses, array generators, and correlation filters, nor to endorse a particular design algorithm. Rather, it is to highlight the design process and also the distinctions between direct and indirect approaches that have not been adequately explored.

1. J. R. Fienup, Opt. Eng. **19**, 297-306 (1980).
2. J. W. Goodman, *Introduction to Fourier Optics* (McGraw-Hill, New York, 1968), chap. 3.
3. Data supplied by Michael Feldman through personal communication.
4. J. R. Rowlette, T. Bowen, R. Roff, J. Stack, J. E. Morris, W. H. Welch, and M. R. Feldman, Proc. Annual Meeting IEEE LEOS (93CH3297-9), 474-475 (1993).
5. W. H. Welch, J. E. Morris, and M. R. Feldman, ``Design and fabrication of radially symmetric computer generated holograms," Annual Meeting of the Optical Society of America (1991).
6. F. Wyrowski, Opt. Lett. **16**, 1915-1917 (1991).
7. U. Krackhardt, J. N. Mait, and N. Streibl, Appl. Opt. **31**, 27-37 (1992).
8. J. N. Mait, *Holographic Optics: Computer and Optically Generated*, I. N. Cindrich and S.-H. Lee, eds., Proc. SPIE **1555**, 53-62 (1991).
9. J. N. Mait, J. Opt. Soc. Am. A **10**, 2145-2158 (1995).

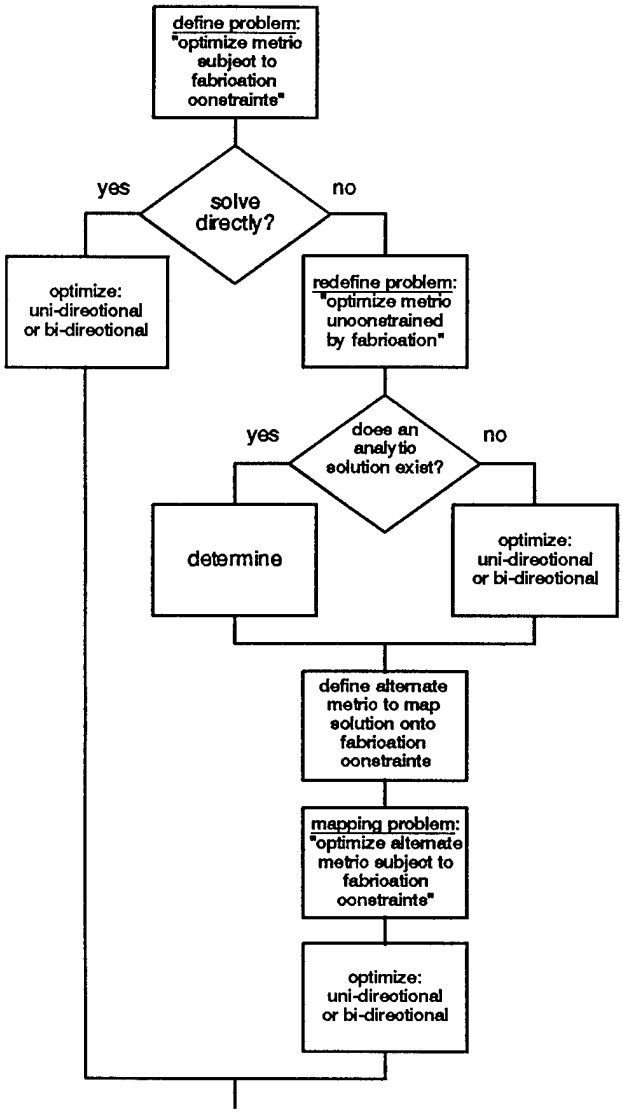


Fig. 1 Flowchart representation of design highlighting the distinction between direct and indirect designs.

phase levels	η_{ub} (%)	minimum feature size (μm)	design	η (%)
2	40.5	0.5	quantization	29.0
			RSIDO	32.0
		1.0	quantization	24.0
			RSIDO	31.0
4	81.0	0.5	quantization	61.0
			RSIDO	64.0
		1.0	quantization	41.0
			RSIDO	46.0

Table 1. Performance of diffractive *f*/1 lenses with 100-μm diameter.

phase levels	η_{ub} (%)	design	η (%)	error ($\times 10^{-4}$)
2	75.74	quantized	79.77	247.08
		iterated	67.51	79.83
		annealed	67.94	79.35
4	78.81	quantized	77.52	31.45
		iterated	77.26	31.90
		annealed	76.84	33.90
8	89.73	quantized	89.44	4.98
		iterated	89.25	2.72
		annealed	89.23	2.60
16	92.94	quantized	93.02	3.22
		iterated	92.72	0.21
		annealed	92.44	0.29
∞	94.06	quantized	94.13	3.69
		iterated	93.88	0.00

Table 2. Performance of multilevel quantized phase array generators designed to generate a 3×3 fan-out.

DOE performance measure	design	$c1(x,y)$	$c2(x,y)$
MACE filter		1	1
	indirect		
minimum mean square error	quantized	757.76	675.16
	iterated	628.04	593.15
minimum (average energy plus correlation peak energy)	quantized	609.98	595.54
	direct		
minimum (average energy plus correlation peak energy)	annealed	609.97	609.97

Table 3. Performance of binary-phase diffractive elements designed to perform as correlation filters.

High Efficiency Dielectric Reflection Gratings

B. W. Shore, M. D. Perry, J. A. Britten, R. D. Boyd, M. D. Feit, H. Nguyen,
R. Chow, G. Loomis,
Lawrence Livermore National Laboratory, PO Box 808, Livermore Ca 94550
and Lifeng Li
Optical Sciences Center, University Of Arizona, Tucson AZ 85721

Summary

We discuss examples of designs for all-dielectric high-efficiency reflection gratings that tolerate high intensity laser pulses and are, in theory, capable of placing 99% of the incident light into a single diffraction order. The designs are based on placing a dielectric transmission grating atop a high-reflectivity multilayer dielectric stack. We comment on the connection between transmission gratings and reflection gratings and note that many combinations of gratings and multilayer stacks offer high efficiency. Thus it is possible to attain secondary objectives in the design. We describe examples of such designs aimed toward improving fabrication and lowering the susceptibility to laser-induced damage.

Introduction

A reflection grating must incorporate two optical functions: it must combine high reflectivity with diffraction. Traditional metallic gratings combine these two functions in a single conducting surface. The conductivity of the metal forces reflection, while periodic grooves create diffraction. Because metallic gratings owe their reflectivity to conductivity, expressible as a complex-valued refractive index, they have a disadvantage for applications that subject the grating to intense radiation. The absorption of radiation causes heating and damage [1]. Transparent dielectric materials have much smaller absorption coefficients than do metals, and therefore optical devices based on dielectrics have potential for withstanding intense radiation [2]. When used to create grating structures, they have unique properties that can offer additional benefits [3].

Contemporary techniques of interference lithography (or holographic grating fabrication) offer opportunities for producing a variety of all-dielectric gratings. Such gratings, useful for a variety of applications as transmission gratings, can be combined with suitable all-dielectric multilayer structures to create reflection gratings. In our work the multilayer thin-film stack is used as a substrate for the grating, which we create using previously described procedures[1] .In brief, we first coat the substrate with a carefully controlled uniform layer of photoresist. Next we expose this photosensitive surface to the stabilized interference pattern at the intersection of two collimated laser beams in a two-arm interferometer. We develop the latent image to create a corrugated surface, using in-situ monitoring to control the profile by terminating the development step at the optimal moment

[4]. Although the developed photoresist could serve as the grating [5], it is more fragile than other materials. To create a more robust structure, the photoresist can be overcoated with dielectric material or, as in our work, the pattern can be transferred to the underlying substrate using lithographic etching techniques.

For use in chirped pulse amplification [6], diffraction gratings must be able to withstand intense radiation. This requirement imposes restrictions on the acceptable materials, largely to such transparent oxides as hafnia, scandia and silica [7]. There remain many possibilities for grating profile and material thicknesses. As we shall show, the action of the combined grating-multilayer structure can be considered in two parts, the diffractive transmission and the reflection. In particular, the required highly reflective multilayer stack can be designed in many ways. This variety of designs allows us to impose additional constraints on the design, beyond the primary requirement of producing high reflectivity.

Our designs are based on numerical modeling of discretized grating profiles and the transcription of the exact Maxwell equations into coupled algebraic equations using the multilayer modal method of Li [8]. The computer codes provide not only efficiencies but also field distributions within the grating.

Relationship between transmission and reflection

Our gratings owe their high efficiency, in part, to the choice of groove spacing and angle of incidence: the spacing $d < 3\lambda/2$ and near-Littrow mount (angle of incidence equal to diffraction angle) allows only orders 0 and -1 to propagate. Under such conditions both the simple single-dielectric transmission grating and the multilayer dielectric reflection grating exhibit regular maxima and minima of diffraction efficiency as a function of groove depth. However, conditions which produce high diffraction efficiency for transmission will produce low diffraction efficiency for reflection. This result is because the reflection grating requires interference between the two transmitted orders, after reflection, in order to place the radiation into order -1 rather than as specular reflection into order 0. When a dielectric transmission grating places a large fraction of the incident light either into order -1 or 0 of transmission (light incident at angle θ_i and emerging at angle θ_t say), then the time reversed situation (radiation at angle θ_t within the medium flowing out of the grating from below into angle θ_i), will also apply. Detailed computations, to be exhibited, bear out this intuitive observation.

Multilayer Grating Designs

Multilayer stacks of thin dielectric films are widely used in the optics industry as antireflection coatings, polarizers, beam splitters, filters, and highly reflecting mirrors. Rather than relying on conductivity or absorption to produce reflection, multilayer dielectric stacks rely on interference. A succession of horizontal plane layers are created with thicknesses such that, for light of a specified wavelength and polarization, incident from above at a given angle, the phases of upward and downward traveling waves within each layer either reinforce the upward wave (for reflection, or HR coating) or the downward wave (for transmission, or AR coating).

It is obviously desirable to have a point design that has relatively little sensitivity to small variations in design parameters, such as layer thicknesses, groove depth, and duty cycle. From a purely theoretical standpoint (disregarding fabrication considerations), robust designs can be obtained by allowing some portion of the top layer to lie beneath the grooves -- the grooves are not etched entirely through the top layer. However, it is often simpler to produce a grating whose groove depth is fixed by a discontinuity in chemical

composition, i.e. a grating whose grooves extend entirely through the uppermost layer. This is one of several subsidiary constraints that may be imposed upon the overall structure, in addition to having high efficiency.

The quarter wave stack

The most common form of highly reflecting multilayer dielectric stack is the (H L)^n stack based on n pairs of high index (H) and low index (L) material, each of which offers one quarter wave of phase shift at the desired angle [9]. As the number of layers increases, the reflectance approaches closer to unity, within a wavelength band whose width is set by the ratio of refractive indices. With this stack in mind, the simplest high efficiency multilayer grating designs are based on placing a dielectric grating atop such a quarter-wave stack. Either an H or L layer may be made the top layer; in general the grooves will be shallower the higher is the index of refraction of the grating layer. The design problem then becomes one of choosing the thickness of the grating layer and the depth and shape of the grooves. (That is, the exact structure of the HR stack need not be considered, only the ability to reflect waves .)

Problems with quarter-wave stacks

The quarter-wave stack provides one easily-understood possibility for creating a high efficiency reflection grating. However, in our holographic method it has one drawback. The dielectric stack, intended to be highly reflecting at the use angle of 52° for 1053 nm light, is also highly reflecting near the exposure angle of 17° for 413 light. (This light is near the reflectivity maximum associated with third harmonic of the design wavelength). This undesired reflectance can be diminished by altering various layer thicknesses.

The HLL design

A very simple alternative to the quarter wave design (HL)^n is an (HLL)^n design, comprising quarter waves of high index material H and half waves of low index material L. Rather than define the quarter waves for the usage wavelength and angle, we choose a shorter wavelength and normal incidence. We have chosen for the stack-design wavelength 830 nm (a choice that simplifies the monitoring of the layer deposition). Such a design greatly diminishes the reflected exposure light and thereby eliminates the need for special antireflection or absorbing coatings between the photoresist and the stack.

As with the quarter wave designs, grating designs based on this stack can achieve reflection efficiency exceeding 99%. Such high efficiencies are available for a range of groove depths and duty cycles, and with either the H or the L dielectric as the uppermost layer.

The efficiencies obtained with the HLL design (at the usage wavelength and angle) are almost indistinguishable from those obtained with the quarter wave stack: Both designs have the same far-field Rayleigh expansion. However, the two designs differ appreciable in the near-field region within the grating grooves. Because the designs have high efficiency, there is a strong standing wave pattern of electric field, with antinodal planes where the electric field is twice the value of a free-space traveling wave. With the quarter wave design, the enhanced-field regions extend into the surface, where they may cause photo-induced breakdown and damage. With the HLL design, the enhanced-field regions fall within the grooves, where they have no harmful effects on damage.

Acknowledgments

This work was supported under the auspices of the U.S. Department of Energy at Lawrence Livermore National Laboratory under contract W-7405-Eng-48.

References

[1]. R. Boyd, J. Britten, D. Decker, B. W. Shore, B. Stuart, M. D. Perry and L. Li, "High-efficiency metallic diffraction gratings for laser applications" Appl. Opt. **34,** 1697-1706 (1995)

[2]. B. C. Stuart, M. D. Feit, A. M. Rubenchik, B. W. Shore and M. D. Perry, "Laser-induced damage in dielectrics with nanosecond to subpicosecond pulses" Phys. Rev. Lett. **74,** 2248-2251 (1995)

[3]. M. D. Perry, R. D. Boyd, J. A. Britten, D. Decker, B. W. Shore, C. Shannon, E. Shults and L. Li, "High-efficiency multilayer dielectric diffraction gratings" Optics Lett. **20,** 940-2 (1995)

[4]. J. A. Britten, R. D. Boyd and B. W. Shore, "In situ end-point detection during development of submicrometer grating structures in photoresist" Opt. Eng. **34,** 474-9 (1995)

[5]. M. G. Moharam, T. K. Gaylord, G. T. Sincerbox, H. Werlich and B. Yung, "Diffraction characteristics of photoresist surface-relief gratings." Appl. Opt **23,** 3214-20 (1984)

[6]. M. D. Perry and G. Mourou, "Terawatt to petawatt subpicosecond lasers" Science **264,** 917-924 (1994)

[7]. M. R. Kozlowski, R. Chow and I. M. Thomas, "Optical coatings for high power lasers" in *CRC Handbook of Laser Science and Technology Supplement 2* ed. M. J. Weber (CRC Press, Boca Raton, 1995), pp. 767-812

[8]. L. Li, "Multilayer modal method for diffraction gratings of arbitrary profile, depth, and permittivity" J. opt. Soc. Am. A **10,** 2581-91 (1993)

[9]. A. MacCloud, *Thin Film Optical Filters* (Adam Hilger, Bristol, 1986)

Design of phase–shifting masks for enhanced–resolution optical lithography

Guo–Zhen Yang, Zhi–Yuan Li, Bi–Zhen Dong, Ben–Yuan GU, and Guo–Qing Zhang

Institute of Physics,Academia Sinica, P. O. Box 603, Beijing 100080, China
Phone : 086–10–2553101, Fax. : 086–10–2562605

1. Introduction

As integrated circuit (IC) technology continues to push further into the submicrometer regime, considerable effort has been devoted to finding new approaches for extending the resolution limits of optical lithographic systems. The idea of using phase–shifting masks in optical lithography is one of such resolution–enhancing techniques and is commonly attributed to Levenson.[1] The problem of the design of phase–shifting mask is how to determine the phase of the mask that produces a predesignated image. There are several approaches to deal with this problem such as simulated annealing algorithm[2] and optimal coherent approximations.[3] In this paper we present an approach of the design of the phase–shifting mask for the enhancement of optical resolution in lithography based on general theory of amplitude–phase retrieval in optical system and an iteration algorithm. For several model objects the numerical investigating results are given.

2. Theoretical formulas

The schematic of a typical optical system considered is shown in Fig. 1. This optical system is composed of an input plane P_1, one Fourier–transform lens and an output plane P_2. The spacings between the two consecutive planes are l_1 and l_2, respectively. The focal length of the lens is l_f. The wave functions on the input plane P_1 and output plane P_2 are denoted by

$$U_1(x_1, y_1) = \rho_1 \exp(i\phi_1) \quad \text{and} \quad U_2(x_2, y_2) = \rho_2 \exp(i\phi_2),$$

respectively. The z-axis is chosen along the optical axis of the system. The output wave function is related to the input wave function by a linear transform function $G(x_2, y_2; x_1, y_1)$ in the form

$$U_2(x_2, y_2) = \int\int G(x_2, y_2; x_1, y_1) U_1(x_1, y_1) dx_1 dy_1. \tag{1}$$

As the discrete form we have

$$U_{1l} = \rho_{1l} \exp(i\phi_{1l}), \quad U_{2m} = \rho_{2m} \exp(i\phi_{2m}), \tag{2}$$

and

$$U_{2m} = \sum_{l=1}^{N_1} G_{ml} U_{1l}, \quad l = 1, 2, 3...N_1, \; m = 1, 2, 3..N_2, \tag{3}$$

where N_1 and N_2 are the numbers of sampling points for the input and the output wave functions, respectively. Consequently, the design of phase–shifting masks for the imaging system can be generally addressed as follows: Given the linear transform $\widehat{G}$ and amplitudes of $U_1(x_1, y_1)$ and $U_2(x_2, y_2)$,how can we determine the phase distribution ϕ_1 in the input plane to satisfy Eq. (3) to high accuracy?

To describe the closeness of $\widehat{G}U_1$ to U_2, we introduce a distance measure equal to the L_2 norm as

$$D(\rho_1, \phi_1; \rho_2, \phi_2) = \| U_2 - \widehat{G}U_1 \| = [\sum_{m=1}^{N_2} | U_{2m} - (\widehat{G}U_1)_m |^2]^{1/2}. \tag{4}$$

The problem may thus be formulated as the search for the extremum of the function D^2 with respect to the function arguments ϕ_1 and ϕ_2.

Through standard algebraic manipulations, we can derive a set of equations satisfied by ϕ_1, and ϕ_2 as follows[4]

$$\phi_{1k} = \arg[\frac{1}{A_{kk}}[\sum G^*_{jk}\rho_{2j}\exp(i\phi_{2j}) - \sum_{j\neq k}{}' A_{kj}\rho_{1j}\exp(i\phi_{1j})]], \tag{5a}$$

$$\phi_{2k} = \arg[\sum_j G_{kj}\rho_{1j}\exp(i\phi_{1j})], \tag{5b}$$

where $\widehat{A} = \widehat{G}^+\widehat{G}$ is an hermitian operator. Equations (5a) and (5b) can be numerically solved by an iterative algorithm starting with an arbitrary initial phase of ϕ_1.[4]

3. Numerical Simulations

According to the general theory of the optical transform,[5] when the lens law is satisfied, i.e., $1/l_1 + 1/l_2 = 1/l_f$, this system performs a linear transform as

$$G(x_2, y_2; x_1, y_1) = \frac{1}{\lambda^2 l_1 l_2}\exp[i\frac{\pi}{\lambda l_2}(x_2^2 + y_2^2)]\exp[i\frac{\pi}{\lambda l_1}(x_1^2 + y_1^2)]$$

$$\times \int\int P_a(x, y)\exp\{-i\frac{2\pi}{\lambda l_2}[(x_2 + Mx_1)x + (y_2 + My_1)y]\}dxdy, \tag{6}$$

where P_a represents the finite aperture of the lens defined by $P_a(x) = 1$, for $| x | \leq a$, $| y | \leq a$; and 0, otherwise. $M = l_2/l_1$ is the amplification factor of the system. Performing the integral operation and neglecting the irrelevant phase factor $\exp[i\pi(x_2^2 + y_2^2)/\lambda l_2]$, we obtain a simple form of the transfer kernel

$$G(x_2,y_2;x_1,y_1) = M\exp[i\frac{\pi}{\lambda l_1}(x_1^2+y_1^2)]\frac{\sin[2\pi a(x_2+Mx_1)/\lambda l_2]}{\pi(x_2+Mx_1)}$$
$$\times\frac{\sin[2\pi a(y_2+My_1)/\lambda l_2]}{\pi(y_2+My_1)}. \quad (7)$$

In the case of 1–D system, we have the transform function as

$$G(x_2;x_1) = \sqrt{M}\exp[i\frac{\pi}{\lambda l_1}x_1^2]\frac{\sin[2\pi a(x_2+Mx_1)/\lambda l_2]}{\pi(x_2+Mx_1)}. \quad (8)$$

In the simulations we choose system parameters as follows : Wave length of the illumination light $\lambda = 365nm$, the numerical number $NA = 0.5$, the focal length $l_f = 40cm$, the diameter of the lens aperture $2a = 40cm$. The system amplification is $M = 0.01$. In the typical optical lithographic system, it requires that the amplitude of output function is proportional to that of the input function, i.e., $U_2(x_2) = \sqrt{1/M}U_1(-x_2/M)$ for 1–D system while for 2–D system $U_2(x_2,y_2) = (1/M)U_1(-x_2/M,-y_2/M)$. Therefore, in solving to Eqs. (5a) and (5b) we set $\rho_2(x_2) = \sqrt{1/M}\rho_1(-x_2/M)$ for 1–D case and $\rho_2(x_2,y_2) = (1/M)\rho_1(-x_2/M,-y_2/M)$ for 2–D case.

We first investigate the design of the phase–shifting–masks for 1–D model images that consist of equal–spacing lines with submicron width, such as two lines, three lines, and four lines, as shown in Fig. 2(a), (b), (c),respectively. The patterns generated by the conventional transmission mask and the designed mask are also shown in Fig. 2. It is evident that the performance of the optical resolution has been substantially improved when using the phase–shifting–mask, compared to conventional imaging system. Therefore, the new algorithm has been proven to be effective. The binary phase distribution (0 and π) for ϕ_1 is automatically derived, as shown in Fig. 3(a), (b), (c),respectively. This is the first time by means of solving the inverse problems to derive the well–known result due to Levenson.[1] As for 2–D system we investigate more complex image shown in Fig. 4(a). Our algorithm also presents an improved result compared to the conventional imaging system, as shown in Fig. 4(b), (c).

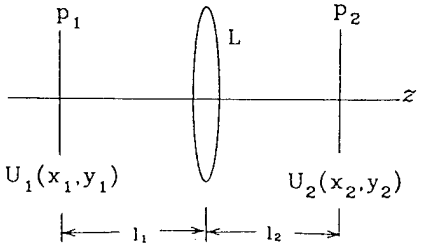


Fig.1. Schematic of an imaging system

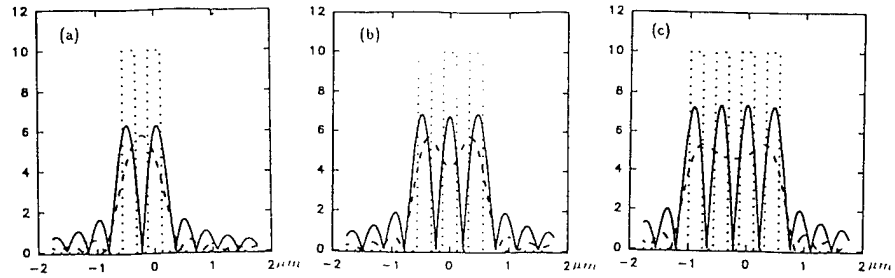


Fig.2. Phase-shifting mask design for 1-D $0.22\mu m$ equal-spacing lines. Dotted lines, dashed lines and solid lines correspond to ideal images, conventional transmission masks and designed masks,respectively.

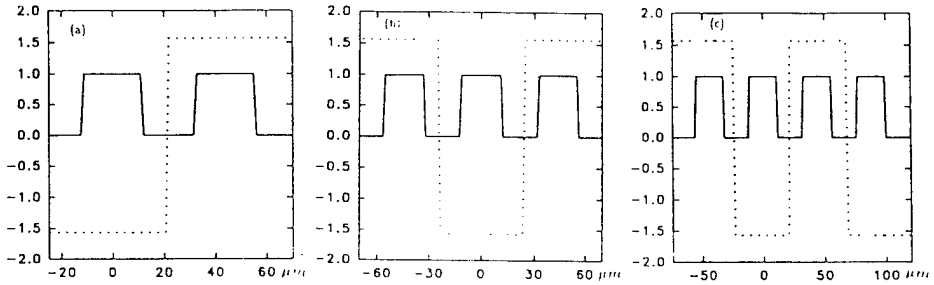


Fig.3. Binary phase distribution of ϕ_1(dotted lines) for designed masks. Solid lines correspond to distribution functions of objects.

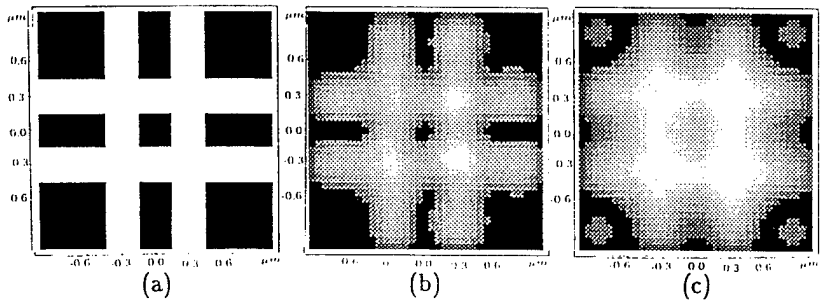


Fig.4. Phase-shifting mask design for 2-D image.(a) The ideal image with $0.30\mu m$ space between two lines.(b) Image due to designed mask.(c) Image due to conventional transmission mask.

3. References

[1] M. D. Levenson, N. S. Viswanathan, and R. A. Simpson, IEEE Trans.Electron Devices **ED–29**, 1828 (1982).

[2] Y. Liu and A. Zakhor, IEEE Trans.Semicon. Mfg. **5**, 138 (1992).

[3] Y. C. Pati and T. Kailath, J. Opt. Soc. Am. A **11**, 2438 (1994).

[4] Guo–Zhen Yang, Ben–Yuan Gu, Bi–Zhen Dong, Jie–Yao Zhuang, and Okan K. Ersoy, Appl. Opt. **33**, 209 (1994).

[5] J. W. Goodman, *Introduction to Fourier Optics* (McGraw–Hill, New York, 1968).

Flattop Beam Generation Using An Iteratively-Designed Binary Phase Grating

Jun Amako and Tomio Sonehara
Seiko Epson Corp., R & D Division
Owa 3-3-5, Suwa-shi, Nagano-ken, 392 Japan
Tel: 0266-52-3131 /Fax: 0266-58-9848

1. Introduction

Various approaches for flattop beam generation have been reported.[1-4] Here we focus on a grating approach in which a phase grating is used to modulate a beam wavefront and shape its Fourier spectrum. We designed a grating-type beam shaper in an iterative manner, where an optimal grating phase is sought under the constraints of amplitude and phase both in the grating and Fourier planes.

Generating a flattop intensity distribution, which is a uniform amplitude and phase distribution, requires that we consider the phases as well as amplitudes of diffracted waves when designing the grating. This phase consideration enables the adjoining diffracted waves to be produced in phase so they can interfere constructively to form a flat-topped field.

2. Physical Basis

Our beam shaper consists of a window and a binary phase grating[5] (see Fig. 1). The function of the window is auxiliary but important.
We let the phase depth of the grating equal π. If a phase function comprising 0 and π is even-symmetric, its Fourier field is also real and even and has the phase of 0 and π. Using this relation makes it easy to find grating structures meeting the demand that some adjacent waves acting for the beam shaping (the wanted waves) have to be in phase. For a depth other than π, its Fourier transform will become complex, which means the diffracted waves can be proven out of phase.
The four requirements for grating design are given below.
(1) As much light energy as possible should be directed to the wanted waves, from the -mth to the +mth order. Other higher orders should be so fully suppressed that their interference with the wanted waves can be minimized.
(2) The wanted waves should have equal amplitudes.
(3) There must be no phase jumps among the wanted waves.
(4) The grating's smallest feature should be made as large as possible.

3. Grating Design and Fabrication

By using the simulated-annealing (SA) algorithm,[6] we sought a one-dimensional binary phase structure that reconstructs three in-phase diffracted waves, the 0th, and ±1st orders. One period of a grating is divided into plural segments. Each segment has a phase value of 0 or π, alternately. The positions of these dividing points are optimized under the afore-mentioned requirements. Solutions obtained for 187 iterations and their diffraction properties are given in Table 1 and Table 2, respectively. The efficiency is the summation of the diffraction efficiencies of the three waves. The uniformity is the ratio of minimum and maximum intensity among these waves. S/N is defined as the ratio of the minimum intensity of the three orders to the maximum intensity of the higher orders (up to ±100th).

We fabricated the grating by means of projection-photolithography and a reactive ion-etching technique. In the translation of the design output into computer-aided design data used to operate a mask writer (laser beam), the quantizing-error was $\leqq \pm 0.0625 \mu$m. The photo mask was manufactured by the mask writer which can write a line-width of $\geqq 2\mu$m with a positioning accuracy of $<0.1\mu$m. The resist-patterned quartz glass substrate was etched at a rate of 400Å/min.; using CHF^3 the RF power was 70W and the pressure was 26mTorr.

4. Simulations and Experiments

By computer simulation we examined the profile's dependence on the incident beam width and the window width for a given grating period. We then determined the optimal dimensions of these factors for the grating period of 8.0mm, the lens focal length of 2000mm, and the beam wavelength of 0.633μm: the beam was 8.0mm ($1/e^2$) wide and the window was 9.0mm wide. Figure 2 shows the results; on the horizontal axis the width of 20 divisions equals 326μm.

In the experiment, the aperture slit, 2.0mm in height and adjustable in width, was placed before the grating. A He-Ne laser beam (0.633μm) hit the grating and the transmitted wavefront was optically Fourier-transformed by a lens. The focused intensity distribution was detected by a CCD camera and the camera's video output was fed, via a frame memory, to a computer for display and analysis. Figure 3 shows the results; on the horizontal axis the width of 20 divisions equals 222μm. Our estimate of the light use efficiency is ~50% from both the grating's efficiency of 57% and the window width which is greater than the beam width ($1/e^2$).

5. Conclusion

We recommend the use of a compact beam shaper composed of a window and a binary phase grating. By computer-simulating the shaped profiles, we have obtained the optimal relation among the beam width, the window width, and the grating period. Through optical experiment we confirmed that the shaper achieves a good approximation to a flattop profile.

References

1) W.W. Simmons, G.W. Leppelmeier and B.C. Johnson, Appl. Opt., 13 (1974) 1629.
2) J.W. Ogland, Appl. Opt., 17 (1978) 2917.
3) P.W. Rhodes and D.L. Shealy, Appl. Opt., 19 (1980) 3545.
4) W.B. Veldkamp and C.J. Kastner, Appl. Opt. 21 (1982) 345.
5) J. Amako and T. Sonehara, Opt. Rev. 2 (1995) 339.
6) M.R. Taghizadech, J.I.B. Wilson, J. Turunen, A. Vasara, and J. Westerholm, Appl. Phys. Lett. 54 (1989) 1492.

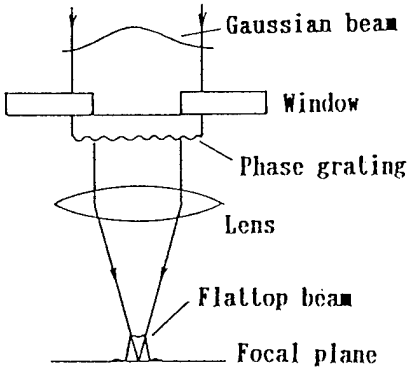


Fig. 1. Schematic drawing of the beam conversion using our beam shaper.

Table 1. Data for a Binary Phase Grating

Dividing positions (in fraction of period)			
0.039166	0.069447	0.133235	0.148085
0.185804	0.814196	0.851915	0.866765
0.930553	0.960834		

Table 2. Diffraction properties

Items	Simulated results
Efficiency	57 %
Uniformity	0.99
S/N	8.1

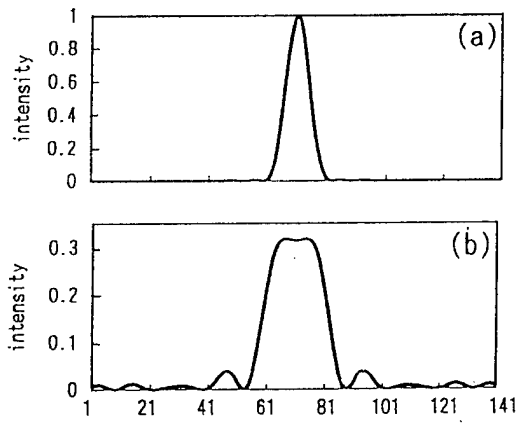


Fig. 2. Computer-simulated profiles (a) without any grating, (b) with the grating.

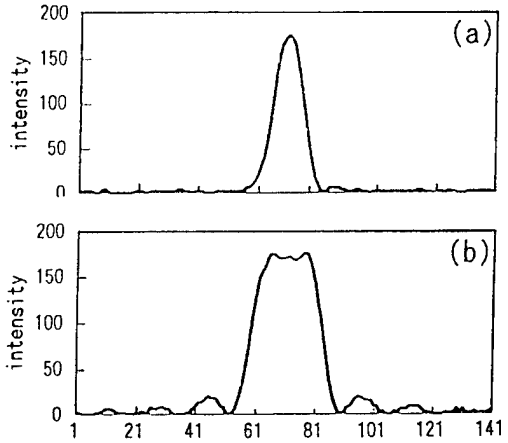


Fig. 3. Experimentally-obtained profiles (a) without any grating, (b) with the grating.

Surface-relief Gratings with Sharp Edges: Improvement of the Convergence of the Coordinate Transformation Method

Lifeng Li
Optical Sciences Center, University of Arizona, Tucson, Arizona 85721
Tel: (520) 621-1789, Fax: (520) 621-4358

1. Introduction

Since it was first proposed one and a half decades ago, the coordinate transformation method of Chandezon *et al.*[1] (the C method) for analyzing surface-relief gratings has gone through many stages of improvement and extension.[2-10] By now, it is truly one of the most efficient and versatile theoretical tools for modeling gratings of arbitrary permittivity and (reasonably) arbitrary profiles. The most distinctive features of the C method, not shared with any other rigorous grating methods, are its virtually uniform convergence with respect to the incident polarization (TE, TM, or conical) and the medium permittivity (dielectric or metal), and its perfect suitability for modeling multilayer-coated gratings.

However, one weakness of the C method remains: it converges slowly at large depth-to-period ratios ($h/d \sim 1$) when the groove profile has sharp edges. This weakness prevents effective application of the C method to some practically important cases, such as triangular and trapezoidal gratings.

In this paper, the C method is reformulated using the recently developed proper procedure for Fourier-analyzing the differential equations that contain periodic discontinuities.[11] The newly formulated C method converges much faster than the old one for grating profiles with sharp edges.

2. Review of the C method

For the purpose of this paper, it suffices to consider only one periodic triangular interface, as shown in Fig. 1. *Oxyz* is a rectangular Cartesian coordinate system. The profile function $a(x)$ is independent of z and its period is d. Furthermore, it is only necessary to consider the TE polarization (the electric field vector parallel to the grooves) because, as explained in Ref. 5, the solutions of Maxwell's equations for the TM polarization and conical mounts can be obtained easily from the TE solutions. Here, only a sketch of the steps of the C method leading to the eigenvalue equation is given. The reader is referred to the above-cited papers for more details.

In the C method, a curvilinear coordinate system is introduced in the x-y plane:

$$v = x, \quad u = y - a(x). \tag{1}$$

The relevant Maxwell's equations expressed in this coordinate system are

$$\frac{\partial E_z}{\partial u} = i\mu k_0 (H_v - \dot{a} H_u), \tag{2a}$$

$$\frac{\partial E_z}{\partial v} = i\mu k_0 [\dot{a} H_v - (1 + \dot{a}^2) H_u], \tag{2b}$$

$$\frac{\partial H_v}{\partial u} - \frac{\partial H_u}{\partial v} = i\epsilon k_0 E_z, \tag{2c}$$

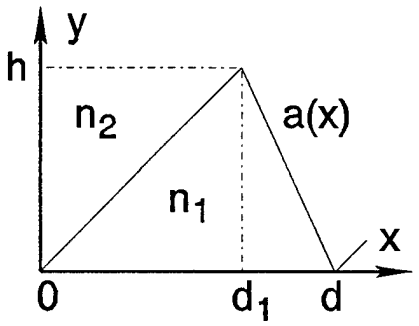


Fig. 1. The Cartesian Coordinate system and a triangular grating profile.

where k_0 is the vacuum wavevector, $\mu = 1$, ϵ is the permittivity, $\dot{a}$ denotes the derivative of $a(v)$, and H_v, H_u, and E_z are the covariant component of the field vectors. In this paper, the Gaussian

system of units and the time dependence $\exp(-i\omega t)$ are used. Eliminating H_u from Eqs. (2), we have

$$\frac{\partial E_z}{\partial u} = D(v)\frac{\partial E_z}{\partial v} + i\mu k_0 C(v) H_v, \tag{3a}$$

$$\frac{\partial H_v}{\partial u} = \frac{\partial}{\partial v}[\, D(v) H_v \,] + i\epsilon k_0 E_z + \frac{i}{\mu k_0}\frac{\partial}{\partial v}\left[C(v)\frac{\partial E_z}{\partial v}\right], \tag{3b}$$

where

$$C(v) = \frac{1}{1 + \dot{a}^2(v)}, \qquad D(v) = \frac{\dot{a}(v)}{1 + \dot{a}^2(v)}. \tag{4}$$

Since the fields are pseudo-periodic in v, we can convert Eqs. (3) into their counterparts in the discrete Fourier space by simply using the transformation rules:

$$\phi \rightarrow \phi_m, \qquad \frac{\partial}{\partial v} \rightarrow i\alpha_m, \tag{5}$$

where ϕ is any term in the equations, ϕ_m is its Fourier coefficient, and $\alpha_m = \alpha_0 + m K$, with $K = 2\pi/d$ and α_0 being the Floquet exponent. If ϕ is a product of functions of v, we suppose that the following rule applies:

$$fg \rightarrow \sum_n f_{m-n} g_n. \tag{6}$$

Thus, Eqs. (3) become,

$$\frac{1}{i}\frac{\mathrm{d}}{\mathrm{d}u} F = M F, \tag{7}$$

with

$$M = \begin{pmatrix} D_{m-n}\alpha_n & \mu k_0 C_{m-n} \\ \dfrac{1}{\mu k_0}(\epsilon\mu k_0^2 \delta_{mn} - \alpha_m C_{m-n}\alpha_n) & \alpha_m D_{m-n} \end{pmatrix}, \tag{8}$$

and $F = (E_{zm}, H_{vm})^{\mathrm{T}}$, where E_{zm}, H_{vm}, C_m, and D_m are Fourier coefficients of the corresponding non-subscripted quantities. The total fields everywhere in the grating structure are given by the superpositions of the eigen-solutions of Eq. (7), which can be solved by standard techniques. Hence, the solution of the grating problem is completed.

3. Reformulation of the C method

Although a computer program based on the theory outlined in Section 2 converges quickly for gratings with smooth profiles, it does not do so for gratings whose profiles have sharp edges. The source of the problem lies in the use of the Fourier factorization rule, Eq. (6), for a product of two functions that have complementary jumps.[11] Two functions, f and g, are said to have a pair of complementary jumps at x_0 if both functions have jumps at x_0 but their product remains continuous there. In Ref. 11, it is proved that in the case of complementary jumps the following Fourier factorization rule should be used, instead of Eq. (6):

$$fg \rightarrow \sum_n [\![1/f]\!]^{-1}_{mn} g_n, \tag{9}$$

where $[\![\phi]\!]$ denotes the matrix generated by ϕ_m. If the jumps of f and g are concurrent but not complementary, then neither Eq. (6) nor Eq. (9) is valid. In addition, the procedures for correctly Fourier-analyzing the differential equations resulting from Maxwell's equations are also given in Ref. 11. In the sequel, these procedures are followed to reformulate the eigenvalue problem. We first need to identify the continuous and discontinuous functions of v in Eqs. (2).

Within a homogeneous medium characterized by a constant ϵ, the continuous functions of v in Eqs. (2) are E_z, H_u, $\partial E_z/\partial u$, and $H_v - \dot{a} H_u$, and the discontinuous functions are $\dot{a}$, $\dot{a}^2$, H_v, $\partial E_z/\partial v$, $\partial H_u/\partial v$, and $\partial H_v/\partial u$. The reader is reminded that the field components here are the covariant components in the curvilinear coordinate system. Perhaps the best way to verify the above classification of field components and their derivatives is to consider the field components at $v_0 + 0$ and at $v_0 - 0$ as being associated with two distinct local coordinate systems, where v_0 is one of the abscissae of the discontinuities of $\dot{a}$. Then, by applying the tensorial transformation rule for the covariant vector components, the nature of the field components can be easily identified.

Equations (2a) and (2c) can be readily Fourier analyzed, yielding

$$\frac{\partial E_{zn}}{\partial u} = i \mu k_0 \left(H_{vn} - \sum_m [\dot{a}]_{n-m} H_{um} \right), \tag{10a}$$

$$\frac{\partial H_{vn}}{\partial u} - i \alpha_n H_{un} = i \epsilon k_0 E_{zn}, \tag{10c}$$

because they do not contain products that have complementary jumps. Equation (2b) contains the product $\dot{a} H_v$, which has a pair of non-complementary jumps at v_0. To circumvent this problem, we rewrite it as follows,

$$\frac{\partial E_z}{\partial v} = i \mu k_0 [- H_u + \dot{a} (H_v - \dot{a} H_u)]. \tag{11}$$

Now, the second term on the right hand side is a product of a continuous function and a discontinuous function, for which Eq. (6) is valid. To complete the missing part in Eqs. (10), we have

$$\alpha_n E_{zn} = \mu k_0 \left[- H_{un} + \sum_m [\dot{a}]_{n-m} \left(H_{vm} - \sum_p [\dot{a}]_{m-p} H_{up} \right) \right]. \tag{10b}$$

From Eqs. (10a), (10c) and (10b), we rederive an equation identical to Eq. (7), but this time with the M matrix of Eq. (8) replaced by

$$M' = \begin{pmatrix} \mathbb{C}[\![\dot{a}]\!]\alpha & \mu k_0 \mathbb{C} \\ \frac{1}{\mu k_0} (\epsilon \mu k_0^2 - \alpha \mathbb{C} \alpha) & \alpha \mathbb{C} [\![\dot{a}]\!] \end{pmatrix}, \tag{12}$$

where α is a diagonal matrix with α_n along the diagonal and

$$\mathbb{C} = (1 + [\![\dot{a}]\!][\![\dot{a}]\!])^{-1}. \tag{13}$$

Once the eigen-solutions of M' are found, the remaining tasks in solving the grating problem are the same as in the conventional C method.

4. Numerical Results

For all numerical examples in this section, the wavelength $\lambda = 1.0$, the incident medium $n_2 = 1.0$,

the truncation order N is half of the matrix dimension of M or M', the solid and dashed lines correspond to TM and TE polarizations, respectively, and the thick and thin lines correspond to the improved and the old C methods, respectively. For the C method, the sum of all diffraction efficiencies is a good indicator of the convergence of individual diffraction orders, therefore only the efficiency sums are presented here.

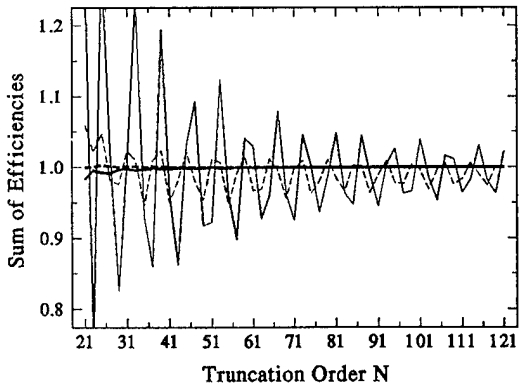


Fig. 2

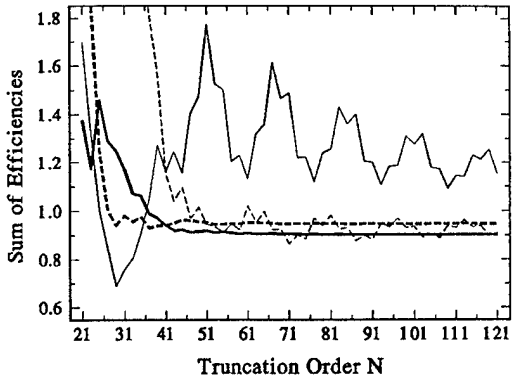


Fig. 3

Figure 2 is for a triangular grating at -1 order Littrow mount, with $d = h = 1.7$, $d_1 = 0.5$, and $n_1 = 0 + i\,5$. Figure 3 is for a symmetrical trapezoidal grating at 45° incident angle, with $d = h = 2.0$, and $n_1 = 0.3 + i\,7.0$. The upper width of the trapezoid is 0.75 and the lower one is 1.25. Figure 4 is for the same geometry as in Fig. 3, but $n_1 = 1.5$. The substantial improvement of convergence by the newly formulated C method is evident.

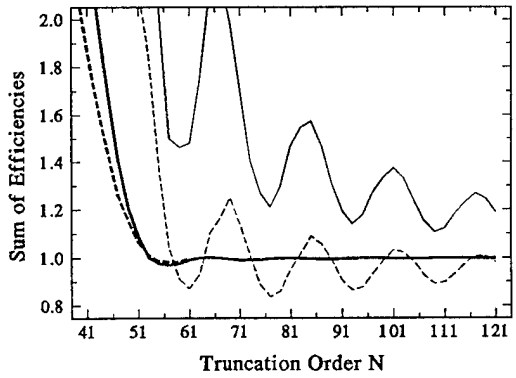


Fig. 4

5. Conclusion

The convergence of the C method for grating profiles with sharp edges has been improved by the reformulation of the eigenvalue equation. Without the mathematical understanding developed in Ref. 11, this improvement would have been impossible.

References

1. J. Chandezon, D. Maystre, and G. Raoult, J. Optics (Paris) **11**, 235 (1980).
2. J. Chandezon, M. T. Dupuis, G. Cornet, and D. Maystre, J. Opt. Soc. Am. **72**, 839 (1982).
3. E. Popov and L. Mashev, J. Opt. (Paris) **17**, 175 (1986).
4. S. J. Elston, G. P. Bryan-Brown, and J. R. Sambles, Phys. Rev. B **44**, 6393 (1991).
5. L. Li, J. Opt. Soc. Am. A **11**(11), 2816 (1994).
6. N. P. K. Cotter, T. W. Preist, and J. R. Sambles, J. Opt. Soc. Am. A **12**, 1097 (1995).
7. G. Granet, J. P. Plumey, and J. Chandezon, Pure Appl. Opt. **4**, 1 (1995).
8. T. W. Preist, N. P. K. Cotter, and J. R. Sambles, J. Opt. Soc. Am. A **12**, 1740 (1995).
9. L. Li, G. Granet, J. P. Plumey, and J. Chandezon, Pure Appl. Opt. (to be published).
10. J. B. Harris, T. W. Preist, and J. R. Sambles, J. Opt. Soc. Am. A **12**, 1965 (1995).
11. L. Li, "Use of Fourier series in the analysis of discontinuous periodic structures," J. Opt. Soc. Am. A (to be published).

Liquid Crystal Phase Modulation Technique to Reduce the Spatial Frequency of Interferometric Fringes

P. Douglas Knight, Jr.
UNC-Charlotte Physics Department
University of North Carolina at Charlotte
Charlotte, NC 28223
Phone: 704-547-2536 Fax: 704-547-3160

Interferometric surface analysis involves looking at a fringe pattern and deriving information concerning the surface being imaged. By counting the fringes, one is able to find the surface deformation relative to a reference point. But a problem is encountered when the fringes are too dense for the fringe analysis software to count them. This limits the resolution of the system. But if a spatial light modulator (SLM) could modulate the phase profile in one arm of the interferometer so that the spatial frequency of the fringes is decreased enough to be counted, this problem would be solved.

The technique to reduce interferometric fringe density involves placing a liquid crystal television (LCTV), acting as a phase modulating SLM, in one arm of an interferometer. A phase profile is then imaged onto the SLM that reduces the fringe density in the region of interest. Assume we have an interferometric pattern where the phase of the pattern varies linearly across the pattern. If we select a point on a fringe pattern captured by a CCD to have a phase shift of zero, then we can express the phase of another point on the image as a function of position as

$$\phi_1(x) = 2\pi(x/a) \tag{1}$$

Here a is the change in image pixel position that gives a phase shift of 2π. Now let us assume we have a phase ramp on the LCTV that mimics the effect of a glass wedge placed in one arm of an interferometer. Therefore we now have phase varying linearly with respect to position across the LCTV. We now write a function for the variance of phase across the LCTV as

$$\phi_2(x) = 2\pi(x/b) \tag{2}$$

where b is the number of pixels (change in x) across the LCTV that gives a phase shift of 2π. Since the LCTV acts as an SLM that retards phase, the SLM in the measurand arm of the interferometer will cause the resulting phase of that point on the output image to be the difference between ϕ_1 and ϕ_2. Notice this only occurs if the region of interest on the SLM and the region of interest on the captured image have a one-to-one correspondence. Therefore the phase-modulated captured image phase has the form of

$$\phi_3(x) = 2\pi x\left(\frac{1}{a} - \frac{1}{b}\right) \tag{3}$$

where $\phi_3(x)$ is the phase as a function of position of this captured image. Since a and b are changes in position for a phase shift of 2π, they are also the change in position of one fringe pattern (light to dark to light). So then $1/a$ and $1/b$ can be thought of as fringe spatial frequencies f_a and f_b. Equation 3 then becomes

$$\phi_3(x) = 2\pi x(f_a - f_b) \tag{4}$$

So if f_b is less than f_a and in the same direction, the resulting fringe pattern would have a phase shift that has a lower spatial frequency than the original pattern. Since this lower spatial frequency in phase corresponds to a lower spatial frequency of fringes in the interferometric pattern, we now have a theoretical technique able to lower output fringe density. Note that if f_b is greater than f_a or in the opposite direction, the resulting fringe pattern would have a phase shift with a greater spatial frequency and/or opposite direction than the original pattern. Also note that equation 4 is valid for any direction as long as f_a and f_b are in the same direction. If we wish to reconstruct the original fringe pattern, we easily see that the original phase can be found using

$$\phi_1(x) = \phi_2(x) + \phi_3(x). \tag{5}$$

Since the modulated fringe pattern and the phase profile on the LCTV each have phase intensity values for each pixel, a reconstructed fringe pattern of the original interferometric output can be generated to prove the initial image is recoverable from the resulting fringe pattern and the phase profile placed on the SLM.

For the twisted, nematic liquid crystal display to produce mainly phase modulation, certain modifications are necessary. Initially, the crossed polarizers on opposite ends of the LCTV are removed to eliminate amplitude modulation due to polarization. Also, the polarization angle of the laser beam is aligned to be parallel to the liquid crystal alignment at the front surface of the LCTV. Also, the bias voltage value for the LCTV is set below the optical threshold to reduce polarization modulation while inside the device.

Referring to Figure 1 as the optical apparatus, a Mach-Zender interferometer is set up using a 488 nm argon laser to produce the fringes. This beam is incident on P1 aligned with the plane of polarization angle of the AR laser. The light is then incident on a half-wave plate

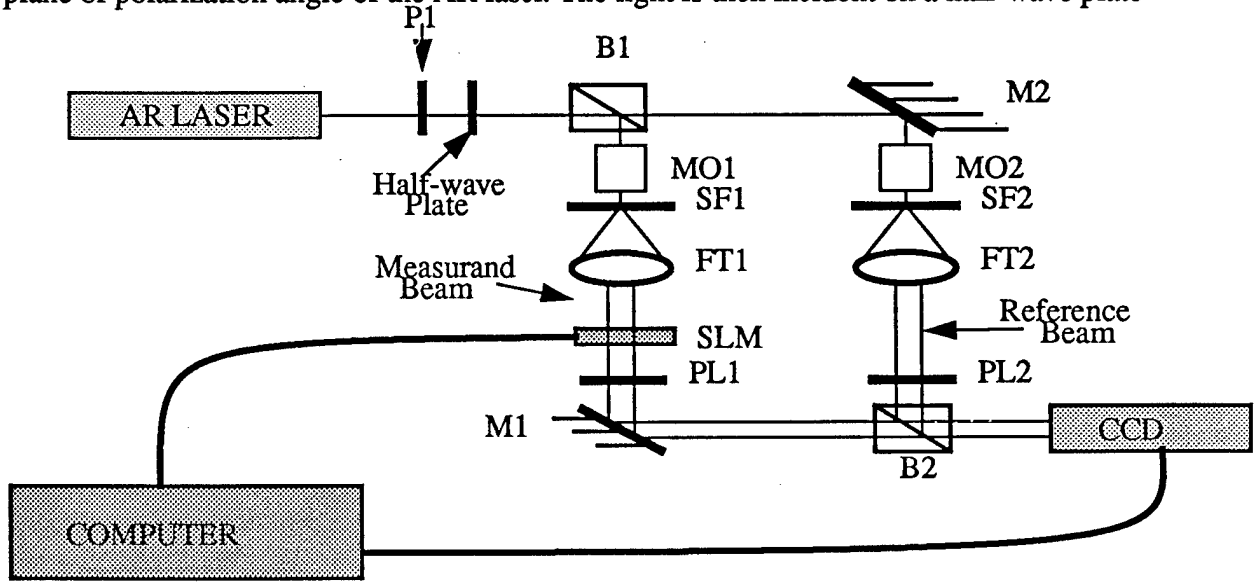


Figure 1

B1, B2, B3: Beamsplitters
MO1, MO2: Microscope Objectives
FT1, FT2: Fourier Transform Lens
SLM: Spatial Light Modulator
M1: Mirror, P1: Polarizer
SF1, SF2: Spatial Filters
CCD: Imaging Camera
PL1,PL2: Plastic Lens

that is oriented so that the outgoing polarization angle is parallel to the alignment of the liquid crystals on the front surface of the SLM. Next, B1 amplitude divides the beam into the reference and measurand arm of the interferometer. For the measurand arm, MO1 focuses the light through pinhole SF1 that spatially filters the beam. FT1 then is placed a focal length away from SF1 so that a plane wave exits FT1. This plane wave is then modulated by a SLM placed perpendicular to the direction of propagation of the wave. M1 then directs the beam so that it is recombined with the reference wave by B2 and imaged onto the CCD. For the reference arm, a plane wave is created similar to how the plane wave for the measurand arm is created. The only difference is the absence of a phase modulator in the reference arm of the interferometer. Plastic lenses of n=1.498 are then used as phase objects. PL1 is placed in the measurand arm right after the LCTV and before M1. PL2 is placed between FT2 and B2 of the reference arm. These are placed at positions appropriate to create a viable interference pattern. For coarser fringe patterns, another phase object (a small piece of clear 35 mm film) is placed before PL2 in the reference arm of the interferometer. Depending on the angular position of the phase object or objects relative to the reference beam, varying coarse phase patterns are generated.

A somewhat linear fringe pattern is initially created by the interferometer. A phase ramp similar to Figure 2a is imaged upon the SLM. This phase ramp is a linear pattern of intensity 0 to intensity b scaled across a set width of pixels. For Figure 2a, the phase ramp width is 20 pixels and b has an intensity of 170. Figure 2b shows fringe density reduction for a fringe pattern of increasing density within the region of interest. Notice the phase ramp is modeled to be similar in form to the fringe pattern. This is necessary for this fringe reduction technique to be valid.

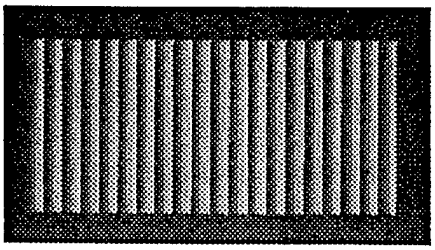


Figure 2a

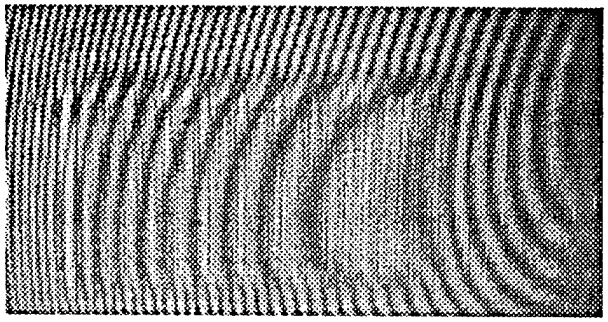


Figure 2b

With the goal of the research being increased resolution of surface profiles, the initial fringe pattern needs to be recoverable. Therefore a technique must be developed to reconstruct the original fringe pattern. Using equation 5, the modulated fringe pattern must first be mapped from an intensity pattern to a phase distribution. Using a gradient technique to map phase, the modulated fringe pattern was mapped to a phase-related intensity distribution using the formula

$$I_2 = \left(\frac{b}{2\pi}\right)\text{asin}\left(\frac{I_1 - A_1}{B_1}\right). \tag{6}$$

where I_2 is the phase related intensity of the modulated fringe pattern, b is as defined earlier, I_1 is the intensity of the modulated fringe pattern, A_1 is the bias intensity of the fringe pattern, and B_1 is the amplitude intensity of the fringe pattern. Equation 6 is derived from equation 2 and the equation for the intensity of a fringe pattern,

$$I_1 = A_1 + B_1 \sin\phi. \tag{7}$$

The intensity distribution from equation 6 and the intensities of the phase ramp placed on the

SLM are then added to get the original phase mapped intensities. These are converted to CCD pixel intensities using equation 7 to reconstruct the original fringe pattern. Figure 3a shows the original fringe pattern, 3b shows the phase ramp imaged onto the SLM, 3c shows the resulting modulated fringe pattern, and Figure 3d shows the computer generated fringe pattern using the described reconstruction technique. The noise in Figure 3d comes mainly from Figure 3c.

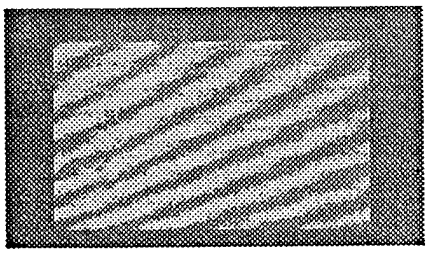


Figure 3a

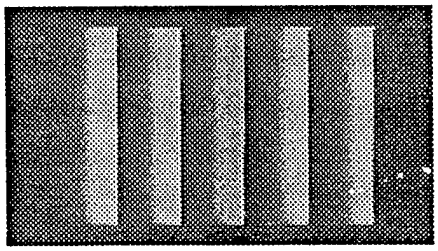


Figure 3b

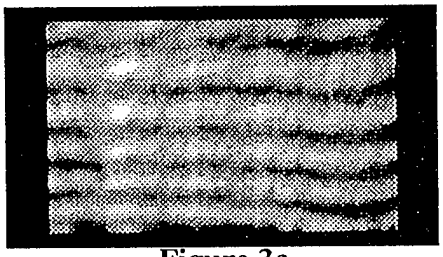


Figure 3c

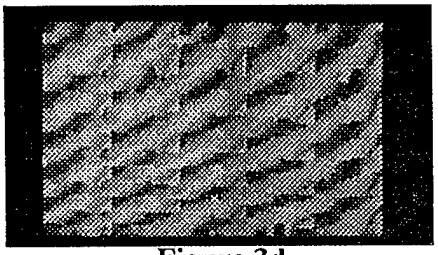


Figure 3d

From Figure 2, it is shown that the spatial frequency of an interferometric fringe pattern can be reduced using an LCTV as a phase modulating SLM. From Figure 3d, it is shown that the original fringe pattern can be recovered using a computational technique. This allows the original fringe pattern to be known only from the phase function placed on the SLM and the resultant modulated fringe pattern captured by a CCD.

Applications of this technique are varied. Flat surfaces with large bumps or pits not mappable using interferometric means could now be mapped. This would involve circular or elliptical phase ramps to initially try to reduce the fringe density.Also, curved surfaces with bumps or pits could be mapped using a phase ramp modeled to fit the surface anomaly. Path noise could also be removed using this technique similar to an adaptive optics system. Currently, pixel size and response time limit the use of LCTV as phase modulating SLMs. With future improvements, applications toward more detailed and complex analysis should be possible.

The author wishes to thank Dr. Eddy Tam for his guidance during the project.

References

1. N. Konforti, et al, Phase-only Modulation with Twisted Nematic Liquid-Crystal Spatial Light Modulators, Optics Letters, Vol. **13**, 251-253 (1988).
2. Eddy Tam, Modulation Properties of a TNLC SLM and its Applications in a Joint Transform Correlator, (1990).
3. Jurgen R. Meyer-Arndt, Introduction to Classical and Modern Optics, Prentice-Hall, (1984).
4. Clifford R. Pollock, Fundamentals of Optoelectronics, Irwin, Chicago (1995).
5. Rafael C. Ganzalez and Paul Wintz, Digital Image Processing, Addison-Wesley, Reading, Mass. (1987).
6. Rensheng Dou and Michael Giles, Closed-Loop Adaptive-Optics system with a Liquid-Crystal Television as a Phase Retarder, Optics Letters, Vol **20**, 1583-5 (1995).

Synthesis of fully continuous phase screens for tailoring the focal plane irradiance profiles

Sham Dixit and Mike Feit

Lawrence Livermore National Laboratory
L-493, P. O. Box 5508, Livermore, California 94551

Tel: (510) 423-7321 Fax: (510) 422-1930
e-mail: dixit1@llnl.gov

In laser driven inertial confinement fusion systems, it is desirable to produce smooth focal plane intensity profiles [1]. Traditionally, binary random phase plates (RPPs) have been used to produce a focal plane irradiance profile which consists of a smooth Airy function shaped envelope and a superimposed fine scale speckle pattern. The speckle is smoothed by conduction smoothing in the laser produced plasma and/or by externally imposed temporal smoothing methods. Although easy to fabricate and use, the RPPs have very limited flexibility in producing arbitrary shaped irradiance profiles. In addition, the secondary maxima of the Airy profile lead to a 15% loss of the energy from the desired region in the focal plane. This loss of the laser energy requires the operation of the fusion lasers at higher energies thereby increasing their cost of operation. Additionally the scattered energy could also cause optical damage to detection equipment near the target.

In order to overcome these limitations of the RPPs, we have recently proposed [2] new phase plate designs for producing arbitrary shaped focal plane intensity profiles which contain greater than 95% of the incident energy. We presented a robust, iterative algorithm based on the phase retrieval algorithms for generating the appropriate phase screens (called kinoform phase plates or KPPs) for producing quite complex intensity profiles in the focal plane. In this procedure, an initial random phase screen is systematically improved upon by repeatedly transforming the complex electric fields between the near-field and the far-field planes and applying appropriately chosen constraints in each plane. The process was successfully

applied to design KPPs that produce complex far-field profiles such as the logo of our Laboratory.

As robust as the algorithm is, it suffers from one serious limitation: if one launches the iterative process using a random phase screen as an initial guess, the algorithm stagnates at the positions of the intensity zeros in the near-field and phase vortices are introduced at these points. Further iterations are unable to remove these vortices. These vortices lead to ~ 2:1 intensity modulations immediately following the phase screen and also to a few percent scattering loss of energy in the focal plane. The inherent singularities at these vortices also make it impossible to unwrap the phase screen into a continuous phase profile.

Continuously varying phase screens offer several advantages over those containing 2π discontinuities. One important advantage is that the propagated field past such a KPP exhibits a low level of intensity modulation. This should minimize the damage threat to the downstream optics. Since the phase appears continuous for the fundamental and harmonic wavelengths as well, the intensity modulations remain small at these wavelengths and hence the unconverted laser light also does not experience any significantly increased level of intensity modulation because of the KPP. The absence of 2π jumps also eliminates the large angle scattering losses from these edges and increases the energy concentration inside the central spot. Phase screens without 2π discontinuities are also useful when fabrication techniques such as ion exchange methods or volume holographic methods are used.

In spite of the advantages of continuous phase screens, the problem of designing such phase screens has eluded us for some time. Typically, smoothly varying phase screens lead to Gaussian envelopes in the far-field whose size is related to the correlation length and the variance of the phase profile. Recent attempts [3] to improve on the iterative algorithm have been unsuccessful where the authors used a continuous phase as a starting point in an iterative algorithm and concluded that the 2π line discontinuities crept in after only two iterations.

We have developed an iterative procedure for constructing fully continuous phase profiles for producing arbitrary focal plane intensity profiles. While continuous phase screens can be easily designed in simpler situations such as circularly symmetric phase profiles and x-y separable phase profiles, the new algorithm is applicable to fully two-dimensional non-

separable situation. The algorithm is launched with a continuous phase profile as an initial guess. The continuous nature of the phase is maintained throughout the iteration cycles by a careful application of the constraints in the near-field and the far-field. The details of the procedure will be presented during the presentation.

We have applied this new algorithm to generate continuous phase profiles for producing superGaussian focal plane intensity distributions. The converged phase continuous phase screen and its corresponding far-field intensity profile are shown in figure 1. The azimuthally averaged far-field profile corresponds to an approximately 12th power superGaussian and contains greater than 98% of the incident energy inside it. We have also applied the algorithm to generate complex far-field profiles. The results will be presented.

This work was performed under the auspices of the U. S. Department of Energy by the Lawrence Livermore National Laboratory under Contract No. W-7405-Eng-48.

References:

[1] J. D. Lindl et al *Physics Today* **45** 32 (1992)

[2] S. N. Dixit et al *Opt Lett* **19** 417 (1994)

[3] Y. Lin et al *Opt. Lett.* **20** 764 (1995).

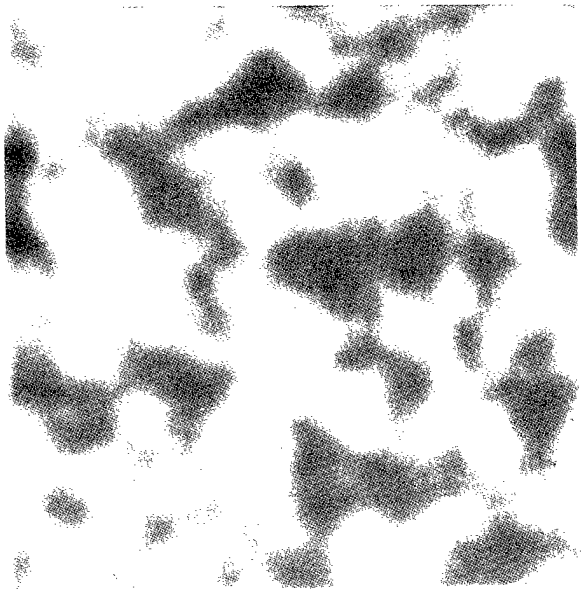


Figure 1a. Continuous phase screen for producing a superGaussian focal plane intensity profile. The phase values range from 0 (black) to 43 radians (white). The gray scale is linear between black and white.

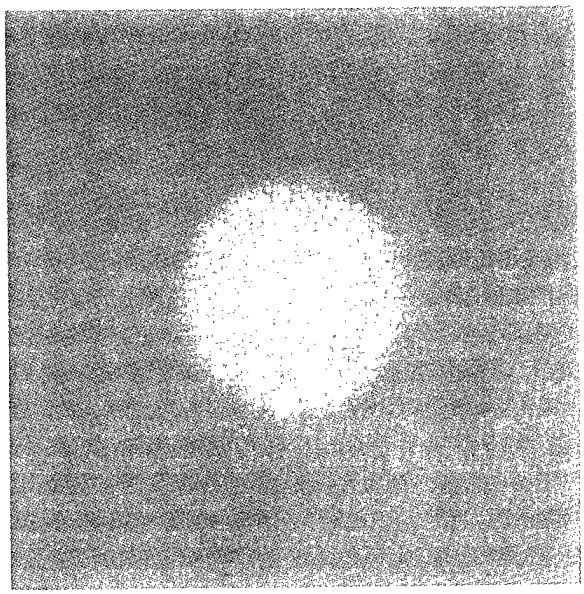


Figure 1b. Far-field intensity distribution produced by the phase screen shown in figure 1a. The far-field has an approximately 12th power superGaussian profile and contains 98% of the incident energy inside it.

Fabrication of large aperture kinoform phase plates in fused silica for smoothing focal plane intensity profiles

Mike Rushford, Sham Dixit, Ian Thomas and Mike Perry

Lawrence Livermore National Laboratory
L-493, P. O. Box 5508, Livermore, California 94551

Tel: (510) 423-7321 Fax: (510) 422-1930

e-mail: dixit1@llnl.gov

In laser driven inertial confinement fusion systems, it is necessary to produce smooth focal plane intensity profiles [1]. The desired intensity distribution consists of a superGaussian envelope with a superimposed speckle on it. The speckle pattern is smoothed either by the plasma or by other temporal smoothing techniques. Binary random phase plates (RPPs) are inadequate for spatial smoothing as they lead to Airy function envelopes in the far-field and are only 84 % efficient. Furthermore RPPs also introduce large intensity modulations in the propagated intensity past the RPP which can potentially damage the optics downstream from the RPPs.

In order to overcome these limitations of the RPPs, we have recently designed new phase plates for producing superGaussian focal plane intensity profiles. Such phase plates consist of smoothly varying phase profiles only a few waves deep. The propagated field past such a KPP exhibits a low level of intensity modulation. The absence of 2π jumps also eliminates the large angle scattering losses from these edges and increases the energy concentration inside the central spot. The calculated far-field profile contains greater than 98% of the incident energy inside the superGaussian spot.

The kinoform phase plates can be fabricated either as a several waves deep smooth surface relief pattern or as a one-wave deep pattern after re-wrapping the phase. The latter design contains 2π jumps that occur either as closed loop structures or as lines extending from one edge to another edge on the input aperture. Use of the phase plates in fusion laser systems also requires that they be resistant to optical damage under high fluence

irradiances (several J/cm2). Moreover, the phase plates have to be located at the end of the fusion laser chains (where the laser beam size is large ~ 40 cm for the Beamlet laser) in order to prevent any potential optical damage to downstream optics. These requirements imply that the phase plates have to fabricated on large fused silica substrates.

Fabrication of continuous phase plates requires patterning the required surface relief structure in a photoresist layer and its subsequent transferring into fused silica by some form of dry etching (reactive ion etching or chemically assisted ion beam etching). The aperture sizes that can be fabricated using this approach are currently limited to a few centimeters in diameter due the size of available ion etching machines. On the other hand, a one wave deep, mod-2π phase profile can be easily fabricated using the lithographic process with binary masks and wet etching of fused silica in hydrofluoric acid. We have demonstrated the scalability of such process to large apertures (up to 80-cm diameter) in our binary RPP fabrication for smoothing the Nova laser focal spot. For these reasons we have chosen to fabricate 40-cm size KPPs in fused silica using the multiple-mask, wet-etch method.

The continuous KPP phase screen was first rewrapped to a one-wave deep structure and was quantized to 16 levels. This quantized phase screen can be fabricated using four binary masks combined with differential etching for each mask step. This quantization leads to about 1% decrease in the efficiency.

The required binary masks were patterned in chrome coated fused silica substrates by patterning an overlayer of photoresist and etching away the unprotected chrome. We used fused silica substrates for the masks as well in order to equalize the thermal expansion coefficients of the KPP and the mask substrates. The mask substrates (also ~40 cm)were chrome coated by vapor deposition and were subsequently coated with a ~ 350 nm layer of photoresist using a large aperture meniscus coater developed at our Laboratory. The patterning of the photoresist was done on a large aperture photoplotter developed in our laboratory. Here the photoresist is exposed by delivering the 414 nm light from an Kr-ion laser through a 300 μm aperture placed approximately 15 μm above the substrate. The long time required for writing the masks (~3 days for each mask) required us to control the temperature of the plotter table (made of aluminum) to 0.02 degrees

centigrade throughout the plotting period. This enabled us to prepare the binary masks with about 1μm precision (positioning as well as pixel size) over the entire aperture.

The KPP was fabricated by transferring these binary patterns into a photoresist layer deposited over the fused silica substrate by exposing under a UV lamp, developing away the exposed resist and etching the unprotected fused silica in a buffered hydrofluoric acid solution. This process was repeated for each of the four masks. The etch depth for the first mask step is $\lambda/2(n-1)$ where λ is the operating wavelength (351nm) and n the substrate refractive index at this wavelength. It is reduced by a factor of 2 with each subsequent mask step. The alignment accuracy between various masks is about 1-2μm.

To evaluate the optical performance of the 16-level KPP, we illuminated a 30-cm diameter portion of the KPP by a spatially coherent 351 nm laser and investigated the focal plane irradiance distribution produced by it. Preliminary results indicate that the far-field spot resembles a super-Gaussian and contains approximately 94% of the incident energy inside it. This compares well with the predicted efficiency of about 97% after allowing for the quantization and mask misalignment losses. Detailed results including the sources of the efficiency loss will be discussed during the presentation.

This work was performed under the auspices of the U. S. Department of Energy by the Lawrence Livermore National Laboratory under Contract No. W-7405-Eng-48.

References:

[1] J. D. Lindl et al *Physics Today* **45** 32 (1992)

[2] S. N. Dixit et al (preceding paper).

Speckle-free phase Fresnel holograms and beam shaping elements

Luiz Gonçalves Neto* and Yunlong Sheng

Université Laval, Centre d'Optique, Photonique et Laser
Départment de Physique, Québec, Canada G1K 7P4, sheng@phy.ulaval.ca
*Address after January 1996: São Paulo University, Laboratory of Integrated Systems
EPUSP, Dept. Engenharia Eletrônica, C.P.8174, 01065-970 São Paulo, SP, Brazil
Fax:(55)(11)211-4574, lgneto@lsi.usp.br

1. Introduction

Computer-generated holograms (CGH's) have proved effective as non-periodic diffractive elements for beam shaping. The elements are usually designed with the iterative algorithms based on the Gerchberg-Saxton Algorithm [1-3]. However, the initial random phase and the phase freedom in the image plane used in those algorithms introduce speckle noise in the reconstructed image [4]. Several techniques have been proposed for designing speckle-free CGH's.

In this paper we describe speckle-free phase-mostly Fresnel holograms. In our design we use the linear spatial filter for computing the Fresnel transform and apply the band-limitation constraint on the Fourier spectrum of the reconstructed image. We choose the constant initial phase for iterations, that can avoid the speckles caused by isolated point zeros in the reconstruction plane. We show that the constant initial phase is suitable in the case of Fresnel holograms as the spherical initial phase is suitable for Fourier holograms. We demonstrate good quality speckle-free phase-only Fresnel holograms using a coupled-mode modulation LCTV as phase-mostly spatial light modulator (SLM) [5].

The design technique is also used for a non-periodic beam-shaping Fresnel hologram which is under fabrication in Honeywell through the CO-OP/ARPA diffractive optics workshop. The element was designed to shape a laser diode elliptical pattern into a square flat top pattern. In the design we consider that the laser diode pattern is approximately a gaussian energy distribution in the x-y plane.

2. Speckle-free design technique

When designing a CGH or a non-periodic beam shaping element a random phase is usually added to the image in order to spread out its Fourier spectrum. Also with the iterative method, the phase of the image in the reconstruction plane is used as a free parameter in order to provide the degree of freedom for the iteration to converge. However, in the optical implementation of such holograms the introduction of the random phase can cause problems because the Fourier spectrum of the image can be spread over the entire Fourier plane, whereas the CGH is of finite size. As a result, a severe information loss will occur and the optically reconstructed image from the resultant CGH will contain strong speckle noise [6], which is not desirable in many applications.

The speckle noise can do not appear in the design of the CGH, because the discrete Fourier transform in the computation gives the amplitude and phase information of the reconstructed image only at the sampled points. However, the optical reconstruction is continuous. The finite CGH aperture leads to interpolation among the sampled image values by a sinc function. When the image with random phase is not a band limited function, the interpolation with the sinc function leads to large intensity variations, e.g. speckle noise, on the optically reconstructed image.

Figure 1 shows how the random phase affects the optical reconstruction. The top part of figure 1 depicts 16 sample values of an one-dimensional image $|f_m|$. We multiply $|f_m|$ by a phase function, compute its Fourier transform and then reconstruct the image. In the example of Fig.1b the phase is constant, resulting in no changes of the image bandwidth. The interpolation with the sinc function does not lead to a large amplitude variation in the reconstructed image. In the example of Fig.1a the phase function is $\exp(2\pi n_m)$, where n_m is a white noise. The random phase introduces higher frequency components and enlarges the bandwidth of the image spectrum, resulting in large amplitude variations in between the sampled values of the reconstructed $|f_m|$. To show the effect of the interpolation with sinc functions in the computer simulation, we increase the sampling rate of the reconstructed image. The bottom part of Fig.1 shows 32 sample values of the reconstructed image at the double sampling rate. The reconstructed image $|f_m|$ in the example of figure Fig.1b is smooth, and that in the example of Fig.1a has large amplitude variations,e.g. speckle noise. Note, however, that the 16 sample values of $|f_m|$ at the initial sampling locations are still equal to that of the original image $|f_m|$ in both examples.

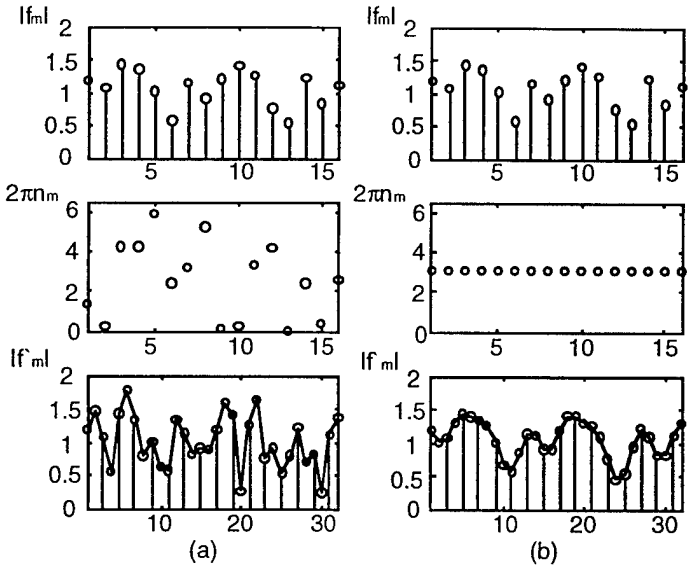


Figure 1: Top: Sampled image; Middle: phase factors added to the image; Bottom: Reconstructed images from $f_m \exp[j2\pi n_m]$ with a double sampling rate.

Three factors should be considered in the iterative designing of the speckle-free CGH's. One is that the sampling rate should be increased in the reconstruction plane in order to simulate the speckle noise which will appear in the optical reconstruction. Another factor is that a Fourier plane constraint should be applied, such that the reconstructed image is a band-limited function. Finally, as shown by Wyrowski et.al., although the iterative technique with band-limitation constraint can smooth out most π-phase jumps in the reconstructed image, and remove most speckle noise, there could be still some isolated point zeros in the reconstructed image. Tracing the phase along a closed circle around those point zeros, the phase can shift by 2π. When a π-jump on those circle is removed by the iteration, a new π-jump will occur on the same circle, so that those point zeros can not be removed by the iteration. Wyrowski suggested to choose initial phase of the iteration and Teiwes [4] used an initial spherical phase to effectively remove those isolated point zeros in Fourier holograms. We show below the implementation of the above three considerations in the design of speckle-free Fresnel holograms.

3. Speckle-free phase-mostly Fresnel holograms

Figure 2 shows the design scheme. We start the design by positioning the desired image $a_{mn} = i_{mn}^{1/2}$ in window of M x N size centered in a 2M x 2N matrix, that results in a image $f_{mn,z}$ in the reconstruction plane. Inside the reconstruction window we have freedom of phase. Outside the window we have freedom of phase and amplitude. The initial phase is chosen as a constant phase.

$$f_{mn,z} = FT^{-1}\left[F_{kl,z}\right] = FT^{-1}\left\{AF_{kl,0}\exp\left[j2\pi\frac{z}{\lambda}\sqrt{1-\left(\lambda\frac{k}{Md_x}\right)^2-\left(\lambda\frac{l}{Nd_y}\right)^2}\right]\right\} \quad (1)$$

The Fresnel diffraction is calculated using a linear spatial filtering [7]. The free propagation at a distance z from the hologram $f_{mn,0}$ to the reconstructed image $f_{mn,z}$ is described by Eq.1 where $F_{kl,0}$ is the Fourier transform of $f_{mn,0}$; $F_{kl,z}$ is the Fourier transform of $f_{mn,z}$; m and n are the image plane coordinates, k and l are the Fourier plane coordinates; A is the amplitude of the plane wave; λ is the wave length; MxN are the number of elements of the hologram matrix structure and d_x and d_y are the size of each hologram element. From Eq.(1) the free propagation is characterized by a transfer function $H_{kl,z}$, given by:

$$H_{kl,z} = \frac{F_{kl,z}}{F_{kl,0}} = A\exp\left[j2\pi\frac{z}{\lambda}\sqrt{1-\left(\lambda\frac{k}{Md_x}\right)^2-\left(\lambda\frac{l}{Nd_y}\right)^2}\right] \quad (2)$$

To calculate the inverse propagation from the reconstruction plane to the hologram plane, we apply the inverse propagation filter

$$f_{mn,0} = FT^{-1}\left[\frac{F_{kl,z}}{H_{kl,z}}\right] \tag{3}$$

The constraint in the hologram plane is the phase modulation characteristic of the SLM, which is a phase-mostly liquid crystal television (LCTV) with a slight coupled amplitude modulation [6].

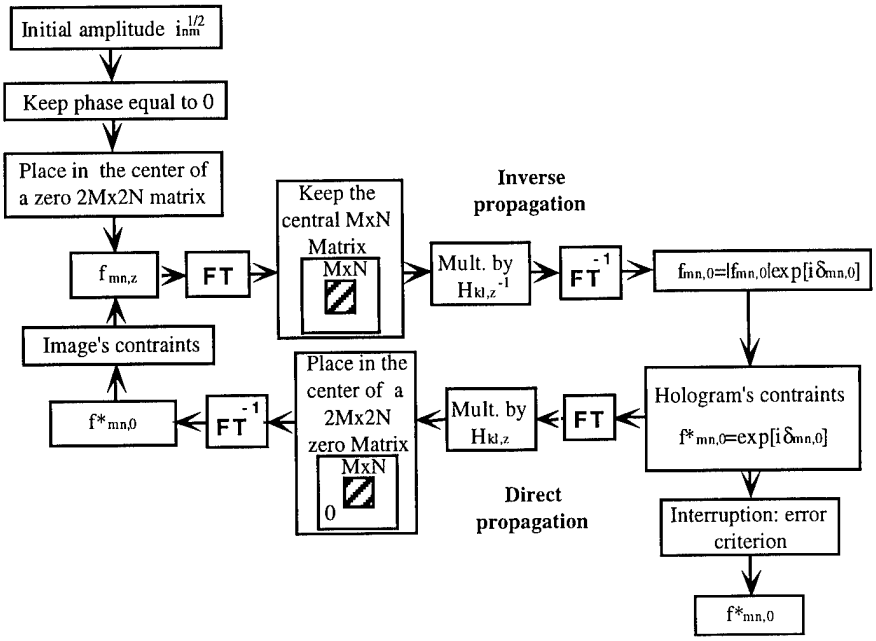


Figure 2: The Iterative Algorithm applied in design of speckle free phase-only fresnel holograms.

The hologram is of M x N size. For computing the free propagation from the hologram plan to the image plan, we use the Fourier transform of $f_{mn,0}$ which is $F_{kl,0}$ of M x N size. We multiply it with $H_{kl,z}$. In this step we introduce the M x N spectrum $F_{kl,0}H_{kl,z}$ inside a 2M x 2N zero matrix before computing the reconstructed image, that doubles the sampling rate of the image in order to simulate the optical reconstructed image with the speckle noise.

The image plane constraint is that the amplitude $|f_{mn,z}|$ must be proportional to a_{mn} inside the reconstruction window g_r. The band-limited constraint is applied on the Fourier transform $F_{kl,z}$ of the image $f_{mn,z}$, that is $F_{kl,z} = 0$ outside a center square of M x N size. The new information $f_{mn,z}$ is used in the next iteration. The iterations continues until no significant reduction in the mean square error is achieved.



(a) (b) (c)

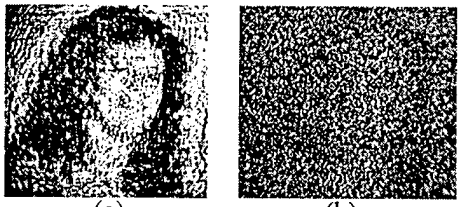
Figure 3: (a) desired reconstruction; (b) resulted hologram; (c) speckle-free reconstruction

For Fourier holograms, the initial spherical phase is a suitable choice because it is naturally band limited in the Fourier plane (hologram plane). By adjusting its radius we can spread the light only in the region of the

hologram. For Fresnel holograms, the initial constant phase is a suitable choice because we are forcing the spectrum of the function $F_{kl,z}$ to be concentrated in the center of the Fourier plane, and consequently, band limited. During the calculus of the inverse and direct propagation, the phase variation of the phase function $H_{kl,z}$ is more smooth in the center of the frequency plane, what does not introduces a strong phase variation (deviation) in $F_{kl,z}$, resulting in a smooth hologram.

4 Experimental results

We designed a phase-mostly Fresnel hologram with the dimensions of 200 x 200 pixels, that is to be displayed in a coupled-mode LCTV [5]. The desired reconstruction is the intensity of the image shown in figure 3a with a size of 400 x 400 pixels. This image is placed in a reconstruction region g_r with the same size, 400x400 pixels (we use only the freedom of phase in the reconstruction). Figures 3b and 3c show the computer generated hologram and computer reconstruction after 50 iterations. The distance z for the free propagation is 3 m, the LCTV pixels size are d_x=10.9 10^{-5} m and d_y=9.0 10^{-5} m, and the light wavelength is λ=632.8 10^{-9} m. The figure 4a shows the optical reconstruction. We note the absence of the speckle noise. To compare the quality of our result, we generated a Fresnel hologram using a initial random phase and an iterative algorithm without force the reconstruction $f_{mn,z}$ to be a band limited distribution. Figure 4b shows the noisy optical reconstruction.



(a) (b)

Figure 4: (a) optical speckle-free reconstruction; (b) noisy optical reconstruction

Acknowledgements: Luiz Gonçalves Neto thanks CNPq - Brazil by their support.

References

1. R.W. Gerchberg and W.O. Saxton. A Practical Algorithm for the Determination of Phase from image and Diffraction Plane Pictures, Optick 35, 237-46, 1972.
2. J.R. Fienup. Iterative method applied to image reconstruction and computer-generated holograms. Optical Engineering, vol.19 no.3, p.297-305, June 1980.
3. Frank Wyrowski. Iterative quantization of digital amplitude holograms. Applied Optics, vol.28 no.18, p.3864-3870, Sep. 15, 1989.
4. Stephan Teiwes, Heiko Schwarzer, Harald Aagedal, Michael Schimid, Thomas Beth, Frank Reichel and Frank Wyrowski, Speckle-free signal reconstruction with non-periodic diffractive elements on liquid-crystal SLM, OSA topical meeting, spatial light modulator, thech. Digest series, vol.9, 24-27 (1995).
5. Luiz Gonçalves Neto, Danny Roberge and Yunlong Sheng. Programmable optical phase-mostly holograms with coupled-mode modulation liquid-crystal television. Applied Optics, Vol. 34, No. 11, p.1944-1950, 10 april 1995.
6. Luiz Gonçalves Neto and Yunlong Sheng. Optical implementation of image encryption. Submitted to Optical Engineering, October 1995.
7 Joseph W. Goodman. Introduction to Fourier Optics. McGraw-Hill Publishing Company, p.48 54, 1968, 1988.

High efficiency fast diffractive lens for beam coupling

Yunlong Sheng and Dazeng Feng
Université Laval, Centre d'Optique, Photonique et Laser,
Département de Physique, Québec, Canada G1K 7P4.
Tel: 418 656 3908, Fax: 418 656 2623 sheng@phy.ulaval.ca

Diffractive lenses for laser diode beam focusing collimating and coupling have wide applications. Large numerical aperture and high light efficiency are important issues for the coupling lenses. Numerical aperture of a typical laser diode beam can be as large as NA ~ 0.5. To capture the highly divergent beam the lens must have a low F-number of F/1 ~ F/2. Coupling the laser beam into an optic fiber with an acceptance angle of NA ~ 0.1 - 0.2 needs even larger numerical aperture of the lens.

We designed a focusing and shaping lens which is fabricated in the Honeywell/CO-OP diffractive optics workshop. The lens is of ϕ = 5 mm, minimum feature size δ = 1.5 μm and phase levels N = 8 for wavelength λ = 850 nm. With the conventional design the outermost Fresnel zone will have a minimum width of Nδ = 12 μm, resulting a lens of about F/7. Reducing the phase levels to N = 2 leads to a minimum zone width Nδ = 3 μm and F/1.7, resulting in a diffraction efficiency of 40%. The uniform etching depths in the workshop foundry does not allow us to make multi-order lens[1].

To design a high efficiency fast focusing lens we choose the method proposed by Welch et.al.[2], which is useful for encoding radially symmetric discrete phase lenses. In the encoding the photomask resolution $\Delta\rho$ is used instead of the minimum feature size δ as the sampling interval. The minimum feature size δ is still respected. The feature sizes become δ, $\delta+\Delta\rho$, $\delta+2\Delta\rho$ ... instead of δ, 2δ, 3δ ... Since $\Delta\rho << \delta$ the degrees of freedom for the iterative simulated annealing optimization are dramatically increased. In this paper we design high efficiency large aperture focusing and shaping lenses with elliptical incident beam using this technique. We estimate aberrations and effects of the sampling rate and of the fabrication errors of those particular type lenses.

1. Simulated annealing algorithm

In the photolithographic process the position accuracy of mask features is determined by the e-beam mask writing, while the minimum feature size δ depends on the mask alignment. We divide a radially symmetric diffractive lens into P ring-shaped cells of equal radial width of $\Delta\rho$, where $\Delta\rho << \delta$ is the resolution of the photomasks. Then, we regroup the cells into T rings. Each ring has a constant phase $\phi(\rho)$ for $\rho_t \le \rho \le \rho_{t+1}$ and the minimum feature size is respected $\rho_{t+1} - \rho_t \ge \delta$.

In the simulated annealing[3] we change randomly the phase value ϕ_t and the locations of the phase transition points ρ_t and ρ_{t+1}. The latter corresponds to change the number of cells in a ring. Then, we calculate the cost function. When the cost is reduced the change is accepted. When the cost is augmented the change is accepted with a probability, which decreases with the decrease of a temperature parameter. In one iteration all the rings are visited consecutively from the innermost to outermost ring. The iteration is then repeated with a lower temperature until the temperature becomes sufficiently low. The initial state of the lens should not affect the final solution of the simulated annealing if the initial temperature is sufficiently high.

The near field diffraction of the fast lens is computed with the Rayleigh-Sommerfeld formula as,

$$U(r,\psi) = \frac{1}{j\lambda}\iint_{\Sigma} A(\rho,\theta)\exp[j\phi(\rho)] \frac{\exp(jkr_{01})}{r_{01}}\cos(\hat{n},\hat{r}_{01})\,\rho d\rho d\theta \qquad (1)$$

where $j = \sqrt{-1}$, λ is the wavelength, $k = 2\pi/\lambda$, $A(\rho,\theta)$ is the incident amplitude, $\exp[j\phi(\rho)]$ is the lens, r_{01} is the displacement vector from a point (ρ,θ) in the lens plane to a point (r,ψ) in the focal plane. The directional factor $\cos(n,r_{01}) = f/r_{01}$, where f is the focal length. For a given $A(\rho,\theta)$ the integral with respect to θ in the right-hand side of Eq.(1) is independent of the lens and can be computed and stored in the computer before the design. Hence, the diffraction output can be updated quickly for each change in the simulated annealing process. The cost function is defined for maximizing the diffraction efficiency η as,

$$e_1 = 1 - \eta = 1 - \frac{\sum_m \sum_n |U_{mn}|^2 m(\Delta r)^2(\Delta\psi)}{I} \qquad (2)$$

where I is the incident power on the lens and U_{mn} is sampled $U(r,\psi)$ with $r = m\Delta r$ and $\psi = n\Delta\psi$. The η is calculated in an area of five times of the Airy size of the lens.

Optimized for high efficiency, the designed lens can have discrete phase levels N at the center, but less than N in the outer region of the lens. Welch et. al. obtained η = 90% for a F/1 lens with the minimum feature size δ = 0.7 μm and λ = 1.3 μm. We obtain η = 89% for a F/3 lens with δ = 1.5 μm for λ = 0.85 μm. We note that the efficiency was high only for a Gaussian incident beam and was much lower for a uniform incident beam. The loss of power due to the lower number of phase levels in the outer region of the lens is less important for Gaussian beam than for uniform beam.

2. Design considerations

(1) Elliptical incident beam: When $A(\rho,\theta)$ is radially symmetric the diffraction output $U(r,\psi)$ is also radially symmetric, we need to compute the output only on one radius in the focal plane. The integral with respect to θ in Eq.(1) becomes a function only of the radial coordinates ρ in the lens plane and r in the focal plane. The data stored in the computer for fast updating the cost function is a 2-D array. When $\Delta\rho$ = 0.1 μm for sampling the lens radius R_0 = 2.5 mm and $r = m(\Delta r)$ is sampled with m =0, 1, ... 30, for radially sampling the focal plane the storage requires 6 Mbytes memory.

We designed focusing lenses for elliptical laser diode incident beam $A(\rho,\theta)$. In this case the diffraction output is no longer radially symmetric. The data to be stored are a 3-D array, which depends on ρ, r and the angular coordinate ψ in the focal plane. The storage requires a much larger memory. Fortunately, for on-axis focusing the diffraction pattern $U(r,\psi)$ has a reflection symmetry. We need to compute the data only for a quarter of the focal plane. The focal plane was sampled by m = 30 points in the radial direction and by every 6° in angular direction. We had to use a larger sampling interval for the lens with $\Delta\rho$ = 0.5 μm, the storage memory was about 18 Mbytes. We needed about 3 hours in the Silicon Graphic Power Indigo 2 Computer for calculating the 3-D array and one hour for optimizing the lens with the simulated annealing.

(2) Sampling interval: In the Rayleigh-Sommerfeld diffraction Eq.1, the phase term $\exp(jkr_{01})$ is very sensitive to r_{01}, the sampling rate $\Delta\rho$ must satisfies the following condition,

$$k\Delta\rho\left\{\frac{\partial r_{01}}{\partial\rho}\right\}_{\max} < 2\pi \qquad (3)$$

The maximum value of $\partial r_{01}/\partial\rho$ occurs at $\rho = R_0$ for the on-axis focal point, where R_0 is the lens radius. Hence, we have,

$$\Delta\rho < \lambda\sqrt{1 + (2F/\#)^2} \qquad (4)$$

The $\Delta\rho$ is limited by the accuracy in mask writing and by the size of the 3-D data stored in the computer. We find that when $\Delta\rho$ varies from 0.05 μm to 0.5 μm for F/# = 1 and 3 the diffraction efficiency varies less than 5%, because in this case the sampling interval,

$$\Delta\rho \approx 0.1\lambda F/\# \sim 0.2\lambda F/\# \qquad (5)$$

the condition described in Eq.4 is satisfied.

(3) Beam shaping: With the elliptical incident beam the focal spot is elliptical(see Fig.1). We designed a lens that shapes the beam to yield a circular focal spot. In the design we added one term in the cost function e_1 as,

$$e_2 - e_1 + \frac{\sum_m \sum_n (|U_{mn}|^p - |U_{m0}|^p) m(\Delta r)^2 \Delta\psi}{I} \quad (6)$$

where U_{m0} is a target circular amplitude distribution whose diameter is equal to the long axis of the elliptical focal spot. The elliptical focus is then expanded along the short axis to a circular spot(see Fig.2). The lens is still radially symmetrical. Its focal length is in fact changed by the simulated annealing, resulting in the circular spot in the original focal plane for the elliptical incident beam.

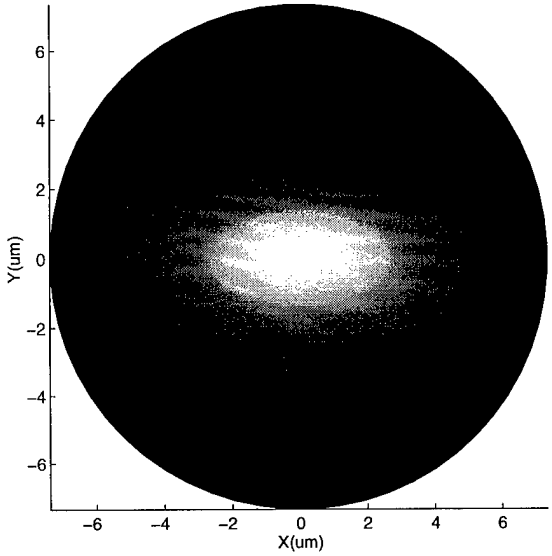


Figure 1. The intensity distribution of the elliptical spot.

(4) Aberrations: The encoding process optimizes the discrete phase values and the locations of the phase transition points in order to maximize the diffraction efficiency. As a consequence, the zone boundaries and phase profile of a diffractive lens are violated, resulting in an important wavefront aberration. We interpolated the discrete phase profile of the designed lenses with a polynomial and estimated the spherical aberrations with the CODE V. Figure 3 shows the axial spherical aberration of the designed focusing and shaping lens of F/3. The transverse spherical aberration (TSA) is smaller than the Airy size for ray heights smaller than 68% of the maximum ray height. Outer this region the TSA increases very fast with the ray height. As a result the lens focuses most energy of the Gaussian beam into

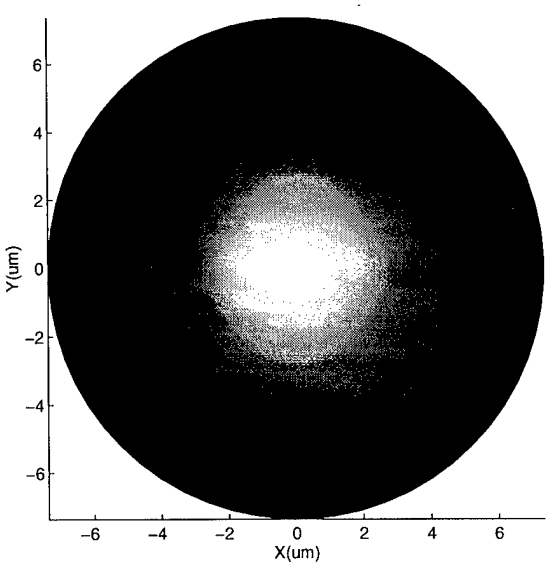


Figure 2. The intensity distribution of the circular spot.

the diffraction limited focal spot. The outer region of the Gaussian incident beam go far beyond the focal point. Its energy is lost.

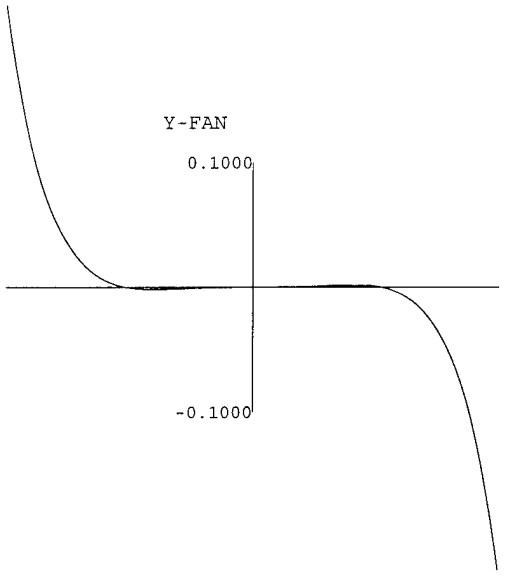


Figure 3. Axial spherical aberration.

3. Estimation of fabrication error effect

There are basically two systematic errors in the photolithographic fabrication: that in the etching depth and that in the mask alignment. Their effects on the lens diffraction efficiency can be estimated by numerical simulation.

For simulating the etching depth error we introduced random phase errors $\Delta\phi_n$ in each of three etching process with n = 1, 2, 3. The values of $\Delta\phi_n$ were randomly distributed within $-\Delta\phi_{max} \leq \Delta\phi \leq \Delta\phi_{max}$. The mean value of η and the standard deviation σ were computed as a function of $\Delta\phi_{max}$ and $\eta\pm\sigma$ are plotted in Fig.4. One sees that when the etching depth errors are controlled under 300 A (0.24 rad for $\lambda = 0.85$ μm), the efficiency decreases only by 1 - 3 % for both F/1 and F/3 lenses.

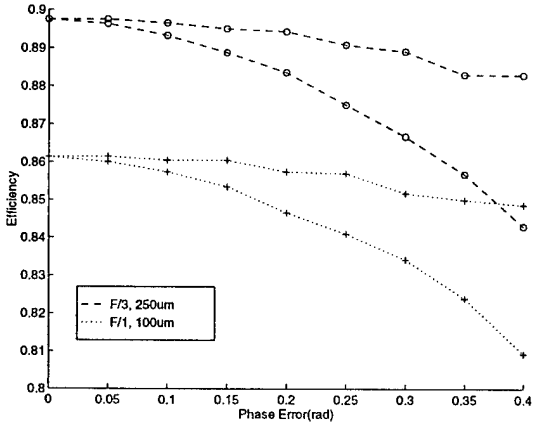


Figure 4. Etching depth error

For simulating the mask alignment error, we shifted the second mask in the x-axis by a distance of Δ with respect to the first mask and the third mask in y-axis by the same distance. With those alignment errors the diffractive lens were no longer radially symmetric. The focal plane light amplitude distribution was calculated with the Rayleigh-Sommerfeld formula. The Efficiency η is computed as a function of Δ and is plotted in Fig.5. The efficiency is reduced by 10% for F/3 lens when Δ = 0.4 μm and by 15% for F/1 lens when Δ = 0.2 μm. Misalignment of the mask can introduce new high spatial frequency features to the lens and reduce the diffraction efficiency significantly.

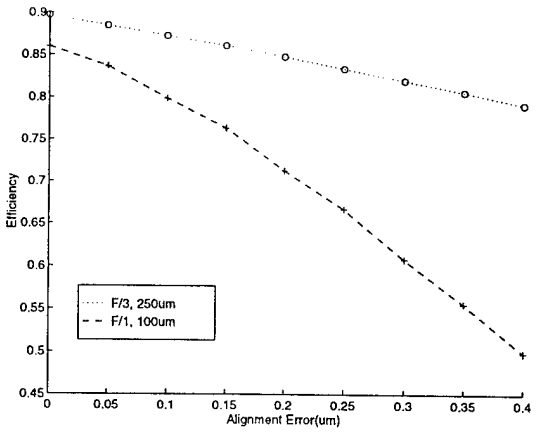


Figure 5. Mask alignment error

5. Results

We have designed focusing and shaping lenses for elliptical shaped input beams. The phase levels of the lenses is N = 8 in the center and N < 8 in outer regions. The TSA of the lens is estimated. The rays within the circle of 68% radius of the lens are focused into the Airy circle. High efficiency is only for Gaussian input beams. For uniform beam the efficiency was poor. Our best design provides efficiency of 89.4% for F/3 lens for minimum feature size of 1.5 μm and $\lambda = 0.85$ μm.

References

1. G. M. Morris, D. Faklis, "Achromatic and apochromatic diffractive singlets", OSA Topical Meeting "Diffractive Optics", Tech. Digest **11**, 57-60 (1994).

2. W. H. Welch, J. E. Morris and M. R. Feldman, "Iterative discrete on-axis encoding of radially symmetric computer-generated holograms", J. Opt. Soc. Am. A, **10**, 1729-1738 (1993).

3. S. Kirkpatrick, C. D. Gelatt Jr. and M. P. Vecchi, "Optimization by simulated annealing ", Science, **220**, 671-680 (1983).

Effective medium theory of symmetric two-dimensional subwavelength periodic structures

Philippe Lalanne
Institut d'Optique Théorique et Appliquée, CNRS, BP 147, 91403 Orsay Cedex, France
tel: 33-1-69-41-68-46 fax: 33-1-69-41-31-92 e-mail: philippe.lalanne@iota.u-psud.fr

1. Introduction

Recent experimental and theoretical investigations have shown that periodic subwavelength structured surfaces with periods small compared to the illumination wavelength behave as homogeneous medium, and have suggested interesting applications, such as fabrication of anti-reflection coatings[1,2,3], quarter wave plates[4] , polarizers[5], and graded-phase diffractive elements[6]. The replacement of the periodic structure by a homogeneous medium is often referred as homogenization or effective medium theory (EMT). EMT can be applied to a large variety of physical material properties, such as diffusion constant, magnetic permeability, thermal conductivity, etc. To facilitate the design and fabrication of artificial dielectric elements, one must be able to relate the effective index of the subwavelength structured surface in a simple way.

The properties of one-dimensional (1-D) periodic structures have been analyzed in great detail, and the equivalence of 1-D gratings and homogeneous uniaxial thin films has been rigorously derived in the long wavelength limit. Limited research has been done in the area of two-dimensional (2-D) gratings. Jackson and Coriell[7] derived upper and lower bounds of the zeroth-order effective index of 2-D periodic structures. More recently, Grann et al.[21] used rigorous coupled-wave analysis (RCWA) to estimate the effective index of 2-D gratings by computer simulations.

In this paper we study the EMT of 2-D symmetric periodic structures for a wave propagating normally to the grating. We use a Fourier expansion method. Closed-forms of the zeroth- and second-order effective indices are provided. By 2-D symmetric structures, we mean structures presenting a center of symmetry. It does not imply that the periods are the same, and for gratings composed of parallelepipeds of one given medium immersed in an other medium, it does not imply that the two fill factors are equal. To our knowledge, this work is the first to present a rigorous approach for the EMT of 2-D periodic structures.

2. Effective medium theory

Notations

To establish our notation, let us first consider a 2-D periodic structure along the x and y axis with an arbitrary relative permittivity profile $\varepsilon(x,y)$. Two examples are shown in Fig. 1. The structure is assumed to be constant in the z direction perpendicular to the plane of Fig. 1. The grating period along the y direction is noted Λ. The period in the x direction Λ_x can be simply written $\Lambda_x=\Lambda/\rho$, where ρ is a dimensionless coefficient. The grating vector K is simply defined as $K = 2\pi/\Lambda$. Using ε_{mn} to denote the (m,n)th Fourier coefficient of periodic structures, we have

$$\varepsilon(x,y) = \sum_{m,n} \varepsilon_{mn} \exp jK(\rho mx + ny) . \qquad (1)$$

Similarly a_{mn} will be used to denote the (m,n)th Fourier coefficients of the inverse relative permittivity. In the following, we restrict the discussion to symmetric periodic structures with

$$\varepsilon_{m,n}=\varepsilon_{-m,n}=\varepsilon_{m,-n}=\varepsilon_{-m,-n}. \qquad (2)$$

Note that it does not imply the equality of the periods along the x and y directions, but simply that a center of symmetry exists.

Methodology

We consider a wave with wavelength λ in a vacuum and wave vector k ($k=2\pi/\lambda$). The wave is propagating in the periodic structure along the z-direction and is polarized in either the x or y direction. In the following, only a

polarization along the y direction will be investigated for the sake of simplicity. The z-dependence of the wave is assumed to be

$$\exp(j\sqrt{\eta}kz), \tag{3}$$

where the constant η is read as the square of the effective index of the periodic structures for the z direction and the given polarization.

We look for a wave propagating in the z direction and periodic in the x and y direction with period $\rho\Lambda$ and Λ, respectively. Expending the x and y components of the wave electric field in a Fourier series, we have

$$E_x = \exp jk\sqrt{\eta}z \sum_{(m,n)\neq(0,0)} s_{xmn} \exp jK(m\rho x + ny) \tag{4a}$$

$$E_y = \exp jk\sqrt{\eta}z \sum_{m,n} s_{ymn} \exp jK(m\rho x + ny), \tag{4b}$$

where s_{xmn} and s_{ymn} are constants, and only E_y has a DC component. On spatial averaging along the x and y directions of the periodic structure, E_x equals zero and E_y equals s_{y00}, since only E_x has a non-null DC component. Note that when looking for a wave polarized in the x direction, Eqs. 4 hold except that, in that case, only E_x has a DC component (i.e. $s_{y00}=0$ and $s_{x00} \neq 0$).

The wave electric field of Eq. 4 is used in satisfying Maxwell's equations inside the periodic structure. Obviously such a solution is not correct. But for small period-to-wavelength ratios, an approximate solution can be derived[8] by expanding η, s_{xmn} and s_{ymn} in a power series of $\alpha = \lambda/\Lambda$. The EMT expansion for η can be written

$$\eta = \eta_0 + \eta_1\alpha^{-1} + \eta_2\alpha^{-2} + \ldots, \tag{4}$$

where η_o is the square of the zeroth-order effective index and η_i, i=1,...,N is the ith-order coefficient of the series expansion. In general η depends on the permittivity ε, the period Λ, the wavelength λ, and on ρ for 2-D periodic structures. (2)

Solution

By solving Maxwell's equations inside the periodic structure, we find[9]

$$\eta_0 = \varepsilon_{00} - \sum_{p,q\neq 0} \sum_{m\geq 0, n>0} \varepsilon_{m,n} a^{p,q}_{m,n} \varepsilon_{p,q} n, \tag{5a}$$

$$\eta_1 = 0, \tag{5b}$$

$$\eta_2 = \sum_{p,q\neq 0} \sum_{m\geq 0, n>0} \varepsilon_{p,q} a^{p,q}_{m,n} c_{mn} + \sum_{p\neq 0} \frac{\varepsilon_{p,0}}{p^2\rho^2} \left(\varepsilon_{p,0} - \sum_{\substack{(r,t)\neq(0,0) \\ u\geq 0, v>0}} \varepsilon_{p-r,t} a^{u,v}_{r,t} \varepsilon_{r,t} t \right). \tag{5c}$$

For numerical purpose, the Fourier series of Eq. 4 have to be truncated. We denote by M the truncation rank so that, in Eq. 4, m and n vary between -M and M. The computation of $a^{p,q}_{m,n}$ and c_{mn} coefficients requires the inversion of a M(M+1)xM(M+1) matrix not defined here.

3. Comparison with rigorous computations

3.1 Jackson and Coriell[7] derived upper and lower bound expressions for the zeroth-order EMT of several simple symmetric periodic structures composed of two-phase materials, like those of Fig. 1. These structures are composed of two homogeneous media indexed by 1 and 2. In our simulation, media 1 and 2 have optical permittivities equal to 1 and 16, respectively. The periodic structure of Fig. 1a is composed of parallelepipeds of high index inserted in a medium of low index. Similarly, the periodic structure of Fig. 1b is composed of cylinders of low index inserted

in a medium of high index. We define the fill factor of the two structures as the ratio between the width (resp. the diameter) of the parallelepiped (resp. cylinder) and the period Λ. The solid lines of Fig. 2 are the upper and lower bounds derived by Jackson and Coriell[7]. They are plotted as a function of the fill factor. Circle-, cross-, and plus-marks are the zeroth-order (η_0) effective index obtained for different truncation ranks. Circle-marks were derived with M = 40, cross marks with M = 20, and plus-marks with M = 7. Basically, the EMT prediction of Eq. 5a lies in between the upper and lower bounds. For the parallelepiped case and for fill factors about 0.8 and 0.9, it is noticeable that the truncated expansion is slowly converging. For a fill factor equal to 0.9, even with M = 40, η_0 remains just above the upper bound.

3.2 In Fig. 3, the transmittance for normal incidence of a 6-grid stack of alternate layers is shown as a function a the wavelength. Each grid is composed an homogeneous thin film of relative permittivity 13 and a 2-D grating with a cubic filling geometries of relative permittivity 1 immersed in a medium of relative permittivity 13. The grating period, fill factor and depth are 0.16, 0.56 and 0.09, respectively. The homogeneous layer depth is 0.07. The solid curve is obtained with rigorous computation and the dashed curve is derived with the second-order EMT of Eqs. 5. Once homogenized, the periodic structure is equivalent to a thin film stack. Basically, there is a good agreement between rigorous computation and the EMT prediction. A significant mismatch is visible for wavelength smaller than 0.6, i.e. for period-to-wavelength ratios larger than 0.27. In that case, the 2-D EMT presented in this paper is a valuable technique to explain and predict the existence of a gap for wavelength larger than 0.9 and smaller than 1.2.

This work was supported by the Direction Générale de l'Armement under contract DRET-DGA # 94-1123.

References

[1] T.K. Gaylord, W.E. Baird and M.G. Moharam, "Zero-reflectivity high spatial-frequency rectangular-groove dielectric surface-relief gratings", Appl. Opt. **25**(24), 4562-4567 (1986)

[2] Y. Ono, Y. Kimura, Y Otha and N. Nishida, "Antireflection effects in ultrahigh spatial-frequency holographic relief gratings", Appl. Opt. **26**(6), 1142-1146 (1987)

[3] D.H. Raguin and G.M. Morris, "Antireflection structured surfaces for the infrared spectral region", Appl. Opt. **32**(7), 1154-1167 (1993)

[4] L. H. Cescato, E. Gluch and N. Sreibl, "Holographic quaterwave plates", Appl. Opt. **29**(15), 3286-3290 (1990)

[5] P. Yeh, "A new optical model for wire grid polarizers", Opt. Comm. **26**(4), 289-292 (1978)

[6] F.T. Chen and H.G. Craighead, "Diffractive phase elements based on two-dimensional artificial dielectrics", Opt. Lett. **20**(2), 121-123 (1995)

[7] J.L. Jackson and S.R. Coriell, "Transport coefficients of composite materials", Journ. Appl. Phys. **39**(5), 2349-2354 (1968)

[8] Ph. Lalanne and D. Lemercier-Lalanne, "On the effective medium theory of subwavelength periodic structures", submitted for publication.

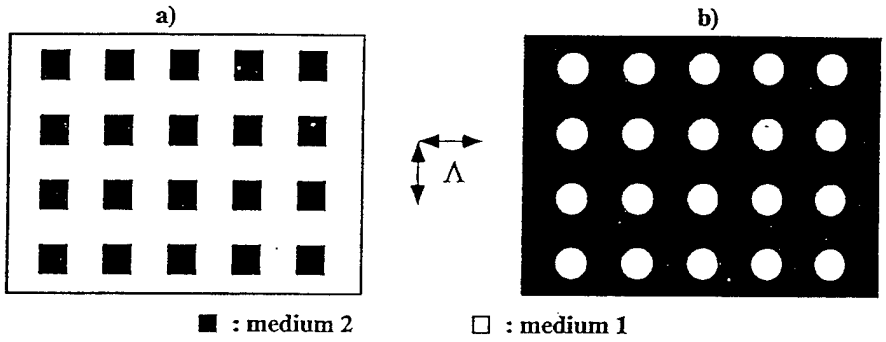


Fig.1 **a)** periodic structure composed of parallelepipeds of high index inserted in a medium of low index
b) periodic structure composed of cylinders of low index inserted in a medium of high index

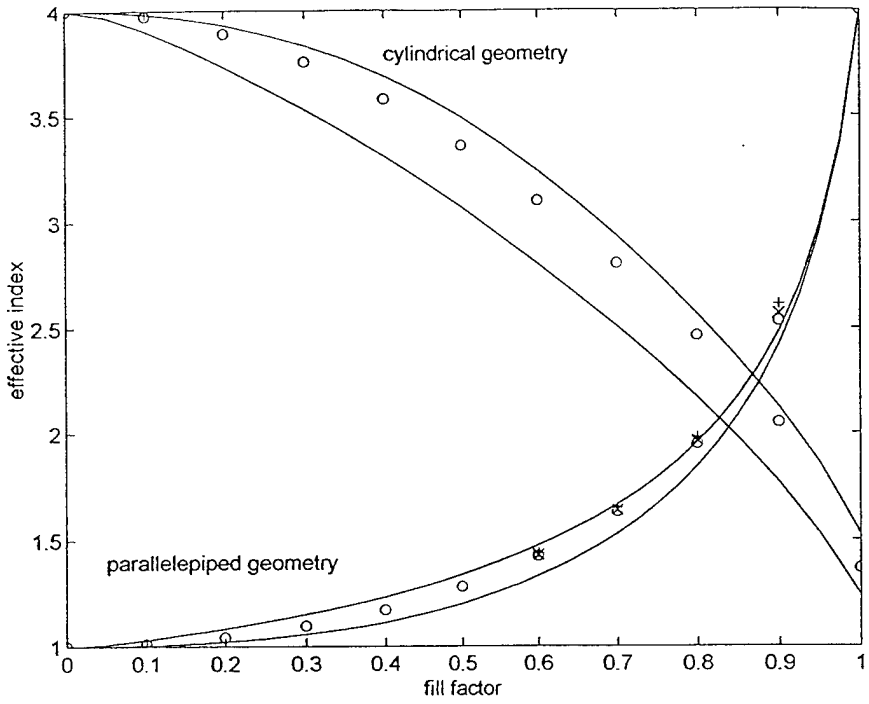


Fig.2 Zeroth-order effective index. The solid curves are the upper and lower bounds derived in Ref. 7 for the zeroth-order effective index and for the periodic structures of Fig. 1. Plus-marks, cross-marks and circle-marks are respectively the effective indices of Eq. 5a for truncation ranks M equal to 8, 20 and 40.

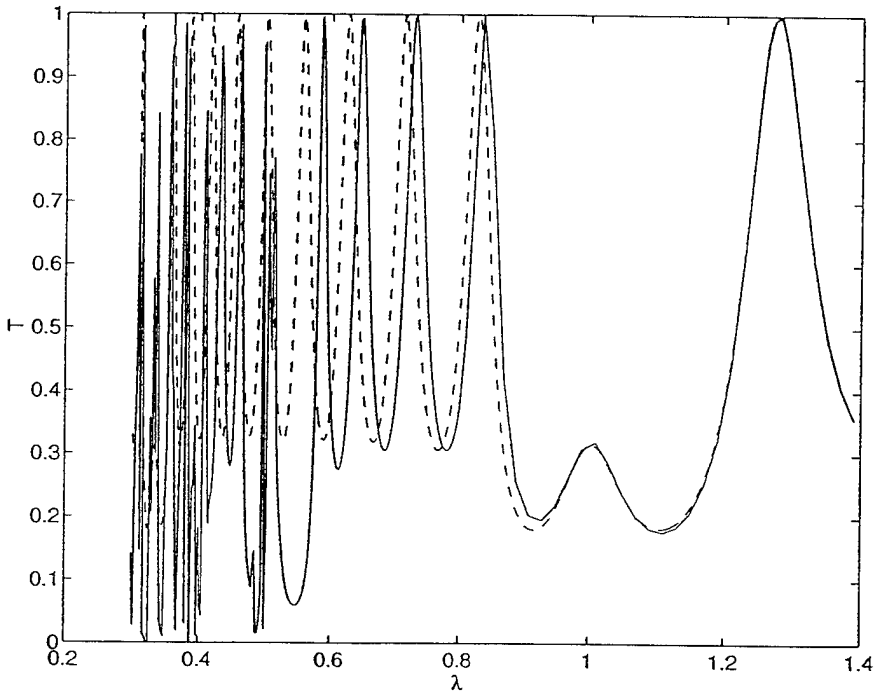


Fig.3 Comparison between the EMT prediction of Eq.5 and rigourous computations.

Z-Scan Measurement in Amorphous As_2S_3 Thin Film

Yeung Joon Sohn, Chong Hoon Kwak, Ok Shik Choe
Department of Physics, Yeungnam University,
Kyongsan, 712-749, Korea
(Fax:+82-53-813-4465, e-mail:chkwa@ynucc.yeungnam.ac.kr)

1. Introduction

Z-scan technique is very useful method for measuring the magnitude and the sign of the nonlinear refractive index due to its simple geometry and high sensitivity compared with nonlinear interferometry, degenerate four-wave mixing, nearly degenerate three-wave mixing, ellipse rotation, beam distortion measurement.[1, 2] With this technique the measurements and analysis for several nonlinear optical materials such as CS_2, ZnSe, GaAs, CdTe had been succesfully acomplished by using high power pulse laser.[1-3] In this paper, we present a cw pump-probe z-scan method for determining the optical nonlinearity of an amorphous As_2S_3 thin film. In an amorphous chalcogenide As_2S_3, thin film the optical nonlinearity originates from the photostructural changes of the material by band gap illumination (bandgap energy of $E_g \simeq 2.5$eV corresponding to Ar-ion laser wavelength of 514nm), which results in photodarkening and photoanisotropy. These effects have been extensively investigated as holographic recording medium for optical information processing, polarization hologram and binary phase gratings such as Dammann grating.[4-6]

2. CW Pump-probe Z-Sscan Experiments

Figure 1 shows the experimental geometry for pump-probe Z-scan method. The sample to be measured is placed and scanned along the z direction in the focal region of two focused laser beams: the one is strong pump beam of Ar-ion laser with wavelength of 514.5nm and the other weak probe beam of He-Ne laser with 632.8 nm. Amorphous As_2S_3 thin film is prepared on slide glass by vacuum evaporation and the thickness is about 4㎛. The transmitted intensity through an aperture is detected in the far field region by photodiode and stored in IBM-PC. The sample is mounted on the sample holder and scanned by using a linear moter along the z-direction. We performed three kinds of experiments: (i) pump inducing-probe scanning method, (ii) (probe inducing) probe scanning method, and (iii) (pump inducing) pump scanning method. These experiments are conducted by controlling shutters S_1 and S_2, as shown in Fig. 1.

3. Experimental Results and Discussions

Figure 2 illustrates the typical experimental results of the z-scan measurements obtained by using (a) pump inducing-probe scanning method, and (b) (probe inducing) probe scanning method, as mentioned above. In obtaining Fig. 2(a), the sample is illuminated with a strong pump beam of $100mW/cm^2$ for a long time (about 10 min.) in order for making the refractive index changes unaltered for further pump beam illumination before Z-scan experiment by probe beam. It is also noted in Fig. 2(b) that although the probe beam intensity is weak compared with pump beam intensity and the wavelenth of the probe beam corresponds to the transparent regions of the material, the intensity near the focal point of the lens is sufficient to induce nonlinear refractive index changes. The sign of the nonlinear refractive index n_2 can be determined from the type of the z scan curve and the magnitude from the valley-peak difference in normalized transmittance. It is found from Fig. 2 that amorphous As_2S_3 thin film is a kind of self-focusing material having a positive Kerr coefficient. We also estimate $\triangle n \simeq 10^{-4}$ for Ar-ion laser intensity of $100mW/cm^2$, which is reasonably agree with that of obtained by holographic method.[4, 6] The curves of two kinds of measurement look like similar to each other except for their relative magnitude of valley to peak value. Figure 3 illustrates the experimental curves for (pump inducing) pump scanning method with various sizes of apertures and depicts the deep well curves. It can be understood from the strong nonlinear absorption of Ar-ion laser wavelength of 514.5nm. Since the absorption coefficient of As_2S_3 for 514.5nm wavelength (about $3x10^3cm^{-1}$) is much larger than that for 632.8 nm (about $3x10^2cm^{-1}$), the absorption significantly influences the z scan curve rather than the nonlinear refraction, and so the absorption curve is predominate over the nonlinear refraction curve.

References

[1] M. Sheik-Bahae, A. A. Said, and E. W. Van Stryland, Opt. Lett. **14**, 955 (1989).

[2] M. Sheik-Bahae, A. A. Said, T. Wei, D. J. Hagan, E. W. Van Stryland, IEEE J. Quantum Electron. **26**, 760 (1990).

[3] A. A Said et al., J. Opt. Soc. Am. **B9**, 405 (1992).

[4] C. H. Kwak, J. T. Kim, and S. S. Lee, Opt. Lett. **13**, 437 (1988).

[5] C. H. Kwak, J. T. Kim, and S. S. Lee, Appl. Opt. **28**, 737 (1989).

[6] C. H. Kwak, S. Y. Park, H. M. Kim, and E.-H. Lee, Opt. Comm. **88**, 249 (1992).

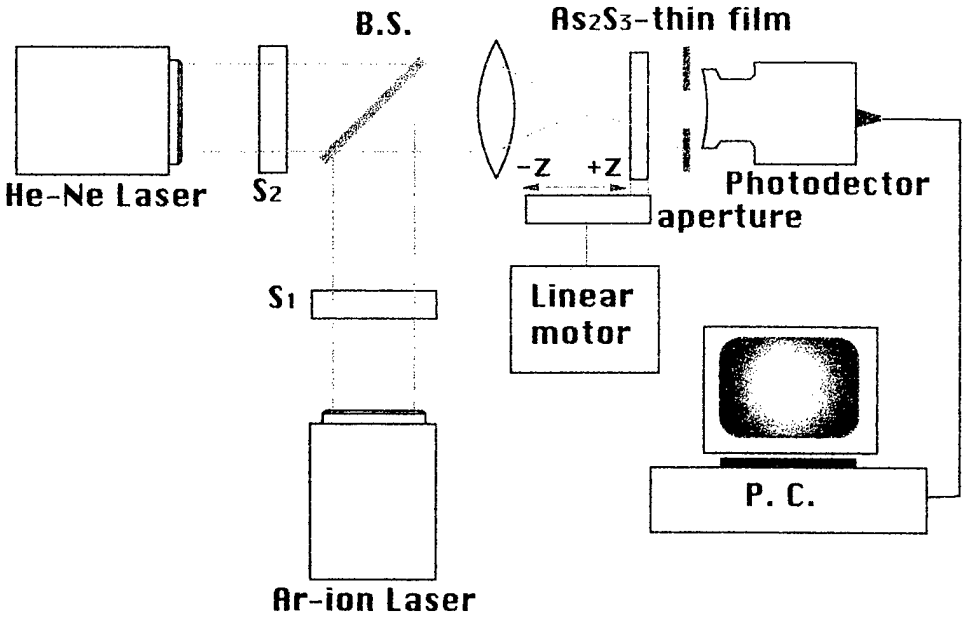


Fig. 1. Experimental geometry for pump-probe z-scan technique.

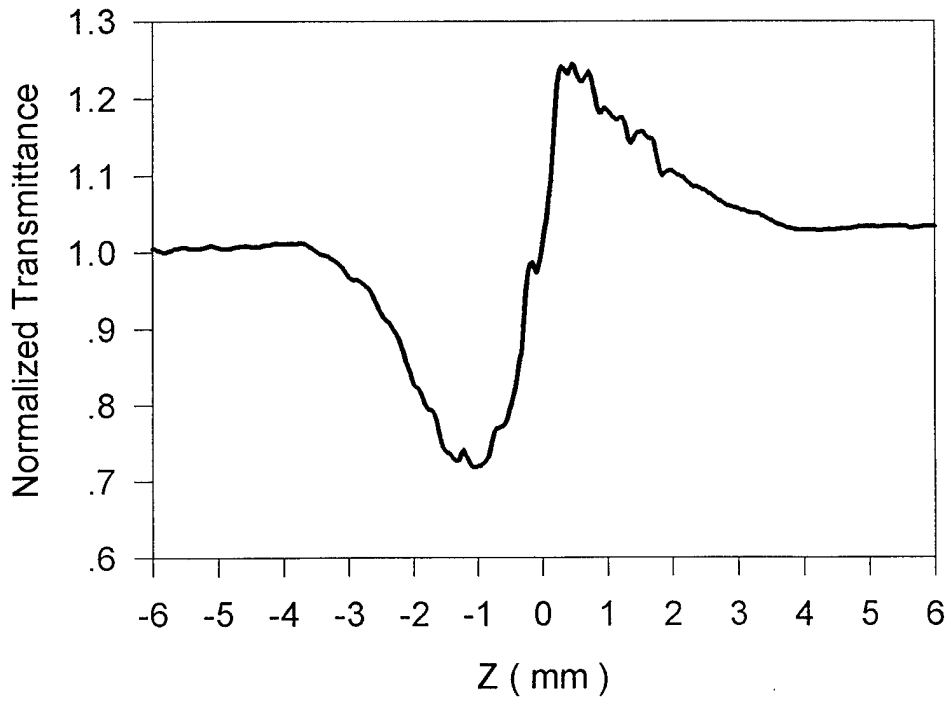
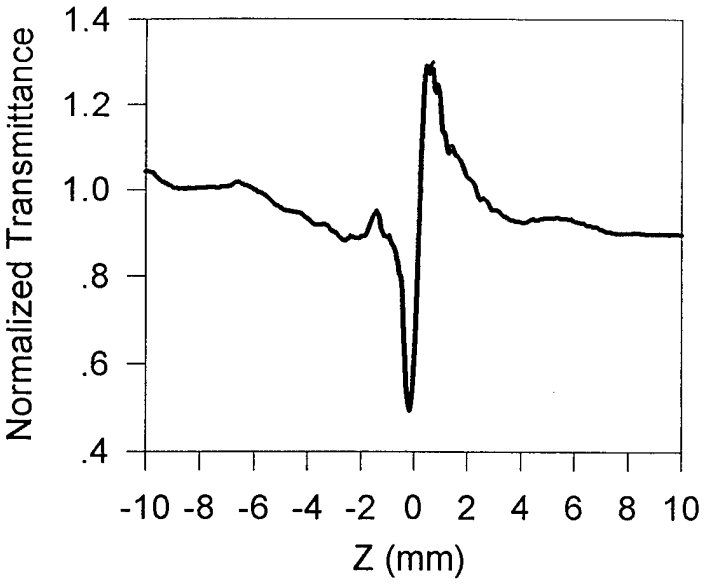


Fig. 2. Experimental z-scan curves for normalized transmittance: (a) pump inducing and probe scanning data and (b) probe beam alone(the next page)



(b) probe beam alone

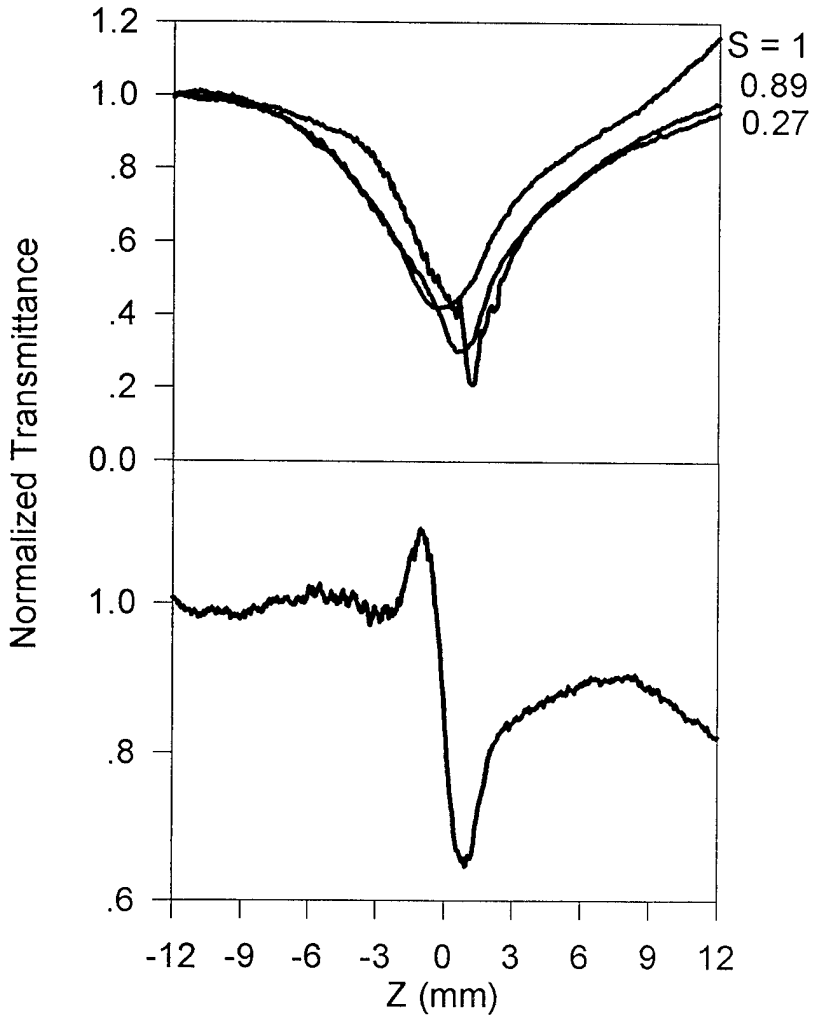


Fig. 3. Experimental z-scan curves obtained from pump beam alone.: (a) Normalized transmittance against sample position for various aperture transmittance S, (b) Aperture transmittance(S=0.4) divided by open aperture transmittance(S=1).

Simplified Processing Method of Dichromated Gelatin Derived from Agfa 8E75HD Plates

Yong Seok Im, Young Lak Lee, Chong Hoon Kwak and Ok Shik Choe
Department of Physics, Yeungnam University,
Kyongsan, 712-749, Korea.
(Fax: +82-53-813-4465, e-mail: chkwak@ynucc.yeungnam.ac.kr)

Sang Cheol Kim
Samsung Aerospace Industries, LTD.
P.O. Box111, Suwon, 440-600, Korea

Introduction

Dichromated gelatin (DCG) is one of the best recording materials for phase volume holograms. Since DCG has large refractive-index modulation, high resolution, high diffraction efficiency (DE), and good signal-to-noise ratio, it is suitable for preparing holographic optical elements. Several papers on the hologram formation mechanism in DCG have been reported in the literature.[1-5] The simplest way to obtain a good hologram is by use of photographic plates, dissolving the silver halide in a fixing bath, and sensitizing it with a solution of ammonium dichromate. Upto now, most of the works has been done using the gelatin layer of Kodak 649F plates. Oliva *et al.*,[8] presented the holographic characteristics of the DCG plates obtained from Agfa 8E75HD plates. The processing procedures for preparing high-quality DCG holographic optical elements (HOEs) developed by Oliva, however, are tedious, since it takes at least 12 hours to process one HOEs. In this work, we present very simple method for making highly efficient DCG hologram starting with Agfa 8E75HD plates. Beginning with Agfa 8E75HD plates, the complete processing time including preprocessing, sensitization, and development is just 2 hours. In addition, DCG hologram has a high DE of 81.5%.

Basic Principle

Assuming the refractive-index modulation of gelatin film is due to a hardness differential,[3-7] the DE of the DCG hologram would be dependent on the initial degree of hardening of the gelatin layer. If the initial hardening is too high, the refractive-index modulation capability will be reduced. Whereas if it is too low, the gelatin will be partially dissolved in the development bath and noisy holograms of low DE will be formed. The degree of hardness of the gelatin layer can be measured by swelling factor and is expressed as a percentage increase in weight, $k_p=(W-W_o)/W_o(\%)$, where W_o is the weight of the dry film and W is that of the swelled film. During development, the initial refractive index modulation in water, $\triangle n_w$, depends on the hardness differential $\triangle h$ between the exposed and unexposed regions and the two swelling factors $\triangle k_p$ and $\triangle k_w$, i.e.,

$$\triangle n_w = k_p k_w \triangle h \quad (1)$$

where k_w is the swelling factor during the water development. The initial refractive index modulation $\triangle n_w$ is further amplified by the final alcohol development. The final refractive index modulation $\triangle n$ can be expressed by

$$\triangle n = k_f \triangle n_w \quad (2)$$

where k_f is a constant gain factor or swelling factor. According to the Kogelnik's coupled wave theory, the diffraction efficiency for transmission phase volume holograms is given by

$$DE = \sin^2\left(\frac{\pi \triangle nd}{\lambda \cos\theta_0}\right) \quad (3)$$

where λ is the reconstruction wavelength in air, θ_0 is the Bragg angle, and d is the hologram thickness.

Experimental Results and Discussion

To study the effects of various parameters and holographic exposure characteristics on the high drying method of the sensitized DCG plate, transmission holographic gratings with spatial frequency of about 1500 lines/㎜ have been recorded by using Ar-ion laser with a wavelength of 457㎚. The irradiance of each beam was taken to be equal, and the angle between the two beams was 40°. The Agfa 8E75HD plates whose gelatin thickness is about 7㎛. The physical characteristics investigated include DE, absorption spectrum of the sensitized DCG, Bragg angle deviation, and degree of hardness. All the chemicals are dissolved in tap water (pH 7.63) and the processes are conducted at room temperature. The detailed preparation and development method for DCG plate developed in this work is shown in Table Ⅰ.

The DE was measured simultaneously during the hologram recording by placing a detector in one of the diffracted beams of the He-Ne laser at 633㎚ wavelength.(Fig. 1) He-Ne laser beam is not absorbed by the Cr ions in DCG and does not affect the hologram formations. Figure 2 illustrates the typical experimental result for DE against exposure time. The absorbance of the unexposed DCG at 457㎚ light is the order of 0.28. From the experimental curve, we estimated the maximum refractive index modulation was about $\triangle$n=0.022, and the corresponding phase shift is $\triangle \psi_{max}$=1.126. We also measured the reconstruction angle response as shown in Fig. 3. It is noted that after the development processing the maximum reconstruction angle corresponding to maxmium DE is shifted about 1.4 degree from Bragg angle at the initial recording. Figure 3(a) shows the reconstruction angle of the maxmium DE as a function of exposure and Fig. 3(b) shows angular response of the grating (1500 lines/㎜) in the gelatin layer.

Figure 4 represent the DE curves according to various processing conditions. The final hologram thickness mainly depends upon two step preprocessing parameters.

The curve C represents the DE of the gratings formed by Georgekutty and Liu's method.[6] The maximum DE is obtained about 28%. There are swelling proportion of 3.8 times as compared with curve D method. The curve D presents the DE of the gratings formed by Table-Ⅰ, which is obtained from the process without hot water (step 5) and using hardener fixer instead of non-hardener fixer (step 1). The maximum DE were

obtained about 8.6%. This result indicates that the gelatin of Agfa 8E75HD plates is extremely hard. The curve B presents the DE by method of Table I without hot water (step 5) and using non-hardener fixer (step 1). The maximum DE is about 38%. The relative swelling value increases to the proportion of 5.4 times as compared with curve D method. The curve A presents the DE by method of Table- I . The maximum DE is about 80%. The relative swelling value increases to the proportion of 9.2 times as compared with curve D method. The crucial step in producing the efficient strong phase hologram recording is immersion in non-hardener fixer and hot water (80℃). We think that the process increases the optical path length differences of the plate such a large value that efficient phase holograms can be produced. The gelatin hardness is an important parameter because it almost influences the optical property of DCG holograms. The result implies that DE depends on non-hardener fixer and hot water (step 5) in processing method. Finally, our simplified method also includes the baking the sensitized DCG plate in the oven (85±5℃) for 10 min. This is not necessary to have overnight drying of the gelatin plate in stringent temperature and relative humidity conditions proposed by Oliva's method. In conclusion, a simple method preparing high efficient DCG plates from Agfa 8E75HD plates, is presented, and it is easy to obtain DCG HOE's of high diffraction efficiency over 80%. Furthermore, one can see that the whole process only requires 2 hours, and the present process is relatively less sensitive to relative humidity when compared to Oliva's process.

Table I . Simplified Fabrication Procedures of DCG film with Agfa 8E75HD Plates

(1) Soak in non-hardener fixer for 15 min.
(2) Wash in running water for 15 min.
(3) Soak in methyl alcohol for 10 min.
(4) Soak in clean methyl alcohol for 10 min.
(5) Soak in hot water (80℃) for 10 min.
(6) Soak in 5% ammonium dichromate solution
(with 1% of Kodak photo-flo 200) for 15 min.
(7) Bake for 10 min at 90±5℃.
(8) Exposure (Ar+ laser, λ=457㎚)
(9) Soak in 0.5% ammonium dichromate solution for 5 min.
(10) Wash in running water for 10 min.
(11) Dehydrate in 50% isopropyl alcohol for 5 min.
(12) Dehydrate in 100% isopropyl alcohol for 5 min.
(13) Dry over 10 min with flowing hot air at 85±5℃.

REFERENCES

[1] T. A. Shankoff, Appl. Opt. **7**, 2101 (1968).
[2] R. K. Curran and T. A. Shankoff, Appl. Opt. **9**, 1651 (1970).
[3] D. Meyerhofer, Appl. Opt. **10**, 416 (1971).
[4] D. Meyerhofer, RCA Rev. **33**, 110 (1972).
[5] B. J. Chang and C. D. Leonard, Appl. Opt. **18**, 2407 (1979).
[6] T. G. Georgekutty and H-K. Liu, Appl. Opt. **26**, 372 (1987).
[7] T. Keinonen and O. Salminen, Appl. Opt. **27**, 2573 (1988).
[8] J. Oliva, P. G. Boj and M. Pardo, Appl. Opt. **23**, 196 (1984).

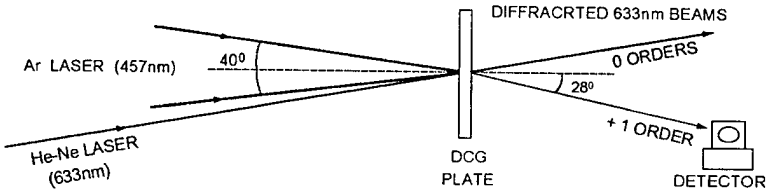
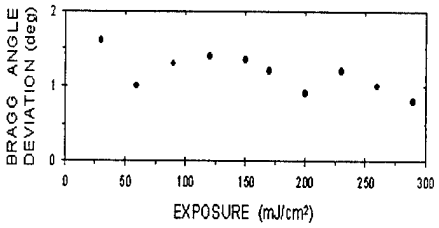


Fig. 1. Experimental arrangement for measuring the phase change due to exposure alone.



(a)

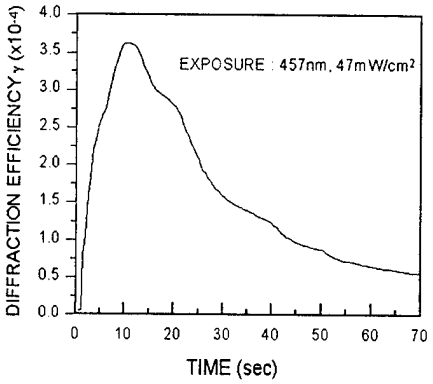
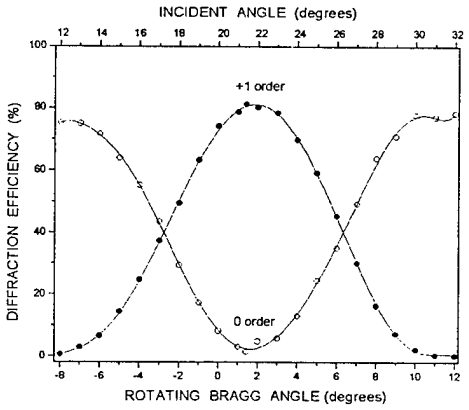


Fig. 2. Diffraction efficiency against time



(b)

Fig. 3. (a) Reconstruction angle for obtaining maximum diffraction efficiency, and (b) Angular response of the diffraction efficiency against Bragg angle deviation.

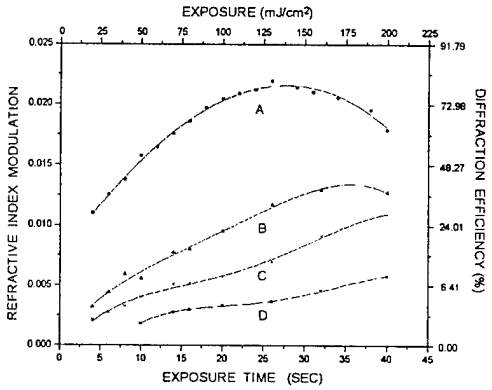


Fig. 4. Effect of the initial degree of hardening on the diffraction efficiency (measured at 457nm).

Analysis of Focal Tolerance and Fine Pattern Resolutions Formed by Phase Conjugation in Dichromated Gelatin Hologram

Yong Seok Im, Young Lak Lee, Chong Hoon Kwak and Ok Shik Choe
Department of Physics, Yeungnam University,
Kyongsan, 712-749, Korea
(Fax: +82-53-813-4465, e-mail: chkwak@ynucc.yeungnam.ac.kr)

Introduction

Submicrometer photolithography necessitates high resolution imaging system. Optical holography is one of the promising candidates for realizing such high resolution imaging systems. Several optical system utilizing holograms have been demonstrated until now including far-field holograms, image holograms, and focused image holograms. In order to achieve the required high resolution, there is to decreasing the wavelength or to increasing the numerical aperture. Two fundamental parameters limiting an optical system are the numerical aperture, NA, and the size of the image field of the imaging optics.[1] For a given wavelength, the resolution is improved by increasing the numerical aperture. As a result, the increasing NA lead to decreasing the focal tolerance. In this paper we present the high resolution holographic imaging system using a focused imaging hologram with phase conjugate wave and demonstrated a long focal tolerance of an image.

Holographic Principles

Figure 1 illustrates the focused holographic construction and reconstruction processing. The minimum construction beam angle, $\theta_{\min}$, required to insure that the re-constructed image can be observed without any interference from its twin image as well as from the surrounding halo of scattered light is given by[2]

$$\theta_{\min} = \sin^{-1}(3NA_{hologram}) \qquad (1)$$

The use of a lens to focus the image onto the holographic recording material permits a larger numerical aperture. The numerical aperture as seen by the high resolution recording material is defined as

$$NA_{hologram} = \frac{NA_{object}}{M_{mag}} \qquad (2)$$

where $NA_{hologram}$ is the numerical aperture at the hologram plane, NA_{object} is the numerical aperture at the object plane, and M_{mag} is the magnification of the

object at the hologram plane. The spatial frequency is frequently used to refer to either the angular direction of propagation of a plane-wave component of a complex wavefront or to the spatial rate of change of the holographically recorded interference pattern. When it used to define the direction of propagation of a plane wave component, the spatial frequency refers to the spatial rate of change of the phase of the wavefront across a suitably chosen the axis of an optical system. The spatial frequency is related to the angle of the wavefront (θ) by[3]

$$\nu_w = \frac{\sin\theta}{\lambda} \tag{3}$$

When this wavefront is allowed to interfere with a reference wavefront, whose angle of arrival is ψ, the resulting interference pattern has a spatial frequency give by

$$\nu_r = \frac{\sin\theta - \sin\psi}{\lambda} \tag{4}$$

When the reference wave propagates along the normal to the observation plane

$$\nu_w = \nu_r \tag{5}$$

The intensity distribution near focus is of particular importance in estimating the tolerance in the setting of the receiving plane in an image-forming system. The properties of the out-of-focus monochromatic images of a point source by a circular aperture were first discussed in Ref. [4]. It follows that focal tolerance $\triangle z$ is approximately given by[4]

$$\triangle z = \pm 3.2 \frac{\lambda}{2\pi} \left(\frac{f}{a}\right)^2 \tag{6}$$

where f is the distance of the focal plane from the hologram mask of aperture, a is the radius of the hologram mask of aperture. Since the numerical aperture of the hologram is given by $NA_{hologram} = a/fq$, for the case of $f \gg a$, $q \approx 1$ (equivalently $f \cong fq$). Hence, the ratio a/f can be defined as the numerical aperture of hologram. We have the expression for the focal torelence of the hologram of the form:

$$\triangle z \approx \pm 3.2 \frac{\lambda}{2\pi} \left(\frac{1}{NA_{hologram}}\right)^2 \approx \pm \frac{4.58}{\lambda \nu^2} \tag{7}$$

Experimental Results and Discussion

The holographic imaging system for both constructing a hologram of the mask and reconstructing the image of the mask is shown in Fig. 1. The theoretical resolution of the fully coherent imaging system is λ/2NA=0.57μm (λ=457nm, NA=0.4). Figure 2 shows the theoretical maximum resolution of the imaging system. The numerical aperture $NA_{hologram}$ of the hologram is plotted as a function of line width. TEM_{00} mode of Ar-ion laser at 457nm wavelength is used as a

light source. A light beam is splitted into two beams by using a variable beam splitter. Both illuminating beams are first focused to a diffraction limited spot with a microscope objective, and then collimated with a lens corrected for infinite image to object ratio. To form a focused hologram, the beam is focused by a condenser lens to trans-illuminate the mask by imaging the source into the entrance pupil of the imaging lens. The hologram mask is formed at this plane using the dichromated gelatin (DCG) as the high resolution recording material.[5-6] The preparation and the development of DCG derived from Agfa 8E75HD plates. The DCG is exposed simultaneously to both the focused image and the second collimated beam, as shown in Fig. 1(a). The focused image holograms were constructed using the IC pattern mask or the USAF-1951 resolution target mask. In order to test the focal tolerance of an image formed by the holographic phase conjugation, the recorded images are reconstructed at the focal point and then the hologram mask is scanned along the optic axis by using the linear motor (Encoder Mike: 0.05㎛/sec) along optical axis. Theoretical focal tolerance of 1㎛ and 2.2㎛ line width of the hologram mask were ±40.12㎛ and ±192.94㎛, respectively. The corresponding focal tolerance observed are about ±37㎛ and ±180㎛, respectively. Figure 3(a) shows a photo-micrograph of the reconstructed image (1㎛ line width of the IC pattern mask) in the forward moved position of 37㎛, and Fig. 3(b) is a photo-micrograph of the reconstructed image (2.2㎛ line width of the USAF-1951 resolution target mask) in the forward moved position of 180㎛.

References

1. Victor Pol, James H, Bennewitz, Gary C. Escher, Martin Feldman, Victor A. Firtion, Tanya E. Jewell, Bruce E. Wilcomb, and James T. Clemens, "Excimer laser-based lithography: a deep ultraviolet wafer stepper", Optical/Laser Microlithography V, **633**, 6-16, SPIE, (1986).
2. G. Addiego and W.G. Oldham, "High-Resolution Imaging Using Focused-Image Holography with Wave-Front Conjugation", Optical/Laser Microlithography, **922**, 18-25, SPIE, March2-4, (1988).
3. Marvin J. Weber, "*Handbook of Laser Science and Technology*", Vol **V**, CRC Press, Florida, (1988).
4. Max Born and Emil Wolf, "*Principles of Optics*", Pergamon Press, Oxford, 1983.
5. J. Oliva, p. G. Boj, and M. Pardo, "Dichromated gelatin holograms derived from Agfa 8E75HD plates", Applied Optics, **23**, 196, (1984).
6. B. J. Chang and C. D. Leonard, "Dichromated gelatin for the fabrication of holographic optical elements", Applied Optics, **18**, 2407, (1979).

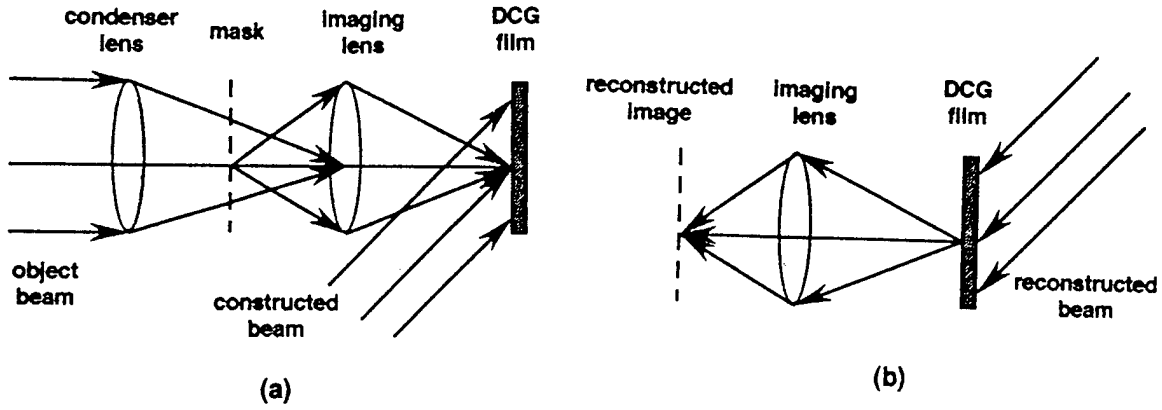


Figure 1. Schematic of the construction and reconstruction process for focused image holography.

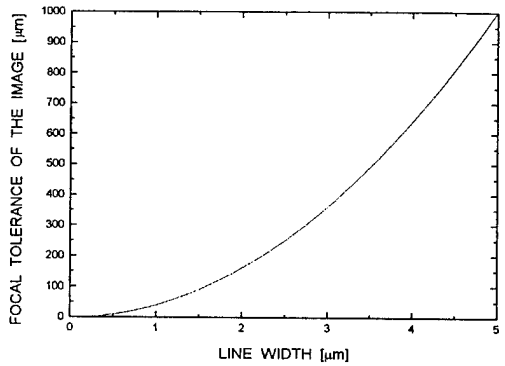
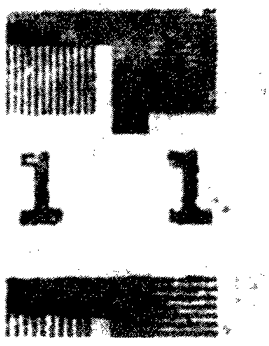
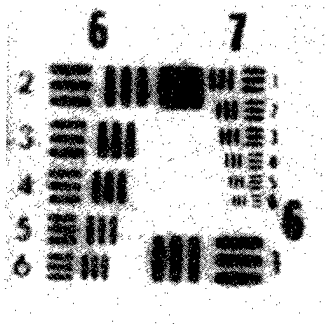


Figure 2. Theoretical focal tolerance $\triangle z$ of the imaging system versus the line width of the hologram mask.



(a) Imaging of 1μm line width position of 37μm in the forward



(b) Imaging of 2.2μm line width position of 180μm in the backward.

Figure 3. Photo-micrograph of the reconstructed aerial image of the hologram mask.

Wavelength agile fluorescence microscopy filter using photorefractive barium titanate.

Robert Kersten and Salvador Fernandez
Ciencia Inc.
111 Roberts St, Suite C
East Hartford, CT 06108.

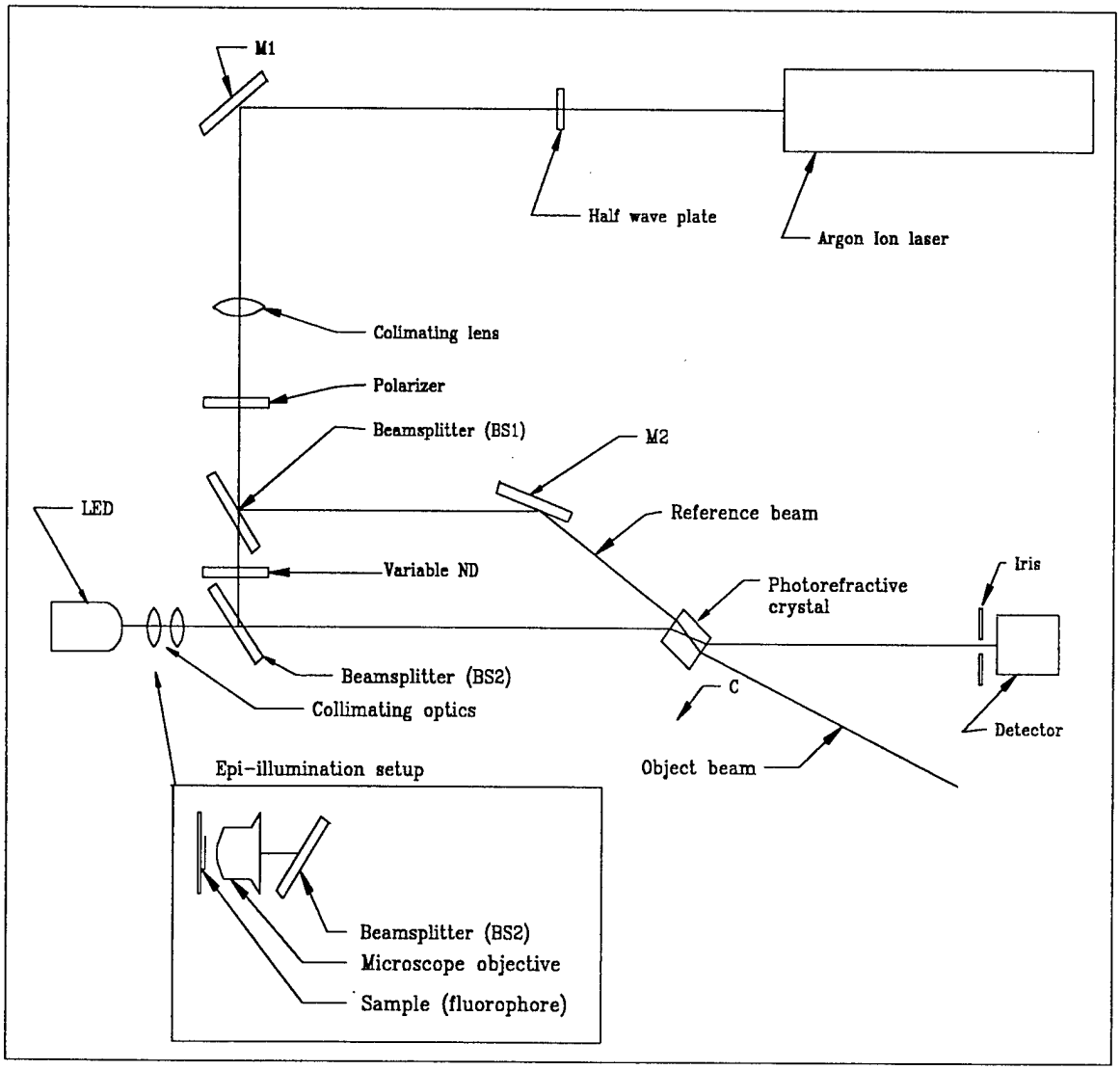
George Fischer and Robert Boyd
Institute of Optics
University of Rochester
Rochester, NY 14627.

We describe a wavelength-agile holographic notch filter (WAHNF) suitable for attenuating scattered laser light from the fluorescence signal in laser induced fluorescence (LIF) applications. The WAHNF utilizes a photorefractive material, specifically $BaTiO_3$, and the technique of two beam coupling to attenuate the coherent portion of the signal to be detected[1]. Static holograms recorded in film emulsions are routinely used for this purpose but have the limitation that they are fixed notch-band devices. In contrast, the WAHNF enables tuning or switching the excitation wavelength while passively adapting to maintain the notch band centered on the laser wavelength.

Two-beam coupling, with its ability to transfer energy from one beam to another, is the method chosen to accomplish the filtering[2]. A 5mm x 5mm x 5mm $BaTiO_3$ crystal with a 90 degree C axis geometry is used and oriented so that the energy from the object beam is transferred to the transmitted reference beam. In LIF applications, the signal is comprised of the very narrow band portion from the excitation laser light and the broad band fluorescence emission which is Stokes-shifted away from the excitation light .

The experimental configuration shown in Figure 1 was initially used without the LED to demonstrate the WAHNF's wavelength-agility. First, two-beam coupling was achieved at 514nm and the extinction coefficient measured; then the wavelength from the argon ion laser was changed to 488nm and the extinction coefficient was measured again. The photorefractive holographic filter was shown to maintain good energy transfer at both wavelengths without any adjustments to the experimental configuration.

Figure 1



For the next step, a broad band 650 nm LED light source was made colinear with the object beam by inserting a dielectric beamsplitter in the position of BS 2. The 650nm wavelength was chosen because it was the highest power visible LED available. This setup demonstrates the WAHNF's capability to attenuate the coherent laser light while passing the broad band LED incoherent light which

simulates the fluorescence emission that would be obtained in a LIF application. The final step was to replace the LED setup with an epi-illumination fluorescence microscopy arrangement as shown in the box in figure 1. The object beam is reflected off BS 2 into a microscope objective and onto a small cuvette which holds the fluorophore. At the detector, the laser excitation light is attenuated by approximately two orders of magnitude while the Stokes-shifted fluorescence is unaffected. Rhodamine was used as a fluorophore since it exhibits significant excitation at both 488nm and 514nm, allowing us to demonstrate wavelength-agility with this configuration.

Our results demonstrates the ability to use a wavelength-agile photorefractive holographic filter in a biological application to achieve greater spectral flexibility. This is important in many LIF applications where multiparameter or ratiometric measurements at more than one excitation wavelength are required.

References.

1. Theo Tschudi, Andreas Herden, Joachim Goltz, Harald Klumb, Franco Laert and Johan Albers, IEEE J. Quantum Electron., QE-22, Aug 1986, p. 1493-1502.
2. S.W. McCahon and M.B. Klein, SPIE 1105, 1989, p.119-122.

Holographic Interferometry Methods for Conducting Stress Analysis on Quartz Crystal Components

Jill A. Brosig
Senior Development Engineer
Motorola, Quartz Products Division
1301 E. Algonquin Rd.
Schaumburg, IL, 60196
Phone 708-576-5673
Fax 708-576-1689

The technique of holographic interferometry has aided in Motorola's Quartz Products Division's continuous pursuit of higher quality quartz crystal components. QPD's portfolio consists of several models of quartz crystals, which are sold as resonators, oscillators, and filters. The crystal frequency for the various products ranges from 12 MHz to 100 MHz.

Products discussed in this paper include AT-cut quartz resonators and quartz filters. Both leaded and surface mount packages were studied. Surface mount parts are attached directly to the radio board whereas the lead formed pieces are hand soldered on.

An oscillator is any device that resonates at a selected frequency or range of frequencies. In simple terms, a tuning fork is an oscillator. In the electronics industry, however, an oscillator is a device that uses the principles of the piezoelectric effect to produce a predetermined output frequency. The basic construction consists of a resonator, in this case a quartz crystal, a power source, and required circuitry. The quartz crystal resonator is equivalent to an inductor connected in series with a capacitor and a resistor.

A crystal filter is a device which allows the receiver circuitry to efficiently select and process the chosen frequency. This is necessary since the overflow of wireless communications has limited the number of radio channels. As the radio channel spacing becomes tighter, the need for higher performing filters increases.

The production of an AT quartz crystal component begins with the cutting of 2" x 2" wafers from a bar of manmade or cultured quartz. The angle at which the quartz bar is cut determines the end product's frequency stability over temperature, and the thickness of the cut wafer determines the frequency. After the cutting process, a series of metals are then deposited on the wafers, followed by a photolithographic process which produces 140 crystals per wafer. The finished crystals are then mounted in appropriate housings.

When an AT cut crystal approaches the infinite plate approximation and is in a stress free environment, the generalized frequency-temperature relationship follow what is known as Bechmann curves. Within this scenario, the inflection temperature is 26 C. Depending on how stress affects the crystal lattice, the inflection temperature can range from as low as 22 C to well above 30 C. By lowering the inflection temperature, the frequency stability of the crystal becomes more controlled. As the industry moves to smaller and smaller telecommunication devices, these types of components become highly desirable as they can replace their larger counterpart, the oscillator.

One theory as to how the inflection temperature can be lower than that at the stress free condition is through the presence of a beneficial stress, either tensile or compression. The beneficial stress hypothesis can be accepted or nullified by using holographic interferometry to relate stress patterns to yields.

Understanding the mechanics of the leaded and surface package will aid in optimizing both product lines. Through the use of holographic interferometry, studies were conducted which determined the stress patterns of the quartz crystal over several environmental perturbations, including temperature, vibration, and drive level. The temperature studies will be discussed here.

The first objects used in the first holographic interferometry experiments consisted of crystal resonators. These crystals were 300 mil in diameter, set at 19.1 MHz, had an unpolished surface, and were mounted in leaded packages. These units were built on two different designs, either a clamp or slot post, and using two types of adhesives, referred to as A and B. At 25 C the slotted mount exerted a tensile stress on the blank, while the clamp design held the quartz under compression. Those products, which recorded inflection temperatures between 22 and 24 C, used a slotted mount design.

The experimental parts were manufactured identical to those run through production, except they were not sealed or plated. The sealing process prevents the blank from being seen and the gold plating interferes with hologram developing by reflecting the laser beam rather than diffusing the light.

These pieces were tested for both in-plane and out-of-plane displacements over the temperature ranges 25 C to 70 C, 35 C to 70 C, and 45 C to 70 C. All the various build cells of this experiment were studied simultaneously, in order to eliminate time and temperature as factors between successive runs. Unfortunately, the equipment used in the crystal design experiment was not capable of performing sandwich holography. Instead, real time holography was used with reference holograms taken at 25 C, 35 C, and 45 C.

The holography setup used was a workstation, manufactured by the Newport Corporation. The light source was a HeNe laser, with a wavelength of 632.8 nm. The system consisted of a free standing enclosed unit and a control console, which creates a hologram within one to two minutes.

These crystal resonators were cycled through temperature vial a hot plate, which was controlled by a Thermo/cense temperature controller. The temperature controller used an RTD capable of accurately reading temperature to +/- 0.2 C. The temperature controller resided outside the optics table for easy access and viewing during the holographic studies.

The holocamera consisted of the camera module and the electronics module. The former holds the thermoplastic plate, on which the hologram is recorded, and the components needed for the recording process. The later module contains the operating panel, control logic and power supplies. The electronics have the capability of activating a variety of holocamera functions.

Throughout the holographic experiments they are viewed via both a video monitor and computer monitor. The resulting fringe patterns are stored on video taper for future viewing and image analysis. The software used for image analysis is manufactured by Automatix, Inc. of Billerica, MA. In conjunction with McRail software, strain is calculated in the x-y direction. This software is limited by only being able to measure strain in two dimensions, however due to the geometric nature of the quartz blank this is sufficient.

The interference patterns obtained from these experiments were examined for fringe number, movement, and location. Experiments were then replicated for repeatability. These additional experiments eliminated part location and orientation as a factory.

The fringe patterns for the out-of-plane displacement studies showed the greatest movement occurred with the clamp mount and adhesive B. For example, when examining those runs where the reference hologram was taken at 25 C, the fringe rotation of this design was 360 degrees. The designs of the adhesive A and the clamp mount and adhesive B and the slot mount showed comparable fringe movement, both near 180 degrees. Adhesive A and the slot mount showed the least movement with under a 90 degree fringe rotation. Initial in-plane displacement measurements did not detect localized strains.

In addition to those crystal packages built for holography, similar production pieces were plated and sealed. These units were then placed in an environmental chamber and run through a temperature cycle (-30 C to 70 C), which measured frequency and resistance at eight temperature points. Corresponding inflection temperature values were derived from this data.

In general, the higher the inflection temperature, the greater the displacement over temperature. It is interesting to note that regardless of the mount design, and inflection temperature near 27.75 C is recorded when the adhesive B is in contact with the quartz. In fact, this is true across product lines. This indicates that adhesive B decouples any stress associated with the mounting package, and only introduces a localized stress between itself and the quartz blank.

Note that at 25 C the slot mount holds the quartz blank in a tensile state, while the clamp mount holds the piece in compression. When adhesive A is used, the quartz blank can be thought of as coupling directly to the mount. The clamp mount has a wider range since holographic results indicated that it undergoes up to twice as much movement as the slot design. In fact, it may surpass the tensile value of the slot mount on the cold temperature end.

Therefore, this experiment used holographic interferometry to aid in optimizing the crystal package by relating stresses exerted on the blanks due to mount design. The observed fringe patterns showed object displacement as a function of time and temperature. Results were that the rigid clamp mount undergoes greater change of displacement than the more forgiving slot mount. A direct relationship was made between quartz displacement and the inflection temperature. The quartz blanks, which were mounted with adhesive B, showed more movement that those on the same design mounted with adhesive A. Results indicated that adhesive A coupled the blank to the mount, similar to a C-clamp, while adhesive B acted like a spring between the two interfaces. Therefore, based on this experiment, QPD was able to optimize the frequency stability of their round blank crystal resonator products by going to a slot mount design and using adhesive A.

Similar experiments are also being conducted on crystal filters. As with the crystal resonators, these parts are being cycled through temperature, however in this case the initial cure phase is also being studied. It appears that the curing process, in conjunction with the makeup and placement of the adhesive, is producing a localized stress upon the quartz blank. The introduction of this stress is resulting in broken blanks as a function of normal usage. Various types and placements of adhesives are being studied via holographic interferometry in order to correct this issue.

A Computational Model for Holographic Sensing

Ben Bakker
University of Massachusetts at Lowell
Val Bykovski
VirTek, Inc. and University of Massachusetts at Lowell

1. *Introduction.* An existing analytical concept based on spectral decomposition has been developed more than hundred years ago, and is presently close to its limits in terms of performance and reliability, in particular, for complex samples. For molecules, a spectrum is a very complex pattern of sharp lines and continuous bands. So, in a classical spectrometer, detection is pruned to *overlapping* errors when two or more components of a sample have overlapping lines, and their separation is, generally, *a non-unique* problem. Indeed, a line can be assigned to, at least, two different transitions (in the same or different atom/molecules in a sample). Such an assignment based on line positions and transitions has limitations, and may not work at all for complex samples. As samples are getting more and more complex, the problem becomes increasingly intractable. In particular, algorithms and data processing to analyze complex spectra become very complex, require sophisticated peak analysis, etc. A mathematical "inversion" procedure for assignment and identification of components (species) also becomes unstable. That is, the current situation has all signs of a *critical botlleneck*, and requires an innovative approach. Meanwhile, *selectivity* is the first priority for many industries and applications. For instance, in the field of air toxics detection, the US EPA requires 189 components to be detected and regulated, and it is highly doubtful that any existing spectrometer is able to analyze reliably such a complex gaseous medium.

2. *An approach* [4]. The proposed approach *revises* the existing analytical paradigm and is aimed to create a foundation for a new class of high performance *knowledge-based* sensors. We replace a "dumb" prism or diffraction grating (DG) by a recordable optical holographic storage which makes the sensor a programmable *knowledge-based* device that is able to store light patterns for various species. Light from a sample interacts with the *reference* light patterns recorded holographically in the sensor memory and reconstructs *an output species mapping*, for example, a position-sensitive mapping of the species in the sample. It may be detected, say, by a CCD array and then used for any process control application. In other words, the holographic sensor is a *knowledge-based* one, and can be species- or application-specific. It makes analysis easier as the primary measurement immediately generates the final result, a sample composition, without any need for sophisticated data analysis and processing such as peak identification.

Holographic recording of a spectrum was first demonstrated by Stroke and Funkhouser [1]. They used a holographic method of Fourier-transform (FT) spectroscopy which permits one "to obtain the spectrum without any computation, and indeed in an interferometric system having completely stationary elements and medium". The interference fringe system was proportional to a non-coherent superposition of the monochromatic fringe systems for each wavelength λ. Experimentally, a light of a cold mercury arc has been recorded holographically on a photoplate and then successfully reconstructed with the 632 nm HeNe laser. A symmetrical spectrum has been obtained

with all characteristic mercury line systems. Holographic FT spectroscopy allows one "recording" spectra on a lensless, slitless and completely static interferometric assembly of two mirrors, simply pointed in the general direction of a diffuse source. Another way to record interferometrically mercury spectrum has been demonstrated in [2].

The proposed method combines two normally separated functions: (1) identification (recognition) of a light pattern (not necessarily a spectral one) from a sample and (2) its decomposition or mapping in the "space of species" rather than in the spectral, wavelength space. Another advantage of the proposed detection concept is that the holographic sensor is highly selective (it is a volume Bragg selective grating), whereas the conventional dispersing element, a periodical diffraction grating is, in fact, an extreme case of *nonselectiveness*. In the proposed method, a multi-wavelength light pattern rather than a single spectral line of a species is used for detection and mapping. This is why the *overlapping error* is quite unlikely.

The holographic sensor may as well respond to a *combination* of components of a sample which seems to be important for many applications. The optical holographic sensors do not require sophisticated data processing thus opening a way to compact, reliable, *in-situ* sensors/analyzers. Additionally, an *all-optical* sensor is noise-resistant in industrial and combat environments. Power supply may also be not needed as optical output may indicate directly a species detected (say, by its position on a calibrated range).

3. *A model.* We consider a simplified model of computer-generated holographic sensor (CGHS). We use a species spectrum to build CGHS. A software was developed to select the n major peaks from an absorption spectrum. An n-plexed hologram was created using a point source object and plane wave reference beam in each case. Figure 1 shows 256 gray-scale image of an CGHS for acetone (CH_3COCH_3). The computational resolution is 500x500 pixels. Seven peaks were selected and multiplexed. Spectral data was obtained from the EPA/AEDC Spectral Database.

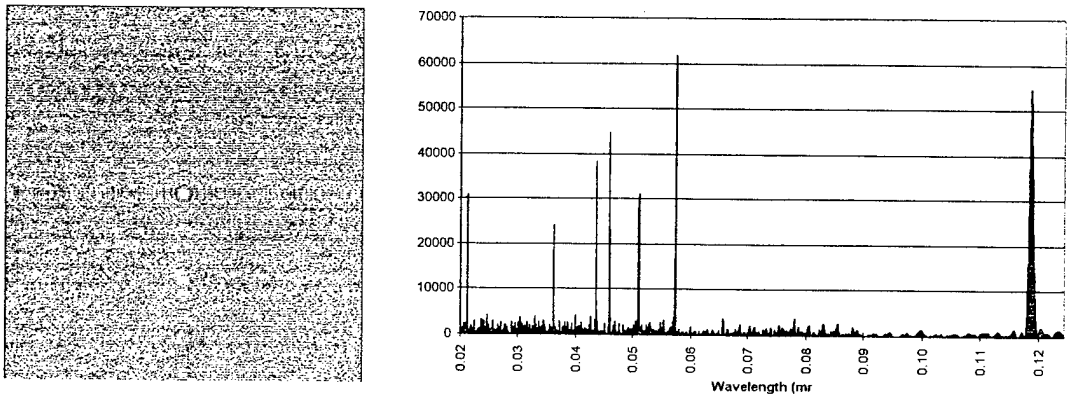


Fig. 1: (a) Computed 256 gray-scale image of multiplexed CGHS for seven spectral peaks from acetone. (b) A spectral response obtained by multiplexing of a scanned spectrum of acetone (7 lines are taken). Each of the seven original acetone peaks is reconstructed, and a high spectral selectivity of the CGHS is obvious.

Both recording and reconstruction were accomplished using a discretized Fresnel integral. The reconstruction using the original acetone spectrum generates a response at the central maximum which is more than 100 times greater than the reconstruction is done with a spectrum of toluene. Further computational experiments revealed a nearly linear dependence on the number of acetone lines present. With five acetone lines present (0.0211, 0.0362, 0.0437, 0.0460, and 0.0576 mm), the intensity of the central maximum was 228,814. With two acetone lines present (0.0437 and 0.0576 mm) the central maximum was 106,155. That is, the proposed detection method is robust to individual spectral lines that may be removed from spectrum without affecting significantly the response. Simply flat "white" background which simulates a thermal one leads to response .016 times acetone response. That, in turn, means that the detection is robust to thermal background.

Further simulation results will be presented including the demonstration of *generalization* capabilities of the holographic sensor which can be designed and built to detect families of chemical components such as "toxic metals", "aromatic cancerogenes", etc.

Acknowledgment. Authors thank Prof. Mike A. Fiddy and Dr. Drew Pommett of University of Massachusetts at Lowell for very useful discussions. Support for Dr. Val Bykovski from the National Science Foundation Grant No. DMI-9523207 to VirTek, Inc. is gratefully acknowledged.

References:

1. G.W. Stroke, A.T.Funkhouser, "Fourier-Transform Spectroscopy Using Holographic Imaging without Computing and with Stationary Interferometers", *Physics Letts.* **16**, n3, pp.271-74 (1965)
2. K. Yoshihara, A. Kitade, "Holographic Spectra Using a Triangle Path Interferometer", *Japanese J. Appl. Phys.* **6**, 167 (1967)
3. H.J. Caulfield, "Holographic Spectroscopy", *In: Advances in Holography,* v.2, Dekker, N.Y., 1976
4. V. Bykoski, M. A. Fiddy, "A Novel Holographic Analyzer Concept and Apparatus". *Patent Pending,* 1995

Computer-generated hologram for reconstruction of unusual mode image

Gao Wenqi Tan Suqing Zhou Jin
(Department of Physics, Nanjing University, Nanjing210093)

Introduction

Usually in reconstruction of Fourier computer-generated hologram[FCGH] the lens is necessary to make imaging at finite distance instead of imaging at infinite originally. The reconstructed images are mutual inverted (one upright image,another inverted image) both appear in a same plane. Whether the imaging lens in reconstruction FCGH will be able to omit? Whether two reconstructed images will be able to separate in spatial? Whether two images have an identical direction and different shape in the same plane? It is the motivation for us to do this study.Through theoretic analysis and experimental reconstruction these assume can be realized essentially.

Principle

In reconstruction configuration of FCGH, as shown in Fig.1 only by virtue of the Fourier lens (F.T.lens) to complete Fourier transform,computer-generated Fourier hologram can reconstruct the image of original object and the conjugate image.The transmission function of Fourier lens in reconstructive geometry is :

$$T = \exp[-jk(x^2+y^2) / 2f] = \exp[i\,\theta\,(x,y)]^1 \quad (1)$$

where f indicates the focal length of a lens, k is wave number, $k=2\pi/\lambda$, λ is the wave length. Here the constant phase delay associated with the lens has been omitted since it dose not affect the result in any significent way .

Thus it can be seen that the effect of a lens in reconstruction is equal to introduce a qudratic phase factor $\exp[-jk(x^2+y^2) / 2f]$.If U(x,y) expresses optical field behind FCGH, thus the optical field U'(x,y) behind the positive lens is:

$$U'(x,y) = U(x,y)\exp[-jk(x^2+y^2) / 2f] \quad (2)$$

That shows the quadratic phase factor may be added in frequency spectrum of FCGH directly.

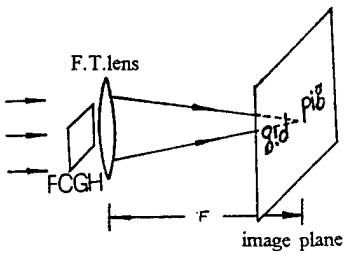


Fig1. The reconstruction configuration of the usual FCGH

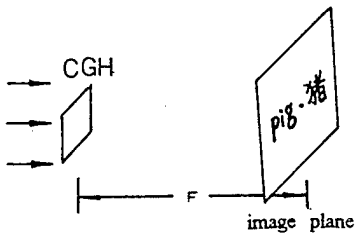


Fig2. The reconstruction configuration of the unusual CGH

Following,this hologram has been further discussed dividing into three cases. In order to explain physical principle conveniently, the continuous function is adopted in discussion instead of discrete form in practical calculation.

1). Adding directly positive lens factor into frequency spectrum of a object.

Assuming objecte function is f(x,y),object's frequency spectrum function is $\mathcal{F}f(x,y)$, when adding the quadratic phase factor the optical filed is:

$$U(f_x,f_y) = \mathcal{F}f(x,y) \cdot \exp[i\,\theta\,(f_x,f_y)] \quad (3)$$

where $\theta(f_x,f_y)]$ is the added quadratic phase factor,

$$\theta(f_x,f_y)] = [-k(f_x^2+f_y^2)/2f]$$

When CGH has recorded information of $U(f_x,f_y)$,the optical filed +f distance away from this CGH is:

$$U_0(x_0,y_0) = [\exp(jkf)]/j\lambda f \cdot \exp[jk(x_0^2+y_0^2)/2f] \cdot \iint U(f_x,f_y) \cdot \exp[jk(f_x^2+f_y^2)/2f] \cdot \exp[-j2\pi(x_0f_x+y_0f_y)/2f]df_xdf_y$$
$$= [\exp(jkf)]/j\lambda f \cdot \exp[jk(x_0^2+y_0^2)/2f] \cdot \mathcal{F}\mathcal{F}[f(x,y)]] \quad (4)$$

In formula, except phase factor the $\mathcal{F}\mathcal{F}[f(x,y)]]$is Fourier transform of object's frequency spectrum, i.e. $\mathcal{F}\mathcal{F}[f(x,y)]]$ is the image filed of original object, the phase factor not acts on observing intensity.

Because detour phase encoding method[2-3] is adopted in CGH, the phase of −1 order and -1 order are mutual conjugate in reconstruction.When adding the positive lens phase factors, image of original object can be reconstructed exactly on +1 order. For -1 order, the added positive quadratic phase factor converts sign that is equal to qudratic phase factor of negative lens $\exp[-i\theta]$. For -1 order, the optical filed also became $U^*(f_x,f_y)$,thus,inverted image of original object can be recontructed on -1 order -f distance away from the CGH. Therefore,when unit-amplitude parallel light illumnates this CGH, one reconstructed image appears on +1 order location; For -1 order,which is equivalent to add a negative lens, a light spot is seen in -1 order location and -1 order reconstructed image is actually in negative focal length -f (here the light spot is defocussed image of -1 order reconstructed image). Thus, the lensless spatial separation of reconstructed images at −1 order and -1 order comes ture. Similarly, adding negative quadratic phase factors into frequency spectrum of object, conjugate image appear in -1 order location and a light spot appears in +1 order location.

2). Adding positive lens factors into frequency spectrum of object and adding negative lens factors into conjugate frequency spectrum of object.

Assuming object function is f(x,y), the function of object's frequency spectrum is:

$$\mathcal{F}[f(x,y)]=A(f_x,f_y)\exp[i\phi(f_x,f_y)] \quad (5)$$

the function of object's conjugate frequency spectrum is:

$$\mathcal{F}^*[f(x,y)]=A(f_x,f_y)\exp[-i\phi(f_x,f_y)] \quad (6)$$

let formula (5) add positive lens factor $\exp[i\theta(f_x,f_y)]$and formula (6) add negative lens factor $\exp[-i\theta(f_x,f_y)]$ respectively then adding:

$$A(f_x,f_y)\exp i[\phi(f_x,f_y)+\theta(f_x,f_y)] + A(f_x,f_y)\exp -i[\phi(f_x,f_y)+\theta(f_x,f_y)]$$
$$= 2A(f_x,f_y)\cdot\cos[\phi(f_x,f_y)+\theta(f_x,f_y)] \quad (7)$$

obviously, now only two times real part exist,virtual part vanish.Thus, two identical direction images appear simultaneously at +1order location and - 1 order location on the same plane when reconstructing.

3). Adding positive lens factor into frequency specturm of oneobject and negative lens factors into conjugate frequency spectrum of another different object respectively.

Assuming a object f(x,y) through Fourier transform,function of object's frequency spectrum is:

$$\mathcal{F}[f(x,y)]=A(f_x,f_y)\exp[i\phi_A(f_x,f_y)] \quad (8)$$

Assuming another object g(x,y) through Fourier transform,function of object's conjugate frequency spectrum is:

$$\mathcal{F}^*[g(x,y)]=B(f_x,f_y)\exp[-i\phi_B(f_x,f_y)] \quad (9)$$

Let formula (8) add positive lens factor $\exp[i\theta(f_x,f_y)]$ and formula (9) add negative lens factor $\exp[-i\theta(f_x,f_y)]$ repectively then adding:

$$A(f_x,f_y)\,\mathrm{expi}[\,\phi_A(f_x,f_y)+\theta(f_x,f_y)] + B(f_x,f_y)\,\mathrm{exp\text{-}i}[\,\phi_B(f_x,f_y)+\theta(f_x,f_y)]$$
$$= C(f_x,f_y)\,\mathrm{expi}[\,\beta(f_x,f_y)] \qquad (10)$$

where $C(f_x,f_y)$ and $\beta(f_x,f_y)$ express amplitude and phase of combined frequency spectrum repectively. when unit-amplitude parallel light illumnates this type CGH,two identical directional different reconstructed images appear simultaneously at +1 order location and -1 order location on the same plane away from the CGH

Experiment

Lee's delay sampling method[4-5] is adopted in CGH. The sampling point of object is 64 × 64. Before FFT transform, the object function addsa random phase factor to prvent dynamic range of Fourier frequency spectrum too big. The size of the CGH drawing by plotter is 256 × 256mm^2 , then reducing the drawing (100x) by photograph, the required CGH is obtained.

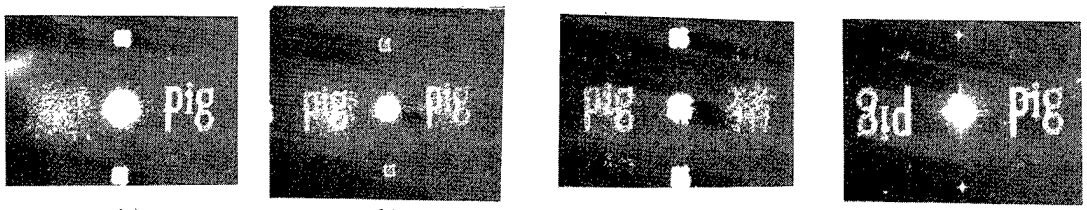
When reconstructing, the parallel He-Ne laser (λ =633nm) illuminates the CGH, the configuration is shown in figure 2. Because of adding the quadratic phase factor (which is equavalent to a lens),the CGH has the function of self-focusing.The reconstruction image will be a focal length f away from the CGH (in our experiment f is 61cm). For the CGH that positive lens factor is added in frequency spectrum of the object (English word 'pig'), one upright image of originally object appear in +1 order location and one light spot appear in -1 order location when reconstructing as shown in figure.3 (a)

For the CGH that positive lens factor is added into frequency spectrum of the object and negative lens factors is added into conjugate frequency spectrum of the object respectively, two image having identical direction appear at +1 order location and -1orderlocation on the same plane when reconstructing as shown in figure.3 (b)

For the CGH adding positive lens factor into frequency specturm of one object and negative lens factors into conjugate frequency spectrum of another different object repectively, two identical direction different reconstructed images appear at +1 order location and -1 order location on thesame plane f away from the CGH. The reconstructed image of this CGHis shown in figure.3 (c)

If illumnating the CGH is not parallel light,the position of reconstructing image plane may be calculated by lens equation, which is decided by the divergence and convergence of incident light.The experimental results is identical to thoeretic analysis but the noise is largger in latter two situations .

For the convenience of comparison, the reconstructed images of usual CGH is shown in figure 3.(d)



(a) (b) (c) (d)

Fig.3. reconstructed images of CGH's unusual mode and usual mode. (a). spatial spectrum of two recontruction images. (b).two reconstruction images having an identiacal direction .(c).two different shape reconstruction images having identical direction . (d).two mutual inverted recontruction images.

Conclusion

The new type CGH that the quadratic phase factor is directly added in frequency spectrum of object has the function of self-focusing and self-imaging objectively, the imaging lens can be omitted in CGH's reconstruction. The optical configuration becomes more simple and more compact.The reconstructed images break through traditional mode (one upright ,another inverted both appear in a same plane), The spatial separation of reconstructed

images comes true. +1 order's upright image and -1 order's inverted image may be appear in diffenert plane respectively When reconstructing;two upright image (having identical direction) of same object or different object appear at +1 order location and -1 order location respectively in the same plane.This study explores a singnificant new way for making particalar reconstructive demand CGH, if increasing diffraction efficiency and the signal-to-noise ratio, a good future for application could be exepected.

Refenerce:

1. "Introduction To Fourier Optics" J.W. Goodman McGraw-Hill Inc.
2. A.W.Lohmann and D.P.Paris, Appl. Opt., 6, 1139 (1967)
3. R.J.Colleir, et al., Optical Holograpy, Academic press, New York and london ,(1971)
4. W.H.Lee, Appl.Opt., 9,639 (1970)
5. W.H.Lee, Progress in Optics, ed. by E.Wolfe, Vol.XVI (1978)

Measurement and Analysis of Compound Amplitude and Phase Holographic Gratings

Y. J. Wang[1], M. A. Fiddy[1], Y. Y. Teng[2], D. A. Pommet[1], and L. Malley[1]

Center for Electromagnetic Materials and Optical Systems
[1] Department of Electrical Engineering
[2] Department of Physics
University of Massachusetts Lowell
Lowell, MA 01854
508 934 3359; fax 3024

Introduction

A hologram on which an interference pattern is recorded, appears transparent after exposure, developing and bleaching. However, these types of holographic transparencies are found to have both some periodic variations of optical density and surface relief when measured using microdensitometer and profilometer. We refer to this kind of holographic grating as a compound hologram, i.e. it contains variations in both amplitude and phase.

It is well known that the diffraction efficiency of this kind of bleached holographic grating is a function of the exposure. Under ideal conditions one can control the exposure and bleaching process to maximize the diffraction efficiency of the first order diffracted beam (approaching 33%) or one of the higher order diffracted beams.

We analyze the diffraction property of this kind of grating below. We assume that the transmittance function of a compound holographic grating is

$$t(x',y') = \{[(1/2) + (m_a/2)\sin(2\pi f x')] \exp[j(m_p/2)\sin(2\pi f x')\} * \mathrm{rect}(x'/L)\mathrm{rect}(y'/L) \qquad (1)$$

where m_a is the peak to peak excursion of the amplitude transmittance
m_p is the peak to peak excursion of the phase delay
L is the width of the square aperture bounding the grating

The sinusoidal variation of the amplitude is caused by the residual amplitude of the partially bleached grating. The sinusoidal variation of the phase is caused by refractive index variation associated with the surface relief of the bleached emulsion. The variations of both amplitude and phase are in phase. Substituting the identity

$$\exp[j(m_p/2)\sin 2\pi f x')] = \sum_{q=-\infty}^{\infty} J_q\,(m_p/2)\exp(j2\pi q f x')$$

where J_q is the Bessel function of the first kind, of order q, into equation (1) gives the expression for the transmittance function,

$$t(x',y') = \{(1/2)\sum J_q\ (m_p/2)\exp(j2\pi qf\,x') + (m_a/4j)\sum J_q\ (m_p/2)\exp(j2\pi(qf+f)x') - (m_a/4j)\sum J_q\ (m_p/2)\exp(j2\pi(qf-f)x')\} * \mathrm{rect}(x'/L)\mathrm{rect}(y'/L) \quad (2)$$

Thus, when a compound grating is illuminated by a normalized monochromatic wave, the field distribution just behind the aperture is assumed proportional to t (x',y'). Fourier transforming this field distribution and using the shifting property of δ - functions, we obtain

$$FT[\,t(x',y')\,] = L^2\,\mathrm{sinc}(Lf_y)\{(1/2)\sum J_q\ (m_p/2)\mathrm{sinc}[L(f_x - qf_0)] + (m_a/4j)\sum J_q\ (m_p/2)\mathrm{sinc}[L(f_x - qf - f)] - (m_a/4j)\sum J_q\ (m_p/2)\mathrm{sinc}[L(f_x - qf - f)] \quad (3)$$

After substituting $f_x = x/\lambda z$, $f_y = y/\lambda z$, it is simple to show that the intensity distribution is

$$I(x,y) = (L^2/2\lambda z)^2\,\mathrm{sinc}^2(Ly/\lambda z)\sum J_q^2\ (m_p/2)\mathrm{sinc}^2[(L/\lambda z)(x - qf\lambda z)] + (m_a^2/4)\sum J_q^2\ (m_p/2)\mathrm{sinc}^2[(L/\lambda z)(x - qf\lambda z - f\lambda z)] + (m_a^2/4)\sum J_q^2\ (m_p/2)\mathrm{sinc}^2[(L/\lambda z)(x - qf\lambda z + f\lambda z)]\} \quad (4)$$

Equation (4) is thus the diffraction pattern of a compound holographic grating. If we choose $m_p = 0$, then

$$\sum J_q\ (m_p/2) = J_0(0) = 1$$

The intensity distribution reduces to the diffraction pattern of a pure sinusoidal amplitude grating. If $m_a = 0$ then expresses the diffracted intensity distribution of a pure sinusoidal phase grating. If we assume that q = 0 in Eq. (4), we have

$$I_0(x,y) = (L^2/2\lambda z)^2\,\mathrm{sinc}^2(Ly/\lambda z)[J_0^2(m_p/2)\mathrm{sinc}^2[(L/\lambda z)x] + (m_a^2/4)J_0^2(m_p/2)\,\mathrm{sinc}^2[(L/\lambda z)(x - f\lambda z)] + (m_a^2/4)J_0^2(m_p/2)\,\mathrm{sinc}^2[(L/\lambda z)(x + f\lambda z)] \quad (5)$$

While $q = \pm 1$, it becomes

$$I_{\pm1}(x,y) = (L^2/2\lambda z)^2 \,\mathrm{sinc}^2(Ly/\lambda z)[J_{\pm1}^2(m_p/2)\mathrm{sinc}^2[(L/\lambda z)(x \mp f\lambda z)]$$

$$+ (m_a^2/4)J_{\pm1}^2(m_p/2)\mathrm{sinc}^2[(L/\lambda z)(x \mp 2f\lambda z)]$$

$$+ (m_a^2/4)J_{\pm1}^2(m_p/2)\mathrm{sinc}^2[(L/\lambda z)x]\} \qquad (6)$$

Eqs (5) and (6) indicate that there always exist three terms for any one of the values of q. These terms are similar to the three components diffracted by a pure sinusoidal amplitude grating. In other words, each diffraction order of a compound grating actually consists of three components: the central maximum of q order, and the two side maxima of (q+1) and (q-1) orders. From Eq. (4) we can explain the behavior of the diffraction efficiency. When the exposure time increases, m_p increases also. The phase component of a compound grating plays an increasingly important role in diffraction with increasing m_p. The maximum diffraction efficiency evolves from the zero order to higher order terms due to the properties of the Bessel function of the first kind.

Since the sinusoidal amplitude grating is always present, then in a compound hologram, every order of the Bessel function is actually diffracted into three components. When m_p is such that the diffracted intensity of the qth order of a pure phase grating is equal to zero, then there will still be the left side maximum of (q+1) order and the right side maximum of (q-1) order at the position of the qth order for the grating. Therefore the order is not absent.

References

1. M. C. Hutley, Diffraction Gratings, Academic Press Inc. Ltd., London, 1982.
2. J. W. Goodman, Introduction to Fourier Optics, McGraw--Hill, 1968.
3. F. T. S. Yu, Appl. Opt., **8**, 2350, 1969.
4. J. N. Latta, Appl. Opt., **7**, 2409, 1968.
5. W. T. Cathey, Jr., J. Opt. Soc. Amer., **56**, 1167, 1966.

Joint Session on Diffractive and Micro-Optics and Holography II

JTuC 1:30 pm-3:00 pm
Gardner A&B

Michael Gale, *Presider*
Paul Scherrer Institute

Diffraction Optics - A century from basic studies to mass production

Erwin G. Loewen
Spectronic Instruments, Inc.
Rochester, NY 14625

Introduction:

Diffractive Optics, defined as the use of diffraction to aid or perform the imaging process, belongs to the large familiy of 19th century concepts in optics that have moved from obscurity to important technology thanks to a fascinating confluence of recently discovered needs with development of a whole collection of new enabling technologies. These include computational methods, optical materials, and finally precision engineering processes that convert the impossible into the possible . Not one of these basic developments originated because of demands from the Diffraction Optics community. They came from the outside world and were conveniently appropriated as needs arose.

Early History

The first serious study of possibilities of diffraction modified imaging was due to Cornu, who was stimulated by reports of the effects of systematic groove spacing errors on diffraction gratings, which shifted the focal plane of his imaging optics. An 1875 paper describes his work, first with standard gratings, but quickly recognizeing that results apply equally well for spherical waves combined with circular grooved gratings. He went so far as to build a special ruling engine designed to allow deliberate program errors to be introduced. He ruled Fresnel patterns into a layer of soot on glass, with 8.5 mm focal length. He noted other orders at integral multiples. Further work was reported in 1893, but practical applications were not on his mind.

Lord Rayleigh experimented with Fresnel Zone plates at about the same time, and noting that no more than 10% was imaged in any one plane suggested that the opaque zones be replaced with transparent ones etched deep enough to give them a $\pi/2$ phase difference. It remained for R.W. Wood some 25 years later to produce such a 'lens' and he was happy to find as much as 40% in the principal image plane. Excessive stray light inhibited any thought he might have had of

actually using it.

Wood, who was the first to blaze a standard diffraction grating by giving the grooves a triangular shape (~1910), must have considered applying this idea to his lens, but evidently could find no good way to actually carry out the idea. This was to take another 40 years, which gives a clear indication of how difficult a job this is.

Enabling Technology for Blazing

The first outside development that proved critical to diffractive optics was precision diamond turning machines. Originally built at Phillips research labs, passed on to DuPont, it found its first U.S. home in Oak Ridge and Lawrence Livermore Labs. The first applications were for generating precision spheres, but they were also treated as an academic prospect (1960). These machines were not only equipped with accurate slides, but were the first to apply programmable digital interferometric feedback position control. Crucial also were the recently developed air bearing spindles with axial run-out at the 50 nm level or better, and finally they taught the all important lesson that temperature of the entire machine and its environment both could and should be held constant to 0.01 C or less. The development of corresponding diamond tools should not be overlooked.

A quite different and to some extent more versatile approach was introduced in the 1980's capable of giving similar results. This was the oddly named concept of binary optics, which rested on the proposition that there is little optical difference between a smooth triangular groove face and its approximation by a series of steps (4 to 16). It could never have been put to use without the great advances in microlithography, in all its aspects. It requires a set of accurately made masks and means to align them. Making masks requires special pattern generators, 'writing' with either laser or electron beams. The latter can write finer patterns, but are slow, expensive, and work in a vacuum. Thanks to digital programming they have the advantage of being able to produce off axis and other non-symmetrical patterns when required, hardly reasonable to do on lathes.

Replication

An important step in making volume diffraction optic elements is replicating the modulated surface of a master onto the product optic. The goal invariably is how to combine high fidelity

with low cost. This describes injection molding quite well, but presupposes that limitations inherent in a plastic lens are acceptable, especially changes of index with temperature. More accurate, but much slower, is the casting process. The master is 'glued' to the glass product with a low viscosity monomer which is then polymerized, usually with the aid of UV radiation. If properly prepared, the two surfaces can be separated without damage, so that the process can quickly be repeated. Another potentially useful process involves embossing the master pattern, usually in the form of a nickel electroform, against the product that has been coated with a special film that must adhere tightly to the substrate, is readily deformed and finally cured with UV light.

Some applications

The simplest diffractive lens, and used in the greatest volume, is the small collimating lens found in every CD system for the last 15 years. It is made by a molding process. At the other end of the scale are large high grade IR lenses made out of germanium. The material is heavy and expensive, giving every incentive to use singlets. To reduce resulting aberrations and chromatism with a diffractive surface is an excellent solution. With volume low, it makes sense to turn the pattern directly into the surface of each lens.

Quite another problem is a reflecting system where simple design calls for skew rays, yet all mirrors are required to be spheres for low cost. A diffractive optic with skew pattern provides an ideal tool for suppressing aberrations. One cannot overlook in such cases the fact that any diffractive surface will change its angular behavior with wavelength. This is desirable for taking advantage of chromatizing possibilities, but it may in some instances limit the wavelength band over which it can be used.

A totally unique application of diffractive optics is found in the vacuum alignment tunnel of the Stanford Linear Accelerator. It supplies the straightness reference over the full 2 miles to an accuracy of 0.025 mm, as checked every 8 m. This is done with a set of 296 Fresnel lenses made by etching their patterns into 10 inch square sheets of 0.01 inch thick nickel. There is a laser illuminated pinhole at one end and an elegant quadrant detector at the other, which recognizes any off axis condition of the lenses (1 at a time) with accuracy to spare. This was set up in 1966 and to this day no alternative concept has been proposed that could do the job.

Liquid crystal grating based on modulation of circularly polarized light.

Jay E. Stockley,

NSF Optoelectronic Computing Systems Center University of Colorado at Boulder, Boulder, Colorado 80309-0525 phone (303) 492-2195 fax (303) 492-3674

Gary D. Sharp, Steven A. Serati, and Ping Wang,

Boulder Nonlinear Systems, Inc. 1898 S. Flatiron Ct. Boulder, Colorado 80301 phone (303) 786-8958 fax (303) 786-8598

Kristina M. Johnson

NSF Optoelectronic Computing Systems Center University of Colorado at Boulder, Boulder, Colorado 80309-0525 phone (303) 492-7967 fax (303) 492-3674

Introduction

Liquid crystals are frequently used as active diffractive optical elements [1,2]. These materials offer several advantages, including rapid response [3], large aperture, and low cost. The simplest liquid crystal diffractive structure is a one dimensional grating comprised of a linear array of electrodes [4]. Application of different voltages along the electrode array results in a multi-level phase structure which may take the form of a blazed grating or phased array. For such devices, the phase front across the grating aperture is constructed from periodic and quantized phase steps up to 2π.

Conventionally, birefringence modulation has been used to obtain the phase modulation for liquid crystal gratings. This is achieved by electrically changing the extraordinary refractive index encountered by the optical field. Changing the birefringence to induce a phase modulation is inherently chromatic. That is, the phase difference, Φ, induced on the field is wavelength dependent and is in general given by:

$$\Phi = 2\pi n_{ex}(V)d/\lambda \quad . \tag{1}$$

Here $n_{ex}(V)$ is the voltage induced change in the extraordinary index of refraction, d is the liquid crystal thickness, and λ is the wavelength of the optical field.

If instead the phase is due purely to polarization modulation, as is the case described here, the phase induced on the optical field is achromatic. This is because the phase modulation depends on the optic axis orientation of the liquid crystal retarder in the plane transverse to the direction of propagation and not on the refractive indices.

Such a broad band active grating structure has a distinct advantage over conventional phase modulation based on retardation. If the reset phase of 2π for the grating is independent of wavelength, then there will be no material dispersion and the only dispersive effects will be due to the grating structure itself. Grating dispersion is a consequence of the far field propagation of the diffracted light. Such propagation effects can be theoretically compensated for by a diffractive system, such as an achromatic Fourier transformer [5].

Phase Modulators Using Chiral Smectic Liquid Crystals

Multiple phase levels can be achieved by rotating the optic axis of a half-wave plate in a plane transverse to a circularly polarized optical field [6]. A few microns of planar aligned chiral smectic liquid crystal (CSLC) between electrodes results in an electrically activated half-wave plate with a rotatable optic

axis. The phase induced on a circularly polarized field is equal to twice the rotation of the optic axis of the half-wave retarder with respect to a reference orientation.

$$\Phi = 2k\alpha \quad . \tag{2}$$

Where k is the number of half-wave retarders or the number of passes through a half-wave retarder and α is the optic axis rotation. The advantage of CSLC's is that the optic axis can be reoriented within submicrosecond times [3].

There are several structures that can produce such a phase modulation. The basic structure is a CSLC half-wave retarder sandwiched between two passive quarter-wave retarders [6]. Here the induced phase is $\Phi = 2\alpha$, where α is the relative optic axis orientation of the CSLC retarder. These materials exhibit maximum optic axis reorientations that vary from a few degrees for electroclinic [7] materials to nearly 90° for Smectic C^{*} materials [8]. Since the phase is twice the reorientation of the optic axis per pass through a half-wave retarder, multiple half-wave plates, reflection-mode configurations or resonantly enhanced devices are needed to obtain enough phase to produce efficient diffractive elements having more than two phase levels.

We have recently implemented a reflection-mode modulator at 632.8 nm using a ferroelectric half-wave retarder and polymer cholesteric liquid crystal mirror [9]. The device demonstrated nearly 2π radians of analog phase modulation.

In this meeting one of the things we will present is our continued effort to obtain large analog phase modulation using a single active device. One such structure, a resonant device which employs a quarter-wave thick retarder of electroclinic material between a high reflector and a partially reflecting (65%) cholesteric mirror has been implemented at 1064 nm. This device demonstrated a phase modulation of $\Phi = 8\alpha$, or just over π radians. This is the first integrated active resonant device using a cholesteric mirror and conventional mirror. Another new phase modulator is a two pass device which is an extension of the phase modulator discussed in reference 9. A $4\mu m$ thick CSLC retarder was fabricated onto a $8.5\mu m$ thick polymer cholesteric mirror which reflected 86% of left hand circularly polarized light at 1064 nm. An analog phase modulation depth of over $3\pi/2$ radians was observed. Figure 1 is a plot of the phase modulation as a function of electric field demonstrated by this new modulator.

Chiral Smectic Liquid Crystal Gratings

The diffraction characteristics of the liquid crystal grating depend on the aspect ratio of the grating thickness and grating period [10]. For a large grating period the diffraction efficiency may be obtained using scalar diffraction theory. As the grating period becomes smaller and the diffraction angles increase, the theoretical diffraction efficiency must be obtained using rigorous coupled wave theory [11]. A system of equations has been derived from Maxwell's curl equations and implemented numerically.

The number of resolvable spots can be shown to first order to vary as twice the square root of the number of electrodes, $2\sqrt{m_e}$, [12]. However, the flexibility of addressing imparted by the electrode structure allows a significant increase in the number of resolvable spots over $2\sqrt{m_e}$.

The chromatic effects of the liquid crystal retarder have also been determined. The retardation change on switching results in a small amplitude grating which will direct some of the incident light to the -1 and +3 orders. However, for a typical amplitude modulation of 10% the amount of light directed to these undesired orders is 0.2% each. Moreover, this amplitude grating does not reduce the number of resolvable spots.

Theoretical results including diffraction efficiency, number of resolvable spots, and chromatic effects will be presented at the meeting.

We will also present, for the first time, experimental results obtained from the implementation of a reflection mode liquid crystal grating using a quarter-wave CSLC retarder and a two pass configuration. The device exhibits a preferential direction for the primary diffracted beam depending on the direction of

increasing phase. Preliminary results indicate a 5:1 contrast ratio between the ±1 orders.

A reflection-mode grating which employs a half-wave CSLC retarder and a polymer cholesteric mirror as the back plane is currently being fabricated. A schematic of this device is shown in Figure 2. The diffraction characteristics of this grating will also be presented at the meeting.

Acknowledgements

We are grateful to Dr. Robert Maurer of the Consortium für Elektrochemische Industrie, GmbH Munich, Germany for supplying the polymer liquid crystal material. We would also like to express our thanks to Scott Gilman of the University of Colorado for fabrication of the resonant modulator.

This Research has been supported in part through the C.A.T.I./O.C.S. business program, Air Force Contract AF1091, Air Force Contract 1745, and Lawrence Livermore Contract LL301.

References

[1] S. T. Kowel, D. S. Cleverly, and P. G. Kornreich, Appl. Opt. **23**, p.278, 1984.

[2] G. D. Love, J. V. Major, and A. Purvis, Opt. Lett., **19**, p.1170, 1994.

[3] N. A. Clark, and S. T. Lagerwall, Appl. Phys. Lett., **36**, p.899, 1980.

[4] P. F. McManamon, E. A. Watson, T. A. Dorschner, and L. J. Barnes, Opt. Eng., **32**, p.2657, 1993.

[5] G. M. Morris, Appl. Opt. **20**, p.2017, 1981.

[6] G. D. Sharp Ph. D. Thesis University of Colorado 1992.

[7] S. Garoff and R. B. Meyer, Phys. Rev. Lett. **38**, p.848, 1977.

[8] J. S. Patel and J. W. Goodby, Mol. Cryst. Liq. Cryst., **144**, p.117, 1987.

[9] J. E. Stockley, G. D. Sharp, S. A. Serati, and K. M. Johnson, Opt. Lett., **20**, p.2441, 1995.

[10] T. K. Gaylord, and M. G. Moharam, Appl. Opt. **20**, p.3271, 1981.

[11] E. N. Glytsis and T. K. Gaylord, J.O.S.A. **4**, p.2061, 1987.

[12] J. D. Zook, Appl. Opt. **13**, p.875, 1974.

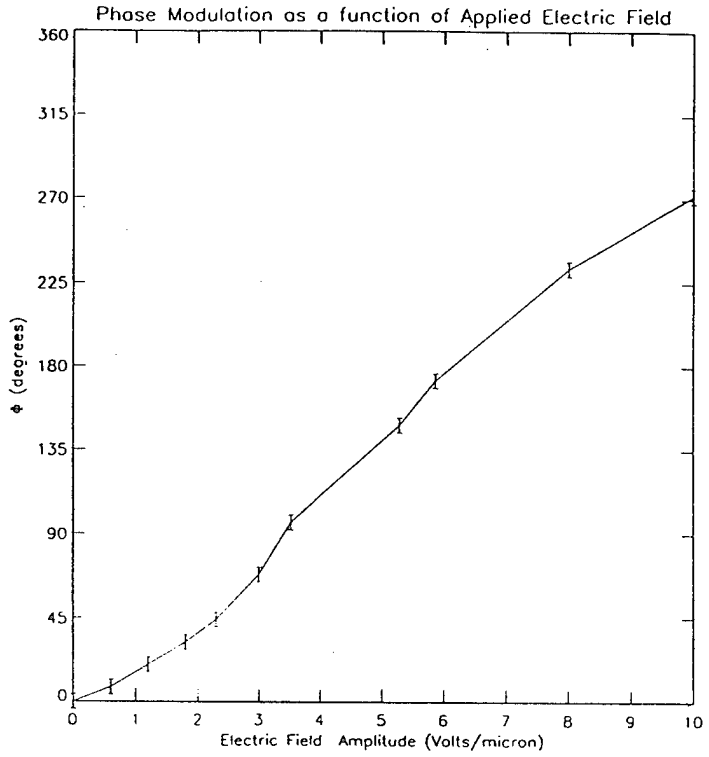


Figure 1. Experimental measurements of phase modulation as a function of electric field for the integrated two-pass modulator.

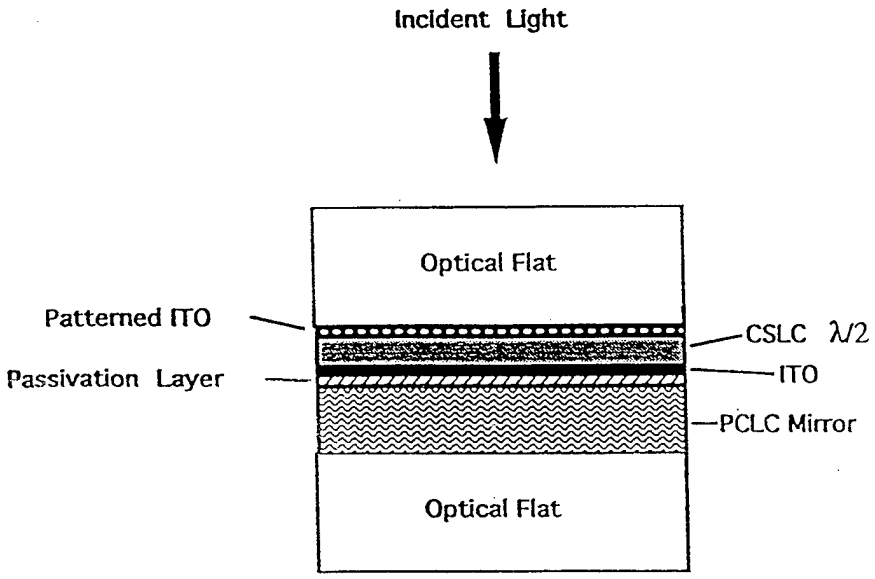


Figure 2. Schematic of the CSLC grating with a polymer cholesteric liquid crystal backplane.

Diffractive Optical Elements for 3-D Displays Based on the Partial Pixel 3-D Display Architecture

G. P. Nordin, M. W. Jones, R. G. Lindquist, J. H. Kulick, and S. T. Kowel

The University of Alabama in Huntsville
Electrical and Computer Engineering Department
Huntsville, Alabama, 35899

Tel.: (205) 895-6215 x410
Fax: (205) 895-6618

Introduction

Real-time holographic display architectures are currently of significant interest,[1-2] in part due to intense international competition to develop advanced displays for high definition television, three-dimensional (3-D) workstations, and virtual reality systems. We have recently invented an alternate approach to holographic displays for such applications. Our 3-D display architecture (referred to as the "partial pixel architecture") is functionally equivalent to a holographic stereogram, yet lends itself to real-time implementation using flat panel liquid crystal technology in conjunction with diffractive optical elements.[3] A key innovation of the architecture is the encoding of very high space-bandwidth product components typical of holographic displays into a fixed diffractive optical element (DOE), while the lower space-bandwidth product components of actual images are displayed in real-time on a conventional liquid crystal display (LCD). In this paper we discuss diffractive optical element design considerations and implementation issues for real-time 3-D displays based on the partial pixel architecture.

Background

The basic geometry of the partial pixel architecture is illustrated in Fig. 1. A pixelated display is present in the x-y plane, and a viewing region is located a distance d_v from the plane. One can think of the viewing region as a series of adjacent virtual slits that are approximately one pupil diameter wide. As in a holographic stereogram, each eye of an observer sees a different image on the display. When the appropriate set of stereopair images are simultaneously presented on the display (with a single image visible through each virtual viewing slit), the scene appears three-dimensional. In addition, the display exhibits one-dimensional (1-D) motion parallax as an observer moves his or her head from side to side within the viewing region. Since special headgear is not required to view the display, it is also autostereoscopic.

In order to simultaneously display separate images through each virtual viewing slit, each pixel of the display must (1) direct light into each virtual viewing slit and (2) independently

control the amount of light directed to each virtual viewing slit. A pixel fulfilling these requirements could thus appear "on" (i.e., bright) when viewed through virtual viewing slit m, while simultaneously appearing "off" (i.e., dark) when observed through virtual viewing slit m+1.

In the partial pixel architecture, these pixel requirements are achieved by subdividing the area of each pixel into smaller regions (i.e., "partial pixels"). Since the display is designed such that the size of each pixel is at the resolution limit of an eye in the viewing region, these partial pixels are not visually distinguishable. Each partial pixel is responsible for directing light into a single virtual viewing slit, as well as controlling how much light is directed towards that slit. Construction of a display that functions like a holographic stereogram is thus reduced to the implementation of partial pixels that provide this basic functionality.

Current Real-time Implementations

We have recently implemented a small real-time monochrome display based on these principles.[4] As illustrated in Fig. 2, it utilizes a conventional liquid crystal display in conjunction with a suitably designed diffractive optical element. Each pixel of the LCD corresponds to one partial pixel and is physically aligned with a single diffraction grating on the DOE as illustrated in Fig. 3. The diffraction grating diffracts light to the appropriate virtual viewing slit, and the LCD pixel acts as an amplitude modulator. The minimum DOE feature size is approximately one micron. Diffraction from the effective partial pixel aperture determines the size of the virtual viewing slit in the plane of the viewing region. The partial pixel apertures are designed such that the virtual viewing slits have a small degree of overlap in this plane.

A top view of the display readout geometry is illustrated in Fig. 4. The viewing region is located 30 cm from the display and consists of 16 virtual viewing slits, each of which is approximately 6 mm wide. Virtual viewing slits –9 to –2 correspond to left-eye images, and slits 2–9 to right eye images. When a set of eight stereo image pairs are simultaneously presented on the display, a 3-D scene with horizontal motion parallax is observable. We have created sequences of such stereo image pairs such that real-time motion in the 3-D scene is achieved at video frame rates. We use a monochrome LCD display from Kopin Corporation, which allows us to drive the display with a standard VGA signal from a notebook PC.

We have recently extended the above display to full-color viewing using a technique that is analogous to rainbow holography. The number of partial pixels per display pixel is increased by a factor of three over the monochrome version, and an incoherent white light source is used to illuminate the display. Each partial pixel is designed to diffract a specific spectral component to

the desired virtual viewing slit. Color filters are not required to implement this particular design, although such filters represent an alternate path to achieving full-color displays.

DOE's

Our work to-date has demonstrated that the partial pixel 3-D architecture does indeed allow the realization of real-time displays that are functionally equivalent to holographic stereograms. However, there are a number of critical issues to be addressed in significantly scaling-up partial pixel architecture displays to useful sizes. Several of these issues are discussed below.

It is clear that future partial pixel architecture displays will require LCD's with very large numbers of pixels. For example, the 3072 × 2048 pixel display currently being developed by Xerox would allow approximately 20 separate 2-D images to be displayed, each with VGA resolution. For higher resolution images with a significant degree of motion parallax, even larger pixel counts are needed.

In addition, significant advances are required for the requisite diffractive optical elements. For example, DOE's are needed with deep submicron feature sizes over large areas (i.e., 11" diagonal or larger displays). The DOE's also need to incorporate an alternate method of defining the physical size of the virtual viewing slits. Currently, each partial pixel architecture display is designed such that diffraction from the aperture of each partial pixel is used to form the virtual viewing slits. A new method is needed to create a significantly taller viewing region in order to greatly enhance the size of the region from which the display can be viewed. We will describe our method of integrating a vertical diffuser function with the individual beam steering gratings for each partial pixel, and analyze the expected performance and potential limitations of such structures when integrated directly with LCD's.

References

1. P. St. Hilaire, S. A. Benton, M. Lucente, M. L. Jepson, J. Kollin, H. Yoshikawa, and J. Underkoffler, "Electronic Display System for Computational Holography", Proc. Soc. Photo-Opt. Inst. Eng. 1212, 174-182, (1990).
2. L. Onural, G. Bozdagi, and A. Atalar, "New High-Resolution Display Device for Holographic Three-Dimensional Video: Principles and Simulations", Opt. Eng., 33(3), 835-844, (1994).
3. J. H. Kulick, G. P. Nordin, A. Parker, S. T. Kowel, R. G. Lindquist, M. Jones, and P. Nasiatka, "Partial pixels: a three-dimensional diffractive display architecture", J. Opt. Soc. Am. A 12(1), 73-83, (1995).
4. M. W. Jones, G. P. Nordin, J. H. Kulick, R. G. Lindquist, and S. T. Kowel, "Real-Time Three-Dimensional Display Based on the Partial Pixel Architecture", Opt. Lett. 20(12), 1418-1420 (1995).

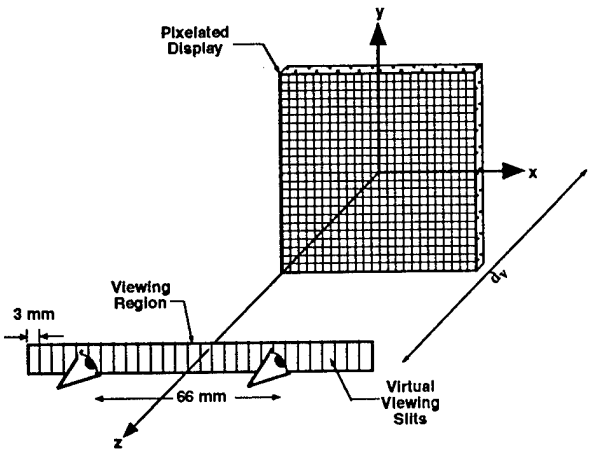


Figure 1. Geometry of the partial pixel architecture.

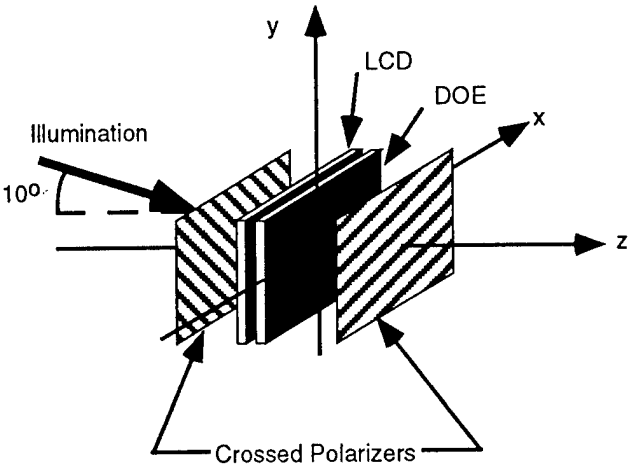


Figure 2. Schematic diagram of a liquid crystal panel-based partial pixel display.

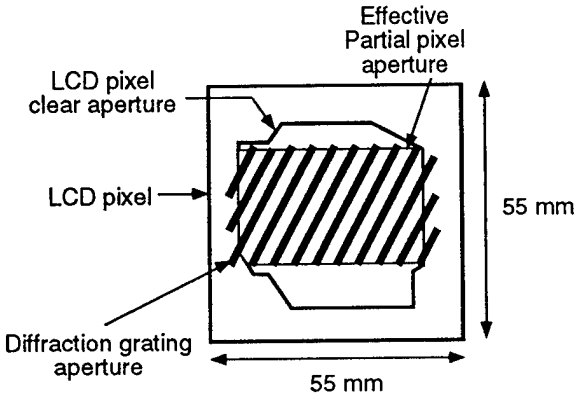


Figure 3. Schematic diagram of a LCD pixel and corresponding diffraction grating.

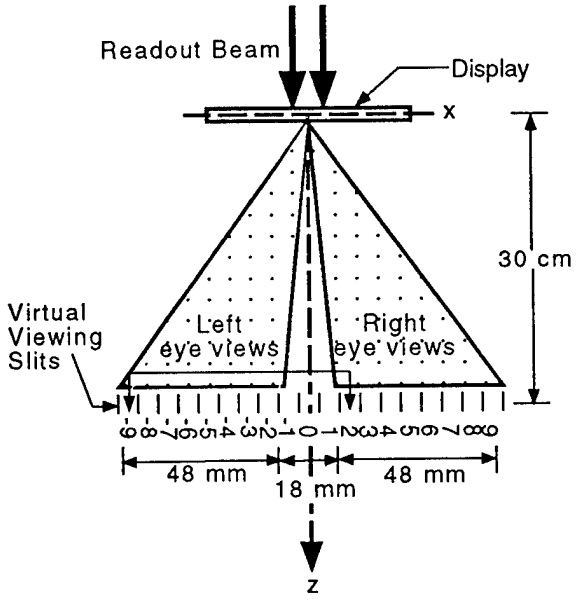


Figure 4. Top view of the readout geometry for the Kopin LCD-based partial pixel architecture display.

Beam-Pointing Stabilization and Ladar Heterodyne Mixing Efficiency Increase Using a Liquid Crystal Phased Array Device

Mark J. Missey
Vincent Dominic
University of Dayton
Center for Electro-Optics
300 College Park
Dayton, Ohio 45469-3433
513-229-2597
mmissey@engr.udayton.edu

Edward A. Watson
Wright Laboratory
WL/AARI-2 Bldg. 622
3109 P Street
Wright-Patterson Air Force Base, Ohio
45433-7700
513-255-4340

Introduction

Laser radar imaging systems often require the ability to accurately point the transmitted laser beam as well as the ability to mix the return light with a single mode receiver. An addressable liquid crystal phased array provides the precise spatially dependent phase shifts needed to achieve such beam stability and increased ladar heterodyne mixing efficiency. The device consists of a layer of nematic liquid crystals sandwiched between two substrates. One substrate is uniformly grounded, while the other is etched with narrow, closely spaced individual 1-D electrodes. The liquid crystals underneath a given electrode are rotated by applying an appropriate voltage, thus generating a birefringent phase delay. Two of these writable one-dimensional gratings can be cascaded to implement two dimensional phase profiles.

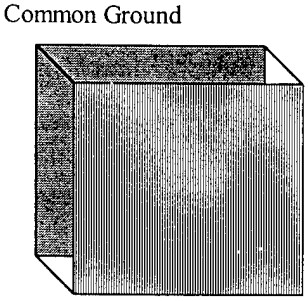


Figure 1. Liquid crystal addressable grating

The device used in this work has a 4 cm by 4 cm clear aperture, an 80 μm electrode spacing with a fill factor of unity, and an achievable phase depth of 2π radians for 1.064 μm light.

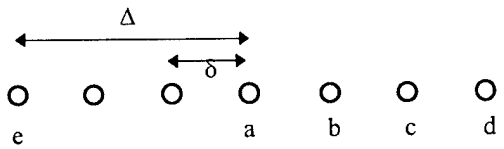
Beam-Pointing Stabilization

This device was originally intended to demonstrate non-mechanical agile beam steering through the use of "blazed" phase gratings; active beam stabilization is thus a natural application of the device's capabilities. Ideally, beam steering is achieved by applying a linear phase ramp across the device mimicking the presence of a prism. Unfortunately, the response time of the liquid crystals precludes the use of LC layers thick enough to provide deflections greater than a few millidegrees. In practice, thinner layers are used, and the prism effect is achieved by resetting the phase ramp after every 2π radians of phase delay. The phase grating behaves like a true blazed grating, with the angle of beam deflection determined by:

$$\sin\theta = \frac{\lambda}{\Lambda}$$

where Λ is the phase ramp periodicity. However, unlike etched blazed gratings, the periodicity here may be changed by altering the voltage profile across the device; a beam can then be arbitrarily steered through a range of angles determined by the device electrode spacing. The device used in this experiment has an 80 μm electrode spacing, so a 2π phase ramp spanning four electrodes yields, at 1.064 μm, a steering angle of 0.190°. Clearly, a device with this electrode spacing cannot be used for large angle beam stabilization. However, since the steering angle is entirely determined by the electrode spacing, a beam can be steered to smaller angles with remarkable precision and repeatability. Furthermore, similar devices have been produced with electrode spacings sufficient to yield steering angles of up to five degrees[3].

Since beam deflection with these devices has been previously demonstrated, the question is not if they can be used to actively stabilize a laser beam, but how well. The response time of the liquid crystals and the required degree of beam confinement fundamentally determine the angular disturbance frequencies for which the device can correct. To illustrate this, consider the following diagram where Δ is the maximum angular perturbation, δ is the desired beam confinement, and position 'a' is the center position.

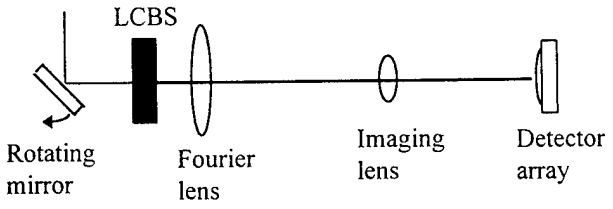


As the angular disturbance deflects the beam to 'b', the liquid crystal device must compensate by applying a phase grating to steer the beam through δ back to the center position. As the beam wanders to 'c', the device must compensate with an additional angle δ, making the entire compensated angle 2δ. Following through the cyclic sequence 'abc...e...a', the maximum cyclic frequency able to be compensated will be:

$$f_{\max} = \frac{\delta}{4\Delta\tau_{LC}}$$

where τ_{LC} is the response time of the liquid crystals. Note that LC device cannot continuously compensate because of the 2π grating resets. Although this calculation of f_{max} is approximate, it serves to provide an order-of-magnitude figure for the range of frequencies over which stabilization may be achieved. The measured response time of the grating device of interest is 50 ms; for Δ/δ=10, this yields f_{max}=0.5 Hz. Given this estimate, it is reasonable to expect stabilization of noise bandwidths on the order of 1-10 Hz.

To determine the stabilization performance of the device, the following setup is used.



The rotating mirror provides angular disturbances for which the liquid crystal beam steerer (LCBS) compensates. To detect such small angular movements, an imaging lens is used to magnify the Fourier plane of the first lens onto the detector array. The output beam location is continuously recorded on an oscilloscope, and stored for processing.

Initial experiments will provide a user-defined angular disturbance sequence to both the rotating mirror and the liquid crystal beam steerer. Later experiments will provide the beam steerer with corrupted information, simulating motion sensor inaccuracies. Finally, a true closed loop system is constructed where beam position information is provided from the oscilloscope to the beam steerer. The overall beam confinement and compensation bandwidth of all three systems are measured, and are shown to be inversely related.

Increased Coherent Laser Radar Mixing Efficiency

Coherent laser radar systems are generally designed so that the waist of the transmitted gaussian beam is at the exit aperture of the system; that is, the system is focused at infinity. Such a configuration is ideally suited for far-field target detection, but efficiency decreases for targets in the near field. To demonstrate this behavior, the overall heterodyne-detected signal from a resolved, perfectly diffuse speckle target is investigated. Following previous works[4,5], the average target return power obeys:

$$P_{\text{det}} = \langle \tilde{i}_{\text{det}} \rangle^2 \, R$$

where i_{det} is the intermediate frequency signal current out of the photodetector, and R is the load resistance of the detection circuit, presumably an oscilloscope. The IF signal current obeys the standard target-plane integral:

$$\tilde{i}_{\text{det}}(t) = \Re \iint_{A_t} d\bar{\rho}_t \, \tilde{\underline{T}}\left(\bar{\rho}_t, t - \frac{L}{c}\right) \underline{U}_t\left(\bar{\rho}_t, t - \frac{2L}{c}\right) \underline{U}^*_{LO}(\bar{\rho}_t, t)$$

where $\Re$ is the detector responsivity, $\tilde{\underline{T}}$ is the random, complex reflectivity of the target, $\underline{U}_t$ is the transmitted beam at the target, and $\underline{U}^*_{LO}$ is the complex conjugate of the local oscillator field back propagated to the target plane. Assuming the local oscillator and transmit beams are identical gaussians with $1/e^2$ intensity radii of w_{ea} and phase curvature radii R_{ea} at the exit aperture, the average signal power output from the laser radar system as a function of target distance L is:

$$P_{\text{det}} = \frac{R\Re^2 P_{LO} P_{trans} \tau \left(\frac{w_{ea}}{L}\right)^2}{1 + \Omega^2}$$

$$\Omega = \frac{\pi w_{ea}^2}{\lambda}\left(\frac{1}{L} + \frac{1}{R_{ea}}\right)$$

where P_{LO} and P_{trans} are the powers of the local oscillator and transmitted beams, and τ is the target reflectivity.

Note that if the radius of phase curvature of the transmitted Gaussian beam at the exit aperture satisfies R_{ra} = -L, then Ω=0, and the average power detected is a maximum. Since this condition, R_{ea} = -L, corresponds to a geometric-optics focus at a distance L from the exit aperture, the system exhibits the highest efficiency when the transmitted beam is geometrically focused at the target. Because a resolved, perfectly diffuse target has been assumed, the total amount of energy incident on the

target and reflected back to the system is independent of the radius of curvature of the Gaussian beam at the exit aperture, and so the term $E_h=(1+\Omega^2)$ can be thought of as the heterodyne mixing efficiency of the system, which determines the percentage of the light returned from the target that is mixed with the local oscillator to produce a detectable signal.

For an adaptively controlled focus, the mixing efficiency of the system can, in principle, be 100% for any target distance, while a fixed system focused at infinity decreases in the manner shown in Fig. 2.

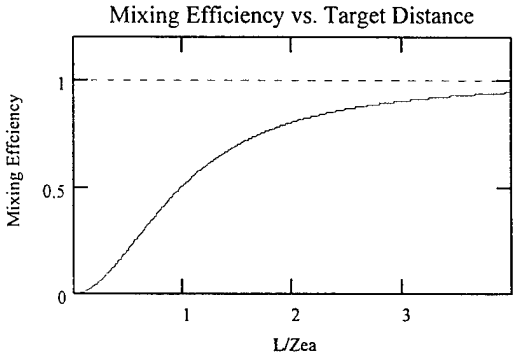


Figure 2. Heterodyne mixing efficiency for adaptively focused system (dashed) and a static system focused at infinity (solid) as a function of normalized target distance L/z^o_{ea}.

Although, the mixing efficiency for a laser radar focused at infinity decreases as the target moves into the near field, the total energy returned to the system increases as $1/L^2$, so that overall the system signal is larger for closer targets, as shown in Fig. 3.

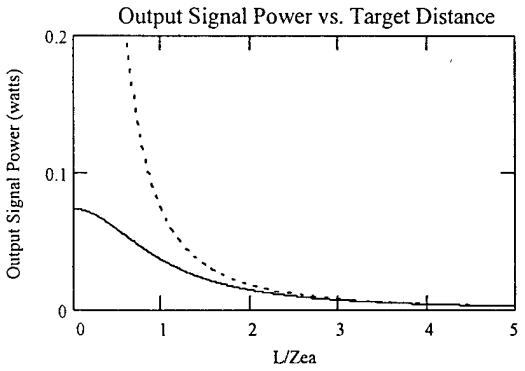


Figure 3. Output signal power of an adaptively focused system (dashed) and a static system focused at infinity (solid) as a function of normalized target distance L/z^o_{ea}. Relevant parameters are: a 1 mJ, 10 ns pulse, λ=1.5 μm, w_{ea}=5 cm, τ=0.8, $\Re$ =.09 A/W.

For this reason, few efforts have attempted to adaptively focus the transmitted beam on the target.

If the end goal of a ladar system were simply detection - is a target present or not - then a fixed focus system is sufficient for any target range.

When target characterization and identification are required, then the returned signal will be separated into different spatial bins. Having more bins allows more spatial information to be extracted, but reduces the total energy contained in each bin, eventually power-limiting the system.

Since,

$$\frac{P_{ret}(R_{ea}=-L)}{P_{ret}(R_{ea}=\infty)}=E_h=1+\left(\frac{z^o_{ea}}{L}\right)^2,\quad z^o_{ea}=\frac{\pi w^2_{ea}}{\lambda}$$

the benefit of an adaptive focusing lens is only substantial for target ranges $L \le z^o_{ea}$. For typical ladar systems, w_{ea}=5 cm and λ=1.5 μm, yielding z^o_{ea}=5.2 km. Achieving a focus at this distance requires such a slight phase curvature that the phase shift at the $1/e^2$ intensity point is only $\lambda/6$. The addressable liquid crystal device, possessing precise voltage controlled phase shifts, is ideally suited for this task.

Since the paraxial lens equation will be well satisfied for the target distances of interest, 2-D quadratic phase curvatures are used to implement focal lengths from about 7 km to about 5 m; the upper limit is determined by the device uniformity and phase quantization levels while the lower limit is determined by the onset of spatial aliasing and multiple focus spots, which are products of the spatially quantized nature of the device. Furthermore, the response time of the device (~50 ms) allows the system to switch focal lengths in just a fraction of a second.

The laboratory setup shown below is used to confirm the previously discussed theory, and to demonstrate the ability of the liquid crystal device to implement very long focal length lenses.

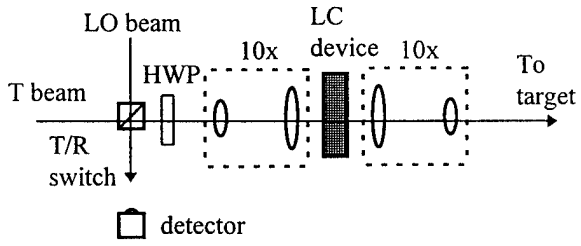


Figure 4. Laser radar system setup consisting of local oscillator (LO) beam, transmitted (T) beam, transmit/receive (T/R) switch, photodetector, half-wave plate, magnifying telescope, liquid crystal phase profile device, and demagnifying telescope.

The second telescope is aligned for demagnification so that the critical z^o_{ea} distance is less than 10 m, allowing demonstration within a closed laboratory environment. The return signal power as a function of target distance for both a static and dynamically focused system is measured and compared to predicted values.

Acknowledgments

This work was funded and supported by Technology/Scientific Services, Inc. and the University of Dayton Center for Electro-Optics. Special thanks to Larry Barnes, Art Serano, Don Tomlinson, and Paul McManamon for their respective contributions.

References

1. P. F. McManamon, E. A. Watson, T. A. Dorschner, and L. J. Barnes, "Applications look at the use of liquid crystal writable gratings for steering passive radiation," *Opt. Eng.* **32**(11), 2657-2664 (1993).
2. T.A. Dorschner, R. C. Sharp, D. P. Resler, L. J. Friedman, D. C. Hobbs, R. L. Chandler, and A. Legere, *Basic Laser Beam Agility Techniques (BATS)*, final report by Raytheon Co. prepared for Wright Laboratory WL-TR-93-1020 (1993).
3. P. F. McManamon, T. A. Dorschner, D. C. Corkum, L. J. Friedman, D. S. Hobbs, M. K. O. Holz, S. Liberman, H. Ngyuyen, S. P. Resler, R. C. Sharp, and E. A. Watson, "Optical Phased Array Technology," Manuscript submitted for publication in *Proceedings of the IEEE* (Special Issue on Laser Radar) February 1996.
4. J. H. Shapiro, B. A. Capron, and R. C. Harney, "Imaging and Target Detection with a Heterodyne-Reception Optical Radar," *Appl. Opt.* **20**, 3292-3313 (1981).
5. D. K. Jacob, "Optical Waveguide Mixing for Coherent Ladar Carrier to Noise Ratio Optimization," M.S. Thesis, University of Dayton (1994).

Programmable Wavefront Generation with Two Binary Phase Spatial Light Modulators

Guoguang Yang and Seth Broomfield

Department of Engineering Science, University of Oxford
Oxford, OX1 3PJ, UK

In this paper we propose a programmable wavefront generation system using two binary phase spatial light modulators (BPSLMs). The output of the binary phase hologram has inversion symmetry and is restricted to be space–invariant, if the output of the hologram is viewed in the Fourier plane of a lens. Inversion symmetry may be broken by introducing a fixed binary phase hologram [1,2] but in this case diffraction efficiency η_d is not increased. Alternatively, an asymmetric output may be generated by increasing the number of phase levels [3]. Results obtained in this way increase η_d but the output remains space–invariant.

It has been pointed out by Bartelt [4] and Yang [5,6] that the restriction of space–invariance can be removed by effectively cascading two phase masks in two Fourier–transforming stages. In this paper we consider a similar binary phase scheme [6] except that fixed phase holograms are replaced by binary phase SLMs and the design method to achieve a given wavefront is based on simultaneous, iterative optimization of both SLMs. The system is demonstrated by producing an asymmetric output. Simulation of its performance as a reconfigurable optical interconnect is also presented. Both utilize the space–variant performance of the system.

The two binary phase SLM system and its experimental implementation

The system is shown in Fig 1. The system consists of two cascaded Fourier transforms. It is easy

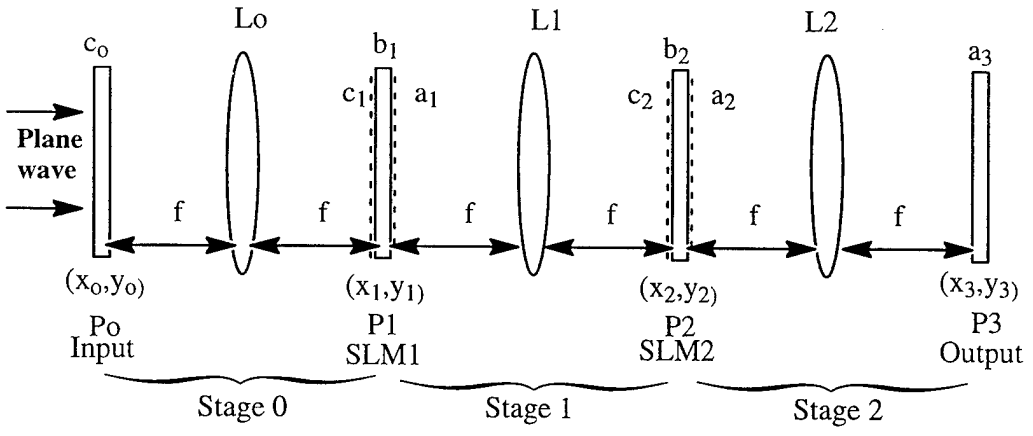


Fig. 1: The two binary–phase SLM system.

to proof that the system is a space–variant system. This is to be contrasted with the impulse response of a single phase SLM system which is a space–invariant system.

Assume the input function is a point at $x_0=y_0=0$, i.e. the complex amplitude of its Fourier transform $c_1(x_1,y_1)=1$. Two Fourier transforms are performed by the system. The system characteristic can be analyzed according to the Fourier theorem. Schemes for producing outputs with different properties using this system are shown in Table 1. It indicates that *all wavefronts with real symmetric, complex Hermitian, real asymmetric and complex asymmetric properties can be generated with the proposed system using binary phase modulation.*

Scheme	b_1, BPSLM1	c_2, Input of b_2	b_2, BPSLM2	a_2, Input to L2	a_3, Output
1	real and even (symmetric)	real and even (symmetric)	real and even (symmetric)	real and even (symmetric)	real and even (symmetric)
2	real and asymmetric	complex and Hermitian	real and even (symmetric)	complex and hermitian	real and asymmetric
3	real and even (symmetric)	real and even (symmetric)	real and asymmetric	real and asymmetric	complex and Hermitian
4	real and asymmetric	complex and Hermitian	real and asymmetric	complex and asymmetric	complex and asymmetric

Table 1. The configuration schemes of two binary phase SLM systems

In the general two dimensional case, to achieve a space–variant operation from an input wavefront specified by N^2 sampled values to an output wavefront specified by N^2 sampled values, the number of sampling points of the transform matrix which is represented by a hologram with amplitude and phase modulation should equal to N^2xN^2. The complex transmission values of the BPSLMs are only +1 and –1, however. This restricts the wavefront transforms which the system can achieve. In general it is impossible to find the exact solution for large N. An optimisation algorithm has to be used to find the closest approximate solution. Therefore, in the sense of an approximate solution, *general transformations with binary phase SLMs can still be achieved.*

In order to demonstrate the system performance, several patterns shown in Fig.2 are selected as the target functions for the calculation. To provide a comparison, most of the patterns are the asymmetric patterns used in references [1,2]. The direct binary search algorithm is used in the design. Simulation results for the target patterns of Fig.2 are given in Table 2 in which the non–uniformity of the output is defined as $NU=(I_{max}-I_{min})/(I_{max}+I_{min})$. This shows that about 75% efficiency is obtained by using the two BPSLM system with 128x128 pixels for generating the patterns. This is a remarkable increase over the results obtained with a single BPSLM which are shown for comparison in table 2. This comparison shows that not only is the diffraction efficiency higher, but the uniformity is improved with the two BPSLM system.

In the experimental system the binary phase SLM is created by placing a ferro–electric liquid crystal (FLC) SLM between crossed linear polarizers as described in [7]. The calculated designs are loaded to the two SLMs from a computer. The asymmetric pattern shown in Fig. 2.(e) is generated in the experiment. Fig.4 is the experimental output when the optimized binary phase patterns shown in Fig.5 are loaded on the two SLMs. Black and white in Fig.5 correspond to 0 and π phase shift. The measured efficiency is 58% with 6% non–uniformity. The diffraction efficiency

of the experiment is lower than the theoretical prediction. This is due to the aberration of the optical system and not including the diffraction effect in the optimization process.

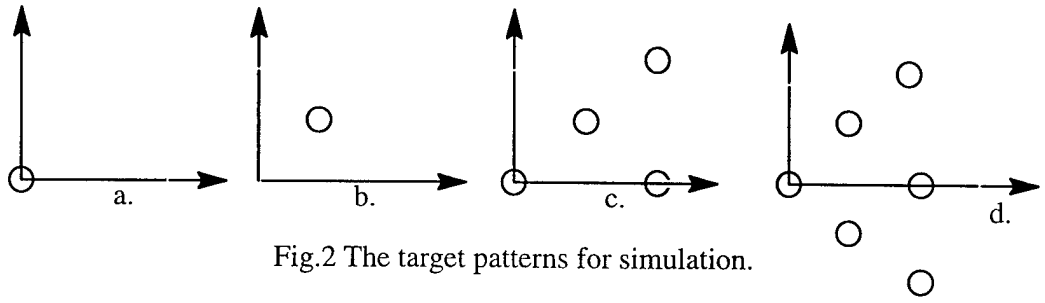


Fig.2 The target patterns for simulation.

Target pattern	calculated η_d (%)	calculated NU(%)	compared η_d (%)	compared NU(%)
a	81.2			
b	81.6			
c	73.8	3.2	41.1 in [3]	7.3 in [3]
d	76.2	0.5	40.4 in [3]	3.0 in [3]
e	75.0	1.0	40.0 in [2]	

Table 2. The simulation results and comparison

The programmable one–to–one optical interconnection system using two BPSLMs

A typical example for which shift variant performance is the programmable optical crossbar one–to–one interconnection system. Most of proposed schemes suffer from the drawback of low efficiency and large spot size. Our system with two BPSLMs can achieve high diffraction efficiency with diffraction–limited spot size. For simplicity, we shall discuss that N 1D light sources are connected to N 1D detectors with one–to–one connectivity. In order to realize the interconnection operation, sampling number of N^2 has to be employed in each SLM. The intensity input C_0 and desired output A_t matrices for N=4 in our simulation are taken to be

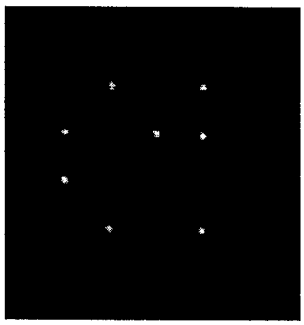


Fig.4 The experimental output pattern created by the cascaded SLM system.

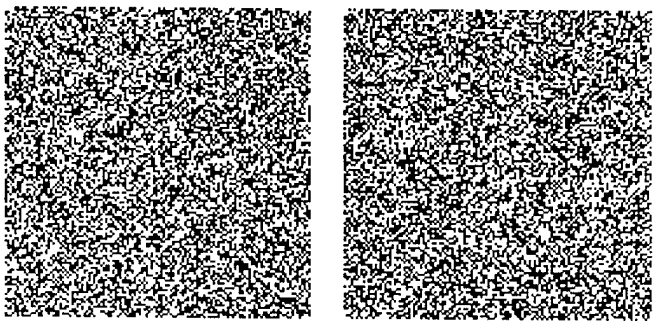


Fig.5 SLM arrays used to create asymmetric output

$$[C_0] = \begin{bmatrix} 1 & 0 & 0 & 0 \\ 0 & 1 & 0 & 0 \\ 0 & 0 & 1 & 0 \\ 0 & 0 & 0 & 1 \end{bmatrix} \qquad [A_t] = \begin{bmatrix} 1 & 0 & 0 & 0 \\ 0 & 0 & 1 & 0 \\ 0 & 0 & 0 & 1 \\ 0 & 1 & 0 & 0 \end{bmatrix} \tag{1}$$

The system connects the first light source to the first detector, the second to the third, the third to the fourth and the fourth to the second. According to the design procedure discussed above, the optimized actual output for N=4 is

$$[A_t]_{actual} = \begin{bmatrix} \underline{\mathbf{0.816}} & 0.074 & 0.105 & 0.002 \\ 0.080 & 0.016 & \underline{\mathbf{0.758}} & 0.175 \\ 0.005 & 0.036 & 0.245 & \underline{\mathbf{0.767}} \\ 0.055 & \underline{\mathbf{0.750}} & 0.110 & 0.065 \end{bmatrix}, \tag{2}$$

The results show that high efficiency can also be achieved with the two BPSLM system used for optical interconnection. It is independent of the dimension of the interconnection. As for implementing crossbar switching by using a multiple facet hologram the main drawback of the scheme is that it is not difficult to obtain a small spot size in order to efficiently couple light into a fibre as the full aperture is used for all inputs, instead of using a facet hologram. These make the scheme attractive for interconecting between a large number of nodes with programmable capability.

The crosstalk in the system is still high, about 20%. If the signal to be interconnected is binary, a threshold detector might be used to suppress the cross-talk. However, the required computation time in optimising the system is considerably longer than the time required for a single binary phase hologram. The optimisition of the two SLM system takes several hours run on a Convex machine which is a parallel processing high speed computer.

Conclusions

We conclude that the programmable wavefront generation system with two binary phase SLMs is a high diffraction efficiency and space–variant system. The amplitude and phase of a wavefront can be modulated with the system. It is experimentally implemented by two FLC SLMs. The experimental results are consistent with the theoretical prediction. A programmable optical crossbar interconnection system can also be based on the two BPSLM scheme.

References

1. M.A.A.Neil and E.G.S.Paige, Proc. of 4th Int. Conf. on Holographic Systems, Components and Applications, IEE Conf. Publication 378, 1993, p.85–90
2. M.S.Kim and C.C.Guest. Appl. Opt. 32 (1993) 678
3. S.E.Broomfield, M.A.A.Neil, E.G.S.Paige, Electronics Letters 29 (1993) 1661
4. H.Bartelt, Appl. Opt. 23 (1984) 1499
5. G.G.Yang, D.L.Lian, J.J.Zhang, J.P.Chen and Y.P.Ho, Opt. Lett. 16 (1991) 162
6. G.G.Yang, Proc. of 3nd Int. Conf. on Holographic Systems, Components and Applications, IEE Conf. Publication 342, 1991, p.45–49
7. S.E.Broomfield, M.A.A.Neil, E.G.S.Paige and G.G.Yang, Electronics Letters 28 (1992) 26

Tuesday, April 30, 1996

Scalar Design

DTuD 3:30 pm-5:00 pm
Gardner A&B

Joseph N. Mait, *Presider*
U.S. Army Research Laboratory

A Rogues' Gallery of CGH Null Tests

Steven Arnold
Diffraction International Ltd.

CGH null testing of aspheric optics was first demonstrated by MacGovern and Wyant in 1971 but has only recently become available as a commercial product. This talk describes a variety of CGH null test configurations using both commercial and customized interferometers. Several of the aspheres and their associated CGH nulls will be shown to exhibit various pathological traits.

Rigorous Design of Flat-Top Generators

Markku Kuittinen, Jari Turunen, and Pasi Vahimaa
Department of Physics, University of Joensuu, P.O. Box 111, 80101 Joensuu, Finland
Voice/fax: +358 73 151 2110/3290

1 Introduction

One of the most common tasks in beam shaping is the transformation of a Gaussian laser beam into a uniform far-field distribution. We present both non-periodic and periodic resonance-region structures that convert a narrow beam (waist size of the order of the wavelength) into a nearly flat-top distribution over a wide angular range.

2 Theoretical model for index modulated apertures

Consider the structure shown in Fig. 1. The space is divided into three regions, of which regions I (half-space $z < 0$) and III (half-space $z > h$) are assumed dielectric and homogeneous with refractive indices n_{I} and n_{III}, respectively. The intermediate region II ($0 \leq z \leq h$), however, is modulated such that it has a perfect conductivity when $x \leq 0$ or $x \geq c$, and dielectric with $n(x) = n_l$ when $x_l \leq x < x_{l+1}$, $l = 1, \ldots, L$ ($x_1 = 0$ and $x_{L+1} = c$). Diffraction by this refractive index modulated aperture can be treated in much the same manner as in Ref.[1], where periodic structures are considered. Consider first TM-polarization, i.e., the only non-vanishing component of the magnetic field vector is H_y. In region I ($z \leq 0$) the solution of the Helmholtz equation is of the form

$$H_y^{\mathrm{I}}(x,z) = \int_{-\infty}^{\infty} A(\alpha) \exp\{\jmath[\alpha x + r(\alpha) z]\} d\alpha + \int_{-\infty}^{\infty} R(\alpha) \exp\{\jmath[\alpha x - r(\alpha) z]\} d\alpha \,, \quad (1)$$

where $A(\alpha)$ is the angular spectrum of the incident field, $R(\alpha)$ represents the unknown angular spectrum of the diffracted field in the region I, and

$$r(\alpha) = \begin{cases} [(kn_{\mathrm{I}})^2 - \alpha^2]^{1/2} & \text{if } |\alpha| \leq kn_{\mathrm{I}} \\ \jmath[\alpha^2 - (kn_{\mathrm{I}})^2]^{1/2} & \text{otherwise} \end{cases} \,, \quad (2)$$

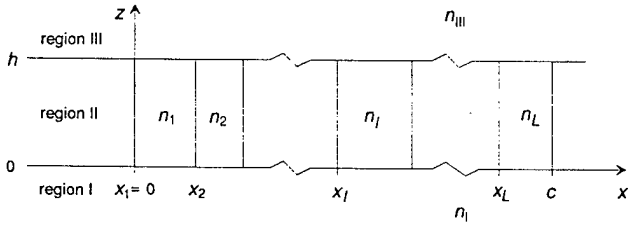


Figure 1: A lamellar dielectric diffractive structure inside an aperture in a perfectly conducting screen, illuminated by an arbitrary two-dimensional electromagnetic wave.

where $k = 2\pi/\lambda$, and λ is the vacuum wavelength. Similarly, in region III ($z > h$)

$$H_y^{\mathrm{III}}(x,z) = \int_{-\infty}^{\infty} T(\alpha) \exp\{j[\alpha x + t(\alpha)(z-h)]\} d\alpha \ , \tag{3}$$

where $T(\alpha)$ is the unknown angular spectrum of the diffracted field in this region and

$$t(\alpha) = \begin{cases} [(kn_{\mathrm{III}})^2 - \alpha^2]^{1/2} & \text{if } |\alpha| \leq kn_{\mathrm{I}} \\ j[\alpha^2 - (kn_{\mathrm{III}})^2]^{1/2} & \text{otherwise} \end{cases} \ . \tag{4}$$

The field $H_y^{\mathrm{II}}(x,z)$ is expressed as a superposition of eigenmodes of the refractive index modulated aperture, which form a discrete set because ot the perfectly conducting boundaries of the aperture at $x = 0$ and $x = c$:

$$H_y^{\mathrm{II}}(x,z) = \sum_{m=1}^{\infty} \left\{ a_m e^{j\gamma_m z} + b_m e^{j\gamma_m (z-h)} \right\} X_m(x) \ , \tag{5}$$

where γ_m is the eigenvalue of the eigenmode $X_m(x)$. These are found by applying the theory of stratified media to connect the fields H_y and E_z at $x = 0$ and $x = c$, and the fact that E_z must vanish at perfectly conducting boundaries. Either the exact eigenmodes may be used as in Ref.[1], which leads to an algebraic eigenvalue equation, or the eigenvalues may be expressed as superpositions of orthogonal polymomials [2], which leads to a matrix eigenvalue equation. In Eq. (5) a_m and b_m are constants that are finally solved from the boundary conditions at $z = 0$ and $z = h$. Once this is done, the unknown angular spectra $R(\alpha)$ and $T(\alpha)$ are obtained from

$$R(\alpha) = A(\alpha) - \frac{n_{\mathrm{I}}^2}{r(\alpha)} \frac{1}{2\pi} \sum_{m=1}^{\infty} \gamma_m (a_m - b_m e^{j\gamma_m h}) I_m(\alpha) \tag{6}$$

$$T(\alpha) = \frac{n_{\mathrm{III}}^2}{t(\alpha)} \frac{1}{2\pi} \sum_{m=1}^{\infty} \gamma_m (a_m e^{j\gamma_m h} - b_m) I_m(\alpha) \ , \tag{7}$$

where $I_m(\alpha)$ is the angular spectrum of the mth mode. In the case of TE-polarization we consider $E_y^{\mathrm{II}}(x,z)$ instead of $H_y^{\mathrm{II}}(x,z)$. Furthermore, Eqs. (6) and (7) lose the factors $n_{\mathrm{I}}^2/r(\alpha)$ and $n_{\mathrm{III}}^2/t(\alpha)$. Finally the far field distribution may be expressed by means of radiant intensity as is customary in physical radiometry:

$$J(\theta_{\mathrm{III}}) = \left(\frac{\pi}{\omega \epsilon_{\mathrm{III}}} \right) (kn_{\mathrm{III}})^2 \cos^2 \theta_{\mathrm{III}} |T(kn_{\mathrm{III}} \sin \theta_{\mathrm{III}})|^2 \ , \tag{8}$$

where θ_{III} denotes the angle with respect to z-axis. In TE-polarization, the first factor in Eq. (8) is replaced by $(\pi/\omega\mu_{\mathrm{III}})$.

3 Theoretical model for periodic structures

Diffraction of a plane wave by a periodic dielctric structure can be treated by rigorous grating theory, using for example Knop's model [3]. When dealing with Gaussian beams, the angular spectrum representation is used, $A(\alpha)$ is sampled, the

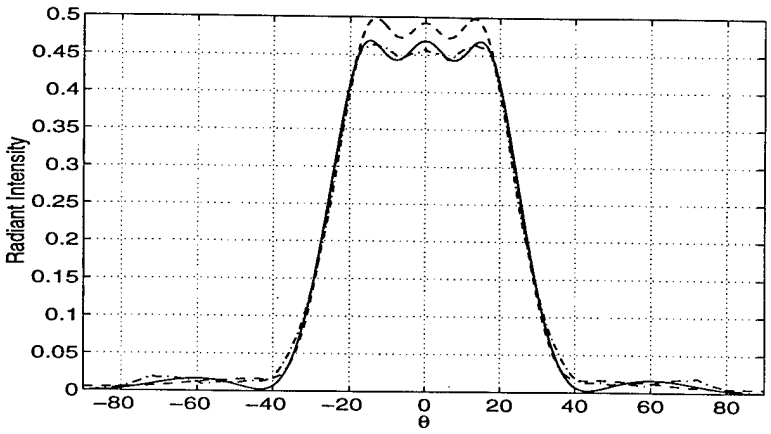


Figure 2: The radiant intensities in diffraction of a Gaussian beam from a single groove. The half width of the illuminating beam waist is 1.18λ and the groove width is 1.75λ. The best groove depths are $h = 0.67\lambda$ for TE-polarization (continuous line), $h = 0.72\lambda$ for TM-polarization (dashed line) and $h = 0.63\lambda$ for the grating solution in TE-polarization (dash-dotted line).

grating diffraction problem is solved for each plane wave component separately, and the results are then summed up coherently for the reflected and transmitted fields. If the beam waist is narrower than the grating period, no discrete diffraction orders are observed, and continuous beam shaping becomes possible.

4 Numerical results

To compare these two methods we designed elements which convert a Gaussian beam of $1/e^2$ half-width 1.18λ into a flat-top distribution of opening angle 33°. For the binary grating we know that most of the incoming energy is diffracted into diffraction orders $p = 0$ and $p = \pm 1$. The relative intensities of these orders depend on the relief height h. It therefore appears reasonable to assume that also most of the energy of the diffracted Gaussian beam might fall between the first order diffraction angles. For a normally incident plane wave we can solve from the grating equation $\sin\theta_{\mathrm{III}} = p\lambda/\Lambda$, the grating period Λ, which gives diffraction angles $\sim \pm 16.5°$ for the first diffraction orders $p = \pm 1$: we get $\Lambda = 3.5\lambda$. The only free parameter is now the relief height h of the binary grating. By varying this height we can adjust the efficiencies of the diffraction orders, which has a direct effect in the flatness of the farfield distribution. (We note, however, that the simple convolution model of Fraunhofer diffraction is not valid in the resonance region.) If we aim the Gaussian beam into the groove of the grating, we find out that a suitable relief height is $h = 0.63\lambda$: see Fig. 2, dash-dotted line. In the analysis we used TE-polarized light and refractive indices $n_{\mathrm{I}} = 1.5$, $n_{\mathrm{III}} = 1$, and $n = 1.5$ for the grating material. We analyzed this same structure with the method described in Sec. 2. We selected value $c = 7\lambda$ and placed a groove of width

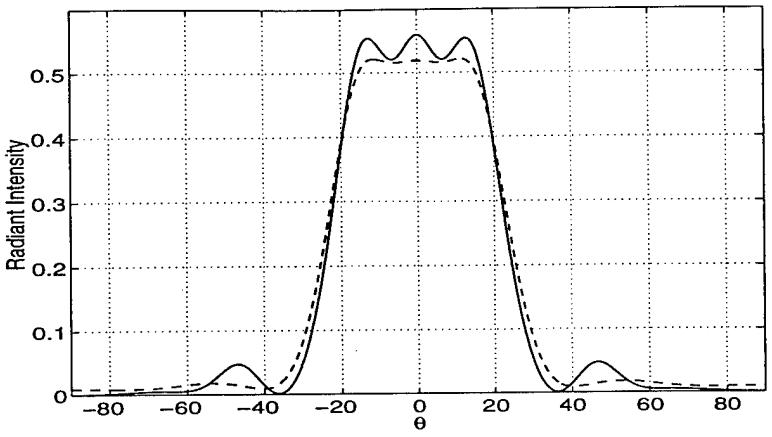


Figure 3: Radiant intensities when the Gaussian beam (same as in Fig. 2) is diffracted from a single ridge. The ridge height is 0.81λ for TE-polarization (continuous line) and 0.80λ in TM-polarization (dashed line).

1.75λ in the middle of the aperture. Because the aperture is wide compared to the incident beam we can assume that the perfectly conducting walls have little effect. For TE-polarization we find that the best groove depth is $h = 0.67\lambda$. For TM-polarization we find that the best flatness is achieved when $h = 0.72\lambda$. The radiant intensities for diffraction by the groove are presented in Fig. 2 as continuous and dashed lines for TE- and TM-polarizations, respectively. We notice that, although the structure is non-periodic, we still can recognize three tops comparable to the solution for the grating (dash-dotted line).

For the ridge we find $h = 0.81\lambda$ and $h = 0.80\lambda$ for TE- and TM-polarizations, respectively (see Fig. 3). It is remarkable in Fig. 3 that the radiant intensity is almost constant throughout the flat-top region for TM-polarization. Furthermore, this ridge solution works with almost the same relief height for both polarizations.

References

[1] J. M. Miller, J. Turunen, E. Noponen, A. Vasara, and M. R. Taghizadeh, "Rigorous modal theory for multiply grooved lamellar gratings," *Opt. Commun.*, **111**, 526–535 (1994).

[2] R.H. Morf, "Exponentially convergent and numerically efficient solution of Maxwell's equations for lamellar gratings," *J. Opt. Soc. Am. A*, **12**, 1043-1056 (1995).

[3] K. Knop, "Rigorous diffraction theory for transmission phase gratings with deep rectangular grooves," *J. Opt. Soc. Am.*, **68**, 1206-1210 (1978).

Diffraction Efficiency of High-NA Continuous-Relief Diffractive Lenses

M. Rossi, C.G. Blough, D.H. Raguin
Rochester Photonics Corporation, 330 Clay Road, Rochester, NY 14623
Phone (716) 272 3010, Fax (716) 272 9374, e-mail: rpc@eznet.net

E.K. Popov*, D. Maystre
Laboratoire d'Optique Electromagnetique, Faculté des sciences et techniques de Saint-Jerome
Ave. Escadrille Normandie-Niemen, 13397 Marseille Cedex 13, France
* on leave from: Institute of Solid State Physics, 72 Tzargradsko Chaussee, Sofia 1784, Bulgaria

1. Introduction

Diffractive lenses are key elements in a large variety of optical systems. In hybrid refractive/diffractive optical systems they are used as powerful elements for aberration correction. Other applications, such as fiber coupling and optoelectronic devices, benefit from the fact that diffractive structures are thin and lightweight, enabling very compact systems. In addition, low-cost replication processes with a high profile fidelity make the use of diffractive lenses in prototype systems as well as in volume production very attractive.

Diffractive phase elements can be fabricated by either a series of photolithographic processes that approximate the surface relief with a multilevel structure (binary optics) or by direct write technologies, such as single-point laser beam writing in photoresist [1] and single-point diamond turning [2]. In contrast to the multimask and etch process, these two fabrication methods require a single fabrication step and are capable of generating the continuous surface-relief profiles required to achieve high (> 90%) diffraction efficiencies.

In this paper we describe the design, the fabrication and the optical characterization of an F/2 diffractive lens for a fiber coupling application. The measured diffraction efficiencies are compared to rigorous electromagnetic calculations and results obtained with a simple and fast algorithm based on phase-sensitive ray tracing. The replicated elements show an excellent profile fidelity and high efficiency.

2. Design and fabrication of high-NA fiber coupling lens

The optical setup of the fiber coupling system is shown in Fig. 1. The diffractive lenses are replicated on both sides of a fused silica substrate. Both lenses have a focal length of $f = 10$ mm and a diameter $D = 5$ mm, resulting in a numerical aperture of NA = 0.24. The aspheric wavefront represented by diffractive lenses can be written as

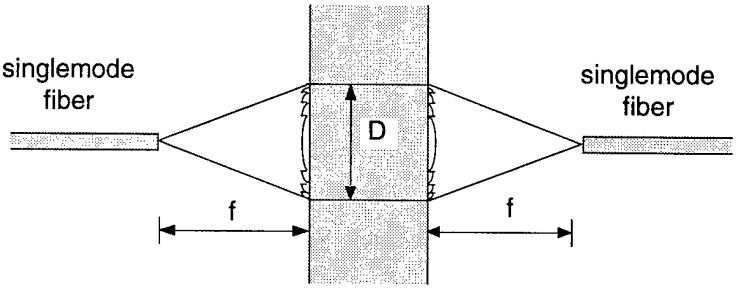


Fig. 1. Optical fiber coupling setup.

$$\phi(r) = \frac{2\pi}{\lambda_0}\left(\frac{\beta_1}{f}\cdot r^2 + \frac{\beta_2}{f^3}\cdot r^4 + \frac{\beta_3}{f^5}\cdot r^6\right), \text{ with } \beta_1 = -\frac{1}{2}, \beta_2 = \frac{1}{8}, \beta_3 = -\frac{1}{16}. \quad (1)$$

The design wavelength λ_0 is 1.55 µm. The required phase shift $\phi(r)$ for scalar diffraction theory is realized by a surface relief profile $d(r)$ in a substrate of refractive index $n(\lambda_0)$ given by

$$d(r) = \frac{\lambda_0}{2\pi\left[n(\lambda_0) - 1\right]}\cdot \mathrm{mod}\left[\phi(r), 2\pi m\right]. \quad (2)$$

The parameter m denotes the blaze order of the lens and determines the width and depth of the zones. Using Eqs. (1) and (2), the minimum zone width Λ_{min} and the scalar zone depth d_{sc} can be calculated by

$\Lambda_{min} \approx 2m\lambda \cdot f/\#$ and

$$d_{sc} = \frac{m\lambda}{n(\lambda)-1}, \text{ respectively.} \quad (3)$$

For multimask fabrication techniques, a lens of order $m > 1$ requires m times as many masks and fabrication steps in order to achieve the performance of an equivalent first-order lens. In contrast, direct-write fabrication methods can profit from the interesting optical properties of higher order lenses [3] without imposing additional fabrication problems. Moreover, the wider but deeper zones of lenses with $m > 1$ are more adapted for the resolution achievable by the fabrication with a laser beam [4] or a diamond tool with a finite tip size.

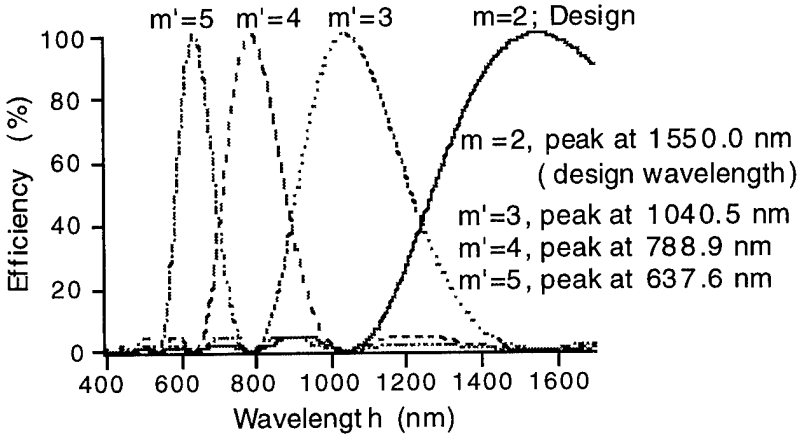


Fig. 2. Efficiency in different diffraction orders as a function of the illumination wavelength λ_1 for replicated F/2 diffractive lens.

For the diffractive lens presented here, $m = 2$ was chosen, leading to a minimum zone width Λ_{min} of 12.8 μm and a depth of $d_{sc} = 5.73$ μm. An analysis in the paraxial domain shows that the lens efficiency in the diffraction order m' as a function of the wavelength is given by [5]

$$\eta_{m'}(\lambda_1) = \mathrm{sinc}^2(\alpha\mu m - m'). \quad (5)$$

The parameter μ describes a potential profile depth error and

$$\alpha = \frac{\lambda_0[n(\lambda_1)-1]}{\lambda_1[n(\lambda_0)-1]} \quad (6)$$

quantifies the phase delay for an illumination wavelength λ_1 differing from the design wavelength λ_0. The plot of Eq. (5) in Fig. 2 reveals that a lens designed for $\lambda_0 = 1.55$ μm and $m = 2$ has an efficiency maximum in the 5th diffraction order for $\lambda_1 \approx 0.64$ μm. Therefore, the optical properties of the replicated near-IR diffractive fiber coupling lenses can be tested with a HeNe laser.

The master surface used for replication was generated using single-point diamond turning techniques. Diamond turning is a mature technology that provides the ability to generate robust metal master surfaces, which are essential for repeated replication cycles. By utilizing a well-behaved diamond turning machine, a correctly sculpted diamond tool, and classical grating replication techniques, high fidelity diffractive elements can be fabricated [6]. An SEM cross-sectional view of a replicated F/2 fiber-coupling lens is shown in Fig. 3. One notes that the relatively small features exhibit exceptional fidelity, sharp zone transitions and smooth surface profiles. The measured surface roughness in the central zone is approximately 45 Å rms [7]. The ability to sculpt the diamond tool provides the means to achieve the remarkably steep sidewalls of the zone transi-

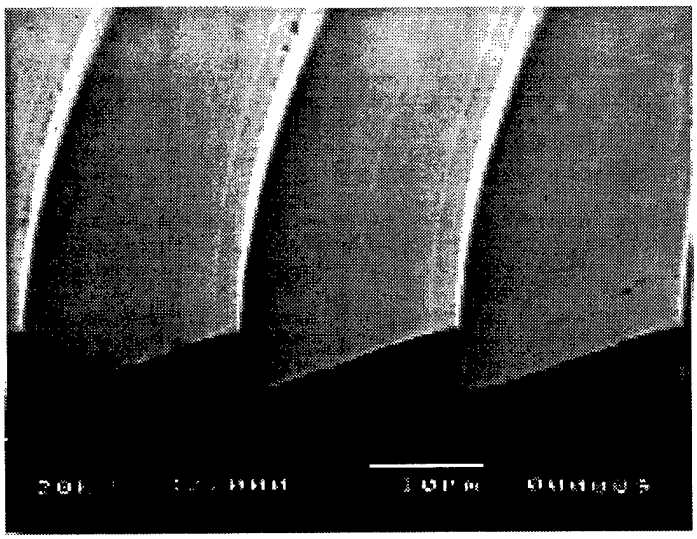


Fig. 3. SEM picture of a replicated diamond-turned diffractive lens with NA = 0.24.

tions, which are critical for obtaining high diffraction efficiency [8].

3. Diffraction efficiency of high-NA diffractive lenses

The surface-relief profile of a diffractive lens locally acts as a blazed grating to which we will apply theoretical models. Scalar theory, Eqs. (1) - (5), leads to accurate results as long as the ratio between the local grating period Λ and the wavelength satisfies $\Lambda/m\lambda \gg 1$ [9]. Since the F/2 lens described in this paper is on the border line of the validity of scalar theory, rigorous electromagnetic theory has to be applied to calculate accurate theoretical diffraction efficiencies. Since these rigorous calculations are usually computation intensive, we applied a refined scalar theory that leads to remarkably accurate results in short computation times [5].

Besides neglecting polarization effects, scalar design methods calculate the phase shift of a diffractive element given in Eq. (1) in an infinitely thin plane. In the ray tracing method, also referred to as the "extended scalar theory" by Swanson [10], some of the effects of the finite thickness of the grating are taken into account. The finite grating thickness is treated by tracing an array of rays through the grating structure and calculating their position and optical phase in a tangential grating plane σ as shown in Fig. 4. Each intersection point in the plane σ is regarded as an ideal point source in the sense of the Huygens-Fresnel principle. Depending on the distance to the observation plane, Rayleigh-Sommerfeld, Fresnel or Fraunhofer diffraction equations are used to determine the amplitude and phase distributions.

For perfectly blazed gratings, this algorithm predicts the highest diffraction efficiency for a grating depth d_{rt} that is shallower than d_{sc}:

$$d_{rt} = \frac{m\lambda}{n(\lambda) - \cos\theta_m}, \tag{7}$$

where the angle θ_m is given by the grating equation:

$$\sin\theta_m = \frac{m\lambda}{\Lambda}. \tag{8}$$

Moreover, it can be shown that due to the so-called "shadowing effect" (cf. Fig. 4) in the tangential grating plane σ, a maximum diffraction efficiency of

$$\eta_{rt} = \frac{\Lambda'}{\Lambda}, \text{ with } \Lambda' = \Lambda\left(1 - d_{opt}\tan\theta_m\right) \tag{9}$$

can be obtained. As will be shown in the next Section, these results correspond well with values obtained with a rigorous integral formalism [11]. Aside from giving an estimate of the diffraction efficiency at small grating periods, the most valuable benefit of the ray tracing algorithm is that the effects of small fabrication errors (e.g. originating from the diamond tool geometry or from overlaying Gaussian beams in direct laser beam writing) can be estimated with little additional computational effort.

The extended scalar theory predicts a maximum diffraction efficiency of $(\eta_{rt})^2$ for the case of multilevel blazed gratings [10]. Using ray tracing arguments, this reduction of the classical scalar theory value can be explained by additional shadowing at each facet of the multilevel structure.

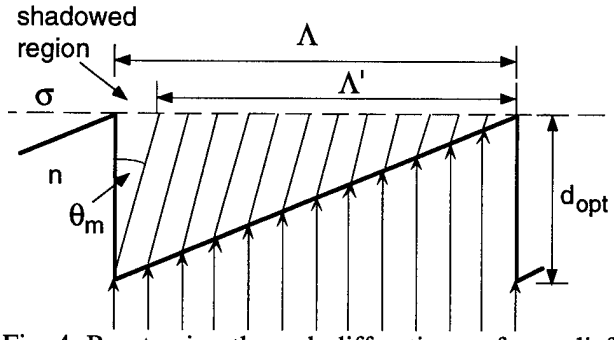


Fig. 4. Ray tracing through diffractive surface-relief structures.

4. Theoretical and experimental results for F/2 fiber coupling lens

We have compared the results for perfectly blazed gratings from the ray tracing algorithm and the rigorous integral formalism. The grating period modelled was chosen to be $\Lambda = 12.78\ \mu m$, corresponding to the minimum zone size of the fabricated F/2 lens with $m' = 5$, see Eq. (3). Both models obtained an optimum profile depth of $d_{rt} = 5.38\ \mu m$. The zone depth of the fabricated

lens was kept at a constant value of $d_{sc} = 5.73$ µm over the whole clear aperture. Therefore, the profile ended up too deep by a factor of $\mu \approx 1.07$ for the smallest zones. From Eq. (5), one notes that the resulting reduction in the diffraction efficiency is more severe in the 5th diffraction order where the lens is tested than in the 2nd order for which the lens is designed. Nevertheless, we will present results for diffractive lenses with locally varying zone depths according to Eq. (7). The diffraction efficiencies obtained by rigorous calculations and the ray tracing algorithm are listed in Table 1. All values are normalized to the total transmitted energy. The ray tracing results illustrate good agreement with the rigorous vector diffraction results.

Table 1. Theoretical diffraction efficiencies for blazed gratings with $\Lambda = 12.78$ µm at different profile depths.

profile depth	$m = 2, \lambda_0 = 1.55$ µm		$m' = 5, \lambda_1 = 0.6328$ µm	
	rigorous	ray tracing	rigorous	ray tracing
5.38 µm	–	90.4%	85.8%	90.5%
5.73 µm	81.0%	85.6%	63.0%	62.4%

Knowing the geometry of the diamond tip and the diamond turning machine's fabrication data, the shape of the fabricated surface relief profile can be calculated. Even for the smallest zone sizes of 12.8 µm, the ray tracing algorithm predicts a loss of less than 3% due to the finite tool size. This is not unexpected considering the excellent profile fidelity illustrated in Fig. 3.

The diffraction efficiency of the replicated lenses at different radii was measured by illumination with a HeNe laser beam ($\lambda_1 = 0.6328$ µm) through a pinhole with a diameter of 110 µm. For a local grating period of $\Lambda \approx 13.5$ µm an efficiency of $\eta_5 = 64\%$ was obtained, at $\Lambda \approx 19$ µm a value of $\eta = 85\%$ was measured. Both measurements show a good coincidence with the theoretical results. The local diffraction efficiency rises well above 90-95% for zones with $\Lambda > 25$ µm. The wavefront performance of the fiber coupler was interferometrically tested to be less than a quarter of a wave at $\lambda_1 = 0.6328$ µm. This corresponds to less than $\lambda/10$ for the design wavelength of $\lambda_0 = 1.55$ µm.

5. Conclusions

A pair of F/2 diffractive lenses is used in a fiber coupling application. Designing the lenses for the second diffraction order in the near-IR allowed their testing with a HeNe laser. The fabrication by single-point diamond turning and subsequent replication resulted in an excellent fidelity of the surface relief profile and high diffraction efficiencies. A ray tracing algorithm developed for fast estimation of the efficiencies of small zones proved good agreement with rigorous vector theory.

6. References

[1] M.T. Gale, M. Rossi, J. Pedersen, and H. Schütz, "Fabrication of continuous-relief micro optical elements by direct laser writing in photoresist," Opt. Eng. 33, 3556 (1994).

[2] C. Londono and P. P. Clark, "The design of achromatized hybrid diffractive lens systems," Proc. SPIE **1354**, 30 (1990).

[3] D. Faklis, G.M. Morris, "Spectral properties of multiorder diffractive lenses," Appl. Opt. **34**, 2462 (1995).

[4] M. Rossi, G.L. Bona and R.E. Kunz, "Arrays of anamorphic phase-matched Fresnel elements for diode-to-laser coupling," Appl. Opt. 34, 2483 (1995).

[5] M. Rossi, R.E. Kunz and H.P. Herzig, "Refractive and diffractive properties of planar microoptical elements," Appl. Opt. **34**, 5996 (1995).

[6] C. G. Blough, *et al*, "High efficiency replicated diffractive optics," Proc. SPIE **2600**, 15 (1995).

[7] Zygo New-View Surface Profilometer, 40X microscope objective.

[8] T. Fujita, H. Nishihara, and J. Koyama, "Blazed gratings and Fresnel lenses fabricated by electron-beam lithography," Opt. Lett. **7**, 578 (1982).

[9] E. Noponen, J. Turunen and A. Vasara, "Electromagnetic theory and design of diffractive-lens arrays," J. Op.t Soc. Am. A **10**, 434 (1993).

[10] G.J. Swanson, "Binary optics technology: theoretical limits on the diffraction efficiency of multilevel diffractive optical elements," MIT Technical Report **914** (1991).

[11] D. Maystre, "A new general integral theory for dielectric coated gratings," J. Opt. Soc. Am **60**, 490 (1978).

Pseudorandom Encoding of Fully Complex Modulation to Bi-Amplitude Phase Modulators

Robert W. Cohn and Wenyao Liu
University of Louisville, Electrical Engineering Dept., Louisville, Kentucky 40292
(502) 852-7077, Fax (502) 852-6807, Rwcohn01@Ulkyvm.Louisville.Edu
Liu's permanent address is Precision Instrument Engineering Dept., Tianjin Univ., Tianjin, 300072, China

Pseudorandom encoding is a statistically-based, pixel-by-pixel mapping of complex valued modulations onto modulators that do not produce all complex values.[1] The resulting far-field diffraction pattern closely approximates that from the desired, but unimplementable, complex modulation. Since the methed is point-oriented, the desired complex modulation can be synthesized and encoded without resorting to time consuming constrained global optimizations *e.g.* simulated annealing,[2] genetic,[3] and Gerchberg Saxton[4] algorithms. In addition to reducing design time, the resulting diffraction patterns can have reasonably high diffraction efficiencies and low levels of background noise.

As originally described, the method was applied to phase-only modulators.[1] In this paper we consider phase modulators that have one additional transmittance state, namely, zero amplitude transmittance. The addition of this single state can improve performance over phase-only modulation, and it is fairly straightforward to add a patterned opaque layer to the current fabrication processes for diffractive optical elements (DOEs). Our design method does specify analog, rather than discrete, phases. This does not preclude the use of discrete level diffractive optics as long as there are enough phase levels to adequately reduce the effects of quantization error.[5,6]

An objective of this paper is to introduce the concept of pseudorandom encoding in as simple a manner as possible. Encoding for bi-amplitude modulators is ideal for this purpose because the statistical properties of amplitude are more obvious than of phase, as were originally reported in ref. 1.

A second objective is to compare the method with a recently-developed non-random, point-oriented encoding algorithm. This specific algorithm is referred to as MEDOF (for minimum Euclidean distance optimal filter).[7] Design using MEDOF begins by specifying an optimal complex valued filter. Each complex value is then mapped to the modulator value that is closest to the desired complex value. The distances can be minimized by varying two parameters. One parameter G gain, scales the magnitude of the complex values with respect to the modulator operating curve. The second parameter β rotates the complex values with respect to the modulator curve. For the problem for which MEDOF was originally developed, that of single object (i.e. non-composite) correlation filters, MEDOF does produce the optimal solution.

For phase-only modulators the minimum distance MEDOF mapping is identical for any values of these two parameters G and β. For this special case the MEDOF filters are identical to Horner and Gianino's phase-only filter.[8] It has been shown that object recognition of composite filters mapped to phase-only modulators is somewhat better when using pseudorandom encoding instead of MEDOF.[9] In this paper we compare MEDOF and pseudorandom encoded spot array generators. For these DOEs pseudorandom encoding clearly outperforms MEDOF, at least as MEDOF had originally been described. However, this does not rule out the use of MEDOF for diffractive optics design. As will be shown, several aspects of MEDOF have been incorporated into the new encoding algorithm.

Pseudorandom encoding background. The algorithm, in general, is described as follows. The complex value $\boldsymbol{a}$ of a given modulator pixel is a single number drawn from a random number generator. The statistical properties (e.g. mean value and standard deviation) of the random number generator are varied so that the desired fully complex design value $\boldsymbol{a}_c$ equals $\langle \boldsymbol{a} \rangle$ the expected value of the random number generator. This procedure is repeated for each pixel of the modulator. The resulting far-field/Fourier plane diffraction pattern of the actual modulation values $\boldsymbol{a}$ closely approximates the Fourier transform of the desired values $\boldsymbol{a}_c$.

The basis of this approximation can be understood in terms of the law of large numbers.[10] The complex amplitude of the far-field pattern can be viewed as a linear combination of wavefronts. The i'th pixel, a source of strength $\boldsymbol{a}_i$ produces a wavefront of complex amplitude $A_i(f_x)$ across the

Fourier plane. The N total wavefronts coincide at the Fourier plane to form an ensemble. According to the law of large numbers, an ensemble of a large number of random occurences (the wavefront amplitudes A_i) approaches the average result (the desired diffraction pattern $\Sigma\langle A_i\rangle=\Sigma A_{c\,i}$.) The errors in this approximation depend on the number of pixels in the modulator and amount of noise introduced by using random modulation values.

The noise level is apparent in the expected far-field intensity pattern which is[1]

$$\langle I\rangle = \left|\sum_i A_{c\,i}\right|^2 + \sum_i \left\{\left\langle |A_i|^2\right\rangle - |A_{c\,i}|^2\right\} . \quad (1)$$

The first summation is the desired intensity pattern and the second summation (of the terms inside the braces) corresponds to the average intensity of background noise.[1] This noise is observed as a speckle pattern that fills the envelope of the diffraction pattern of a single pixel. The speckle energy is a measure of the degree of randomness used in the design. For example, if there is no randomness then the terms inside the braces cancel and the remaining summation is precisely the desired diffraction pattern. Ref. 1 also evaluates the standard deviation of the intensity pattern.

Encoding the design value a_c using random bi-amplitudes. Since the specified modulator can directly produce any value of phase, we will directly set ϕ the phase of the modulator equal to ϕ_c the desired phase. The amplitude of the modulator $a=|\boldsymbol{a}|$ can be set to either 1 or 0. We define a to be a discrete random variable having a value of 1 with probability p and a value of 0 with probability q=1-p. The average amplitude is simply

$$\langle a\rangle = 1\cdot p + 0\cdot q = p \quad (2)$$

which we use to represent any desired amplitude $a_c=|\boldsymbol{a}_c|=p$ between 0 and 1. The pseudorandom selection is directly performed using the standard uniform random number generator ran(*iseed*). If $0\le \text{ran} < p$ then a=1 and $\phi=\phi_c$. If $p\le \text{ran}\le 1$ then a=0. For random bi-amplitudes the expected intensity of the diffraction pattern, eq. (1), reduces to

$$\langle I\rangle = \left|\sum_i A_{c\,i}\right|^2 + \sum_i p_i q_i \quad . \quad (3)$$

It is clear that the second term describing the speckle background is small if the desired amplitudes $a_{c\,i}$ are clustered near either 1 or 0, and this term is large if the amplitudes are clustered near .5 . The level of the speckle indicates to what degree noise is affecting the accuracy of a design. Eq. (3) also shows that noise reduces the useful diffraction efficiency of the design.

Incorporation of MEDOF into Pseudorandom Encoding. Eq. (3) shows that for a given set of design amplitudes $a_{c\,i}$ (that are proportional to $|A_{ci}|$) the noise level is fixed. However, the noise level can be varied if we scale the design values by the gain factor G. The value of G is defined to be the maximum value of $a_{c\,i}$. In pseudorandom encoding as described in the previous section, we usually normalize the complex values so that G=1. The algorithm can be applied without modification for any value of G less than 1. Reducing G increases the number of zero states which reduces energy utilization.

Consider the alternative case in which the value of G is greater than 1. Eq. (2) cannot implement those values of $Ga_{c\,i}$ that now exceed unity radius (See fig. 1). We choose to set these amplitudes to 1 which corresponds to the MEDOF prescription. As with the original MEDOF algorithm, we search for the value of G that optimizes the performance of the diffractive optic. A value of G in excess of unity usually optimizes a specific design. Our interpretation[9] of this is that increasing G reduces the random errors, since fewer values are now pseudorandom encoded. There is now a second source of error, that we refer to as systematic error, for those desired amplitudes in excess of unity.[5] In performing this search over G we find that the optimal solution tends to balance the contributions due to random and systematic errors.

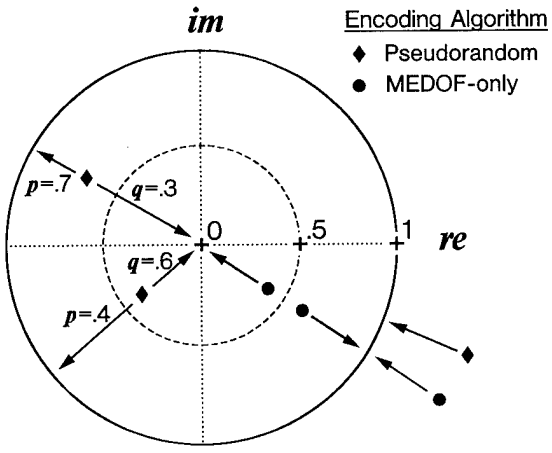


Fig. 1. Mapping desired complex values using pseudorandom and MEDOF-only encoding

Design example and comparison of pseudorandom and MEDOF-only encoding. Our objective is to design a 300 x 300 pixel diffractive optic that produces 64 spots of equal intensity in an 8 x 8 array. Ideally, the background noise is zero and we would like it to be as small as possible for the encoded design. The phases of the spots are varied in an attempt to maximize average intensity transmittance (hence, energy utilization) of the design values $\boldsymbol{a}_{c\,i}$. A set of desired complex values was found that have a diffraction efficiency of η=.23 for G equal 1.

These desired values are pseudorandom encoded a number of times for values of G between 1 and 1.82 . For purposes of comparison we also performed the MEDOF-only encoding as a function G. The mappings for these algorithms are illustrated in fig. 1. The MEDOF-only prescription sets the modulator value to $a_i = 0$ if $Ga_{c\,i}$ is less than .5, and to $a_i = 1$ otherwise. (We also verified by simulation that .5 gives the best solution for all possible threshold settings.) As with pseudorandom encoding, ϕ_i is set to $\phi_{c\,i}$ in all cases.

The various encodings of the desired $\boldsymbol{a}_{c\,i}$ into $\boldsymbol{a}_i$ were calculated and the resulting modulations were Fourier transformed with a 300 x 300 point discrete Fourier transform (DFT) subroutine. Various performance measures were calculated and are graphed in fig. 2. A conservative measure of signal to background noise is the average intensity of the 64 spots divided by the maximum noise intensity in the entire DFT file. We refer to this measure as signal to peak noise ratio (SPR). The ratio of the average signal to average noise intensities is typically one to two orders of magnitude larger than SPR. The non-uniformity is defined as a relative error; specifically, the standard deviation of the 64 spot intensities divided by the average intensity. The maximum peak-to-peak fluctuation in each case is roughly 2-3 times larger than the measure of non-uniformity plotted in fig. 2. The efficiency of the encoding in approximating the desired complex design η_e was calculated as the sum of the 64 spot intensities divided by the total energy in the Fourier transform plane. The average intensity transmittance of the modulator is $\eta_t = N_{on}/N$, where N_{on} is the number of modulator pixels set to unity amplitude. The energy utilization efficiency is then $\eta = \eta_t\eta_e$. The results in fig. 2 were found for values of G between 1 and 1.82 . Though G is not shown, note that diffraction efficiency η increases monotonically as a function of G.

Fig. 2 shows that the best pseudorandom encoded design outperforms the best MEDOF-only design in SPR (212 *vs.* 19.5) and non-uniformity (2.5 % *vs.* 17.8 %). The measured efficiency η_m of the best MEDOF-only encoding is higher than the best pseudorandom encoding (59 % *vs.* 32 %), but even this difference can be reduced by sacrificing some uniformity and SPR. For instance, even at an efficiency of 57 % the pseudorandom encoded design outperforms MEDOF in all other measures.

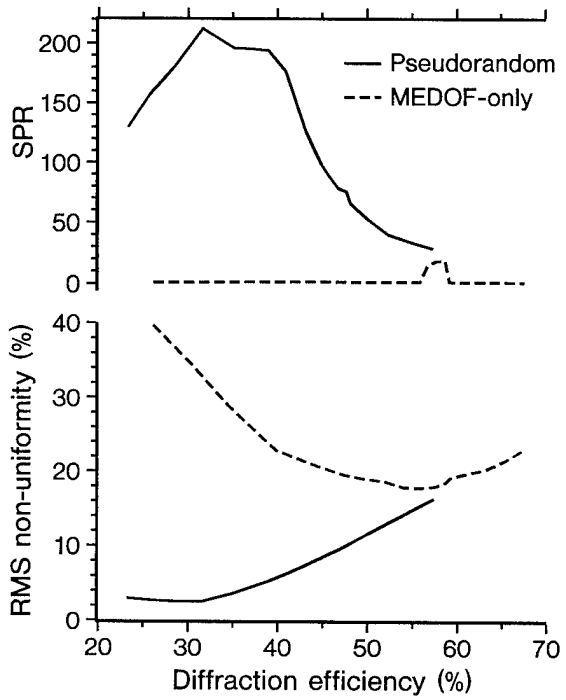


Fig. 2. Performance of encoding algorithms

The differences between MEDOF and pseudorandom encoding can be appreciated by considering the differences in the background noise of their diffraction patterns. The images shown (fig. 3) are for the designs for which SPR is maximum. The noise has been brought out by saturating the maximum grayscale in each intensity pattern by a factor that is roughly the same value as its respective SPR. The MEDOF design shows a series of harmonically related noise orders. Orders like these are quite common in many binary optics designs. The noise orders can be thought of as intermodulation distortion products that are known to result when two or more frequencies are passed through a nonlinearity. With multiple harmonically related frequencies there can be substantial interference and competition between desired frequencies, as well, which accounts for the large

non-uniformity. The pseudorandom design is subject to the same nonlinearity, but random encoding greatly reduces these effects. By using randomness, the noise (which is equivalent to the errors in the approximation to the $a_{c\,i}$) has been distributed more uniformly over the entire observation plane, as indicated by eq. (1) or eq. (3). Even if there is more total energy in the background noise, its peak level is usually much lower than the peak levels produced by MEDOF and other systematic approaches.

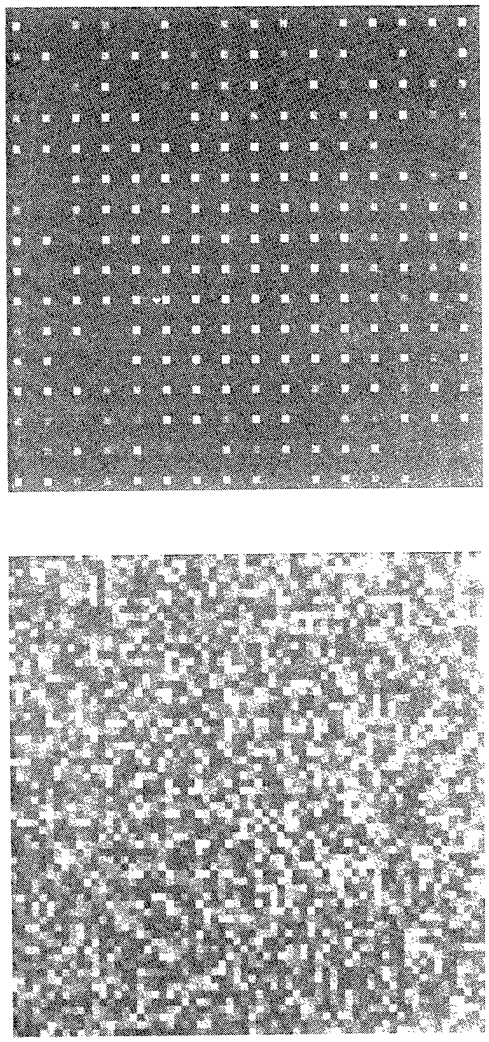


Fig. 3. Background noise of MEDOF-only (top) and pseudorandom encoded (bottom) spot arrays. Grayscale satuaration is 26x and 212x respectively.

Pseudorandom encoding can be viewed as attempting to maxmize the entropy of the approximation errors. In selecting gain G of greater than 1 some intermodulation products are accepted as long as an overall better performance in SPR, uniformity, etc. is achieved.

Pseudorandom encoding of bi-amplitudes produces results that are excellent for many critical applications and the devices require no new developments in fabrication art. We believe that these general pseudorandom encoding concepts can be used to the develop of substantially faster algorithms for globally optimal designs of diffractive optics.

1. R. W. Cohn, M. Liang, "Approximating fully complex spatial modulation with pseudo-random phase-only modulation," *Appl. Opt.*, **33**(20), 4406-4415. (1994)
2. M.P. Dames, R.J. Dowling, P. McKee, D. Wood, "Efficient optical elements to generate intensity weighted spot arrays: design and fabrication," *Appl. Opt.*, **30**(19), 2685-91 (1991).
3. E. G. Johnson, M. A. Abushagur, "Microgenetic-algorithm optimization methods applied to dielectric gratings," *JOSA A*, **12**(5),1152-1160. (1995)
4. R.W. Gerchberg, W.O. Saxton, "Practical algorithm for the determination of phase from image and diffraction plane pictures," *Optik* **35**(2), 237-250 (1972).
5. R. W. Cohn, "Performance Models of Correlators with Random and Systematic Phase Errors," *Opt. Eng*,**34**(6),1673-1679. (1995)
6. W. J. Dallas, "Computer-Generated Holograms," Ch.6, pp.332-334. *The Computer in Optical Research*, B. R. Frieden, Ed., Springer, Berlin. (1980)
7. R. D. Juday, "Optimal realizable filters and the minimum Euclidean distance principle," *Appl. Opt.*, **32**(26), 5100-5111. (1993)
8. J.L. Horner, P.D. Gianino, "Phase-only matched filtering," *Appl. Opt.*, **23**, 812-816. (1984)
9. L.G. Hassebrook, M.E. Lhamon, R.C. Daley, R.W. Cohn, M. Liang, "Random Phase Encoding of Composite Fully Complex Filters," to appear in *Opt. Lett.*
10. A. Papoulis, *Probability, Random Variable and Stochastic Process*, 3rd ed, pgs. 107, 211. McGraw-Hill, New York. (1991)

Analysis and synthesis of 2-D diffractive lens using the local linear grating model and the coupled-wave theory

Yunlong Sheng, Simon Larochelle and Dazeng Feng
Université Laval, Centre d'Optique, Photonique et Laser,
Département de Physique, Québec, Canada G1K 7P4.
Tel: 418 656 3908, Fax: 418 656 2623 sheng@phy.ulaval.ca

Large numerical aperture diffractive lenses have many applications for imaging and beam coupling. Since the minimum Fresnel zone width of a diffractive lens is approximately proportional to F-number: $r_M - r_{M-1} = 2\lambda F/\#$, the grating period in the region close to the lens edge is comparable with the wavelength λ for a fast lens. The diffraction of such surface relief wavelength-scale structures should be solved with rigorous electromagnetic theory. Most methods with the resonance domain diffraction theory for analysis and synthesis of diffractive optics elements are for 1-D and 2-D separable gratings, 1-D cylindrical lens and 2-D lens arrays[1]. Those elements are treated with the 1-D grating model. However, rigorous analysis of a single 2-D radially symmetrical diffractive lens needs solutions of the 3-D Maxwell equations. The numerical solutions with the finite-element methods[2] are usually computational expansive.

In this paper we present a simple method for estimation and optimization of the diffraction efficiency of 2-D radially symmetric diffractive lenses, using a local linear grating model of the lens and the coupled-wave theory[3]. The numerical experiments show that the model is self-consistent and is consistent with the scalar theory when the feature size of the lens structure is large compared to the wavelength.

The full-period Fresnel zones of a diffractive lens are defined so that the optical path from the edge of the m-th zone is equal to $m\lambda$. The radii of the m-th zone is given by:

$$r_m = \sqrt{2m\lambda f + (m\lambda)^2} \qquad (1)$$

The zone width decreases approximately as $1/r_m$. At the center the zones are much larger than λ. The diffraction efficiency of this part of the lens may be 100% for continuous phase profile and 95% for eight discrete phase levels. Near the edge the zone widths are comparable with λ. The scalar approximation may introduce important errors in analyzing this part of the lens.

The difficulty of the vector theory of diffraction in analyzing the 2-D lens is that most theoretical methods are developed for 1-D linear gratings, presented by a cylindrical surface whose generatrices are infinitely long. Only in this case the Maxwell equations are 2-D and are of scalar nature. Many existing methods can provide numerical solutions. Otherwise, solution of the Maxwell equations is a 3-D problem that can be solved only by computational expansive numerical methods, such as the finite element methods.

In order to apply the 1-D grating theory to the analysis and synthesis of a 2-D lens, we introduce an approximative local linear grating model for the radially symmetrical lens. We divide the lens into two regions. In central region the scalar theory may be still applied. Only in the outer ring-shaped region the rigorous vector theory should be applied. Then, we divide the ring into N angular sections. Let θ_j be orientation of the j-th section with j =0, 1,..., N-1. Each

of the N identical sections is considered as a 1-D linear grating whose period decreases with the radius r. The curvature of the linear grating groove is null. Thus, the lens is approximated by a N-polygon. When $N \rightarrow \infty$, the polygon tends to the circular lens. There is a trade-off between the validity of the linear grating model and that of the approximation to the circular lens by a N-polygon. We keep the shortest groove length longer than 10λ: $2\pi r_0/N > 10\lambda$, where r_0 is the inner radius of the ring. For r_0=1 mm and λ=0.62μm, N<1000, the N-polygon is very close to the circular lens.

The linear grating model may be justified since the interaction between electromagnetic field and substrate is essentially local and the groove length of the angular section grating is much larger than 10λ. The validity of the model can be also justified by the computation results compared with that provided by other methods.

In order to estimate diffraction of the angular section grating whose period decreases with r, we divide the section into L local gratings of constant period. The i-th local grating has the boundary of r_i and r_{i+1} with i = 0, 1, ..., L-1 and r_0 and r_L is the inner and outer radius of the ring, respectively. The constant period of a local grating is the local mean of the varying period. This approximation may be justified since variation of the period is smooth. Our computation results, which will be given in Figure.3, show that the computed diffraction efficiency is not sensitive to the grating divisions for arbitrary radial divisions r_i.

Now we compute the diffraction of a local grating (i,j). Let the incident beam be a plane wave with uniform amplitude, and $x\mathbf{E}_{+1})_{i,j}$ be the transmitted first order of diffraction just behind the local grating (i,j). First we consider an angular section with θ_j = 0. Its grooves are parallel to the y-axis. The radial direction of the lens is parallel to the x-axis.

The components of $(\mathbf{E}_{+1})_{i,0}$ are computed from the two fundamental TE and TM polarizations: E_y is solved from the TE polarization and E_x and E_z are solved from the TM polarization. The rigorous coupled-wave analysis is implemented in the computation.

According to Eq.(1) the optical paths from every zone to the focal point have a difference of λ. Hence, the propagation from lens to the focus introduces no additional phase shift. All the first orders diffracted by local gratings are directed to the focus. However, the field $(\mathbf{E}_{+1})_{i,0}$ is complex valued, whose amplitude and phase depend on the grating period and groove profile, and thus vary with r_i. Figure 1 and 2 show the intensity and phase of the first order of diffraction as a function of the grating period for TE and TM polarization. When the grating period is smaller than 3λ. the intensity of the first order of diffraction decreases dramatically (<50%) and their phase varies very fast with the grating period, resulting in fast drop of the diffraction efficiency.

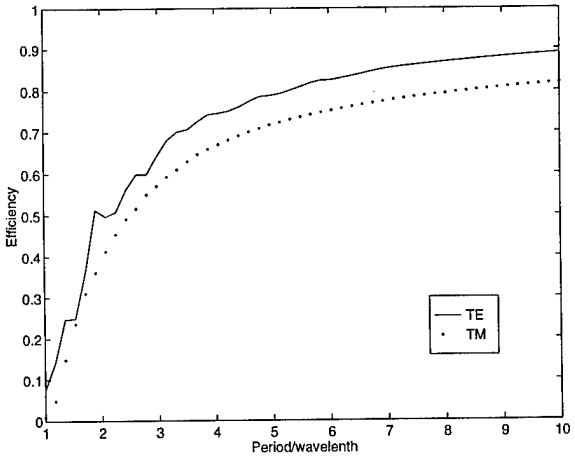


Figure 1. The first order intensity as a function of the grating period.

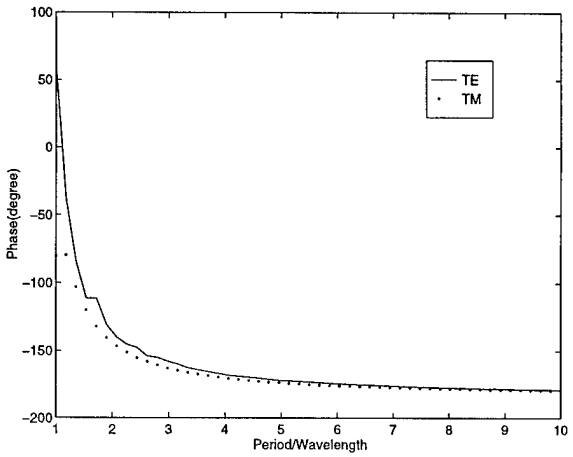


Figure 2. The first order phase shift as a function of the grating period.

The contributions to the field at the focus from all the local gratings i = 0, 1, 2, ..., L-1 in the angular section with j = 0 may be simply added up :

$$E_{j=0} = \sum_{i=0}^{L-1} c_i (E_{+1})_{i,0} \qquad (2)$$

where c_i^2 is proportional to the area of the surface of the i-th grating

$$c_i = \sqrt{r_{i+1}^2 - r_i^2} \qquad (3)$$

Equation 2 is in fact the vector transmittance of the angular section grating $\theta_j = 0$ which is illuminated uniformly.

In order to compute the contribution to the field at focus of the angular section j $\neq 0$, we assume that the incident beam $\mathbf{E}_1$ is polarized along the y-axis. First we rotate an angle θ_j of the coordinate system x-y to X-Y. In the new X-Y coordinate system, the j-th angular section grooves are parallel to the Y axis, and the incident beam becomes to $\mathbf{R}(\theta_j)\mathbf{E}_1$. Then we multiply a matrix of transmittance $\mathbf{T}$ to obtain the transmitted beam in X-Y coordinate system, the matrix $\mathbf{T}$ is defined using the vector $\mathbf{E}_{j=0}$ from Eq.2 as:

$$T = \begin{vmatrix} E_x & 0 & 0 \\ 0 & E_y & 0 \\ E_z & 0 & 0 \end{vmatrix} \qquad (4)$$

Finally, we rotate back to the original x-y coordinate system by the matrix of $\mathbf{R}(-\theta_j)$ and the transmitted beam is given by:

$$E_j = R(-\theta_j) \cdot T \cdot R(\theta_j) \cdot E_1 \qquad (5)$$

where the matrix of rotation is:

$$R(\theta_j) = \begin{vmatrix} \cos(\theta_j) & \sin(\theta_j) & 0 \\ -\sin(\theta_j) & \cos(\theta_j) & 0 \\ 0 & 0 & 1 \end{vmatrix} \qquad (6)$$

Then, we add up the vector fields diffracted from all the angular sections j = 0, 1, 2,... N-1 of the lens. Since the lens is radially symmetrical and the incidence is normal, the resultant field is along the z-axis. The diffraction efficiency is easily estimated. This results is in fact the efficiency of the outer ring-shaped region of the lens. That of the central part of the lens is estimated with the scalar theory.

In order to establish the relevance of our approximative local linear grating model of the 2-D lens, we computed a lens of small numerical aperture with f = 10 mm and F/4 with 4 discrete phase levels. The computed diffraction efficiency of 75.4% tends to that of 81% predicted by the scalar theory. The difference between the scalar and the vector theory results is even smaller because the vector theory shows a reflection loss of about 3%. The scalar theory does not give the reflection loss.

Figure 3 and 4 show the estimated diffraction efficiency of a lens as a function of the randomly changed radial divisions of the angular sections and as a function of the number of angular divisions N. The computation was done for a F/1 lens with f

= 1 mm and 16 phase levels. The inner radius r_0 of the ring-shape part of the lens is the radius of the 11-th zones, $r_0 = r_{m=11}$, where r_m is defined by Eq.1. The radial divisions generate about 16 local gratings. Each grating contains about 10 zones (grooves). We shifted randomly all the transition points in the angular section with a maximum shift of 2 Fresnel zone widths. The variations of the estimated diffraction efficiency were less than 1%. Also, when the number N of the angular divisions of the lens varies form 4 to 100, the estimated diffraction efficiency varied less than 0.1%.

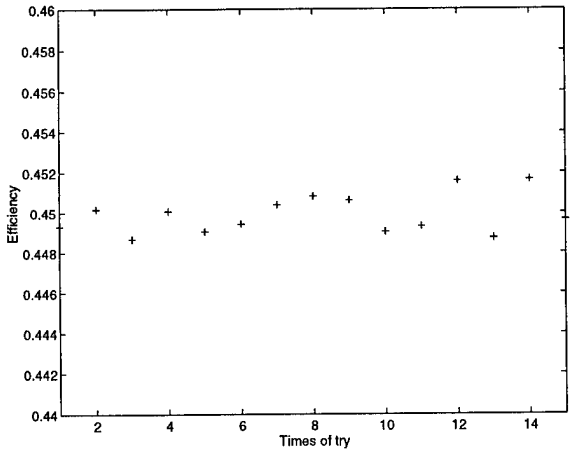


Figure 3. Lens efficiency as a function of the randomly changed radial divisions of the angular sections.

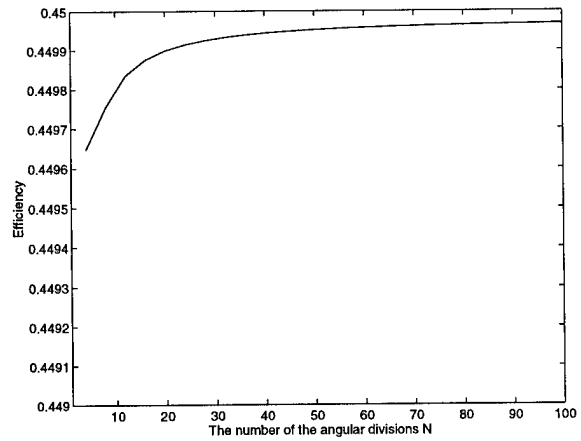


Figure 4. Lens efficiency as a function of the number of angular divisions.

Synthesis and optimization of the 2-D lens for high efficiency using the local linear grating model are under way. The local grating groove shape should be changed and optimized, and both the intensity and the phase of the first diffraction order of the local grating are important in the optimization.

We have introduced an approximative local linear grating model for estimating the diffraction efficiency of the 2-D radially symmetrical diffractive lens using the coupled-wave theory. We have shown that the local linear grating model is self-consistent and is consistent with the scalar theory results when the feature size is large compared to the wavelength.

References

1. E. Noponen, J. Turunen and A. Vasara, "Electromagnetic theory and design of diffractive-lens arrays", J. Opt. Soc. Am. A, **10**, 434-443(1993).

2. B. Lichtenberg and N. C. Gallagher, "Numerical modelling of diffractive devices using the finite element method", Opt. Eng, **33**, 3518-3526(1994).

3. M. G. Moharam and T. K. Gaylord, "Diffraction analysis of dielectric surface-relief gratings", J. Opt. Soc. Am, **72**, 1385-1392(1982).

Wednesday, May 1, 1996

Subwavelength Structures

DWA 8:30 am-10:00 am
Gardner A&B

Yeshayahu Fainman, *Presider*
University of California, San Diego

Thin-film filters with diffractive and waveguiding layers

R. Magnusson, S. Tibuleac, Z. Liu, D. Shin, and P. P. Young
Department of Electrical Engineering
The University of Texas at Arlington
Arlington, Texas 76019
Phone: (817) 272-3474
Fax: (817) 272-2253

S. S. Wang
Motorola Inc.
5555 North Beach Street
Fort Worth, Texas 76137

By merging traditional thin-film optics with diffractive and waveguide optics, it has been shown theoretically that optical reflection filters can be designed with 100% efficiency, symmetrical lineshapes, near-zero nonoscillatory sidebands over extended wavelength regions, narrow (or wide) controllable linewidths, and other favorable attributes [1]. Thus, single- and multilayer reflective filters with near ideal features have been theoretically demonstrated by utilizing anti-reflection design to suppress reflections adjacent to the resonance peak [2]. In addition, a transmission bandpass filter can be designed using guided-mode resonance effects with a highly reflecting dielectric multilayer stack [3]. This new transmission filter produces broad-range low-transmission sidebands with nearly 100% transmission efficiency at the passband. Numerous applications have been identified including laser resonator frequency-selective polarizing mirrors, laser cavity tuning elements, mirrors and phase-locking elements for vertical-cavity surface emitting laser arrays, and sensor elements [4]. Experimental results verifying the theoretically predicted high resonance efficiencies for reflection filters have been reported in the optical spectral region [5,6], in the millimeter wave region [7], and in the microwave region [8].

A very general diffraction problem (Fig.1) has been mathematically formulated using rigorous coupled-wave theory [9] resulting in computer codes applicable to a wide range of physical situations. Variables include wavelength of the incident plane wave, angle of incidence, layer thicknesses, layer permittivities, grating period, grating profile, modulation amplitudes, and grating slant angle. Any polarization state can be handled. Multilayer structures with arbitrarily many, arbitrarily-ordered, modulated and homogeneous layers and arbitrary surrounding materials can be treated.

Accordingly, the guided-mode resonance properties of single-layer, planar, dielectric waveguide gratings (i. e., the canonical structure) have been studied and explained in great detail. It has been shown that these structures function as reflection filters producing complete exchange of energy between forward and backward propagating diffracted waves with smooth lineshapes and arbitrarily narrow filter linewidths. Simple expressions based on rigorous coupled-wave theory and on classical slab waveguide theory are found to give a great deal of insight into these phenomena. Parametric resonance locations can be determined approximately and quantification of the inherent TE/TM polarization separation and the free-spectral ranges of the filters are obtained in simple terms. Furthermore, the resonance regimes, defining the parametric regions within which the guided-mode resonances arise, can be directly visualized. It has been shown that the linewidths of the resonances can be controlled by the grating modulation amplitude and by the degree of mode confinement (refractive-index difference at boundaries) [4].

Additionally, it has been shown that ideal reflection filters can be designed by combining guided-mode resonance effects in waveguide gratings with antireflection effects of thin-film

structures. Since the guided-mode resonance effect overrides the antireflection effect, the filter possesses a symmetrical line shape with near-zero reflectivity over appreciable wavelength bands adjacent to the resonance wavelength. In the single-layer filter, the same layer functions as the waveguide grating supporting the resonance and as the antireflection layer suppressing reflection around the resonance. As shown in Fig. 2, a multilayer design allows the filter resonance peak a wide surrounding region of low reflectance. The central resonance wavelength, the filter linewidth, the range of the low sidebands, and the resonance line shape depend on the chosen parameters [1,2].

Further, it has been shown that a narrow-line, polarized transmission bandpass filter (as opposed to the reflection bandpass filters referred to above) can be obtained by combining the asymmetrical guided-mode resonance response of waveguide gratings with the dielectric mirror effect of multilayer structures. As illustrated in Figs. 3 and 4, this filter exhibits low-transmission sidebands with high efficiency within the passband. The location of the transmission peak can be controlled by the grating period with a fixed angle of incidence. These filters have attractive features such as polarization sensitivity and high transmission efficiency with narrow linewidths; a drawback is the increased fabrication complexity relative to homogeneous layered structures.

In conclusion, the resonance effects discussed in this paper are induced by and controlled by the proper combination of diffractive optics, thin-film optics, and waveguide optics. These effects open up new possibilities for design and applications of optical elements and devices.

1. S. S. Wang and R. Magnusson, "Design of waveguide-grating filters with symmetrical line shapes and low sidebands," *Optics Letters* , vol. 19, pp.919-921, June 15, 1994.

2. S. S. Wang and R. Magnusson, "Multilayer waveguide-grating filters," *Applied Optics* vol. 34, pp. 2414-2420, May 1995.

3. S. S. Wang and R. Magnusson, "Transmission bandpass guided-mode resonance filters," accepted for publication by *Applied Optics* .

4. R. Magnusson and S. S. Wang, "Theory and applications of guided-mode resonance filters," *Applied Optics*, vol. 32, pp. 2606-2613, May 1993.

5. M. T. Gale, K. Knop, and R. H. Morf, "Zero-order diffractive microstructures for security applications," Proc. SPIE on Optical Security and Anticounterfeiting Systems, vol. 1210, pp. 83-89, 1990.

6. S. M. Norton and G. M. Morris, "Embedded grating structures: Use of the scattering operator in design," Optical Society of America Annual Meeting, Portland, Oregon, September 10-15, 1995.

7. V. V. Meriakri, I. P. Nikitin, and M. P. Parkhomenko, "Frequency characteristics of metal-dielectric gratings," *Radiotekhnika i elektronika*, no. 4, pp. 604-611, 1992.

8. R. Magnusson, S. S. Wang, T. D. Black, and A. Sohn, "Resonance properties of dielectric waveguide gratings: Theory and experiments at 4 - 18 GHz," *IEEE Transactions on Antennas and Propagation* , vol. 42, pp. 567-569, April 1994.

9. T. K. Gaylord and M. G. Moharam, "Analysis and applications of optical diffraction by gratings," Proc. IEEE, vol. 73, pp. 894-937, 1985.

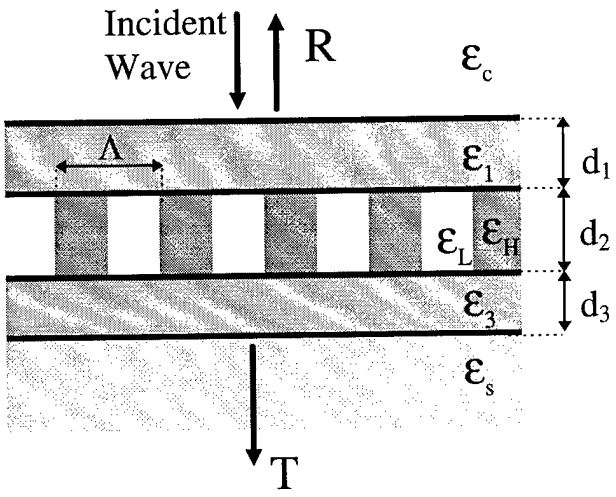


Fig. 1 Generic multilayer, square-wave-profile waveguide-grating filter with normal incidence. R is the filter reflectance and T is the filter transmittance. Layer thicknesses are d and relative permittivities are ε.

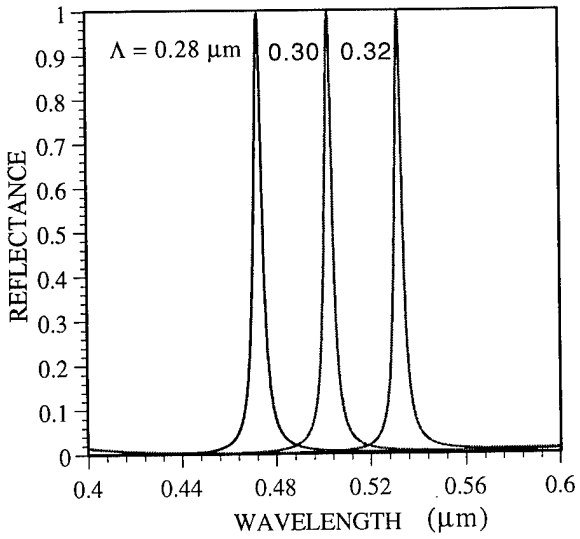


Fig. 2 TE polarization spectral response of a triple-layer waveguide-grating filter. Note the resonance wavelength depedence on the grating period Λ. The parameters are $\varepsilon_C = 1.0$, $\varepsilon_S = 2.31$, $\varepsilon_1 = 1.77$, $\varepsilon_{2H} = 4.75$, $\varepsilon_{2L} = 3.24$, $\varepsilon_3 = 3.42$, $d_1 = 94$ nm, $d_2 = 63$ nm, and $d_3 = 65$ nm (AR design).

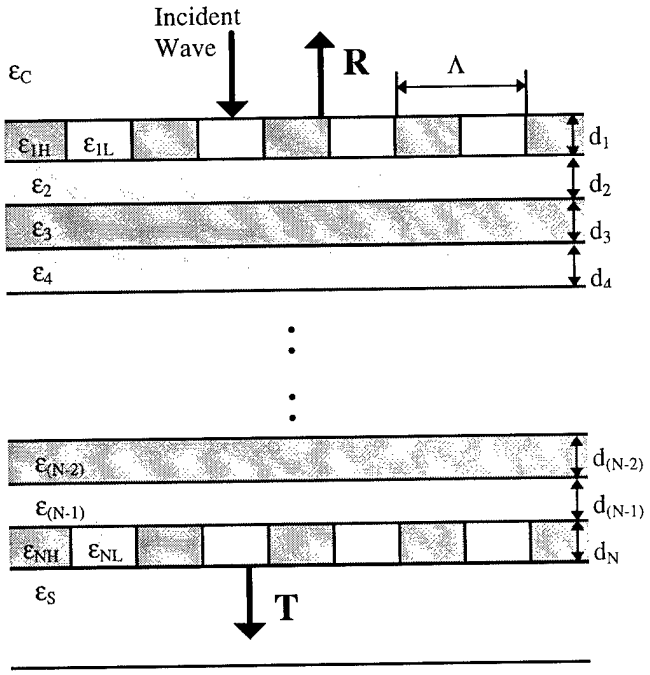


Fig. 3 Multilayer waveguide-grating transmission filter with high-reflection design for efficient transmission at the resonance wavelength and suppressed transmission off resonance.

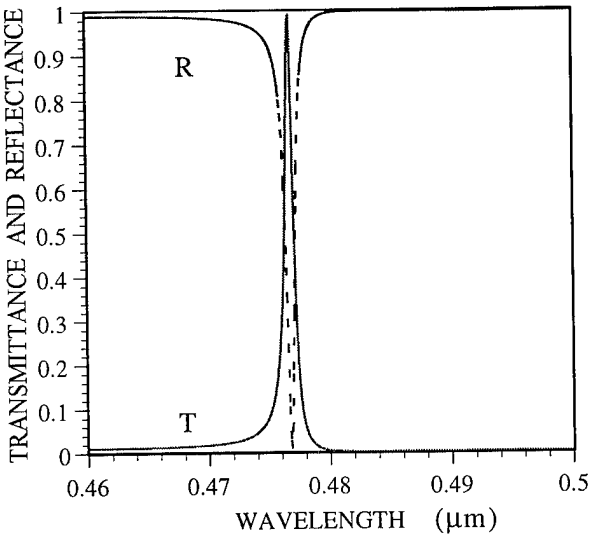


Fig. 4 TE polarization spectral response of an 11-layer transmission filter with layers 1 and 11 being waveguide gratings. The gratings have period $\Lambda = 0.3$ μm, thickness d = 51 nm, and permittivities $\varepsilon_H = 6.25$, $\varepsilon_L = 4.84$. The parameters for the homogeneous layers are d = 51 nm, ε = 5.52 for odd-numbered layers and d = 87 nm, ε = 1.9 for even-numbered layers.

Design of Resonant Grating Filters

Scott M. Norton
G. Michael Morris
Turan Erdogan

The Institute of Optics
University of Rochester
Rochester, NY 14627
Phone:(716)275-8008
FAX (716)271-1027

1.0 INTRODUCTION

Resonant grating filters offer high-contrast, narrowband reflectivity and transmissivity for an incident plane wave. They differ from other optical filters in that they operate on the principle of resonance excitation, rather than a bragg-type or Fabry-Perot effect. The principle of resonance excitation has been equated with the excitation of a leaky waveguide mode.[1] Connecting the resonance to a leaky mode excitation has led to new design principles for resonance grating filters. For instance, the ideal waveguide dispersion relation has been used to locate the position of the resonance in wavelength or angle.[2] However, connecting resonant width to leaky waveguide excitation has largely been ignored. We will show how the waveguiding concept can be extended to give approximations to resonant width. This approach is based on three different models: homogeneous RCWA[3], an approximate homogeneous modal analysis, and an approximate coupled-mode approach. Note, the term homogenous refers to solving the problem without the existence of an incident plane wave field.

2.0 GENERAL THEORY OF RESONANT GRATING FILTERS

A resonant grating filter is illustrated in Fig.1. This particular type of filter is a sinusoidal-type, because the periodic region has a sinusoidal permittivity variation. When a plane wave with the proper wavelength and angle is incident on the structure, it is possible to achieve 100% reflection of the field.

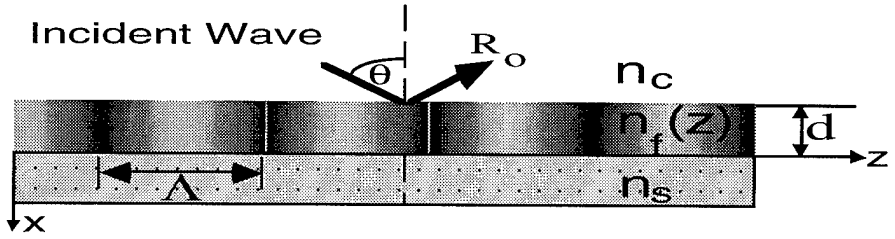


Figure 1. Resonant grating filter with refractive index profile $n_f^2(z) = n_{av}^2(1 + M\cos(\frac{2\pi}{\Lambda}z))$.

As explained earlier, the resonance reflection is due to the excitation of a leaky waveguide mode centralized in the periodic region. The process of resonance excitation can be understood as follows. An incident plane wave scanning over wavelength, for instance, is incident upon a structure at a particular angle. At some specific wavelength, a leaky mode is excited, assuming the structure is designed properly. Near the excitation wavelength an excited mode begins to re-radiate above and below the periodic region. The scattered field

over the excitation wavelength range has a rapidly changing phase term which, at some point, will be completely in phase with the directly reflected field and completely out of phase with the directly transmitted field. An example of a resonance reflection is plotted in Fig. 2.

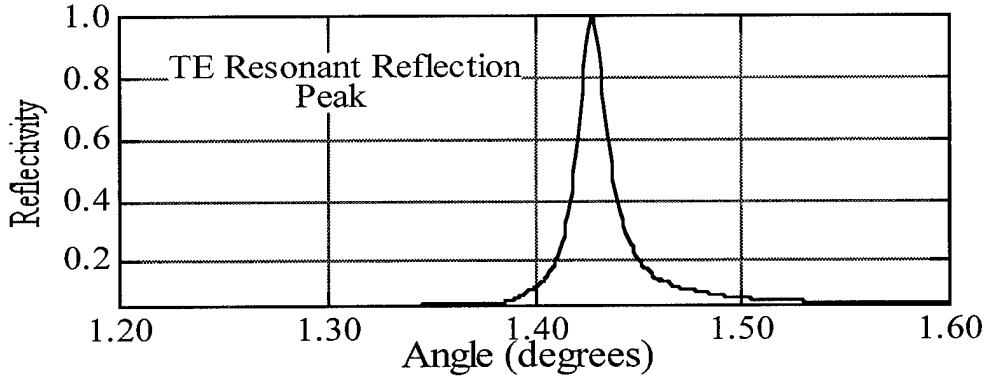


Figure 2. An example of a TE resonant reflection peak. Important parameters in design of grating filters includes center wavelength and angle and the corresponding bandwidths.

Mathematically, a leaky waveguide mode can be described by a pole in the complex propagation constant domain, β. A plane wave can excite the leaky waveguide mode through the coupling relation

$$\mathcal{R}e(\beta) = k_z - m\frac{2\pi}{\Lambda} \qquad \text{m=integer} \qquad (1)$$

where β is the complex propagation constant of a leaky waveguide mode, k_z is the tangential wave vector of the incident field, and Λ is the period of the grating. From the above coupling relation we see that it is the real part of the propagation coefficient which is related to the resonance position in wavelength or angle. Wang and Magnusson[1,4] made use of this by averaging over the periodic index region and using the ideal waveguide relation to obtain an approximation of Re(β). In this case, the imaginary part is lost by the averaging. However, they were able to show that the real propagation coefficient along with the coupling relation gives a good approximation for resonant position. Up until now, the imaginary part of β has been largely ignored. It has been shown in other grating literature that the imaginary part of the propagation constant can be linked to the resonant width through a Lorentzian relation.[5] We are interested in showing the different methods to obtain the imaginary part of the propagation coefficient and its relation to the actual resonant width (FWHM as determined by inhomogeneous RCWA). Our end goal is to show that the approximate methods (homogeneous modal and coupled-mode) are more than adequate to provide the designer with an approximation of resonant width.

3.0 METHODS OF DETERMINING Im(β)

There are two main advantages for finding the resonant width through the imaginary part of the propagation constant. One, it can significantly decrease computation time. In order to find the resonant width using standard rigorous vector methods which compute diffraction efficiency, one must plot out the reflectivity over the resonance and actually measure the resonant width. This requires the computation of many different points over the resonance and in fact, requires the designer to know where the resonance is located

beforehand (assuming a resonance even exists). The approximate methods, however, require the computation of just one point for each resonance peak - a significant decrease in computation time. The second advantage of computing Im(β) through the approximate methods, is the ability to quickly determine overall trends in resonant width for a particular design structure. In other words, the designer can quickly learn how the resonant width changes over the whole range of a structure parameter, such as depth.

The first method to obtain Im(β) is by homogeneously solving the rigorous coupled wave problem (rather than inhomogeneously). The inhomogeneous solution requires knowledge of the incoming exciting field, while the homogeneous solution involves locating the resonance position through a root search of the complex β-plane. The location of the root provides the information about what type of incoming field would excite it. This method is, in fact, rigorous in the sense that the designer has the option of increasing the accuracy by increasing the number of diffraction orders included.

Another method for determining Im(β) is to homogeneously solve the equations of modal analysis. This method is similar to the coupled-wave approach except that the author's implementation took into account only the zeroth mode and its corresponding diffracted order. The approximation, however, for dielectric resonant grating structures holds very well. In the symmetric case ($n_s=n_c$), the approximation results in a close form transcendental equation, the solutions of which, are the complex poles, β. Otherwise, the non-symmetrical case($n_s \neq n_c$) is also very easy to implement.

The final approach is based on coupled-mode theory. It is the most interesting because it is the most "physical" approach. In other words, the method allows the designer to understand the origins of the trends he observes in loss versus a given physical parameter. But most important, it is possible to obtain an explicit closed-form formula for the loss.

4.0 THE RESONANT WIDTH FROM Im(β)

To establish a relationship between resonant width and the imaginary part of β, we can use an approximation introduced by Neviere.[5] Basically, we assume that the resonance has a Lorentzian form. We start by assuming the reflected amplitude can be given by

$$r = \frac{c}{k_{zm} - \beta} \qquad \text{where } k_{zm} = k_z - m\frac{2\pi}{\Lambda} \tag{2}$$

and where c is an arbitrary constant and k_z is the tangential component of the incident field vector. The reflected intensity is therefore given by

$$R = |r|^2 = \frac{|c|^2}{(k_{zm} - \beta_r)^2 + \beta_i^2} \tag{3}$$

where $\beta_r = \mathcal{R}e(\beta)$ and $\beta_i = Im(\beta)$. As can be seen by Eq.(3), the maximum in R occurs when $k_{zm} = \beta_r$, which was given earlier as the coupling condition for resonance excitation. At half of the maximum reflectivity, β_i must be equal to $(k_{zn} - \beta_r)$. Therefore, in this approximation, the full width of the resonance at half maximum (FWHM) is given by $2\beta_i$.

5.0 RESULTS AND DISCUSSION

Each of the models described above were used to generate Im(β) vs. depth plots. The Im(β) values were then converted to resonant width values, Δk_z, using the Lorentzian model. The resonant grating structure in Fig. 1 was examined with a modulation of M=0.1. A plot comparing final results for Δk_z to the FWHM determined from measuring RCWA diffraction efficiency data is given in Fig.3.

The plot demonstrates peaks in resonant width with each peak decreasing in amplitude with depth. As can be seen, each of the models gives an excellent match to FWHM as calculated by RCWA. In fact, the approximate modal method and the approximate coupled-mode method overlap almost exactly. The deviations in the actual width data at the top of the first peak are not due to any approximation in the calculation of Im(β) but are due to the breakdown of the Lorentzian model. At these deviated points the resonance has an asymmetrical profile rather than symmetrical Lorentzian profile of Fig.2. The resonance reflectivity plot is asymmetrical because of an associated zero near the pole in the complex domain. Thus, the reflectivity near a resonance shows a 100% peak but with a 0% reflectivity on one of the sidelobes of the resonance.

These types of resonant width plots are extremely valuable to the designer. Very little calculation gives the designer the complete width profile over any of the structural parameters and thus significantly aids the design process.

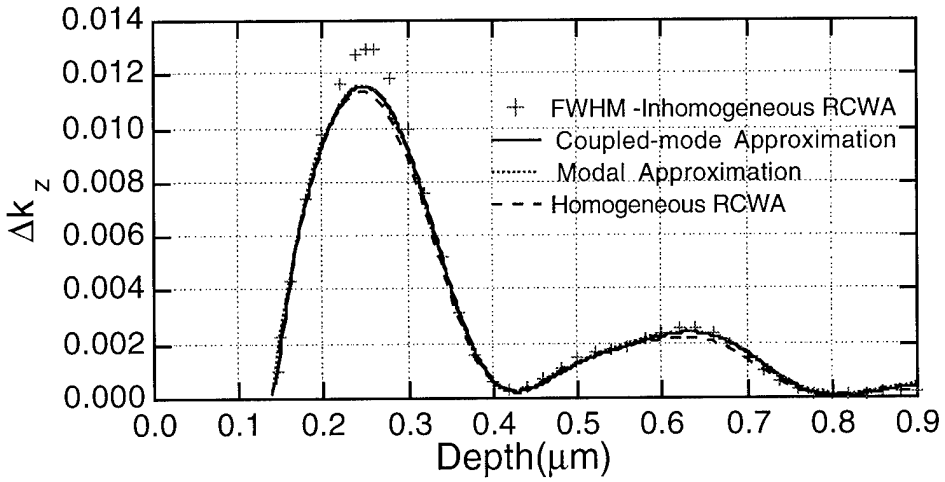


Figure 3. Resonant width comparison between FWHM of RCWA and three different methods which calculate Im(β). (n_c=1.0, n_{av}=1.6, n_s=1.45, λ=0.6μm, Λ=0.38, M=0.1)

---

1. A. Hessel and A. A. Oliner, "A new theory of Wood's anomalies on optical gratings," *Appl. Opt.* **10**, 1275-97 (1965).
2. Magnusson, R. and Wang, W., "New Principle for Optical Filters", *Appl. Phys. Lett.* **61**, 1022-24 (1992).
3. S. Peng, G.M. Morris, "Efficient implementation of rigourous coupled-wave analysis for surface-relief gratings," *J. Opt. Soc. Am. A* **12**, 10876-96 (1995)
4. . Wang, S.S. and Magnusson, R. "Theory and applications of guided-mode filters," *Appl. Opt.* **23**, 2606-13 (1993)
5. Neviere, M., Petit, R., Cadilhac, M., "About the theory of optical grating coupler-waveguide systems," *Opt.. Comm.* **8**, 113-17 (1973)

ZEROTH-ORDER COMPLEX-AMPLITUDE MODULATION BY LAMELLAR SURFACE PROFILES

Ville Kettunen, Pasi Vahimaa, Jari Turunen, Marko Honkanen, Olli Salminen

Department of Physics, Univ. of Joensuu, P.O. Box 111, FIN-80101 Joensuu, Finland

Eero Noponen

Department of Technical Physics, Helsinki Univ. of Technology, FIN-02150 Espoo, Finland

1. Introduction

In diffractive optics phase-only elements provide the highest diffraction efficiencies, but they also generate noise in the neighborhood of the signal window W. Moreover, this noise tends to be strongest in the immediate neighborhood of W. In many applications, such as space-invariant optical interconnection, one must suppress the noise from some given spatial-frequency frame around W. This can be accomplished with a phase-only modulating element, but it requires an effective increase of the size of W to include also the frame. Consequently the numerical complexity of performing the design increases considerably.

To delete the noise entirely, one may modulate both the amplitude and the phase of the incident field continuously. The amplitude modulation results in a decrease of the diffraction efficiency of the element. Also, and this is often the most critical factor, the fabrication of amplitude and phase modulated transparencies is difficult [1]. To overcome the problem one often modulates the efficiency and the phase of the first carrier-grating order [2], but then the signal is moved off-axis and the efficiency is futher reduced.

We propose to employ the zeroth diffraction order of a lamellar carrier grating instead of the first order: amplitude and phase modulation of the incident wave are accomplished through the combined effect of groove depth and width modulation. In this method the signal remains on axis and the efficiency can be as high as it is for the original element with continuous amplitude and phase modulation.

2. Design of amplitude and phase modulated elements

Let us proceed to determine the extent of the decrease of diffraction efficiency when amplitude and phase modulated elements are employed in place of purely phase-modulating elements. Consider, as a simple example, diffractive elements that split a plane wave into a one- or two-dimensional array of plane waves (Fourier-type array illuminator). The diffraction efficiency is defined as the proportion of incident energy that is diffracted into the N signal orders.

Let us denote by $\hat{T}_m$ the complex amplitude associated with mth plane wave component of the signal wave. This corresponds to mth diffraction order of the (periodic) element. Then

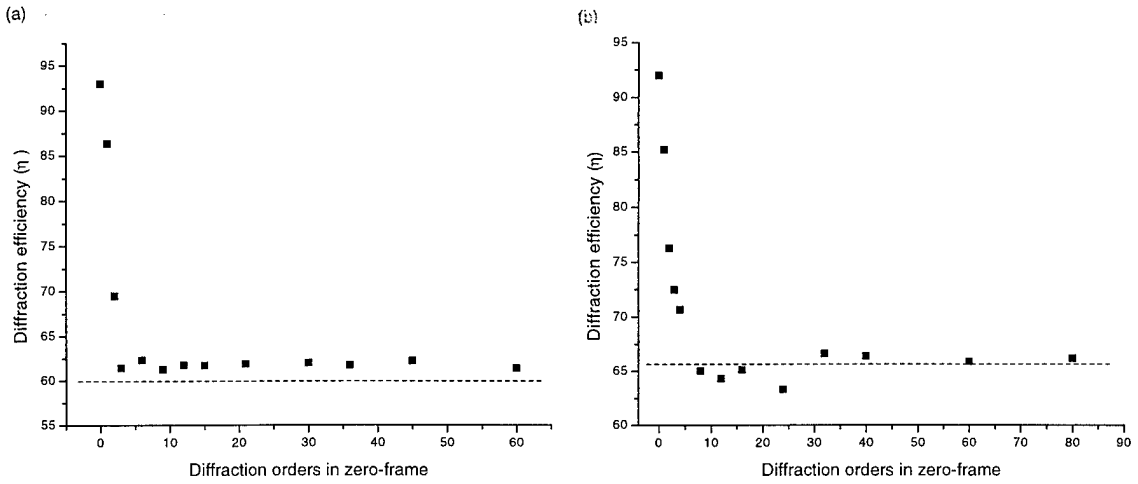


Figure 1: Diffraction efficiency as a function of the width of the frame for the (a) 3-beam splitter and (b) 4-beam splitter. The horizontal dashed lines give the optimum efficiencies of the amplitude and phase modulated elements.

the signal wave intensity distribution at the exit plane of the element may be written as

$$I_s(x) = \left| \sum_{m \in W} \hat{T}_m \exp\left(i2\pi m x\right) \right|^2 , \tag{1}$$

where the period of the element has been assumed equal to unity and we assume a normalization $\sum_{n \in W} \left|\hat{T}_m\right|^2 = 1$. Since no thin (paraxial-domain) diffractive element can have a complex-amplitude transmittance greater than unity, the diffraction efficiency of an element that reproduces the signal wave exactly (by amplitude and phase modulation) is given by

$$\eta_{\mathrm{ca}} = I_{\max}^{-1}, \quad \text{where} \quad I_{\max} = \max_{x \in (0,1)} \left\{ I_s(x) \right\} . \tag{2}$$

Let us assume that phase freedom is available, i.e., the phases of $\hat{T}_m$ may be chosen freely. This permits us to optimize η_{ca} by minimization of $I_{\max}$. Analytic solutions are possible at least for $N \leq 4$: for $N = 2$ we have $\eta_{\mathrm{ca}} = 8/\pi^2$, for $N = 3$ $\eta_{\mathrm{ca}} = 3/5$ and, $N = 4$, $\eta_{\mathrm{ca}} \approx 65.4\%$.

Figure 1 illustrates the rapid convergence of the efficiencies of continuously phase modulated elements with $N = 3$ and $N = 4$ towards the efficiencies η_{ca} when the width of the frame around the signal window is increased. The phase-only modulated elements are designed by a standard iterative Fourier-transform algorithm.

For more complicated signals the optimization of the phases must be performed numerically. We have used to methods to do this. First, we have simply taken the signal phase obtained by optimization of Wyrowski's upper bound for diffractive phase elements [3] and computed η_{ca} from Eqs. (1) and (2). This, of course, yields a completely error-free signal, but (somewhat unexpectedly) the efficiencies η_{Ub} thus obtained are not always very high: see the second column of table 1; the signal phases have been taken from Ref. [4].

Table 1: Efficiencies of complex-amplitude modulating diffractive elements obtained by two different methods.

N	η_{Ub} (%)	η_{clip} (%)
2	50	50
3	60	60
4	56.5	65.8
5	55.6	66.6
6	43.2	62.6
7	65.2	71.1
8	56.5	76.2
9	75.7	79.4

In the second approach we use a modified type of iterative Fourier-transform algorithm. The signal-plane constraints are such that the amplitude of the signal is set equal to the desired value in W and equal to zero outside W. Phase freedom is used fully. In the plane of the element the signal wave is clipped during the iteration according to a certain scheme, with the aim of reducing $I_{\max}$. The results are shown in the third column of the table.

3. Zeroth-order encoding of amplitude and phase

As already mentioned, it is difficult to realize continuous distributions of amplitude and phase modulation simultaneously. First-order carrier techniques, of which Lohmann's classic method [2] is an example, can solve the problem. However, the signal is generated off-axis. Moreover, since the first carrier order is modulated, the efficiency η_{ca} of the original element with continuous phase and amplitude modulation must be multiplied by the first-order efficiency of the carrier grating, which is just over 40% for a binary phase carrier.

Our approach is to employ the zeroth order of a carrier grating. In this method the noise is deflected far away from the optical axis, i.e., around the higher diffraction orders of the carrier grating. It can be shown by means of the complex-amplitude transmittance method that if we modulate both the widths and the depths of the grooves of a lamellar carrier grating, the amplitude and the phase of the incident field can be controlled through the efficiency and the phase of the zeroth carrier order. All possible combinations of amplitude and phase are possible in view of this simple approach, which however fails when the carrier period d_{c} is less than $\sim 10\lambda$. In that case one must use rigorous electromagnetic diffraction theory to determine the available amplitude-phase combinations as illustrated in Fig. 2. The design algorithm must then quantize the amplitude and phase to this set of permitted values.

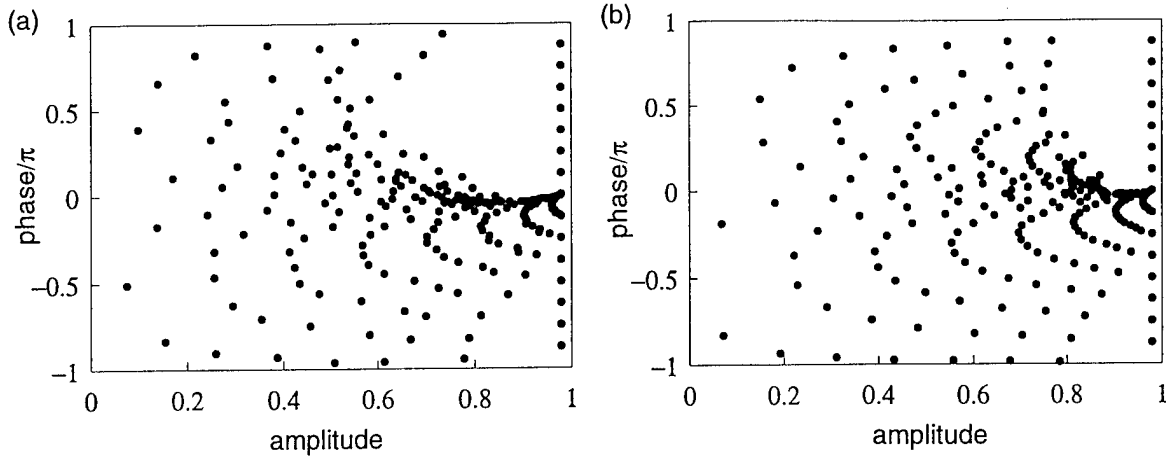


Figure 2: Achievable combinations of amplitude and phase when the groove width and depth both have 16 permitted, equally spaced values and (a) $d_c = 4\lambda$ (b) $d_c = 8\lambda$.

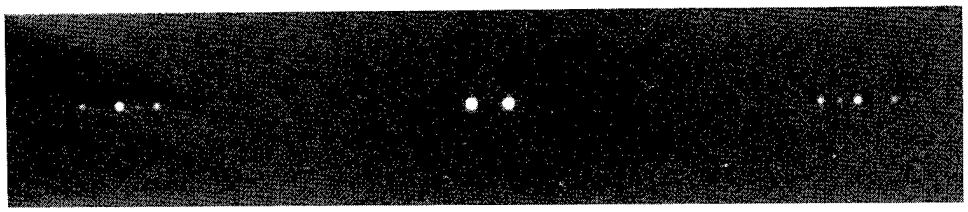


Figure 3: Optical reconstruction of a two-beam splitter encoded with zeroth-order complex-amplitude modulation.

It is straightforward to extend the design and encoding methods to two-dimensional structures. For example, we obtained an efficiency η_{clip} of 50.1% for a 2×2 signal and 51.76% for a 3×3 signal. In two-dimensional encoding one can also employ rectangular pillars or holes.

4. Experiment

In Fig. 3 we show a photograph of a two-beam splitter encoded using the scheme introduced here and fabricated by direct-write electron-beam lithography in PMMA. Note the large frame around the two-spot signal and the noise in the neighborhood of carrier orders ± 1.

References

1. D. C. Chu, J. R. Fienup, and J. W. Goodman, Appl. Opt. **12**, 1386 (1973).
2. A. W. Lohmann and D. P. Paris, Appl. Opt. **6**, 1739 (1967).
3. F. Wyrowski, Opt. Lett. **16**, 1915 (1991).
4. U. Krackhardt, J. N. Mait, and N. Streibl, Appl. Opt. **31**, 27 (1992).

Sub-nanometer linewidth resonant grating filters

Song Peng and G. Michael Morris
Institute of Optics
University of Rochester
Rochester, NY 14627

INTRODUCTION

Narrowband filters are important optical components that have numerous applications. Conventional interference narrowband filters suffers low peak efficiency due to the roughness of the film coatings especially the roughness of the spacer layers. The minimum linewidths of interference filters are typically 1 nm for the visible regime, while the peak efficiencies are less than 40%. Spectral stability of interference filters is poor because spacer layers absorb water vapors and cause shifting of the peak wavelength. Usually the coatings have to be sandwiched in between two substrates, which are then sealed along the side. In addition, narrowband interference filters are structure-complex; 60 layers are not uncommon for 1 nm interference filters. The large number of layers imposes great difficulty in the use of advanced film deposition techniques such as chemical vapor deposition (CVD) methods.

Interference filters are based on multiple-beam interference in Fabry-Perot cavities. To overcome the difficulties associated with interference filters, new filter mechanisms are called for. Resonance phenomena of grating diffraction is a suitable candidate. Resonant anomalies in grating diffraction has attracted much attention recently. The sharp reflection peaks have been suggested for use in reflection filters[1, 2], security marks[3], and dichroic reflectors in microwave antennas.[4] A few experimental results have been reported in the literature. Machev and Popov[1] experimentally demonstrated the resonant anomalies from a coated grating. Gale[3] presented the measured anomalous reflectivity of an embedded lamella grating. Magnusson et, al.[5] observed notches in the transmission spectrum of a waveguide grating in the microwave region. Resonant scattering phenomena in diffraction from two-dimensional (2D) gratings, i.e. doubly periodic or crossed gratings, has also been investigated both theoretically[6] and experimentally.[7] In Ref. 7 we demonstrated a 1-nm FWHM filter based on a 2D grating structure.

In this presentation we will address several practical considerations involved in the design and fabrication of narrowband resonance filters.

THEORY

Theoretical studies attribute resonant anomalies to the excitation of guided modes supported by the grating structure.[8] The resonant response can be calculated by using rigorous electromagnetic theory of diffraction gratings. For the purpose of this presentation an intuitive picture is helpful for understanding device operation. Figure 1 illustrates a multiple-beam interference picture of grating resonance phenomena. As the incident light impinges on the grating structure it excites a leaky waveguide mode. Because of the periodic modulation of the waveguide structure, the radiation is coupled back out as the leaky mode propagates along the waveguide. The light that is coupled out can be considered a combination of beams scattered out at each grating period. This view of scattering establishes a picture of multiple-beam interference. At a particular incident angle and wavelength, the scattered beams constructively interfere with each other, resulting in a large reflected or transmitted intensity. When the incident wavelength deviates from the resonance condition, the scattered beams dephase and their amplitudes decrease, thus the reflection and transmission rapidly return to their static values.

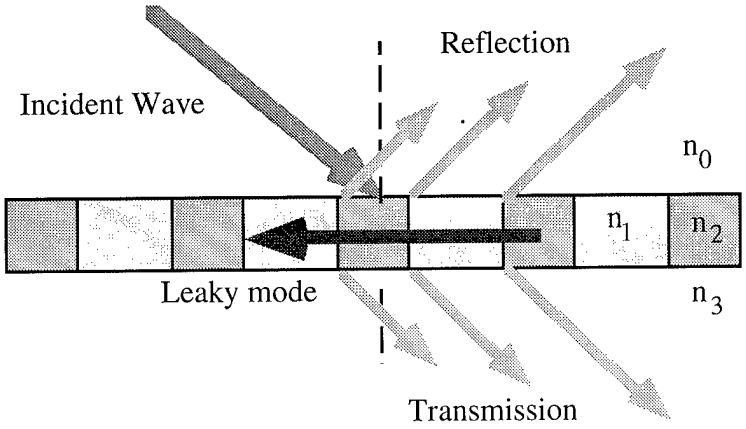


Figure 1. Multiple beam interference picture of grating resonance phenomenon.

Practical structures can have more than one layer. To support a guided mode, one of the layers needs to have an index of refraction higher than the incident medium and the substrate. I addition, the layers must also satisfy thickness constraints. In order to excite a particular mode of the structure, the tangential component of the incident wave vector must be matched via the grating periodicity to the propagation constant of the waveguide mode. This resonance condition is given by

$$k_{ix} + jK = \mathrm{Re}(\beta), \tag{1}$$

where k_{ix} is the tangential component of the incident wave vector, j represents any integer, K is the grating vector which is equal to $2\pi/\Lambda$, and β is the propagation constant of the leaky waveguide mode. When the coupling condition represented by Eq. (1) is satisfied, the incident field will

excite a leaky waveguide mode. Therefore, Eq. (1) can be used to determine the peak wavelength of resonance filters. The filter linewidths are governed by the rate at which the radiation is scattered out of the structure. The faster the rate, the wider the filter width. This is quite intuitive because if the leaky waveguide mode decays faster, there will be less number of beams. On the other hand, it is known from multiple-beam interference concept that the filter width is inversely proportional to the number of beams. The decay rate of the leaky mode, thereby the linewidth of the filter, is determined by the imaginary part of its propagation constant, i.e., $\mathrm{Im}(\beta)$.[8]

FABRICATION ISSUES

Arbitrarily-narrow linewidths can be designed for resonance reflection filters without complicating the structure. Basically a very weak grating will do. The theoretical efficiency is unity as long as the materials involved are non absorbing.[9] Practically, the filter performance such as peak efficiency is limited by several factors that must be considered in the design and fabrication processes.

In contrast to thin-film interference filters, a resonant grating filter can be considered as a transverse resonance structure because the resonance occurs along the grating plane. This type of structure is highly sensitive to absorption of the waveguide materials, because the distance that the leaky mode has to propagate is much larger compared to the thickness or the period of the structure. Resonant grating filters are also highly sensitive to the roughness of the grating structures, because grating roughness adds random phase into each scattered beam thus diminishing the constructive interference effect. Note that narrower linewidth implies a larger number of beams and a greater decaying (coupling) length. Thus for given materials and level of grating roughness, the narrower the linewidth the lower the peak efficiency. Furthermore, excessive material absorption may also have the effect of broadening the linewidth.

The divergence or the size of the incident beam is another factor that can limit the peak efficiency[6], because in general a narrow spectral response is associated with a sharp angular response. For a collimated beam, the diameter of the beam needs to be a few times larger than the decay length so that the degradation of the peak efficiency is negligible. The size of the grating needs to be only slightly larger than the size of the beam so that the leak waveguide mode does not see the edge of the grating.

Despite these limits, resonance structures with linewidth of 1 nm (FWHM) or less and high efficiency have been fabricated. The peak efficiency and linewidth obtained already well exceed

that of commercial interference filters. Figure 2 illustrates the measured spectral and angular response of a 1D grating resonance structure. It can be seen that the peak efficiency is greater than 90% while the FWHM is 1.2 nm. The sidelobe is relatively high because for this initial experiment the film thickness was not designed for the 780-nm wavelength.

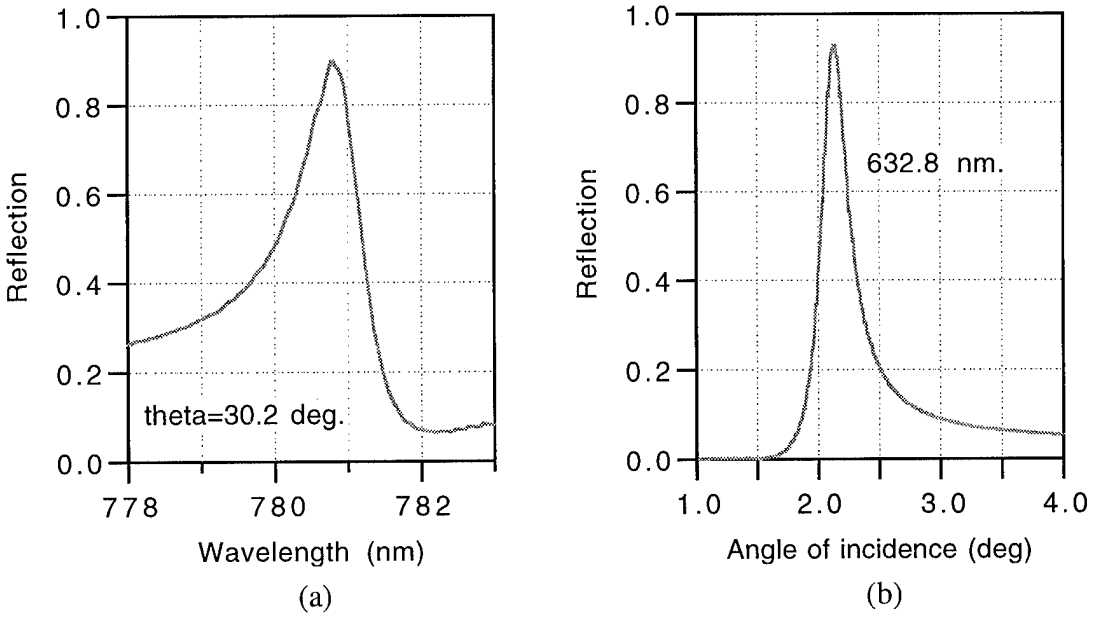


Figure 2. Measured spectral and angular response of a 1D grating resonance structure.

REFERENCE

1. L. Mashev and E. Popov, "Zero order anomaly of dielectric coated gratings," Opt. Commun. **55**, 377-380 (1985).

2. R. Magnusson and S. S. Wang, "New principle for optical filters," Appl. Phys. Lett. **61**, 1022-1024 (1992).

3. M. T. Gale, K. Knop and R. Morf, "Zero-order diffractive microstructures for security applications," SPIE **1210**, 83-89 (1990).

4. H. L. Bertoni, L.-H. S. Cheo and T. Tamir, "Frequency-selective reflection and transmission by a periodic dielectric layer," IEEE Trans. Antennas Propag. **AP-37**, 78-83 (1989).

5. R. Magnusson, S. S. Wang, T. D. Black and A. Sohn, "Resonance properties of dielectric waveguide gratings: theory and experiments at 4-18 GHz," IEEE Trans. Antennas Propag. **42**, 567-569 (1994).

6. S. Peng and G. M. Morris, "Resonant scattering from two-dimensional gratings," J. Opt. Soc. Am. A, accepted for publication , (1995).

7. S. Peng and G. M. Morris, "Experimental demonstration of resonant anomalies in diffraction from two-dimensional gratings," submitted to Optics Letters , (1995).

8. R. Petit, ed., *Electromagnetic theory of gratings* (SpringerVerlag,Berlin,1980).

9. P. Vincent and M. Neviere, "Corrugated dielectric waveguides: a numerical study of the second-order stop bands," Appl. Phys. **20**, 345-351 (1979).

Optimisation of guided-mode resonance and Bragg gratings designed using rigorous diffraction theory.

Ben Layet, Malcolm T.M. Lightbody and Mohammad R. Taghizadeh
Department of Physics, Heriot-Watt University
Edinburgh EH14 4AS, UK
Tel: (+44) 131 451 3068 Fax: (+44) 131 451 3136

Introduction

We consider the implementation of several standard optical components by means of diffraction gratings. The motivation depends on the particular grating employed. A binary surface relief grating, in fused silica, for example, may provide greater robustness than, say, a multi-layer thin film. This is significant for high power laser systems. Alternatively, gratings manifesting the so-called guided-mode resonance (GMR) [1], or resonance type Wood anomaly, are of interest because ideally they give a very high performance for certain optical functions.

In particular, we discuss the use of GMR and Bragg gratings as beam deflectors. In the former case we attempt to maximise the bandwidth and fabrication error tolerance. The term Bragg grating implies that the grating is designed for incidence beams satisfying the Bragg condition. We study these more thoroughly as beamsplitters and polarising elements, where we concentrate on restricting the relief depth of the grating as far as possible. Finally, the performance of a 3 wavelength harmonic separation filter (HSF) designed by scalar diffraction theory is examined as the resonance domain is entered. The results are significant for optical systems of large aperture or short length. In these cases the period of a grating HSF needs to be small enough to ensure the unwanted higher orders, containing the discarded wavelengths, do not overlap the required 0th order beam at the entrance pupil of the element following the HSF.

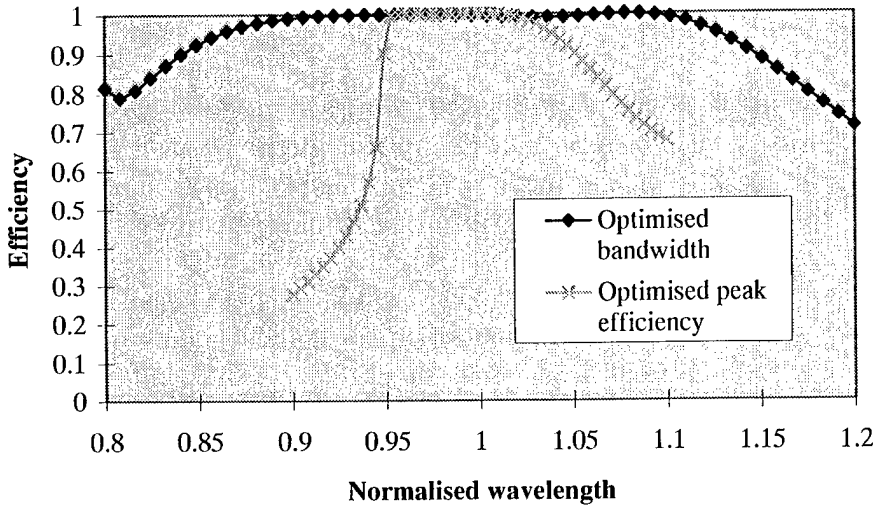
Beam Deflectors

Single groove square profile high spatial frequency Bragg gratings are generally known to be capable of providing high efficiency beam deflection into the -1st transmitted order. For example, a fused silica grating (refractive index, $n = 1.45$) with a period, $d = 1/\sqrt{2}\ \lambda$, a thickness, $t = 1.47\ \lambda$ and an almost central transition point, p, gives 96.9% efficiency when illuminated with a TE polarised plane wave at 45° to the normal. Gratings of this sort are being considered for use in very high power laser systems [2,3].

It is also easy to design square profile GMR gratings, operating in reflection, which are capable of beam deflection with 100% peak efficiency. Methods of controlling the resonance shape and sidelobes have been discussed in reference [4]. The practical problem we address here is the extremely tight fabrication tolerances required to achieve a specified design. We attempt to maximise the (wavelength) bandwidth in the hope that the performance of the resulting grating will be less susceptible to variations in all design parameters, and hence ease the fabrication difficulties. The device will then not be so suitable as a narrowband filter, of course, but alternative applications become possible.

We optimise the GMR beam deflectors using a simple 1D optimisation technique, which we apply in turn to all free parameters: period, thickness and transition point. The incidence angle is fixed at 45°, ensuring 90° deflection. The refractive index of the grating, i.e. of the rectangular blocks on the substrate, is 3.4 (e.g. silicon in the infra-red) and the substrate index is 1.45 (e.g. fused silica in the near infra-red, and barium fluoride over a wider range in the infra-red). The bandwidth is maximised by calculating the performance for many wavelengths at each stage in the optimisation process. In figure (1) the increase in bandwidth is shown by comparison with that obtained for an optimisation based solely on peak efficiency. Unfortunately, there is not a corresponding increase in the tolerance to fluctuations in design parameters. Clearly, the link between bandwidth and tolerances is not strong enough. The merit function must specify our requirements more precisely. The results of this further stage in the study will be presented at the conference.

Figure 1: Bandwidth of GMR Beam Deflectors



Polarising Elements

The second device we investigate is a binary phase grating, operating at Bragg incidence, which is optimised for near 100% 0th order efficiency for TM polarised waves and near 0% 0th order efficiency for TE waves. The grating is designed by optimising the thickness, transition point and period. We ensure Bragg incidence is maintained when the period is altered, by changing the incidence angle to the appropriate value. The dependency of the incidence angle reduces the number of parameters and allows the optimisation to proceed more successfully. This, of course, would not be true if Bragg gratings were not good solutions to the problem. The optimised grating is described by the following data: $t = 1.235\ \lambda$, $d = 0.601\ \lambda$ and $p = 0.4155$. It diverts all (99.9%) the TM polarised light in a mixed polarisation beam, incident at the Bragg angle, into the 0th transmitted order, acting as a linear polariser. The TE light is almost wholly distributed between the -1st transmitted and 0th reflected orders. Only 0.05% appears in the 0th transmitted order. However, there is a fabrication challenge. The optimal design requires a large aspect ratio (grating thickness to smallest transverse structural distance) of about 5, which is near the limit of what can be routinely fabricated.

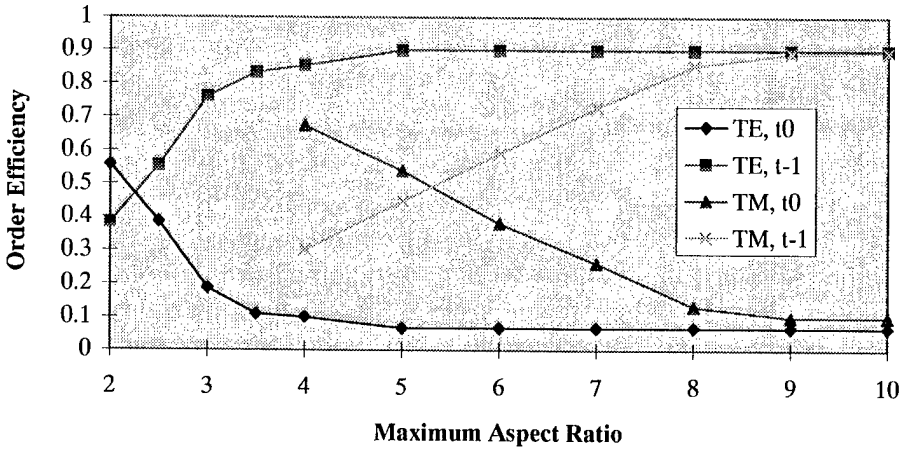
A polarisation beamsplitter, providing 93.6% TE in the -1st transmitted order and 99.9% TM in the 0th transmitted order, and with a similar aspect ratio, has also been designed. This performance is marginally inferior to the polarising beamsplitter reported by Noponen et al. [5], but the aspect ratio is much superior. Their grating groove width is narrow and results in an aspect ratio of nearly 17. This comparison demonstrates the relevance of aspect ratio control in grating design.

Beamsplitters

Often it is necessary to divide a beam into two or more component parts with a pre-specified power ratio between beams. We concentrate, here, on the two output beam device, i.e. the standard beamsplitter. We use simple Bragg gratings operating in the resonance regime. The grating period is $1/\sqrt{2}\ \lambda$ to ensure that the -1st order makes an angle of 90 degrees to the input beam, which is incident at an angle of 45 degrees to the grating normal. We attempt to split the linearly polarised incident beam between the 0th and -1st transmitted orders, with relative efficiencies corresponding to the required beamsplitting ratios. We present design parameters for splitting ratios ranging from 1:9 through to 9:1. The ratio is given as the 0th order efficiency followed by the -1st order efficiency. All the gratings were presumed to have a refractive index of 1.45, corresponding to fused silica at optical wavelengths.

We found that the thickness and transition point could be optimised to produce gratings whose diffracted orders closely approached the required efficiencies. To assess the ease of fabrication of the gratings we use the aspect ratio, i.e. the ratio of grating thickness to minimum transverse feature size. A large aspect ratio implies a deep groove grating which is difficult to fabricate. The success of the optimisation often depends strongly on the maximum aspect ratio which the grating is allowed, as figure (2) illustrates. It is easier to obtain an optimal design with a small aspect ratio, for TE than for TM illumination, and when the amount of power in the zeroth transmitted order is greatest.

Figure 2: The Efficiency of a 1:9 Beamsplitter vs. Maximum Aspect Ratio

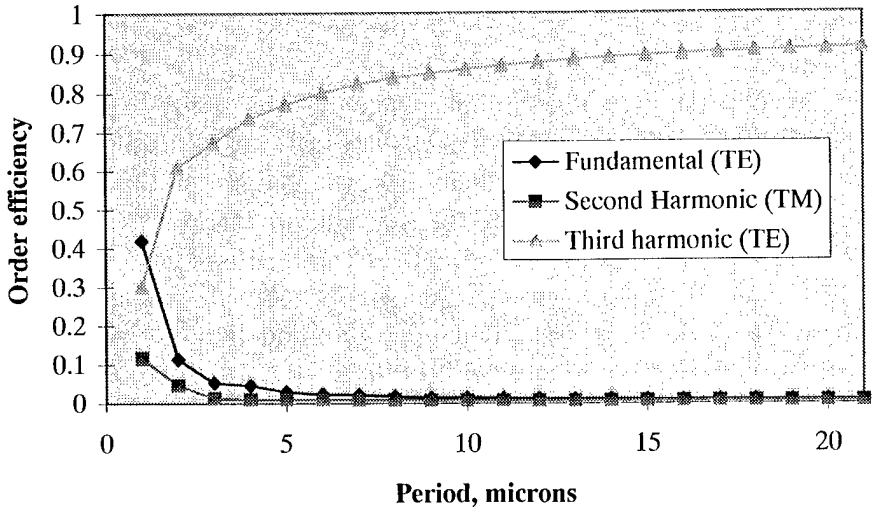


Harmonic Separation Filter

HSF's are useful in frequency doubling and tripling schemes where it is necessary to eliminate unwanted harmonic components. We look in detail at a frequency tripled Nd:YAG 1.054 μm wavelength laser, assuming a type I - type II tripling scheme. Significant amounts of fundamental (TE polarised) and second

harmonic (TM polarised) frequencies are left in the main beam as a result of the non-linear mixing process. They can be eliminated using a grating, based on work on colour separation gratings by Dammann [6], which puts all the $\lambda/3$ into the 0th transmitted order and all the $\lambda/2$ and λ into the 1st and -1st transmitted orders respectively. The grating consists of a three level staircase surface relief profile with a carefully chosen thickness. For large period components the angular separation between the different harmonics is small, implying a large post filter propagation distance in order to effectively discriminate between them. However, as the period is reduced the approximations of scalar theory under which the original design was produced become less valid. For this reason it is important to investigate the performance using rigorous diffraction theory, as is clearly shown in figure (3). Rigorous re-optimisation of the structure provides no significant improvement in the performance in this regime.

Figure 3: Performance of a 3 wavelength HSF as the period varies.



References

[1] S.S.Wang, R.Magnusson, J.S.Bagby and M.G.Moharam, "Guided-mode resonances in planar dielectric-layer diffraction gratings", J. Opt. Soc. Am. A, Vol 7, No 8, August 1990

[2] J.Paye, J.-L. Bruneau and P. Coffin, "Protection of final optics in megajoule-class lasers by steering of UV beams using diffraction gratings", SPIE Conference on High Power Lasers, Monterey, 1995

[3] Malcolm Lightbody, Ben Layet and Mohammad Taghizadeh, "Application of Resonance Domain Diffractive Optics Beam Deflectors to High Power Laser Systems", accepted for publication by J. Mod. Opt.

[4] S.S.Wang and R.Magnusson, "Design of waveguide-grating filters with symmetrical line shapes and low sidebands", Opt. Lett., Vol 19, No 12, June 1994

[5] E.Noponen, A.Vasara, J.Turunen, J.M.Miller and M.R.Taghizadeh, "Synthetic diffractive optics in the resonance domain", J. Opt. Soc. Am. A, Vol 9, No 7, July 1992

[6] H.Dammann, "Color separation gratings", Appl. Opt., Vol 17, No 15, August 1978

Wednesday, May 1, 1996

Micro-Optics Applications

DWB 10:30 am-12:00 m
Gardner A&B

Ravindra A. Athale, *Presider*
George Mason University

Giant Microoptics: Wide Applications in Liquid Crystal Display (LCD) Systems

Shigeru Aoyama, Tsuyoshi Kurahashi, Daidou Uchida,
Masayuki Shinohara and Tsukasa Yamashita
Omron Corporation, Central R&D Laboratory
20 Igadera, Shiokaiinji, Nagaokakyo City Kyoto 617, JAPAN
Telephone: 075-957-9819
Fax: 075-953-7604

Microoptic devices[1,2] as shown in fig.1 are becoming standard optical components by recent development in optical imaging systems and fiber communication systems because of 2-D configuration facility and mass productivity using replicating technique[3]. In particular, LCD systems have been grown up very fast in these few years and will be a promising industrial field of microoptic devices. For this purpose, area size must be increased from a few mm to a few 10 cm, while μm feature size is still remained, and this is called giant microoptics.

In this paper, we review the giant microoptic devices using replicating technique for the LCD systems.

A novel planar microlens array[4] for the use in high definition LC- projectors, in which microlens array is built in the counter substrate of the LCD, is shown in fig.2. In a conventional structure, focal length is restricted by the thickness of the counter substrate so that it is difficult to achieve high light power passing through the pixel aperture in proportion to the increasing pixel density. A main advantage of the planar microlens array is to realize the short focal length and optimize the focal spot size correspondent to the pixel aperture size so as to enhance screen brightness as shown in fig.3. The microlens array consists of 1.3million rectangular microlenses of 24μm×34μm and is formed onto the base glass substrate with a diameter of 8" using stamping replication method. A cover glass substrate with thickness as small as 100μm is stacked onto the micronlens array using an optical adhesive as shown in fig.4. The electrode and the black-matrix are formed on to the cover substrate. The substrates have same material as that of the LCD in order to achieve thermal reliability during LCD fabrication process. The replication accuracy of size less enough than pixel aperture size for 8" wafer is required. Another requirement is to realize the accuracy of thickness of optical adhesive to be less than focal depth. We have developed a stamping replication system, in which replication accuracy

of size less than ±2μm and that of thickness less than ±10μm was achieved, respectively. Consequently, the screen brightness was improved 1.7 times higher for high definition LC-projector.

Fig.5 shows an optical low pass filter with sinusoidal cross sectional profile. LCDs comprising a regular structure of pixel selectively induce undesirable image sampling noise. Optical low pass filter, which is located between the LCD and viewer, is one of the suitable methods to effectively reduce the sampling noise as shown in fig.6. Applying optical low pass filter to the LCDs , it is necessary to reduce sampling frequency without reducing image spectrum in order to avoid image degradation. For this purpose, the development of optical low pass filter with efficiency as high as 70% is one of the crucial issues, in which efficiency means the ratio of the sum of transmitted light power and first diffracted light power to total input light power. We have developed an optical low pass filter with 2-D sinusoidal cross sectional profile. The sinusoidal pattern was formed onto 4" square substrate using molding replication method. The pitch size and pattern depth is 10μm and 0.5μm, respectively. The measured efficiency was as high as 85% and the deviation less than 5% for 4" square was obtained, which corresponds to pattern thickness of 0.04μm.

Fig.7 shows the pictures of color image displayed on the LCD with low pass filter (a) and without low pass filter (b). One can recognize that the image quality is effectively improved by low pass filtering effect. These low pass filters are now commercially available.

A microprism array with asymmetry cross sectional profile is shown in figure 6. Low power consumption is thought to be attractive for portable flat LCDs because of long battery life time. The microprism array functions as light output angle selective devise, whereby the light output at normal angle is emitted and the other light is reflected to the lightguide. In addition, the reflected light is scattered in the lightguide and strikes to this device again. This operation enables to enhance the light output intensity at normal angle. Taking account of the asymmetry of light output distribution from the lightguide, the microprism was designed to have asymmetry right-angled triangle configuration, which was formed onto flexible film using stamping replication method. This structure makes it possible to effectively select the light output at normal angle. The area size and pattern pitch is 5" square and 50μm, respectively. Fig.7 shows the experimental results of light output distribution from the lightguide. The light output intensity at normal angle 1.4 times as large as that without microprism array was achieved.

We introduced giant microoptic devices for LCD systems. This technology will be very helpful for the development of not only the LCD systems but also other advanced optical imaging systems.

References

1. T.Yamashita and S. Aoyama, "Micro grating device using electron beam lithography," in *Holographic Optics III: Principle and Applications, Proc. SPIE* **1340** , 11-14(1991).

2. K.. Iga and S. Misawa, "Distributed-index planar microlens and stacked planar optics: a review of progress," *Appl. Opt.* **25** , 3388-3396 (1986).

3. M. Tanigami, S. Ogata, S. Aoyama, T. Yamashita and K. Imanaka," Low-Wavefront Aberration and High-Temperature Stability Molded Micro Fresnel Lens," *IEEE Photon. Technol. Lett.* **11**, 384-385 (1989).

4. H. Hamada, A. Fujii, Y. Mizuguchi, T. Shibatani, F. Funada and K. Awane, "A New High Definition Microlens Array Built in p-Si TFT-LCD Panel," Asia Display'95, Oct. 16-18, 1995, Hamamatsu, Japan, paper P3.6-1.

Figures

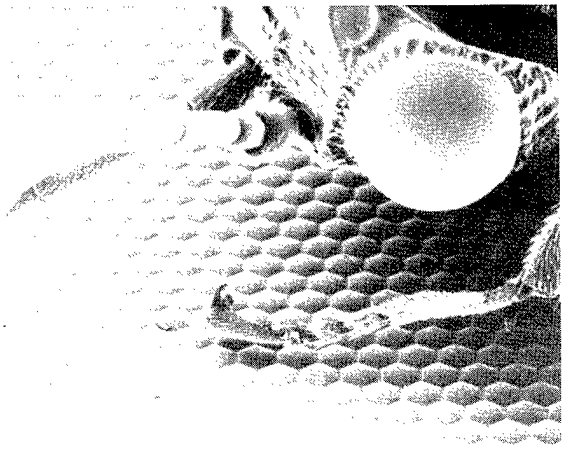


Fig. 1. Microlens array with hexagonal aperture.

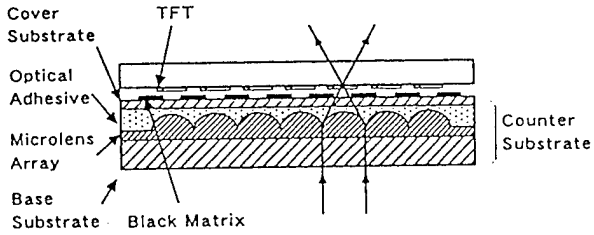


Fig.2. Schematic illustration of the planar microlens array.

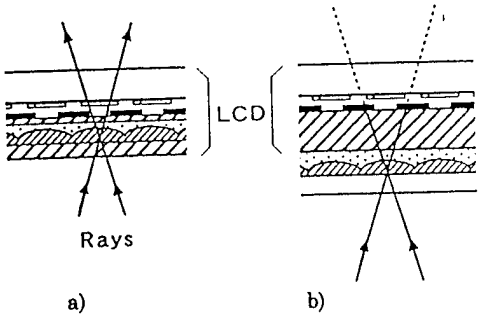


Fig.3. Focusing effect of microlens: a) planar microlens b) conventional.

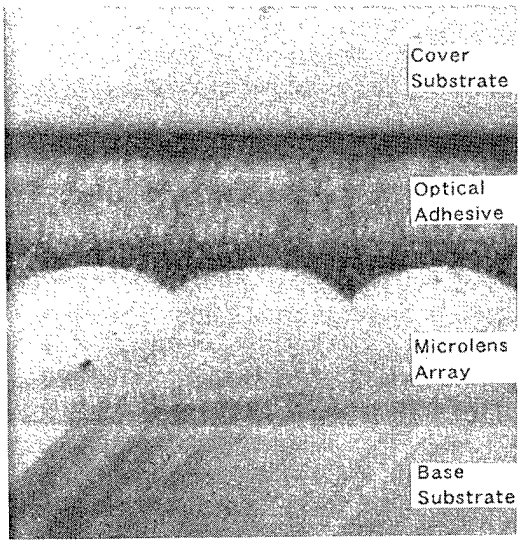


Fig.4. Photograph of cross section of the planar microlens array.

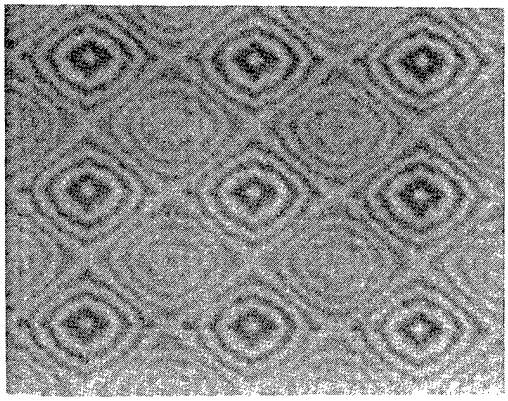
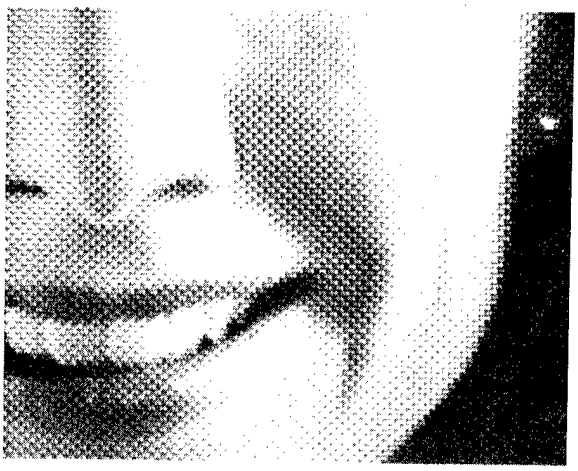


Fig.5. Top view of the optical low pass filter: equal thickness fringes.



a)



b)

Fig.7. Experimental results for color image displayed on the LCD: a) with low pass filter b) without low pass filter.

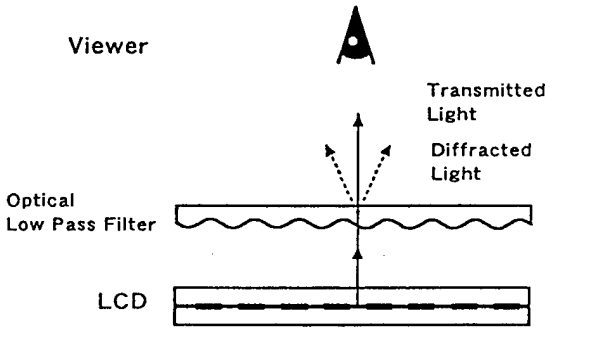


Fig.6. Configuration of LCD setup with optical low pass filter.

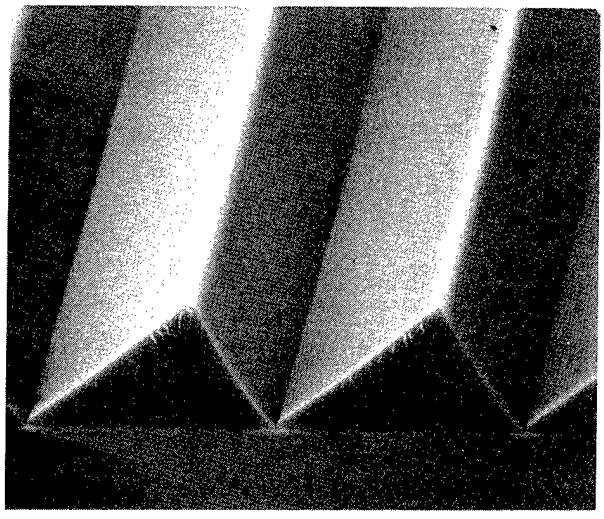


Fig.8. SEM photograph of the microprism array.

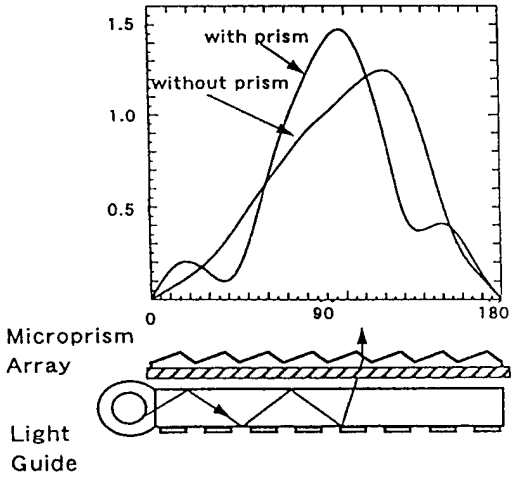


Fig.9. Experimental results of light output distribution: relative light intensity to angle with respect to the surface of microprism array.

Color Separation Echelon Gratings

Margaret B. Stern and Gary J. Swanson

Lincoln Laboratory, Massachusetts Institute of Technology

Lexington, MA 02173-9108

Color discrimination by wavelength bands has a large number of military and commercial applications. In the infrared portion of the spectrum, wavelength separation allows better temperature discrimination of thermally emissive objects.[1] In the visible portion of the spectrum, a device which separates white light into red, green, and blue wavebands without loss of energy could increase the efficiency of color sensors. An echelon-like grating structure [2,3] separates electromagnetic radiation of different wavelengths according to diffraction order rather than by dispersion within one diffraction order as would be the case for a conventional prism-type grating, as shown schematically in Figure 1.

A prototype grating has been designed to disperse red light (650 nm) into the -1 order, green light (525 nm) into the 0 order, and blue light (420 nm) into the +1 order. When combined with a collimated illuminator and a microlens array, it produces arrays of red, green, and blue spots that can be individually controlled. The echelon grating has a 4-μm grating period, a four-phase-level profile and a 96 mm diagonal (75 mm × 60 mm rectangle). The grating consists of 4 steps, each with a physical depth of $d=\lambda_0/(n_0-1)$, where λ_0 is the wavelength at which the zero-order diffraction efficiency is maximized, and n_0 is the refractive index at λ_0. The grating period is determined by λ_0 and the spatial coherence of the illumination source (currently having a divergence of ~6°). For a center design wavelength of 525 nm and n_0 of 1.46, each of the 1-μm-wide steps is 1.14 μm deep, for a total etch depth of 3.42 μm. Fabrication of echelon-like color separation gratings requires critical control over the etch depth (within 10-30 nm), the etch profile (vertical sidewalls), and etch uniformity across the grating area.

The gratings were processed in a silicon fabrication facility according to the usual binary optics technology prescription, i.e., two cycles of lithography and etching were needed to produce the four phase levels. Processes were developed to fabricate the transparent, nonconducting fused silica wafers without modifying the Si-processing equipment. The gratings were patterned using an i-line (365 nm), 5× reduction, projection step and repeat optical lithography system. The i-line stepper had a 15 mm × 15 mm field. Accordingly, four rows of five 15-mm square grating blocks were stepped across the wafer to create the 75 mm (x) × 60 mm (y) continuous patterned area. Stitching errors in the y-direction ranged between 0.2 - 1 μm. Strict control of both exposure and development parameters are needed to achieve the 50% duty cycle required for these binary optics gratings. Overlays between the two lithography levels of better than 0.2 μm across the 4" wafer (0.15 μm±0.1 μm for a test pattern) were achieved on the stepper using global alignment. Wafers were then etched in a parallel-plate reactive ion etching (RIE) system to the target depth. Etch depths were controlled by etch time.

The performance of the echelon grating has been modeled using scalar diffraction theory (which is valid for periods much larger than the wavelength and shallow etch depths) and rigorous EM diffraction calculations, as shown in Figure 2. The EM calculations assume TE polarization and normal incidence (TM polarization results are slightly worse). Results are normalized to the

total transmitted light. Because the grating depths for the echelon are not negligible, 50-60% efficiency is predicted by the EM calculations vs the 80-90% efficiency predicted by scalar theory. The effects of processing variations on grating performance have also been modeled. The simulations indicate that the etch depth errors must be less than 3% of the minimum step height for the device to function well. Variations in etch depth shift the center frequency to shorter wavelengths if the grating is too shallow and to longer wavelengths if the grating is too deep.

The grating operation can be observed using a transmission microscope and a microlens array. The microlens array (either 200 μm ≈F/2 photoresist lenses or 500 μm diameter F/4 Corning SMILE lenses) placed on top of the grating which is illuminated from below collects the dispersed light. Color is analyzed via a series of color filters placed over the light source. Preliminary evaluation of the color separation optic reveals that the central zero order transmits green light, with the red diverted into the -1 order and the blue diverted into the +1 order. More detailed spectroscopic and efficiency measurements made on these grating will also be presented.

Acknowledgment

We would like to acknowledge J. E. Curtin for her expert assistance in device fabrication. This work was sponsored by the Advanced Research Projects Agency. Opinions, interpretations, conclusions, and recommendations are those of the author and are not necessarily endorsed by the United States Government.

References

1. M. W. Farn, M. B. Stern, W. B. Veldkamp, and S. S. Medeiros, "Color separation by use of binary optics," *Opt. Lett.* **18**, 1214 (1993).

2. H. Dammann, "Color separation gratings," *Appl. Opt.* **17**, 2273 (1979).

3. M. W. Farn, R. E. Knowlden, M. B. Stern, and W B. Veldkamp, "Color separation gratings," *NASA Conf. Publ.* **3227**, 409 (1993).

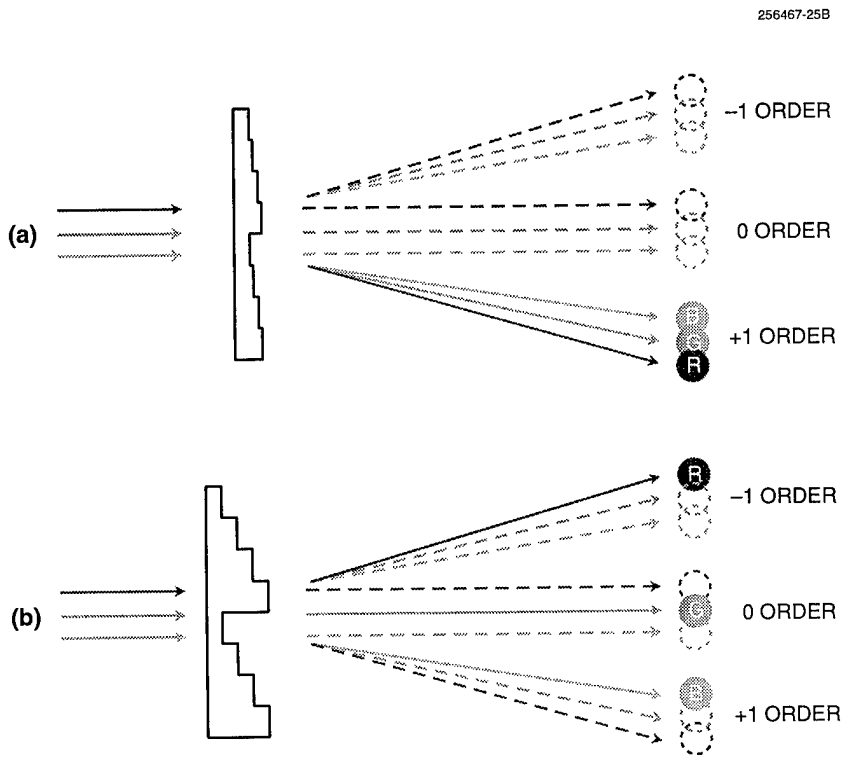


Figure 1 Color separation by dispersion in a conventional stepped grating (a) versus the binary optics echelon grating (b).

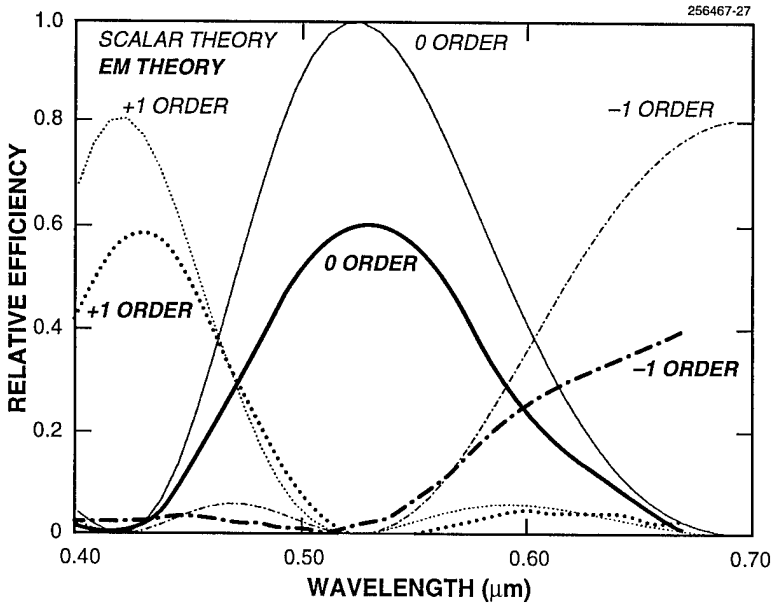


Figure 2 Predicted spectral efficiency as a function of wavelength for both the scalar diffraction theory model and rigorous electromagnetic calculations. The -1, 0, and +1 order efficiencies are plotted as a function of wavelength. The diffraction efficiencies of all other orders are summed and plotted as "all other orders".

A Multiview Fast Optical Tomography System Using Microlens Arrays

K. P. Bishop, R. E. Pierson, E. Y. Chen
Applied Technology Associates, 1900 Randolph SE, Albuquerque, NM 87106, 505/846-6110, FAX: 505/768-1391

L. McMackin
U.S. Air Force Phillips Laboratory, Kirtland AFB, NM 87117, 505/846-2046, FAX: 505/846-2045

1.0 Introduction

In this paper, we present an application of microlens-based Hartmann wavefront sensors. The wavefront sensors, which employ arrays of one-dimensional cylindrical microlenses, are used in a multiview optical tomography system to provide a nonintrusive measurement of a dynamic heated air jet flow. A number of linear Hartmann sensors is arranged around the circumference of the region of interest (Figure 1). The tomography system uses the multiple simultaneous wavefront measurements around the circular jet to reconstruct two-dimensional estimates of the index-of-refraction variations in the flow. High speed sampling of the flow enables reconstruction of three-dimensional organized structures present in the flow.

One-dimensional Hartmann sensors enable high resolution wavefront measurements at rates of several kilohertz. These one-dimensional Hartmann sensors consist of an array of cylindrical microlenses that focus an incident wavefront onto a linear charge-coupled device (CCD) detector array. The Hartmann sensors measure the tilt variations on the wavefront in the direction perpendicular to the flow axis by measuring the displacement of each focused spot on the CCD array from its on-axis position. The wavefront error or optical path difference (OPD) is then calculated by integrating the microlens deflection measurements. The OPDs from the multiple sensor system are combined by a reconstruction algorithm to produce a two-dimensional estimate of flow structures in the area of the sampling plane, where all the beams intersect (see Figure 1). Here, we present results using the Algebraic Reconstruction Technique (ART),[1] although other reconstruction methods are being investigated for this application.

For the tomographic system, the lens array was designed to match the CCD array in length. The CCD array of the Dalsa CL-C4 2048 cameras contain 2,048 pixels in 28.4 mm, thus each pixel is 14 μm across. The microlens design currently in use consists of 64 microlenses each 448 μm in width.

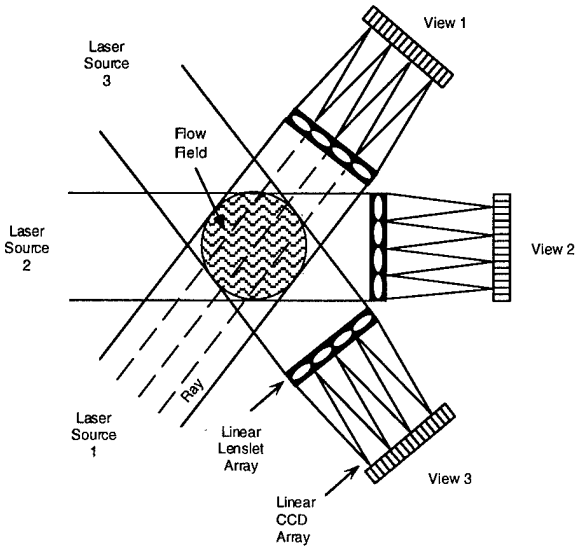


Figure 1. Optical phase tomography measurement system. In this system, a number of wavefront sensor measurements is made simultaneously around the region of interest.

The microlenses were designed for use with laser diodes at a wavelength of 670 nm, and the lenses have a focal length of 37.4 mm. The Hartmann wavefront sensor is the basic unit of the tomography system described in the following sections.

2.0 Single View Subsystem

A wavefront sensor is combined with a laser light source to form one view of the optical tomography system. A schematic diagram of a single view unit is shown in Figure 2. The light source consists of a 670 nm laser diode and a laser beam expander. Laser diodes were chosen because of their small physical size and inexpensive cost. The laser diode produces an astigmatic beam. However, this does not cause a problem for the one-dimensional Hartmann sensor since the laser beam perpendicular to the sensor axis only has to be as large as the dimension of a pixel in the CCD array. The laser beam expander was chosen to over expand the output beam in relation to the length of the Hartmann sensor so that the central portion of the beam is sampled. This provides a more uniform intensity profile across the entire

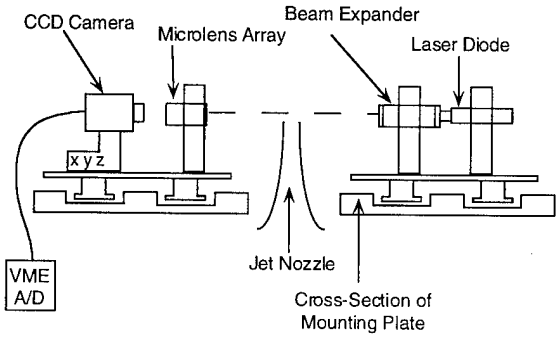


Figure 2. A single view of the tomography system consisting of the wavefront source and the Hartmann wavefront sensor.

Hartmann sensor, thus maintaining approximately the same signal-to-noise ratio for each microlens.

While the spatial resolution of the system in the reconstruction plane is fixed by tomographic performance, the spatial resolution in the direction perpendicular to the reconstruction plane is determined by the dimension of the pixel and the rate at which the wavefront measurements are taken. The flow generation system is designed to produce a 3-8 m/s flow. At the 8 m/s flow speed and a 5.0 kHz sample rate, the 14 μm pixels integrate a 1.6 mm region of the flow in the streamwise direction. The integration size is decreased to approximately 1.0 mm using electronic gating of the cameras. The height alignment of the views of the system to each other is critical due to the 14 μm pixel height. The design requirement to resolve millimeter sizes in the flow determines the alignment error that can be tolerated between the views of the system.

The measurement of the wavefront aberration consists of two parts. First, a reference measurement is taken with no aberrating media. The second measurement is taken with the aberration in place. Using the difference between two spot locations at the CCD array eliminates exact positioning requirements of the microlenses with respect to the CCD array and also eliminates some problems attributable to the quality of the wavefront. The time lag between the initial and displaced spot measurements must be small enough to minimize changes in the environment and in the wavefront which affect the spots.

Noise levels in the system were found to be larger than expected due to environmental conditions.[2] The optical mounting system was chosen to ensure stability and to reduce the effect of vibrations on the system. A small movement in the alignment between the cameras and the microlens array produces a change in the reference spot location for each measurement, creating vibration isolation issues in the mounting design. Therefore, large mounting hardware was used to increase the stability of all the components in the system. Another cause for errors, which grows worse with time, is the heating of the cameras. The wavefront sensor can measure the convection of hot air off the faceplate of the cameras, therefore a cooling system was required. The cameras were cooled by water flowing through a tube built into the faceplate mount of the camera. The water rate and pressure were kept low to ensure that no noise was induced due to any vibrations from water surges through the cameras.

3.0 Multiview Tomographic System

A schematic diagram of the 8-view tomographic system is shown in Figure 3. In our current system, each view is equally spaced around the jet, although variations of this configuration will be investigated in the future.

Both the source and wavefront sensor portions of each view were placed on a mounting disk with circular rails in order to make the alignment of the system easier. The rail mounting system also simplifies reconfiguring the optics for a different arrangement. The nozzle was designed to move up and down in the middle of the optical system without effecting the optical alignment, so that various downstream locations in the flow could be examined.

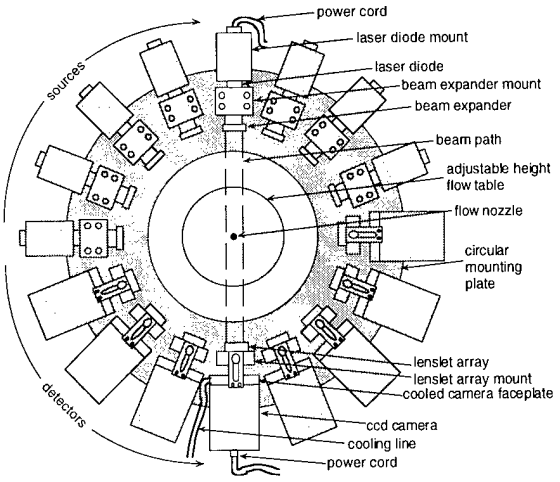


Figure 3. Multiview Tomography System

The use of one-dimensional Hartmann sensors greatly simplifies the recording of the data from multiple sensors in the tomography system at the speed desired. However, the aggregate rate of eight one-dimensional cameras exceeds the common acquisition systems currently available. Each camera contains a 2,048 x 1 CCD array and can be read out at rates of 60 Mega-pixels/s. Off-the-shelf VME analog-to-digital converter boards were found that could sample 4 channels simultaneously with 12 bits of resolution at rates up to 31 MHz. Two such boards were used in the 8-view system. Timing electronics were custom made to provide the signals to synchronize and operate the cameras simultaneously. The electronics also enable the cameras to be electronically gated to reduce the exposure time; this gating ensures that the flow is considered 'frozen' with respect to the scale sizes present, reducing the smearing of objects across the wavefront sensor.

The performance of the tomography system in reconstructing the density fluctuations in the flow was estimated using simulations of propagating light through a known model of varying phase structures. These simulations were performed to determine the requirements of the number of views in the system and the number of microlenses required in the Hartmann sensor for adequate spatial resolution. The number of microlenses chosen was 64 based on previous results[3] and research described in an accompanying paper at this conference.[4] The number of views was selected based on a trade between cost and the ability to adequately resolve the objects of interest in the flow.

A novel image quality metric was used to quantitatively evaluate the performance of the reconstruction.[5] This metric indicates the amount of correlation between a truth image and the reconstructed image as a function of spatial frequency. The correlation metric is particularly useful for discriminating signal from noise when the reconstruction is corrupted by high spatial frequency noise introduced by the tomographic reconstruction process.

We define the effective resolution of our tomography system as the smallest feature size in flow reconstruction that has a correlation above 60 percent. Features larger than this limit are well resolved by the system. Figure 4 shows a plot of the effective resolution as a function of the number of views with varying amounts of noise added. The plot

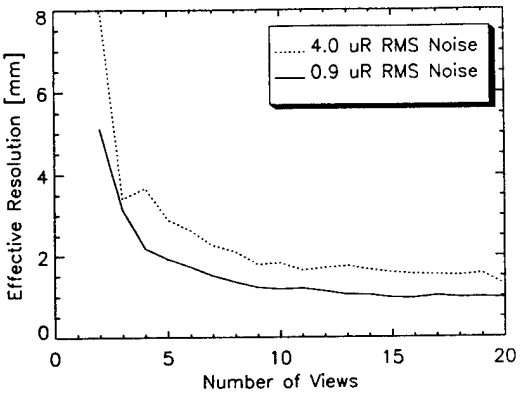


Figure 4. The correlation performance metric result as a function of the number of views in a tomography system.

shows that the benefit of using more than 8-10 views is small in comparison to the increasing cost and design complexity of adding more views. Eight views were chosen in our particular system, which is also a convenient number for obtaining the fast data acquisition system needed to record the camera data.

4.0 Results

The 8-view tomography system is operational and has been used to image index of refraction and temperature in air flow cross-sections. A photograph of the implemented tomography system is shown in Figure 5. Figure 6 shows results for a "known" object formed by placing a mask over the flow nozzle. The mask produces three circular regions of warm air

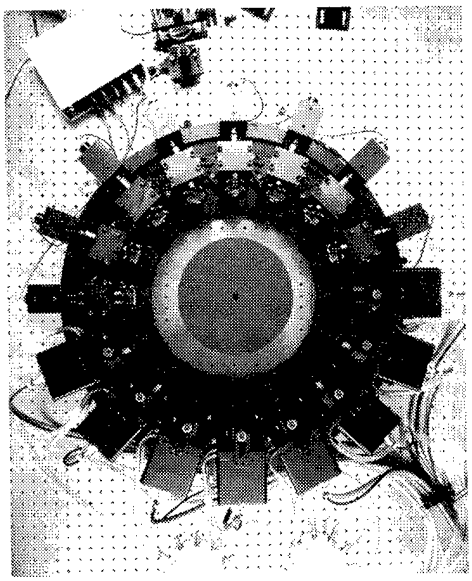
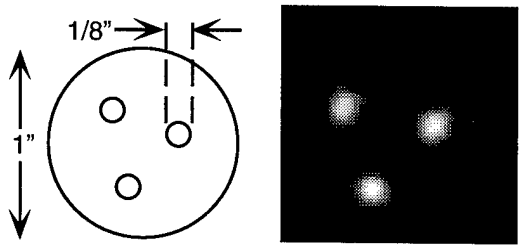


Figure 5. The laboratory setup of the optical tomography system in the Fast Optical Tomography of Turbulent Organized Structure (FOTTOS) laboratory at Phillips Laboratory, KAFB, NM.

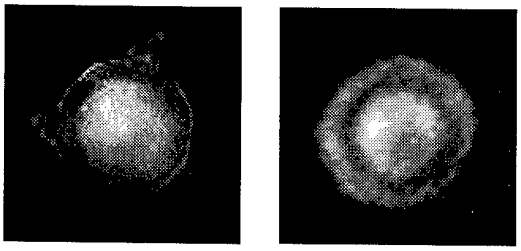
with a lower index of refraction than the surrounding areas. A drawing of the mask used is shown in Figure 6a. The optical tomography system was aligned as close to the nozzle subapertures as possible in order to reconstruct the laminar region of the flows. The system was used to measure the index-of-refraction variations caused by the mask, and the resultant reconstruction is shown in Figure 6b.

Figure 7a is an image obtained by filling the half inch diameter flow generating system with smoke and taking a picture of the cross-sectional smoke variations in the jet. This flow visualization technique is intrusive, unpredictable, and does not give any indication of the magnitude of density fluctuations. It is only an indication of the type of structures that might be expected in the flow. Figure 7b is a reconstructed image of the jet flow measured using the tomography system. This measurement was taken in a 8 m/s flow at 2.5 nozzle diameters downstream from the nozzle exit.



(a) Drawing of Mask *(b) Reconstructed Image from Mask Measurement*

Figure 6. Measurement of Hot Air through Mask



(a) Representative Visualization of Flow Cross-Section Using Smoke *(b) Tomographic Reconstruction of Actual Flow Measurement*

Figure 7. Flow Field Measurement

Conclusions

A fast optical tomography system has been developed for nonintrusive measurement of density fluctuations in a heated jet flow. The system provides measurements at higher rates than other current techniques. It eliminates the need for interpreting interferograms and performs the measurement at high temporal and spatial resolutions. The system is being used to investigate the various parameters of the heated jet flow and other index of refraction structures. Improvements are being considered to both ease the calibration currently required in the system and to improve performance by reducing system noise.

References

1. Gordon, R., "A Tutorial on ART," *IEEE Transactions on Nuclear Science*, Vol. NS-21, June 1974.

2. Neal, D., Pierson, R., Chen, E., Bishop, K., McMackin, L., "One-Dimensional Wavefront Sensor Development for Tomographic Flow Measurements," SPIE, August 1995.

3. McMackin, L., Masson, B., Clark, N., Bishop, K., Pierson, R., Chen, E., "Hartmann Wavefront Sensor Studies of Dynamic Organized Structure in Flowfields," *AIAA Journal*, Vol. 33, No. 11, pp. 2158-2164, November 1995.

4. Pierson, R., Bishop, K., Chen, E., Neal, D., McMackin, L., "Evaluation of Wavefront Sensors Based on Etched Microlenses," *Optical Society of America Conference on Diffractive Optics and Micro-Optics*, Boston, Massachusetts, April 29 - May 3, 1996.

5. Pierson, R., Chen, E., "Narrow-Band Spatial Frequency Correlation Metric," Applied Technology Associates, Albuquerque, NM, ISME Informal Technical Report 95Ir0001, January 1995.

MICROLENS LITHOGRAPHY

R. Völkel, H. P. Herzig, Ph. Nussbaum, W. Singer, R. Dändliker
Institute of Microtechnology, Rue Breguet 2, CH-2000 Neuchâtel, Switzerland
Tel. +41-38-234276, Fax +41-38-254276, e-mail: voelkel@imt.unine.ch

BACKGROUND AND OBJECTIVES

The future demands for flat panel display (FPD) manufacturing is a resolution of 3-5 µm for large substrates of 550 x 650 mm^2 size. Standard lithographic techniques, like wafer stepping or proximity printing can be used. Unfortunately, these methods have some severe drawbacks which significantly increase the fabrication costs. Using a wafer stepper, the small printing area will cause numerous exposure steps. The stepping has to be very accurate, because stitching errors can be easily seen in the display pattern. Using a proximity printer, the substrate is set some 20-50 µm behind the mask to achieve a resolution of 3-5 µm. This is not an easy task for large substrates. The costs for these highly planar substrates are immense. A direct contact may easily damage the expensive photomask.

Microlens lithography[1] is a new lithographic method that uses microlens arrays to print a mask onto a substrate layer. The lithographic system consists of a stack of microlens arrays forming an array of micro-objectives. Each micro-objective images a small part of the mask pattern, the images overlap in the image plane. Microlens lithography provides a resolution of 2-5 µm for an almost unlimited print area. A working distance (system-to-substrate) of 1-3 mm allows fast loading and alignment of the substrate. The large depth of focus (e.g. >100 µm for 5 µm resolution) significantly reduces the flatness requirements for the substrates and as well might be useful for printing into thick photoresist layers (e.g. for micromechanics) or onto curved surfaces.

MICROLENS ARRAYS

In the past, the fabrication methods for lens arrays were complicated and the optical performance was often poor. Nowadays, high quality microlens arrays are available, e.g. ion exchange lenses, photo-thermal lenses, melting photoresist lenses and diffractive lenses. The most promising fabrication method for very large refractive microlens arrays is the melting resist technology.[2,3,4] Photoresist cylinders are formed by lithography and melted at a temperature of T≈150°C. Surface tension forms an almost perfect sphere. Melting resist microlenses are well suited for high resolution imaging. An almost diffraction limited optical performance is observed. Figure 1 shows the image of a test pattern imaged with a melted resist lens. A resolution of 1.2 µm (≈400 lines per mm) is observed in a microscope with white light illumination. To obtain high transmission in the UV, the shape of the resist lens is transferred into fused silica by reactive ion etching (RIE) as shown in Fig. 2. Melting resist lenses are fabricated on top of a fused silica substrate. Atoms from the resist surface and the silica are simultaneously removed by energetic ions until the lens shape is completely transferred. The reacting gas is normally a mixture of CHF_3 and O_2 gases. Depending on the O_2 content of the reacting gases, the etch rates of photoresist and silica may differ up to a factor of three. The higher the O_2 content, the higher is the etch rate of the resist. Spherical aberrations can be corrected during the etching by changing the O_2 content of the reacting gas to vary the slope in the rim region of the microlenses.[5,6]

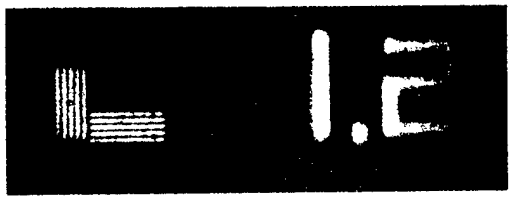


Figure 1. Image of a test pattern imaged with a single melting resist microlens (Ø=250µm, NA=0.36).

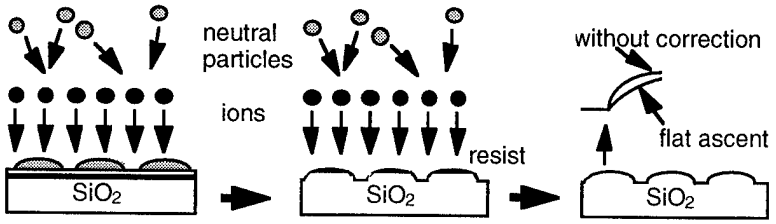


Fig. 2. Scheme of the RIE transfer process. A correction of the lens profile at the rim is obtained by changing the O_2 content during the etching process.

Standard semiconductor processes, like photolithography, resist technology and RIE are used for the fabrication of melting resist microlens arrays. Microlens lithography is therefore available for all manufacturable display sizes.

MICROLENS IMAGING SYSTEM

Microlens lithography is based on the well known concept of multiple lenses or bee's eye lenslet-array imagers.[7,8,9,10,11,12,13] Figure 3 shows the principle of the microlens lithography imaging system. The imaging system consists of a stack of three microlens arrays forming an array of micro-objectives. Each micro-objective independently transports a part of the mask pattern. The images from different channels overlap. The overlapping areas coincide in the final image to provide a single, complete image of the mask pattern. A demagnification of the intermediate image avoids crosstalk between adjacent imaging channels. A field lens array (FL) located in the intermediate image plane improves the radiometric efficiency of the system. The optical performance can be improved by using two field lens arrays (FL1,2) instead of one. Both field lenses are situated near the intermediate image plane. The optical system in Fig. 3 is fully symmetrical. One half of the system is identical to the other half, including object and image. Due to this geometry, the antisymmetrical wavefront aberrations (coma, distortion and magnification chromatic aberrations) are minimized or zero. The spherical aberrations can be significantly reduced by using aspherical lenses, e.g. hyperboloids. Figure 4 shows an aberration-corrected microlens imaging system suitable for lithography.

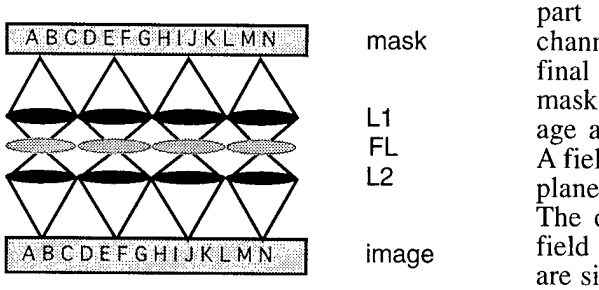
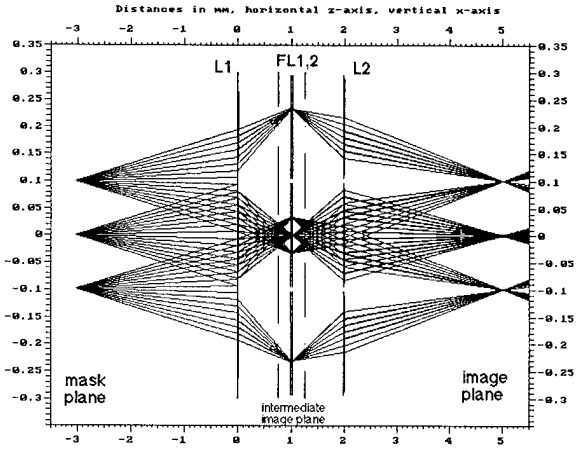


Figure 3. Microlens imaging system used for microlens lithography.



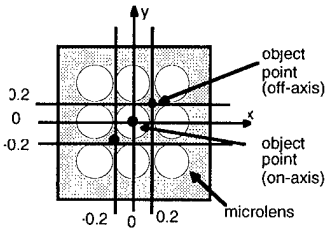


Figure 4. Raytracing through a four layer microlens array system. Three object points (as indicated in the scheme above) are transported by multiple imaging channels. Two lens arrays (L1,2: Ø=190µm, f=750µm) are used for imaging. Two arrays (FL1,2: f=500µm) act as field lenses. The images overlap perfectly in the image plane.

Two lens arrays (L1,L2) are used for imaging, two lens arrays (FL1,FL2) act as field lenses. The numerical aperture of the system was 0.05. A diffraction limited optical performance is achieved.

MULTIPLE PUPIL IMAGING

The microlens imaging system shown in Fig. 4 transports the light simultaneously through separate, independent imaging channels. The corresponding images from the different channels overlap in the image plane. Such systems are so-called multiple pupil imaging systems.[14,15] Figure 5 shows the modulation transfer function (MTF) calculated for two different object points transmitted by the 3x3 pupil system shown in Fig. 4. The on-axis object point (0/0) is transmitted by one imaging channel (MTF shown left). The off-axis object point (0.2/0.2) is transmitted by four adjacent imaging channels (MTF shown right). The calculation is based on ray-tracing.

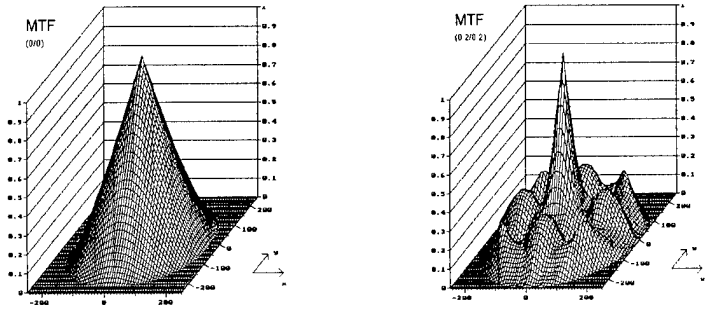


Figure 5. Modulation transfer function (MTF) of the 3x3 pupil system shown in Fig. 4.

Compared to conventional optics, the MTF of multiple pupil imaging (right) looks quite different. The distribution of the spatial frequency peaks and valleys is depending on the lens array geometry.

WORKING DISTANCE, DEPTH OF FOCUS

The microlens imaging system (planar, overall thickness 3-4 mm) is integrated into standard proximity printers. The imaging system creates an erect unit image of the mask on the substrate layer.

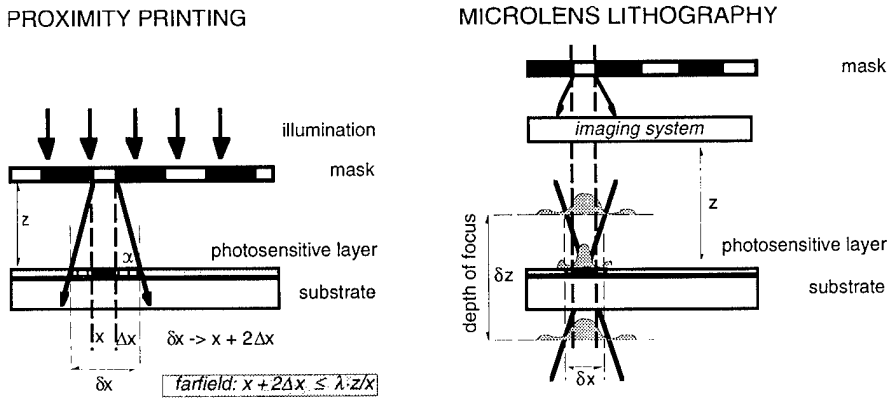


Fig. 6: Working distance z, resolution δx and depth of focus δz for (left) standard proximity printing and (right) microlens lithography.

Figure 5 compares the working distance z, resolution δx and depth of focus δz for (left) standard proximity printing and (right) microlens lithography. There are two basic advantages of microlens lithography compared to proximity printing:

- A larger **working distance**: For microlens lithography the distance between the substrate and microlenses is z=1-3 mm (compared to z=20-50 µm).
- A larger **depth of focus**: For proximity printing, the resolution decreases rapidly with the distance z. For microlens lithography, the highest resolution is observed in the image plane. The image is extented in forward and backward direction. A resolution of 5 µm (imaging system with NA=0.04, λ=400 nm) corresponds with a usable depth of focus of 100 µm.

DEMONSTRATION SYSTEM

A three lens array demonstration system, similar to Fig. 3, has been built. Two arrays of melted resist microlenses (Ø=190 µm, NA=0.15, hexagonal closely packed) were used for imaging. The intermediate image was demagnified to ß=0.6. A third microlens array (Ø=190 µm, NA=0.23) served as a field lens array. The image plane was observed in a microscope with white light illumination. Figure 7

shows (a) the image plane of a mask used for the fabrication of FPDs and (b) the image plane of a standard resolution target. Both were imaged using the demonstration set-up described above.

a) b)

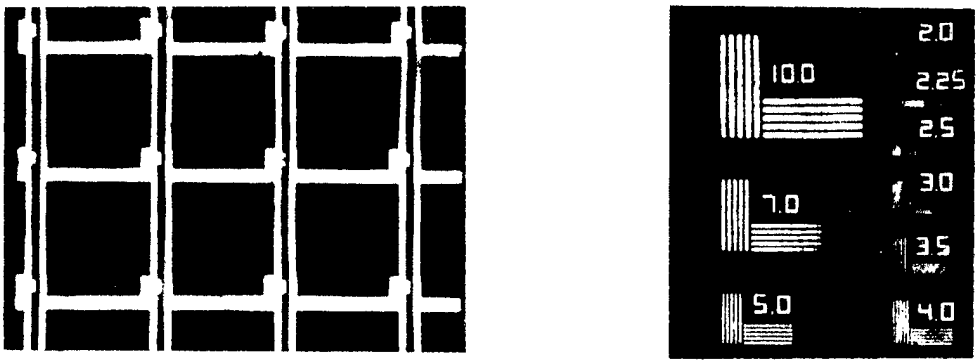


Figure 7. Image plane of a three layer microlens micro-imaging system similar to Fig. 3. (a) Image of a mask used for FPDs. (b) Image of a resolution target.

A resolution in the order of 100 lines per mm (5 µm minimum feature size) was observed for white light illumination.

SUMMARY

Microlens lithography provides a resolution of 2-5 µm for an almost unlimited print area. A working distance (system-to-substrate) of 1-3 mm allows fast loading and adjustment of the substrate. Potential applications are the fabrication of large area flat panel displays (FPDs) and color filters. The large depth of focus (typically 50-100 µm might be very useful for printing in thick photoresist layers (e.g. for micromechanics) or on curved surfaces.

ACKNOWLEDGMENT

This project was partially supported by Hugle Lithography and the Swiss Priority Program 'Optique'.

REFERENCES

1 W. B. Hugle et. al., U.S. patent appl., #08/114,732 (1993).
2 Z.D. Popovic, R.A. Sprague, G.A. Neville Connell, Appl. Opt. 27, 1281 (1988).
3 M.C. Hutley, SPIE Opt. in Compl. Syst., **1319** 491 (1990).
4 S. Haselbeck, H. Schreiber, J. Schwider, N. Streibl, Opt. Eng. **6** 1322-1324 (1993).
5 M. Eisner, S. Haselbeck, H. Schreiber, J. Schwider, EOS Meeting Series 'Microlens Arrays', UK (1993).
6 M. B. Stern, T. R. Jay, Opt. Eng. **33** 3547-3551 (1994).
7 H. Käufer, E. Burger, H. P. Huber, FRG patent 1.260.178 (Aug. 8, 1968), U.S. pat. 3.447.438 (June 3, 1969).
8 I. Kitano, K. Koizumi, H. Matsumura, K. Ikeda, T. Uchida, U.S. patent 3.658.407 (April 25, 1972).
9 H. H. Anderson, U.S. patent RE 28.162 (1974).
10 R.H. Anderson, Appl. Opt. **18** 477-484 (1979).
11 I. Glaser, A.A. Friesem, Appl. of hologr. and optical data processing, E. Moram (ed) Pergamon Press (1977).
12 I. Glaser, U.S. patent 4.175.488 (November 27, 1979).
13 M. Kawazu, Y. Ogura, Appl. Opt. **19** 1105-1112 (1980).
14 S. Fender, Proc. SPIE **440** 2 (1983).
15 R. Völkel, W. Singer, H.P. Herzig, R. Dändliker, MOC '95, Hiroshima, Japan 156-159 (1995).

Laser Beam Relaying with Phase-Conjugate Diffractive Optical Elements

Siamak Makki
James Leger

Department of Electrical Engineering
University of Minnesota
Minneapolis, Minnesota 55455
Tel:(612) 625-0838 , Fax:(612) 625-4583

In many high power optical systems, it is necessary to relay a beam from one component to another or from the laser output to the target. Simple Gaussian beams can be easily relayed with conventional optics; however more complex profiles, such as a flat-top laser mode, require an afocal imaging system to reproduce the mode profile and phase front. Fig. 1a shows a conventional afocal system. For high Fresnel number applications, the intermediate focal point can result in undesirable concentration of light and subsequent air breakdown.

Beam relaying can also be accomplished by phase conjugation. In this case, the image is generated without any intermediate focal points. The conjugate wave simply traverses the same path in reverse until it has reconstructed the complex conjugate of the original field. Dynamic phase conjugation techniques, such as stimulated brillouin scattering or four-wave mixing[1], have been used in laser relay systems and can compensate for time-varying aberrations. However, in many laser systems a fixed diffractive optical element can also provide the required phase conjugation, resulting in a simple and low-cost solution to relaying laser beams.

We have demonstrated a beam relaying system that uses a single custom-made diffractive element and does not require any conventional lenses. The system is sketched in Figure 1b. The diffractive optic is designed by calculating the diffraction pattern from a specific light distribution at the element surface using the Rayleigh-Sommerfeld diffraction formula[2]. We start with the original light field and then determine the diffraction pattern at half the distance between the object and image planes. The plate is then designed to produce the phase conjugate of the arriving distribution. It is easy to show that propagation from the plate to the image plane results in the phase conjugate of the original object profile. Since the transmittance of the element is phase-only, it can be fabricated as a diffractive optical element. Having calculated the phase profile of the plate, we can perform a modulo-2π operation and phase-level quantization. By making the size of the element large enough, we minimize the diffraction losses. Since it is possible to design and fabricate virtually any desired profile, this technique can be used to relay any light field distribution to any distance.

When using a phase conjugation system to relay a beam in the near field, the maximum intensity of the propagating beam is close to the original mode intensity (Fig. 1b). In an afocal imaging system, however, the maximum intensity at the intermediate focal point can be much higher. Consider, for example, relaying a square beam profile of width d a distance z using an afocal system. It is straightforward to show that the intensity at the intermediate focal point $I_2(x,y)$ is given by

$$I_2(x,y) = \left(\frac{4d^2}{\lambda z}\right)^2 \mathrm{sinc}^2\left(d\frac{4x}{\lambda z}\right)\mathrm{sinc}^2\left(d\frac{4y}{\lambda z}\right)$$

resulting in a concentration factor over object intensity profile $I_1(x,y)$ of

$$\frac{I_2(0,0)}{I_1(0,0)} = \frac{16d^4}{\lambda^2 z^2} = 16(N)^2$$

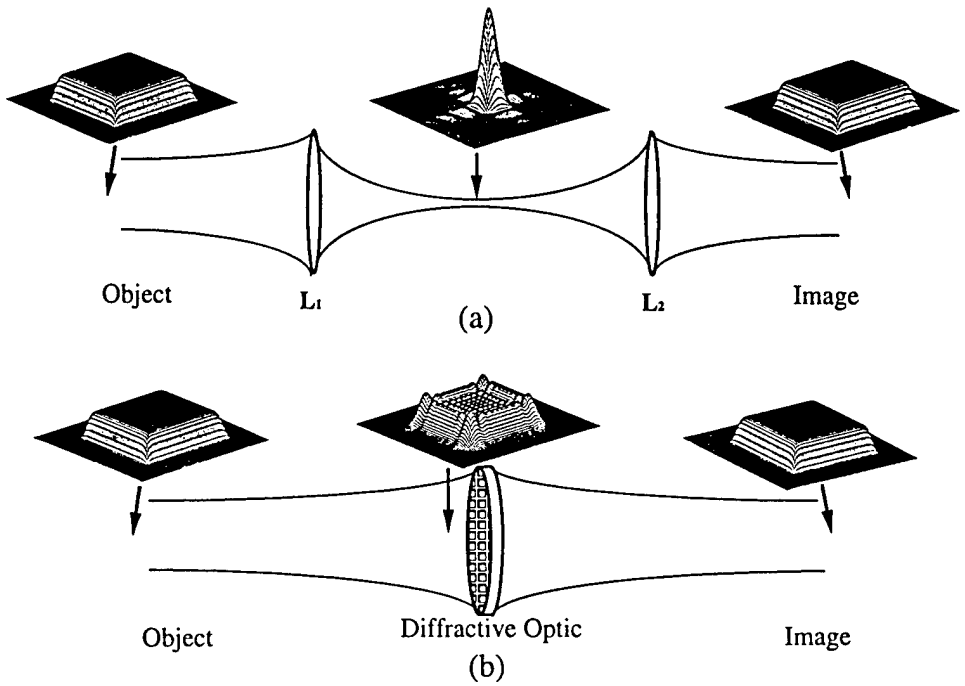


Figure 1: Propagation of a flat-top laser beam along optical axis of: (a) an afocal imaging system (b) a phase-conjugate system

where $N = \frac{d^2}{\lambda z}$ is the Fresnel number of the system. Therefore in systems with Fresnel numbers larger than 1/4, the peak intensity at the intermediate focal point is higher than the intensity level of the object profile.

As an experimental demonstration, we have chosen to relay a flat-top laser mode (width equals 1.2 mm) a distance of 2 meters. The diffractive plate was fabricated with a minimum feature size of 50 μm and 16 phase levels which results in 97.9% modal reflectivity. In the experiment, a square aperture of width 1.2 mm was illuminated by a uniform plane wave with a wavelength λ=1.064 μm. Fig. 2 shows experimental measurements of the mode intensity both before and after the diffractive element. The effect of the phase conjugation produced by the diffractive optic is to generate a faithful copy of the original mode with high efficiency. The intermediate diffraction patterns are seen to mirror each other on either side of the diffractive element.

We will next investigate the effects of misalignment and different mode size on the quality of the image in a diffractive optic phase conjugation imaging system. Since the phases of the diffractive plate are fixed, the plate only works properly for a mode of specific size, shape and location. This is in contrast to conventional imaging, where proper imaging is essentially independent of these parameters. Figure 3 shows the experimental and theoretical images for modes that are 10% smaller and 10% larger. To determine uniformity, we have calculated the ratio of rms error to perfect image intensity. The calculation was performed within the central 80% of the original mode profile width. Figure 4a shows the ratio of rms error to image intensity, and figure 4b the power contained in the image profile versus percent object size difference for a system with Fresnel number of $1/\pi$. It is worth noting that smaller sizes only result in reduced contained power, whereas the uniformity does not degrade.

The relative position of the laser mode with respect to the diffractive plate is also very important. Figure 5 shows the resulting image when the object profile is shifted by 10% of its total width in a plane perpendicular to the optical axis. It is important to note that, due to the principle behind the phase conjugation technique, a shift of object will not simply result in an image shift (as would be the case in conventional system) but will also introduce distortion due to improper phase

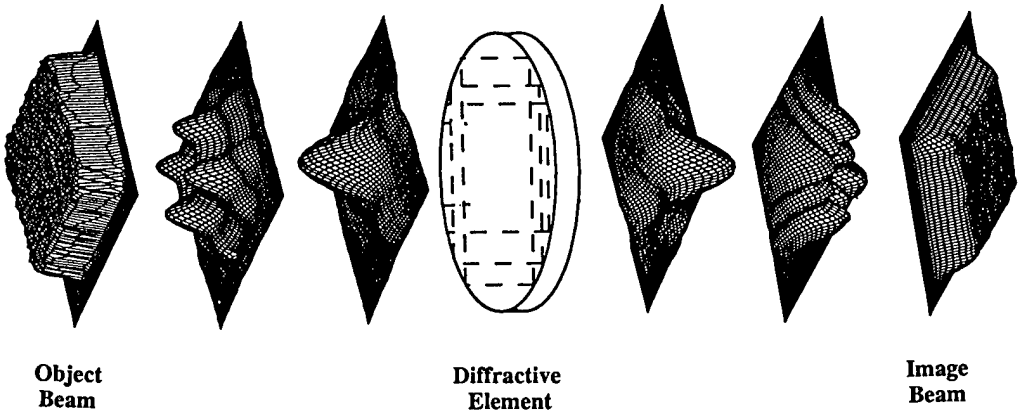


Figure 2: Experimental measurements of intensity patterns before and after diffractive optic phase plate. After propagating the design distance, the complex conjugate of the original distribution is reproduced, resulting in an identical intensity pattern.

conjugation. Figures 6a and 6b are the plots of rms error and power versus percent shift of the object for a system with Fresnel number of $1/\pi$.

In conclusion, we have introduced a unique imaging system that uses a diffractive optical element to relay complex beam profiles without going through a focal point. For high Fresnel number applications, the system has been found to be quite advantageous compared with conventional afocal systems, although it can also be employed in lower Fresnel number applications. Tolerances were simulated on a computer and found to be acceptable for many laser systems.

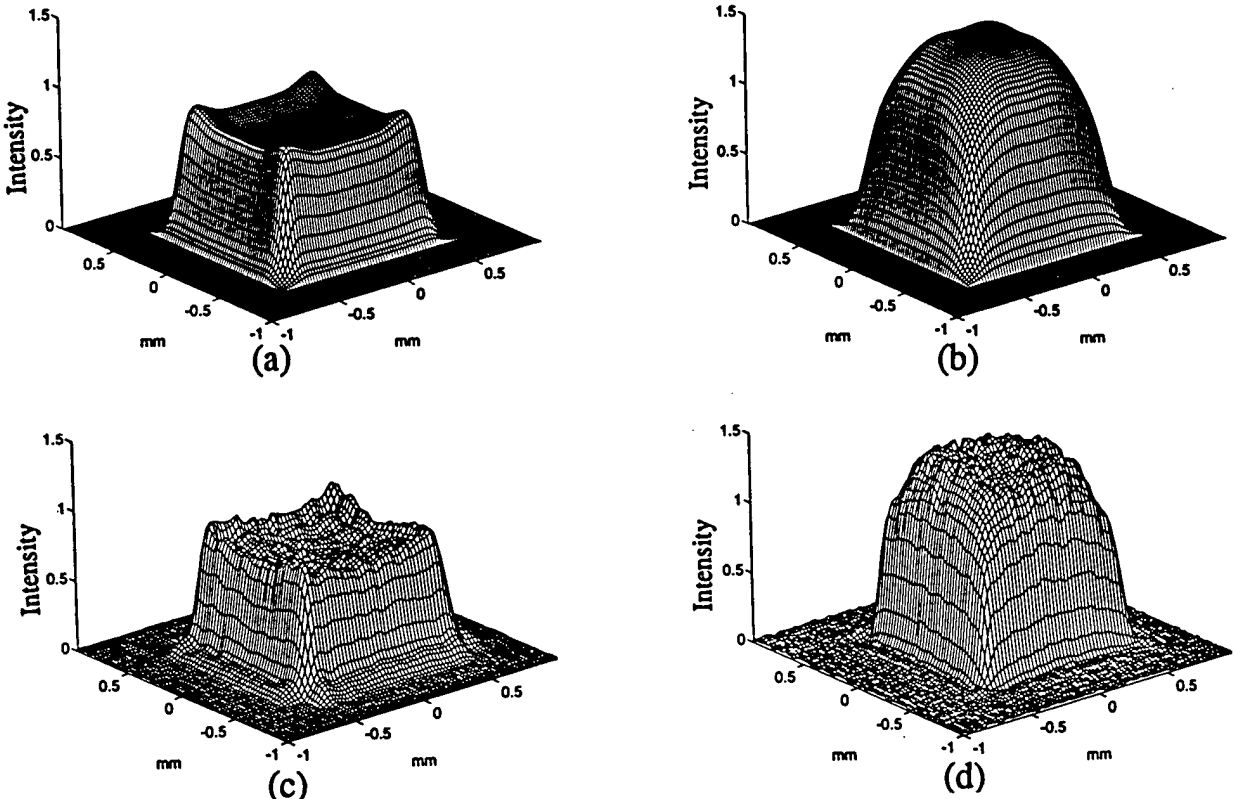


Figure 3: Size tolerance results: (a)10% smaller (theory) (b)10% larger (theory) (c)10% smaller (experiment) (d)10% larger (experiment)..

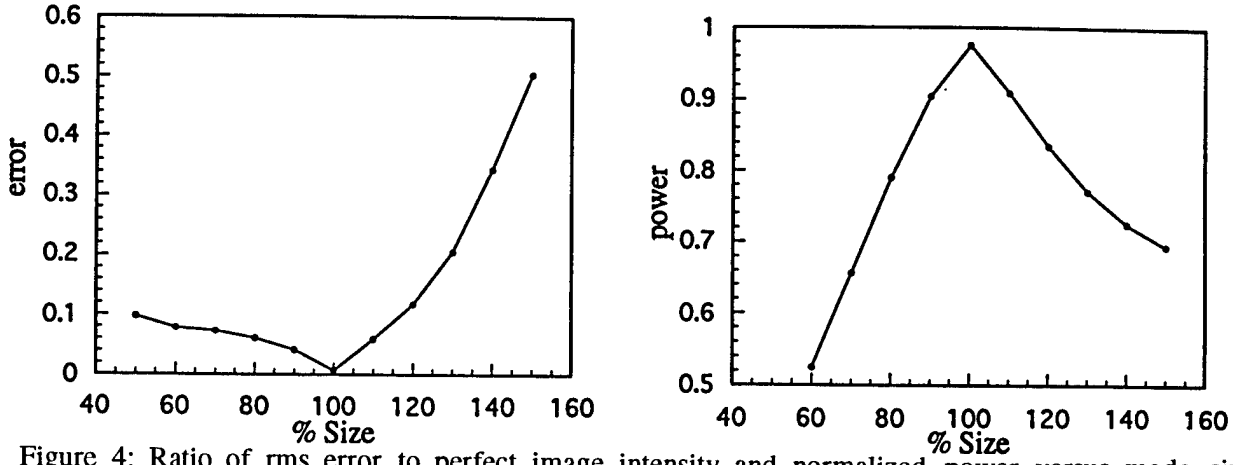


Figure 4: Ratio of rms error to perfect image intensity and normalized power versus mode size change.

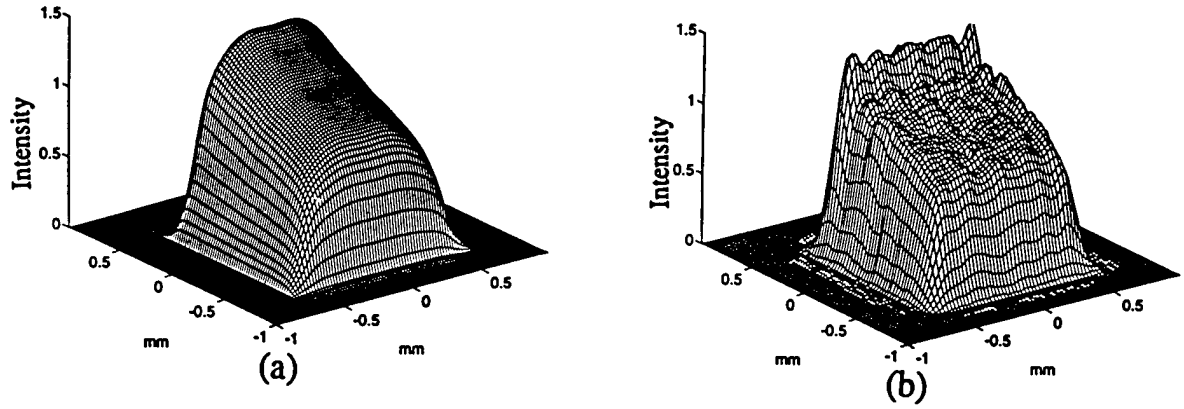


Figure 5: Shift tolerance results: (a)10% shift (theory) (b)10% shift (experiment).

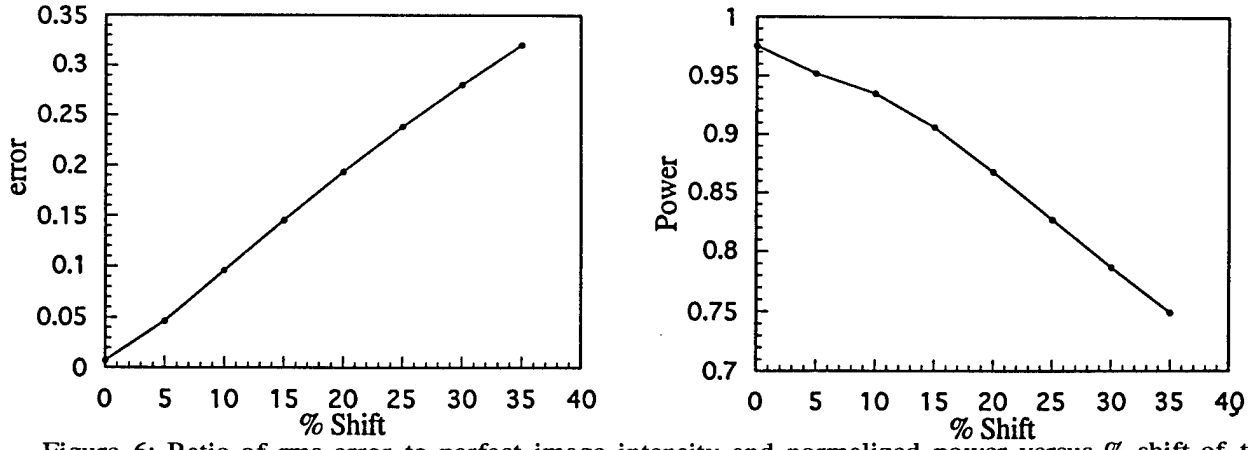


Figure 6: Ratio of rms error to perfect image intensity and normalized power versus % shift of the mode.

References

1. J. Auyeung, D. Fekete, A. Yariv, and D. M. Pepper, IEEE J. Quantum Electron. **QE-15**,1180-1188 (1979)
2. J. R. Leger, Diana Chen, and Zhong Wang, Opt. Lett. **19**, 108-110 (1994)

Wednesday, May 1, 1996

Testing & Evaluation

DWC 1:30 pm-3:00 pm
Gardner A&B

Hans Peter Herzig, *Presider*
University of Neuchatel, Switzerland

Interferometric Tests for Micro-Optics

N. Lindlein, J. Schwider
Lehrstuhl fuer Optik, University of Erlangen
Staudtstr. 7/B2, D-91058 Erlangen, Germany
Fax: ++49/9131/13508
e-mail: norbert@move.physik.uni-erlangen.de

1. Introduction

Micro-optics comprises different kinds of optical elements. This paper will mainly deal with the testing of microlenses, not of mirrors, prisms and other microoptical devices. Microlenses can be classified into two types: refractive and diffractive lenses. Since the diffractive lenses are normally computer generated it is not necessary to test their global optical function, only the microstructure has to be measured. In the case of refractive microlenses there are several properties which have to be determined: paraxial parameters (e.g. focal length, diameter), surface quality (deviations from the ideal form) and wave aberrations. The measurement of these parameters with the help of interferometers in reflected and transmitted light, as well as the advantages and problems of these interferometers, will be discussed.

2. Measurement of the surface quality and sphericity

A Twyman-Green interferometer [1] can be used to determine the deviations of the surface of a refractive microlens from an ideal sphere. A scheme of such an interferometer is shown in fig. 1. A plane wave is focused with the help of a microscopic objective onto the micro sphere to be tested. In the ideal case of an exact micro sphere and exact alignment of the set-up the focus of the spherical wave coincides with the center of curvature of the micro sphere. Then, the light is reflected back by the micro sphere and the microscopic objective collimates the light to a plane wave which interferes with the plane wave of the reference arm. If there exist deviations of the micro sphere from an ideal sphere the interferogram will show these aberrations. Since the reflectivity of the micro spheres can vary within wide margins it is necessary to balance the light intensity between the test arm and the reference arm of the interferometer. This is done with the help of

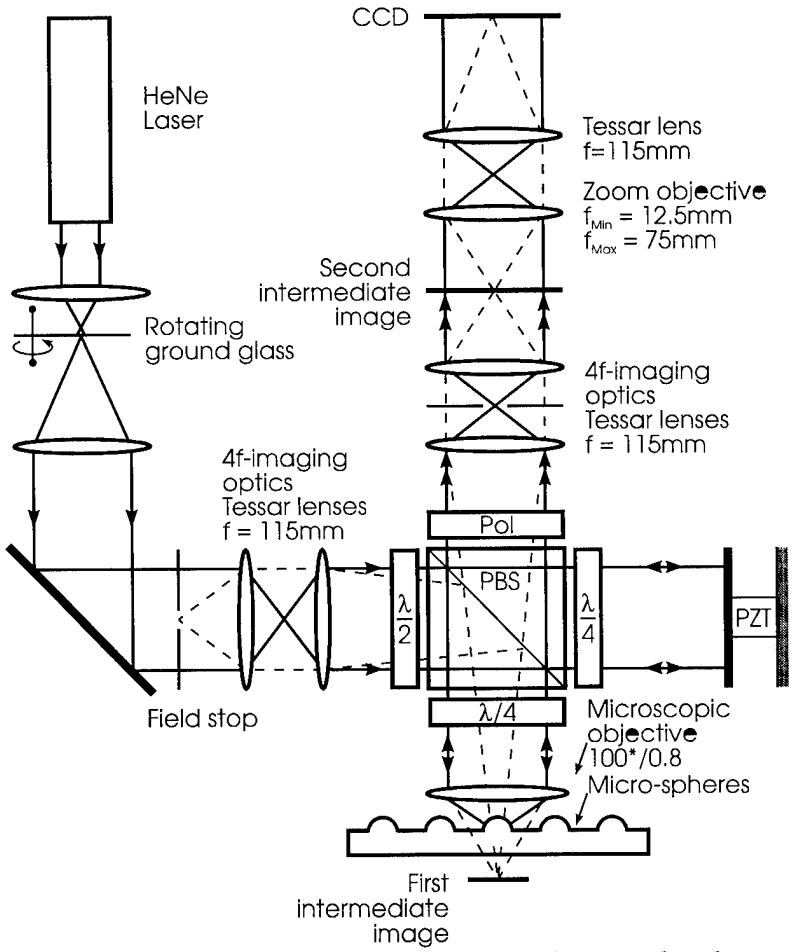


Fig.1: Twyman-Green interferometer with partial coherent illumination and polarizing optics.

polarizing optics. Although, the temporal coherence of the laser light is advantageous for the interferometer the spatial coherence gives rise to spurious interference effects and speckle noise (see fig. 2).

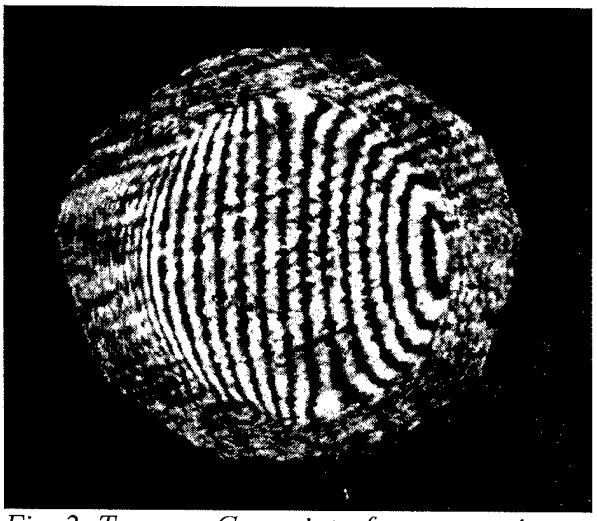


Fig. 2: Twyman-Green interferogram using coherent illumination.

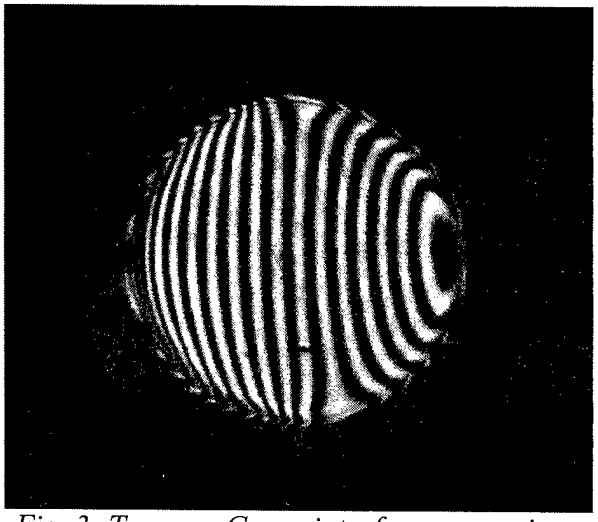


Fig. 3: Twyman-Green interferogram using partial coherent illumination.

If a rotating ground glass is used to destroy the spatial coherence of the laser light the smoothness of the interference fringes can considerably be improved (see fig. 3). To maintain sufficient contrast of the fringes the reference mirror has to be positioned adequately.

The Twyman-Green set-up can also be used to measure the radius of curvature of the micro sphere by moving the micro sphere to the so called cat's eye position where the spherical wave is focused onto the vertex of the micro sphere and an inversion of the wave occurs. Because of this inversion it is necessary to use spatial coherent light so the rotating ground glass has to be removed in the case of the cat's eye adjustment. The length of the translation between the normal measuring and the cat's eye position is equal to the radius of curvature of the micro sphere.

3. Measurement of the wave aberrations

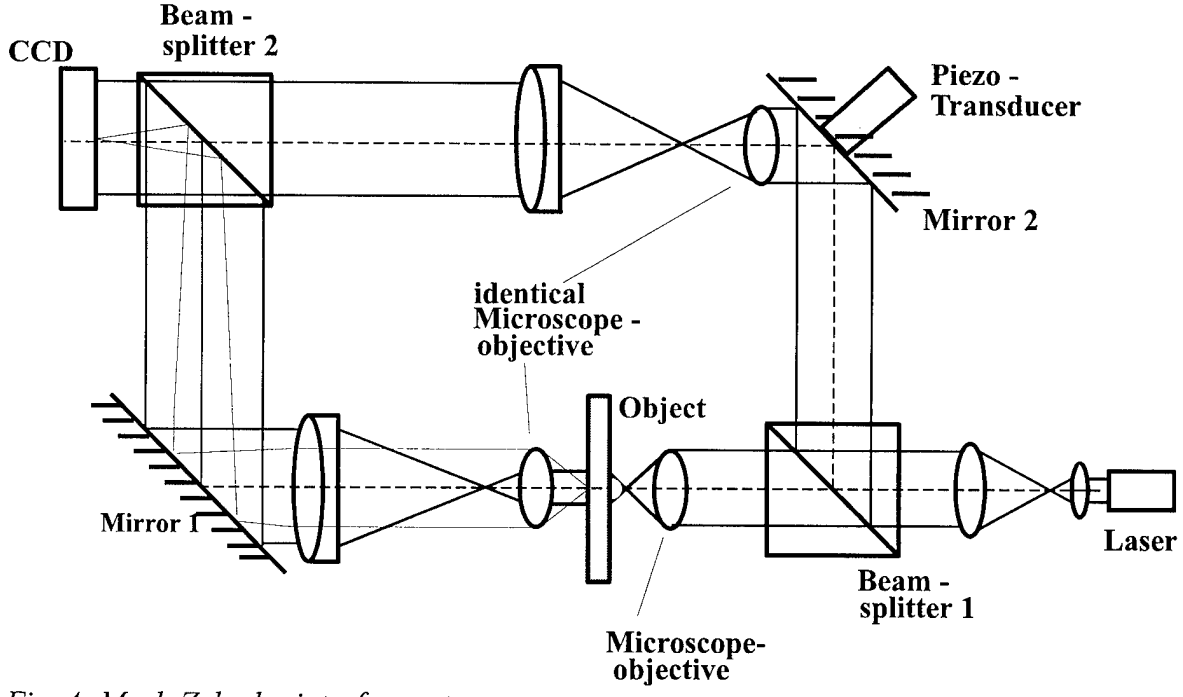


Fig. 4: Mach-Zehnder interferometer.

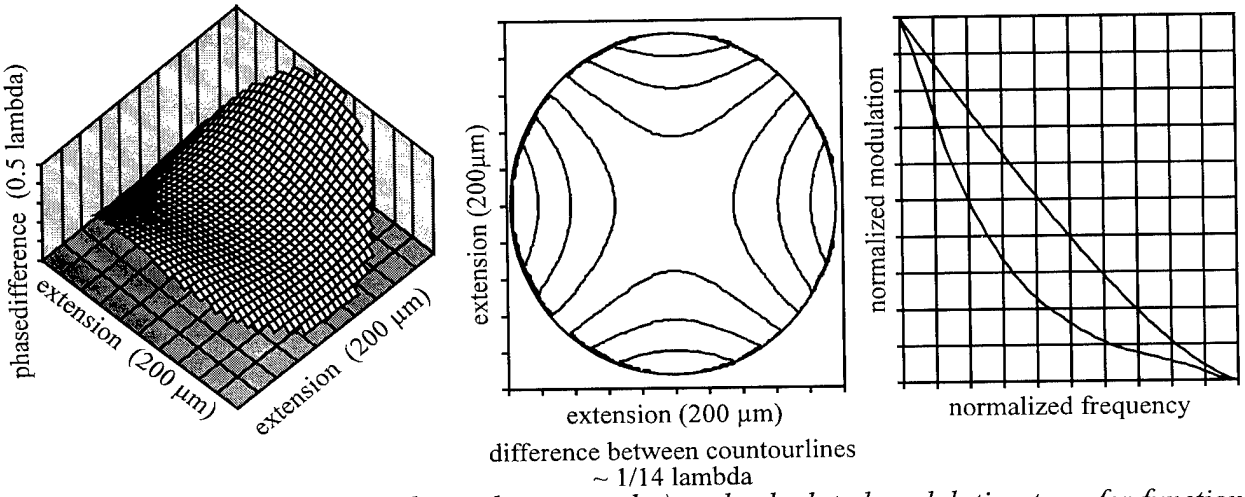


Fig. 5: Wave aberrations (3D plot and contour plot) and calculated modulation transfer function of a microlens measured with the help of a Mach-Zehnder interferometer using phase shifting evaluation techniques.

The measurement of the wave aberrations of a microlens should be carried out with the help of a transmitted light interferometer. The Mach-Zehnder interferometer shown in fig. 4 allows for the measurement of the wave aberrations (fig. 5) [2].

The principle of the Mach-Zehnder interferometer is the following: A plane wave is focused with the help of a microscopic objective in such a way that the focus of the spherical wave coincides with the focus of the microlens under test. The microlens aperture is then imaged via a microscope onto a CCD-detector. The scaling factor can be adapted by changing the micro-objective of the microscope.

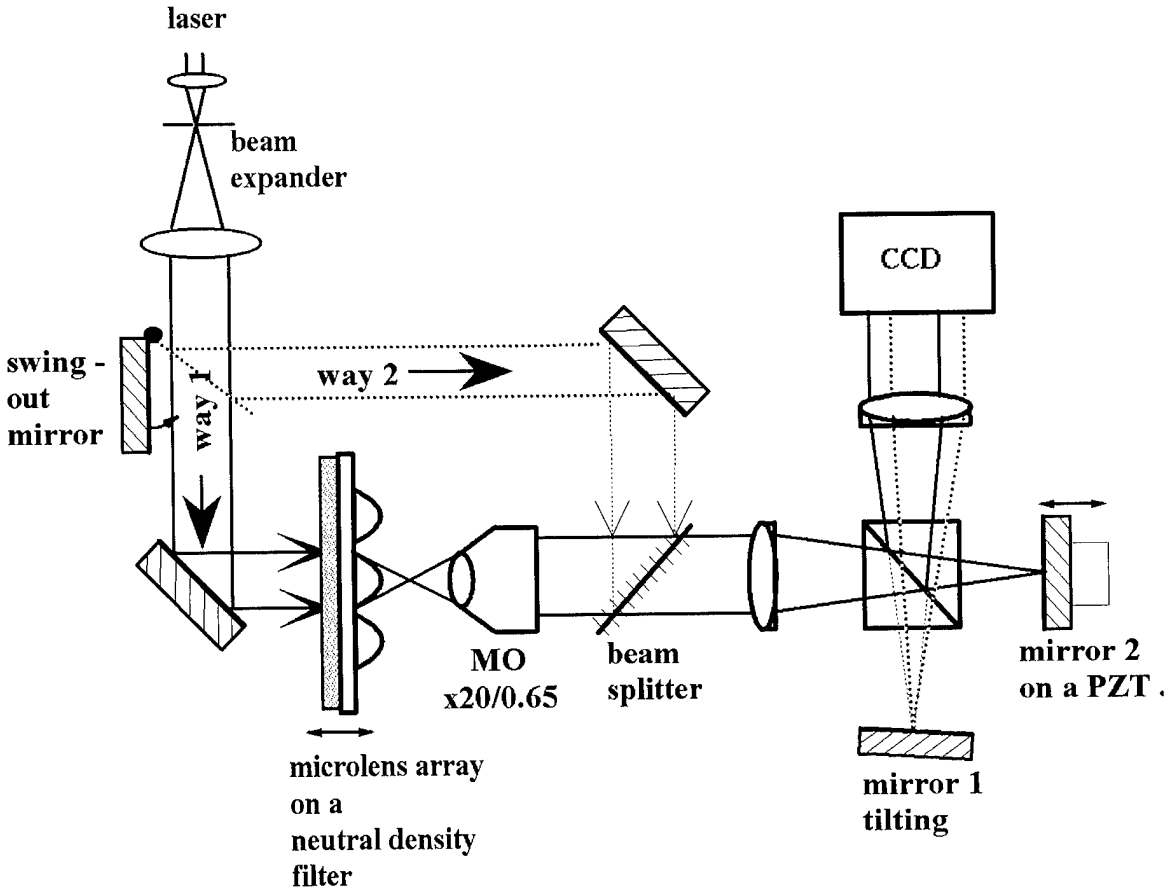


Fig. 6: Scheme of a shearing interferometer.

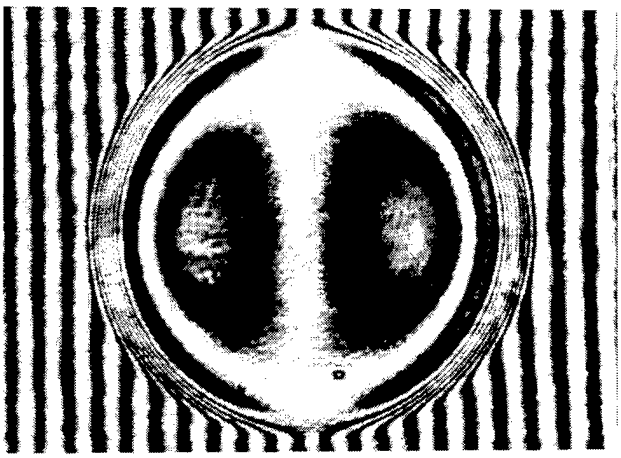


Fig. 7: Shearing interferogram of a microlens with spherical aberration.

The wave aberrations of a microlens can also be measured by using a shearing interferometer (see fig. 6). There, the aberrated wavefront behind the microlens is sheared laterally by itself and forms on the CCD-detector an interferogram of one partial derivative of the wavefront (fig. 7). By shearing in the x- or y-direction both partial derivatives can be determined. With the help of the phase shifting evaluation technique and a least squares fitting algorithm [3] the wave aberrations can be calculated from the interferograms.

The shearing interferometer can also be used to measure the focal length of the microlens [4]. The principle is sketched in fig. 8 together with an interferogram typical for the cat's eye position.

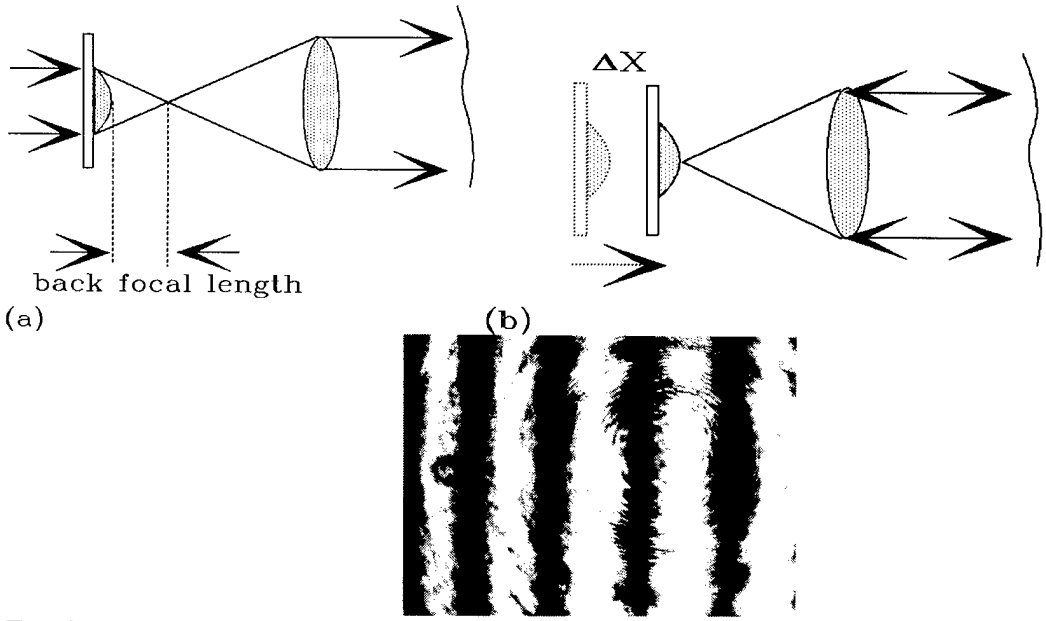


Fig. 8: Positions (a) and (b) for the measurement of the focal length of a microlens and interferogram in the cat's eye position (b).

4. References

[1] J. Schwider, O. Falkenstörfer: *„Twyman-Green interferometer for testing microspheres"*, Opt. Eng. **34** (1995) 2972-2975.

[2] G. Schulz, J. Schwider: *„Interferometric testing of smooth surfaces"*, Prog. in Opt. **13** (1976), ed. E. Wolf, North Holland Publishers, Amsterdam.

[3] H. Sickinger, O. Falkenstörfer, N. Lindlein, J. Schwider: *„Characterization of microlenses using a phase-shifting shearing interferometer"*, Opt. Eng. **33** (1994) 2680-2686.

[4] M.C. Hutley, D. Daly, R.F. Stevens: *„The testing of microlens arrays"*, IOP Short Meet. Ser. **30** (1991) 67-81.

Evaluation of Wavefront Sensors Based on Etched Microlenses

R. E. Pierson, K. B. Bishop, E. Y. Chen
Applied Technology Associates, 1900 Randolph SE, Albuquerque, NM 87106, 505/846-6110, FAX: 505/768-1391

D. R. Neal
Sandia National Laboratories, P.O. Box 5800, Albuquerque, NM 87185-0601, 505/844-0854, FAX: 505/844-6098

L. McMackin
U. S. Air Force Phillips Laboratory, Kirtland AFB, NM 87117, 505/846-2046, FAX: 505/846-2045

1.0 Introduction

Since etched microlenses are produced by digital technology, it is inherently easy to fabricate optics customized for a particular application. However, optimization of wavefront sensors requires an ability to predict their complex behavior. In previous work,[1,2] we demonstrated binary microlens arrays for wavefront sensing in a visible wavelength tomographic imaging system. An eight-view tomographic system based on microlens array sensors is now operational and is described in a separate paper at this conference.[3] The current paper addresses error budgeting and optimal design for wavefront sensors; it describes modeling and test procedures and illustrates one design approach.

2.0 Etched Microlens Wavefront Sensors

The principle of Shack-Hartmann wavefront sensing is well documented.[4,5] Figure 1 depicts a single-etched microlens with a detector array at its focal plane. The edge-to-edge wavefront optical path difference over the lens aperture is translated into a displacement of the focal spot at the detector array. A computer records the intensity profile at the detector array, calculates spot motion, and reconstructs the corresponding tilt at the microlens.

The microlenses are fabricated from a series of optical masks produced by commercial mask layout software. The mask pattern is transferred to the microlens substrate by coating the substrate with photo-resist, exposing through the mask with ultraviolet light, developing the substrate, and etching into the substrate using reactive-ion etching. The process is repeated with a sequence of masks, each etched to twice the depth of the preceding mask. For our application, we used four masks to produce 16 etched levels. Fewer etched levels cause power to be dissipated from the center of the focal spot to its tails; more levels require more etching and narrower etches. The manufacturing process restricts the narrowest possible etch width as well as the total sag across the

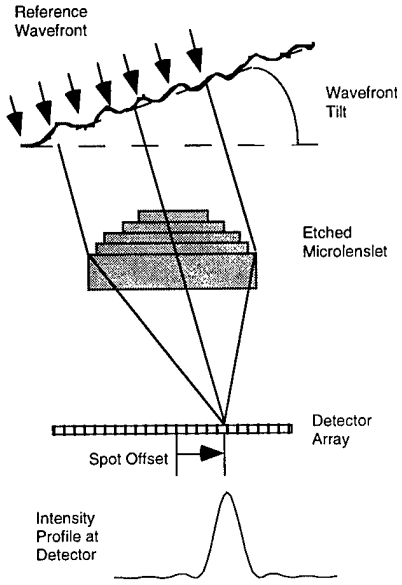


Figure 1. Binary microlenses from focal spots on a fast readout CCD array. Spot motion at the focal plane records wavefront tilt across the microlens.

microlens. For our application, the microlenses are on the order of 200-500 microns with an f-number of 90. The resulting surfaces are approximately spherical with a total sag of one to two waves.

Figure 2 depicts a section of a microlens array in a Shack-Hartmann configuration. The motion of each microlens's focal plane spot is calculated and the corresponding tilt is integrated to reconstruct the impinging wavefront. The wavefront measuring ability of a sensor is often described in terms of range and sensitivity where range is the maximum detectable tilt at each microlens and sensitivity is the minimum detectable tilt. For example, air flow simulations indicate that our application requires a sensitivity of about 3 μrad at a range of +/- 100 μrad. However, one- and two-dimensional microlens arrays demonstrate more complex behavior than a single microlens. Attempts to achieve high sensitivity and

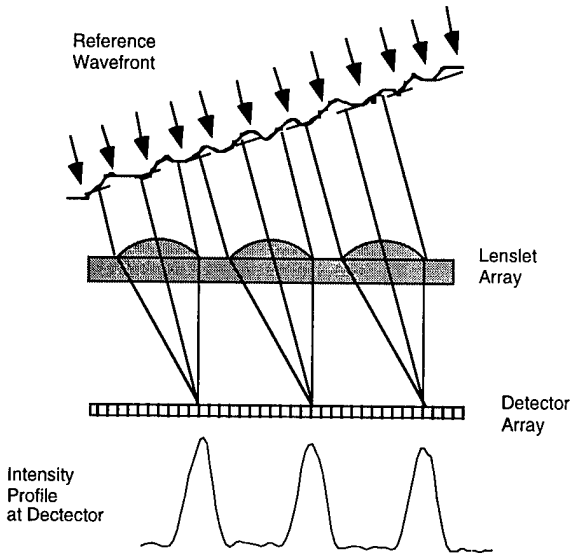


Figure 2. An array of etched microlenses samples wavefront tilts. Interference between focused spots increases with decreasing microlens spacing.

use coherent illumination may severely restrict the tilt measurement range due to interference between spots. The spot intensity profiles in Figure 2 for a microlens array show a markedly different form than the single spot in Figure 1 for a single microlens; this difference is due to destructive interference between spot side lobes.

3.0 Error Budget, Computer Models, and Laboratory Tests

Although the principle of the wavefront sensor system is simple, evaluating performance for a particular binary microlens design may be complicated. Figure 3 indicates this complexity by outlining the error budget for our wavefront sensor.

Random, short time-scale errors appear as noise in the spot location measurements from one time sample to the next. These errors include detector noise, electronic interference, and accuracy limits in the spot location algorithm. These errors can be mitigated by careful design but not removed. In contrast to short time-scale errors, long time-scale errors appear to accumulate with time. These errors are primarily due to changes in the reference wavefront that result in a "fixed pattern" in the wavefront tilt measurements. These errors can be mitigated by careful design, frequent calibration, and good experimental technique.

Deterministic errors result in consistent false measurements of tilt that vary from microlens to microlens over a whole array. These errors are due to physical system problems such as misalignment, positioning errors, or lens-to-lens differences. Deterministic errors can be removed by calibration against wavefronts of known tilt. In contrast, signal-dependent errors are induced by the wavefront being

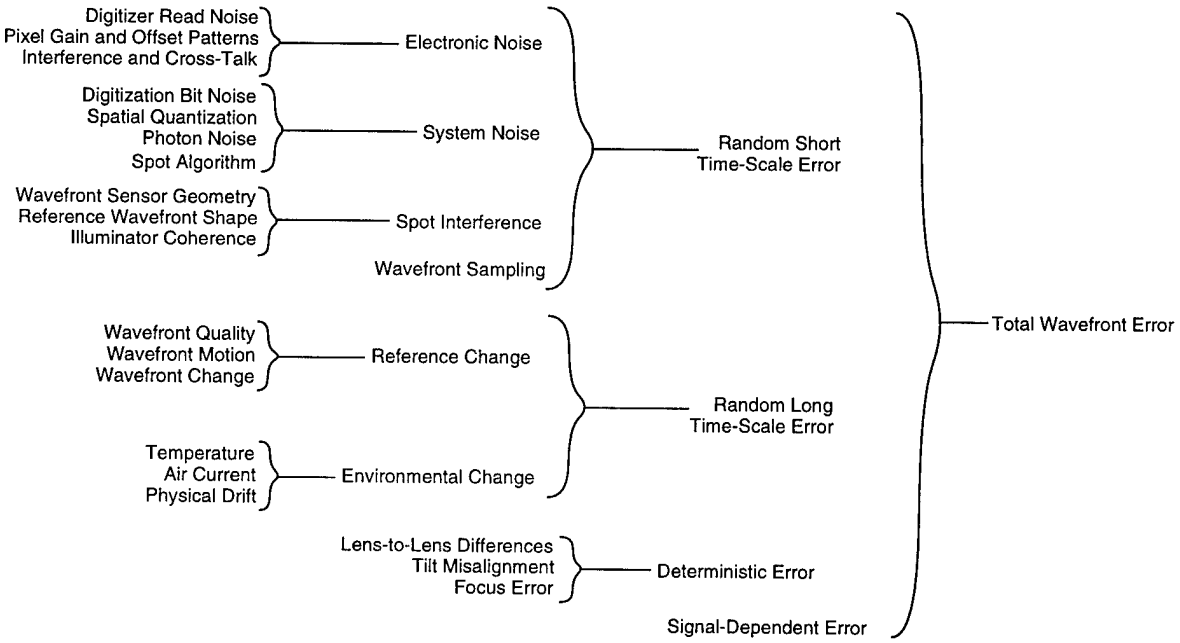


Figure 3. This error budget indicates both short and long time-scale noise sources in wavefront sensing.

measured and are very difficult to correct. Large distortions may cause complex behaviors due to shifting of the reference wavefront or significant interference among focal plane spots.

Over the past year, we have quantified the error sources for our application. A full analysis of these results is beyond the scope of this paper. However, our method for evaluating the error budget is based on computer modeling anchored by laboratory tests.

The modeling system diagrammed in Figure 4 is implemented in software using Khoros and IDL image processing and visualization tools. The model performs a Monte-Carlo simulation of the wavefront sensing process. It creates a finely sampled reference wavefront, propagates it through the distortion, through the microlens array, and to the detector. The detected intensity is digitized, processed to locate focal plane spots, and converted back to wavefront tilts. The resulting tilts are compared to true tilts, or the integrated wavefront is compared to the known wavefront at the microlens array.

Figure 5 shows the laboratory test configuration. A collimated source is reflected off of a mirror at 45 degrees onto the microlens array. To calculate random short time-scale errors, all components of the system are kept fixed while focal plane measurements are repeated at 2.5 kHz over a period of 4 ms. The root-mean-square motion of all the focal plane spots over this short time period provides a measure of short time-scale error. In the same way, the system is kept fixed while data is collected over 30 minutes at intervals of 30 seconds. The root-mean-square difference between average focal plane spot locations at any time and the average positions at the beginning of the run is taken as the measure of accumulated long time-scale error. Deterministic errors are

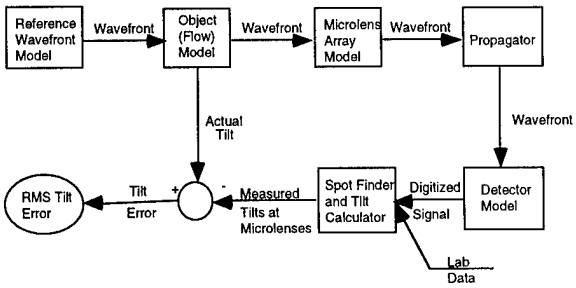


Figure 4. Computer simulations predict microlens array performance under realistic conditions of illumination and noise for expected flow conditions.

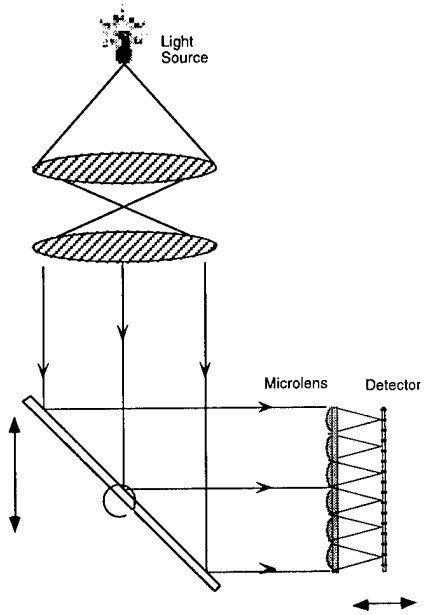


Figure 5. In this test configuration, the light source, microlens to detector distance, wavefront tilt, and wavefront position may all be controlled.

evaluated by introducing tilt at the mirror and measuring lens-to-lens response. If the exact amount of induced tilt is known, both relative and absolute errors may be corrected by appropriate scaling of the measured tilts. In contrast, signal-dependent errors are not directly measured. However, errors due to reference wavefront quality can be assessed by translating the reference wavefront across the sensor using the mirror. Changes in measured tilt, as the wavefront is translated, measure roughness and structure of the wavefront.

4.0 A Design Approach

The parameter space for microlens-array-based wavefront sensor design is very large. However, many of the parameters are fixed by the application. After limiting the degrees of freedom, the computer model described in the preceding section may be used to evaluate performance within the remaining design space. In addition, an error budget allows decoupling of weakly interrelated error sources. Random long-term error, random short-term error, deterministic error, and signal-dependent error may all be essentially independent over the range of possible designs being considered.

Figure 6 illustrates the method of optimal design for short-term error based on assumptions of two degrees of freedom: the number of microlenses per fixed length array and the focal length of these microlenses.

To begin, we fix the number of microlenses and run performance simulations as a function of focal length. Our design parameter is root-mean-square tilt error due to random short time-scale errors. The resulting curve in Figure 6a shows optimal performance for focal lengths from 40-100 mm . Performance is worse at shorter focal lengths because of decreased sensitivity and focal plane spot size. At longer focal lengths, performance is limited by interference among the focal plane spots. In Figure 6b, we determine the optimum performance for each microlens density; each point in this plot is the minimum of a curve similar to 6a for a given number of microlenses per millimeter. Figure 6b indicates that the tilt error increases with the number of microlenses due, primarily, to decreasing spot size. Figure 6c changes error metrics to add information about the wavefront to be reconstructed. Here the measure of error is the root-mean-square error between the reconstructed wavefront and the true wavefront measured as optical path difference. For a small number of microlenses, the wavefront error is large due to wavefront undersampling. For a large number of microlenses, the error is dominated by noise in the measured tilts. From this analysis, the optimum design point is near 2.8 lenses/mm, and the focal length at this design point happens to be 48 mm.

In our application, our actual operating point is at 2.23 microlenses/mm and a focal length of 37.5 mm. Our measured short time-scale root-mean-square tilt error at this configuration is 1.0 μrad, which matches the simulation prediction. Actual performance in our system is limited by long time-scale errors which have been measured at 3.0 μrad over 30 minutes. It is our hope to present more details of the error budget and measured errors in a subsequent report.

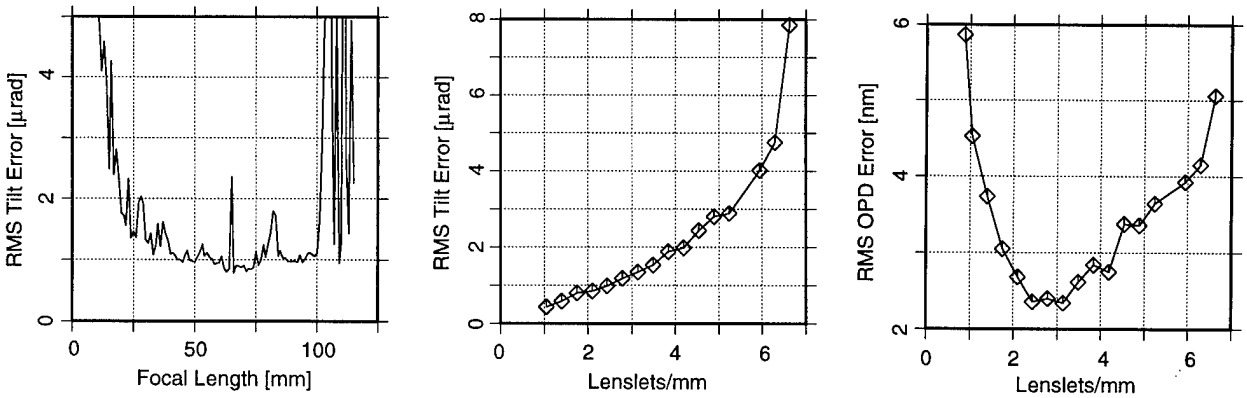
5.0 Conclusions

Microlens-based designs are versatile and adaptable due to the ability to specify and fabricate microlenses optimized to a particular application. For Shack-Hartmann wavefront sensing, the complex system behavior can be simulated by computer and verified by simple laboratory tests. In addition, an error-budget-based design approach allows discrimination of an optimal design for a particular wavefront sensing application.

This paper addressed only design issues for the wavefront sensor. A separate paper[3] at this conference addresses design and operation of a full tomographic system based on microlens arrays.

6.0 References

1. McMackin, L., Masson, B., Clark, N., Bishop, K., Pierson, R., Chen, E., "Hartmann Wavefront Sensor Studies of Dynamic Organized Structure in Flowfields," *AIAA Journal*, Vol. 33, No. 11, pp. 2158-2164, November 1995.
2. Bishop, K., Chen, E., McMackin, L., Neal, D., Pierson, R., "One-Dimensional Wavefront Sensor Development for Tomographic Flow Measurements," SPIE, August 1995.
3. Bishop, K., Chen, E., McMackin, L., Pierson, R., "A Multiview Fast Optical Tomography System Using Microlens Arrays," *Optical Society of America Conference on Diffractive Optics and Micro-Optics*, Boston, Massachusetts, April 29 - May 3, 1996.
4. Schack, R. V., "Direct Phase Sensing Interferometer," *Journal of the Optical Society of America*, Vol. 61, No. 5, p. 655, 1971.
5. Schack, R. V. and Platt, B. C., "Production and Use of a Lenticular Hartmann Screen," *Journal of the Optical Society of America*, Vol. 61, No. 5, p. 656, 1971.



a) Tilt Error versus Focal Length

b) Tilt Error versus Number of Lenslets

c) Wavefront Error versus Number of Lenslets

Figure 6. Design optimization is based on predicted performance evaluated over the free parameter space -- in this case f-number and microlens density.

REALIZATION OF MULTILAYER DIFFRACTIVE COMPONENTS
-
EXPERIMENTAL METHODS OF CHARACTERIZATION

H. GIOVANNINI, H. AKHOUAYRI and C. AMRA
Laboratoire d'Optique des Surfaces et des Couches Minces URA 1120 CNRS
Ecole Nationale Supérieure de Physique de Marseille
13397 Marseille cedex 20 - France
Tel: (33) 91-28-83-28 Fax: (33) 91-28-80-67

1) INTRODUCTION

It has been shown that multilayer coatings permit to modify the optical properties of diffraction gratings[1], which increases the fields of application of gratings, especially in micro-optics domain. For example, the efficiency of a grating for s or p polarization can be varied by depositing an optical coating on the diffracting surface[2]. Several techniques can be used to realize such components. One can mention the evaporation techniques (Electron Beam Deposition, Ion Assisted Deposition, Ion Plating) already used for thin film applications. These techniques have been used in our laboratory to realize various diffractive components. The optical properties (efficiency of diffracted orders and phase difference of the scattered field between s and p polarizations) of such components, have been measured by using two devices: one based on a goniometric ellipsometer[3], the other based on a recently developed grating interferometer[4]. The results obtained with these two techniques have been analyzed and compared to the results given by a numerical simulation based on a rigourous method, and the absorption has been measured by using a photothermal technique[5].

2) CHARACTERISTICS OF BARE GRATINGS BEFORE COATING

Characterization of diffractive components is realized with a device (fig. 1) that has already been used to measure the intensity and the phase of the scattered field in each direction of space[6]. This device is based on an ellipsometric goniometric mounting. It permits to measure the phase difference ϕ_{sp} between s and p polarizations together with the intensity of the light in the plane of incidence[7]. This technique gives the efficiency of different diffracted orders (angle θ is varied thanks to a rotating plate) and the corresponding value of ϕ_{sp}. Incidence angle i can be varied thanks to another rotating plate.

A grating interferometer (fig. 2) can also be used to measure the phase difference between s and p polarizations by a two-wave interferometric technique[8], when G_1 and G_2 are in Littrow

mounts for the diffracted orders m and n respectively. The change of polarization is obtained with the help of a nematic liquid-crystal retarder. The gratings can be rotated around a verical axis to study different diffraction orders for a Littrow mounting.

These two techniques of characterization are compatible with the use of different wavelengths.

The measured optical properties of gratings can be used to solve the inverse problem[9] and to determine the physical parameters (spacing, substrate complex index). A theoretical method based on differential formalism[10] has been used to recover these parameters.

3) CHARACTERISTICS OF COATED GRATINGS

The numerical simulation has also been used to determine *a priori* the characteristics (thicknesses, complex refractive indices) of the thin film layers to be deposited, in order to obtain diffractive components with specific optical properties. For example, the grating efficiency in one order and the phase change after diffraction between s and p polarizations, can be varied by coating the grating[11]. The first result is of particular interest for adressing applications, while the second one can find applications in the field of fiber optic sensors[4].

In case of multilayer coated gratings, the numerical simulation of the grating behaviour must take into account all the free space and guided mode diffracted orders.

In our laboratory several deposition techniques (Electron Beam Evaporation, Ion Assisted Deposition and Ion Plating) are available; they give very hard and dense materials independent of humidity, temperature,... Monitoring of all deposited optical thicknesses is quasi-perfect with the help of a spectral monitoring system.

The measured optical properties of the realized diffractive components have been compared to those given by theory. In particular, this allowed us to compute and to measure the phase difference of the diffracted field between s and p polarizations for dielectric-coated gratings and for bare metallic gratings near the plasmon resonances. However, for deep coatings and for thick multilayers, numerical simulation still remains a problem.

4) MICRO-OPTICS

In order to realize bi-dimensional diffractive components, it is first possible to deposit multilayer coatings through grids, on a plane substrate. In this case, superpolished glass substrates can be used to realize diffractive components with very low scattering losses (down to 10^{-5}). This technique, which is easy to setup, is compatible with the use of other types of substrates, like crystals, polymers, sol-gels,... Various optical components have been realized in our laboratory and tested with the methods described in the previous sections. The bi-dimensional pattern can be also obtained by ion-etching technique. This method permits to obtain gratings with low spacing (typically 1 μm).

These components appear to be an alternative solution to realize anti-reflection filters, or to replace arrays of micro-lenses. However, to determine the physical parameters of the diffractive components for specific applications, some theoretical problems (computation in case of thick layers, simulation of bi-dimensional gratings) have to be solved.

5) PHOTOTHERMAL MEASUREMENTS OF GRATINGS' ABSORPTION

Absorption is one of the most important characteristics of gratings for high power laser applications. Photothermal deflection[12] of a laser probe beam, when the grating is illuminated by an intensity modulated pump beam, permits to measure the grating absorption. This technique has been used to test diffractive components realized in our laboratory.

6) CONCLUSION

Techniques of deposition used in the field of thin films can be adapted to realize coated diffraction gratings. In this case, diffractive components with specific optical properties can be obtained. The same techniques can be adapted to realize bi-dimensional diffraction gratings for micro-optics applications. In all these cases, the techniques of characterization based on ellipsometry, on two beam interferometry and on photothermal deflection can be used to determine the optical performances of the components. However, design of components is limited, for the moment, by the performances of numerical methods.

REFERENCES

[1] R. Petit, M. Cadilhac, D. Maystre, P. Vincent and M. Nevière, *in Electromagnetic theory of gratings*, R. Petit ed., vol 22 of Topics in Current Physics (Springer-Verlag, Berlin, 1990), pp 1-225.

[2] M. G. Moharam and T. K. Gaylord, J. Opt. Soc. Am. A **3**, 1780 (1986).

[3] C. Deumié, H. Giovannini, G. Albrand, H. Akhouayri and C. Amra, "Ellipsometry of light scattering from thin films multilayers", Int. Conf. on Optical Interference Coatings, Tucson, pp 255-256 (1995).

[4] H. Giovannini, D. Yeddou, S. Huard, M. Lequime, C. Froehly, Opt. Lett., **18**, 2074 (1993).

[5] M. Commandré and P. Roche, "Charcterization of optical coatings by photothermal deflection", Int. Conf. on Optical Interference Coatings, Tucson, pp 207-209 (1995).

[6] C. Amra, D. Torricini and P. Roche, Appl. Opt. **32**, 5462 (1993).

[7] C. Deumié, H. Giovannini and C. Amra, to be published in Appl. Opt.

[8] H. Giovannini and H. Akhouayri, Opt. Lett., **20**, 2255 (1995).

[9] A. Roger, Opt. Comm., **32**, 11 (1980).

[10] P. Vincent in [1] pp 101-121.

[11] M. Nevière in [1], pp 123-157.

[12] M. Commandré and E. Pelletier, Appl. Opt., **29**, 4276 (1990).

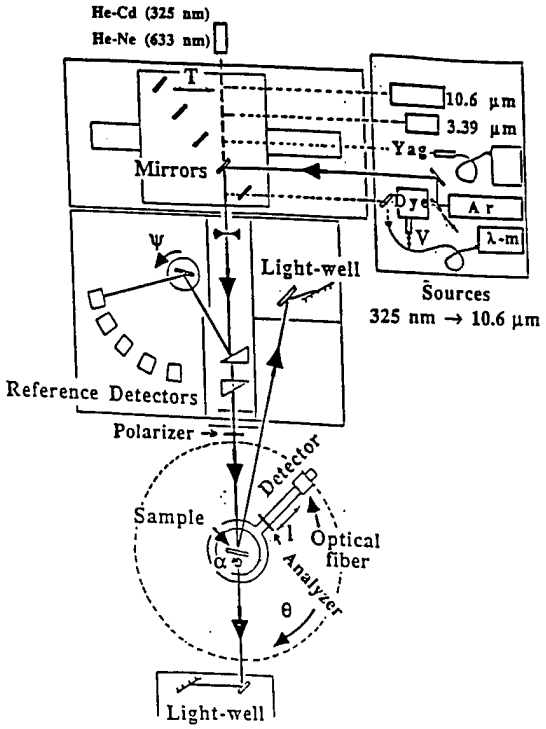


FIGURE 1: Ellipsometric goniometric mounting

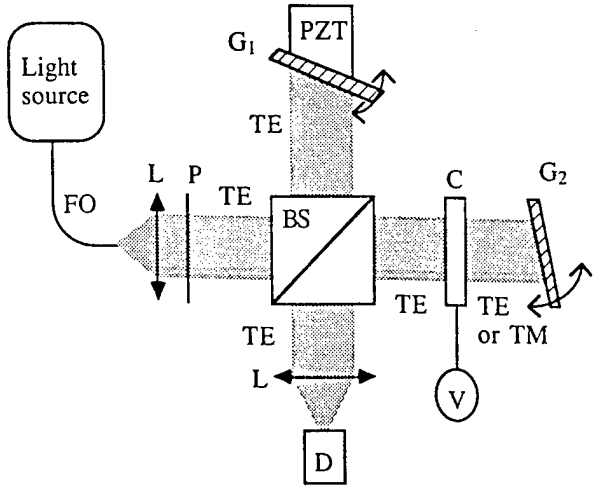


FIGURE 2: Grating interferometer. The length of one arm is modulated thanks to piezoelectric transducer PZT. G_1 ang G_2 can be rotated around a verical axis. BS: beamsplitter cube, FO: fiber-optic, D: photodiode, P: polarizer,
C: nematic liquid-crystal cell.

Experimental studies of Talbot array illuminators

Thomas J. Suleski and Donald C. O'Shea
School of Physics and
Center for Optical Science and Engineering
Georgia Institute of Technology
Atlanta, GA 30332-0430
Tel:404-894-3992 Fax:404-894-9958

Introduction

An experimental study of Talbot array illuminators (TAIs) has been performed. These devices, first proposed and implemented by Lohmann,[1] are binary phase gratings that, when properly illuminated, give rise to periodic, concentrated areas of light with uniform intensities through Fresnel diffraction. This phenomenon is generally referred to (somewhat misleadingly) as Talbot self-imaging.

The relative ease with which these devices can be fabricated and their high efficiency make them excellent choices for optical systems requiring beam fanouts. However, the vast majority of work performed on TAIs to date has been theoretical in nature. Experimental work has largely been restricted to proof-of-principle studies in which photographs have been taken of the intensity distributions in Talbot planes of the devices. Further work is needed to verify the predictions of current models and to suggest new uses for these devices. We have performed detailed experimental measurements of the output of TAIs. Additional theoretical results are also presented in support of the experimental work.

Background

The Talbot distance from a periodic structure is defined as $Z_T = 2d^2/\lambda$, where d is the grating period and λ is the wavelength of the illuminating radiation. Under coherent, plane-wave illumination, amplitude gratings form field distributions at integer multiples of the Talbot distance that replicate the amplitude and phase of the field directly behind the grating itself; thus the phrase "self-imaging." Multiple images are formed at certain rational fractions of the Talbot distance.[2] These gratings are easily understood, but inefficient.

The promise of higher efficiency makes the use of phase gratings desirable for Talbot imaging. However, patterns in the Talbot planes of binary phase gratings are generally more complex than those for amplitude gratings. The degrees of freedom affecting the diffraction patterns are the opening ratio w, the phase step ϕ, and propagation distance z. Several combinations of these parameters do give rise to 100% modulated intensity distributions that match the spatial structure of the phase grating.[3] These distributions are virtually 100% efficient for large arrays.

When modeling and designing Talbot array illuminators, researchers have generally required that the Talbot intensity distributions be 100% modulated and that the distributions be located at simple, rational fractions of the Talbot distance. These limitations have allowed useful diffraction patterns to go undiscovered. It would take a great deal of computer time to simulate all of the possible Fresnel patterns over any significant distance for TAIs. Experimentally, the propagation distance can be varied continuously and the diffraction patterns observed in real time.

Experimental Setup

An experimental system has been constructed for precision measurement of Fresnel diffraction patterns from amplitude and phase gratings. Illumination is provided by a spatially filtered, expanded, collimated beam from a helium-neon laser at 632.8 nm. An optical rail is used to hold a carrier that can be translated along the optic axis of the system. The carrier is used to hold either (a) a solid-state CCD camera or (b) the detector head of a laser beam profiling system. The camera allows visual measurement of the intensity patterns. The beam profiler, typically used for characterization of Gaussian laser beams, allows precision measurement of the diffraction patterns with a rotating 5 micron slit. Patterns measured with the CCD camera are analyzed using Image Analyst™ image processing software. Data obtained from the beam profiler is exported as an ASCII text file and imported into MATLAB™ for analysis. A sample intensity distribution is shown in Fig. 1.

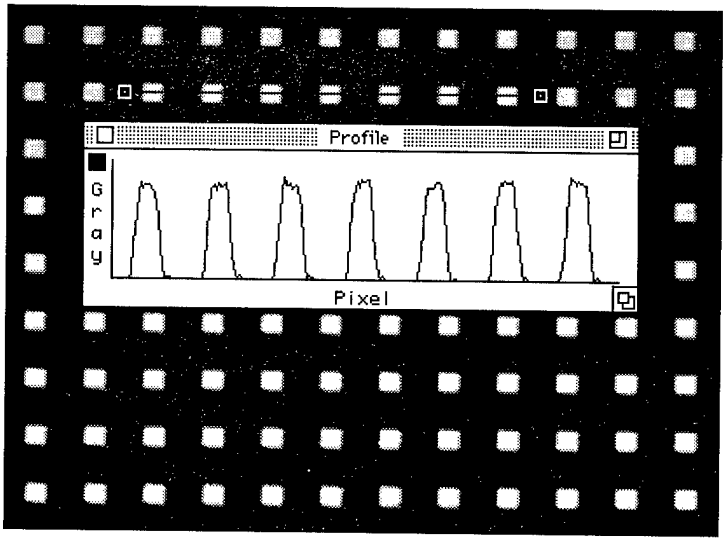


Fig. 1: CCD image of a Fresnel diffraction pattern. The image was formed in the 1/3 Talbot plane from 2 orthogonally crossed 1-D binary phase gratings, each with an opening ratio of 1/3 and phase step of $2\pi/3$. The grating and image periods are 400 μm.

Results

Experimental measurements of Fresnel diffraction patterns from Talbot array illuminators have shown intensity distributions that can be more useful than those in "standard" Talbot planes. For example, a one-dimensional TAI with an opening ratio of 1/3 and a phase step of $2\pi/3$ creates a 100% modulated intensity pattern with the same opening ratio in the 1/3 Talbot plane, as shown in Fig. 2a. The peak intensity of the one-dimensional pattern is increased threefold over the illuminating intensity. Taking two of these 1-D gratings and orienting them at 90 degrees gives a 2-D array of square peaks in the same plane with 9 times the original intensity (shown in Fig. 1). Increasing the propagation distance slightly to 0.355 Z_T results in the distribution shown in Fig. 2b. The peak intensity in this plane for the 1-D case is approximately 70% higher than the peak in the 1/3 Talbot plane. The corresponding 2-D pattern has a peak height more than 26 times higher than the illuminating intensity.

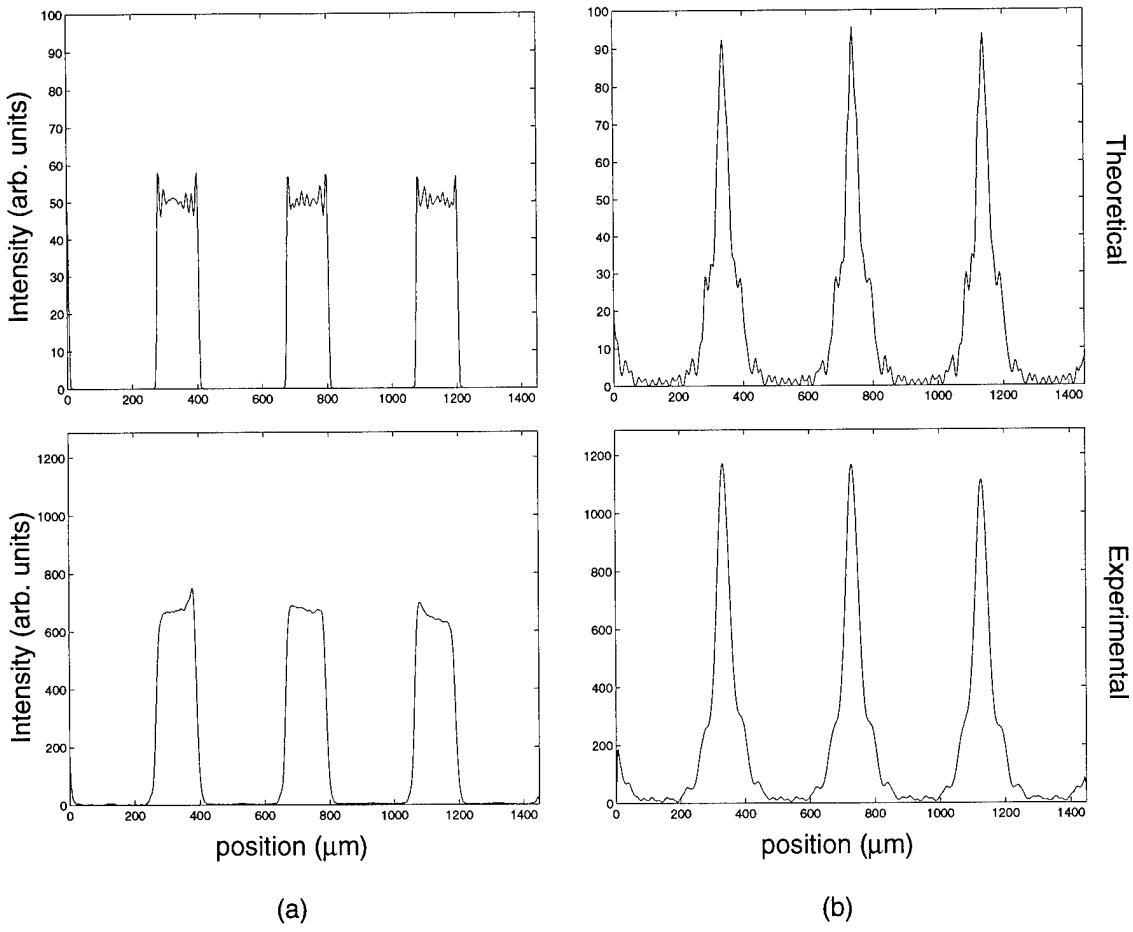
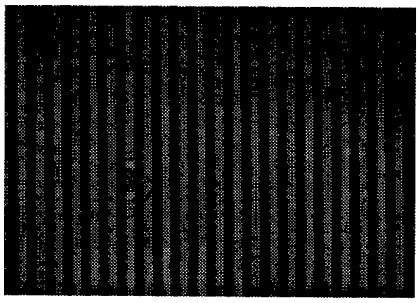
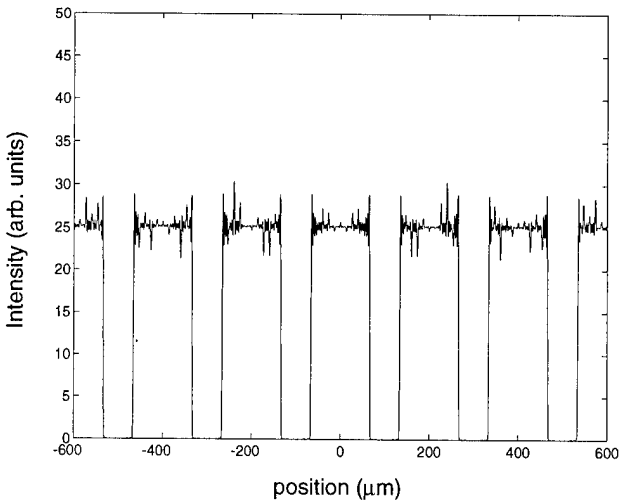


Fig. 2: Theoretical and experimental intensity profiles from a 1-D binary phase grating with an opening ratio of 1/3 and phase step of $2\pi/3$ at two different distances from the grating. (a) $z = 0.333\ Z_T$, (b) $z = 0.355\ Z_T$.

Other patterns have been discovered that, while not 100% modulated, may still be of use for applications requiring a minimum threshold intensity before physical effects occur, such as in photolithography and photoablation. We also present evidence for the first time (to the best of our knowledge) of 100% modulated Talbot image doubling from a binary phase grating, as shown in Fig. 3. The spatial frequency of the image is double that of the grating that created it. Theoretical models confirm this finding.



(a)



(b)

Fig. 3: (a) CCD image of a Fresnel diffraction pattern. The image was formed in the 1/12 Talbot plane from a 1-D binary phase grating with an opening ratio of 1/3 and phase step of $2\pi/3$. The spatial frequency of this pattern is twice that of the grating that created it. (b) Theoretical intensity distribution for the same grating and location (the original grating period was 400 μm).

References

[1]A.W. Lohmann, "An array illuminator based on the Talbot-effect," Optik **79**, 41-45 (1988).

[2]J.R. Leger and G.J. Swanson, "Efficient array illuminator using binary-optics phase plates at fractional-Talbot planes," Opt. Lett. **15**, 288-290 (1990).

[3]V. Arrizón and J. Ojeda-Castañeda, "Talbot array illuminators with binary phase gratings," Opt. Lett. **18**, 1-3 (1993).

Submicron gratings with dielectric overcoat: performance and stability

C. Heine R. H. Morf and M. T. Gale

Paul Scherrer Institute
Badenerstrasse 569, CH-8048 Zürich, Switzerland
Tel. +41 1 492 63 50 Fax +41 1 491 00 07

1. Introduction

Submicron gratings show increasing potential in applied optics, often presenting attractive alternatives to thin film technology solutions. Gratings on light-weight plastic materials can replace heavy and expensive glass devices. Embossing techniques can be used for cheap mass production. The coating of gratings with thin films leads to additional degrees of freedom for component design. For practical applications, it is important not only to investigate the possibilities of such structures, but also the limiting factors such as fabrication considerations and stability properties.

In the first part of this paper we discuss stability aspects of surface-relief submicron grating structure overcoated with a thin dielectric film. Measurements on a broadband antireflection structure are presented. We also give an interpretation of the results of our measurements. The second part describes an experiment which shows that the symmetry of the grating can strongly be influenced using directional evaporation. In the third part we propose a new kind of polarizer and discuss fabrication possibilities.

High frequency surface-relief gratings can exhibit broadband antireflection characteristics. This has been investigated over several years in theoretical [1] as well as experimental [2,3] work. Recently, we reported on the realization of a broadband antireflection (BAR) structure for solar energy applications [4,5]. It consists of a lamellar surface grating in a polycarbonate (PC) substrate with a dielectric thin film overcoat. Coating the grating structure with a thin MgF_2 layer is one essential step to achieve the excellent broadband antireflection performance shown by these devices. A practical problem is that for evaporating MgF_2, the best coating results are obtained when the substrate temperature is relatively high, ~200°C [6]. At this temperature PC starts to flow and the gratings disappear due to surface forces. The dielectric has therefore to be deposited on the cold PC substrate and the mechanical properties have to be investigated.

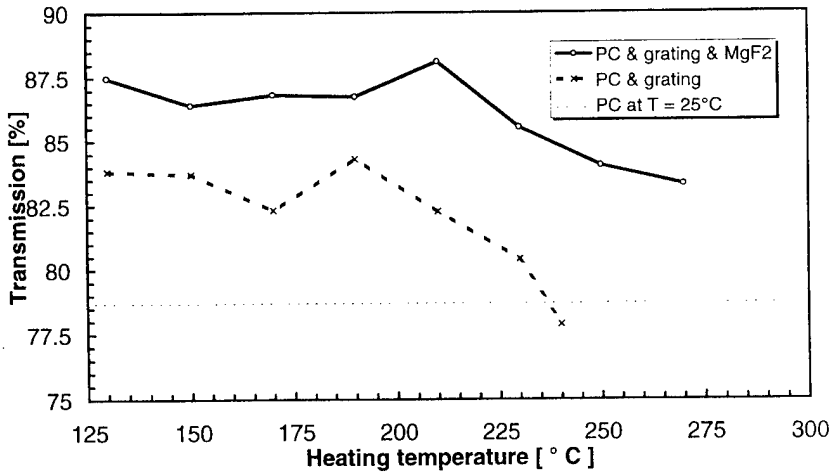


Fig. 1: Measured transmission of bare and MgF_2 coated gratings after heating. The angle of incidence was 45° and the measurement wavelength 800 nm. Coated gratings not only have better antireflection performance but are also stable up to higher temperatures.

2. Stability of thin film coated gratings

a) Temperature:

We have investigated the stability of bare surface gratings and the BAR structures as a function of temperature. Only the front side of the devices was structured. The transmission performance was measured before and after tempering them for several minutes on a hot plate, with a small distance between hot plate and PC-foil in order to avoid separation problems. The temperatures given correspond to the temperatures at the hot plate.

Figure 1 shows the measured transmission of E-polarized light (E-vector perpendicular to grating vector) for an angle of incidence of 45°. The transmission of the device with the bare grating starts to decrease at temperatures higher than 190°C (measured on the hot plate). This coincides with a disappearance of the grating as visible to the naked eye. The MgF_2 coated structure not only shows better transmission, but also withstands significantly higher temperatures. The coating appears to stabilize the grating which, in contrast to a bare grating, does not disappear. At higher temperatures, parts of the polycarbonate started to become dull.

b)Adhesion:

The evaporation of MgF_2 was performed on the cold substrate. In order to test adhesion on the surface, we used the tape test, applying a strip of adhesive tape to the surface and removing it again [5]. Figure 2 shows the measured transmission for E-polarized light at normal incidence. Shown is the transmission as a function of wavelength for coated, structured PC-foils (continuous line and dots) and coated unstructured PC-foils (cross symbols). Measurements were performed before applying the tape test and afterwards. For the unstructured but MgF_2 overcoated PC-foil, we see that the transmission is the same as for the uncoated PC-foil (broken line) - the MgF_2 coating was completely lifted off. For the structured PC foils, the tape test had no significant effect on the transmission performance. This can be explained by the roughness of the surface on a scale which does not give rise to straylight, but helps to improve MgF_2-PC adhesion. In addition, the structure may relax the intrinsic tensions at the boundary of the two materials and thus lead to higher stability.

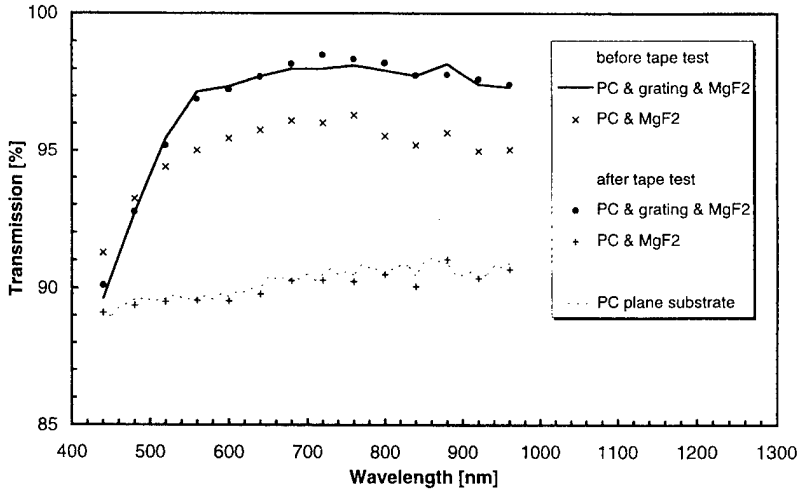


Fig. 2: Transmission of coated substrates before and after tape test. The measurements show that MgF_2 deposited on cold unstructured substrates is lifted off the surface when a tape test is applied, leading to a significant reduction in transmission. By contrast, the test applied on coated gratings did not have an effect on the transmission performance. The MgF_2-films adheres well to the structured substrate.

c) Conclusion: The experiments show that:

- a grating in PC is (temperature) stabilized by a thin film coating of MgF_2.
- MgF_2 shows better adhesion to the substrate if the latter is structured.

This can be important for applications in optics in two very different ways. The first point opens the possibility to apply antireflection structures onto substrates by hot transfer ("melting"), including application onto curved substrates such as lenses. We have 'melted' thick PC-foils (up to now without BAR-structure) on BK7 glass and were not able to separate them without damaging the glass surface. The second point opens the possibility to coat substrates which may not be heated. Provided there is possibility to etch a submicron grating structure into this substrate, thin films evaporated onto the cold substrate cab be expected to exhibit good adhesion.

The BAR-structures are intended to be used outdoors for solar energy applications. Handling the tempered devices gave us the impression that the MgF_2 coating stability is increased after tempering them up to 210°C. This can be due to a better contact between substrate and coating as it is the case when MgF_2 is deposited on hot substrates. The tempered structures are also less sensitive to finger prints. An exposure of the structures to extreme weather conditions over several months will give insight in medium range lifetime properties.

3. Non-symmetric gratings:

Light coupling and light trapping are two other interesting applications for submicron gratings. Depending on the application, it is favorable to use non-symmetric- rather than symmetric gratings. Light which couples into diffraction orders will be totally reflected at the surface opposite to the structure and impinge again on the grating. According to the reciprocity theorem, part of the light will couple to an outgoing zero order wave. This effect limits the coupling efficiency. The effect can be reduced with a nonsymmetric grating geometry such as blazed gratings. Light trapping in solar cells was improved by use of such structures [4]. A nonsymmetric grating (see inset of Figure 3)can be realized by means of directional evaporation of a dielectric at an angle not perpendicular to the grating surface. Using rigorous calculations, we found grating geometries having a high ratio of the first transmission orders (T_{+1}/T_{-1}).

In order to demonstrate this effect, we coated the PC-gratings in such a way on both the front and the backside of the PC-foil (see Figure [3] inset). The transmission measurements were performed with light incident at an angle of 45° (plane of incidence parallel to the grating vector). The second measurement was taken after turning the grating by 180° around an axis normal to the surface. This introduces no difference for a symmetric grating. By contrast, we measured a strong coupling effect not found in the first measurement (see Figure 3). This can only be explained by the introduced asymmetry of the coating.

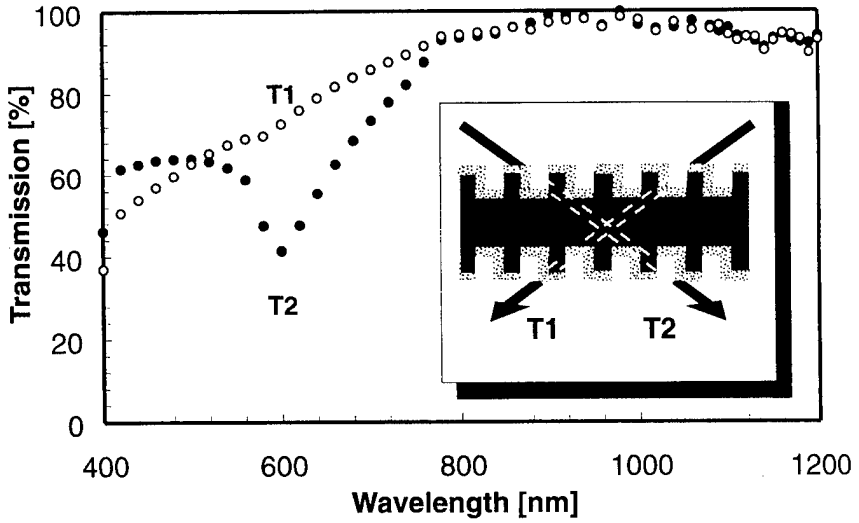


Fig. 3: Transmission spectrum for asymmetric grating structure. T1 and T2 are the measured spectra for off-axis illumination upon rotating the grating by 180°.

4. Other types of thin film coated gratings:

The use of high frequency gratings is a well known approach to realize polarizing components. We propose a dielectric polarizer based on submicron gratings and materials commonly used in thin film technology. It consists of a TiO_2 grating on a SiO_2 substrate, overcoated with MgF_2 (Figure 4, inset). The outer MgF_2/air grating will act as antireflection grating for the H-polarization and improve the polarizer's performance. It is surprising to find that the polarizing performance is excellent for a wavelength at which the first order of transmission is already evanescent and the first order of reflection just starts to be non-propagating. Therefore, moderate grating periods have to be used, which can be realized by holographic techniques. It is clear that in this region, rigorous diffraction theory has to be used to calculate the efficiencies. Figure 4 shows the transmission for the H-polarization (H-vector perpendicular to grating vector) as well as the inverse polarization contrast ratio (inverse PCR) which is the ratio of the transmitted energy of H- and E-polarization. The calculations were performed with the method described in Ref. [7]. Note that solely the grating period, which can be realized very accurately, determines the wavelength of optimum polarization performance.

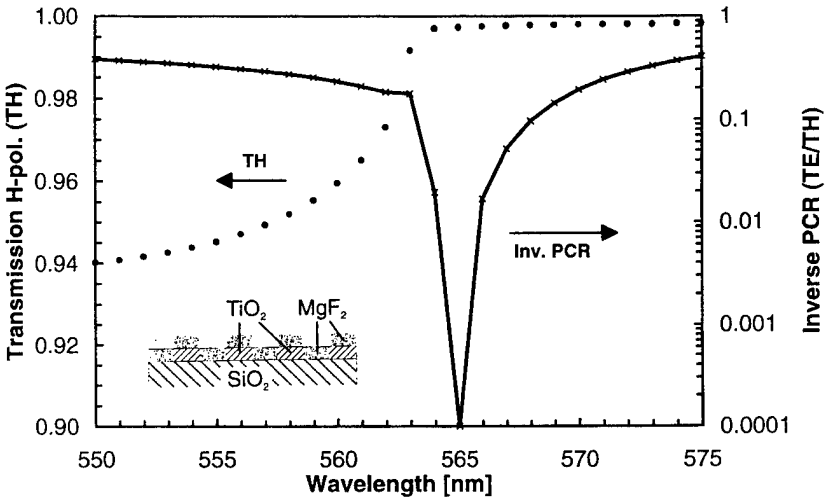


Fig 4: With usual thin film materials and the appropriate grating period an excellent polarizer can be realized, as rigorous calculations show.

5. Conclusions

Thin dielectric films on submicron gratings present a simple and effective possibility to manipulate their optical properties such as reflectivity, polarization selectivity or symmetry of coupling to diffraction orders. Our tests on BAR-structures showed that mechanical properties of microstructures on polycarbonate can be significantly improved by the additional thin film coating. Similarly, adhesion of coating materials to the substrate can be improved by structuring the substrate.

References

[1] E. B. Grann, M. G. Moharam, and D.A. Pommet, "Optimal design for antireflection tapered two-dimensional subwavelength grating structures", *J. Opt. Soc. Am. A.* **12,** 333-339, (1995).

[2] S.J. Wilson and M.C. Hutley, "The optical properties of 'moth eye' antireflection surfaces", *Opt. Act.*. **29,** 993-1009, (1982).

[3] R. C. Enger and S. K. Case, "High-frequency holographic transmission gratings in photoresist", *J. Opt. Soc. Am.* **73,** 1113-1118, (1983).

[4] C. Heine and R.H. Morf, "Submicrometer gratings for solar energy applications", *Appl. Opt.* **34,** 2476-2482, (1995).

[5] C. Heine, R.H. Morf, and M.T. Gale, "Coated submicron gratings for broadband antireflection in solar energy applications", *submitted to J. Mod. Opt in October1995.*

[6] H.A. Macleod, "Thin-Film optical Filters", 2nd ed., p 390 *(Macmillan, New York, 1986).*

[7] R. H. Morf, "Exponentially convergent and numerically efficient solution of Maxwell's equations for lamellar gratings", *J. Opt. Soc. Am. A.* **12,** 1043-1056, (1995).

Fabrication

DWD 3:30 pm-5:00 pm
Gardner A&B

Michael Feldman, *Presider*
Digital Optics Corporation

Rapid Fabrication of Diffractive Micro-Lenses Using Excimer Laser Ablation

Xiaomei Wang

Cynosure Inc., 35 Wiggins Ave., Bedford, MA 02170
Tel. (617) 275-5007 Fax: (617) 275-5449

James R. Leger

Department of Electrical Engineering, University of Minnesota
4-174 EE/CSi Building, 200 Union St. S.E., Minneapolis, MN 55455
Tel. (612) 625-0838, Fax (612) 625-4583

Robert H. Rediker

Cynosure Inc., 35 Wiggins Ave., Bedford, MA 02170
Tel. (617) 275-5007 Fax: (617) 275-5449

Introduction

Diffractive optical elements (DOEs) provide solutions for applications that require complex phase profiles which are difficult or impossible to make with conventional optics. Because of their planar nature, they have small volume and are light-weight, both of which are attractive features for many applications. Diffractive optical elements are typically fabricated by multi-mask-level photoresist patterning and sequential reactive-ion etching to form the multi-level phase profile[1,2]. Other fabrication techniques include direct E-beam writing, direct laser writing, single-point ablation by excimer laser[3], and thin film deposition. Here we describe a new technique for rapid fabrication of diffractive optic elements and arrays using deep-UV excimer laser ablation. We have fabricated 8-level diffractive micro-lenses which have diffraction-limited focusing and near-theoretical diffraction efficiency. This technique provides a flexible means for rapid prototyping and for applications where other techniques cannot be applied or are not cost-effective.

Fabrication Technique

The original goal of this experiment was to fabricate a uniquely prescribed array of micro-lenses in real-time for diode laser array beam correction. The fabrication technique employs the direct ablation of the substrate material by a high-power pulsed UV laser. To generate binary phase structures on the substrate, a mask with the required intensity-modulated patterns is imaged on the substrate with a UV objective. A binary structure is created by single- or multiple-pulse ablation by the UV laser. To generate multi-level diffractive elements, for example a 2^M-level phase structure, a set of M masks is used, as in the standard lithography technique. The significant advantage of this technique is that the complex and time-consuming process of photoresist deposition, lithography, and etching employed in the standard lithography technique is simply replaced by rapid ablations on a time scale of seconds. This capability allows us to fabricate in real-time an arbitrary arrangement of different DOEs from a pre-determined collection of suitable masks. For example, an array of micro-lenses with each lens uniquely prescribed can be fabricated for laser array beam correction. This technique provides a

flexible new way for rapid prototyping. It is a simpler and faster process compared to single-point etching with laser or E-beam because it is a parallel process.

Figure 1 shows a schematic of the laser ablation system. We used the 193 nm deep-UV output from a Lambda-Physik COMPex 205 excimer laser. This wavelength not only provides the best optical resolution, but also generates micro structures that are sharper and smoother than those fabricated with longer wavelengths at 248 nm and 308 nm. A uniform intensity light field is produced at the mask plane by a homogenizer. The mask set, printed on a single quartz substrate by E-beam writing, contains a set of masks for 21 different focal length lenses. Based on the prescription for each lens, a given mask from the mask set is positioned in the beam path rapidly by a high-speed air-bearing stage. The in-position mask is imaged onto the polyimide sample by an objective. A 10x objective is used for de-magnification. As each lens prescribed from the 21 choices is to be fabricated to form an array, the polyimide sample is stepped accordingly. The system is designed to fabricate an 8-level lens in a few seconds and an array of 100 lenses in a few minutes.

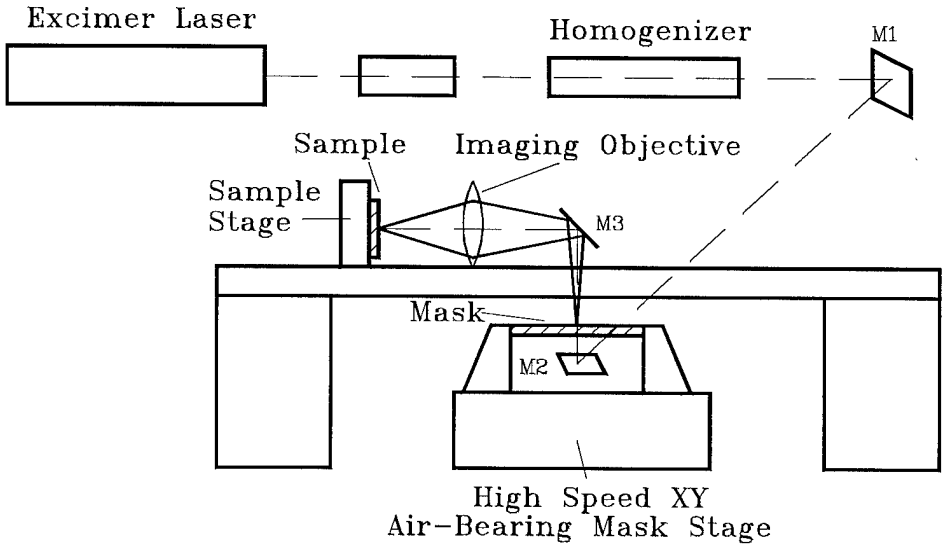


Figure 1. Schematic of the excimer laser ablation system.

The fabrication quality is influenced by laser wavelength, laser beam uniformity and stability, substrate material, and very importantly, the mask alignment accuracy and imaging objective quality. The mask-stage positioning accuracy is 2.3 μm for full 4-inch travel. Thus the pattern alignment on the substrate is 0.23 μm or less with 10x de-magnification. The height of the binary structure, determined by the design wavelength, is influenced by the ablation laser wavelength, the fluence at the substrate, the type of the substrate material, and the number of pulses applied. The general behavior of the ablation depth as a function of the laser fluence at 193 nm has been studied previously for several types of polymers[4]. We have measured this function specifically for the polyimide samples we used. The optimum unit step height is d_8=180 nm for refractive index of 1.56 and the design wavelength λ_0 = 805 nm. The fluence is adjusted such that the ablation depth from a single pulse corresponds to 180 nm. Four pulses are applied with the level 1 mask, two pulses applied with the level 2 mask, and 1 pulse applied with level 3 mask.

Lens Quality

An example of 8-level diffractive lenses is shown in Fig. 2 — a photomicrograph of a f/4.5 positive lens with diameter of 440 μm. Each of the eight levels as well as the Fresnel zone boundaries can be distinctly observed. The smallest feature resolvable in this element is 1 μm.

The diffraction efficiency of this lens is 92% ± 3%. It is measured by the following method using a laser diode source with output at 803 nm (SDL-5400). The beam is formed with a focusing lens and has a matching F/number to that of the lens to be tested. The lens under test then collimates the beam. A detector is placed in the far-field to detect the power in the collimated beam. The contributions from other orders to the power measurement are negligible. The diffraction efficiency is the power in the collimated beam in the far-field, divided by the power measured in the near-field without the lens under test but with only the polyimide flat substrate. The measured diffraction efficiency for the pictured lens is 92%. Within the

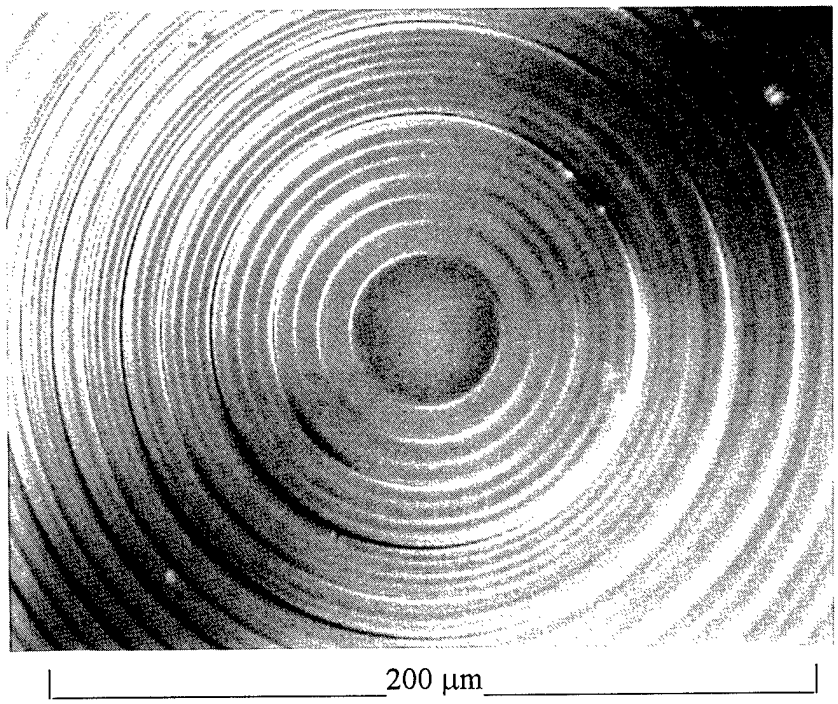


Figure 2. A microscope picture of an 8-level f/4.5 diffractive lens fabricated with 193 nm excimer laser in polyimide. Its diffraction efficiency is 92%.

experimental errors, efficiencies measured for several other similar lenses are the same. This efficiency is very close to the theoretical value of 95% predicted by the scalar theory. It should be noted that although scalar theory works reasonably well for lenses with F/number of 4.5, it still gives an efficiency number larger than that obtained from the rigorous electromagnetic theory[3]. The diffraction efficiency was also measured using an input beam of much larger F/number (lower N.A.) for different lens-offsets. The results are plotted in Figure 3.

To further test the performance of the fabricated diffractive lenses, we measured the point-spread-functions for these lenses, and compared with theoretical scalar diffraction calculations. In the experiment, the diffractive lens under test is illuminated with a collimated

uniform laser beam. The 2-D intensity profile at the focus is measured using a CCD sensor equipped with an objective that images the laser beam profile onto the CCD sensor with 10x magnification. The measured intensity distribution in one axis is compared with that of calculations in Figure 4. The two theoretical curves are the calculated intensity with (solid line) and without (dotted line) the convolution effect of the imaging optics and the detector resolution included. Comparison shows that the diffractive lenses fabricated with the technique described here have diffraction-limited performance. Point-spread-functions for different input beam diameters were also measured. Comparison with theoretical calculations for these cases will be discussed.

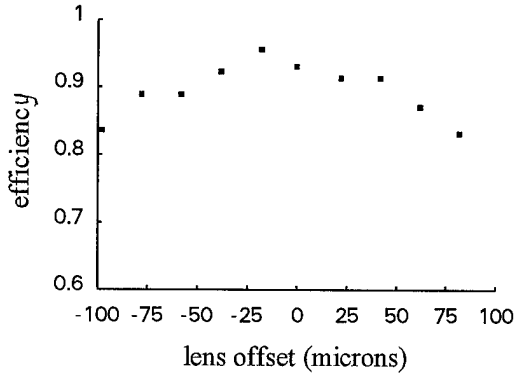


Figure 3. Measured diffraction efficiency for different lens offset positions.

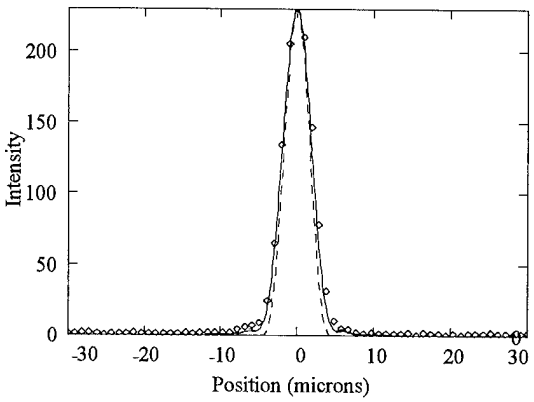


Figure 4. Comparison of measured (diamond symbols) and calculated (solid and dotted lines) intensity distributions in x-direction at the focus. The solid line is the calculations with convolution and the dotted line is the calculation without convolution.

In this talk, we will also present results for diffractive micro-lenses with smaller F/numbers and results for arrays which have either identical lenses or pre-prescribed unique lenses. We will discuss the system performance including the fabrication time and resolution.

The authors thank E. Motamedi and H. Sankur of Rockwell International for providing the polyimide samples, and thank X. Liu and F. Durville for helpful discussions. This work was supported by the Department of Commerce under the Advanced Technology Program.

References

[1]M. E. Motamedi, W. H. Southwell, R. J. Anderson, W. J. Gunning, and M. Holtz, "High speed binary microlens in GaAs," *Proc. SPIE,* **1544**, 33-44 (1991).

[2]Margaret B. Stern and Theresa R. Jay, "Dry etching for coherent refractive microlens arrays," *Optical Engineering,* **33**, 3547-3551, (1994).

[3]M. T. Duignan, "Micromachining of diffractive optics with excimer lasers," *1994 Technical Digest Series,* **11**, Diffractive Optics Topical Meeting, Rochester, NY, (June 6-9, 1994).

[4]R. C. Crefer and P. J. Oakley, "Laser processing in manufacturing," page 196.

Excimer laser micromachining for rapid fabrication of binary and blazed diffractive optical elements

Michael T. Duignan and Gregory P. Behrmann

Potomac Photonics, Inc., 4445 Nicole Drive, Lanham, MD 20706
Phone: (301) 459-3031 Fax: (301) 459-3034
e-mail: 76217.1357@compuserve.com

Introduction

For all their power and promise, diffractive optical elements (DOEs) are generally so difficult to fabricate and so costly to prototype that their full commercial potential has yet to be realized. Although microfabrication techniques that stem from VLSI semiconductor processes are well-developed, they usually require mass production to be economically feasible.[1] Even when unit cost is not a primary consideration, the time period from design to realization of even the simplest custom DOEs can frequently run to weeks or even months. We show that we are able to produce practical diffractive elements in minutes to hours. A user has the ability to design, fabricate, gauge, and refine the diffractive structure at a single workstation. We have constructed a wide spectrum of DOEs, including spherical lenses, aspheres, toroids, as well as cylindrical and conical lenses—each in a fraction of the time required using more conventional microfabrication techniques.

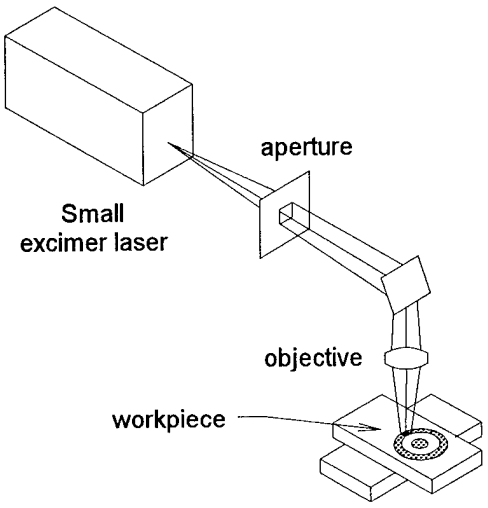


Fig. 1. Direct-write microfabrication of diffractive optical structures.

In general, our approach[2] is to use a small, high repetition-rate pulsed excimer laser operating at 248 nm to ablate the grating into the substrate material. As illustrated in Figure 1, the laser beam remains fixed while precision X-Y or X-θ servo-driven stages move the workpiece under the focusing objective. An appropriate cutting "tool" shape and size is chosen and is achieved by projecting a demagnified image of a custom beam aperture (created on this same micromachining workstation) onto the substrate. This simple approach thus avoids the expense and complexity associated with mask generation, maintenance, and alignment. The minimum feature size is determined by the ablation spot size. Approximately 2-4 μm period structures are a practical minimum for the current system.

True 3-dimensional contours are attained by controlling laser fluence (J/cm²/pulse) or the number of laser shots per unit area or both. We have very recently incorporated an optical profilometer (Wyko RST-Plus) directly into our DOE micromachining system. This has greatly enhanced our ability to characterize depth and smoothness and is helping to accelerate the refinement of the process.

π-Phase Diffractive Structures

True binary (2-level or π-phase) diffractive structures are generally the easiest to fabricate by any method. Their chief disadvantage is that at most 40.4% of the incident light is diffracted into the order of choice.[3] However, the relative intensity of the 1st diffracted order at the focus of a π-phase lens may exceed that of all others by many orders of magnitude. Off-axis designs can be used to further reduce scattering from undesired orders.[4] Thus reduced efficiency may not be a significant drawback for many applications, especially when the relative cost benefits are considered.

Figure 2 diagrams our process for rapid fabrication of binary elements. A ~405 nm thick layer of polyimide is spin-coated onto a fused silica window and cured. The polyimide thick-

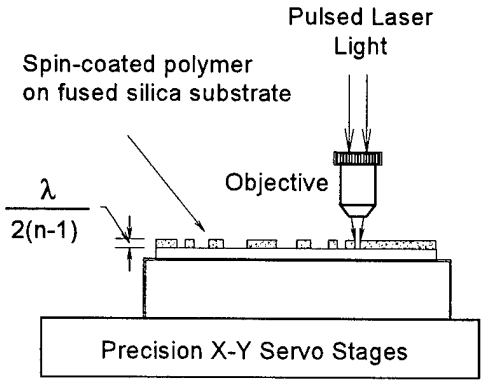


Figure 2. Direct-write fabrication of a binary grating. Diffractive elements are generated by photo-ablative removal of portions of a ~0.4 μm thick polyimide layer on fused silica.

ness is chosen to correspond to a π-phase shift with respect to air for the design wavelength, typically 633 nm for our sample elements. These substrates may be made in bulk and can be stored indefinitely. Polyimide is relatively durable, nonhygroscopic, chemically inert, and is transparent through much of the visible and near-infrared. It absorbs strongly at the 248-nm KrF machine laser wavelength and ablates cleanly but the transparent fused silica below remains undamaged. Therefore, depth accuracy depends primarily on the thickness of the original polymer layer, which can be controlled to ±5%. Incident fluence is of the order of ~1 J/cm². The laser spot size and shape used depends on the feature size required for the cut and the available laser pulse energy. Typically it may range from ~2 μm to >100 μm.

A personal computer based motion control system drives the servo stages over a travel range of 100 mm by 250 mm. The stages are addressable to 0.25 μm and are specified by the manufacturer to be accurate to ±1 μm over the full range of travel. The excimer laser is externally triggered and firing is coordinated with stage motion such that shots can be fired at specified incremental distances, even for arcs or arbitrary curves. The maximum writing speed depends ultimately on the required shot spacing and the maximum laser repetition rate of 2000 Hz. The required shot spacing, in turn, is usually determined by the minimum feature size and therefore the machining laser spot size. Using a spot diameter of ~14 μm, we have written 1 mm × 1 mm DOE's in ~6 minutes. We are currently developing methods for significantly decreasing fabrication time still further. We will report on a simple technique for varying the cutting laser aperture size (Fig. 1) under computer control. This will permit the use of a large laser swath for larger features, *e.g.*, the innermost zones of a Fresnel lens, then decreasing the laser kerf for finer features, resulting in a substantial increase in speed.

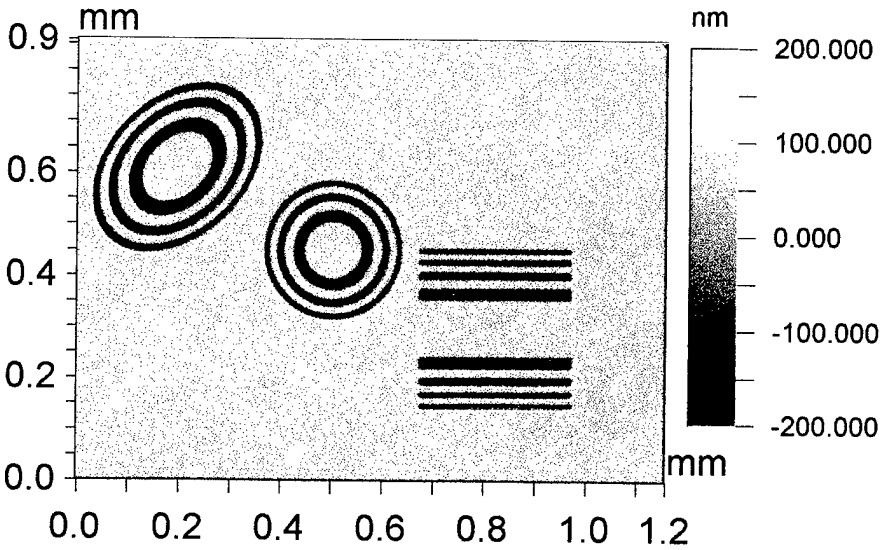


Figure 3. Some simple π-phase diffractive optical elements fabricated by excimer laser micromachining: a toroidal lens with primary focal lengths of 10 and 5 mm (top left); spherical lens, 250 μm diam., f.l.= 5 mm; cylindrical lens, 250 μm square., f.l.=5 mm (bottom right). the step height for each structure is ~400 nm.

Depending on the application, the desired motion program may be generated directly from a CAD program and executed much like a pen plotter. We have written simple Visual Basic™ programs as well as Microsoft Excel™ macros that define the structures, then command the motion and laser firing directly. The sample elements in Fig. 3 were each created in Excel™.

For example, in the case of the toroidal lens, the user enters the overall size of the element, the focal lengths in both major axes, and the angle of rotation (here 45°). The laser machining parameters such as laser kerf and stage velocity may also be adjusted. The program uses these parameters to determine a series of elliptical tool paths that will result in the desired structure. Clicking the "Machine Now" button executes the motion. In minutes a completed and functioning diffractive element is produced. No subsequent processing is required. Typical diffraction efficiency into the m=+1 order is 38-40% of transmitted light.

Blazed or Contoured Structures

Improving the diffraction efficiency beyond the ~40% limit for 2-level structures requires blazing of the grating. The literature documents many examples of precisely fabricated sawtooth-like diffractive structures with demonstrated efficiencies that approach 100%. Production of these elements using traditional lithographic techniques is a complex and costly process requiring multiple exposure and etch cycles. Excimer micromachining of these blazed gratings represents a formidable challenge. Accuracy and precision in the plane of the structure depends mainly on the laser spot size and the quality of motion control. Extending the process to the third dimension, depth, adds new factors, including laser fluence, beam homogeneity or intensity profile, and shot-to-shot reproducibility, as well as spot overlap or "stitching" patterns. Deviation from an ideal depth profile often results in light scattering into undesired orders. Smaller scale surface roughness leads to diffuse scattering. Either implies a loss of diffraction efficiency.

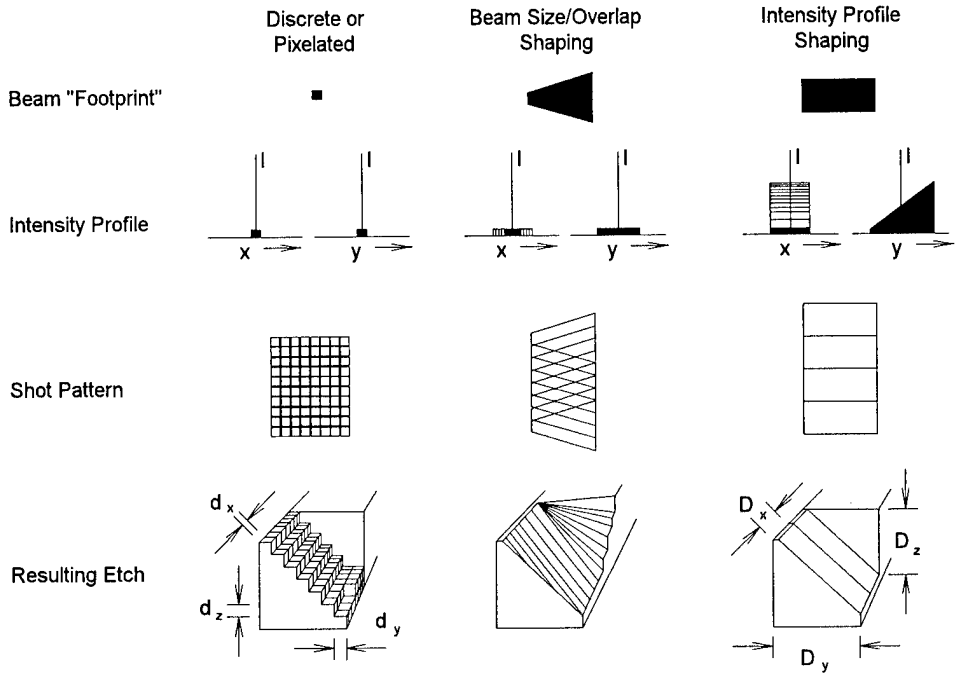


Figure 4. Three approaches to 3-dimensional direct-write ablative micromachining of diffractive structures.

Figure 4 outlines three general approaches to direct-write micromachining of blazed gratings. The first is to simply focus the beam to a size that is small compared to the grating period. The laser intensity is adjusted such that the depth of material removed per shot is small compared to the maximum desired depth. In this way, 3D-pixel-like volume elements can be removed with each laser shot. Control of depth is achieved by varying the beam intensity and number of shots per unit area. Although this method is the most versatile in that arbitrary 3-D surface structures can be fabricated, it has a number of disadvantages. Chief among them is the relatively slow writing speed. The small spot size and low intensity

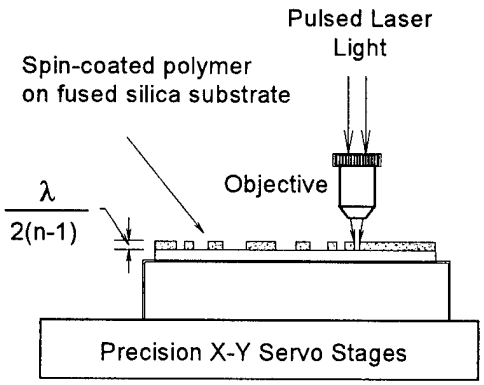


Figure 2. Direct-write fabrication of a binary grating. Diffractive elements are generated by photo-ablative removal of portions of a ~0.4 μm thick polyimide layer on fused silica.

ness is chosen to correspond to a π-phase shift with respect to air for the design wavelength, typically 633 nm for our sample elements. These substrates may be made in bulk and can be stored indefinitely. Polyimide is relatively durable, nonhygroscopic, chemically inert, and is transparent through much of the visible and near-infrared. It absorbs strongly at the 248-nm KrF machine laser wavelength and ablates cleanly but the transparent fused silica below remains undamaged. Therefore, depth accuracy depends primarily on the thickness of the original polymer layer, which can be controlled to ±5%. Incident fluence is of the order of ~1 J/cm². The laser spot size and shape used depends on the feature size required for the cut and the available laser pulse energy. Typically it may range from ~2 μm to >100 μm.

A personal computer based motion control system drives the servo stages over a travel range of 100 mm by 250 mm. The stages are addressable to 0.25 μm and are specified by the manufacturer to be accurate to ±1 μm over the full range of travel. The excimer laser is externally triggered and firing is coordinated with stage motion such that shots can be fired at specified incremental distances, even for arcs or arbitrary curves. The maximum writing speed depends ultimately on the required shot spacing and the maximum laser repetition rate of 2000 Hz. The required shot spacing, in turn, is usually determined by the minimum feature size and therefore the machining laser spot size. Using a spot diameter of ~14 μm, we have written 1 mm × 1 mm DOE's in ~6 minutes. We are currently developing methods for significantly decreasing fabrication time still further. We will report on a simple technique for varying the cutting laser aperture size (Fig. 1) under computer control. This will permit the use of a large laser swath for larger features, *e.g.*, the innermost zones of a Fresnel lens, then decreasing the laser kerf for finer features, resulting in a substantial increase in speed.

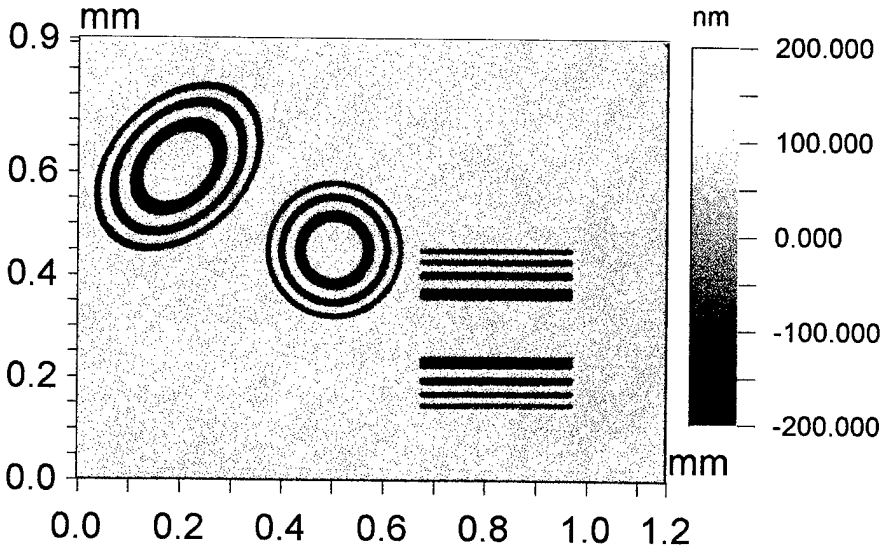


Figure 3. Some simple π-phase diffractive optical elements fabricated by excimer laser micromachining: a toroidal lens with primary focal lengths of 10 and 5 mm (top left); spherical lens, 250 μm diam., f.l.= 5 mm; cylindrical lens, 250 μm square., f.l.=5 mm (bottom right). the step height for each structure is ~400 nm.

Depending on the application, the desired motion program may be generated directly from a CAD program and executed much like a pen plotter. We have written simple Visual Basic™ programs as well as Microsoft Excel™ macros that define the structures, then command the motion and laser firing directly. The sample elements in Fig. 3 were each created in Excel™.

For example, in the case of the toroidal lens, the user enters the overall size of the element, the focal lengths in both major axes, and the angle of rotation (here 45°). The laser machining parameters such as laser kerf and stage velocity may also be adjusted. The program uses these parameters to determine a series of elliptical tool paths that will result in the desired structure. Clicking the "Machine Now" button executes the motion. In minutes a completed and functioning diffractive element is produced. No subsequent processing is required. Typical diffraction efficiency into the m=+1 order is 38-40% of transmitted light.

Blazed or Contoured Structures

Improving the diffraction efficiency beyond the ~40% limit for 2-level structures requires blazing of the grating. The literature documents many examples of precisely fabricated sawtooth-like diffractive structures with demonstrated efficiencies that approach 100%. Production of these elements using traditional lithographic techniques is a complex and costly process requiring multiple exposure and etch cycles. Excimer micromachining of these blazed gratings represents a formidable challenge. Accuracy and precision in the plane of the structure depends mainly on the laser spot size and the quality of motion control. Extending the process to the third dimension, depth, adds new factors, including laser fluence, beam homogeneity or intensity profile, and shot-to-shot reproducibility, as well as spot overlap or "stitching" patterns. Deviation from an ideal depth profile often results in light scattering into undesired orders. Smaller scale surface roughness leads to diffuse scattering. Either implies a loss of diffraction efficiency.

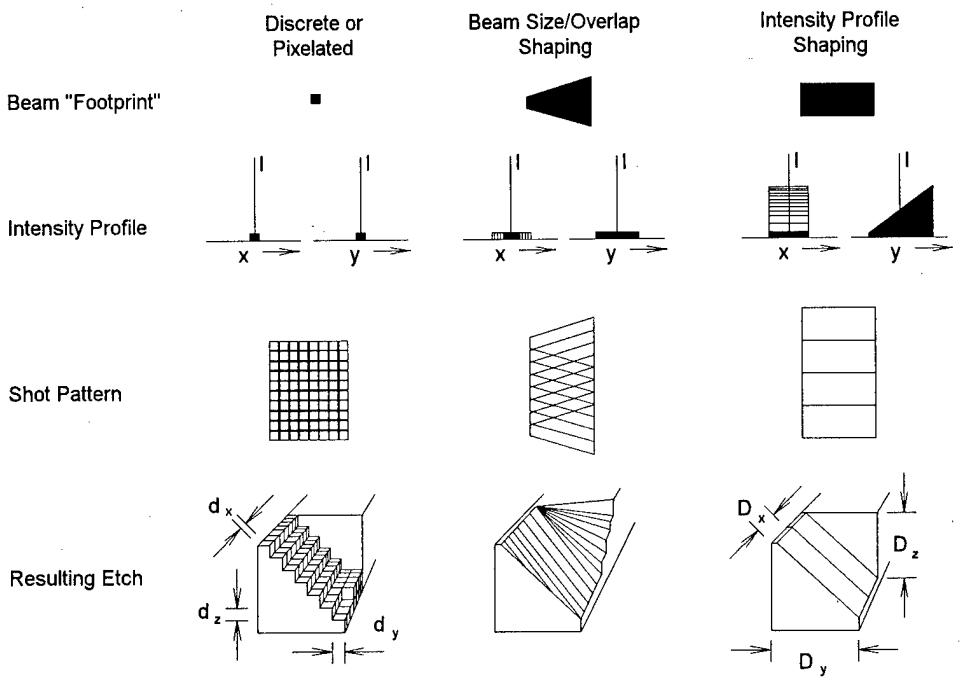


Figure 4. Three approaches to 3-dimensional direct-write ablative micromachining of diffractive structures.

Figure 4 outlines three general approaches to direct-write micromachining of blazed gratings. The first is to simply focus the beam to a size that is small compared to the grating period. The laser intensity is adjusted such that the depth of material removed per shot is small compared to the maximum desired depth. In this way, 3D-pixel-like volume elements can be removed with each laser shot. Control of depth is achieved by varying the beam intensity and number of shots per unit area. Although this method is the most versatile in that arbitrary 3-D surface structures can be fabricated, it has a number of disadvantages. Chief among them is the relatively slow writing speed. The small spot size and low intensity

required to remove ~100 nm/shot, means that most of the available pulse energy is discarded. For a blaze that corresponds roughly to an 8-level ramp, between 0 and 7 shots must be provided for each pixel. For example, a 1 cm^2 grating with 16-μm period (2 μm pixel size) would require ~24 hours of writing time with the laser averaging 1 kHz pulse repetition rate.

The second approach uses beam shaping to dramatically increase the writing speed. A trapezoidal aperture (Fig. 1) is imaged onto the workpiece. The distance between the parallel sides of the trapezoid determine the grating period. The stage is translated (or rotated) in a direction parallel to these sides and the laser pulse spacing is set so that there is little overlap at the narrow side. The wider side receives multiple overlapped shots resulting in greater depth. The ratio of the lengths of the parallel sides determines the blaze angle. The trapezoid need not be regular. Nonlinearity in machining depth may be compensated by curving the nonparallel sides appropriately. A great advantage in speed is realized because a much larger fraction of the laser pulse energy is utilized. The same 1 cm^2 sample grating that took 24 hours to produce with the discrete method can now be realized in under 1 hour. Fig. 5 shows profiles of two test gratings made with these two methods. Although this work is in an early stage, we have already demonstrated grating efficiencies of >70% for 633 nm light.

Finally, a further increase in writing speed can be attained by the third method, laser intensity profile shaping. The laser passes through a graded attenuator resulting in a ramped intensity profile in the image plane. The blaze angle may be achieved in as little as a single shot. Work with this technique is just getting underway. We plan to present a comparison of each of these methods.

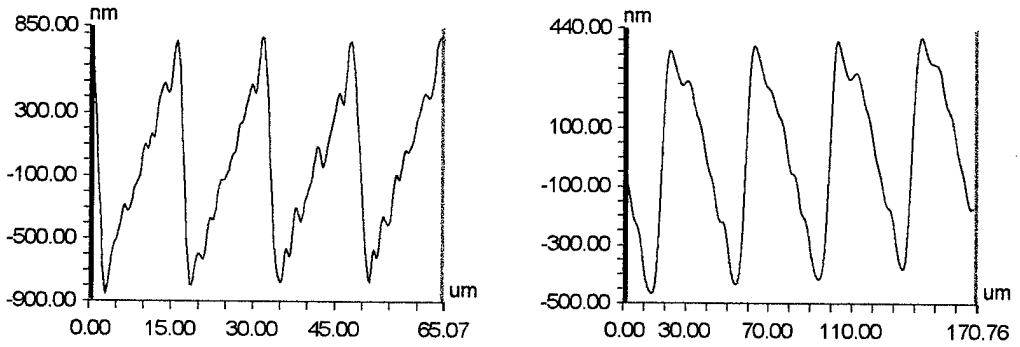


Figure 5. Depth profiles of some preliminary ramped structures micromachined into polyimide. The left shows a 16-μm period, ~1.5 μm deep and was fashioned by rastering a ~3.5-μm diam. beam up to 7 times per row or 28 times per grating period (Discrete method Fig. 4). The right shows a 40-μm period, ~0.8 μm deep grating fabricated by overlapping trapezoid-shaped beams. The measured efficiency for this preliminary structure was >70%. Note that each grating period requires only one pass with this method vs. 28 for the raster. Profiles obtained with the integrated Wyko RST.

Acknowledgment

This work is supported by a Phase II Small Business Innovative Research contract with the National Aeronautics and Space Administration (Contract No. NAS8-40572).

References

1. M. R. Feldman, invited paper MGG1, OSA Annual Meeting, Portland, OR, Sept., 1995.
2. M. T. Duignan, in *Diffractive Optics*, Vol. 11, 1994 OSA Technical Digest Series (Optical Society of America, Washington, DC, 1994), pp. 129-132.
3. G. J. Swanson, "Binary optics technology,: The theory and design of multi-level diffractive optical elements," *MIT/Lincoln Lab Technical Report 854*, 14 89.
4. F. S. Roux, *Opt. Eng.* **33**, 2843-2848 (1994)

Fabrication of Submicron Feature Diffractive Elements using Near-Field Direct-Write Ultra-Violet Lithography

Igor I. Smolyaninov, Joseph N. Mait,† David L. Mazzoni, and Christopher C. Davis

Electrical Engineering Department
University of Maryland
College Park, Maryland 20742
e-mail: smoly@eng.umd.edu

†U.S. Army Research Laboratory
AMSRL-SE-EO
2800 Powder Mill Road
Adelphi, Maryland 20783
e-mail: mait@arl.mil

The fabrication of surface relief diffractive elements using a series of binary exposures and etches in photo-resist is attractive because it relies upon standard lithographic techniques [1]. Disadvantages of this process include the necessity for mask generation prior to photoresist exposure and the logarithmic relationship between the desired number of phase levels and number of exposures. To overcome the latter restriction, the generation of gray level masks has been proposed [2]. However, both restrictions can be overcome if the photoresist is exposed directly. Electron beam [3] and laser beam direct-write [4] procedures have been proposed. Electron beam writing is attractive for its high resolution and laser beam writing for its cost. Both high resolution and low cost are possible if a tapered fiber is used to deliver energy to the photoresist [5,6]. We report on the fabrication of diffractive gratings with submicron features using a tapered fiber to deliver ultra-violet (UV) energy to a layer of photoresist.

By placing a small aperture some distance from a surface, where the distance is much less than the wavelength of the illumination, it is possible to resolve, or create lithographically, structures that are significantly smaller than one wavelength [7-9]. These "near-field" optical experiments are generally performed with an aperture determined by the tip of a tapered optical fiber. A tapered multimode or single-mode optical fiber always becomes single mode (HE_{11}) as the tip is approached. If the taper is sufficiently gradual, or adiabatic, minimal mode conversion loss occurs and substantial power reaches the tip.

Lithographic spatial resolution of 200-300 nm has been obtained with a 454 nm Ar^+ ion laser and uncoated fiber tips [5]. When metal coated fiber tips were used the resolution was improved to approximately 80 nm. We have demonstrated a spatial resolution on the order of 100 nm with a 248-nm KrF excimer laser even with uncoated fiber tips [6], which is comparable to results generated by metal coated tips [5]. Uncoated fiber tips are more convenient in practical applications. In addition, these techniques have allowed us to study local nonlinear photochemistry processes that occur during photolithographic writing. This is the only experimental technique to our knowledge that makes such measurements possible.

Our experiments were performed using a reflection mode near-field scanning optical microscope (NSOM). The NSOM is represented schematically in Fig. 1. For course positioning,

the sample is placed on a tri-axis translation stage driven by three New Focus™ Picomotors. The sample is illuminated by an adiabatically-tapered fiber tip which is held at a constant distance from the sample by means of shear force feedback [10]. The tip is mounted on a piezotube that provides both three axis motion in the nanometer range and dithers the tip for shear force measurement. By recording the shear force feedback signal during writing, we are able to measure the topography of the sample with nanometer resolution. The fiber tip is drawn at the end of 100 μm UV fiber by heating it with a CO_2 laser beam in a micro-pipette puller.

The source of illumination is an excimer laser coupled into the fiber using a reflective microscope objective. The laser is operated at a 200 Hz pulse repetition rate with a pulse duration of 60 ns. The average laser power was 5 mW. For lithography, the laser was gated so that single pulses could be used to write patterns on the sample. This enables proper control of the exposure of thin (200-500 nm) films of photoresist.

The use of shear force feedback allows us to detect changes in the photoresist film prior to development. The photochemical reactions in the photoresist film lead to morphological changes that alter the volume of the irradiated areas and lead to variations in the height of the film. These changes are easily detected due to the extreme sensitivity of the shear force technique to variations in sample height. After exposure, the sample is immediately raster scanned by the same tip used for writing and the shear force feedback signal is recorded.

Figure 2 contains two images of diffraction gratings written into the surface of photoresist. The images were obtained after exposure but prior to development. The scales below the images indicate height variations in the surface, which we expect to deepen after development. The grating periods for Figs. 2(a) and (b) are approximately 500 nm and 250 nm, respectively. The feature sizes in both cases are slightly less than the period. The power used to write the 250-nm grating was roughly one-third that which was used to write the 500-nm grating. Our observations show that the intensity of light is the most decisive factor that determines size of a single spot [6].

In conclusion, we have demonstrated direct-write UV lithography using a NSOM with uncoated fiber tips and also developed a convenient technique that uses shear force methods to adjust experimental parameters during lithography experiments. Diffraction gratings with 500 nm and 250 nm periods were fabricated. A portion of this research was supported by the Department of Defense through contract number MDA 904-92-C-M023.

References

1. W. B. Veldkamp and G. J. Swanson, in *International Conference in Computer-Generated Holography*, Proc. SPIE **437**, 54 (1983).
2. T.J. Suleski and D. C. O'Shea, Appl. Opt. **34**, 7507 (1995).
3. N. Streibl, J. Schwider, M. Schrader, and U. Krackhardt, Opt. Eng. **32**, 781 (1993).
4. D. Zaleta, W. Daschner, M. Larsson, B. C. Kress,, J. Fan, K. S. Urquhart, and S.-H. Lee, in *Diffractive and Miniaturized Optics*, SPIE Critical Review **CR49**, 117 (1993).
5. G. Krausch, S. Wegscheider, A. Kirsch, H. Bielefeldt, J. C. Meiners, and J. Mlynek, Opt. Commun., in press.
6. I. I. Smolyaninov, D. L. Mazzoni, and C. C. Davis, "Near-field direct-write ultra-violet lithography and shear force microscopic studies of the lithographic process," Appl. Phys. Lett., in press.
7. D. W. Pohl, W. Denk, and M. Lanz, Appl. Phys. Lett. **44**, 651 (1984).
8. E. Betzig, J. K. Trautman, T. D. Harris, J. S. Weiner, and R. L. Kostelak, Science **251**, 1468 (1991).
9. H. Heinzelmann and D. W. Pohl, Appl. Phys. A **59**, 89 (1994).
10. S. I. Bozhevolnyi, I. I. Smolyaninov, and O. Keller, Appl. Opt. **34**, 3793 (1995).

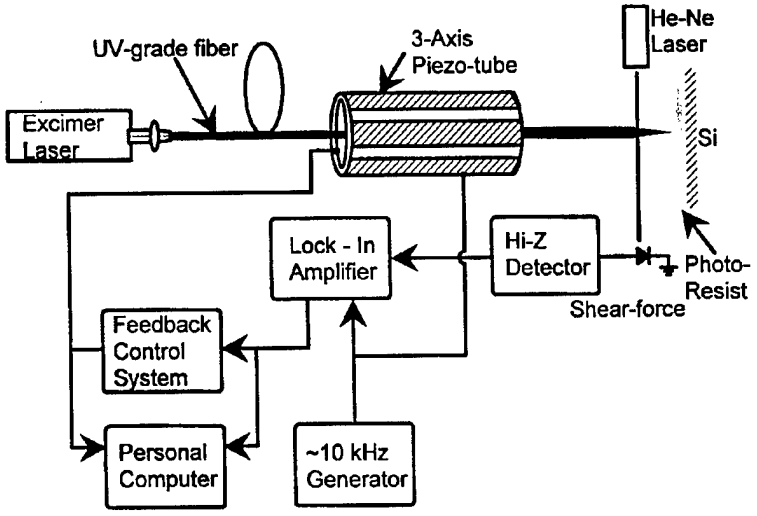
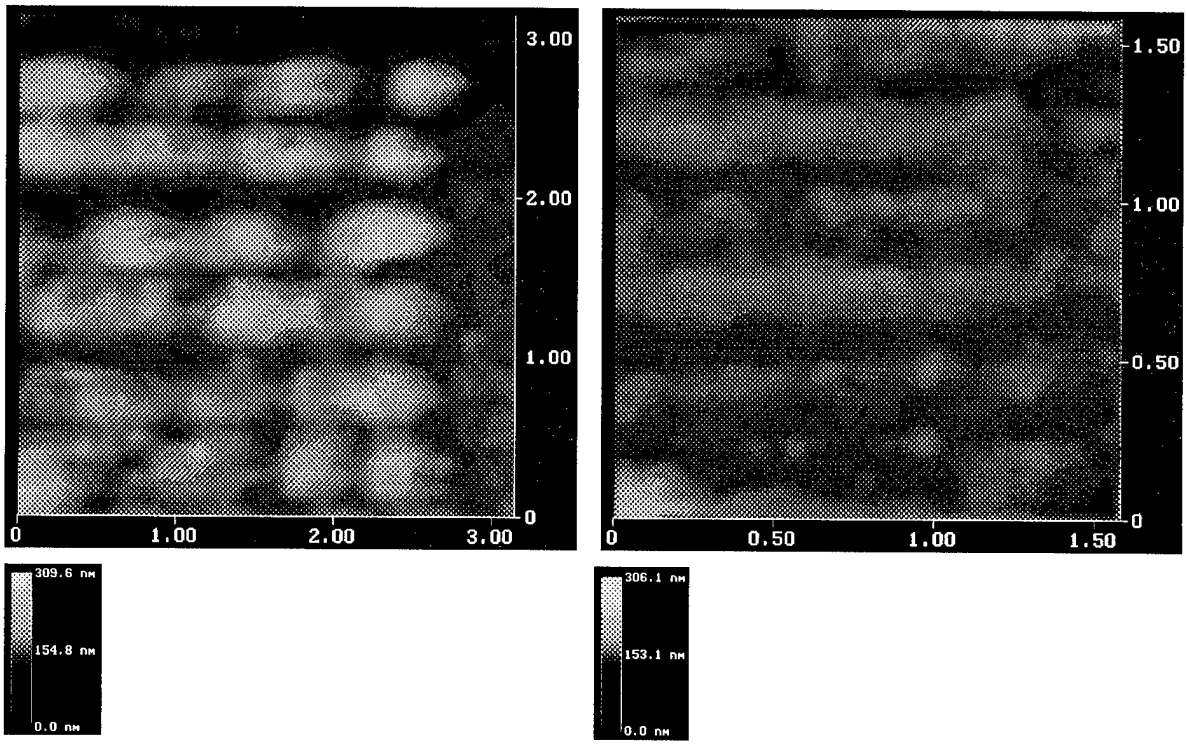


Fig. 1. Schematic representation of near-field scanning optical microscope used for direct-write lithography.



(a) (b)

Fig. 2. Topographical changes in the surface of photoresist, after UV exposure and prior to development, detected using shear force feedback. Image scales are μm. Diffraction gratings with periods of (a) 500 nm and (b) 250 nm.

One-step lithography for mass production of multilevel diffractive optical elements using High Energy Beam Sensitive (HEBS) gray-level mask.

Walter Däschner, Robert Stein, Pin Long, Chuck Wu* and Sing H. Lee

Dept. of Electrical and Computer Engineering, University of California San Diego, La Jolla, CA, 92093-0407
*Canyon Materials, Inc. 6665 Nancy Ridge Drive, San Diego, CA 92121

In order to satisfy the growing industrial need for Diffractive Optical Elements (DOEs), fabricated at a low price, we investigated the gray level mask fabrication aproach. Our apoach allows mask fabrication by a single e-beam direct write step without any involved resist processing. The mask can then be used in a optical lithography tool to generate a DOE structure in photoresist. This DOE structure will then be transfered into the substrate material by the use of a chemically assisted ion beam etching (CAIBE) process.

HEBS-Glass [1] is a mask material sensitive towards e-beam exposure, an exposure with a certain electron beam dosage changes the optical density of the material according to Fig. 1.

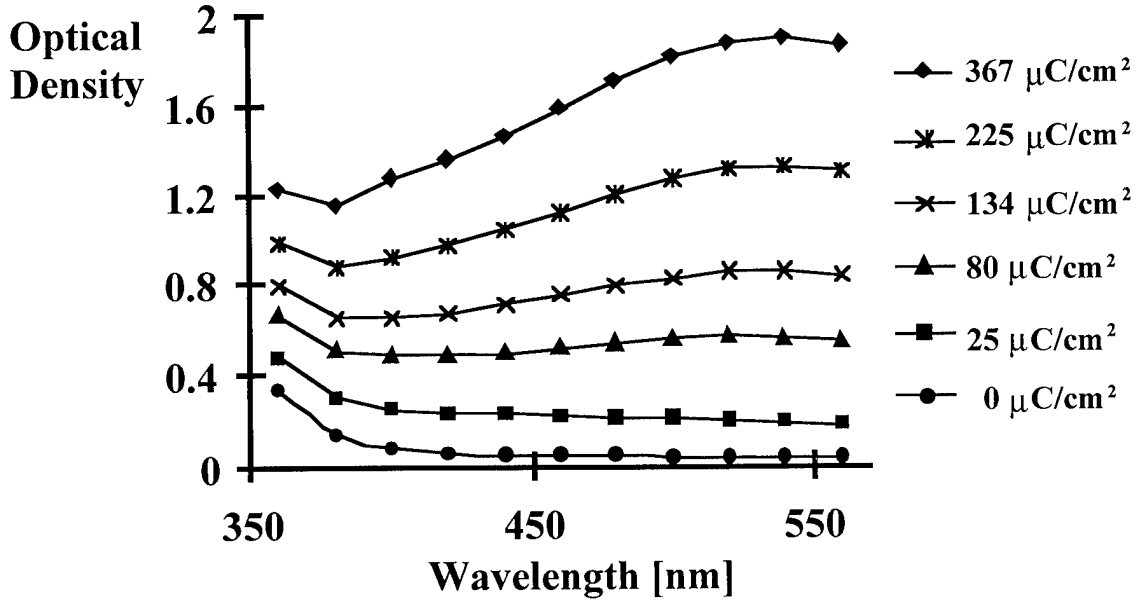


Fig. 1 Optical density of HEBS material after exposure with 30 kV e-beam acceleration Voltage.

The exposure necessary for this measurement was done in our Cambridge EBMF-10.5 using a 25 nA writing current, a 0.1 micron addressing grid size and an acceleration Voltage of 30 kV.

This transmission data was collected using a Hitachi U-2000 photo spectrometer. After e-beam exposure the mask needs no further development or fixation process. The mask with varying optical densities can then be used to expose a photo resist in a contact aligner. This allows to associate a certain resist thickness after development with each optical density. The information was used to determine the e-beam dosages for each of the (i.e. 32) phase levels necessary to generate a DOE. Software, previously written in house, to support mask making and direct write approaches [2] for the fabrication of DOEs, was used to generate the necessary e-beam data. The so generated HEBS-Glass gray-level mask can be used to expose numerous DOEs using an optical lithography tool. After many copies of the mask on the photo resist are developed, many substrates with the developed photo resist will be placed in a CAIBE [3] system, to simultaneously transfer the microstructures from the analog resists onto the surfaces of the substrates. The number of substrates that can be etched simultaneously will depend on the relative size of the ion source in the CAIBE system and the size of the substrate. The DOE array shown in Fig. 2 was generated this way. This scanning electron micrograph shows an array of 10 by 10 spherical on axis lenses with an f# of 3.1, the aperture size of the lenses is 100 by 100 microns and the lenses are designed for the use with 830 nm wavelength.

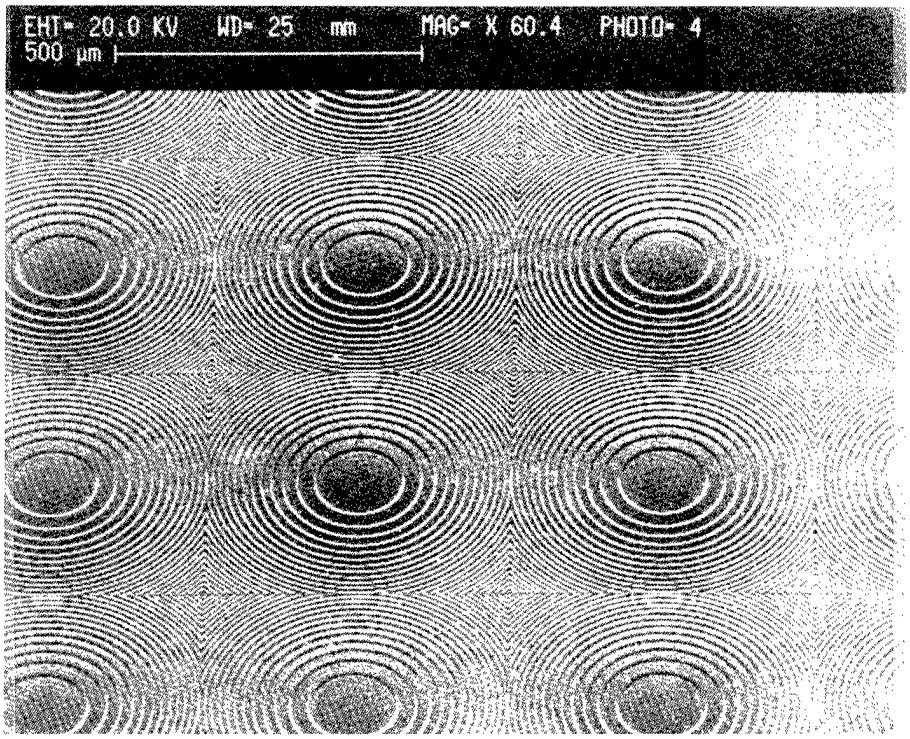


Fig. 1 Scanning electron micrograph of lenslet array fabricated by employing a HEBS-Glass gray level mask and a CAIBE process.

The described fabrication method shows a possibility for cost effective mass fabrication of DOEs. There is a number of advantages to the newly developed approach.

The mask fabrication is simplified and more cost-effective. Instead of a set of masks (i.e. 5 masks for 32 phase levels) with all the associated resist processing, only a single mask needs to be exposed in the e-beam writer and no resist processing is associated with the mask generation.

All phase levels are written in a single step on a single mask. The inevitable miss registrations and associated efficiency losses between subsequent exposures are avoided.

Third the number of processing steps for the DOE fabrication compared to a binary mask fabrication method (i.e. 32 phase levels) is reduced by a factor of 5. This will reduce the cost for high quality monolithic DOEs substantially.

Fourth even with a binary fabrication method for master fabrication and a following replication step based on injection molding this replication method only becomes economic with a number of DOEs to be fabricated in the 10's of thousands. Since the proposed fabrication method greatly reduces the involved fabrication steps resulting in a cost reduction, the number at which molding based methods become economically feasible will grow considerably. This will allow to avoid the problems associated with the molding approach. The material which is best suited for the application, can be chosen without being limited by the constraints of the molding material (i.e. limited temperature range of operation or limited wavelength range). Also all the involved materials and tools are compatible with VLSI fabrication so that no new fabrication or software tools need to be established unlike in the case of replication by injection molding or casting.

There is a considerable gain in turn around time since the number of production steps has been reduced and the mask fabrication steps have been simplified.

References:

1. C. Wu "Method of making High Energy Beam Sensitive Glasses" U.S. Patent No. 5,078,771, Jan. 7th 1992.

2. J. Fan, D. Zaleta, K. Urquhart, S.H. Lee, "Efficient encoding algorithms for computer-aided-design of diffractive optical elements by the use of electron-beam fabrication". Appl. Opt. **34**(14): 2522-2533, May 1995.

3. W. Däschner, M. Larsson and S.H. Lee, "Fabrication of monolithic diffractive optical elements by the use of e-beam direct write on an analog resist and a single chemically assisted ion-beam-etching step." Appl. Opt. **34**(14): 2534-2539, May 10, 1995.

Subwavelength Diffractive Elements Fabricated in Semiconductor for 975 nm

R.E. Smith, M.E. Warren, J.R. Wendt and G.A. Vawter

Sandia National Laboratories

Albuquerque, NM 87185-0603

Diffractive optical elements can be realized by fabricating surface relief structures with features shorter than the wavelength of light.[1-4] These structure have the properties of homogeneous layers of material but with effective indexes of refraction determined by the duty cycle of the surface features. Lateral variations in those duty cycles lead to lateral gradients in refractive index and, potentially, surface elements with very high diffraction efficiencies.

Here we present a high-efficiency, dielectric, subwavelength surface relief "blazed grating," [5-6] — a single "blazed-tooth" of which is shown in the scanning electron micrograph (SEM) in Fig. 1 — and report recent results on a subwavelength "anti-reflection" (AR) surface shown in the SEM in Fig. 2. These structures were designed for use at 975 nm. To our knowledge, this is the shortest wavelength for which semiconductor structures of these types have been successfully demonstrated. The structures were fabricated in GaAs substrates. Our choice of wavelength and substrate material was motivated by interest in integrating diffractive optical elements with vertical-cavity surface-emitting laser diodes and other semiconductor optoelectronic devices.

The subwavelength diffractive structures use a single lithographic fabrication and still have high efficiencies, even for fast lenses. In contrast, conventional diffractive optical elements with high efficiency require multiple lithographic steps to produce modulo 2π stepped profiles that approximate the ideal refractive surface profile. The precise alignment needed for each lithographic step in a multilevel process is challenging.

Various schemes for modulating the grating features have been proposed.[7] In our approach we simultaneously vary all the free parameters: the etch depth, width and spacing, rather than artificially constraining our optimization to be analogous to pulse-width or pulse-position modulation. Instead we rely on fabrication based constraints, such as minimum lithographic line width and maximum groove aspect ratio. In each case the merit function for the optimization is comprised of a rigorous coupled wave theory (RCWT) calculation of the light transmitted into the desired diffracted order.[8] The optimization in accomplished by using a straightforward gradient method.[9]

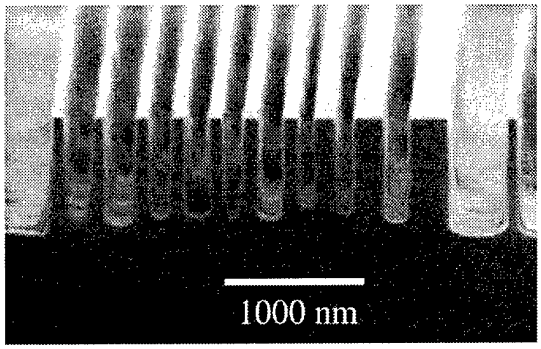


Fig. 1. An SEM of a single subwavelength "blazed tooth" generated by etching 10 subwavelength grooves into a GaAs surface. The resulting "blazed grating" is seen to diffract 85% of the transmitted light into the first order. (See Fig. 3)

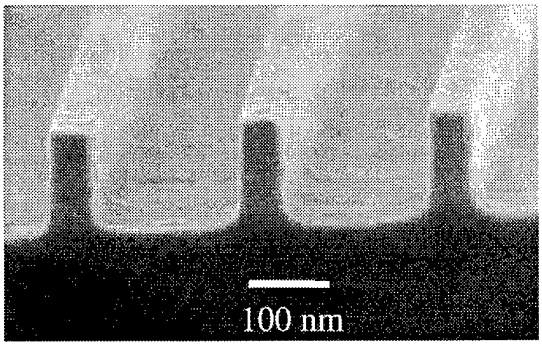


Fig. 2. An SEM of three of the teeth comprising a subwavelength "AR surface" etched into GaAs This surface transmits ~96% of incident light. (See Fig. 4)

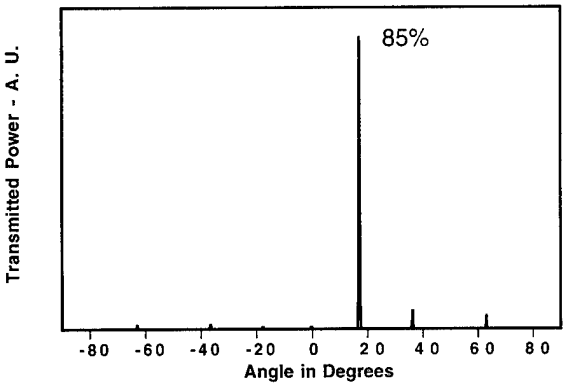


Fig. 3. A scatterometer trace of the light diffracted by the subwavelength blazed grating shown in Fig. 1. 85% of transmitted light is diffracted into the first order.

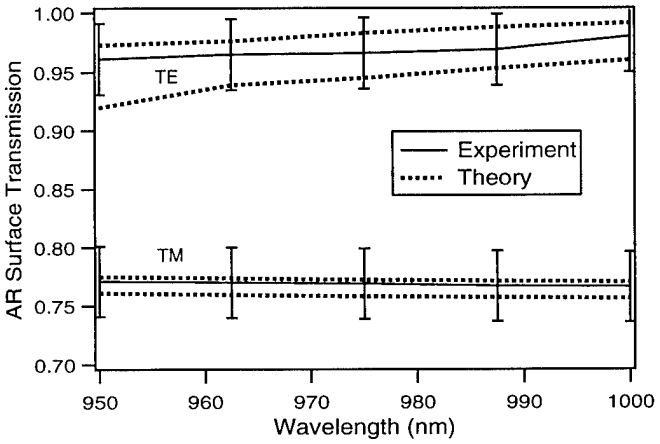


Fig. 4. Measured reflectance for TE and TM light incident on the subwavelength AR surface shown in Fig. 2. The error bars represent the spread in the data over several samples. The theory bands represent the values predicted for variations in teeth widths (47-55 nm).

Table 1. Summary of Results

	AR Surface (Transmission)	Blaze Grating (% in 1st Order)	f#1.5 Lens (% in 1st Order)
Theoretical Maximum	100%	100%	100%
Theoretical Design	100%	99%	92%
Measured	96±2%	85±1%	(In Fabrication)

Table 1 shows a summary of our results in these subwavelength structures. The top row shows the theoretical maximum achievable by using the subwavelength approach. Notice that in each case the maximum is 100%. The second row shows theoretical results obtained using a modified RCWT code to predict output of optimized structures with fabrication constraints. The resulting AR and Blazed grating structures are shown in Figs. 1 and 2. The third row shows the experimentally measured values for these elements. These results are further described in Figs. 3 and 4, respectively. At the time of writing, the lens has yet to be fabricated and tested. It is worth mentioning in passing that the design for this lens is more fabrication tolerant than the design used for the blazed grating.

References:

1. R. C. Enger and Steven K. Case, Appl. Opt. **22** 3220 (1983).
2. Y. Ono, Y. Kimura, Y. Ohta and N. Nishida, Appl. Opt. **26**, 1142 (1987).
3. W. Stork, N. Streibl, H. Haidner, and P. Kipfer, Opt. Lett. **16**, 1921 (1991).
4. M. W. Farn, Appl. Opt. **31**, 4453 (1992).
5. M. E. Warren, R.E. Smith, G.A Vawter, and J. R. Wendt, Opt. Lett. **20**,1141 (1995).
6. J. R. Wendt, G.A Vawter, R.E. Smith, and M. E. Warren, J. Vac. Sci. Technol. **13** Nov./ Dec. (1995).
7. E. Noponen and J. Turunen, J. Opt. Soc. Am. A. **11**, 1097 (1994).
8. T. K. Gaylord and M. G. Moharam, Proc. IEEE **73**, 894 (1985).
9. The Mathworks, Inc., Natick, MA.

This work was supported by the United States Department of Energy under Contract DE-AC04-94AL85000.

Fabrication of Fresnel zone plates for x-ray microscopy: diffractive optics for soft x-rays.

S. J. Spector[1], C. J. Jacobsen[1],D. M. Tennant[2]

1. *Dept. of Physics, SUNY at Sony Brook, Stony Brook, NY 11794, phone#: (516)-632-8097, fax#: (516)-632-8101*
2. *AT&T Bell Laboratories, 101 Crawford Corners Rd, Holmdel, NJ 07733, phone#: (908)-949-5007*

Fresnel zone plates are diffractive optical elements which are currently being used for high resolution x-ray microscopy. Several groups fabricate zone plates for use in specific microscopes [1] and we present here a summary on the fabrication of zone plates for use in the Scanning Transmission X-ray Microscope at the National Synchrotron Light Source. X-ray microscopy has demonstrated imaging with resolution five times superior to that which can routinely be achieved by visible light microscopy. In addition, x-rays with wavelengths between the carbon (4.2 nm) and oxygen (2.3 nm) K absorption edges are absorbed nearly an order of magnitude more strongly by organics than by water. This creates a natural absorption contrast mechanism and allows the viewing of many biological specimens wet and intact (without sectioning) and at atmospheric pressure [2]. By taking advantage of the spectroscopic properties of x- rays, x-ray microscopy can be used to map chemical elements and their binding states. Fluorescent chemical labels and gold labels can also be imaged at high resolution. Furthermore, several labs including ours are developing the capability to view radiation-tough frozen hydrated specimens in x-ray microscopes.

At soft x-ray wavelengths all materials both absorb and phase shift light, so it is not possible to make the usual refractive optical elements for soft x-rays. Fresnel zone plates are the diffractive optical elements currently being used for the highest resolution imaging with soft x-rays. A Fresnel zone plate consists of a series of concentric rings or zones of material. The placement of the zones for a source at infinity is given by the equation $r_n^2 = nf\lambda + n^2\lambda^2/4$, where n is the zone number, r_n is the radius of the n'th zone, f is the focal length and λ is the wavelength. The zones therefore become closer together and smaller towards the outside of the zone plate. The size of the focal spot of the zone plate is roughly equal to the width of the outer zone, which also determines the finest spatial resolution that can be achieved by the microscope. In addition, to achieve this resolution, the zones have to be placed with accuracy better than 1/3 their width. The highest resolution zone plates we have fabricated have 30 nm outer zone widths, and are expected to give Raliegh resolution of 36 nm. Preliminary results indicate an improvement in resolution compared to the 45 nm zone plates used previously.

A diagram of the optical arrangement of the Scanning Transmission X-ray Microscope (STXM) is shown in figure 1, and its operation is described in detail elsewhere [3]. The Fresnel zone plate forms a microprobe, and the sample is placed at its focus. In the typical transmission mode of operation, the sample is scanned and a proportional counter records the intensity intensity through the sample. Because the zone plate is a diffractive optical element, imaging in this arrangement requires coherent illumination of the zone plate. X-rays are provided by a high brightness soft x-ray undulator on the 2.5 GeV ring of the National Synchrotron Light Source. A spherical grating monochromator is used to spectrally filter the beam to $\lambda/\Delta\lambda = 200 - 1500$. Ideally, one has $\lambda/\Delta\lambda \simeq N/2$, where N is number of zone plate zones.

Because zone plates are not 100% efficient optical elements, much of the light is focused into unwanted orders or goes straight through the zone plate as zero order light. Figure 1 shows how the combination of an apodized zone plate, or zone plate with a central stop, and an order sorting aperture removes the unwanted orders of light. Because the central stop is a large area of the zone plate, the central stop needs to be very opaque to soft x-rays. We made the central stop of gold 300 nm thick, which blocks 99.94% of the x-rays incident with a wavelength of 3.1 nm [4] and therefore reduces the central stop integrated flux to satisfactory low levels.

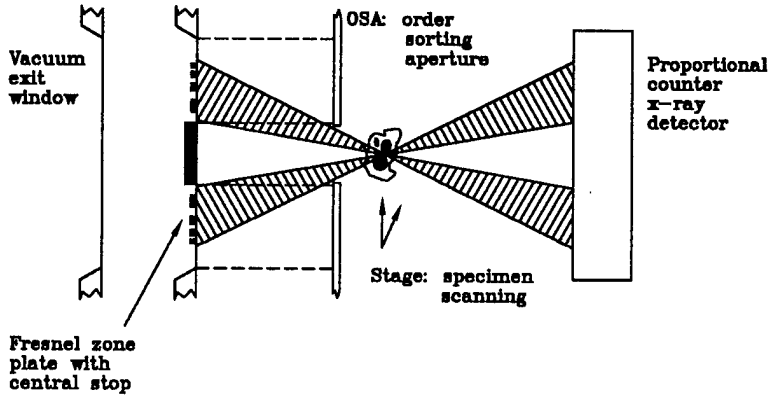


Figure 1: Arrangement of the STXM.

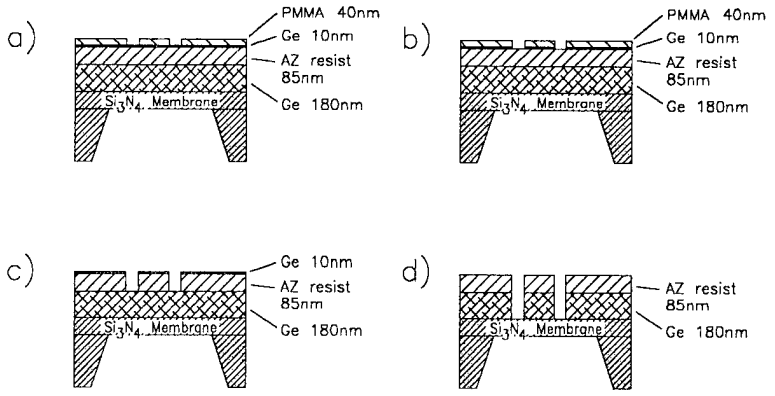


Figure 2: Fabrication with a trilayer resist. a) exposure and development, b) RIE (reactive ion etch) thin Ge mask, c) RIE AZ photoresist d) RIE thick Ge substrate.

The zone plates were fabricated on supporting square Si_3N_4 membranes approximately 0.25 mm wide and 120 nm thick. The fabrication technique for the membranes is similar to methods described elsewhere [5]. After the fabrication of the membranes, a gold central stop was fabricated on each membrane. In the same step gold alignment crosses were also made on the wafer off of the membrane for proper placement of the zones relative to the central stop. The technique used in the fabrication of the gold features is similar to techniques described in more detail elsewhere [6]. A bilayer resist structure was placed on the wafer, and the features were patterned in the resist by electron beam lithography. 300 nm of gold was then evaporated on top of a 10 nm layer of chrome, used to improve adhesion. The resist was then removed in warm acetone, lifting off the unwanted gold and leaving behined the desired gold features.

The trilayer resist structure used for the patterning of the Ge zones is shown in figure 3. The electron-beam exposure was done in a commercially available, JBX-6000FS e-beam lithography system manufactured by JEOL Ltd. This machine can deliver a current of 100 pA into 6 nm spot size, allowing each zone plate to be exposed in less than 5 minutes. (The same machine is also used to expose the central stops and alignment crosses, but at a higher current and larger spot size setting). The machine also has excellent placement precision and can write in an ($80\mu m^2$) field without having to move the sample. These characteristics make it idealy suited for the fabrication of high resolution and relative large zone plates, 80 μm in diameter. (A large diameter zone plate is necessary for reasonable working distances in the microscope). However, the lithography system is not optimized for drawing circular structures and this causes irregularities which will be discussed later.

After exposure and development of the thin, 40 nm, layer of PMMA, the pattern was transferred to the very thin Ge layer, 10 nm, below by reactive ion etching in CF_3Br gas. Reactive ion etching (RIE) is

an anisotropic etching technique that is necessary for the high aspect ratio structures we wish to produce. Next, the Ge acts a mask for the RIE of the 85 nm AZ photoresist in O_2. The final 180 nm Ge layer is then etched by RIE in CF_3Br. The CF_3Br RIE selectively etches the Ge approximately 4:1 over the AZ photoresist which had been previously hard baked at 195 C°. There is only a small amount of AZ resist left afterward, which can then be removed by a O_2 RIE.



Figure 4a: View of all the zones in a zone plate with 30 nm outer zones.

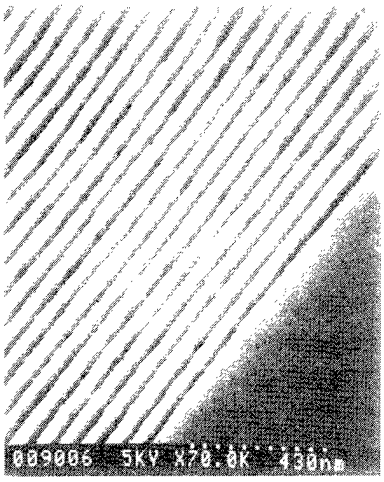


Figure 4b: Close view of the outer zones.

Figure 4 shows a scanning electron micrograph of a zone plate with a 30 nm outer zone width. Although there is some line width variation, the outer zones are cleanly resolved. After inspection of the line width variations and comparison with the pattern data file, we concluded that these variations are due to the method the machine currently uses to draw circular structures. The machine can only natively draw trapezoidal and rectangular structures, and uses a conversion program to convert circles or arcs into a large number of these micro figures which it can draw. The method of conversion being used is not well suited for fine circular structures. It creates an extremely large number of micro figures, and the boundaries between micro figures are exposed twice. We believe this double exposure is responsible for the line width variations we see, as there is a good correspondence between the patterns in the zone plate and the boundaries of the micro figures. We are working to improve the method used to draw circular structures by modification of the manufacturer's software.

Figure 5 shows an image of resolution test pattern taken with the STXM using a 30 nm zone plate. Also shown is a reverse contrast scanning electron micrograph of the test pattern for comparison. The test pattern was fabricated in 200 nm of Ge on a Si_3N_4 membrane in a manner analogous to the fabrication of the zone plate. The inner ring represents features 40 nm in size and these features are easily be resolved. Smaller features, (perhaps as small as 30 nm) can also be resolved although it is difficult to tell exactly because the features in the test pattern are not clearly defined at this resolution.

We also measured the diffraction efficiency of the same zone plate by measuring the flux in the focal spot and comparing this with the flux incident on the Ge. A pinhole aperture of known size was used to determine the flux through an area on the membrane were the Ge has been removed. The same pinhole aperture was used measure the flux in the focal spot. The diffraction efficiency of the zone plate was measured to be 4.3% at a wavelength of 3.1 nm. This efficiency is significantly less than the theoretical efficiency of 10.5%, which was determined from the material and thickness of the zones and its optical properties [7, 4]. However, this efficiency is still high enough for practical use in the microscope. In scanning x-ray microscopy, efficiency is not critical because decreased efficiency does not lead to increased radiation dose to the sample.

There are a few contributing explanations for the loss in efficiency. We believe some of the loss in efficiency is due to the line width variations we have already discussed. Another contribution is from the Ge being less dense than expected. We measured the Ge to be considerably less opaque to x-rays than

would be expected from the thickness and known scattering factors. When we recalculated the density of the Ge from the transmission of x-rays, we calculated the ideal efficiency of the zone plate to be about 8.0%. Another possible contribution to loss in efficiency would be incomplete etching of the Ge. The scanning electron micrographs we have taken do not clearly indicate whether the Ge is completely etched, so we are continuing to investigate this as a possibility.

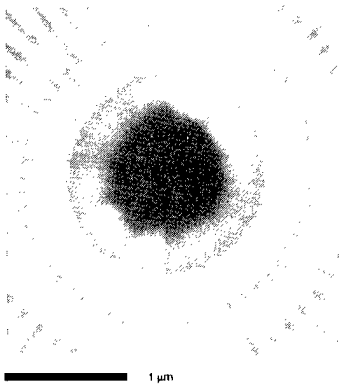


Figure 5a: STXM image of test pattern taken using a zone plate with 30 nm outer zones.

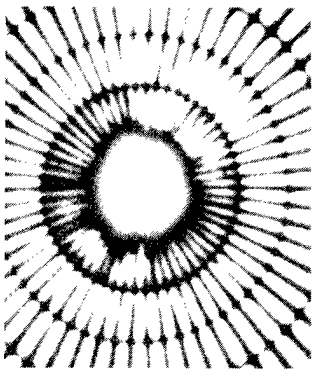


Figure 5b: Reverse contrast SEM image of the same test pattern.

Fresnel zone plates are diffractive optical elements that can be used for imaging with soft x-rays at resolutions superior to that which can be achieved by routine visible light microscopy. We have fabricated zone plates which focus soft x-ray light into a spot size of approximate 30 nm. Focusing soft x-rays in this manner represents the smallest focal spot of electromagnetic waves at any wavelength.

References

[1] G. Schneider, T. Schliebe, and H. Aschoff. Cross-linked polymers for nanofabrication of high resolution zone plates in nickel and germanium. *Journal of Vacuum Science and Technology*, B 0:0, 1995.

[2] J. Kirz, C. Jacobsen, and M. Howells. Soft x-ray microscopes and their biological applications. *Quarterly Reviews of Biophysics*, 28(1):33–130, 1995. Also available as Lawrence Berkeley Laboratory report LBL-36371.

[3] C. Jacobsen, S. Williams, E. Anderson, M. T. Browne, C. J. Buckley, D. Kern, J. Kirz, M. Rivers, and X. Zhang. Diffraction-limited imaging in a scanning transmission x-ray microscope. *Optics Communications*, 86:351–364, 1991.

[4] B. L. Henke, E. M. Gallikson, and J. C. Paris. X-ray interaction: photoabsoption, scattering, transmission, and reflection at E=30–30,000 ev. *Atomic Data and Nuclear Data Tables*, 54:181–342, 1993.

[5] D. M. Tennant, J. E. Gregus, C. Jacobsen, and E. L. Raab. Construction and test of phase zone plates for x-ray microscopy. *Optics Letters*, 16:621–623, 1991.

[6] R. E. Howard, E. L. Hu, L. D. Jackel, P. Grabby, and D. M. Tennant. 400 angstrom line width e-beam lithography on thick silicon substrates. *Applied Physics Letters*, 36:596, 1980.

[7] J. Kirz. Phase zone plates for x rays and the extreme uv. *Journal of the Optical Society of America*, 64:301–309, 1974.

Replication Techniques

DThA 8:30 am-10:00 am
Fairfax A

Michael C. Hutley, *Presider*
National Physical Laboratory, U.K.

Foundry fabrication for diffractive optical elements

Ravi Athale & Kannan Raj

ECE Dept., George Mason University, Fairfax, VA 22030

Batch fabrication of multiple projects to spread the non-recurring costs and therefore reducing the cost of prototype custom circuits has been carried out for silicon integrated circuits (MOSIS). Recent efforts along this line include batch fabrication of optoelectronic devices through the CO-OP program. In this talk, we will discuss issues involved in providing multi-project foundry fabrication of diffractive optical elements through the binary optics approach. Cost comparison with other competing technologies will be made.

Fabrication of continuous-relief micro-optics : progress in laser writing and replication technology

M.T. Gale, Th. Hessler, R.E Kunz and H. Teichmann

Paul Scherrer Institute (PSI), Badenerstrasse 569, CH-8048 Zurich, Switzerland
Tel. +41 1 492 63 50 Fax +41 1 491 00 07 e-mail gale@psi.ch

1. Introduction

Laser writing technology for the fabrication of continuous-relief micro-optical elements is being developed at a number of institutes worldwide [1,2]. It represents a very powerful and flexible fabrication technique and fits well to replication technology in which the resist surface-relief microstructure can be electroformed and replicated into plastic material. Fig. 1 illustrates the essential production steps involved.

Direct laser writing technology is highly suited to the fabrication of *'planar'* continuous-relief micro-optical elements, with typical microstructure of about 5 μm maximum relief and in certain cases up to 10 μm or more. Accurate control of the exposure beam intensity and processing parameters enables continuous-relief microstructures to be fabricated with lateral feature resolution under 5 μm and height resolution better than 10 nm.

At PSI, laser writing and replication technology is used for the fabrication of a wide range of Fresnel lenslets, lenslet arrays and other 'planar' surface-relief micro-optical elements. The work is aimed at establishing routine and reliable technology for the low-cost mass-production of a wide range of planar micro-optical elements, partly in collaboration with commercial replication houses for hot embossing, uv-embossing and injection moulding. Recent developments include the fabrication of deep (>10 μm) Fresnel lenslets for investigating white light applications and the fabrication of lenslet arrays with a focal length uniformity of better than ±0.2 μm in 250 μm for applications in confocal microscopy. This paper presents the current status of laser writing and replication technology at PSI, discusses the fabrication constraints and gives examples of recently fabricated micro-optical elements.

2. Laser writing technology

A 3rd generation laser writing system is currently being installed at PSI for the fabrication of planar micro-optical elements (see Fig. 2). A photoresist-coated substrate is raster scanned under a focused HeCd laser beam (wavelength $\lambda = 442$ nm) whose intensity can be synchronously modulated to 256 discrete levels. In the new system, the raster scan is performed by a roller-bearing xy-stage and the focused laser writing spot is generated by a modified Compact Disc (CD) reader autofocus optic. The current dynamic positioning accuracy of the xy-stage is about 35 nm rms, and the minimum lateral feature (segment) size which can be fabricated is about 5 μm.

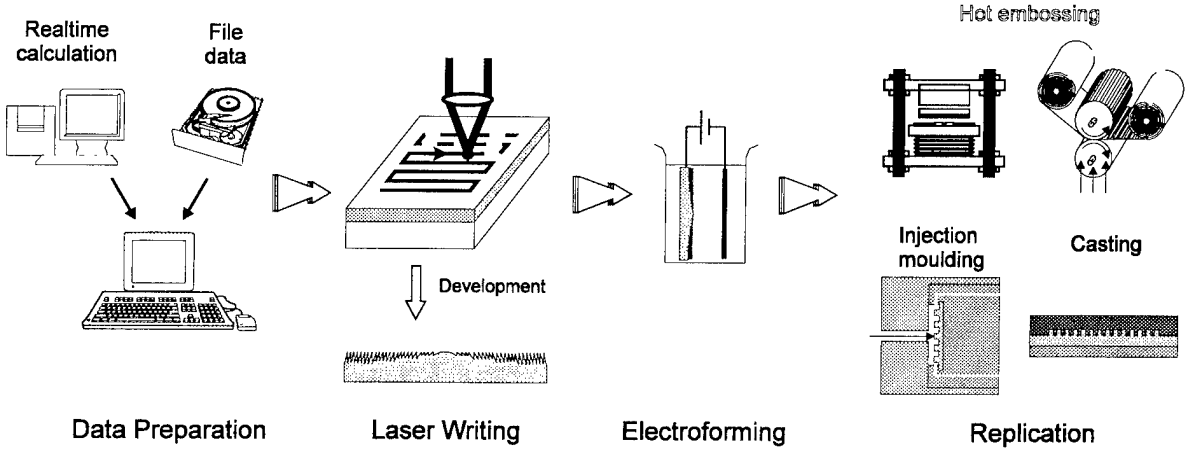


Fig. 1. Essential steps in the production of planar micro-optical elements - design and data preparation, laser writing, electroforming and replication.

• **Fabrication constraints**

There are three main types of fabrication constraints:

a) Positioning errors in the raster scan leading to surface roughness

The dynamic positioning accuracy of the xy-stage is crucial for the optical performance of the fabricated elements. Since the exposure is generated by overlapping Gaussian beams, a modulation in the profile with a grating period of the interscan distance is created. The amplitude is small if the overlap of the Gaussian beams is optimal [2]. If the interscan distance varies however, this modulation can become significant and the resulting grating structure leads to stray light and a reduction in the optical efficiency of the element. The line straightness and separation must thus be controlled as well as possible and the writing spot size for a specific element is chosen as large as possible.

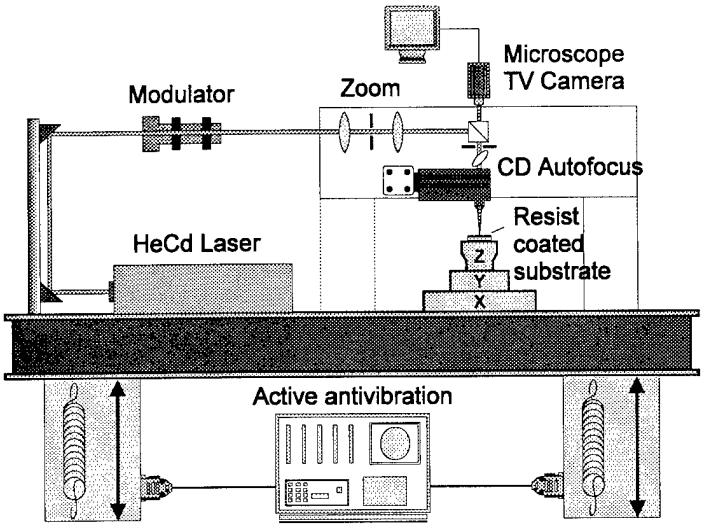


Fig. 2: Schematic of the new laser writing system currently being installed at PSI.

b) Limited resolution due to finite writing spot size

The finite writing spot size (Fig. 3a) leads to limitations in the maximum slope (Fig. 3b) which can be fabricated in the surface relief and thus to straylight in unwanted diffraction orders and an efficiency reduction in the fabricated elements. This has been investigated by writing blazed grating structures of varying periodicity and measuring the profile and diffraction efficiency (Fig. 3c). For a focused spot size (FWHM) of about 1 μm and the same interline distance, the diffraction efficiency in the current (2nd generation) writing system starts decreasing significantly for grating periods $\Lambda < 7$ μm. Reducing the focused spot size and interline spacing leads to longer writing times and increased straylight resulting form the line positioning errors.

This effect limits the minimum feature size which can be fabricated in practice and thus also the maximum lenslet Numerical Aperture (NA). It can be alleviated by using thicker resist films for fabricating deeper lenslets with larger phase steps and segment sizes.

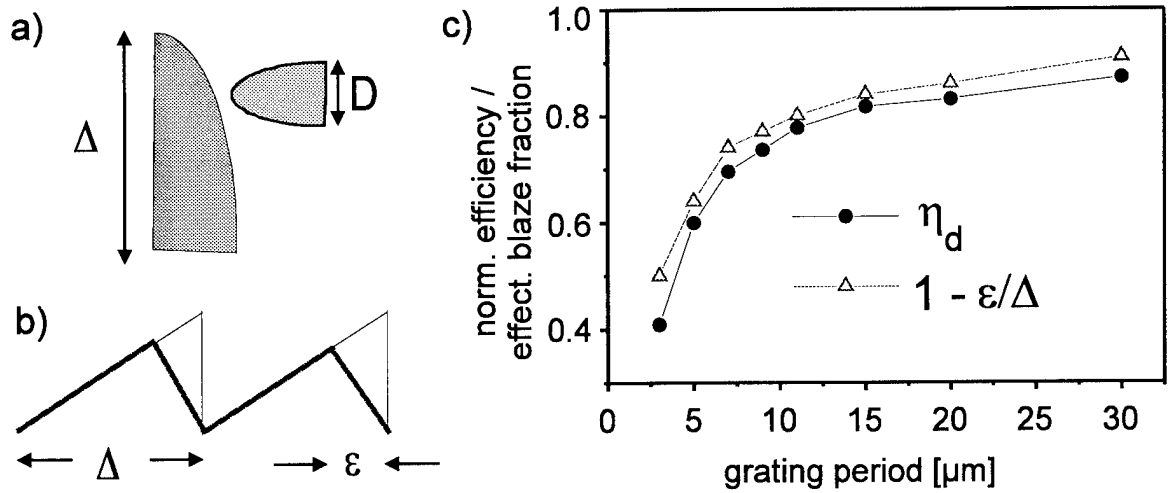


Fig. 3 Effect of finite writing spot size:
a) Writing spot diameter D and segment width Δ; b) blaze fraction (1-ε/Δ);
c) measured blaze fraction and diffraction efficiency as a function of the grating period.

c) Control of the depth in the development of the exposed photoresist

Errors in the depth of fabricated lenslets have different influences depending upon the lens design:

- for purely refractive lenslets, a focus shift results, but the efficiency is not significantly affected.
- for lenslets consisting of several Fresnel zones, the focus position is less strongly affected but the efficiency in this focus decreases in favour of additional foci.
- for deep Fresnel lenses, the sensitivity to depth scaling errors increases.

These effects are discussed in more detail in Ref. 2 and 3. The appropriate lens design must be chosen according to the application requirements. The optical efficiency of microlenses fabricated at PSI varies in practice between about 60 % and 95 %, depending upon the element feature sizes. These limitations in efficiency and straylight are outweighed in many applications by the advantages of a very flexible design and low cost replication in plastic material.

4. Replication technology

The physical copying of surface-relief microstructure by replication techniques such as hot embossing, moulding and casting is expected to become a key technology for the low-cost, mass-production of micro-optical elements with micrometer or nanometer sized features. These replication processes are capable of achieving nanometer resolution over large areas and the cost of replicated microstructure is relatively independent of the complexity of the detailed structure. Replication technology is already used for the commercial production of submicron grating structure (hot embossed diffractive foil and security holograms) and data storage microstructure (injection moulded Compact Discs).

Fig. 4 shows Ni shims and micro-optical structures replicated by embossing and moulding technologies. Measurements on replicated elements show that the increased surface roughness introduced by the replication process can be held to 1 or 2 nanometers for optimised replication technology. The commercial replication of microoptical elements requires further development to routinely handle the deeper and finer microstructures typical for elements such as refractive and diffractive microlenses, binary optics and other phase DOEs.

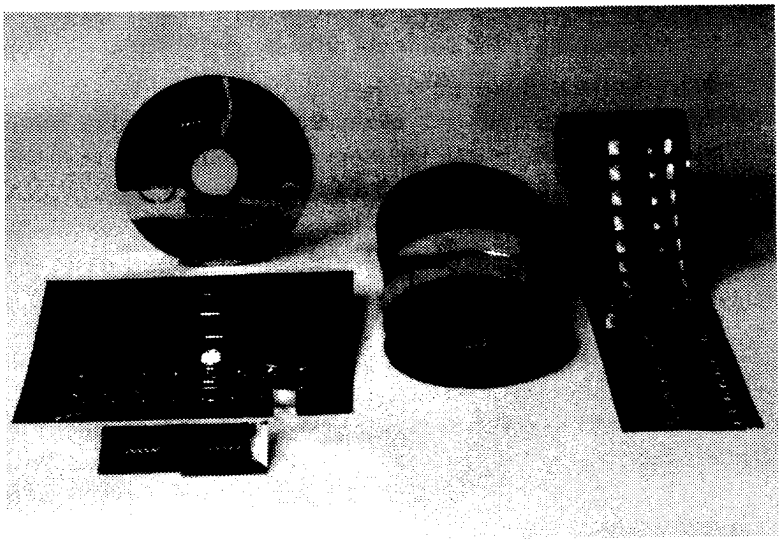


Fig. 4 Test replicas of micro-optical structures:
Ni shims (left) and replicated microstructure (right)

Work is underway together with commercial replication houses to assess the performance of standard and modified replication technology for various types of micro-optical elements. The major replication techniques, illustrated in Fig. 1. can be summarised as:

Hot embossing

Stamping, roller and reciprocating systems are routinely used for reproducing diffractive optical microstructures such as holograms and submicron grating patterns for diffractive foil [2]. Commercial roll embossing systems achieve embossing speeds of up to 1 m/s in polymer foil of up to 2 m width. Typical polymers include PVC and PC (polycarbonate); for fabricating reflective elements, they are often precoated with a thin metal film. Typical costs for hot embossed foil are below \$0.001 / cm^2. Although commercial roller systems are fully capable of submicron resolution, microstructure with relief amplitudes in excess of about 1 µm present considerable problems. Best results for deeper microstructures have been obtained using a reciprocating or stamping hot press.

Injection moulding

Injection moulding is standard replication technology for fabricating CDs and is now being investigated for applications in micro-optics. Injection moulded replicas are of higher cost than those fabricated by hot embossing (typical CD fabrication costs are ~\$0.01 / cm^2), but the technology has the potential of producing higher quality, deeper microrelief structures in stable, thick (>1 mm) PMMA or PC substrates. Initial tests have shown that the reproduction of high aspect ratio (>1:1) microstructure presents problems for the standard CD moulding process. Further work is underway.

Casting

Casting techniques have long been used for producing very high fidelity replicated spectroscopic gratings in epoxy materials. Of particular interest is the replication into a thin film of uv-curable material coated onto a rigid substrate such as glass, or using a roller press to replicate into a uv-curable film on a plastic substrate film, with rapid curing at the contact stage or shortly afterwards ('uv-embossing'). This technology is particularly suited to the replication of deep or high aspect-ratio microstructures. Micro-optical elements are routinely fabricated at PSI using this technology and tests at a commercial uv-embossing house are underway.

4. Examples of fabricated micro-optical elements

Micro-optical elements for a variety of applications have been produced using the PSI laser writing system and replication technology. The elements cover a wide spectrum from very low (0.01) to high (> 0.5) numerical aperture (NA) Fresnel lenslets and lenslet arrays for applications such as wavefront testing, laser diode to fibre coupling, optical computing and confocal microscopy. Two examples are the following:

• Microlens arrays for confocal microscopy

Lenslet arrays with a high uniformity of the focal length for applications in confocal microscopy [4] have been fabricated and evaluated in collaboration with the 'Institut für Technische Optik', University of Stuttgart, Germany. The arrays consisted of 200 by 200 microlenses (each 150 μm x 150 μm in size) with a focal length of 250 μm (NA = 0.28), designed for a wavelength of $\lambda = 780$ nm. The lenslet performance is dominantly diffractive, with the measured focal lengths lying within ± 200 nm of the mean value of 250 μm, with a mean deviation of $\sigma = 90$ nm.

• Deep Fresnel lenses

Lenslets with a deep profile (>10 μm relief) were fabricated by direct laser writing in a thick photoresist film. Such lenslets are of interest for applications in white light micro-optical systems, the aim being to combine the advantages of planar microstructures (compact, lightweight, mass-production by replication) with achromatic or broad-band optical behaviour.

5. Acknowledgements

The authors gratefully acknowledge the contributions of H. Schütz, J. Pedersen and R. Stutz of PSI in the laser writing system and replication technology, and H.J. Tiziani and R. Achi of the "Institut für Technische Optik" at the University of Stuttgart, Germany for the characterisation data on the arrays for confocal microscopy. This work was supported in part by the Swiss Priority Program OPTIQUE.

References

[1] M.T. Gale, M. Rossi, J. Pedersen and H. Schütz, "Fabrication of continuous-relief microoptical elements by direct laser writing in photoresist", Opt. Eng. **33**, 3556-3566 (1994).

[2] M.T. Gale, "Direct writing of continuous-relief micro-optics" and "Replication", in *MICRO-OPTICS*, H.P. Herzig (Ed.), Taylor and Francis (publication mid 1996).

[3] M. Rossi, R.E. Kunz and H.P. Herzig, "Refractive and diffractive properties of planar micro-optical elements", Appl. Opt. **34**, 5996-6007 (1995).

[4] Th. Hessler, M.T. Gale, M. Rossi, and R.E. Kunz, "Fabrication of Fresnel microlens arrays by direct laser writing in photoresist", EOS Topical Meeting Digest Series : Vol. 5, MICROLENS ARRAYS (NPL, London, 11-12 May 1995), ISSN 1167-5357, pp. 37-43 (1995)

Replication of continuous-relief diffractive optical elements by conventional CD injection molding techniques

Fredrik Nikolajeff, Anna-Karin Holmér, Stellan Jacobsson and Sverker Hård
Dep. of Microwave Techn., Chalmers Univ. of Techn., S-412 96 Göteborg, Sweden
Phone: +46 - 31 7721892 Fax: +46 - 31 164513 email: fredrik@ep.chalmers.se

Åke Billman, Lars Lundbladh and Curt Lindell
Toolex Alpha, Box 1176, S-172 24 Sundbyberg, Sweden
Phone: +46 - 8 289030 Fax: +46 - 8 289532

Introduction

Diffractive optical elements (DOEs) are realized either as continuous surface-relief microstructures (e.g. by direct-write electron beam lithography or direct laser writing) or as binary or multilevel reliefs (mostly using semiconductor fabrication technology). In general, the optical performance (especially efficiency) of continuous-reliefs is superior to that of their binary counterparts. One very important feature of DOEs is their ability to be replicated using techniques such as embossing, casting or molding[1]. Although the manufacture cost of one original DOE is relatively high, the piecewise cost is dramatically reduced when large series of one specific DOE is wanted (e.g. in telecommunication). A method particularly well suited for massproduction of DOEs is injection molding[2,3]. We will describe the process of replicating continuous-relief DOEs by conventional CD injection molding, report on successfully replicated DOEs and discuss the fidelity of the process.

Experiments and results

Two typical continuous-relief DOEs, a linear blazed grating and a fan-out element, were chosen as test structures. The blazed grating had a period of 20 μm. The 3x3 fan-out element, with a periodicity of about 18 μm, was iteratively calculated using a modified Gerchberg-Saxton phase-retrieval algorithm without any quantization of the phase. Direct-write electron beam lithography (system JEOL JBX-5DII) was used to fabricate original elements. A circular (98 mm diameter) quartz substrate with a 10 nm layer of Cr was spin-coated with positive electron-resist SAL 110-PL1 (Shipley) to a resist thickness of 2.8 μm. The layout of the DOEs on the substrate had to be made considering the chosen molding process. In the e-beam exposure we used an acceleration voltage of 50 kV with a beam current of 5.0 nA. The number of exposure doses was 64 and these were compensated for the proximity effect. Successive development in SAL-101 (Shipley) developer followed. A total development time of 10 minutes resulted in relief depths of about 1 μm. To sustain the high pressure and temperature in the mold process a copy of the original micro-structure in form of a stamper has to be made. The first step in this process is to form a conductive coating on the resist surface. We sputtered a 100 nm Au-layer. A first-generation Ni master can then be produced by electroplating Ni. The plating was done using a commercial Toolex Alpha optical disc plating system (Toolex P 250). A Ni-thickness of 300 μm was obtained after 3 hours plating. The plating current was

ramped from 0.5 A to 15 A. The Ni copy was easily separated from the original resist micro-structure by merely "knocking" on the backside of the quartz substrate. The resist micro-structure is then destroyed and some of the resist may stick to the Ni master. Plasma etching in oxygen of the Ni master was used to remove any remaining resist. The backside of the Ni master has to be very flat, otherwise the high pressure in the mold will destroy the master. The standard technique of lapping was done using a Toolex PML-300 Lapping machine. The Ni stamper was inserted into a Toolex MD 100 Injection Molding machine. This is a commercial machine which is built with extreme high precision for massproduction of optical discs of various formats. Using the process data shown in Table 1, several thousand DOE replicas have successfully been molded.

Material	Pressure	Injection temp.	Tool temp.	Cycle time
Polycarbonate (T_g = 155° C)	6 MPa	360° C	120° C	≈ 10 sec.

Table 1. Mold data using a Toolex MD 100 Injection Molding machine to replicate continuous-relief DOEs.

Original and replicated DOEs were characterized by optical measurements and AFM. The diffraction efficiency (defined as the measured intensity in one order divided by the sum of the intensities in all the measurable orders) in the first order was measured to be 90 % for the original blazed grating and 94 % for the replicated ones. The diffraction efficiencies differ between the original and replicated gratings which is to be expected due to the difference in indices of refraction of electron-resist (n=1.54) and polycarbonate (n=1.58). Assuming a perfect blazed structure and with the use of scalar diffraction theory, the diffraction efficiency of the original grating would predict a diffraction efficiency of the replicated grating of 96.5 %. That the actual value is lower indicates that the manufactured grating deviates slightly from the ideal blazed shape. In Figure 1 AFM measurements of both original and replicated gratings are shown.

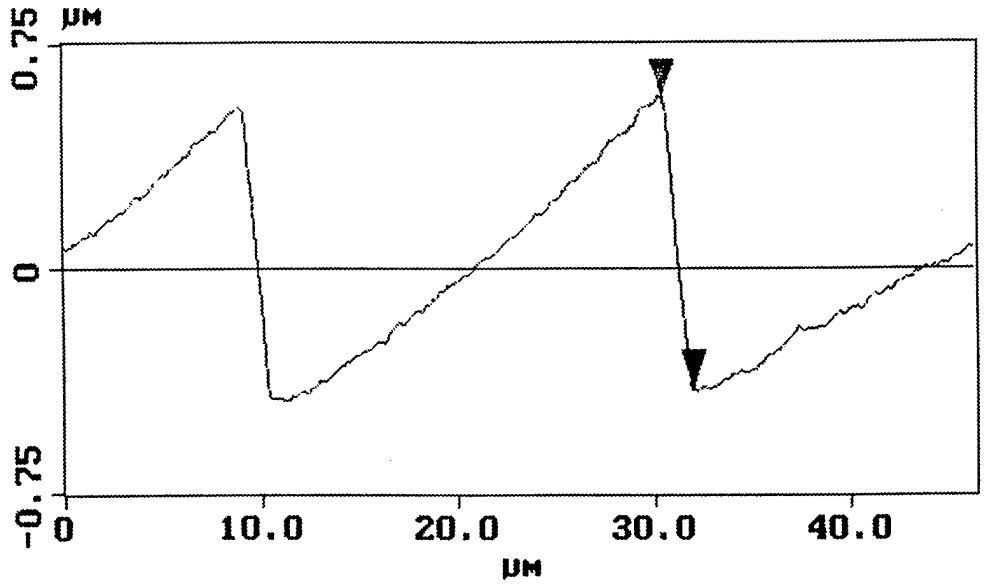


Fig. 1 (a) AFM measurement of linear blazed grating fabricated by e-beam lithograhy. Grating period: 20 µm. Measured relief height: 966 nm.

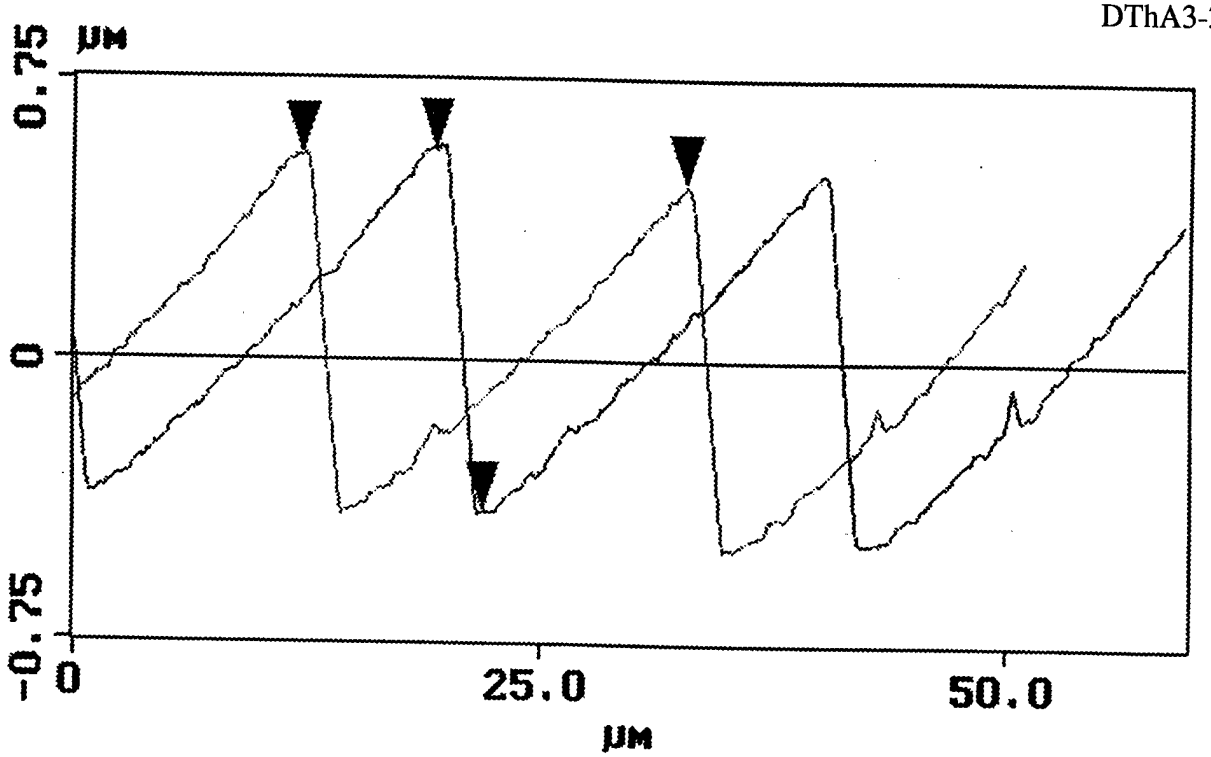


Fig. 1 (b) AFM measurement of grating replicated by injection molding. Measured relief height: 968 nm.

Although it is very difficult to measure exactly the same area on original and replicated gratings, the scans show very nearly identical profiles. Therefore we conclude that, for the dimensions used, the molded replicas have little degradation by shrinkage. The replicated fan-out element was measured to have a diffraction efficiency of 83 % and uniformity error of 16 %. These values are actually very close to the ones we could predict by taking into account the deviation between actual and optimal relief height for the laser wavelength used. However, this test did not aim to optimize the optical performance of the replicated DOEs, but rather investigate the fidelity of the replication process. We intend to further discuss injection molding for high aspect ratio DOEs. We will also demonstrate commercial CDs with different diffractive structures.

References

1. F. P. Shvartsman, "Replication of diffractive optics", Critical Reviews of Optical Science and Technology, Vol. **CR49**, 165-186 (1993)

2. R. D. Te Kolste, W. H. Welch and M. R. Feldman, "Injection molding for diffractive optics", Proc. SPIE, Vol. **2404**, 129-131 (1995)

3. H.-J. Rostalski, A. Mitreiter, J. Guhr, M. Schmidt, F. Wyrowski and H. Mischke, "Replication of diffractive optics by injection moulding", Proc. Workshop on Diffractive Optics, Prague 21-23 August 1995, 38-39

Diamond Turning and Replication of High-Efficiency Diffractive Optical Elements

C. G. Blough, S. K. Mack, R. L. Michaels, M. Rossi
Rochester Photonics Corporation, 330 Clay Road, Rochester, New York 14623
Phone (716) 272-3010, Fax (716) 272-9374, e-mail: rpc@eznet.net

1. Introduction

Diffractive optical elements can provide a significant advantage in the design of many optical systems that require aspheric or chromatic correction. For high-numerical aperture systems that have tight size and weight constraints, a diffractive element can often provide the necessary leverage to obtain a suitable optical design. For extremely narrow wavelength applications, a diffractive singlet can be used to produce the desired aspheric wavefront; however, for large wavelength range applications the diffractive asphericity must be tempered to reduce spherochromatism. The unique dispersion characteristics of diffractive surfaces provide the ability to correct primary or secondary chromatic aberrations.[1,2] Recent literature has shown that there are numerous potential optical designs that could benefit from the application of diffractive optical elements.[3] The main impediments that inhibit system engineers from manufacturing more optical designs containing diffractive elements is uncertainty about predicted performance and cost. We have developed manufacturing techniques that utilize the accurate machining potential of single-point diamond turning (SPDT) to generate robust metal master surfaces suitable for replication. By utilizing several replication techniques, a variety of different optical component configurations can be efficiently manufactured to provide exceptional wavefront performance and high diffraction efficiency.

In the presented paper, important aspects of SPDT high-efficiency diffractive surfaces are outlined. A brief description of replication techniques and special tooling and fixturing requirements needed to replicate hybrid components is also addressed. Diffraction efficiency measurement results are presented for several replicated diffractive surfaces with wavelength to minimum zone width ratios approaching 0.25, (*i.e.*, a F/2 diffractive lens). Broad guidelines are presented for expected diffraction efficiency values as a function of minimum zone width.

2. Single-Point Diamond Turning and Replication Techniques

Diffractive optical elements are typically manufactured using microlithographic techniques, which produce binary optics, or single-point writing techniques such as laser pattern generation and SPDT, which produce continuous blaze structures or kinoforms.[4] Each fabrication technique has its niche applications depending on the particular component requirements. SPDT provides an exceptional method for generating rotationally symmetric metal diffractive surfaces for use in replication processes.[5] In addition, SPDT techniques are widely used to manufacture diffractive surfaces for infrared applications.[6]

2.1 Single-Point Diamond Turning Diffractive Surfaces

SPDT is a mature technology that utilizes fluid bearings and slides to obtain the rigid motion control necessary to achieve nanometer precision during machining processes. A gem-quality diamond tool provides the extremely sharp and smooth cutting surface necessary to produce optical-quality surfaces. A typical diamond tool has a cutting point, which has a nose radius to provide minimal machining crossfeed artifacts. The tool radius is usually selected to be as large as the fabricated surface slope will allow.

For diffractive surfaces, which are discontinuous, the normal tool design often must be drastically modified to provide high diffraction efficiency. The maximum diamond tool radius is dictated by the minimum zone width and/or the maximum sum of the local blaze angle and local surface slope. One of the most sensitive fabrication errors for diffractive surfaces is the side wall of the zone transition step height. If the tool radius can be selected to be small, the effects of the side wall can be minimized. However, a typically more effective approach is to have the diamond tool sculpted so that a vertical side wall can be generated. Since a diamond turned surface is essentially a replica of the cutting tool profile, the bottom of the zone transitions usually have a radius. The cutting tool nose radius provides the ability to achieve smooth zone profiles, which are important in reducing spurious scattered light. A typical SPDT diffractive surface has zone profile surface roughness of 40-50 Å rms. The ability to form smooth continuous blaze profiles and extremely steep zone transitions provides a distinct advantage for SPDT rotationally symmetric diffractive surfaces.

2.2 Replication of Diffractive Elements

Replication provides the ability to economically produce multiple diffractive elements with minimal tooling costs. The most critical step in the replication process is to start with a high fidelity master surface. As discussed above, an excellent technique for generating diffractive master surfaces is SPDT. Diamond turning provides the ability to produce a robust metal surface that can withstand multiple replication cycles. A metal that provides excellent surface finish and durability is electro-less nickel, which is typically plated onto a stainless steel plug. The plug can be precisely fabricated to provide important fixturing and jigging references.

We have developed several replication techniques that are selected according to the particular project constraints; predicted volumes, cost sensitivity, and opto-mechanical tolerances. The replication methods are variations of typical grating replication techniques. The first step generates a sub-master, which has the opposite profile of the master surface. Subsequent fabrication steps generate more sub-masters whose surface profiles alternate between being identical and opposite of the master surface. Although some diffraction efficiency loss occurs with each replication step, the total loss is typically less than a few percent over ten to twenty replication cycles. The life of a sub-master is usually limited by cosmetic defects that progressively occur during separation of the replicas. The replicated layer is usually thermal or UV cured epoxy.

In addition to being able to replicate high-fidelity zones, one must also be able to correctly align the diffractive surface to the substrate. This alignment capability is typically most important when replicating hybrid elements in which at least one surface is curved. A tolerance budget must be established that divides potential fabrication errors between the substrate and the replication process. The most common errors involve the ability to precisely align the substrate's and diffractive surface's opto-mechanical axes. Common potential error sources include substrate centration, diffractive pattern centration, and wedge in the epoxy layer. Other potential error sources that are typically less critical include transmitted wavefront specifications (*i.e.*, test plate fit requirements) and epoxy layer thickness control. Common ranges of tolerances for the replication process are 30" to 5' of wedge in the epoxy and 5 to 100 μm of pattern centration error. Several diffractive elements have been replicated that provide wavefront errors of a quarter to tenth wave at a wavelength of 0.6328 μm. In addition, many diffractive elements implemented in refractive lens systems have helped achieve diffraction-limited performance.

3. Results and Conclusions

The following section provides diffraction efficiency measurement results for several replicated diffractive elements. The efficiency measurements are all taken at the minimum zone width for the particular optic and represent the local diffraction efficiency. The integrated diffraction efficiency will be higher and is dependent upon the diameter of the optic and the illumination.

3.1 Diffraction Efficiency Measurements

A diffractive optical element can be treated as a linear blazed diffraction grating to model the predicted local diffraction efficiency as a function of zone width, Λ. Measured local diffraction efficiency results for several replicated lenses are shown in Fig. 1. The solid line shows the theoretical diffraction efficiency of zones as a function of the illumination wavelength λ divided by their width Λ. The reduction in efficiency for larger values of λ/Λ compared to the scalar theory predicted value of 100% is an effect that can be explained by rigorous vector analysis.[7] However, simple geometrical optical models can give an idea of the causes for this efficiency reduction and lead to quite accurate estimations. Scalar design methods treat the diffractive structure as an infinitely thin layer, an assumption that is no longer valid for small zone sizes. A ray tracing algorithm, also referred to as "extended scalar theory", uses a combination of geometrical optics in the grating region and scalar diffraction in the image space.[8] The loss in efficiency can be explained as a "shadowing effect" resulting from the finite height of the zone profile. Recent work has shown that for continuous-blaze structures, the predicted loss in efficiency is estimated by calculating the "shadowing effect" of the particular grating.[9] This result is significant because binary diffractive structures suffer a loss in efficiency proportional to the square of the "shadowing effect".

The measured efficiency results are not compensated for fabrication errors. In addition, all efficiencies have been measured at visible wavelengths. The degradation increases with the wavelength to period ratio because the relative fabrication errors become progressively larger for smaller zone periods. The last data point, 64% efficiency, results from a diffractive surface that was not properly compensated for optimum grating height at small zone periods. The actual measured and predicted efficiencies are within $\approx$5%. Figure 1 can be used to generate a general guideline for expected local efficiency as a function of zone width: 95-98% for $\Lambda > 25$ μm and 85-95% for 25 μm $< \Lambda <$ 5 μm. Integrated efficiency will be higher, although it is strongly dependent on the illumination.

4. Conclusions

By combining SPDT techniques to fabricate high-fidelity master surfaces and precision replication techniques, diffractive elements of exceptional performance have been manufactured. A general guideline for expected local diffraction effciency as a function of zone width has been presented. Future work as well as that outlined above will be presented during the presentation.

5. References

[1]T. Stone, N. George, "Hybrid diffractive-refractive lenses and achromats," Appl. Opt. **27**, 2960 (1988).

[2]Apochromatic Hybrid Doublets, Melles Griot Corporation, Irvine, CA.

[3]See for example; D. Stephenson, "Diffractive optical elements simplify scanning systems", LFW, 75 (6/95); J. S. Anderson, C. W. Chen, R. A. Spande, "Thermal weapon sight (TWS) AN/PAS-13 diffractive optics designed for producibility'", NASA Conf. Pub. **3227**, 303 (93); C. J. Shackleford, X. Ning, "Design of plastic diffractive/refractive hybrid lenses for CCD cameras", Proc. SPIE 2600-16, (95).

[4]P. P. Clark and C. Londono, "Production of kinoforms by single point diamond machining", Opt. News, 39 (12/89).

[5]C. G. Blough, *et al*, "High-efficiency replicated diffractive optics", Proc. SPIE **2600**-015, (95).

[6]M. J. Riedl, "Predesign of diamond turned refractive/diffractive elements for IR objectives", Proc. SPIE **CR41**, 140 (92); A. P. Wood, "A hybrid refractive-diffractive lens for manufacturing by diamond turning", Proc. SPIE **1573**, 122 (91).

[7]E. Noponen, J. Turunen, A. Vasara, "Parametric optimization of multilevel diffractive optical elements by electromagnetic theory", Appl. Opt. **31**, 5910, (92).

[8]G.J. Swanson, "Binary optics technology: theoretical limits on the diffraction efficiency of multilevel diffractive optical elements," MIT Technical Report **914** , (1991).

[9]Submitted to OSA Spring Topical Meeting 1996; M. Rossi, *et al*, "Diffraction efficiency of high-NA continuous-relief diffractive lenses".

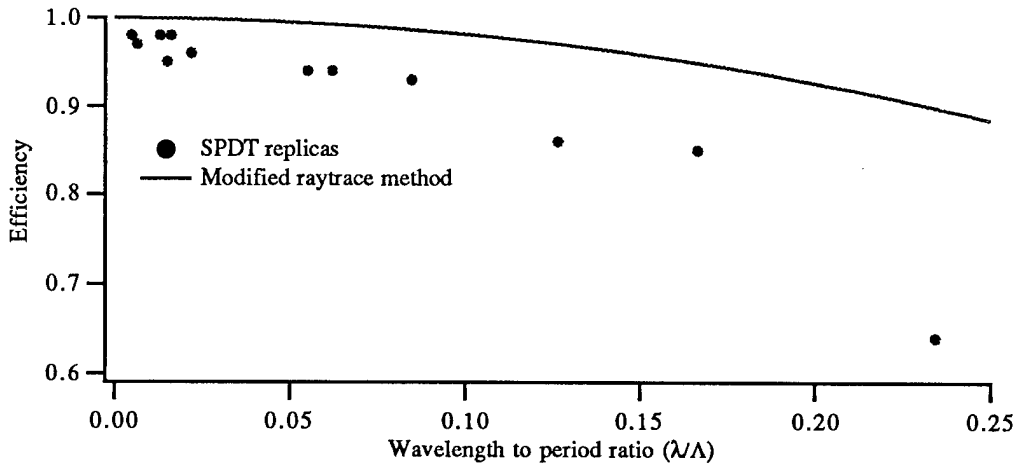


Fig. 1. A graph of measured local diffraction efficiency values and predicted theoretical performance versus wavelength to zone width ratio.

Replication process with a 3D-amplitude/phase mask

Edgar Pawlowski

Heinrich-Hertz-Institut für Nachrichtentechnik Berlin GmbH
Einsteinufer 37, 10587 Berlin, Germany
Tel. +49 30 31002-489, Fax. -213 , pawlowski@hhi.de

1. Introduction

In the last years the interest in low-cost production techniques for integrated optics and diffractive optical elements (DOEs) has rapidly grown. Different methods like embossing, moulding and casting were reported [1,2,3,4]. This technologies are well established for the production of submicron grating structures, like moulded CDs and hot embossed holograms. However, all this methods are not suitable for materials like glasses (e.g. silica) or semiconductors (e.g. InP, GaAs). In order to overcome this problem, grayscale and halftone masks with different gray levels were proposed, were a serie of gray levels corresponds, after a optical lithography process, to different resist depths [5,6]. These structures were finally transferred by dry etching processes to the substrate material. In this paper we present a new 3D-structure replication technique for this wide range of optical and semiconductor materials and for high structure depths. Deep microrelief structures up to 10 μm or more and structures with very high lateral resolution (< 200 nm) can be replicated. Due to the 3D-amplitude/phase mask it is possible to suppress edge ringing by means of modulating the amplitude and the phase of the light. The fabrication process of the mask is based on repeated multi-steps of photolithographic and ion-beam-sputter-deposition techniques. An in situ monitoring system is used to control the optical thickness and the transmission of the mask structures.

2. 3D-replication process

The replication process is based on a single optical lithography step with a 3D-amplitude/phase mask and subsequent dry etching process (Fig.1). The mask consists of transparent and absorptive 3D-structured multilayers (TiO_2 or Si_XO_y). The absorption is controlled by changing the thickness and the O_2-concentration during the ion-beam-sputter-deposition process. More flexible parameters can be obtained by using different exposure wavelengths during the lithography process. The complete DOE-fabrication procedure consists of different stages. First, the 3D-amplitude/phase mask is designed and fabricated. The calculation of the mask data is based on the scalar diffraction theory, on the theory

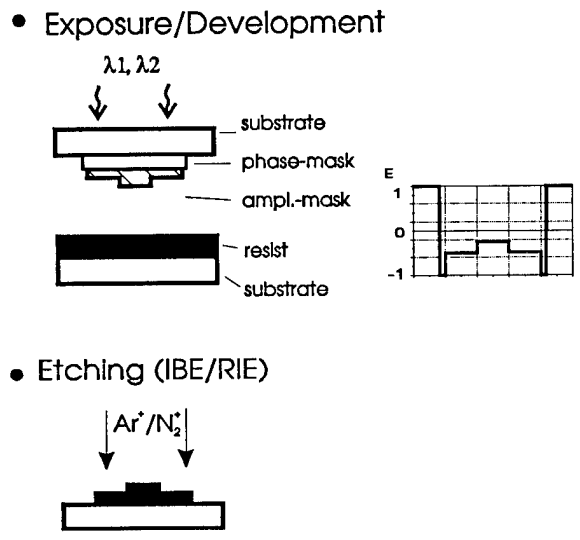


Fig. 1 Replication procedure

of the characteristic matrices [7], optical measurements of the thin film layers, the contrast curves of the resist and the knowledge of the selectivity between the thin film material and substrate during the dry etching process. Second, the image of the 3D-amplitude/phase mask is transferred by optical lithography into the resist and the resist is developed. Finally, the resist patterns are transferred by dry etching techniques into the substrate and the resist is removed.

2.1. Fabrication of the 3D-amplitude/phase mask

The mask can be generated by different microstructuring techniques like e-beam writing, laser beam or ion-beam lithography or the well known binary fabrication techniques. For simple processing, we fabricated the masks by photolithographic processing techniques and thin-film deposition. The masks were fabricated with the aid of computer generated masks (written by electron beam) and with photolithographic and ion-beam-sputter-deposition (IBSD) techniques [8,9]. The optical thickness was controlled by an in situ Reflection-Wideband-Monitoring-System (RWMS) with high accuracy (<0.1%). Different mask-substrate materials (e.g. quartz-glass, BK7 glass) were tested, but due to the high transmission in the UV-region, we used finally quartz-glass for our experiments. Different stages for recording a multi-level amplitude/phase mask were necessary. First, the substrate was cleaned, coated with resist (AZ 5214/5218) and prebaked. Second, the pattern from an e-beam written mask was transferred into the resist (image reversal) by optical contact lithography. This involves exposure and reversal baking (120°). The alignment and exposure was carried out on a mask aligner (Süss MA 100M) at the wavelength of 313 nm. Third, a layer of TiO_2 or Si_xOy was sputtered onto the substrate by ion-beam-sputter-deposition techniques and finally the photoresist is removed with acetone and stripper. For the fabrication process of 8-level 3D-amplitude/phase masks, the lithography- and coating process was repeated two times with two additional masks. To ensure proper overlay between the various masks, we used diffractive alignment marks and conventional alignment marks as common in microelectronics technology. Fig.2a shows the transmittance of the mask material Si_xO_y in dependence of the thickness and the wavelength. The transmittance curve can be separated into two different regions. In the absorption region ($\lambda_a < \lambda s$), where the mask acts as a amplitude mask and in the transmission region ($\lambda_t > \lambda s$), where the mask acts as a phase mask. Both wavelength regions can be utilized during the same exposure process, by using two or more different exposure wavelengths.

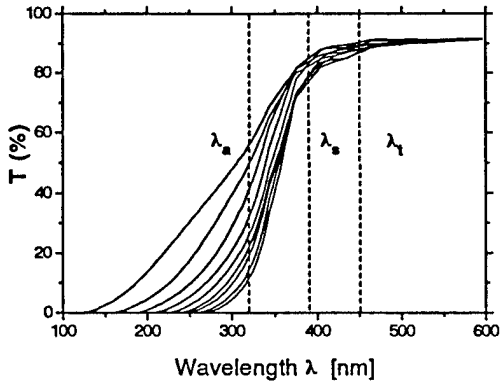


Fig.2a Transmittance of Si_xOy-layers

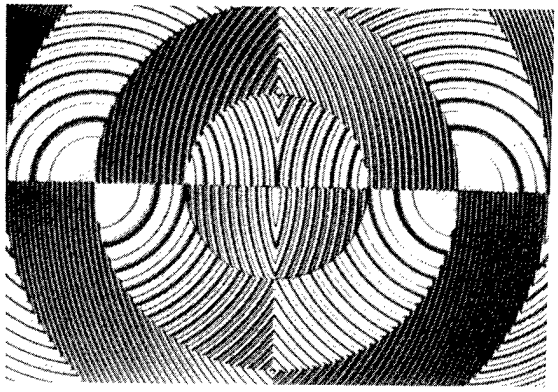


Fig. 2b 3D-amplitude/phase mask

The exposure times must be adjust independently for both wavelengths. Fig. 2b shows a photograph from the central region of a fabricated 3D-amplitude/phase mask. Due to the strong absorption in the visible wavelength region, each phase step is colour encoded.

2.2 Fabrication of DOEs

In order to elucidate the photolithography process, we varied the most important parameters like exposure dose and development time. Figure 3a shows standard contrast curves of the resist AZ 5214 for different development times. The obtained resist patterns after the exposure and development process is shown in figure 3b. The eight individual levels can be seen clearly. It should be noted, that alignment and linewidth errors, which cause significant diffraction efficiency degradation, could not be observed. The replication of the resist mask into the substrate material is realized by IBE with N_2^+-ions (for e.g. InP-substrates) and Ar^+-ions (for e.g. SiO_2-substrates) accelerated to an energy of 700 eV. The structure depth is defined by the etch selectivity between resist and substrate material and can be monitored by in situ mass spectrometry. The measured rms roughness of the replicated structures was smaller than 3 nm.

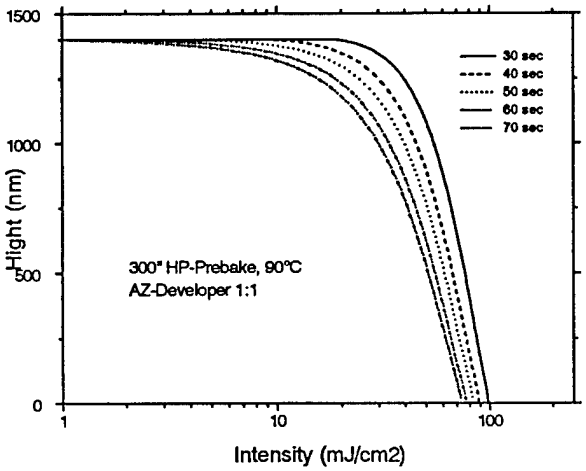


Fig.3a Contrast curves of the AZ5214 resist for different development times

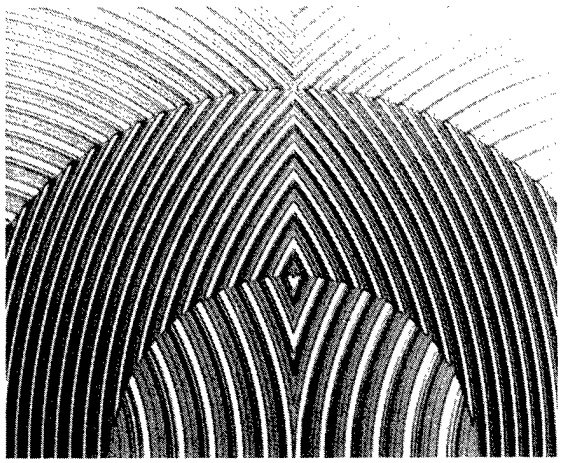


Fig. 3b Photograph of resist patterns

3. Experimental results

We fabricated different DOEs with different apertures and optical functions in order to improve the replication process. The DOEs have different zones, where the phase profile in each zone is approximated by discrete multi-level stepped profiles (2-8 levels). The design of the DOEs is based on the scalar diffraction theory and the use of a raytracing program, where the DOE phase function was determined by a simple optimization procedure. The smallest lateral structure dimensions of these elements are about 0.4 μm. Figure 4a shows a photograph of an etched DOE and figure 4b the measured and calculated intensity distribution in the focal plane. The experimental and theoretical results are in good agreement. More detailed results will be presented on the conference.

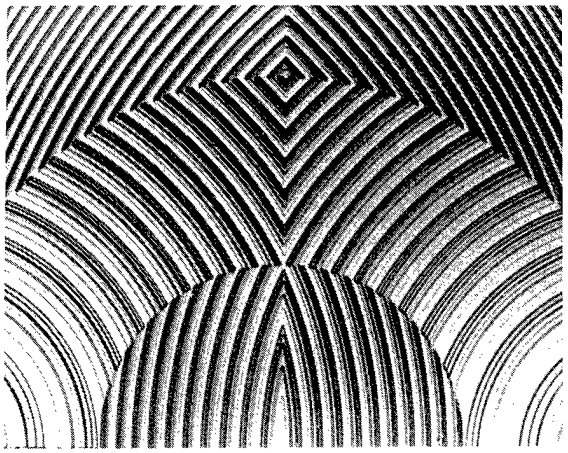


Fig.4a Replicated DOE

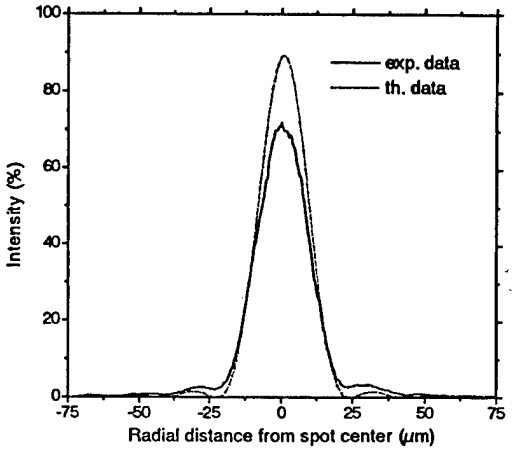


Fig. 4b Calculated and measured intensity distribution in the focal plane of a FZL at 0.63-μm wavelength.

4. Conclusions

To simplify the fabrication process of DOEs, we proposed a new replication process for 3D-structures. First experiments with 3D-amplitude/phase mask demonstrate, that our process is suitable for different optical materials and critical structure dimensions. This process enables the mass-production of DOEs. A further improvement of the DOE-efficiency and the structure resolution should be possible by reducing the fabrication errors with an in situ control of the development process, in order to come closer to the predicted values.

5. References

1. W. Lukosz and K. Tiegenthaler, Optics Lett. 8, 10, p. 537 (1983).
2. B. Kluepfel and F. Ross, Eds., Holography Market Place, Ross Books, Berkely CA, (1991).
3. M. T. Gale, Luca G. Baraldi, Rino E. Kunz, Replicated microstructures for integrated optics, SPIE. Vol 2213, pp.2-10, (1994).
4. H. P. Herzig, Diffractive microoptics in Swizerland, OSA, Ser. Vol. 11, pp.22-25, 1994
5. H. Andersson, et al., Single photomask, multilevel kinoforms in quartz and photoresist: manufacture and evaluation, Appl. Opt. 29, 4259 (1990).
6. D. C. O'Shea, P. L. Thompson, and W. S. Rockward, Grayscale masks for diffractive optics: I. Spatially filtered halftone screeens, OSA, Ser. Vol. 11, pp.119-122, (1994).
7. F. Abelés, Ann. Phys., Paris 12th series, 5 (1950).
8. E. Pawlowski, Thin film deposition: an alternative technique for the fabrication of binary optics with high efficiency, Proc. IEE **379**, pp. 54-59 (1993).
9. E. Pawlowski and B. Kuhlow, Antireflection-coated diffractive optical elements, Opt . Eng. 33(11),3537-3546 (1994).

Thursday, May 2, 1996

Applications II

DThB 10:30 am-12:00 m
Fairfax A

James R. Leger, *Presider*
University of Minnesota

Blazed Diffractive Optics

Madeleine B. Fleming

3M Optics Technology Center, 3M Center Bldg. 260-5A-11, St. Paul, MN 55144-1000
tel. 612-736-9287; fax 612-733-7091; e-mail mbfleming@mmm.com

Introduction

The diffractive optics community has embraced the lithographic methods used in the electronics industry[1]. Typically, binary transmission masks are used to expose resist and produce stepped structures which approximate the ideal, continuous profiles. Since these profiles are approximations of the ideal, continuous profiles, the diffraction efficiency is less than 100%: in theory, a four-level DOE has a first-order efficiency of 81%; an 8-level DOE, 95%[1]. Although the efficiency can be increased by increasing the number of levels and computer-based optimization, the process is limited by the resolutions of the binary masks and of the mask registration to the substrate.

In the meantime, with the advancement of suitable technologies, blazed diffractive optics have received renewed interest. More precise computer modeling of these elements has also been discussed in the literature[2, 3]. Blazed diffractive elements have smooth facets rather than the stepped facets of lithographic DOEs. (In this paper, we do not limit the discussion to kinoform lenses.) In theory, blazed elements with curved facets can be 100% efficient. In addition, the freedom from binary masks in the structure generation process offers other advantages. Single-point diamond turning, wedge-tool diamond turning, and laser-written photolithography are just three of several methods currently used to generate blazed diffractive elements.

Methods

Single-point diamond turning has long been used to generate refractive optical surfaces such as aspheres and flats that are difficult to make via conventional grinding and polishing methods. This method has also been used for diffractive elements[4]. Because of the residual scalloping of the surface (see Fig. 1), light scatter has been a limitation in their use at visible wavelengths. Single-point diamond turning has recently been brought from the infrared into the visible range with the exploitation of sol- gel shrinkage, which reduces the effect of the scalloping[5].

Wedge-tool diamond turning overcomes the scalloping problem by cutting with the edge of the diamond tool, as shown in Fig. 1, rather than with its tip. Although these diamond tools are more subject to wear than radius tools[6], the blazed surfaces they cut can be as smooth as the diamond

edge, within materials limitations. Although it is convenient to use opposite sides of the tool for opposite sides of the groove, this is not necessary; a diamond with a smaller included angle can be use to cut opposite groove faces, and the problem becomes one of precision engineering.

Laser writing in linear photoresist is used to generate arbitrary phase profiles, including blazed elements[7, 8]. By varying the laser intensity, one controls the exposure of the photoresist and thus the profile of the element. The continuous range of intensities eliminates the multilevel limitation imposed by binary mask lithography. Although the lateral resolution is still limited by the laser spot size, the non-uniform spot profile provides a smoothing of this lateral pixellization. Laser writing also has the advantage of allowing non-symmetric profiles. In contrast, diamond turning is limited to linear and circular patterns.

Advantages

In addition to increased efficiency, diffractive elements made by these methods have other advantages over multilevel elements. Diamond turning, for example, is not limited to flat base curves. Hybrid diffractive/refractive lenses are easily generated in a single mastering step. An example of a hybrid lens with a blazed diffractive element is the multifocal ophthalmic lens[9]. This lens, either as a contact lens or an intraocular lens, has a diffractive element with a half-integer wavelength step height, which distributes the light nearly equally between two focal spots, and a curved base, which allows chromatic correction. Another advantage of the blazed element in this application is the reduction in the number of corners and edges on the surface, which could accumulate debris or cause corneal damage, especially as a contact lens[10].

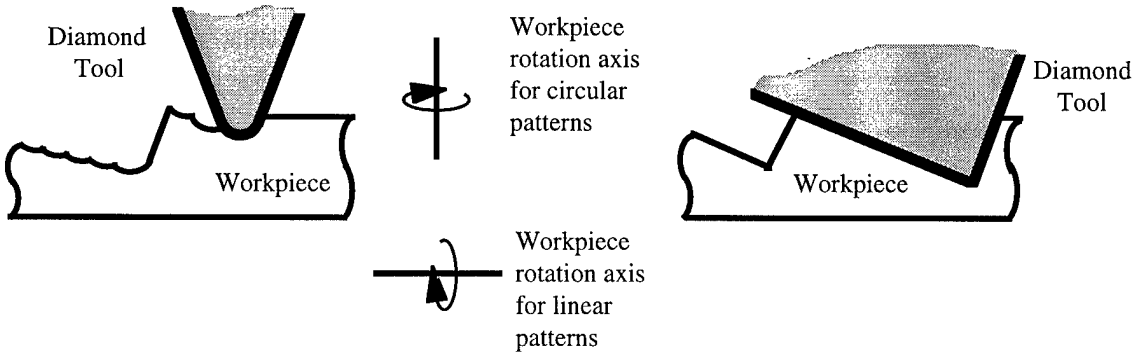


Figure 1. Cross-sectional view of diamond turning configurations. (Left) In single-point turning, a diamond tool with a radius tip is translated incrementally to cut the desired profile as the workpiece spins. The shape of the tool tip can be seen in the turned workpiece as surface scalloping. (Right) In wedge-tool diamond turning, the workpiece is rotated as for single-point diamond turning, but the translation steps of the tool cover the full groove, and the edge of the diamond is used to cut the workpiece.

The step heights of a multilevel diffractive element are chosen to suit a particular design wavelength. These levels are usually the same across the entire element. All the lenslets in an array made from a given set of masks, then, would need to operate at the same wavelength for peak performance. With blazed optics, elements in the same array can easily have different design wavelengths. This can be advantageous in display technology, where red, green, and blue pixels are often treated separately by the associated optics.

It is commonly known that, in a conventional diffractive lens, the zone spacing decreases as the radial position increases. For low F/# lenses, these outer zones can be difficult to generate due to the high resolution that is needed. Once the multi-level restriction is eased, however, the outer zone width can be increased by proportionately increasing the groove depth, as shown in Fig. 2. Such elements have been called superzones[11], higher-order kinoforms[12], and phase-matched Fresnels[13] by separate authors.

Conclusion

Blazed diffractive elements can now be produced by several different methods. These methods have some advantages over multistep diffractive elements, including increased DOE efficiency, non-zero base curvature, multiple-wavelength array capability, and small F/# compatibility.

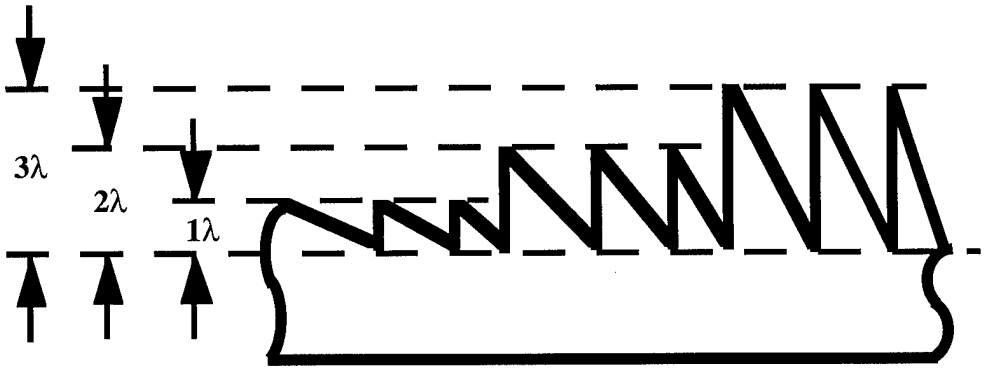


Figure 2. Segment of a superzone diffractive lens. The typical diffractive lens has zones of constant depth and decreasing width as the zone radius increases. On a superzone lens, the groove depth is an integer multiple of the standard depth and the grooves are wide enough to be generated easily.

References

1. G.J. Swanson, "Binary optics technology: the theory and design of multi-level diffractive optical elements," Technical Report 854 (Massachusetts Institute of Technology Lincoln Laboratory, 14 August 1989).

2. W.H. Southwell, "Ray tracing kinoform lens surfaces," Appl. Opt. **31**, 2244-2247 (1992).

3. L.N. Hazra, O. Filali Meknassi, and C.A. Delisle, "Zone characteristics of planar kinoform lenses of any specific order for stigmatic imaging between extra-axial conjugate points," J. Opt. Soc. Am. A **12**, 2463-2470 (Nov 1995).

4. P.P. Clark and C. Londoño, "Production of kinoforms by single-point diamond turning," Opt. News **15** (12), 39-40 (1989).

5. B. Bernacki, in *Optical Manufacturing and Testing*, Dougherty and Stahl, eds., Proc. Soc. Photo-Opt. Instrum. Eng. **2536**, 463-474 (1995).

6. M.M. Meyers and M.E. Schickler, "A method of manufacturing a diffractive surface profile," Patent application #WO 95/18392 (World Intellectual Property Organization, International Bureau, 9 July 1995).

7. C.G. Blough and G.M. Morris, "Diffractive/refractive lenses offer high performance at low cost," Laser Focus World, November 1995.

8. M.T. Gale, M. Rossi, J. Pedersen, and H. Schütz, "Fabrication of continuous-relief micro-optical elements by direct laser writing in photoresist," Opt. Eng. **33**, 3556-3566 (1994).

9. M.J. Simpson and J.A. Futhey, "Multi-focal diffractive ophthalmic lenses," US Patent #5,076,684, 31 Dec 1991.

10. J.A. Futhey, W.B. Isaacson, and R.L. Neby, "Multifocal diffractive lens," US Patent #4,830,481, 16 May 1989.

11. J.A. Futhey, "Diffractive lens," US Patent #4, 936, 666, 26 Jun 1990; J.A. Futhey, "Superzone holographic mirror,", US Patent #5,285,314, 8 Feb 1994.

12. J.C. Marron, D.K. Angell, and A.M. Tai, "Higher-order kinoforms," in *Computer and Optically Formed Holographic Optics* , I. Cindrich and S.H. Lee, eds., Proc. Soc. Photo-Opt. Instrum. Eng. **1211**, 62-66 (1990).

13. M. Rossi, G.L. Bona, and R.E. Kunz, "Phase-matched Fresnel," Opt. Commun. **97**, 6-10 (1993).

Multiple Order Delay Holograms for Polarization and Color Selectivity

Fang Xu, Rong-Chung Tyan, Joseph E. Ford*, and Yeshayahu Fainman
Department of Electrical and Computer Engineering
University of California, San Diego, La Jolla, CA 92093-0497
*AT&T Bell Laboratories
101 Crawfords Corner Rd., Holmdel, NJ 07730

Diffractive optical elements constructed as phase only computer generated holograms (CGHs) are attractive for numerous applications in photonics and optoelectronics. A conventional diffractive optical element (DOE) has a maximum phase delay of 2π between pixels. Therefore, the required etch depth is, in general, shallow (< wavelength λ, see Fig. 1a). These DOEs are relatively insensitive to the polarization and wavelength of the reconstruction field compared to volume gratings. Previously we demonstrated polarization selective diffractive optical elements using two birefringent $LiNbO_3$ substrates with different diffractive microstructures on the interior.[1,2] The required etch depths on both substrates are deeper than that in a conventional DOE because the substrates birefringence is relatively small (see Fig. 1b). Another approach to achieve the same functionality is based on deep etch structure (see Fig. 1c) that corresponds to multiple periods of phase delays (also called modular $2m\pi$) using a single birefringent substrate, as first proposed in reference 1 and later in reference 3. This approach may reduce the cost and simplify the fabrication process of such polarization selective diffractive optical elements. In the following we report the design, fabrication and characterization of multiple order delay (MOD) holograms that posses dual functionality in polarization or color.

To design a MOD hologram with dual impulse responses using single substrate, we use the geometrical optics approximation and find the corresponding phase delays caused by an etched pixel compared to that of an unetched pixel

$$\begin{aligned} k_1(n_1 - n_{t1})d &= 2l\pi + \Phi_1 \\ k_2(n_2 - n_{t2})d &= 2m\pi + \Phi_2 \end{aligned} \tag{1}$$

where $\Phi_1+2l\pi$ and $\Phi_2+2m\pi$ are the phase delays exhibited by the two independent optical reconstruction fields, d is etch depth of the pixel, k_1 and k_2 are the wavevectors of the two reconstruction fields, n_1 and n_2 are the refractive indices of the substrate for the two reconstruction fields, n_{t1} and n_{t2} are the refractive indices of the material surrounding the microstructure, and l and m are integers corresponding to the multiple periods of phase delays exhibited by the two fields. The two independent reconstruction fields can be of different wavelengths or of orthogonal linear polarizations. In general, Eqs. (1) does not have a unique accurate solution for d, if Φ_1 and Φ_2 are arbitrarily specified design values, unless the refractive indexes n_1 and n_2 can be controlled in every pixel of the diffractive element as in a form birefringent artificial dielectric nanostructures[4]. However, for our design with a homogeneous substrate characterized by constant values of n_1 and n_2, there exist only an approximate solutions for d when the values of integers l and m are arbitrarily large such that

$$\begin{aligned} k_1(n_1 - 1)d &= 2l\pi + \Phi_1 + \delta_1 \\ k_2(n_2 - 1)d &= 2m\pi + \Phi_2 + \delta_2 \end{aligned} \tag{2}$$

where δ_1 and δ_2 are small numbers representing the approximation errors and air is used for the medium surrounding the microstructure thus $n_{t2}=n_{t1}=1$. If δ_1 and δ_2 are much smaller than the value of the phase quantization level, this is a valid approximate solution to Eqs. (1). With this

approach, it is possible to design the two independent phase functions within some specified accuracy at each pixel. Therefore, independent multilevel phase holograms can be implemented for the two orthogonal polarizations or two different wavelengths. Solving Eq.(2) we find,

$$d = \frac{(2l\pi + \Phi_1 + \delta_1)\lambda_1}{2\pi(n_1 - 1)} = \frac{(2m\pi + \Phi_2 + \delta_2)\lambda_2}{2\pi(n_2 - 1)} \tag{3}$$

We used the above algorithm to design and demonstrate two types of MOD holograms with dual functionality. The first one is a polarization selective element made of a single birefringent yttrium orthovanadate (YVO_4) substrate and the second one is a wavelength selective element made of BK7. YVO_4 has large birefringence and can be relatively easy to process using microfabrication techniques. We used x-cut YVO_4 crystals grown by CASIX, Inc. The n_o=2.0241 and n_e=2.2600 of YVO_4 were determined at λ=0.5145 μm. Using Eqs. (2) and (3) with these values of refractive indices, we find all the possible combinations of Φ_1 and Φ_2 that are necessary for construction of a binary phase single substrate birefringent computer generated hologram (SSBCGH) (see Table 1). In Table 1, d_l and d_m are the calculated exact etch depths from Eq. 1 that are required to obtain Φ_1 and Φ_2 for various integers l and m. We observe from Table 1 that by choosing a single value for each etch depth will introduce approximation errors of less than about 6% for all cases. This error can be further reduced by taking the value d as the weighted average of d_l and d_m instead of one half of the summation. Other optimizations such as choosing a different set of phase quantization bases may also reduce the approximation errors. Furthermore, because the absolute phase in diffractive optics is of no concern, we can remove an etch depth bias of 1.013 μm (see Table 1) without affecting the desired relative phase values between different pixels. Therefore, only two distinct etches are needed to construct a binary phase level SSBCGH (s and t in Table 1).

For experimental demonstration and characterizations of such a SSBCGH, we constructed a diffractive polarization beam splitter that diffracts one polarization while transmitting the other. This is a special case of the dual functionality element that requires a single value of etch depth. The desired diffractive structure was defined and transferred by electron beam and photo-lithographic processes, and then the element was ion beam etched to 1.032 μm. The duty ratio of the fabricated SSBCGH element was measured to be 1:1. The experimental evaluation of the element shows 70.8% diffraction efficiency and 79.7:1 polarization contrast ratio (PCR) into the zero order, 37.4% diffraction efficiency and 33:1 PCR into the +1st order and, 38.9% diffraction efficiency and 32.5:1 PCR into the -1st order.

To better understand the fabrication accuracy requirements and their effect on the performance of the fabricated SSBCGH elements we used rigorous coupled wave analysis (RCWA)[5] to simulate the performances of our fabricated element. Fig. 2 shows the simulation results for diffraction efficiencies and PCRs as functions of etch depth for grating with 1:1 duty ratio and vertical side-walls. From the simulation results, we can observe that, the good performance (>40% diffraction efficiency and over 100:1 PCR) can be obtained, which is close to our geometrical optics design. The experimental performance of the fabricated element is very close to that predicted by the RCWA (see Fig. 2). From the simulation, we can also see that the performance of a SSBCGH can be further improved with more accurate etch depth. Also, the RCWA results show that the etch depths for the best PCR and the largest diffraction efficiency are very similar but not identical. This important result implies that the desired etch depth can be driven by the application needs and may slightly differ from the values provided by the geometrical optics approximate design listed in Table 1.

Using the same approach, we also demonstrated a wavelength selective element for operation as a color selective beamsplitter for wavelengths of 1.30 μm and 1.55 μm. The substrate material is BK7 glass. The indices of refraction of BK7 were specified by the supplier (Newport Optical Materials Inc.) to be 1.5027 at 1.30 μm, and 1.5004 at 1.55 μm. Using Eq. 1, the phase delay for a 7.75 μm deep etch is 5.994π at 1.3 μm and 5.004π at 1.55 μm. This set of values provides the necessary phase delay for a simple wavelength beam splitter that transmits 1.3 μm light field and deflects 1.55 μm light field. The element was etched to 7.9 μm using chemically assisted ion beam etching method with CHF_3 as the reactive gas.

Figure 3 shows the measured diffraction efficiency and the location of each of the first four orders for the fabricated element. A perfectly fabricated binary phase hologram, neglecting Fresnel reflection losses, should have no energy in the even orders, 40.5% in the +/- 1st orders, and 4.5% in the +/- 3rd orders. At 1.55 μm, the diffraction efficiencies of the fabricated element matched these numbers closely, with 39% in each of the first orders, 3.6% in each of the +/- 3rd orders, and a zero order transmission of 0.83%. At 1.3 μm, the transmission was 83%, while the diffraction into any of the orders was less than 1.2%.

A MOD hologram is more sensitive to changes in the illumination angle than a conventional DOE because of the increased optical path differences. We tested the effect of tilting the element, and found that the performance (first order diffraction efficiency at 1.55 μm and zero order transmission at 1.3 μm) changed by less than 2% for a 5° tilt, and less than 10% for a 10° tilt. In fact, the overall performance was slightly improved with a 5° tilt, suggesting that the etch depth should be increased to 7.93 μm to optimize performance. A field angle of 10° indicates that these elements are compatible with F/3 and larger optics.

In conclusions, we have demonstrated multiple order delay holograms with dual impulse responses in polarization or color. The experimental results indicate good performances. Such elements may be useful in image processing, optoelectronic packaging and photonic switching.

Authors thank P.C. Sun and K. Urquhart for helpful discussions. The research conducted at UCSD is funded by National Science Foundation, Air Force Rome Laboratory and AFOSR.

References:

1 J. Ford, F. Xu, K. Urquhart, and Y. Fainman, Opt. Letts., **18**:456, (1993).
2 F. Xu, J. Ford, and Y. Fainman, Appl. Opt., **34**:256, (1995).
3 S. Liu and Y. Chen, Opt. Lett., **20**:1832, (1995).
4 I. Richter, P. Sun, F. Xu, and Y. Fainman, Appl. Opt., **34**:2921, (1995).
5 M. G. Moharam, T. K. Gaylord, JOSA, **72**:1385, (1982).

		d_l, d_m	$d = (d_l + d_m)/2$	$d_r = d - 1.013$	error (%)	
Φ_o, Φ_e	l, m	(μm)	(μm)	(μm)	δ_l/Φ_o*	δ_m/Φ_e*
0, 0	4, 5	2.010, 2.042	2.0260	1.0130 (= s)	+3.27	-3.9
0, π	2, 2	1.005, 1.021	1.0130	0.0000	+1.63	-3.8
π, 0	2, 3	1.256, 1.225	1.2406	0.2276 (= t)	-6.1	+3.8
π, π	4, 5	2.261, 2.246	2.2535	1.2405 (= s+t)	-2.9	+3.8

Table 1 Design results and the real etch depth required for a binary phase single substrate BCGH. (* When Φ_o and/or Φ_e are zero, they are taken to be 2π for errors evaluations.)

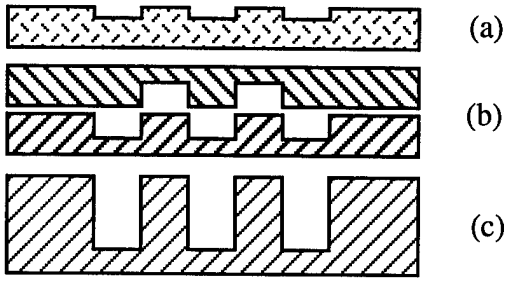


Figure 1. (a) conventional DOE, (b) two-substrate BCGH and (c) multiple order delay DOE.

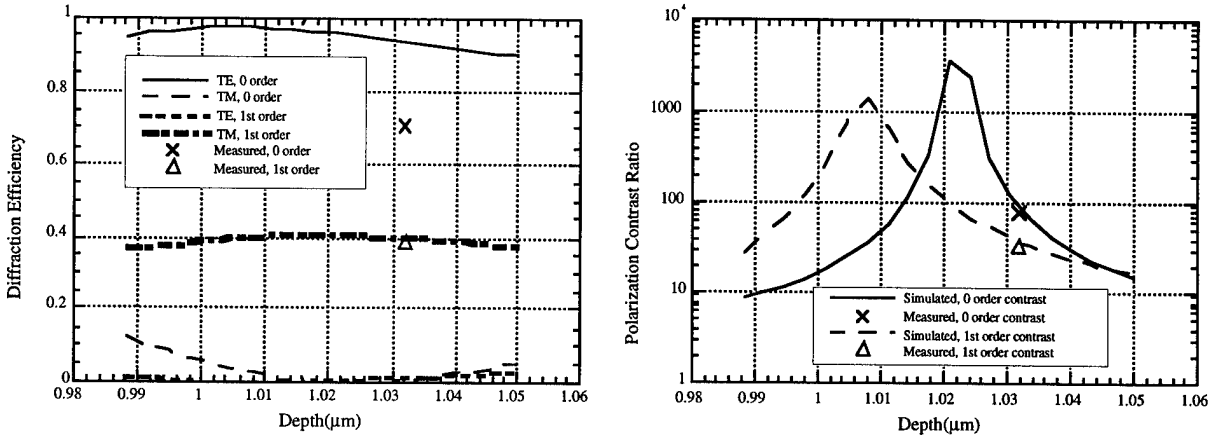


Figure 2. Simulated (curves) and measured (data points) performances of the SSBCGH

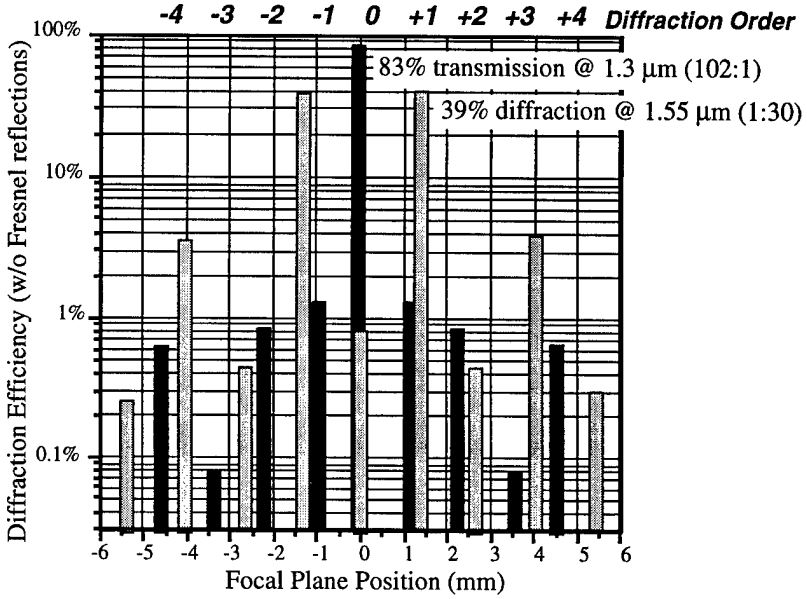


Figure 3. Intensity at diffraction peaks for 1.3 μm (solid) and 1.55 μm (shaded) illumination.

Focusing Waveguide Grating Coupler Using Diffractive Doublet

Stephen Sheard, Tingdi Liao and Guoguang Yang
Department of Engineering Science, University of Oxford
Parks Road, Oxford, OX1 3PJ UK
Telephone : +44 1865 273929; Fax : +44 1865 273905.

Philip Prewett and Jianguo Zhu
Central Microstructure Facility, Rutherford Appleton Laboratory
Chilton, Didcot, Oxon, OX11 0QX, UK
Telephone : +44 1235 821900; Fax : +44 1235 445706.

INTRODUCTION

A focusing waveguide grating coupler (FWGC)[1] implements simultaneously two optical functions. One is to couple out the guided–wave propagating in the waveguide structure; the other is to focus the outgoing beam into a small spot. Although combining two optical functions into a single diffractive optical element is quite attractive, the submicron feature sizes necessary to implement high–numerical–aperture focusing elements impose a significant burden on the lithography. Therefore, focusing waveguide grating couplers with high numerical aperture (NA> 0.25) have been rarely reported[2]. Furthermore, fabrication of such FWGCs usually relies upon direct–write electron beam lithography.

Waveguide grating couplers have been intensively and widely investigated[3–6]. Such uniform gratings can be defined using simple two beam optical interference methods, even though the grating pitch is of submicron order. On the other hand, Fresnel lenses have been successfully used as focusing elements and the fabrication of Fresnel lenses with various numerical apertures can be made by conventional photolithography. In principle, a focusing grating coupler can be realized by using a waveguide grating coupler to couple out the guided–wave into the superstrate (cladding), and then a Fresnel lens to focus the outgoing beam into a spot in the air. It is import that these two diffractive elements should be sufficiently physically separated in the vertical direction so that they manipulate the guided–wave and outgoing beam independently. The resulting "diffractive doublet" is therefore optically equivalent to the single–element FWGC described previously. However, so far to our knowledge, no investigation has been reported on this composite FWGC when considered as a single integrated element. In this paper, the design procedure and fabrication technology of this composite FWGC is presented.

FWGC DESIGN

As described above, the output coupling characteristics of the composite FWGC are determined by the waveguide grating coupler, and the focusing function by the integrated Fresnel lens. Due to their physical separation, the designs of the waveguide grating coupler and the Fresnel lens

can be discussed independently. The device structure is illustrated in Fig.1, which is based on the planar silica waveguide structure developed under the "SOPHI" project funded by EPSRC and the Department of Trade and Industry UK.

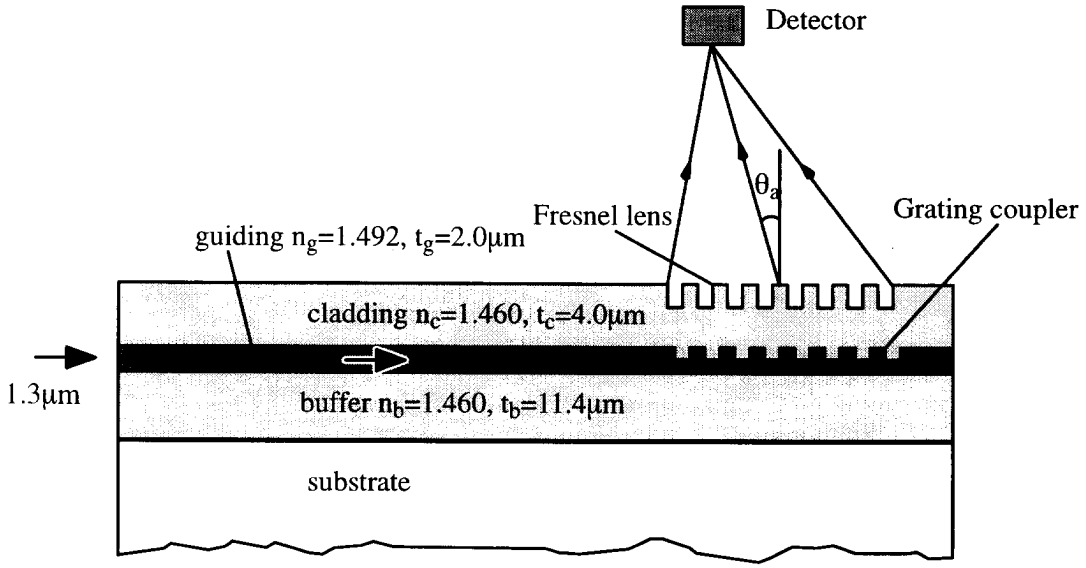


Fig. 1: A composite focusing waveguide grating coupler comprising of a uniform grating coupler and a Fresnel lens.

Grating coupler : A grating coupler with rectangular grooves was designed based on the silica waveguide structure comprising of arseno–silicate glass (ASG) and a SiO_2 buffer layer. To obtain the desirable condition that only a single radiation beam into the cladding is produced by the grating, the pitch of the grating coupler must satisfy

$$\frac{\lambda}{N_e + n_c} < \Lambda < \frac{2\lambda}{N_e + n_s} \tag{1}$$

where n_b and n_c are the index of buffer layer and cladding film, respectively. N_e is the effective index of guided mode (TE_0). The condition $\Lambda \neq \lambda/N_e$ must also be satisfied in order to eliminate Bragg reflection. In our design, the grating pitch is chosen to be 0.80μm such that only a single diffraction beam radiates into the cladding at an angle of $\theta_a = -8.40°$ in the air. The grating etched depth t_g is determined to be 0.20μm, which yields a radiation decay factor of $\alpha = 0.39 cm^{-1}$ and a radiation directionality of 50%[5].

Usually, the thickness of the buffer layer and cladding layer are determined according to the requirements of the waveguide mode profile. Here, the thickness should also be determined so that the Fresnel lens is physically separated from the waveguide grating coupler. Based on the electric field distribution of the optical waveguide mode structure, a cladding film thickness greater than 4.0μm is sufficient to allow independent performance of these two diffractive optical elements. Furthermore, this separation of 4.0μm compared with the aperture size of the Fresnel lens (1.0 ~ 2.0mm), allows us to consider that these two elements are geometrically coplanar.

Fresnel lens : As a diffractive optical element, the Fresnel lens consists of a series of concentric annuli or zones. The phase difference between two successive zones is π. The different dif-

fraction orders of this Fresnel zone plate give rise to a series of both positive and negative focal length. For a normally incident plane wave, the radius of the m–th ring is simply determined by

$$r_m^2 = m\lambda f + (m\lambda/2)^2 \tag{2}$$

with the first–order focal length $f=r_1^2/\lambda$ and the minimum feature size (or ring width)

$$\delta = \frac{\lambda}{D/f} = \frac{0.5\lambda}{NA} \tag{3}$$

where $NA \doteq 0.5D/f$. It is noted that δ is approximately equal to the diffraction–limited focusing spot size (FWHM) for a lens with numerical aperture NA. From (3) it is seen that high numerical aperture, i.e., up to 0.5, can be achieved by using conventional photolithography with one micron resolution. The Fresnel lens can be analytically calculated using Eq.(2) and then a standard photolithographic mask can be used to fabricate the Fresnel lens.

FABRICATION

The fabrication of this composite FWGC, consisting of a grating coupler and a Fresnel lens, are addressed independently in the following.

Fabrication of grating coupler : Shipley S1400–17 positive photoresist mixed with 3–5% (by weight) imidazole[11] is spin–coated upon the waveguide surface at 4000rpm for 30 seconds, resulting in 0.46μm thick resist film, and then soft–baked for 5 minutes at 90°C. A two beam interference method is used to expose the resist mixture to produce a grating with pitch of 0.80μm. Following this exposure, a grating window of $2.0 \times 2.0mm^2$ is defined over the exposed grating regions using a mask aligner and a photolithographic mask with the required window pattern and registration features. The defined resist grating pattern is then baked at 100–110°C for 50 minutes, followed by a further UV flood exposure. After development, a resist grating with a slight undercut resist profile is obtained. Finally, the hardened resist pattern is used as an etching mask, and the grating pattern is transferred into the guiding layer by reactive ion etching using a CF_4 plasma.

Fabrication of Fresnel lens : a cladding film of SiO_2 is sputter–deposited on top of the fabricated waveguiding grating surface. The process should be monitored to ensure that the grating grooves are adequately filled by the cladding film. The deposited film thickness is expected to be about 4.0μm. The Fresnel lens is patterned on top of the SiO_2 cladding layer by conventional photolithography. Once again, the resist pattern is used as an etch mask and reactive ion etching is then used to transfer the binary Fresnel lens pattern approximately 0.40μm deep into the SiO_2 film using a CHF_3 plasma.

FABRICATION RESULTS

The focusing performance of the fabricated composite FWGC is evaluated using a spot size measurement, in which the focusing spot is magnified by a 20× microscope objective. The corresponding CCD image and intensity profiles of the focused spot are shown in Fig.2 and Fig.3. The measured spot size (FWHM) is 4.98μm, while the theoretically determined diffraction–lim-

ited spot size is 1.72μm. The broadening of the focusing spot size may arise from fabrication and alignment errors. There exists astigmatism in the focused spot due to the cylindrical wavefront propagation in the planar waveguide and the oblique incident beam on the Fresnel lens plane.

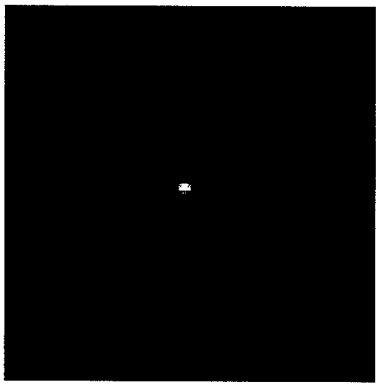


Fig.2: The CCD image of the focused spot produced by the composite focusing waveguide grating coupler.

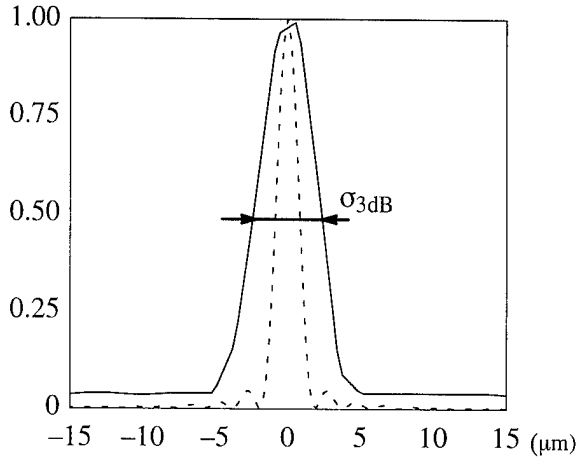


Fig.3: Normalized intensity distribution of focused spot produced by the fabricated FWGC. The focused spot size (FWHM) is determined to be 4.98μm. The broken curve corresponds to the theoretical diffraction–limited intensity.

CONCLUSIONS

A novel focusing waveguide grating coupler consisting of a grating coupler and a Fresnel lens has been successfully fabricated. Although diffraction–limited focusing performance has not been achieved in this device, it is significant to note that the fabrication procedure offers considerable advantages when compared with conventional FWGC fabrication using direct–write electron beam lithography. Fabrication of this device is compatible with microlithography technology and therefore fabrication cost can be reduced. High numerical aperture is achievable with a compact planar structure. A near vertical output focusing beam can be obtained when the pitch of the grating coupler satisfies $\Lambda \approx \lambda / N_e$. In addition, higher diffraction efficiency could be possible by using high efficiency grating couplers and a four–level binary phase Fresnel lens. It is expected that this novel device will find potential applications in integrated optoelectronic systems.

REFERENCES

1. S. Ura, T Suhara, and H Nishihara et al, J of Lightwave Techno., vol. LT–4, 913–917, 1986.
2. I Kawakubo, J Funazaki, and K Shirane et al, Appl. Opt., vol.33, 6855 –6859, 1994.
3. T Tamir and S T Peng, Appl. Physics, vol.14, 235–254, 1977.
4. W Streifer, D R Scifres, and R D Burnham, IEEE J QE–12, 422–428, 1976.
5. M Li and S J Sheard, Opt. Commun., vol.109, 239–245, 1994.
6. R L Roncone, Lifeng Li, and K A Bates et al, Appl. Opt., vol.32, 4522–4528, 1993.
7. H Moritz, IEEE Trans., vol.ED–32, 672–676, 1985.

Imaging in planar optics: system design for oblique deflection angles

Markus Testorf and Jürgen Jahns
FernUniversität Hagen, LG ONT, Elberfelderstr. 95, 58084 Hagen, Germany,
Fax.: +49-2331-332904, e-mail: markus.testorf@fernuni-hagen.de

I. Introduction

Planar optics has been successfully demonstrated to be useful for the integration of free space optical systems[1]. In this context, planar integration means the arrangement of optical elements on the surface of a thick transparent substrate. The light signal travels within the substrate along a folded zig-zag path, reflected at its surfaces. Since planar optics was first proposed, various applications has been demonstrated like array generation[2] or imaging[3].

One inherent property of planar optical systems is the off axis light propagation with respect to planes in which optical elements are located. On the one hand, off-axis propagation is a constraint of planar optics in order to separate input and output signals spatially, which are both located in the same plane. On the other hand, for separating input and output the angle of light propagation can be chosen arbitrarily within a wide range. Therefore, it can be treated as a design parameter which has to be determined from further constraints. In this paper we consider the design of planar optical imaging systems. We ask the question in which way imaging properties depend on the choice of the deflection angle.

II. First order optical systems

We start our considerations with the system presented in Fig. 1 and 2. The whole system consists of three parts: free space, lens and free space.

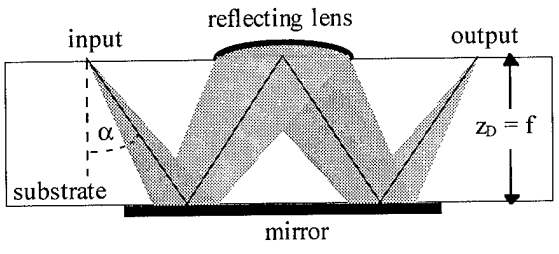


Fig. 1: Planar optical imaging system.

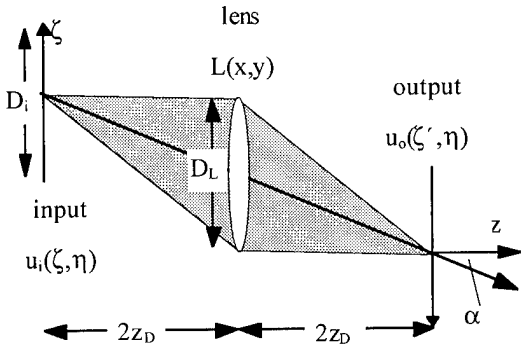


Fig. 2: Unfolded off-axis system.

Light propagation can be described as a convolution of the initial wave front $u_i(\zeta,\eta)$ with the point spread function of free space, h(x,y,z). Small diffraction angles and large propagation distances are assumed for first order optics[4]. For off-axis light propagation, h(x,y,z) becomes

$$h(x,y,z) = -\frac{\cos(\alpha)}{i\lambda z}\exp\left[ik\frac{z}{\cos(\alpha)} + ik\sin(\alpha)x\right]\exp\left[\frac{i\pi}{\lambda z}\left(\cos^3(\alpha)x^2 + \cos(\alpha)y^2\right)\right] \quad (1)$$

where α is the propagation angle due to the normal of the optical elements. The substitution $x = \zeta - z\cdot\tan(\alpha)$ compensates the overall lateral shift due to off-axis propagation. From Eq. (1) the transmission function L(x,y) of an ideal parabolic lens can be determined as[5]

$$L(x,y) = \exp\left[-\frac{i\pi}{\lambda f}\left(\cos^3(\alpha)x^2 + \cos(\alpha)y^2\right)\right] \quad (2)$$

Within the parabolic approximation L(x,y), in Eq. (2), can be regarded a perfect lens for collimating and imaging, analogous to the on-axis case[4], obtained for α=0.

III. Space-Bandwidth Product

For systems without aberrations, the angle α determines the space-bandwidth product of the system, i.e. the number of pixels N_p in the input that can be handled. N_p can be determined as the ratio of the input area $D_i \times D_i$ (Fig. 2) and the area of the point spread function d_{PSF} of the imaging system. From Eqs. (1) and (2) we can estimate d_{PSF} in x and y direction

$$d_{PSF} = d_{PSF,x} \times d_{PSF,y} \quad \text{where } d_{PSF,x} = \frac{2\lambda f}{D_L\cos^3(\alpha)} \quad \text{and } d_{PSF,y} = \frac{2\lambda f}{D_L\cos(\alpha)}. \quad (3)$$

Although we assume a quadratic lens aperture of width D_L, the resolution cell is rectangular. If z_D is the thickness of the glass substrate, a maximum N_P can be obtained for the case $D_L = D_i = 2z_D\tan(\alpha)$ which yields to

$$N_p = 4\frac{z_D^2}{\lambda^2}\sin^4(\alpha) \quad (4)$$

That means, a large space-bandwidth product can be achived with large angles α and thick substrates according to the parabolic approximation. Interestingly, for the one-dimensional case, where only the number of lines in x direction is considered, one finds

$$N_{p,x} = 2\frac{z_D}{\lambda}\sin^2(\alpha)\cos(\alpha) \quad (5)$$

which shows a maximum value for $\alpha = \arcsin\left(\sqrt{2/3}\right) \approx 55°$.

IV. Higher flexibility from additional elements

In order to provide additional freedom for the design of an imaging system we introduce three additional deflection elements (prism or diffraction grating) to allow individual propagation angles α_1-α_4 for every piece of free space[6] (Fig. 3). This additional freedom can be used e.g. to image with arbitrary magnification. We assume $\alpha_1=\alpha_2\neq\alpha_3=\alpha_4$, which means ordinary reflection at element P_1 and element P_3. With $P_2(x,y)=\exp\left[2\pi i\, x \sin(\alpha_3-\alpha_1)/\lambda\right]$ the ideal lens becomes, according to Eq. (2):

$$L(x,y) = \exp\left[-\frac{i\pi}{2\lambda f}\left(\left(\cos^3(\alpha_1)+\cos^3(\alpha_3)\right)x^2+\left(\cos(\alpha_1)+\cos(\alpha_3)\right)y^2\right)\right] \tag{6}$$

For the magnification M_x and M_y in x and y direction, respectively, we obtain

$$M_x = \frac{\cos^3(\alpha_3)}{\cos^3(\alpha_1)} \quad \text{and} \quad M_y = \frac{\cos(\alpha_3)}{\cos(\alpha_1)} \tag{7}$$

We can achieve equal magnification $M_x=M_y$ in both lateral coordinates by placing elements P_1 and P_3 (Fig. 3 and 4) at the bottom side of the substrate with

$$P_1(x,y)=\exp\left[i\frac{2\pi}{\lambda}\sin(\alpha_1)(-x+y)\right] \quad \text{and} \quad P_3(x,y)=\exp\left[i\frac{2\pi}{\lambda}\sin(\alpha_3)(x-y)\right] \tag{8}$$

These gratings rotate the propagation direction from the x-z plane to the y-z plane and vice versa at half the propagation distance before and behind the lens, respectively. This guarantees a symmetrical setup with respect to both lateral coordinates including equal magnification.

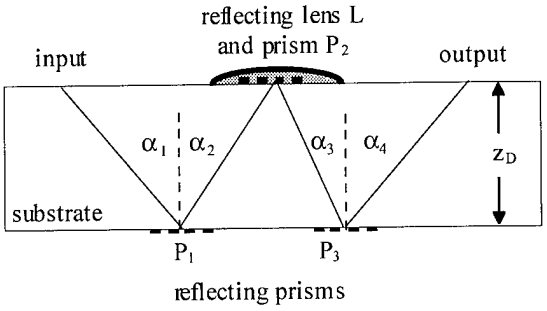


Fig. 3: Planar optical system including additional deflection prisms.

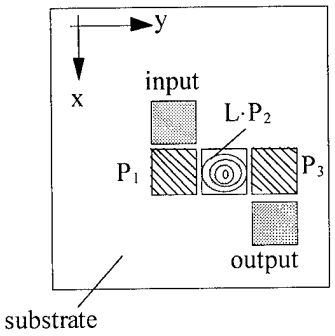


Fig. 4: Top view of planar imaging system, symmetric in x and y.

The additional prisms give access to arbitrary propagation angles. Besides matching of magnification factors, this method can be used whenever asymmetries due to off-axis free space propagation have to be compensated, e.g. to obtain a quadratic area for the point spread function in Eq. (3).

V. Wave aberrations

Now we consider wave aberrations describing imaging properties beyond first order optics. Again we consider the planar optical system in Fig. 1 and 2. We assume perfect imaging for $\zeta=\eta=\zeta'=\eta'=0$. For all other object points ζ, η we find wave aberrations at the plane of the lens. To demonstrate the aberration's influence, we restrict our discussion to astigmatism and defocusing in one dimension, i.e. $\zeta=y=0$. From a Taylor expansion of the point spread function of free space we calculate the phase of the aberrations $(2\pi/\lambda)\cdot W_{ab}(x)$:

$$W_{ab}(x) = -\frac{3\zeta x^2}{z_D^2}\cos^4(\alpha)\sin(\alpha) - \frac{3\zeta^2 x^2}{2z_D^3}\cos^5(\alpha)\left[\cos^2(\alpha) - 4\sin^2(\alpha)\right] \tag{9}$$

We note, that Eq. (9) contains terms which do not occur for on-axis imaging $\alpha=0$. As one application we estimate the maximum space-bandwidth product from the term linear in ζ which dominates W_{ab} even for moderate angles α. If we only tolerate wave aberrations smaller than $\lambda/4$ we can use Eq. (3) to get

$$N_{p,x} < \sqrt{\frac{D_i}{6\lambda}\frac{\cos(\alpha)}{\tan(\alpha)}} \tag{10}$$

As an example we obtain for $\lambda=0.5$, $\alpha=20^o$ and $D_i=500\mu m$, a value $N_{p,x}=20$, which is certainly more realistic than values obtained by Eq. (5).

VI. Conclusion

We demonstrated in which way the oblique propagation angle of light signals in planar optical systems can be used for the design of imaging systems. As typical examples, we showed that the propagation angle can be chosen to

- optimize the space bandwidth product of the imaging system.
- design imaging systems with arbitrary magnification.
- influence imaging properties due to wave aberrations.

References

1. J. Jahns and A. Huang, "Planar integration of free space optical components," Appl. Opt. **28**, 1602 (1989).
2. M. M. Downs and J. Jahns, "Integrated optical array generation," Opt. Lett. 15, 769 (1990).
3. J. Jahns and J. S. Walker, "Imaging with planar optical systems," Opt. Comm. **76**(5,6), 313 (1990).
4. J. Goodman, Introduction to Fourier optics, (McGraw Hill, New York 1968).
5. S. Reinhorn, S. Gorodeisky, A. A. Friesem, and Y. Amitai, "Fourier transformation with a planar holographic doublet," Opt. Lett. **20**, 495 (1995).
6. Z. Zhou and T. Drabik, "Coplanar refraktive-diffractive doublets for optoelectronic integrated systems," Appl. Opt. 34, 3048 (1995)

Diffractive Optics in an Ultraviolet Satellite Attitude Sensor

T. A. Fritz
Honeywell Military Aviation
2600 Ridgway Parkway
Minneapolis, MN 55413

D. B. Pledger
T. R. Werner
Honeywell Technology Center
3660 Technology Drive MN65-2500
Minneapolis, MN 55418

Honeywell's Earth Reference Attitude Determination Sensor (ERADS) is a wide field of view ultraviolet imaging sensor for satellite attitude determination. The sensor was designed for small satellite applications[1], where size, weight, and cost are the primary drivers. Use of the ultraviolet region of the spectrum provides a unique capability to simultaneously image stars, Earth's limb (day or night), and other celestial objects, and to tolerate the sun in the field of view. This is because the solar output is lower relative to the other objects of interest in this waveband, and eliminates the need for expensive and cumbersome sun shields. The field of view consists of a 10° annular region at 71° from axis, and a 10 degree center field. Higher accuracy attitude information is obtained from measurements of stellar location. The accuracy with which these measurements can be made is limited by the number of pixels on the focal plane, the blur spot dimensions, and the photon count rates. The detector array of the sensor was a megapixel CCD. The field of view of the sensor was effectively increased by making use of an array of six folding

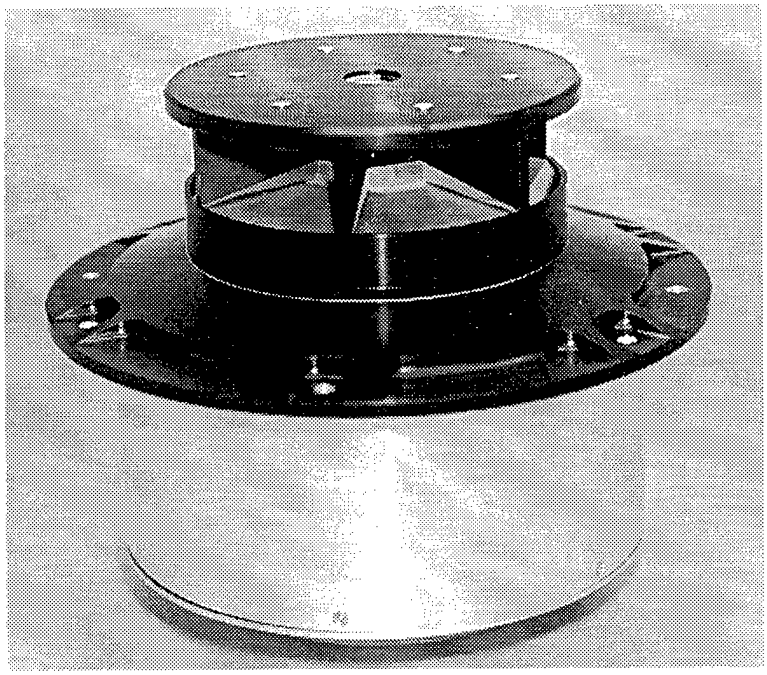


Fig. 1. ERADS wide angle ultraviolet sensor assembly (lower canister diameter = 6.5 in.)

mirrors, and the field remapping effectively increased the pixel density in the area of interest.The optimal blur diameter for the centroiding algorithms proved to be the width of three pixels, if a photon rate of 50 per star for fourth magnitude stars could be maintained.

The photon rate was ultimately limited by the diameter of the aperture stop of the spherical lens and the spectral bandwidth. With a limited choice of UV materials, we could obtain only a 200 Å bandwidth and a 59 square mm aperture, which corresponds to a 10 mm entrance aperture at the center field angle, while holding the required blur diameter. This left us roughly a factor of two short of the required photon count. The conventional approach to increasing the photon rate is to add concentric spherical elements around the lens of different glass than the core, which reduces aberration and allows for a larger aperture. This conflicts with the basic cost/size/weight objectives of the program. The addition of the required elements would have increased the cost and complexity of the system beyond feasibility. In order to resolve this situation, a highly non-conventional approach was taken which allowed all performance objectives to be met.

BASELINE OPTICAL DESIGN

The first generation ERADS sensor used a simple sapphire ball lens with the aperture stop at the center of the lens, which covers the very large field of view (132° - 152°). All refractive surfaces are concentric to the stop, so the only Seidel 3rd order aberrations present are spherical aberration and Petzval curvature. The limiting aberration is spherical aberration, and it is minimized by using a glass with a high index of refraction. Sapphire was chosen, which has an (ordinary) index of refraction of 1.8244 at 280 nm. The spherical aberration can be further reduced by adding meniscus lenses of different glass, whose radii are concentric to the aperture stop, but we preferred to minimize the number of elements. A curved image surface matches the Petzval curvature and the curvature on a fiber optic field flattener. Since coherent bundles of UV-transmitting fiber are not available at this time, the image surface has an acrylic coating with laser dyes to convert the photons from the UV band to visible light for transmission through the fiber bundle. This fiber bundle is the input faceplate for an image intensifier tube, which transfers the image to a million-pixel CCD array.

Because of the obliquity of the wavefront at the aperture stop, the effective aperture at extreme angles is greatly reduced, and there are higher order aberrations present. Also, the mapping from a nearly hemispherical image surface to a flat one greatly increases the footprint of the detector pixel at extreme angles. Therefore, a reflective mirror array is used in front to map the extreme field into a more moderate field of view. This reduces the effects of oblique spherical aberration and distortion of pixels. Six to eight facets are preferred over a continuous mirror (which would be a portion of an axicon) because they don't affect the wavefront, except for some image mapping distortion. Because the attitude determination sensor only needs to view the limb, which is an annular region in object space, the mapping distortion away from the center of these mirror facets is not detrimental to the overall function of the sensor.

BENEFIT OF DIFFRACTIVE OPTICS

The second-generation ERADS sensor (see Figure 1), which is designed for satellite flight, increases the signal energy. A larger ball format is used, and the larger image format of ITT's

Gen III image intensifier. The spherical aberration is reduced dramatically by splitting the ball lens in two and etching a rotationally symmetric diffractive optical element into one flat surface at the stop. By correcting spherical aberration and longitudinal color, we are able to increase the aperture size by a factor of 1.3, double the waveband, and still maintain the same spot size. This yields an increase of greater than three times the energy for the same size ball lens, with only about 10-15% energy loss from using a diffractive optical surface over a wide field of view. The diffractive optical correction also gives performance superior to the conventional solution of adding concentric shells of different optical materials. The diffractive optical surface gains leverage in color correction because of the extremely low number of material choices. Because of the large angle of incidence at the stop for large field angles, optical cement is required in the aperture stop to prevent total internal reflection (TIR) at the sapphire-air interface.

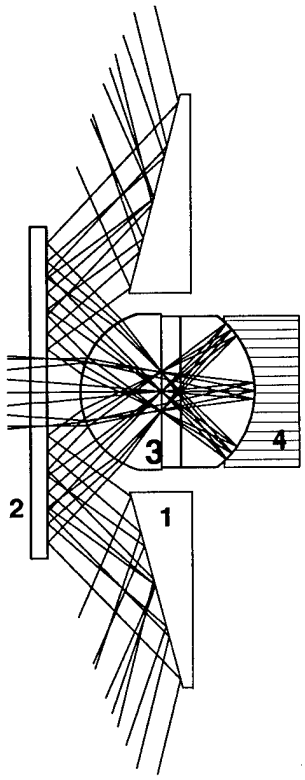


Figure 2. Raytrace of ERADS system, showing annular and on-axis imagery.
1. hexagonal mirror array
2. fused silica window with UV-reflective coating
3. ball assembly
4. fiber optic field flattener

An advantage of the diffractive optic at the stop location is that energy from extra orders of the diffractive optic are undeviated. The spot size increases, but the extra orders are located right on top of the desired first order. This slight change in spot size has no effect on the centroiding algorithms of the sensor.

DOE FABRICATION

The diffractive optic was fabricated on a 1.5 in. diameter sapphire substrate of 0.138 in. thickness, after which the outer diameter of the substrate was ground down to 1.161 in. diameter. A 0.6 micron layer of aluminum was then deposited onto the entire diffractive optical surface

except for a 7.00 mm diameter center portion where the diffractive optical pattern was fabricated, and this opaque annulus defined the aperture stop for the system. This element was then cemented on both sides in between two separate hemispherical sapphire ball lenses with UV-transmitting cement. The diffractive optical pattern had 41 zones with eight steps per zone using the binary optics approach of three mask levels and two alignments, and three separate etches of depths 961 Å, 1921 Å, and 3842 Å, which reflected the index of refraction difference between the sapphire optical elements (n=1.82) and the optical cement (n=1.46). Standard semiconductor processing was used to fabricate the eight-level binary optics and to fabricate the thin film metal aperture.

CONCLUSIONS

The diffractive optical element allowed a larger aperture and waveband than would be possible using all refractive elements for the sensor in a limited photon environment. A flight version of the optical system has been fabricated, assembled and integrated with the software package. ERADS was integrated with the University of Houston's Wake Shield satellite in May 1995. Attachment was made to one of the bottom supports, to achieve nadir pointing of the center aperture. Calibration imagery was obtained with an ultraviolet source inside the assembly facility after integration was complete. The Wake Shield facility was then moved into the cargo bay of the shuttle Endeavour to await the STS 69 launch. Several delays occurred, ultimately moving the launch back to August 30, 1995.

Objectives of the flight experiment were twofold: first, to determine whether the mechanical and optical designs were suitable for space operation; and second, to obtain imagery of all the objects which ERADS would observe during operation. This would include stars, the sun, Earth, Earth's limb under both night and sunlit conditions, and combinations of these. Of particular interest were the effects that direct sun exposure would have on the optical elements. To achieve these objectives, observations were made over four separate orbits during satellite free flight, each covering the complete range of solar illumination conditions. In addition, deep space observations were made for an hour while the Wake Shield was being moved across the bay prior to deployment. Very limited imagery was downloaded during the flight, and 200 megabytes was stored in a flash memory unit.

The flight experiment was completed as scheduled, and the sensor removed from the Wake Shield subsequent to landing. No optical or mechanical abnormalities were found. Post flight image analysis and calibration are scheduled for December. ERADS is currently scheduled to be included in the Wake Shield 3 mission at the end of 1996. This experiment would utilize the same hardware, and the use of real time algorithms to evaluate attitude determination ability.

REFERENCES

1. Billing-Ross, James, Teresa Fritz, Douglas Pledger, Ralph Castain, William Saylor, "Low cost ultraviolet solid state sensor system for the three axis attitude determination," in Advances in the Astronautical Sciences, Univelt Inc., Vol. 81 (1993), pp. 25-32.

Akhouayri, H. — DWC3
Amako, Jun — JTuB12
Amra, C. — DWC3
Andres, P. — JTuB7
Aoyama, Shigeru — DWB1
Arnold, Steven — DTuD1
Athale, Ravindra A. — DWB, DThA1

Bakker, Ben — JTuB25
Behrmann, Gregory P. — DWD2
Billman, Ake — DThA3
Bishop, K. P. — DWB3, DWC2
Blattner, P. — JTuB8
Blough, C. G. — DTuA5, DTuD3, DThA4
Boyd, R. D. — JMC3, JMC4, JTuB10
Boyd, Robert — JTuB23
Britten, J. A. — JMC3, JMC4, JTuB10
Broomfield, Seth — JTuC5
Brosig, Jill A. — JTuB24
Bryan, S. J. — JMC3
Bykovski, Val — JTuB25

Carson, R. F. — DMD2
Chen, E. Y. — DWB3, DWC2
Chen, Yansong — JTuB1A
Choe, Ok Shik — JTuB20, JTuB22
Chow, R. — JTuB10
Climent, V. — JTuB7
Cohn, Robert W. — DTuD4
Cox, J. Allen — DMA2, DTuA3
Crawford, M. Hagerott — DMD2

Dandliker, R. — DWB4
Daschner, Walter — DWD4
Davis, Christopher C. — DWD3
Dianyuan, Fan — JTuB3
Dixit, Sham — JTuB15, JTuB16
Dobson, David C. — DMA2
Dobson, Sarah L. — DTuA2
Dominic, Vincent — JTuC4
Dong, Bizhen — JTuB1A, JTuB1B, JTuB11
Du, T. C. — DMD2
Duignan, Michael T. — DWD2

Ehlert, R. — DMB2
Erdogan, Turan — DWA2
Esener, Sadik C. — DMD1

Fainman, Yeshayahu — DTuA2, DWA, DThB2
Falabella, S. — JMC3
Feit, Michael D. — JTuB6, JTuB10, JTuB15
Feldblum, Avi Y. — DMB1
Feldman, Michael — DWD
Feng, Dazeng — JTuB18, DTuD5
Fernandez, Salvador — JTuB23
Fernandez-Alonso, M. — JTuB7
Fiddy, M. A. — JTuB27
Fischer, George — JTuB23
Fleming, Madeleine B. — DThB1
Ford, Joseph E. — DThB2
Fritz, Bernard S. — DTuA3
Fritz, T. A. — DThB5
Fromer, Neil — DMB3

Gale, Michael T. -DWC5, DThA2, JTuC
Giovannini, H. — DWC3
Goncharenko, Andrey M. — JTuB2
Grot, Annette — DMD3
Grunwald, R. — DMB2
Gu, Benyuan — JTuB1A, JTuB1B, JTuB11

Hard, Sverker — DThA3
Heine, C. — DWC5
Herzig, Hans Peter — JMC5, JTuB8, DWB4, DWC
Hessler, Th. — DThA2
Hoch, John S. — DMD3
Holmer, Anna-Karin — DThA3
Honkanen, Marko — DWA3
Hou, H. — DMD2
Hutley, Michael C. — JMC1, DThA

Im, Yong Seok — JTuB21, JTuB22

Jacobsen, C. J. — DWD6
Jacobsson, Stellan — DThA3
Jahns, Jurgen — DMB, JTuB2, DThB4
Jin, Zhou — JTuB26
Johnson, Kristina M. — JTuC2
Jones, M. W. — JTuC3

Kaganovskii, Yu. — JMC2
Kahn, Joseph M. — DMD3
Kersten, Robert — JTuB23
Kettunen, Ville — DWA3
Keyworth, B. P. — DMD4
Khilo, Nikolay A. — JTuB2
Kilcoyne, S. P. — DMD2
Kim, Sang Cheol — JTuB21
Knapp, Wayne — DTuA5
Knight, Jr., P. Douglas — JTuB14
Kostuk, Raymond — JMC
Kowel, S. T. — JTuC3
Kuittinen, Markku — DTuD2
Kulick, J. H. — JTuC3
Kunz, R. E. — DThA2
Kurahashi, Tsuyoshi — DWB1
Kwak, Chong Hoon — JTuB20, JTuB22

Lalanne, Philippe — DMA4, JTuB19
Lancis, J. — JTuB7
Larochelle, Simon — DTuD5
Lawandy, N. M. — DMB3
Layet, Ben — DWA5
Lear, K. L. — DMD2
Lee, Sing H. — DWD4
Lee, Young Lak — JTuB21, JTuB22
Leger, James R. — DWB5, DWD1, DThB
Li, Dehua — JTuB1A
Li, Lifeng — DMA5, JTuB6, JTuB10, JTuB13
Li, Zhi-Yuan — JTuB11
Liao, Tingdi — DThB3
Liau, Z. L. — DMB4
Lightbody, Malcolm T. M. — DWA5
Lindell, Curt — DThA3
Lindlein, N. — DWC1
Lindquist, R. G. — JTuC3
Liu, Wenyao — DTuD4
Liu, Z. — DWA1
Loewen, Erwin G. — JTuC1
Long, Pin — DWD4
Loomis, G. — JTuB10
Lundbladh, Lars — DThA3

MacDonald, R. I. — DMD4
Mack, S. K. — DThA4
Magnusson, R. — DWA1
Mait, Joseph N. — DMA3, JTuB5, JTuB9, DTuD, DWD3
Makki, Siamak — DWB5
Malley, L. — JTuB27
Marchand, Philipe J. — DMD1
Maystre, D. — DTuD3
Mazzoni, David L. — DWD3
McCormick, Frederick B. — DMD1
McIntyre, Kevin J. — DTuA4, JTuB4
McMackin, L. — DWB3, DWC2
McMullin, J. N. — DMD4
Mersereau, Keith — DMB1, DMD
Michaels, Robert L. — DTuA5, DThA4
Mirotznik, Mark S. — DMA3
Missey, Mark J. — JTuC4
Moharam, M. G. — DMA
Morf, R. H. — DWC5
Morris, G. Michael — DMA4, DTuA4, JTuB, JTuB4, DWA2, DWA4 , JTuB, JTuB4
Morrison, Rick L. — DMD5

Neal, D. R. — DWC2
Neto, Luiz Goncalves — JTuB17
Neviere, M. — DMA1
Nguyen, H. T. — JMC3, JMC4, JTuB10
Nijander, Casimir R. — DMB1
Nikolajeff, Fredrik — DThA3
Noponen, Eero — DWA3
Nordin, G. P. — JTuC3

Norton, Scott M. — DWA2
Nussbaum, Ph. — DWB4

O'Shea, Donald C. — DWC4

Patzold, H. J. — DMB2
Pawlowski, Edgar — DThA5
Peng, Song — DWA4
Perry, M. D. — JMC3, JMC4, JTuB10, JTuB16
Pierson, R. E. — DWB3, DWC2
Piper, Eckhard — JMC5
Pledger, D. B. — DThB5
Pommet, D. A. — JTuB27
Popov, E. K. — DTuD3
Prather, Dennis W. — DMA3
Prewett, Philip — DThB3

Raguin, D. H. — DTuD3
Raj, Kannan — DThA1
Rajkumar, N. — DMD4
Rediker, Robert H. — DWD1
Rosenbluh, M. — JMC2
Rossi, M. — DTuD3, DThA4
Rushford, Mike — JTuB16

Saarikoski, Henri — DMB5
Saarinen, Jyrki — DMB5
Salminen, Olli — DWA3
Salmio, Risto-Pekka — DMB5
Schneider, R. P. — DMD2
Schwarzer, Heiko — DTuA1
Schwider, J. — DWC1
Seigal, P. K. — DMD2
Serati, Steven A. — JTuC2
Sharp, Gary D. — JTuC2
Sheard, Stephen — DThB3
Sheng, Yunlong — JTuB17, JTuB18, DTuD5
Shin, D. — DWA1
Shinohara, Masayuki — DWB1
Shoop, Barry L. — JTuB5
Shore, Bruce W. — JMC3, JMC4, JTuB6, JTuB10
Singer, Wolfgang — JMC5, DWB4
Smith, R. E. — DWD5
Smolyaninov, Igor I. — DWD3
Sonehara, Tomio — JTuB12
Spector, S. J. — DWD6
Stein, Robert — DWD4
Stern, Margaret B. — DWB2
Stockley, Jay E. — JTuC2
Suleski, Thomas J. — DWC4
Sun, Pang-chen — DTuA2
Suqing, Tan — JTuB26
Swanson, Gary J. — DWB2
Sweeney, Donald — DTuA

Taghizadeh, Mohammad R. — DWA5
Tajahuerce, E. — JTuB7
Tan, T. S. — DMD3
Tatian, Berge — DTuA5
Teichmann, H. — DThA2
Teng, Y. Y. — JTuB27
Tennant, D. M. — DWD6
Tervonen, Ari — DMB5
Testorf, Markus — JTuB2, DThB4
Thomas, Ian — JTuB16
Tibuleac, S. — DWA1
Townsend, Wesley P. — DMB1
Tsang, D. Z. — DMB4
Turunen, Jari — DMB5, DTuD2, DWA3
Tyan, Rong-Chung — DThB2

Uchida, Daidou — DWB1

Vahimaa, Pasi — DTuD2, DWA3
Vawter, G. A. — DMD2, DWD5
Volk, Brian — DTuA5
Volkel, R. — DWB4

Walpole, J. N. — DMB4
Wang, Ping — JTuC2
Wang, S. S. — DWA1
Wang, Xiaomei — DWD1
Wang, Y. J. — JTuB27
Wangler, Johannes — JMC5
Warren, M. E. — DMD2, DWD5
Watson, Edward A. — JTuC4
Weible, K. J. — JTuB8
Wendt, J. R. — DMD2, DWD5
Wenqi, Gao — JTuB26
Werner, T. R. — DThB5
Witzmann, H. H. — DMB2
Woggon, S. — DMB2
Wu, Chuck — DWD4
Wyrowski, Frank — DTuA1

Ximing, Deng — JTuB3
Xu, Fang — DThB2
Xuegong, Deng — JTuB3

Yamashita, Tsukasa — DWB1
Yang, Guoguang — JTuC5, DThB3
Yang, Guozhen — JTuB1A, JTuB1B, JTuB11
Yongpin, Li — JTuB3
Young, P. P. — DWA1
Yue, Qiu — JTuB3

Zhang, Guoqing — JTuB1A, JTuB1B, JTuB11
Zheng, Shihai — JTuB1A
Zhu, Jianguo — DThB3

DIFFRACTIVE OPTICS AND MICRO-OPTICS TECHNICAL PROGRAM COMMITTEE

M.G. Moharam, *University of Minnesota, General Chair*

Jurgen Jahns, *University of Hagen, Germany, Program Chair*

J. Allen Cox, *Honeywell Technology Center, Program Chair*

Bernard V. Braunecker, *Leica AG, Switzerland*

Dale Buralli, *Sinclair Optics*

Thomas K. Gaylord, *Georgia Institute of Technology*

Michael J. Hayford, *Optical Research Associates*

H. Peter Herzig, *University of Neuchatel, Switzerland*

Michael Hutely, *National Physics Laboratory, UK*

Raymond K. Kostuk, *University of Arizona*

James Leger, *University of Minnesota*

Joseph Mait, *Army Research Laboratories*

Keith O. Mersereau, *AT&T Bell Laboratories*

G. Michael Morris, *University of Rochester*

M. Oikawa, *Nippon Sheet Glass, Japan*